
Introducing Chirality into 1,3,4-Thiadiazole- and 1,3,4-Oxadiazole-Based Ligands for the Design of Iron(II) Spin-Crossover Complexes

Dissertation

zur Erlangung des akademischen Grades
„Doktor der Naturwissenschaften“
im Promotionsfach Chemie

*am Fachbereich Chemie, Pharmazie,
Geographie und Geowissenschaften
der Johannes Gutenberg-Universität Mainz*

Vorgelegt von

Jens-Georg Becker

geboren in Lahnstein

Mainz, 2025

Betreuerin: Prof. Eva Rentschler

Erste*r Gutacher*in: [REDACTED]

Zweite*r Gutacher*in: [REDACTED]

Nachnutzung unter der Lizenz: CC BY-ND 4.0

Tag der mündlichen Prüfung: 19.01.2026

Eidesstattliche Erklärung bzgl. der Nutzung von KI

Eidesstattliche Erklärung

Hiermit erkläre ich _____,

dass ich die vorliegende Arbeit mit dem Titel: **Introducing Chirality into 1,3,4-Thiadiazole- and 1,3,4-Oxadiazole-Based Ligands for the Design of Iron(II) Spin-Crossover Complexes**, selbstständig verfasst und keine anderen als die angegebenen Quellen und Hilfsmittel (dazu zählen auch KI-basierte Anwendungen oder Werkzeuge*) benutzt habe. Sämtliche wörtlichen oder sinngemäßen Übernahmen und Zitate sind kenntlich gemacht und nachgewiesen (dies gilt auch für Texte, die durch generative KI, wie Chat GPT erzeugt wurden). Ich versichere, dass ich keine Hilfsmittel verwendet habe, deren Nutzung die Prüferin oder der Prüfer explizit ausgeschlossen hat. Im Anhang „Nutzung KI-Tools“ habe ich die verwendeten KI-Tools dokumentiert. Mit Abgabe der vorliegenden Leistung übernehme ich die Verantwortung für das eingereichte Gesamtprodukt. Ich verantworte damit auch jegliche KI-generierten Inhalte, die ich in meine Arbeit übernommen habe. Die Richtigkeit übernommener (KI-generierter) Aussagen und Inhalte habe ich nach bestem Wissen und Gewissen geprüft. Mir ist bekannt, dass ein Verstoß gegen die genannten Punkte prüfungsrechtliche Konsequenzen hat und insbesondere dazu führen kann, dass die Promotionsleistung als mit „nicht bestanden“ bewertet wird. Die Einschreibung kann für bis zu zwei Jahre widerrufen werden, wenn Studierende zweimal oder häufiger bei Prüfungsleistungen täuschen (§ 69 Abs. 4 und 5 HochSchG).

_____ 13.11.2025 _____

Datum



Unterschrift

Danksagungen

In Erster Linie gilt mein Dank [REDACTED] für die Möglichkeiten, die ich während meiner Promotion hatte. Durch Sie habe ich die Chance gehabt mit lockereren Zügeln mich auszuprobieren, aber auch wieder auf Kurs zu finden.

Darüber hinaus danke ich [REDACTED] für die vielfältige Unterstützung. Seine Hilfe war maßgeblich verantwortlich für die zielgerechte Ausarbeitung meiner Ergebnisse. Ohne den Beitrag von [REDACTED], sowohl im Umgang mit defekten Geräten als auch am XRD, wäre die Arbeit nur halb so leicht von der Hand gegangen. Dafür verantwortlich waren auch meine Kollegen, mit denen ich das Privileg hatte zusammenzuarbeiten. [REDACTED] war immer mit einem guten Rat zur Stelle. Eine Mittagspause mit Diskussionsbeiträgen von [REDACTED] [REDACTED] und [REDACTED] werde ich genauso vermissen, wie wissenschaftliche Gespräche mit ihnen. Einen weiteren Dank muss ich an [REDACTED], für das Durcharbeiten meiner Dissertation und ihren direkten Beitrag zu meiner Arbeit während ihres Moduls, richten. Großer Dank gilt auch meinen Bachelorstudenten [REDACTED] und [REDACTED], für die großartige Arbeit. Zusätzlich möchte ich den weiteren Hiwis: [REDACTED] und [REDACTED] [REDACTED], für die wichtigen Beiträge danken. Für mich nicht zu vergessen sind [REDACTED] und [REDACTED] und ich bin sehr dankbar das Privileg zu haben, beide in ihrem ersten Lehrjahr zu begleiten. Auch den ehemaligen Mitarbeitern des Arbeitskreises danke ich für die Arbeit, auf die ich aufbauen konnte und eine Menge guter Ratschläge.

Fernerhin möchte ich [REDACTED], [REDACTED], [REDACTED], [REDACTED] [REDACTED] und [REDACTED] für die Mößbauer- und NIS-Experimente und den Beitrag zu den Publikationen danken. Überdies geht mein Dank auch an [REDACTED] für die vielen NMR-Experimente. Außerdem möchte ich mich für die Möglichkeit bedanken an dem [REDACTED] teilzuhaben.

Neben meinen Kollegen danke ich meiner Familie für ihre Unterstützung und Prägung, wodurch ich die Möglichkeit hatte diese Dissertation, trotz ADHS, zu schaffen. Einen großen Beitrag zu der Vervollständigung dieser Arbeit haben auch meine Freunde, die um so wichtiger sind, wenn man selbst nicht weiterweiß.

Der größte Dank geht an meine Freundin, Partnerin und Frau [REDACTED], welche zu den tiefsten Punkten zu mir stand und mit mir über jeden Berg und durch jedes Tal gewandert ist. Tausend Dank.

[REDACTED]

[REDACTED]

[REDACTED]

[REDACTED]

Kurzzusammenfassung

Die Forschung auf dem Gebiet der molekularen Schalter hat in den letzten Jahrzehnten großes Interesse erfahren, nicht zuletzt durch die Vergabe des Nobelpreises 2016 zum Thema molekulare Motoren basierend auf molekularen Schaltern. Dies ist auf die Möglichkeiten der Miniaturisierung von Datenspeicherung und Sensortechniken zurückzuführen. Spin-Crossover-(SCO)-Komplexe werden in diesem Zusammenhang intensiv untersucht, da ein Schalten zwischen dem High-Spin-Zustand (*HS*) und dem Low-Spin-Zustand (*LS*) durch den Einsatz externer Stimuli wie Temperatur, Druck und Licht möglich ist. Eisen(II) als d^6 -Ion ist für die Forschung an SCO-Komplexen besonders geeignet, da der Spin-Zustandswechsel zwischen dem Low-Spin-Zustand ($S = 0$) und dem High-Spin-Zustand ($S = 2$) erfolgt. Dieser Wechsel ist mit einer starken strukturellen Reorganisation und Änderung der Eigenschaften, beispielsweise der Absorption und dem magnetischen Moment, verbunden. Die molekulare Struktur der Liganden ist hierbei von großer Bedeutung, da die Koordinationsumgebung die SCO-Eigenschaften direkt beeinflusst. Das Einbringen von chiralen Bausteinen erweitert die Anwendungskonzepte, etwa durch ferroelektrische Eigenschaften und die Verwendung als chiroptischem Schalter.

Diese Arbeit untersucht den Zusammenhang zwischen dem Chalkogen im Kernbaustein des 1,3,4-Chalkogendiazol-Heterozyklus in asymmetrischen, mononuklearen Komplexen. Zudem wird der Einfluss des gewählten Arylsystems und der NCE ($E = S, Se$ und BH_3) Co-Liganden untersucht. Ebenso wird die Einbindung chiraler Bausteine als Substituenten durch gezielte Synthese erforscht.

Zunächst wird der Einfluss des Chalkogens und des NCE Co-Liganden ($E = S, Se, BH_3$) in den Komplexen $[Fe(L^{Ph-TDA})(NCE)_2]$ ($E = S, Se, BH_3$) untersucht, wobei für den NCS Co-Ligand das Auftreten von Spin-Zustandsordnung charakterisiert werden konnte. Darauf aufbauend wird das Einbringen von Chiralität durch die Substitution einer Methyl-Gruppe diskutiert. Hierbei konnte eine Korrelation zwischen dem Stereoisomer und dem thermischen SCO festgestellt werden. Darüber hinaus wird die Auswirkung einer Naphthylgruppe als Arylsystem untersucht, wobei eine Wechselwirkung zwischen Emission und Magnetisierung im Festkörper für $[Fe(L^{Naph-ODA})(NCBH_3)_2]$ beobachtet wurde. Das Einbringen einer Methyl-gruppe führt bei den Stereoisomeren überraschenderweise nicht zu abweichenden SCO-Eigenschaften. Der Einfluss der Koordinationsisomerie wird anhand der Solvatomeren von $[Fe(L^{Naph-TDA})(NCBH_3)_2]$ diskutiert. Abschließend dienen dinukleare Komplexe zur Untersuchung helikaler Motive, wobei der 1,3,4-Thiadiazol-basierter Komplex in Zusammenhang mit der Interkalation kleiner Gastmoleküle für supramolekulare Chemie analysiert wird.

Die hier synthetisiert und charakterisierten Komplexe zeigen ein ausgezeichnetes Beispiel der Korrelation zwischen gezieltem Ligandendesign und Einfluss auf die Struktur-Eigenschafts-Beziehung.

Abstract

Molecular switches have gained significant interest in recent decades due to their applications in bottom-up approaches for data storage and sensor miniaturization. Next to the organic molecular switches, which are known from molecular motors represented by Feringa et al., molecular switches based on 3d transition metals are often discussed in literature. Spin crossover (SCO) complexes are well-studied for their ability to switch between high-spin (HS) and low-spin (LS) states in response to external stimuli such as temperature, pressure or light - enabling access to distinct, switchable states. Coordination chemistry and organic synthesis allow precise modulation of spin state behaviour, including transition profiles and the characteristic temperature $T_{1/2}$. Iron(II), a d^6 ion, is particularly favoured for SCO research due to its spin transition between the diamagnetic LS state ($S = 0$) and the paramagnetic HS state ($S = 2$), which involves strong structural reorganization and property changes such as UV-Vis absorption and temperature-dependent magnetization. Ligand design is critical, as the coordination environment around iron(II) directly influences SCO properties. Introducing chirality - well-known for its importance in biochemical enantiosensitivity - can also open pathways to ferroelectric and chiroptical behaviour.

This work investigates the influence of chalcogen in asymmetric, mononuclear 1,3,4-chalcogendiazole-based complexes, the impact of modified π -systems, the role of NCE co-ligands ($E = S, Se, BH_3$) and the substituents resolving in chiral ligands. Additionally, ligand substitution via tailored organic synthesis and complexation reactions is explored, supported by various analytical methods.

Initially, the influence of the chalcogen and the NCE co-ligand ($E = S, Se, BH_3$) in the complexes $[Fe(L^{Ph-TDA})(NCE)_2]$ ($E = S, Se, BH_3$) is investigated, with spin-state ordering being characterized for the NCS co-ligand. Building upon this, the introduction of chirality through methyl-group substitution is discussed. A correlation between the stereoisomer and the thermal spin-crossover (SCO) behavior could be established. Furthermore, the effect of introducing a naphthyl group as an aryl system is examined, revealing an interaction between emission and thermal SCO in the solid state for $[Fe(L^{Naph-ODA})(NCBH_3)_2]$. Interestingly, the incorporation of a methyl group does not lead to significant differences in the SCO properties of the stereoisomers. The influence of coordination isomerism is discussed based on the solvatomers of $[Fe(L^{Naph-TDA})(NCBH_3)_2]$. Finally, dinuclear complexes are employed to investigate helical motifs, with a 1,3,4-thiadiazole-based complex being analyzed in the context of guest-molecule intercalation relevant to supramolecular chemistry.

The complexes synthesized and characterized in this work provide an excellent example of the correlation between rational ligand design and its impact on structure-property relationships.

Table of Contents

Eidesstattliche Erklärung bzgl. der Nutzung von KI	II
Danksagungen	IV
Kurzzusammenfassung	VI
Abstract	VIII
Table of Contents.....	1
List of abbreviations	8
Introduction.....	12
References:	14
Theory Background	16
Further external Stimuli for Spin crossover	23
Analytic approaches to analyse the Spin state Transition.....	26
Ligand design of chiral Spin crossover complexes.....	36
Manuscript: Combining Chirality and Spin Crossover: Design Strategy and Functionality	37
Abstract:.....	37
Introduction:.....	37
1. Bidentate Ligands of the Schiff Base Type	41
2. Tetradentate Ligands Featuring an Ethylenediamine Motif.....	46
3. Tridentate Ligands Incorporating a Pybox Motif.....	51
4. Additional Ligand Designs Beyond these Categories	58
Conclusion	59
Motivation	64
Outline of the Thesis	70
Chapter 1: Achiral 1,3,4-Thiadiazole complexes for quantitative Packing analysis.....	72
Manuscript: Sub Lattice Driven Spin State Ordering and Coordination Elasticity in Fe(II) 1,3,4- Thiadiazole Complexes.....	73
Abstract:.....	73
Introduction:.....	73
Results and discussion:	75
Synthesis:	75

Table of Contents

Temperature dependent magnetic properties:	76
Structural Characterization and Spin Crossover Behavior of Complexes C1–C3	78
Variable-temperature Mössbauer spectroscopy:	81
DFT modelling	83
Conclusions:	88
Experimental:	88
Ligand Synthesis:	90
References:	93
ESI: Sub Lattice Driven Spin State Ordering and Coordination Elasticity in Fe(II) 1,3,4-Thiadiazole Complexes	96
Table of Contents	96
1. NMR-spectra:	97
2. IR-spectra:	100
3. HRES ESI Mass spectra:	102
4. Crystal structure description:	106
5. Crystallographic Data:	124
6. Magnetic data:	133
7. Light-induced excited spin state trapping:	134
8. Solid state UV-Vis measurement:	136
9. DFT-Methods and Model	139
10. Reference:	141
Chapter 2: Chiral 1,3,4-Thiadiazole Complexes for Packing analysis	142
Manuscript: Understanding Polymorphism and Spin Crossover in Chiral Iron(II) Complexes: Structure–Property Insights	143
Abstract:	143
Introduction:	143
Results and discussion:	145
Synthesis:	145
Structural determination of complex C1 and C3	147

Table of Contents

Temperature dependent magnetization:.....	151
Mössbauer spectroscopy.....	152
CD- and UV-Vis spectra.....	154
Packing analysis of both Polymorphs by Nuclear vibrational spectroscopy.....	155
Conclusions:.....	160
Experimental:.....	160
Ligand Synthesis:.....	162
Complex Synthesis:.....	163
References:.....	164
ESI: Understanding Polymorphism and Spin Crossover in Chiral Iron(II) Complexes: Structure- Property Insights.....	1688
1. NMR-Spectra:.....	169
2. IR-spectra:.....	172
3. Mass spectra:.....	174
4. Crystallographic Data.....	178
5. Temperature dependent magnetization measurement.....	190
6. CD-Spectra and chiral HPLC.....	195
7. References:.....	201
Chapter 3: Synergism between the Luminescence of Sensor and Spin Crossover.....	202
Manuscript: Synergetic Spin Singlet-Quintet Switching and Luminescence in mononuclear Fe(II) 1,3,4-Oxadiazole Tetradentate Chelates with NCBH ₃ Co-ligand.....	203
Abstract:.....	203
Introduction:.....	203
Results and Discussion:.....	206
Synthesis:.....	206
Solid Magnetic data:.....	207
Structural determination:.....	209
Photoluminescence spectroscopy:.....	211
Conclusion:.....	214

Table of Contents

Experimental:.....	214
Ligand synthesis:.....	215
Complex synthesis:	217
Acknowledgment:.....	218
Literature:	218
ESI: Synergetic Spin Singlet-Quintet Switching and Luminescence in mononuclear Fe(II) 1,3,4-Oxadiazole Tetradentate Chelates with NCBH ₃ Co-ligand.....	222
1. NMR-spectra:.....	223
2. IR-spectra:.....	230
3. Mass spectra:.....	231
4. Crystal structures:.....	234
5. UV-Vis spectra:.....	238
6. Photoluminescence spectroscopy	240
7. Magnetic Data:.....	242
8. Synthesis of complex precursors	245
9. References:	245
Chapter 4: Unique packing properties of chiral 1,3,4-Oxadiazole Spin Crossover complexes	246
Manuscript: Chirality Without Compromise: Identical Spin Crossover Behavior between the Racemate and the Enantiopure Fe(II) Complexes.....	247
Notes and references.....	252
ESI: Chirality Without Compromise: Identical Spin Crossover Behavior between the Racemate and Enantiopure Fe(II) Complexes	255
1. Experimental Details:.....	256
2. Synthesis:.....	257
3. NMR-Spectra:.....	260
4. IR-spectra:.....	270
5. Mass spectra:.....	272
6. Crystallographic Data:.....	277
6.4. XRD Tables:	298

Table of Contents

6.5. Bond length tables:.....	304
6.6. Bond angle tables:	306
6.7. Stacking Parameters:	309
7. Powder <i>XRD</i> :	309
8. Magnetic Data:.....	311
9.1 Chiral <i>HPLC</i>	312
9.2 <i>CD</i> -spectra:	313
10. References:	315
Chapter 5: Solvent induced coordination Isomers of 1,3,4-Thiadiazole complexes.....	316
Manuscript: Lattice Solvent as a Structural Switch: <i>Mer-Fac</i> Isomerism and Spin Crossover in Fe(II) complexes based on 1,3,4-Thiadiazole	317
Abstract.....	317
Introduction	317
Results and Discussion:.....	318
Synthesis:.....	318
Structural determination:.....	320
Solid Magnetic data:	325
Solution Phase measurements: UV-Vis Absorption spectroscopy:.....	327
Conclusion:	328
Experimental:.....	329
Ligand synthesis:.....	329
Complex synthesis:	331
References:	3322
ESI: Lattice Solvent as a Structural Switch: <i>Mer-Fac</i> Isomerism and Spin Crossover in Fe(II) complexes based on 1,3,4-Thiadiazole	3355
1. <i>NMR</i> -Spectra:.....	3366
2. <i>IR</i> -spectra:.....	33939
3. <i>ESI</i> -Mass spectrometry	3411
4. Crystallographic Data	3444

Table of Contents

5. Temperature dependent magnetization measurement	3644
6. <i>UV-Vis</i> Absorption spectroscopy in solution.....	3666
7. References:	3677
Chapter 6: Helical dinuclear iron(II) complexes with 1,3,4-Oxa- and 1,3,4-Thiadiazole coordination units.....	3688
Manuscript: The Crucial Role of the Heteroatom and Bite Angle Influencing Spin States and Dinuclear Fe(II) Helicate Formation in 1,3,4-Thia/Oxadiazole Ligand.....	36969
Abstract:.....	36969
Introduction:	36969
Results and discussion:	3700
Structural determination of complex C1 and C2 and ligand L ^{ODA-Hel} :	3711
Solution Stability of the complex:.....	3755
Cyclic Voltammetry:.....	3755
Host-Guest chemistry:	3766
Conclusions:.....	3788
Experimental:.....	3788
Ligand Synthesis:.....	3800
Complex Synthesis:	3811
References:	3822
ESI: The Crucial Role of the Heteroatom and Bite Angle Influencing Spin States and Dinuclear Fe(II) Helicate Formation in 1,3,4-Thia/Oxadiazole Ligand	3866
1. <i>NMR</i> -Spectra:.....	3877
2. <i>IR</i> -spectra:	4022
3. Mass spectra:.....	4055
4. Crystallographic Data	4066
5. <i>UV-Vis</i> -Spectra:.....	41313
6. Cyclovoltammetry Data	4144
7. Magnetic Data:.....	4155
8. Molar Conductivity:	4155

Table of Contents

9. References:	4166
Summary and Perspectives	4177
Curriculum Vitae.....	4200
Nutzung von KI-Tools.....	4222

List of abbreviations

<i>SCO</i>	Spin Crossover
<i>HS</i>	High Spin
<i>LS</i>	Low Spin
<i>S</i>	Spin
$L^{\text{Ph-TDA}}$	1-(5-phenyl-1,3,4-thiadiazol-2-yl)-N,N-bis(pyridin-2-ylmethyl)methanamine
$L^{\text{Ph-TDA-AI}}$	1-(5-phenyl-1,3,4-thiadiazol-2-yl)-N,N-bis(pyridin-2-ylmethyl)ethan-1-amine
$L^{\text{Naph-ODA}}$	1-(5-(naphthalen-2-yl)-1,3,4-oxadiazol-2-yl)-N,N-bis(pyridin-2-ylmethyl)methanamine
$L^{\text{Naph-ODA-AI}}$	1-(5-(naphthalen-2-yl)-1,3,4-oxadiazol-2-yl)-N,N-bis(pyridin-2-ylmethyl)ethan-1-amine
$L^{\text{Naph-TDA}}$	1-(5-(naphthalen-2-yl)-1,3,4-thiadiazol-2-yl)-N,N-bis(pyridin-2-ylmethyl)methanamine
<i>XRD</i>	X-ray diffraction
<i>SQUID</i>	Superconducting quantum interference device
<i>CD</i>	Circular Dichroism
$T_{1/2}$	Transition temperature
<i>AI</i>	Artificial Intelligence
<i>DNA</i>	DeoxyriboNucleic Acid
<i>CISS</i>	Chiral Induced Spin Selectivity
<i>SALC</i>	Symmetry Adapted Linear Combination
Δ_o	Octahedral ligandfield strength
<i>P</i>	Spin pairing energy
k_B	Boltzman constant
<i>T</i>	Temperature
<i>LIESST</i>	Light Induced Spin State Trapping
M_s	Spin multiplicity
<i>L</i>	Angular moment
Δ_{oc}	Critical octahedral ligand field splitting
μ	Magnetic moment
<i>r</i>	Distance

List of abbreviations

ΔE_{HL}^0	Energy difference between high spin and low spin state
E_{HS}^0	Energy of the high spin state
E_{LS}^0	Energy of the low spin state
ΔE_{HL}^*	Activation energy between the high spin and low spin state
E_{vib}^i	Vibrational energy of state i
f_{LS}	Force constant for the low spin state
f_{HS}	Force constant for the high spin state
Δ_{LS}	Octahedral ligand field splitting for the low spin state
Δ_{HS}	Octahedral ligand field splitting for the high spin state
ΔG	Gibb's energy
ΔH	Enthalpy
ΔS	Entropy
ΔS_{el}	Electronic entropy
ΔS_{vib}	Vibrational entropy
R	Universal gas constant
solv	Solvent
EtOH	Ethanol
X	Halogenid
trim	4-(4-imidazolylmethyl)-2-(2-imidazolylmethyl)imidazole
H ₂ B(pz)(pypz)}	Bis{dihydro(pyrazol-1-yl)(2-pyridylpyrazol-1-yl)borate}
$T_{1/2}^{\downarrow}$	Critical temperature measured downwards
$T_{1/2}^{\uparrow}$	Critical temperature measured upwards
ΔT	Temperature difference
TIESST	Thermal Induced Spin State Trapping
T_{TIESST}	Critical temperature of the Thermal Induced Spin State Trapping
L _{npdtz}	2-naphthyl-5-pyridyl-1,2,4-thiadiazole
K	Kelvin
min	Minute
cm	Centimeter
nm	Nanometer
mol	Mol
L	Ligand
2-pic	picolylamine
btr	4,4'-bis-1,2,4-triazole

List of abbreviations

λ	Wavelength
<i>MLCT</i>	M etall to L igand C harge T ransfer
<i>ISC</i>	I nter S ystem C rossing
<i>reverse-LIESST</i>	R everse L ight I nduced S pin S tate T rapping
T_0	Temperature constant dependent on the inner coordination geometry of the complex
μ_{eff}	Effective magnetic moment
g_s	gyromagnetic ratio
μ_B	Bohr magneton
χ_m	Molar magnetic susceptibility
N_A	Avogadro constant
y_{HS}	High spin fraction
y_{LS}	Low spin fraction
<i>NMR</i>	N uclear M agnetic R esonance
χ_g	Mass magnetic susceptibility
$\Delta\nu$	Frequence difference
$\chi_g^{solvent}$	Mass magnetic susceptibility of the solvent
$\rho_{solvent}$	Density of the solvent
$\rho_{solution}$	Density of the solution
m	Mass
\bar{d}_{Fe-L}	Distance between iron and ligand
Å	Angström
Σ_O	Octahedral distortion parameter
α_i	Trans-angle alpha
θ_O	Torsional distortion parameter
θ_i	Cis-angle theta
<i>EC</i>	E lectron C apture
l	Core spin
γ	gamma quantum
δ	Isomeric shift
<i>QS</i>	Q uadropolic S plitting
M_l	Core spin multiplicity
Δm_l	Magnetic core spin quantum number
<i>IR</i>	I nfrared

List of abbreviations

<i>DSC</i>	D ifferential S canning C alorimetry
<i>EPR</i>	E lectron P aramagnetic R esonance
<i>NRS</i>	N uclear R esonance S cattering
<i>pDos</i>	P honon D ensity of S tate
<i>μSP</i>	M uon S pin R elaxation
<i>XAS</i>	X -Ray A bsorption S pectroscopy
<i>ESI-MS</i>	E lectrospray I onisation M ass S pectrometry
<i>EA</i>	E lemental A nalysis
<i>NIS</i>	N uclear I nelastic S cattering
<i>HPLC</i>	H igh- P erformance L iquid C hromatography
<i>DOSY</i>	D iffusion O rded S pectroscopy
<i>ESI</i>	E lectronic S upplementary I nformation
<i>LITH</i>	L ight- I nduced T hermal H ysteresis
Λ_m	M olar conductivity
<i>HSQC</i>	H eteronuclear S ingle Q uantum C oherence
<i>HMBC</i>	H eteronuclear M ultiple B ond C orrelation
<i>COSY</i>	C orrelation S pectroscopy

Introduction

Information technology and data processing has become a core element of societies over the past century.

This is evident not only in social sectors, with companies like *Spotify* and *Netflix*, but also in the rise of social media platforms such as *TikTok* and *Facebook*. These companies generate and trade information and information technology to create income, highlighted during the *Cambridge Analytica* scandal.^[1-4]

Information technologies are also essential in warfare. Modern conflicts, such as the *Russian* invasion of *Ukraine*, have demonstrated the strategic use of satellite information from *Starlink* in combat situations, as well as the defence against cyberattacks targeting critical infrastructure, which becomes a part of modern warfare strategy.^[5,6]

In recent years, artificial intelligence (*AI*) has emerged as a major field, relying on vast amounts of information to train widely used models such as *ChatGPT*.^[7,8] The challenge in all these examples is not only to gather information, but also to store and process it efficiently.^[9]

However, information storage is not unique to human technology; it is fundamental to nature itself. For example, deoxyribonucleic acid (*DNA*) and protein-based peptides serve as information storage systems for living organisms, enabling genetic inheritance across generations.^[10,11] In 2021, Yao et al. proposed using peptide sequences - naturally used for protein construction - as materials for data storage.^[10]

“*Green*” technologies based on proteins offer not only sustainability but also biocompatibility, opening up new opportunities for neuromorphic networks that mimic biological synapses and for interfaces between biological and electronic information in implantable devices.^[12]

Another key element in nature is chirality, which also plays a role in information transfer and retention. The importance of the chirality for biochemistry reactions is the key-lock-system for enzymes, where an enantioselectivity of the interaction between the key molecule and the lock (enzyme) is reported for initiation of reactions.^[13] Further chirality dependent mechanism in biochemistry was found Jonathan Williams and colleagues. They demonstrated that (-)- α -pinene is predominantly emitted by vegetation, whereas (+)- α -pinene is mainly released from terpene storage pools. This leads to a relative change in the amounts of each isomer during drought conditions.^[14]

The chiral induced spin selectivity (*CISS*) effect has gained significant importance in the study of chirality effects in living organisms and spintronic device approaches.^[15] It is attributed to the handedness-dependent spin polarization observed during electron transfer through *DNA*.^[16] As demonstrated by

Mishra et al., the *CISS* effect also plays a crucial role in the spin polarization of electron transfer through bacteriorhodopsin.^[17] Further idea of using the *CISS* effect for molecular junctions as spin filters in the field of spintronics, brings up the question of manipulation of this effect by molecular switches.^[18]

Since the first investigations into molecular switches, this field has been directly linked to information storage.^[19] A molecular switch is defined as a molecule that can persist in at least two different states and exhibit a transition between these states in response to external or internal stimuli, such as light, temperature, pressure, pH value, or intercalation.^[20]

Among the extensive research on molecular switches, spin crossover materials form a well investigated family. Research has evolved from studying thermal spin crossover to developing multifunctional materials suitable for a wide range of applications.^[21–24] Spin crossover is only observed in complexes and solid states of 3d transition metals with electron configurations from d^4 to d^7 , enabling transitions between high-spin (*HS*) and low-spin (*LS*) states. These transitions are accompanied by significant changes in geometry and properties such as light emission and conductivity.^[25–31]

The advantage of molecular design based on spin crossover complexes for data storage lies not only in miniaturization, which enables high-density storage devices, but also in the relative ease and cost-efficiency of synthesis and modification compared to organic switches.^[32]

Combining chirality and spin crossover offers the potential to create materials that are optimal for information storage. These materials exhibit bistability, responding not only to changes in magnetic moments due to temperature, but also to light, pressure, and magnetic fields as stimuli for switching. Additionally, they offer the possibility of ferroelectricity output or circular dichroism (*CD*)-signals as chiroptical switching materials or switchable spinfilters based on the chiral induced spin selectivity (*CISS*)-effect for reading out stored information.^[18,21,33]

References:

- [1] X. Amatriain in Proceedings of the 2nd International Workshop on Big Data, Streams and Heterogeneous Source Mining: Algorithms, Systems, Programming Models and Applications, ACM, Chicago Illinois, **2013**, pp. 1-6.
- [2] J. Isaak, M. J. Hanna, *Computer* **2018**, 51, 56-59.
- [3] A. Zulkifli, *Computer* **2022**, 55, 77-80.
- [4] *Strategic Direction* **2013**, 29, 25-27.
- [5] L. Bojor, T. Petrache, C. Cristescu, *Land Forces Academy Review* **2024**, 29, 185-194.
- [6] U. Priyono *JDP* **2022**, 8, 44.
- [7] S. Y. Wang, S. Pershing, A. Y. Lee, *Current Opinion in Ophthalmology* **2020**, 31, 318,323.
- [8] K. I. Roumeliotis, N. D. Tselikas, *Future Internet* **2023**, 15, 192.
- [9] Dept. CSE, Jodhpur National University, Jodhpur, India, Z. K. Lawal, R. Y. Zakari *IJECS* **2016**, *International Journal of Engineering and Computer Science*, 5(3), 15947-15961
- [10] C. C. A. Ng, W. M. Tam, H. Yin, Q. Wu, P.-K. So, M. Y.-M. Wong, F. C. M. Lau, Z.-P. Yao *Nat. Commun.* **2021**, 12, 4242.
- [11] M. Ghai, F. Kader *Biochem. Genet.* **2022**, 60, 1107-1140.
- [12] J. Wang, F. Qian, S. Huang, Z. Lv, Y. Wang, X. Xing, M. Chen, S.-T. Han, Y. Zhou, *Advanced Intelligent Systems* **2021**, 3, 2000180.
- [13] A. Cecconello, F. C. Simmel, *Small* **2019**, 15, 1805419.
- [14] J. Byron, J. Kreuzwieser, G. Purser, J. Van Haren, S. N. Ladd, L. K. Meredith, C. Werner, J. Williams, *Nature* **2022**, 609, 307-312.
- [15] B. P. Bloom, Y. Paltiel, R. Naaman, D. H. Waldeck, *Chem. Rev.* **2024**, 124, 1950-1991.
- [16] T. J. Zwang, S. Hürliemann, M. G. Hill, J. K. Barton, *J. Am. Chem. Soc.* **2016**, 138, 15551-15554.
- [17] D. Mishra, T. Z. Markus, R. Naaman, M. Kettner, B. Göhler, H. Zacharias, N. Friedman, M. Sheves, C. Fontanesi, *Proc. Natl. Acad. Sci. U.S.A.* **2013**, 110, 14872-14876.
- [18] M. Suda, Y. Thathong, V. Promarak, H. Kojima, M. Nakamura, T. Shiraogawa, M. Ehara, H. M. Yamamoto, *Nat. Commun.* **2019**, 10, 2455.
- [19] F. M. Raymo, *Adv. Mater.* **2002**, 14, 401-414.
- [20] B. L. Feringa, W. R. Browne, Eds. , *Wiley*, **2011**.
- [21] A. Bousseksou, G. Molnár, *Comptes Rendus. Chimie* **2003**, 6, 1175-1183.
- [22] A. B. Gaspar, V. Ksenofontov, M. Seredyuk, P. Gütllich, *Coord. Chem. Rev.* **2005**, 249, 2661-2676.
- [23] D. Dattler, G. Fuks, J. Heiser, E. Moulin, A. Perrot, X. Yao, N. Giuseppone, *Chem. Rev.* **2020**, 120, 310-433.
- [24] N. A. A. M. Amin, S. M. Said, M. F. M. Salleh, A. M. Afifi, N. M. J. N. Ibrahim, M. M. I. M. Hasnan, M. Tahir, N. Z. I. Hashim, *Inorg. Chim. Acta* **2023**, 544, 121168.

- [25] Y. Li, M. K. Javed, S.-Q. Wu, A. Sulaiman, Y.-Y. Wu, Z.-Y. Li, O. Sato, X.-H. Bu, *Chinese Chem. Letters* **2023**, 34, 107492.
- [26] B. Benaicha, K. Van Do, A. Yangui, N. Pittala, A. Lusson, M. Sy, G. Bouchez, H. Fourati, C. J. Gómez-García, S. Triki, K. Boukheddaden, *Chem. Sci.* **2019**, 10, 6791-6798.
- [27] J.-L. Wang, Q. Liu, Y.-S. Meng, X. Liu, H. Zheng, Q. Shi, C.-Y. Duan, T. Liu, *Chem. Sci.* **2018**, 9, 2892-2897.
- [28] A. Rotaru, I. A. Gural'skiy, G. Molnár, L. Salmon, P. Demont, A. Bousseksou, *Chem. Commun.* **2012**, 48, 4163-4165.
- [29] S. K. Kuppusamy, A. Mizuno, A. García-Fuente, S. Van Der Poel, B. Heinrich, J. Ferrer, H. S. J. Van Der Zant, M. Ruben, *ACS Omega* **2022**, 7, 13654-13666.
- [30] R. Ishikawa, S. Ueno, S. Nifuku, Y. Horii, H. Iguchi, Y. Miyazaki, M. Nakano, S. Hayami, S. Kumagai, K. Katoh, Z. Li, M. Yamashita, S. Kawata, *Chem. Eur. J.* **2020**, 26, 1278-1285.
- [31] K. S. Woo, A. Zhang, A. Arabelo, T. D. Brown, M. Park, A. A. Talin, E. J. Fuller, R. S. Bisht, X. Qian, R. Arroyave, S. Ramanathan, L. Thomas, R. S. Williams, S. Kumar, *Nat. Commun.* **2024**, 15, 4656.
- [32] K. Senthil Kumar, M. Ruben, *Coor. Chem. Rev.* **2017**, 346, 176-205.
- [33] B. L. Feringa, R. A. Van Delden, N. Koumura, E. M. Geertsema *Chem. Rev.* **2000**, 100, 1789-1816.

Theory Background

The interest in the chemistry of 3d transition metals is based on the occupancy of their d-orbitals, which gives lead to crucial impact on the electronic and magnetic properties.^[1] In an octahedral ligand field, the five d-orbitals split into two sets: the antibonding e_g^* orbitals - *symmetry-adapted linear combinations (SALCs)* of the $d_{x^2-y^2}$ and d_{z^2} orbitals, which point directly at the ligands - and the non-bonding t_{2g} orbitals - SALCs of the d_{xy} , d_{xz} , and d_{yz} orbitals - in systems with purely σ -donating ligands.^[1]

The energy gap between these two orbital sets is termed the ligand field splitting energy (Δ_o), often described using the parameter $10 Dq_o$.^[2] Electron population of these orbitals is further governed by the spin pairing energy (P), which reflects the energetic cost of pairing two electrons with opposite spins due to electron-electron repulsion.^[3]

For 3d transition metals with electronic configurations from $3d^4$ to $3d^7$, three limiting spin states arise:^[2]

- When $\Delta_o > P$, electrons preferentially occupy the lower-energy t_{2g} orbitals, resulting in a **low-spin** state (right in **Figure 1**)
- When $\Delta_o < P$, electrons populate all five orbitals according to Hund's rule, yielding a **high-spin** state. (left in **Figure 1**)
- When $\Delta_o \approx P$, and the energy difference lies within the range of thermal energy ($k_B T$), the system may undergo a **spin crossover** between high- and low-spin states.

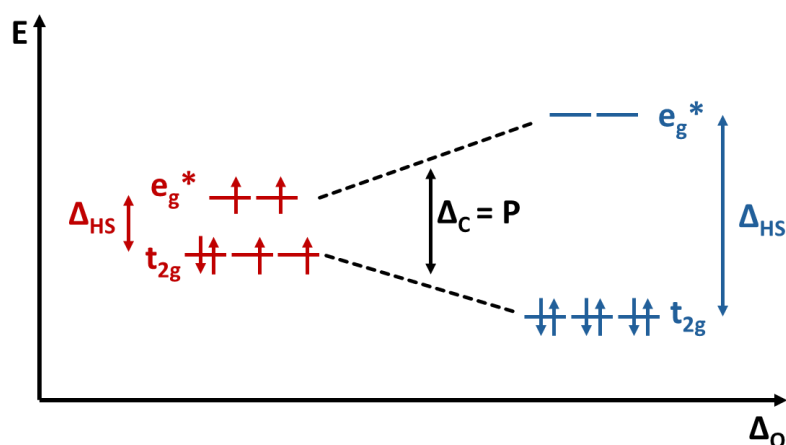


Figure 1: Schematic diagram of the ligand field splitting of the 3d orbitals of iron(II) in an octahedral coordination environment for the high spin state (left) with $\Delta_o < P$ and the low spin state (right) with $\Delta_o > P$ and the given electron population of the orbitals. Δ_c is defined as the critical ligand field splitting energy for $\Delta_o = P$.

The spin crossover can be triggered by external stimuli such as temperature^[4], pressure^[5,6], light (light-induced excited spin-state trapping known as *LIESST* effect)^[7,8], or magnetic fields^[9,10].

Iron(II) is the most extensively studied metal in spin crossover (SCO) chemistry, as it undergoes transitions between a diamagnetic low-spin state ($S = 0$) and a paramagnetic high-spin state ($S = 2$). This bistability makes Fe(II)-based complexes attractive for molecular switches as sensors^[11-13] and data storage applications^[14,15].

Electronic configurations can be described using term symbols of the form ^{2S+1}L , where the superscript denotes spin multiplicity ($M_S = 2S + 1$), and L corresponds to the total orbital angular momentum, noted with "S", "P" or "D", standing for $L = 0, 1$ or 2 .^[16] For a free Fe(II) ion, the ground state is 5D , the term with maximum spin multiplicity. As Δ_o increases, the ground state changes from 5T_2 to 1A_1 - derived from the 1I term of the free ion - at a critical splitting value Δ_{oc} , where $\Delta_o \approx P$.^[17]

This dependence of term energies on ligand field strength is visualized in the *Tanabe-Sugano* diagram (**Figure 2**), which also conveys the symmetry characteristics of each state.

In this footnotes of the termsymbols, subscript indices denote symmetry under specific symmetry operations: a subscript "1" is used if the wavefunction remains unchanged under a C_2 rotation perpendicular to the principal axis; a subscript "2" indicates a sign change. The presence of inversion symmetry results in classification as "gerade" (g) if the wavefunction remains invariant, or "ungerade" (u) if it changes sign.^[16]

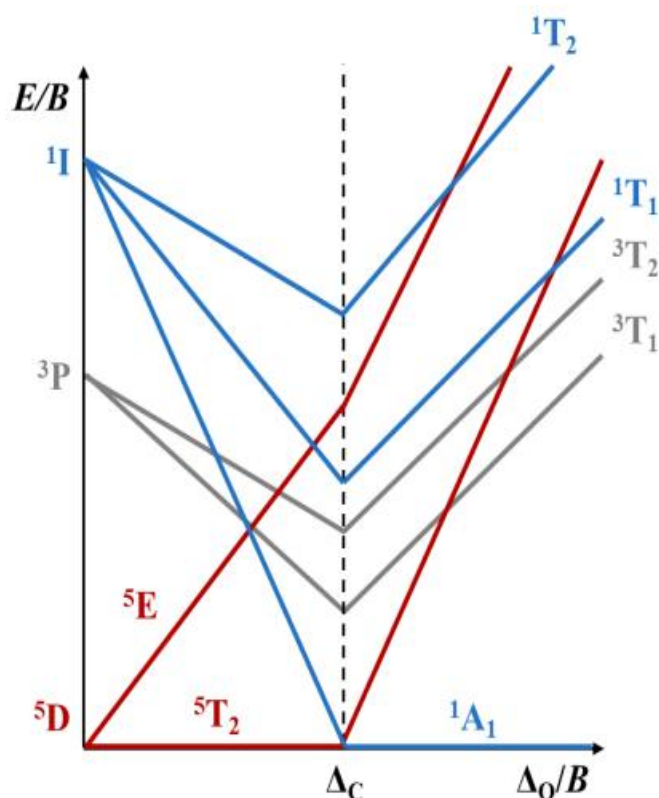


Figure 2: Scheme of the *Tanabe Sugano* diagram for d^6 iron(II)-ion in an octahedral coordination environment with the energy E of the states in *Racah Parameter B* against the octahedral splitting energy Δ_o in *Racah Parameter B*.^[18] Reprinted from literature with permission.

The ligand field splitting energy can be correlated with the metal-ligand bond length.^[19] This relationship can be described through the dipole moment (μ) and the bond length (r) as follows:^[19]

$$10 Dq \sim \Delta_o \sim \frac{\mu}{r^6} \quad (2 - 1)$$

A shorter bond length generally indicates stronger metal-ligand interactions, resulting in a larger ligand field splitting energy (Δ_o), whereas longer bond lengths are associated with weaker field strengths and reduced splitting.^[19]

Both spin states can be represented by harmonic potential energy surfaces, illustrating the energy as a function of the metal-ligand bond length, as shown in **Figure 3**. In the high-spin (*HS*) state, population of the antibonding e_g^* orbitals lead to a reduction in bond order and an elongation of the metal-ligand bonds. This results in a broader potential well and a shift of the electronic ground state to longer Fe-L bond distances.^[19]

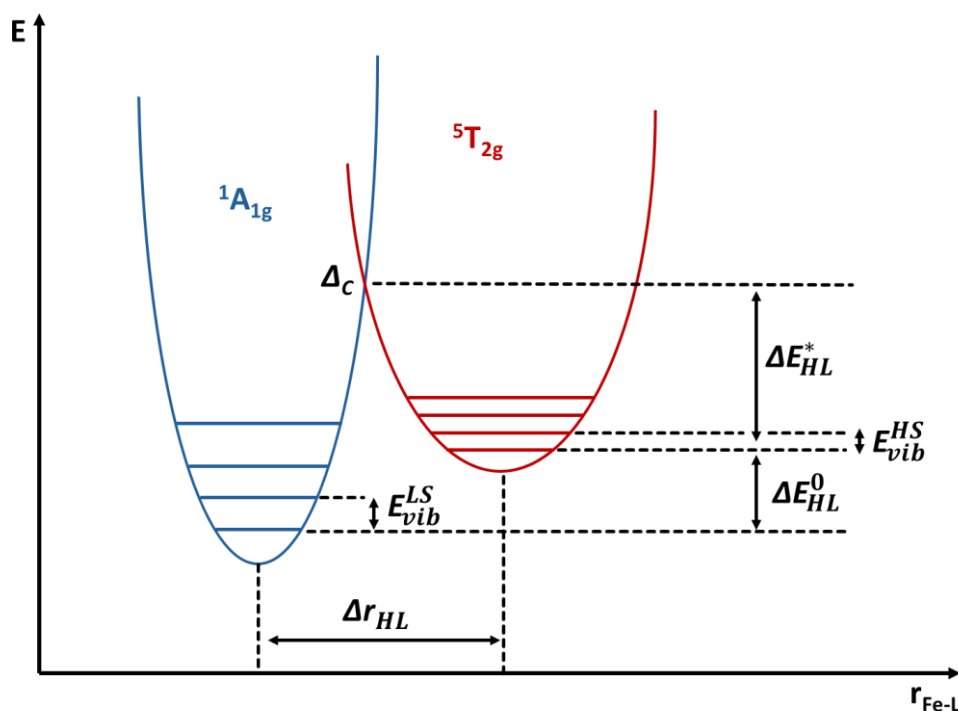


Figure 3: Schematic representation of the harmonic potential for iron(II) of the high spin state $^5T_{2g}$ (red) and the low spin state $^1A_{1g}$ (blue) in an ideal octahedral coordination environment.^[19] Reprinted from literature with permission.

The zero-point energy difference between the high-spin and low-spin (*LS*) states is denoted as ΔE_{HL}^0 and corresponds to the difference between their respective zero-point energies: $E_{HS}^0 - E_{LS}^0$.^[19] The activation energy ΔE_{HL}^* is defined as the energy gap between the crossing point Δ_c of the two potential curves and the zero-point energy of the high-spin state (E_{HS}^0).

The vibrational energy levels E_{vib}^i ($i = HS$ or LS) depend on the vibrational force constant f_i ($i = HS$ or LS), which reflect the stiffness of the potential. Due to the stronger bonding in the low-spin state, the vibrational constant f_{LS} is larger than f_{HS} ($f_{LS} > f_{HS}$).^[20]

Importantly, the crossing point Δ_{oc} represents the intersection of the two potential energy surfaces and does not correspond to a stable configuration. At this specific bond distance, the system cannot reside in either ground state. In an ideal system, the potential energy minima corresponding to the low-spin and high-spin states (Δ_{LS} and Δ_{HS} , respectively) do not coincide with Δ_{oc} .^[19]

To investigate the equilibrium between the high-spin and low-spin states, the *Gibbs* free energy difference (ΔG) must be considered. This can be described using the *Gibbs-Helmholtz* equation:^[21]

$$\Delta G = \Delta H - T \Delta S \quad (2 - 2)$$

where ΔH is the enthalpy difference, ΔS is the entropy difference between the two spin states, and T is the absolute temperature. This equation allows quantification of the thermodynamic driving forces that influences spin state populations and their temperature dependence.

The temperature dependence of the spin crossover is primarily governed by the entropy term in the *Gibbs* free energy. At elevated temperatures, the entropic contribution becomes dominant, while at lower temperatures, the enthalpy difference between the high-spin and low-spin states plays a more significant role in determining the *Gibbs* free energy (ΔG).

The total entropy change (ΔS) associated with the spin crossover can be divided into two main components: a **vibrational** part and an **electronic** part. The vibrational contribution arises from changes in metal-ligand stretching and deformation modes between the two spin states. The electronic contribution, on the other hand, results from differences in spin and orbital degeneracies.^[21]

$$\Delta S = \Delta S_{el} - \Delta S_{vib} \quad (2 - 3)$$

In iron(II) complexes, this electronic entropy change is substantial due to the transition from a non-degenerate singlet low-spin state ($S = 0, M_S = 1$) to a highly degenerate high-spin state ($S = 2, M_S = 5$), which also includes orbital degeneracy. The total degeneracy of the high-spin state are up to 15-fold, significantly increasing the entropy in this state and thereby favouring the high-spin population at higher temperatures.^[21]

$$\Delta S_{el} = R \cdot \ln \left(\frac{(2S + 1)_{HS}}{(2S + 1)_{LS}} \right) \quad (2 - 4)$$

Therefore, thermally induced spin crossover can be regarded as an entropy-driven process.^[22]

For a single iron(II) centre, the spin transition is typically abrupt, with the system residing either in the high-spin or the low-spin state. However, in the case of an ensemble of spin crossover complexes in the solid state, the equilibrium transition is better understood as a first-order phase transition, propagated through the material via cooperative effects.^[21,23]

Cooperativity arises from intermolecular interactions such as hydrogen bonding, π - π stacking, and C-H $\cdots\pi$ interactions, which establish long-range order.^[24] Consequently, in solution, where long-range orders are absent or significantly reduced, cooperativity is weakened. This leads to a gradual, continuous spin transition, which can be described by a *Boltzmann* distribution of the vibronic states.^[25,26]

The influence of the solvent on the spin crossover behaviour has been elegantly demonstrated by Palacios-Corella et al. (2023), who investigated a multifunctional material based on a redox-active polyoxometalate coordinated to iron(II) via a 2,6-bis(pyrazol-1-yl)pyridine ligand, forming $\text{Fe}[\text{V}_6\text{O}_{19}(\text{C}_{16}\text{H}_{15}\text{N}_6\text{O})_2]\cdot\text{solv}$.^[27]

They showed that bulky solvents such as DMF or benzonitrile induce a gradual spin crossover due to reduced cooperativity. In contrast, intercalation of smaller solvents like ethanol (EtOH) induces internal (chemical) pressure, leading to a contraction of the unit cell and stabilization of the low-spin state. Similarly, nitromethane and acetonitrile were found to shift the spin transition temperature to lower values, indicating low-spin stabilization.

Anions can influence the spin crossover due to H-interactions, polarisation and by the size, as often discussed in literature.^[28] A prominent example of anion influence on spin state stability was reported by Lemercier et al. (2006), who studied the complex $[\text{Fe}(\text{trim})_2]\text{X}_2$, where the ligand is 4-(4-imidazolylmethyl)-2-(2-imidazolylmethyl)imidazole and X represents halide anions (F^- , Cl^- , Br^- , I^-).^[29] With increasing anion size and decreasing basicity from F^- to I^- , the strength of the peripheral $\text{N}_{\text{Ligand}}\cdots\text{H}\cdots\text{X}$ hydrogen bonding diminishes. This reduces the inductive effect transmitted through the ligand framework, thereby weakening the Fe(II)-N bond and stabilizing the low-spin state more effectively for iodide, followed by bromide and chloride. In contrast, fluoride results in a stabilization of the high-spin state, yielding an overall high-spin configuration.

Intermolecular π - π interactions between aryl systems also play a key role in tuning cooperativity. Ossinger et al. demonstrated this in the system $[[\text{Fe}\{\text{H}_2\text{B}(\text{pz})(\text{pypz})\}_2]$ (pz = pyrazole, pypz = pyridylpyrazole), which crystallizes in two polymorphs.^[30] In one polymorph (II) strong π - π stacking interactions result in low-spin stabilization and a higher transition temperature ($T_{1/2} = 400$ K). In contrast, the other polymorph (I), lacking such interactions, exhibits a lower transition temperature ($T_{1/2} = 270$ K).

In general, increasing long-range order and intermolecular interactions enhance cooperativity, often leading to an abrupt spin crossover with hysteresis. This bistable behaviour within a defined temperature window is referred to as a memory effect.^[24]

Typically, the spin transition upon cooling ($T_{1/2}^{\downarrow}$) occurs at a lower temperature than upon heating ($T_{1/2}^{\uparrow}$). This hysteresis is a kinetic phenomenon and is scan-rate dependent. In systems with strong cooperativity, rapid cooling can trap the complex in a metastable high-spin state, a process known as the *TIESST* effect (Thermally Induced Excited Spin-State Trapping).^[31,32]

This phenomenon enables access to addressable spin states at low temperatures and opens possibilities for low-temperature switching applications.

The scan-rate dependency of spin crossover behaviour was demonstrated by Kiehl *et al.* (2022) through the investigation of the complex $[\text{Fe}(\text{L}^{\text{nptdz}})_2(\text{NCSe})_2]$, where L^{nptdz} denotes 2-naphthyl-5-pyridyl-1,2,4-thiadiazole.^[32] This complex exhibits strong intermolecular π - π interactions and displays a hysteresis width of $\Delta T = 58$ K during thermal cycling at a constant scan rate of $0.35 \text{ K}\cdot\text{min}^{-1}$. Increasing the scan rate to $10 \text{ K}\cdot\text{min}^{-1}$ did not affect the heating curve ($T_{1/2}^{\uparrow}$ remained constant), nor did it significantly shift the cooling transition temperature ($T_{1/2}^{\downarrow}$). However, the completeness of the spin transition decreased at higher scan speeds. This phenomenon, known as quenching, leads to trapping of the metastable high-spin state and is referred to as the *TIESST* effect.

The *TIESST* temperature (T_{TIESST}) was further investigated by subjecting the metastable high-spin state to different heating rates after rapid cooling. T_{TIESST} was observed to increase with the scan rate, ranging from 70.15 K at $0.5 \text{ K}\cdot\text{min}^{-1}$ to 86.10 K at $10 \text{ K}\cdot\text{min}^{-1}$. Moreover, higher scan rates led to an increasingly incomplete transition to the low-spin state, due to the thermal trapping of the metastable high spin state, underlining the crucial role of scan speed in the interpretation of spin-crossover properties.^[24]

In certain cases, the spin transition profile exhibits multiple steps, corresponding to intermediate states between the fully high-spin and fully low-spin configurations. Several factors may give rise to such multi-step behaviour:^[33]

1. Polynuclear complexes with independently switching metal centres.
2. Mononuclear complexes, where stepwise transitions can occur with or without accompanying phase transitions or symmetry changes.

A well-characterized example of a polynuclear system was reported by Matsumoto *et al.* for the tetranuclear grid complex $[\text{Fe}_4(\text{L})_4(\text{BF}_4)_4] \cdot 2 \text{ CH}_3\text{CN}$, where L is a bis-pyrazolylpyridine-bridged imidazole ligand.^[34] This complex transitions from the fully high-spin state $[\text{HS}]_4$ to a mixed $[\text{HS}]_3[\text{LS}]$

state, as confirmed by Mössbauer spectroscopy. At lower temperatures (< 100 K), a further transition to the symmetric $[HS]_2[LS]_2$ state was observed by both Mössbauer spectroscopy and single-crystal *XRD*, although this transition remained incomplete.

The first full report of a two-step spin crossover in a mononuclear complex was provided by Chernyshov et al. for $[\text{Fe}(2\text{-pic})_3]\text{Cl}_2 \cdot \text{EtOH}$ (pic = picolylamine), originally published by Gütllich et al. in 1994.^[19,35] This complex exhibits two abrupt transitions at $T_{c1} = 114$ K and $T_{c2} = 124$ K, with the intermediate state undergoing a symmetry-breaking phase transition. Single-crystal *XRD* studies revealed transitions from the low-spin phase ($B2_1/c$; nonconventional space group) to an intermediate mixed-spin phase ($P2_1/c$), and finally to a high-spin phase ($B2_1/c$; nonconventional space group). The intermediate phase exhibits long-range order of alternating high- and low-spin iron(II) centres.^[36]

Importantly, a stepwise spin transition in mononuclear systems does not necessarily require a phase transition or symmetry breaking. Garcia et al. (1999) demonstrated this with the complex $[\text{Fe}(\text{btr})_3](\text{ClO}_4)_2$ (btr = 4,4'-bis-1,2,4-triazole).^[37] This compound shows a two-step profile, with an abrupt transition at $T_{1/2} = 222$ K and a lower-temperature hysteresis $\Delta T = 1.5$ K ($T_{1/2}^\uparrow = 185$ K and $T_{1/2}^\downarrow = 183$ K). No phase transition was detected. Instead, the asymmetric high-spin phase already contains two crystallographically distinct iron(II) centres, each with different spin-crossover properties.

These findings highlight the value of single-crystal X-ray diffraction (*XRD*) in elucidating spin-crossover mechanisms and emphasize the need for careful sample handling. Defects or impurities in the crystal lattice can hinder complete spin transitions, a phenomenon referred to as incomplete spin crossover.

Figure 4 schematically summarizes the various thermally induced spin-crossover profiles by plotting the high-spin fraction as a function of temperature, illustrating abrupt, gradual and hysteretic behaviours.

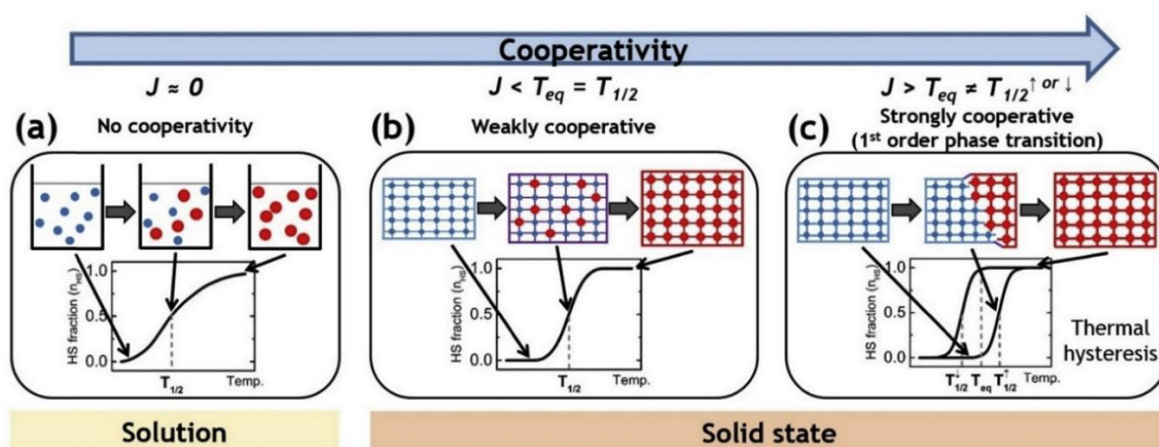


Figure 4: Schematic representation of the influence of the increased cooperativity, given by the interaction parameter J and the impact on the spin crossover perturbation through the packed system.^[23] Reprinted from literature with permission.

Further external Stimuli for Spin crossover

As previously discussed, spin crossover can be induced thermally. However, additional external stimuli have also been explored. Excitation of an iron(II) complex in the low-spin state at low temperature using pulsed light ($\lambda = 514 \text{ nm}$) leads to population of the excited singlet states (1T_1 - and 1T_2 -state) or the metal-to-ligand charge transfer (*MLCT*) state. This is followed by vibrational relaxation and intersystem crossing (*ISC*) through the excited triplet state (3T_2) to the vibrational ground state of the excited triplet (3T_1) state.^[38,39]

From the 3T_1 state, intersystem crossing can proceed either back to the singlet ground state (1A_1), thereby returning to the low-spin configuration, or to the metastable high-spin state (5T_2). At low temperatures, the thermal relaxation from the high-spin metastable state (5T_2) to the low-spin ground state (1A_1) is slow, as the transition is spin- and symmetry-forbidden according to selection rules. This results in a prolonged lifetime of the high-spin state, a phenomenon known as the *LIESST* (Light-Induced Excited Spin State Trapping) effect.^[38,39]

Conversely, irradiation of the high-spin state with light of longer wavelength (e.g.: $\lambda \approx 820 \text{ nm}$) excites the system via the 5E excited state, inducing intersystem crossing back to the low-spin ground state (1A_1). This process is termed the *reverse-LIESST* effect (shown in **Figure 5**).^[40]

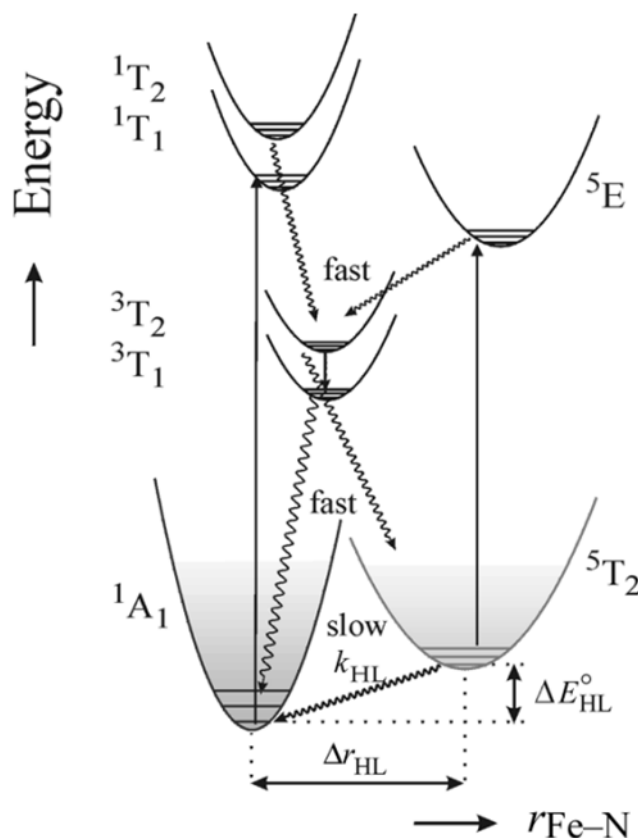


Figure 5: Schematic representation of the harmonic potential wells of the involved states during the *LIESST*-effect and the mechanism of the *LIESST*-effect.^[41] Reprinted from literature with permission.

The critical temperature at which thermal relaxation of the trapped spin states occurs is defined as T_{LIESST} . Létard *et al.* established an empirical correlation between T_{LIESST} and the thermal spin crossover transition temperature $T_{1/2}$, expressed by the relationship:^[42]

$$T_{LIESST} = T_0 + 0.3 T_{1/2} \quad (2 - 5)$$

here T_0 is a temperature constant dependent on the inner coordination geometry of the complex. This constant is similar for complexes sharing comparable coordination environments.^[42,43]

The exploration of hidden spin states through thermally and light-induced spin state transitions opens the door to multistate stability in spin crossover systems. This phenomenon was thoroughly investigated by Boonprab *et al.* for the complex $[\text{Fe}(\text{L}^{\text{naphBzen}})_2]$, which exhibits an incomplete ($\approx 50\%$) spin crossover accompanied by a thermal hysteresis of $\Delta T = 25$ K ($T_{1/2}^\uparrow = 135$ K and $T_{1/2}^\downarrow = 110$ K). Single crystal X-ray diffraction measurements revealed a phase transition characterized by the formation of two sublattices: one containing iron(II) centres in the high spin state, and the other containing iron(II) centres in the low spin state.^[44]

Rapid cooling of the sample leads to an overall high spin state, indicative of the *TIESST* effect, with a $T_{TIESST} = 75$ K. This behaviour reflects the strong cooperativity present in the system. Subsequent irradiation with light at $\lambda = 650$ nm caused an increase in magnetic susceptibility from 2.37 to 2.70 $\text{cm}^3 \cdot \text{mol}^{-1} \cdot \text{K}$, signalling a partial *LIESST* effect on the thermally switched low spin iron(II) centres.^[44]

Complete reversal of the spin state was achieved by irradiation with light at $\lambda = 830$ nm and 980 nm, illustrating an example where certain spin states are accessible exclusively via light irradiation rather than thermal spin crossover. The spin transition to the mixed high spin-low spin state was observed at $T_{1/2}^\uparrow = 60$ K, and direct cooling led to an open hysteresis of $\Delta T = 60$ K. Continuous irradiation at $\lambda = 830$ nm during warming to 100 K followed by cooling to 10 K induced a light-induced thermal hysteresis (*LITH*), enabling access to the low spin–low spin state at $T_{1/2}^\downarrow = 30$ K. Notably, without sustained irradiation, the system could not transition from the high spin-high spin state to the low spin-low spin state. Starting from the thermally quenched high spin-high spin state, full conversion to the low spin state was achieved through light exposure ($\lambda = 830$ nm) without passing through the intermediate mixed spin state phase.

This study elegantly demonstrates the potential for multistate spin stability in mononuclear complexes, highlighting the complementary roles of thermal and light-induced spin crossover processes without the necessity of polynuclear architecture.

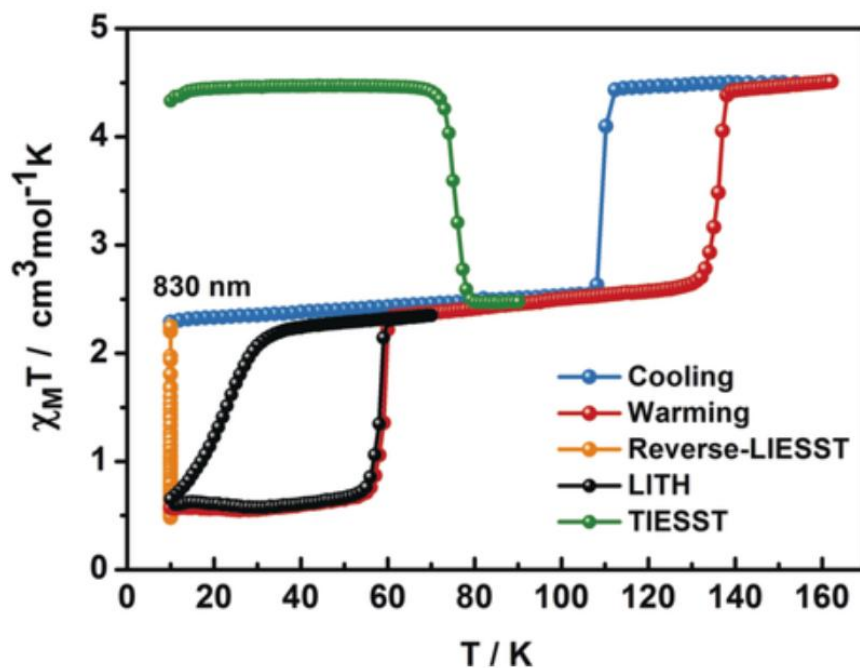


Figure 6: Multistate approach represented by the $\chi_M T$ vs T plot of the complex $[\text{Fe}(\text{L}^{\text{NaphBzen}})_2]$ published by Boonprab *et al.*, showing Light Induced Thermal Hysteresis (LITH) as well as Thermal induced excited spin state Trapping (TIESST).^[44] Reprinted from literature with permission.

As previously discussed, pressure can serve as an external stimulus to induce spin crossover. This is because the spin transition involves a change in metal-ligand bond distances, primarily due to the population of antibonding e_g^* orbitals in the high spin state. With increasing pressure, the high spin state becomes destabilized, which results in a shift of the transition temperature $T_{1/2}$ toward higher values.^[4] Further application of pressure induced spin crossover is based on the barocaloric effect.^[45] Reversible thermal changes in isothermal entropy and adiabatic temperature follow the application or removal of external pressure. Gracia *et al.* provide a representative example using $[\text{Fe}(\text{pap-5NO}_2)_2]$, in which the spin-crossover is identified by powder *X-ray* diffraction under isothermal compression and decompression, based on unit cell volume changes.^[46] The resulting p - V curve demonstrates a pronounced pressure hysteresis, and the observed barocaloric effect is directly linked to the substantial volume change occurring during the spin transition.

Analytic approaches to analyse the Spin state Transition

After the discussion of induced spin state transition by various stimuli, the key characteristics for spin crossover applications - such as the transition temperature $T_{1/2}$ and the transition profile (incomplete, gradual, abrupt, or exhibiting hysteresis) - need to be thoroughly investigated.

The Research developed a toolkit to measure the characteristics of the spin crossover.

As mentioned earlier, the spin transition involves a switch between the diamagnetic 1A_1 low spin state and the paramagnetic 5T_2 high spin state, which directly affects the temperature-dependent magnetization of the material.

One of the most common and reliable methods to study this is by measuring the temperature-dependent magnetic susceptibility using a *Superconducting Quantum Interference Device (SQUID)* magnetometer.

The effective magnetic moment μ_{eff} , assuming negligible angular momentum contribution, can be calculated by the formula:

$$\mu_{eff} = g_s \sqrt{S(S+1)} \mu_B \quad (2 - 6)$$

where the *Landé* factor, which is the ratio of the magnetic moment to the angular momentum and a value of $g_s \approx 2$, for a free electron, and μ_B is the *Bohr* magneton.^[16]

The molar magnetic susceptibility χ_m is directly related to the effective magnetic moment μ_{eff} by the following equation:^[16]

$$\mu_{eff} = \sqrt{\frac{3k_B}{N_A \mu_B^2}} \sqrt{\chi_m T} \approx 2.83 \sqrt{\chi_m T} \quad (2 - 7)$$

The equation includes the temperature T , the *Boltzmann* constant k_B , the *Avogadro* number N_A and the *Bohr* magneton μ_B . The measured $\chi_m T$ values represent a linear combination of the proportions of the high spin state y_{HS} and the low spin state y_{LS} with the magnetic susceptibility of each spin state χ_M^i ($i = HS$ or LS).

$$\chi_M T = (y_{HS} \cdot \chi_M^{HS} + (1 - y_{HS}) \cdot \chi_M^{LS}) T \quad (2 - 8)$$

In the literature, common plots display the product of molar magnetic susceptibility and temperature ($\chi_M T$) against temperature.^[44,47-49]

To eliminate the influence of cooperativity or intermolecular interactions in magnetic investigations, temperature-dependent solution measurements are often performed using 1H -NMR, known as the *Evans NMR* technique.^[26] In this method, the sample is dissolved in a deuterated solvent inside an *NMR*

tube, and a capillary tube containing pure solvent is placed inside the same *NMR* tube. The paramagnetic moment of the high spin complex causes a shift in the $^1\text{H-NMR}$ signal of the solvent in the sample solution, whereas the pure solvent signal remains unaffected. As the complex undergoes temperature-induced spin crossover, the fraction of high spin species decreases at lower temperatures, leading to a decrease in the frequency difference $\Delta\nu$ between the solvent signals. The mass magnetic susceptibility χ_g of the complex can be calculated using the frequency difference $\Delta\nu$, the mass m of the complex, the spectrometer frequency ν , the mass susceptibility of the solvent χ_g^{solvent} , and the densities of both the solvent ρ_{solvent} and the solution ρ_{solution} .^[50]

$$\chi_g = \frac{3\Delta\nu}{4\pi\nu m} + \chi_g^{\text{solvent}} + \chi_g^{\text{solv}} \frac{\rho_{\text{solution}} - \rho_{\text{solvent}}}{m} \quad (2 - 9)$$

As the spin crossover is accompanied by a significant change in bond lengths - up to 10 % - and in the geometry of the metal coordination environment, the transition can be monitored by variable temperature single crystal X-ray diffraction. The bond lengths for both spin states can be compared by calculating the average bond length $\bar{d}_{\text{Fe-L}}$ for each spin state.^[21]

$$\bar{d}_{\text{Fe-L}} = \frac{1}{6} \sum_{i=1}^6 |d_i| \quad (2 - 10)$$

Commonly, the high spin state and low spin state differ, with the average bond lengths for the low spin state ranging from 1.96 Å to 2.00 Å, while the high spin state exhibits longer bond lengths between 2.16 Å and 2.20 Å. The *Jahn-Teller* effect, caused by the asymmetric population of the t_{2g} orbitals in the high spin state, leads to a distortion of the octahedral coordination environment. This distortion can be characterized by the angular distortion parameter Σ_O , which quantifies the deviation of the 12 cis angles α_i from the ideal 90° of a perfect octahedron, and by the torsional distortion parameter θ_O , derived from the triangular faces formed by three donor atoms, with respect to the threefold axis normal vector and the distortion towards a trigonal prism geometry.^[51]

$$\Sigma_O = \sum_{i=1}^{12} |90^\circ - \alpha_i| \quad (2 - 11)$$

$$\theta_O = \sum_{i=1}^{24} |60^\circ - \theta_i| \quad (2 - 12)$$

In the case of a perfect octahedral geometry, the angular distortion parameter Σ_O equals zero. For the high spin state, the distortion can reach values of 80° or more. The torsional distortion parameter θ_O is typically small for the low spin state compared to the high spin state, although these values can vary significantly between different complexes.^[51]

An iron-specific method for determining the spin state is ^{57}Fe -Mössbauer spectroscopy. The starting nucleus for iron(II) is $^{57}_{27}\text{Co}$, which decays via an electron capture (EC) reaction that removes an electron from the K-shell, producing an excited $I = 5/2$ ^{57}Fe nucleus. This excited state subsequently decays to the $I = 3/2$ state. The energy difference between the $I = 3/2$ excited state and the ground state $I = 1/2$ for the iron nucleus is 14.4 keV, at which point the emitter emits a gamma quantum (γ), and the absorber is excited recoillessly.^[52,53]

To modulate the energy of the emitted γ , the *Doppler effect* is employed by moving the emitter and absorber at different relative velocities. Three key pieces of information can be obtained from these measurements.^[52,53]

The *isomeric shift* (δ) arises from differences in the electron density around the iron(II) centre, affected by the oxidation state and coordination environment, relative to the absorber material.^[52,53] This shift differs between the low spin and high spin states. *Quadrupole splitting* (QS) occurs when the coordination environment around the iron(II) ion is distorted, leading to an anisotropic charge distribution due to oxidation state, spin state, and symmetry considerations. For example, a low spin iron(II) centre with a $t_{2g}^6 e_g^0$ configuration in a perfect octahedral environment exhibits no quadrupole splitting, whereas a high spin iron(II) shows measurable quadrupole splitting. Additionally, *magnetic hyperfine splitting* (IS) can be observed when an external magnetic field is applied, splitting the excited $I = 3/2$ and ground $I = 1/2$ states into magnetic sublevels characterized by $M_I = 2I + 1$ with the selection rule $\Delta m_I = -1, 0, +1$.^[52,53]

Mössbauer spectroscopy is a powerful tool for spin state identification due to the variety of accessible information about the electronic and geometric environment of the iron centre.

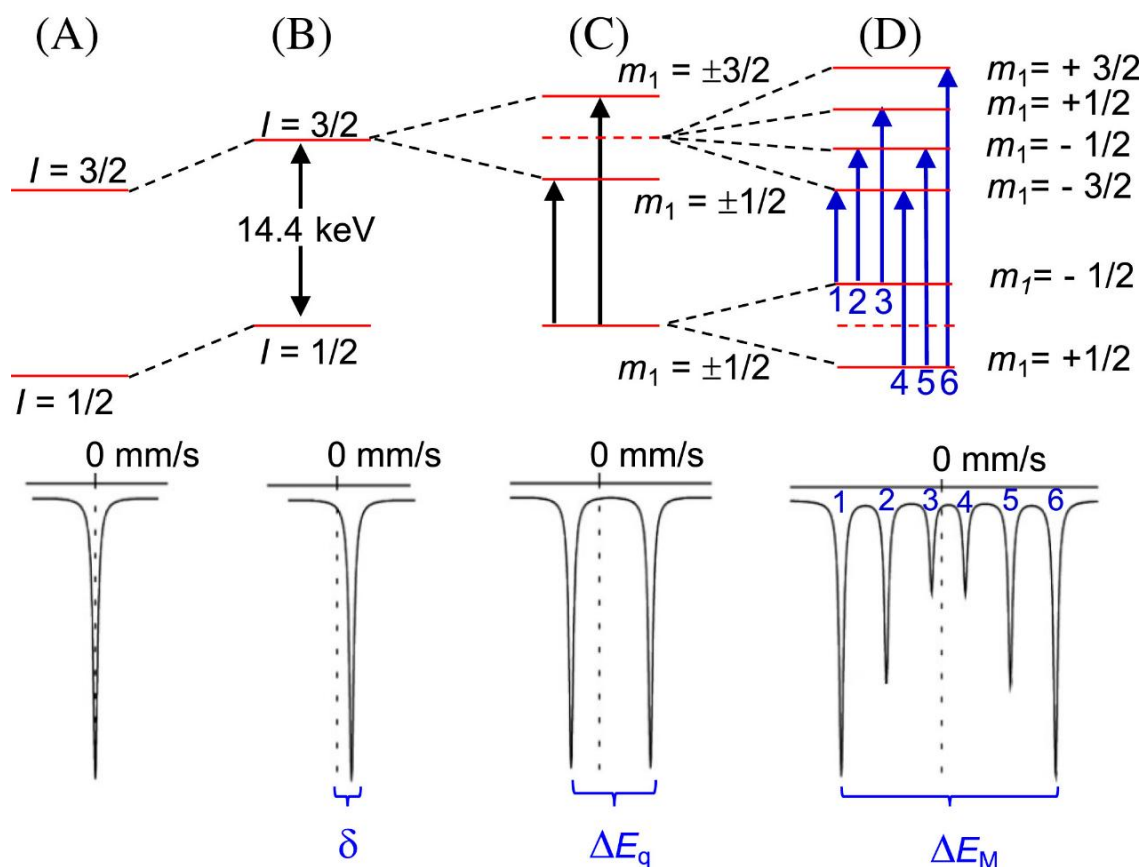


Figure 7: Schematic representation of the impact of the isomeric shift, the quadrupole splitting and the magnetic splitting on the energy difference between the $l = 1/2$ state and $l = 3/2$ state as well as on the measured resonance signal.^[54] Reprinted from literature with permission.

The spin transition involves not only a change in the orbital population between the low spin and high spin states but also a shift in the ligand field splitting energy. This effect can be described as thermochromism. The relevant electronic transitions occur between the t_{2g} orbitals and the antibonding e_g^* orbitals. According to the *Laporte* rule, these transitions are formally forbidden, although they are spin allowed. The low intensity of these transition bands limits the use of spin crossover complexes as materials for light-based readout sensors.^[16,55,56] To overcome this limitation, emissive functional groups have been introduced into the ligand system. The emission of these groups can undergo energy transfer to the ligand field transitions, providing an alternative pathway. In principle, the low spin state quenches the fluorescence of the fluorophoric group by transferring energy to the iron(II) ligand field transitions.^[57–60] Upon spin crossover, this energy transfer is suppressed, allowing the fluorophoric group to emit light. This synergistic effect between spin crossover and luminescence has been demonstrated, for example, by Meneses-Sánchez and coworkers. They studied *Hofmann*-type coordination polymers incorporating anthracenyl units through an intrinsic ligand-based approach using bpan (bis(4-pyridyl)anthracene) as a connecting ligand, as well as extrinsic pyrene molecules in polymers built with bpb (bis(4-pyridyl)butadiyne). Both systems exhibited a strong

interplay between the spin crossover behaviour and luminescence properties, making them promising candidates for magneto-optic switches.^[61]

Further methods for the investigation of the spin crossover are not discussed in detail, but are summarized in the following table:

Table 1: Measurements techniques to investigate the spin transition properties, reported in literature.

Method	Abbreviation	Information	Literature
Infra-Red Spectroscopy	<i>IR</i>	Measuring vibration energy	[20,62]
Raman Spectroscopy	<i>Raman</i>	Measuring vibration energy	[63]
Differential scanning calorimetry	<i>DSC</i>	Identification of phase transition measuring the temperature dependent heat change	[64]
Electron Paramagnetic Resonance Spectroscopy	<i>EPR</i>	Measuring the <i>g</i> -value of the electrons for the high spin iron(II)	[65–67]
Nuclear Resonance Scattering	<i>NRS</i>	Measuring the <i>pDos</i> of the iron(II)-environment vibration	[68–70]
Muon Spin Relaxation	<i>μSP</i>	Information on the electronic structure and dynamics of the thermal spin transition	[71–73]
X-Ray Absorption Spectroscopy	<i>XAS</i>	Information on the local and electronic structure and their change due to spin transition	[74–78]

References:

- [1] J. S. Griffith, L. E. Orgel *Q. Rev., Chem. Soc.* **1957**, *11*, 381.
- [2] A. Hauser in *Spin Crossover in Transition Metal Compounds I* (Eds.: P. Gülich, H.A. Goodwin), Springer Berlin Heidelberg, Berlin, Heidelberg, **2004**, pp. 49–58.
- [3] L. G. Vanquickenborne, L. Haspeslagh *Inorg. Chem.* **1982**, *21*, 2448–2454.
- [4] J. A. Real, A. B. Gaspar, M. C. Muñoz *Dalton Trans.* **2005**, 2062.
- [5] V. Ksenofontov, A. B. Gaspar, P. Gülich in *Spin Crossover in Transition Metal Compounds III*, Springer-Verlag, Berlin/Heidelberg, **2004**, pp. 23–64.
- [6] S. P. Vallone, A. N. Tantillo, A. M. Dos Santos, J. J. Molaison, R. Kulmaczewski, A. Chapoy, P. Ahmadi, M. A. Halcrow, K. G. Sandeman *Adv. Mat.* **2019**, *31*, 1807334.
- [7] A. Hauser in *Spin Crossover in Transition Metal Compounds II*, Springer Berlin Heidelberg, Berlin, Heidelberg, **2004**, pp. 155–198.
- [8] G. Chastanet, C. Desplanches, C. Baldé, P. Rosa, M. Marchivie, P. Guionneau *Chem. Sq.* **2018**, *2*, 2.
- [9] P. O. Ribeiro, B. P. Alho, R. M. Ribas, E. P. Nóbrega, V. S. R. De Sousa, P. J. Von Ranke *J. Magn. Magn. Mater.* **2019**, *489*, 165340.
- [10] A. Bousseksou, F. Varret, M. Goiran, K. Boukheddaden, J. P. Tuchagues in *Spin Crossover in Transition Metal Compounds III*, Springer Berlin Heidelberg, Berlin, Heidelberg, **2004**, pp. 65–84.
- [11] E. Resines-Urien, E. Fernandez-Bartolome, A. Martinez-Martinez, A. Gamonal, L. Piñeiro-López, J. S. Costa *Chem. Soc. Rev.* **2023**, *52*, 705–727.
- [12] C.-M. Jureschi, J. Linares, A. Boulmaali, P. Dahoo, A. Rotaru, Y. Garcia *Sensors* **2016**, *16*, 187.
- [13] J. Linares, E. Codjovi, Y. Garcia *Sensors* **2012**, *12*, 4479–4492.
- [14] F. M. Raymo *Adv. Mater.* **2002**, *14*, 401–414.
- [15] O. Kahn, J. Kröber, C. Jay *Adv. Mater.* **1992**, *4*, 718–728.
- [16] L. H. Gade, Wiley, **1998**.
- [17] P. Gülich, E. Bill, A. X. Trautwein, Springer Berlin Heidelberg, Berlin, Heidelberg, **2011**.
- [18] P. Gülich, A. B. Gaspar, Y. Garcia *Beilstein J. Org. Chem.* **2013**, *9*, 342–391.
- [19] P. Gülich, A. Hauser, H. Spiering *Angew. Chem. Int. Ed. Engl.* **1994**, *33*, 2024–2054.
- [20] J. A. Wolny, R. Diller, V. Schünemann *Eur. J. Inorg. Chem.* **2012**, *2012*, 2635–2648.
- [21] W. Nicolazzi, A. Bousseksou *Comptes Rendus. Chimie* **2018**, *21*, 1060–1074.
- [22] M. Sorai, S. Seki *J. Phys. Chem. Solid.* **1974**, *35*, 555–570.
- [23] K. Ridier, G. Molnár, L. Salmon, W. Nicolazzi, A. Bousseksou *Solid State Sciences* **2017**, *74*, A1–A22.
- [24] S. Brooker *Chem. Soc. Rev.* **2015**, *44*, 2880–2892.

- [25] A. B. Gaspar, M. Seredyuk *Coord. Chem. Rev.* **2014**, *268*, 41–58.
- [26] B. Weber, F. A. Walker *Inorg. Chem.* **2007**, *46*, 6794–6803.
- [27] M. Palacios-Corella, V. García-López, J. C. Waerenborgh, B. J. C. Vieira, G. Mínguez Espallargas, M. Clemente-León, E. Coronado *Chem. Sci.* **2023**, *14*, 3048–3055.
- [28] T. Boonprab, W. Thammasangwan, G. Chastanet, M. Gonidec, P. Harding, D. J. Harding *Crystal Growth & Design* **2024**, *24*, 8145–8152.
- [29] G. Lemerrier, N. Bréfuel, S. Shova, J. A. Wolny, F. Dahan, M. Verelst, H. Paulsen, A. X. Trautwein, J. Tuchagues *Chem. Eur. J.* **2006**, *12*, 7421–7432.
- [30] S. Ossinger, C. Näther, A. Buchholz, M. Schmidtman, S. Mangelsen, R. Beckhaus, W. Plass, F. Tuczek *Inorg. Chem.* **2020**, *59*, 7966–7979.
- [31] A. Dürrmann, G. Hörner, D. Baabe, F. W. Heinemann, M. A. C. De Melo, B. Weber *Nat Commun* **2024**, *15*, 7321.
- [32] J. Kiehl, T. Hochdörffer, L. M. Carrella, V. Schünemann, M. H. Nygaard, J. Overgaard, E. Rentschler *Inorg. Chem.* **2022**, *61*, 3141–3151.
- [33] G. Azzolina, R. Bertoni, E. Collet *J. Appl. Phys.* **2021**, *129*, 085106.
- [34] T. Matsumoto, G. N. Newton, T. Shiga, S. Hayami, Y. Matsui, H. Okamoto, R. Kumai, Y. Murakami, H. Oshio *Nat. Commun.* **2014**, *5*, 3865.
- [35] D. Chernyshov, M. Hostettler, K. W. Törnroos, H. Bürgi *Angew. Chem. Int. Ed.* **2003**, *42*, 3825–3830.
- [36] N. Ortega-Villar, M. Muñoz, J. Real *Magnetochemistry* **2016**, *2*, 16.
- [37] Y. Garcia, O. Kahn, L. Rabardel, B. Chansou, L. Salmon, J. P. Tuchagues *Inorg. Chem.* **1999**, *38*, 4663–4670.
- [38] A. Hauser *Coord. Chem. Rev.* **1991**, *111*, 275–290.
- [39] B. Ordejón, C. De Graaf, C. Sousa *J. Am. Chem. Soc.* **2008**, *130*, 13961–13968.
- [40] G. Chastanet, M. Lorenc, R. Bertoni, C. Desplanches *Comptes Rendus. Chimie* **2018**, *21*, 1075–1094.
- [41] P. Gütllich, Y. Garcia, H. A. Goodwin *Chem. Soc. Rev.* **2000**, *29*, 419–427.
- [42] J.-F. Létard *J. Mater. Chem.* **2006**, *16*, 2550–2559.
- [43] J.-F. Létard, L. Capes, G. Chastanet, N. Moliner, S. Létard, J.-A. Real, O. Kahn *Chem. Phys. Lett.* **1999**, *313*, 115–120.
- [44] T. Boonprab, S. J. Lee, S. G. Telfer, K. S. Murray, W. Phonsri, G. Chastanet, E. Collet, E. Trzop, G. N. L. Jameson, P. Harding, D. J. Harding *Angew. Chem. Int. Ed.* **2019**, *131*, 11937–11941.
- [45] K. Lünser, E. Kavak, K. Gürpınar, B. Emre, O. Atakol, E. Stern-Taulats, M. Porta, A. Planes, P. Lloveras, J.-L. Tamarit, L. Mañosa *Nat. Commun.* **2024**, *15*, 6171.

- [46] D. Gracia, V. Cuartero, C. Popescu, A. Trapali, T. Mallah, M.-L. Boillot, J. Blasco, G. Subías, M. Evangelisti *J. Mater. Chem. A* **2025**, *13*, 17944–17951.
- [47] S. Sundaresan, J. Kiehl, L. M. Carrella, E. Rentschler *Crystal Growth & Design* **2023**, *23*, 1648–1655.
- [48] S. Sundaresan, J.-G. Becker, J. Eppelsheimer, A. E. Sedykh, L. M. Carrella, K. Müller-Buschbaum, E. Rentschler *Dalton Trans.* **2023**, *52*, 13181–13189.
- [49] K. E. Burrows, S. E. McGrath, R. Kulmaczewski, O. Cespedes, S. A. Barrett, M. A. Halcrow *Chem. Eur. J.* **2017**, *23*, 9067–9075.
- [50] R. W. Hogue, S. Singh, S. Brooker *Chem. Soc. Rev.* **2018**, *47*, 7303–7338.
- [51] R. Ketkaew, Y. Tantirungrotechai, P. Harding, G. Chastanet, P. Guionneau, M. Marchivie, D. J. Harding *Dalton Trans.* **2021**, *50*, 1086–1096.
- [52] P. Gütllich *Chemie in unserer Zeit* **1970**, *4*, 133–144.
- [53] P. Gütllich *Chemie in unserer Zeit* **1971**, *5*, 131–141.
- [54] C. L. Bianchi, R. Djellabi, A. Ponti, G. S. Patience, E. Falletta *Can. J. Chem. Eng.* **2021**, *99*, 2105–2114.
- [55] O. G. Shakirova, I. A. Os'kina, E. V. Korotaev, S. A. Petrov, N. V. Kuratieva, A. Ya. Tikhonov, L. G. Lavrenova *IJMS* **2023**, *24*, 9853.
- [56] I. Bräunlich, S. Lienemann, C. Mair, P. Smith, W. Caseri *J Mater Sci* **2015**, *50*, 2355–2364.
- [57] C. Lochenie, K. Schötz, F. Panzer, H. Kurz, B. Maier, F. Puchtler, S. Agarwal, A. Köhler, B. Weber *J. Am. Chem. Soc.* **2018**, *140*, 700–709.
- [58] C. Yi, Y.-S. Meng, L. Zhao, N.-T. Yao, Q. Liu, W. Wen, R.-X. Li, Y.-Y. Zhu, H. Oshio, T. Liu *CCS Chem.* **2023**, *5*, 915–924.
- [59] K. Sun, J.-P. Xue, Z.-S. Yao, J. Tao *Dalton Trans.* **2022**, *51*, 16044–16054.
- [60] O. A. Qamar, F. Jamil, M. Hussain, M. Mustafa, R. U. Rehman, A. Inayat, M. S. Habib, M. Sajid *Chem. Pap.* **2023**, *77*, 7331–7359.
- [61] T. Delgado, M. Meneses-Sánchez, L. Piñeiro-López, C. Bartual-Murgui, M. C. Muñoz, J. A. Real *Chem. Sci.* **2018**, *9*, 8446–8452.
- [62] C. L. Zilverentant, G. A. Van Albada, A. Bousseksou, J. G. Haasnoot, J. Reedijk *Inorganica Chimica Acta* **2000**, *303*, 287–290.
- [63] Z. G. Lada *Magnetochemistry* **2022**, *8*, 108.
- [64] B. Papánková, M. Vrbová, R. Boča, P. Šimon, K. Falk, G. Miehe, H. Fuess *J. Therm. Anal. Calorim.* **2002**, *67*, 721–731.
- [65] E. N. Frolova, O. A. Turanova, L. V. Bazan, I. V. Ovchinnikov, A. N. Turanov *Appl. Magn. Reson.* **2024**, *55*, 987–1010.
- [66] T. A. Ivanova, I. V. Ovchinnikov, R. R. Garipov, G. I. Ivanova *Appl. Magn. Reson.* **2011**, *40*, 1–10.

- [67] N. E. Domracheva, A. V. Pyataev, V. E. Vorobeva, E. M. Zueva *J. Phys. Chem. B* **2013**, *117*, 7833–7842.
- [68] G. Félix, M. Mikolasek, H. Peng, W. Nicolazzi, G. Molnár, A. I. Chumakov, L. Salmon, A. Bousseksou *Phys. Rev. B* **2015**, *91*, 024422.
- [69] H. Paulsen, H. Grünsteudel, W. Meyer-Klaucke, M. Gerdan, H. F. Grünsteudel, A. I. Chumakov, R. Ruffer, H. Winkler, H. Toftlund, A. X. Trautwein *Eur. Phys. J. B* **2001**, *23*, 463–472.
- [70] H. Grünsteudel, H. Paulsen, W. Meyer-Klaucke, H. Winkler, A. X. Trautwein, H. F. Grünsteudel, A. Q. R. Baron, A. I. Chumakov, R. Ruffer, H. Toftlund *Hyperfine Interactions* **1998**, *113*, 311–317.
- [71] S. J. Blundell, F. L. Pratt, T. Lancaster, I. M. Marshall, C. A. Steer, S. L. Heath, J.-F. Létard, T. Sugano, D. Mihailovic, A. Omerzu *Polyhedron* **2003**, *22*, 1973–1980.
- [72] S. J. Campbell, V. Ksenofontov, Y. Garcia, J. S. Lord, Y. Boland, P. Gütlich *J. Phys. Chem. B* **2003**, *107*, 14289–14295.
- [73] O. Roubeau, P. C. M. Gubbens, D. Visser, M. Blaauw, P. Dalmás De Réotier, A. Yaouanc, J. G. Haasnoot, J. Reedijk, S. Sakarya, U. A. Jayasooriya, S. P. Cottrell, P. J. C. King *Chemical Physics Letters* **2004**, *395*, 177–181.
- [74] Y. Garcia, P. J. Van Koningsbruggen, G. Bravic, P. Guionneau, D. Chasseau, G. L. Cascarano, J. Moscovici, K. Lambert, A. Michalowicz, O. Kahn *Inorg. Chem.* **1997**, *36*, 6357–6365.
- [75] K. Hosoya, S. Nishikiori, M. Takahashi, T. Kitazawa *Magnetochemistry* **2016**, *2*, 8.
- [76] K. Kitase, T. Kitazawa *Dalton Trans.* **2020**, *49*, 12210–12214.
- [77] A. Michalowicz, J. Moscovici, J. Charton, F. Sandid, F. Benamrane, Y. Garcia *J Synchrotron Rad* **2001**, *8*, 701–703.
- [78] A. Y. Mohamed, M. Lee, K. Kitase, T. Kitazawa, J.-Y. Kim, D.-Y. Cho *Crystals* **2018**, *8*, 433.
- [79] V. Maliuzhenko, M. Weselski, J. Gregoliński, M. Książek, J. Kusz, R. Bronisz *Inorg. Chem.* **2024**, *63*, 17762–17773.
- [80] D.-H. Ren, X.-L. Sun, L. Gu, D. Qiu, Z. Li, Z.-G. Gu *Inorg. Chem. Commun.* **2015**, *51*, 50–54.
- [81] Z.-G. Gu, C.-Y. Pang, D. Qiu, J. Zhang, J.-L. Huang, L.-F. Qin, A.-Q. Sun, Z. Li *Inorg. Chem. Commun.* **2013**, *35*, 164–168.
- [82] L.-F. Qin, C.-Y. Pang, W.-K. Han, F.-L. Zhang, L. Tian, Z.-G. Gu, X. Ren, Z. Li *Dalton Trans.* **2016**, *45*, 7340–7348.
- [83] T. Hashibe, T. Fujinami, D. Furusho, N. Matsumoto, Y. Sunatsuki *Inorg. Chim. Acta* **2011**, *375*, 338–342.
- [84] L. Tian, C.-Y. Pang, F.-L. Zhang, L.-F. Qin, Z.-G. Gu, Z. Li *Inorg. Chem. Commun.* **2015**, *53*, 55–59.
- [85] L.-F. Qin, C.-Y. Pang, W.-K. Han, F.-L. Zhang, L. Tian, Z.-G. Gu, X. Ren, Z. Li *CrystEngComm* **2015**, *17*, 7956–7963.

- [86] W.-K. Han, L.-F. Qin, C.-Y. Pang, C.-K. Cheng, W. Zhu, Z.-H. Li, Z. Li, X. Ren, Z.-G. Gu *Dalton Trans.* **2017**, *46*, 8004–8008.
- [87] Y. Sekimoto, M. R. Karim, N. Saigo, R. Ohtani, M. Nakamura, S. Hayami *Eur. J. Inorg. Chem.* **2017**, *2017*, 1049–1053.
- [88] G. Li, O. Stefanczyk, K. Kumar, L. Guérin, K. Okuzono, K. Tran, M. Seydi Kilic, K. Nakabayashi, K. Imoto, A. Namai, Y. Nakamura, S. Ranjan Maity, F. Renz, G. Chastanet, S. Ohkoshi *Angew. Chem. Int. Ed.* **2025**, *64*, e202423095.
- [89] H. Ando, Y. Nakao, H. Sato, S. Sakaki *Dalton Trans.* **2010**, *39*, 1836–1845.

Ligand design of chiral Spin crossover complexes

Over the last decades different approaches of introducing chirality in the ligand design for spin crossover complexes were reported. The impact of the chirality and the design strategies are summarized in the next chapter, based on known literature examples of chirality introduced in iron(II) spin crossover complexes. The choice of ligand design in the structures discussed to improve spin crossover will be addressed, as well as the investigation of peripheral influences through ligand modification. Three major families of designed ligands - *Schiff* base ligands, ligands based on the ethylenediamine motif, and the *pybox* system - are discussed, along with ligands that cannot be assigned to these three main families. Additionally, structure-property relationships of complexes with implemented chirality will be presented in these chapter, as the knowledge about the impact of chirality and the possible results is essential for further design strategies.

The results are presented in the form of a scientific review and planned for publication.

Author contribution:

The Manuscript was written by [REDACTED], with input from [REDACTED] and [REDACTED]. [REDACTED]; [REDACTED] had the supervision during the manuscript process. All Authors have read and agreed to the published version of the manuscript.

Manuscript: Combining Chirality and Spin Crossover: Design Strategy and Functionality

████████████████████
¹Department Chemie, Johannes-Gutenberg-Universität Mainz, Duesbergweg 10–14, 55128 Mainz, Germany.
Email: ████████████████████

Abstract:

Investigations into the role of chirality in light-harvesting systems and catalysis have advanced in recent decades. The incorporation of this property, widespread in nature, into coordination units such as molecular switches has attracted increasing interest over the years. In this review, we discuss the various approaches to introducing chirality into well-established spin crossover systems and the impact of ligand design on their properties. Furthermore, we present examples of structure-property relationships between stereoisomers in chiral spin crossover complexes, as well as reports of their multifunctionality.

Introduction:

The investigation of spin crossover (*SCO*) complexes has gained significant interest over the past decades.^[1-3] This phenomenon occurs in 3d transition metals with electron configurations ranging from d^4 to d^7 .^[4] For *SCO* to take place, the crystal field splitting energy (Δ) in an octahedral field - between the e_g and t_{2g} orbitals - must be comparable to the spin pairing energy (P), which favours the high-spin state.^[4] When the energy difference between Δ and P falls within the range of thermal energy (k_bT), a temperature driven transition between two possible spin states can occur: a high-spin state when $\Delta < P$ and a low-spin state when $\Delta > P$.^[4]

This transition can be triggered by external stimuli such as temperature^[4], pressure^[5], magnetic fields^[6], or light irradiation^[7,8] - known as the *LIESST* (Light-Induced Excited Spin-State Trapping) effect. The *SCO* is accompanied by structural changes, as well as temperature-dependent variations in magnetization, optical properties, and electronic behaviour.^[9-12] Among the various transition metal ions, iron(II) is one of the most extensively studied.^[13] Its spin transition occurs between the diamagnetic low-spin state A_{1g} ($S = 0$) and the paramagnetic high-spin state ${}^5T_{2g}$ ($S = 2$), offering opportunities to utilize these complexes as molecular switches, sensors, data storage elements, and in diverse nanotechnological applications.^[3,13,14]

Chirality plays a crucial role in nature, offering a means of information storage and serving as a key factor in structure-directed assembly.^[15-18] Molecular handedness is evident at the biomolecular level

- for instance, in proteins, amino acids, carbohydrates, and terpenes - where it significantly influences both structure and function.^[19] In biomolecules, the most observed form of chirality is point chirality, which arises from four distinct substituents bonded to a central atom. The chirality of individual molecules can also manifest in supramolecular architectures, such as helical structures.^[20]

Helicity can be achieved and stabilized by supramolecular structures in nature, such as DNA or α -helix, through intramolecular interactions, for example, H-bondings or electrostatic interactions.^[21] The rigidity of the peptide helix influences the direction of enzymatic reactions. The low helicity favours the formation of intramolecular cycles, which in turn promotes intramolecular processes.^[22]

Two non-superimposable mirror-image isomers are called enantiomers. While each enantiomer displays nearly identical properties on its own, their behaviour can differ significantly when interacting with other chiral molecules, forming diastereomeric pairs. This distinction is particularly important in nature and modern chemistry^[23], especially in fields such as drug design^[24], asymmetric catalysis^[25], and analytical chemistry for chiral separations^[18]. Chiral effects like the *CISS* (Chiral-Induced Spin Selectivity) effect - where molecular chirality influences electron spin - have attracted substantial interest due to their broad application potential in spintronics (e.g., spin valves), catalysis (e.g., the oxygen evolution reaction, *OER*), and enantioselective separations.^[26]

The interplay between chirality and *SCO* presents exciting opportunities for multifunctional materials, where the response can be modulated by molecular chirality - such as in the proposed *CD-LIESST* (Circular Dichroism-Light Induced Excited Spin State Trapping) effect. The influence of chirality on light-induced spin-state dynamics has been explored by *Oppermann et al.*, who demonstrated that in tris-ligated complexes with bidentate bispyridine derivatives, the relaxation pathway of the *LIESST* effect involves a *Ray-Dutt* twist and a corresponding change in optical activity, as observed by time-resolved circular dichroism (*TRCD*).^[27] Since chirality removes centrosymmetry in a molecular complex, such materials can also exhibit second harmonic generation (*SHG*) in conjunction with light-switchable *SCO*, as demonstrated by *Ohkoshi et al.* or *Iazzolino et al.* - marking a significant step toward magneto-optical devices.^[28,29] Further applications of these multifunctional materials lie in the coupling between *SCO* and ferroelectricity - enabled by non-centrosymmetric crystal structures. Investigations by *Han et al.* or *Ru et al.* have explored this field.^[30,31]

Chirality can be introduced into *SCO* complexes through various strategies. One of the earliest methods involves spontaneous resolution into Δ - and Λ -isomers that crystallize as enantiopure crystals. This was demonstrated by *Bartual-Murgui et al.* for *cis*-[Fe(bqen)(NCE)₂] complexes (bqen = N,N'-bis(8-quinolyl)ethane-1,2-diamine; E = S, Se), where both enantiopure and racemic crystals (with alternating Δ - and Λ -isomers) were observed.^[32]

A similar case was reported by Kühne et al. 2022 investigating the complex $[\text{Mn}(\text{4-OMe-Sal}_2\text{323})]\mathbf{A}$ with various achiral counterions $\mathbf{A} = \text{ClO}_4^-, \text{BF}_4^-, \text{NO}_3^-, \text{Br}^-$ and I^- , verifying the chiral resolution by CD-spectroscopy.^[33] Kelly et al. could reveal the same spontaneous resolution of both enantiomers by crystallisation of the manganese(III) complex $[\text{Mn}^{\text{III}}(\text{R-sal}_2\text{323})]\text{NCS} \cdot \text{EtOH}$, formed via self-assembly of a Schiff base ligand from 1,2-bis(3-aminopropylamino)ethane and 2-hydroxybenzaldehyde, yielding enantiomeric Δ - and Λ -isomers.^[34]

Besides spontaneous resolution, chirality can also be induced through external chiral sources, such as chiral counterions, solvents, or guests in the coordination environment. Gural'skiy et al. employed *L*-camphorsulfonate as a counterion in a 1D SCO polymer based on 4-amino-1,2,4-triazole. This resulted in nanoparticles exhibiting abrupt spin transitions with hysteresis, along with temperature-dependent circular dichroism (CD) signals.^[35]

Chiral recognition by chiral anions was 2019 demonstrated by Jakobsen et al. in a manganese(III) complex $[\text{Mn}\{\text{5-OCF}_3\text{-sal}_2\text{323}\}]^+$. Using (*R,R*)- or (*S,S*)-bis[1,1'-binaphthyl-2,2'-diolato]borate anions, they generated helical 1D structures with defined helicities (*S* \rightarrow *M*, *R* \rightarrow *P*). The system exhibited gradual and incomplete SCO with $T_{1/2}(\text{S}) = 391$ K and $T_{1/2}(\text{R}) = 388$ K, where the differences were attributed to varying degrees of solvation.^[36]

Chiral solvents can also induce chirality.^[37] Gural'skiy et al. demonstrated this using 2-butanol, while Qin et al. reported chiral recognition of solvents like lactonitrile or methylglutaronitrile using chiral iron(II) SCO hosts.^[38,39]

A more direct and effective strategy is the introduction of chirality into the ligand framework itself, where the chiral centre is in close proximity to the metal centre. This approach will form the focus of this review. The scope of the review will not include chiral SCO involving other metals such as cobalt(II) or manganese(III) due to the limited number of examples. One such rare case was reported by Zhang et al. for cobalt(II) complexes with a chiral imine ligand, where enantiopure complexes displayed gradual SCO, whereas the racemate remained in the high-spin state.^[40]

Designing chiral ligands is synthetically more demanding but enables greater control and tunability. Chiral separation methods like HPLC or diastereomeric resolution are costly and inefficient, which restricts their broader application. In contrast, using enantiopure ligands simplifies access to enantiopure complexes and typically results in a single coordination chirality (e.g., Λ or Δ), as observed by Howson et al.^[41]

Introducing chirality at the ligand level also strengthens the chiral influence on the coordination environment, especially when placed close to the metal centre. The flexibility of modifying chiral moieties (e.g., amino acid derivatives) allows further control over the chiral environment and SCO behaviour. This is not as easily achieved with chiral anions or via separation techniques, which remain less common and more limited in variation.^[42,43] Chirality in the ligand backbone has been investigated

across systems of varying nuclearity, including mononuclear complexes, dinuclear helical complexes, and polynuclear frameworks. For instance, Maliuzhenko et al. used (*RR/SS*)-trans-1,2-di(tetrazol-1-yl)cyclopentane to synthesize enantiopure and racemic iron(II) coordination polymers. The racemic coordination polymers stayed in the high-spin state, while the enantiopure version showed *SCO* at $T_{1/2} = 144$ K (solvated) and $T_{1/2} = 228$ K (desolvated), due to differences in the coordination and anion networks.^[44] Similarly, Kawabata et al. created enantiopure and racemic *SCO* networks using iron(II)-NC-niob(IV) frameworks and 1-(3-pyridyl)ethanol as the ligand. The enantiopure networks, due to their non-centrosymmetric space groups, exhibited second harmonic generation - a rare example of spin-state-dependent nonlinear optical behaviour.^[45]

Chirality in polynuclear complexes was also reported by Flood et al., who designed helical Fe₂L₃ complexes via Schiff-base condensation with chiral amines. The handedness of the ligand directly determined the helicity of the resulting complex (*S* → *P*, *R* → *M*). The racemic system exhibited different packing and higher $T_{1/2}$ than the enantiopure forms.^[46]

Ren et al. similarly reported [Fe₄L₄] cage complexes, where ligand exchange and *SCO* behaviour were influenced by the chirality of the ligands.^[47]

This review focuses on mononuclear *SCO* complexes featuring chiral ligands, a class that has been investigated in recent decades in little more than twenty publications. We will highlight the design milestones of chiral ligands, the relationship between intra- and intermolecular interactions, and the influence of homochiral vs. heterochiral systems on *SCO* behaviour, including the spin transition profile and the critical temperature ($T_{1/2}$). We will also examine chirality-induced effects, such as ferroelectricity, resulting from non-centrosymmetric molecular symmetry.

The review is organized into four chapters according to the ligand design, as follows:

1. Bidentate Ligands of the Schiff Base Type
2. Tetradentate Ligands Featuring an Ethylenediamine Motif
3. Tridentate Ligands Incorporating a Pybox Motif
4. Additional Ligand Designs Beyond these Categories

1. Bidentate Ligands of the Schiff Base Type

Schiff-based ligands into which chirality is introduced are used for investigations of spin crossover (SCO) in a well-established family of iron(II) complexes. The design is pictured in **Figure 1**. A key advantage of this ligand system is its great modularity: the aldehyde component can be easily modified via nucleophilic substitution on the imidazole motive^[48], and many aldehydes are commercially available. Similarly, the amine component is affordable in various substituted forms, enabling electronic tuning of the ligand framework by aryllic substitution^[49] or incorporation of larger π -systems such as naphthyl groups.^[50]

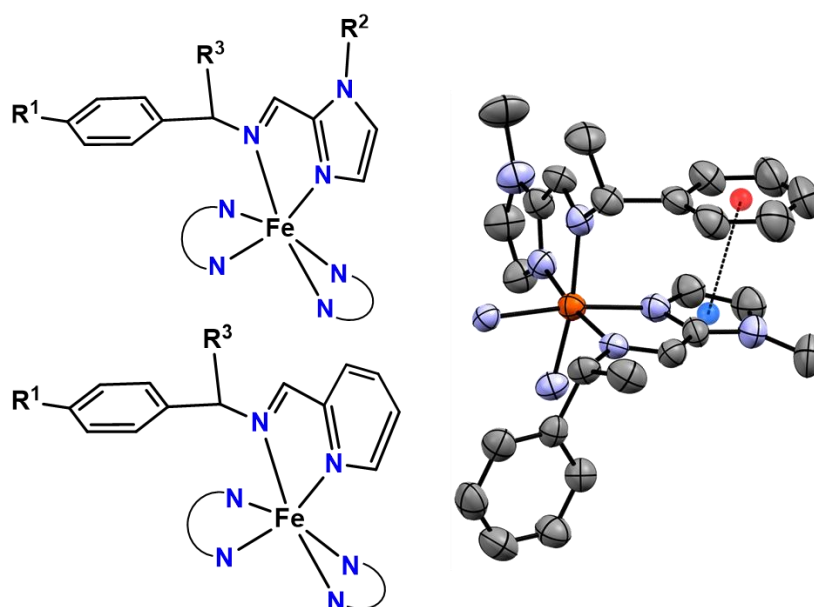


Figure 1: Ligand design for the chiral $[\text{Fe}(\text{L})_3]^{3+}$ based on chiral Schiff base ligands (left) and the intramolecular interaction between the imidazole and phenyl unit leading to the preferred enantiomer based on the chosen ligand chirality.^[51]

The earliest report of complexes containing chiral bidentate *Schiff* base ligands and iron(II) were published by Howson et al. in 2009.^[51] They employed pyridyl-units and focused on the influence of ligand chirality on the preferential formation of coordination isomers (Δ -fac, Λ -fac, Δ -mer, Λ -mer) in optically pure complexes, without investigating SCO properties. Their study demonstrated that the fac-isomer is stabilized by intramolecular interactions, which is shown in **Figure 1**.

In 2011, Howson et al. further investigated the steric impact of the R^3 substituent by varying it from a methyl to the bulkier ethoxymethylbenzene group, studying both zinc(II) and iron(II) complexes.^[41] For the iron(II) complex (**1**) with perchlorate counteranion and $\text{R}^1 = \text{H}$, $\text{R}^2 = \text{Me}$, $\text{R}^3 = \text{Me}$, a gradual SCO was observed, with the magnetic moment increasing from $0.9 \mu_{\text{B}}$ to $1.7 \mu_{\text{B}}$ at 300 K for the *R*-enantiomer. The role of intramolecular stabilization by π - π interactions between the pyridine and phenyl groups was confirmed by $^1\text{H-NMR}$ and *DFT* calculations.

The first complete *SCO* using the imidazole-motive was reported by Hashibe et al 2011., using 2-methylimidazol-4-yl-methylideneamino-*R*-(+)-1-methylphenyl as ligand for complex (**2**).^[52] The *fac-R-Λ* isomer exhibits an abrupt *SCO* with $T_{1/2} = 195$ K, where intermolecular hydrogen bonding was found to be key for strong cooperativity.

Gu et al. synthesized a related iron(II) complex using the Howson ligand design with substitution of the pyridyl- to the imidazole-motif (**3**): $R^1 = H$, $R^2 = Me$, $R^3 = Me$) and the tetrafluoroborate as counter anion (shown in **Figure 1** top). This complex shows an abrupt *SCO* at $T_{1/2} = 365$ K in the solvated form. Heating leads to a more gradual transition with a narrow hysteresis loop of $\Delta T = 3$ K ($T_{1/2}^{\uparrow} = 222$ K and $T_{1/2}^{\downarrow} = 219$ K) for both enantiomers. Interestingly, the *S*-enantiomer yielded the Δ -isomer, while the *R*-enantiomer yielded the Λ -isomer.^[53] This reflects the impact of the chosen counter anion enabling different intermolecular interactions between the *SCO* molecules.^[54-56]

Qin et al. utilized a similar complex to explore chiral recognition of chiral solvents by enantiopure complexes. Solvation in racemic mixture of lactonitrile or methylglutaronitrile leads to crystallization of the complex with enantiopure solvent molecules in the lattice, suggesting potential for optical recognition of small organic molecules. As the boiling point of the used nitriles are higher compared to acetonitrile, this helps to maintain the *SCO* behaviour, unlike the solvent removal effects seen in related complexes.^[39]

Ren et al. studied the influence of alkyl chain length (R^2) and electronic substitution on R^1 in iron(II) perchlorate complexes.^[49] Single crystal *XRD* revealed the correlation between amine chirality and coordination isomer, while the electronic nature of R^1 and alkyl chain length significantly influence *SCO* behaviour. Increasing the alkyl chain length from propyl to hexyl resulted in more abrupt *SCO* and higher $T_{1/2}$ values ($T_{1/2}^{(4)} = 257$ K, $T_{1/2}^{(7)} = 282$ K), due to beneficial packing effects. A gradual and incomplete profile was found for (**5**) $R^1 = Cl$, $R^2 = \text{pentyl}$, $R^3 = Me$ ($T_{1/2} = 137$ K), in contrast to the incomplete but more abrupt *SCO* for (**6**) $R^1 = OMe$, $R^2 = \text{iso-butenyl}$, $R^3 = Me$ ($T_{1/2} = 375$ K).

Potential application in sensors and spintronics, results in investigation of attachment of *SCO* complexes to polymer matrices or surfaces being an active research area.^[57] Tian et al. grafted complexes with naphthyl substitution ($R^3 = Me$, $R^2 = Me$) and Merrifield peptide attachments via the substitution at the imidazole (R^2) motive with tetrafluoroborate and perchlorate as counteranions. Increasing aromatic bulk from phenyl (**3**) to naphthyl (**8**) reduces ligand field strength, resulting in a gradual incomplete *SCO* at $T_{1/2} = 150$ K. Switching the anion from tetrafluoroborate (**8**) to perchlorate (**9**) led to less complete *SCO*, attributed to the anion size. The grafted complexes (**10**) and (**11**) lost *SCO* behaviour, remaining high spin over the measured temperature range, as intermolecular interactions were suppressed by dilution.^[50]

Qin et al. further explored the effect of R^2 chain length (butyl, pentyl) with perchlorate counterions. While propyl complexes (**4**) show *SCO* at 257 K, the butyl derivative (**15**) remains high spin, and pentyl (**16**) shows *SCO* at 291 K. These findings underscore the influence of packing modulated by alkyl chain length, which is shown in **Figure 2**.^[58] Co-crystallization of pentyl and butyl enantiomers (**17**) slightly increases $T_{1/2}$ to 301 K due to packing stabilizing the low-spin state via strong intramolecular π - π interactions, causing less octahedral distortion around iron(II).

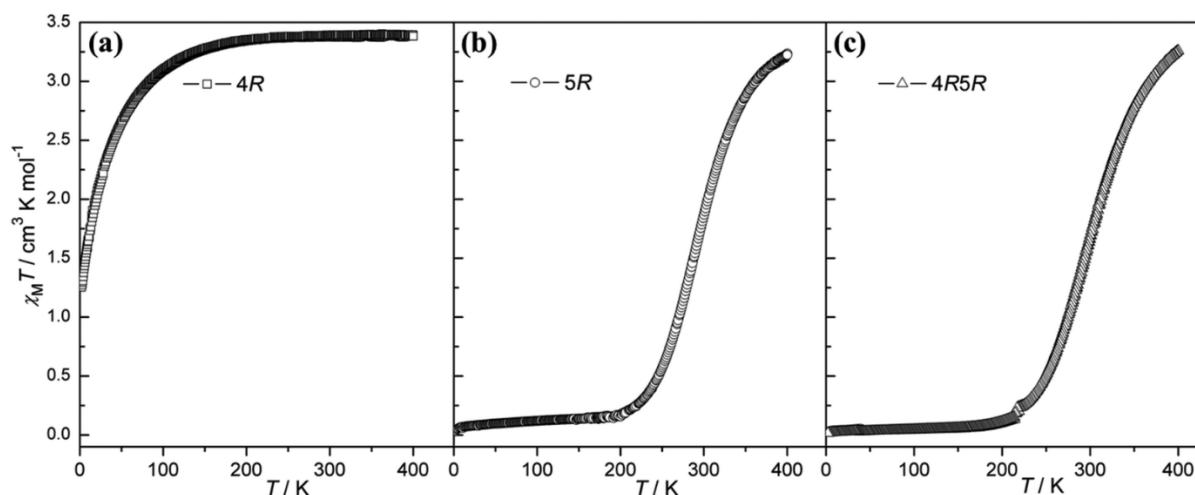


Figure 2: $\chi_M T$ vs T measured plot of the complexes (**15**) (left), (**16**) (middle) and (**17**) (right) to compare the impact of the variable chain lengths of R^2 .^[58] Reprinted from literature with permission.

The racemate mixture of the butyl complex (**18**) was shown by single crystal XRD to contain alternating Δ - and Λ -isomers, resulting in continuous, incomplete *SCO* at $T_{1/2} = 366$ K. This difference in packing and *SCO* behaviour between racemates and enantiopure complexes aligns with Wallach rule, which posits denser packing in racemates compared to the enantiopure complexes leading to increased $T_{1/2}$, due to stronger cooperativity.^[59] For the pentyl racemate (**19**), $T_{1/2}$ shifts to 346 K with a hysteresis of 46 K ($T_{1/2}^{\downarrow} = 369$ K, $T_{1/2}^{\uparrow} = 323$ K). Mixed racemates (**20**) with butyl and pentyl substituents exhibit similar *SCO* behaviour with smaller hysteresis (~ 11 K). Heating causes shifts to lower $T_{1/2}$ due to solvent loss effects. Temperature-dependent *CD* spectroscopy tracked *SCO* for the butyl complex.

Han et al. isolated two polymorphs of the butyl tetrafluoroborate complex: one (**21**) exhibits continuous *SCO* at $T_{1/2} = 294$ K (**Figure 3**), while the other (**22**) remains high spin, similar to the perchlorate complex.^[60] The second polymorph (**22**) crystallizes in a polar space group, exhibiting polarization from distorted iron(II) and ligand dipoles, giving rise to ferroelectricity - a rare example of multifunctionality combining chirality and *SCO*. The difference between the polymorphs arises from packing differences: C-H $\cdots\pi$ interactions localize at meta positions in (**21**) and para positions in (**22**) (**Figure 3**), leading to stronger intermolecular interactions and shorter bond lengths in (**21**).

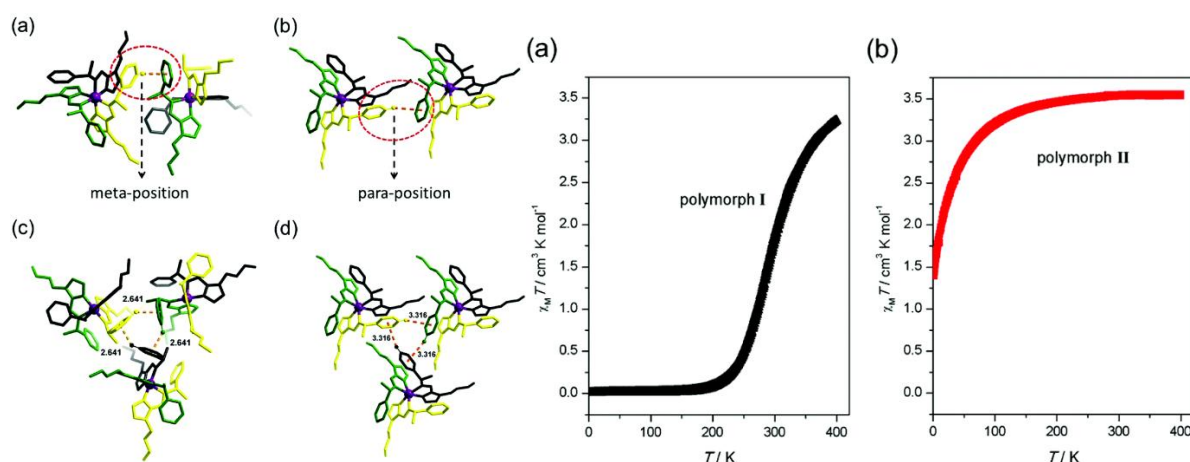


Figure 3: Intermolecular C-H- π -interactions between the complexes and the distance between the centroid and the H in angstrom in case of the polymorph I (**21**) (a) and (c) and (**22**) (b) and (d) (left) and the $\chi_M T$ vs T measured plot of the complexes (**21**) (a) black and (**22**) (b) red (right).^[60] Reprinted from literature with permission.

Sekimoto *et al.* replaced the phenyl ring with a cyclohexyl group, disrupting C-H... π interactions, important for cooperativity, using NCS as co-ligand to form neutral $[\text{FeL}_2(\text{NCS})_2]$ complexes ((**23**) and (**24**)).^[61] This substitution leads to incomplete, gradual SCO profiles in both enantiomers and racemic mixtures, with $T_{1/2} = 230$ K for pure enantiomers (**23**) and 193 K for the racemate (**24**) (single crystal data). Mössbauer spectroscopy and *LIESST* effect measurements confirm spin state transitions, with $T_{\text{LIESST}} = 60$ K.

Based on the presented research on the bidentate Schiff-base ligand design, we could clearly see the advantage of this offering vast tunability: increasing alkyl chain length correlates with higher SCO transition temperatures (propyl < butyl < pentyl < hexyl). Intermolecular interactions, including solvent effects, significantly influence SCO behaviour.^[49,53,58]

The stereochemistry of the ligand dictates the coordination isomer preference and affects SCO behaviour, largely driven by intramolecular interactions.^[41] Particularly the intramolecular interactions between aryl groups as \mathbf{R}^3 , which dictates Stereoisomers (Λ - or Δ -isomer) are different between phenyl and naphthyl substituents and thus show different impact on the SCO properties, as a larger π -system shifts the low spin stabilisation, which resulting in lower transition temperature.^[50,53] The nature of the \mathbf{R}^1 substituent also strongly influences the electronic properties and thus the SCO behaviour. The introduction of a methoxy group by Ren *et al.* resulted in a reduced $T_{1/2}$ of 137 K ($\mathbf{R}^3 = \text{Me}$, $\mathbf{R}^2 = \text{Pentyl}$, $\mathbf{A} = \text{ClO}_4^-$), in comparison to the unsubstituted analogue reported by Qin *et al.*^[49,58] Chirality-induced properties, such as ferroelectricity resulting from the polar packing of chiral ligands, underscore the potential of these materials for multifunctional applications, where spin crossover can be accompanied by temperature-dependent magnetization as well as polarization change.^[60]

Table 1: List of the chiral complexes based on the Schiff based ligand design.

Nr.	Stereoisomer	R ¹	R ²	R ³	A	Profile/Properties	T _{1/2} / K	Citation
1	<i>R</i>	H	Me	Me	ClO ₄	gradual incomplete		[41]
2	<i>R</i>	H	H	Me	ClO ₄	abrupt	195	[83]
3	<i>R/S</i>	H	Me	Me	BF ₄	gradual after desolvation, Hysteresis (3K)	365 222↑ 219↓	[81]
4	<i>R/S</i>	H	n-propyl	Me	ClO ₄	abrupt	257	[80]
5	<i>R/S</i>	Cl	isobutyl	Me	ClO ₄	abrupt incomplete	375	
6	<i>R/S</i>	OCH ₃	n-pentyl	Me	ClO ₄	gradual incomplete	137	
7	<i>R/S</i>	H	n-hexyl	Me	ClO ₄	gradual	282	
8	<i>R/S</i>	naphthyl	Me	Me	BF ₄	incomplete gradual	150	[84]
9	<i>R/S</i>	naphthyl	Me	Me	ClO ₄	incomplete gradual		
10	<i>R/S</i>	naphthyl	Polymer	Me	BF ₄	Polymer associated	HS	
11	<i>R/S</i>	naphthyl	Polymer	Me	ClO ₄	Polymer associated	HS	
12	<i>R</i>	H	Me	Me	ClO ₄	gradual after desolvation	355 220	[85]
13	<i>R</i>	H	Me	Me	ClO ₄		363	
14	<i>R</i>	H	Me	Me	ClO ₄		363	
15	<i>R/S</i>	H	n-butyl	Me	ClO ₄		HS	[82]
16	<i>R/S</i>	H	n-pentyl	Me	ClO ₄		291	
17	<i>R+R/S+S</i>	H	n-butyl + n- pentyl	Me	ClO ₄		301	
18	<i>Rac</i>	H	n-butyl	Me	ClO ₄		336	
19	<i>Rac</i>	H	n-pentyl	Me	ClO ₄	Hysteresis (46K)	323↑ 369↓	
20	<i>R+S/R+S</i>	H	n-butyl + n-pentyl	Me	ClO ₄	Hysteresis (11K)	335↑ 324↓	
21	<i>S</i>	H	n-butyl	Me	BF ₄		302	[86]
22	<i>S</i>	H	n-butyl	Me	BF ₄	ferroelectricity	HS	
23	<i>R/S</i>	cyclohexyl	pyridyl	Me	NCS		230	[87]
24	<i>Rac</i>	cyclohexyl	pyridyl	Me	NCS		193	

2. Tetradentate Ligands Featuring an Ethylenediamine Motif

One common strategy to improve the stability of the complex is to increase the hapticity of the ligands to tetradentate or even higher numbers of donor atoms.

Petzold *et al.* reported a comprehensive $^1\text{H-NMR}$ study on the racemic hexadentate ligand N^1, N^2 -bis([2,2'-bipyridine]-6-yl)methyl)-trans-cyclohexane-1,2-diamine. The kinetics and thermodynamics of the *SCO* were determined in various solvents.^[62] The 1,2-cyclohexanediamine motif for *SCO* iron(II) complexes with optically active ligands was also investigated by Ting-Ting *et al.*, using (*R/S*)- N^1, N^2 -bis(pyridin-2-ylmethyl)cyclohexane-1,2-diamine as ligand, where the iron(II) coordination sphere was accomplished by NCS_e co-ligands.^[63] Both enantiomers form different polymorphs that differ in their intermolecular packing: one polymorph crystallizes in a polar space group ((**26**)-II), while the other does not ((**26**)-I). The difference between the two polymorphs is based on intermolecular $\text{N}_{\text{amino}}\text{-H}\cdots\text{Se}$ hydrogen bonding, which is essential for building the 3D network. For the nonpolar polymorph ((**26**)-I), these interactions are stronger, suggesting stronger cooperative interactions. The packing of the racemate (**28**) follows the *Wallach* rule, as the density of the racemate is higher than that of both enantiopure polymorphs.^[59] In the racemate, the Λ - and Δ -enantiomers alternate in the packing, resulting in additional interactions such as inter-pair $\pi_{\text{pyridine}}\text{-}\pi_{\text{pyridine}}$ and $\text{C-H}\text{-}\pi_{\text{pyridine}}$ interactions. These strong interactions lead to an overall high-spin state, as measured by temperature-dependent *SQUID* magnetometry. This contrasts with the enantiopure polymorphs, where the stronger interactions in polymorph ((**26**)-I) leads to a more abrupt *SCO* at $T_{1/2} = 146$ K, while polymorph ((**25**)-I) exhibit a gradual *SCO* at $T_{1/2} = 160$ K (shown in **Figure 4**). *LIESST* and *reverse LIESST* experiments show an incomplete up to 90% reversible transition over several cycles for polymorph ((**26**)-I), which is promising for applications as photo switches (shown in **Figure 4**).^[64]

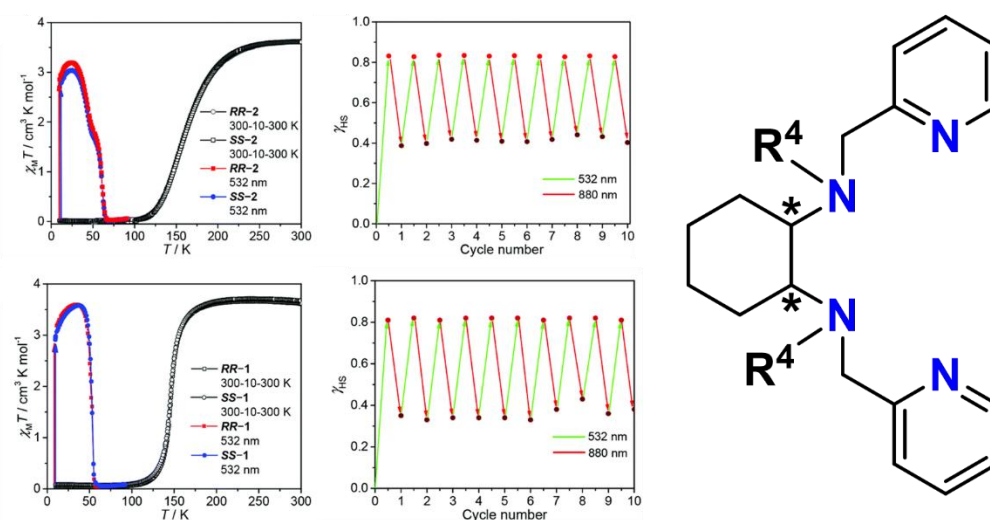


Figure 4: χ_{MT} vs T measured plot of the complexes (**25**) (above) and (**26**) (down) as well as reported *LIESST* measurements for both complexes and the schematic representation of the ligand design featuring the ethylenediamine motive (right).^[63] Reprinted from literature with permission.

By forming the complex with a Schiff base ligand based on pyridine-2-carbaldehyde via a *Manniche* reaction, Regueiro et al. obtained chiral carbon-bearing *RR*- or *SS*-L₁ = (1*R*,2*R*) or (1*S*,2*S*)-N¹,N²-bis(pyridin-2-ylmethyl)cyclohexane-1,2-diamine ligands for complex (**29**) and (**30**).^[65] The keto group forms intermolecular interactions with N–H hydrogen atoms, stabilizing the structure and enabling crystallization of both enantiomers. This reaction exemplifies diastereoselectivity in *Manniche* reactions mediated by iron(II).^[66,67] Complexes with both enantiopure ligands were obtained with NCS and NCS_e co-ligands.^[68,69] Little, to no molecular interactions are observed, also because, no solvent molecules were present for the molecular packing.

Consequently, all four complexes reveal a gradual spin transition profile. The NCS co-ligand leads to an incomplete *SCO* with a lower critical temperature at $T_{1/2} = 110$ K for (**29**), compared to the NCS_e-containing complex (**30**) ($T_{1/2} = 260$ K), which is shown in **Figure 5**, reflecting the stronger ligand field splitting of NCS_e, in accordance with the literature.^[68,69] *LIESST* measurements showed a photoconversion up to 80%, with the photoconversion efficiency being influenced by the sample preparation.

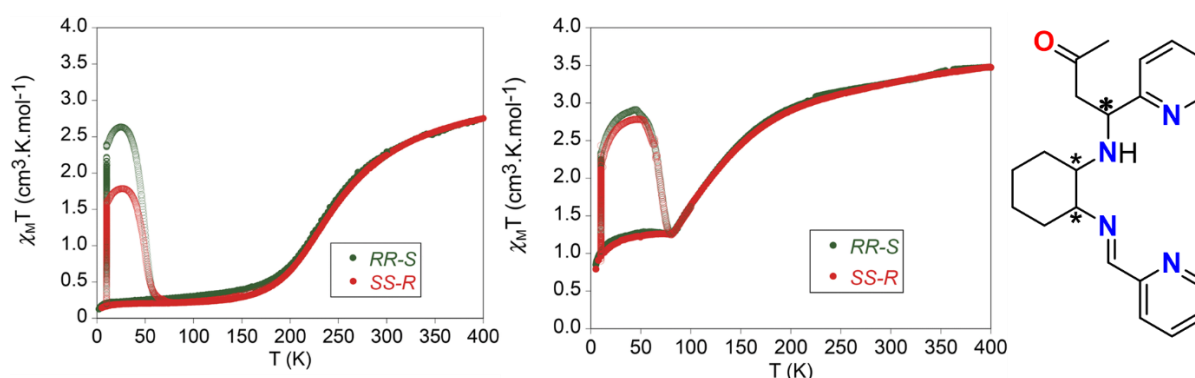


Figure 5: $\chi_M T$ vs T measured plot of the complexes (**30**) (left) and (**29**) (middle) as well as reported *LIESST* measurements for both complexes and enantiomers and the schematic representation of the ligand design featuring the ethylenediamine motive.^[65] Reprinted from literature with permission.

The well investigated motive was chosen by Zhao et al. to improve flexibility by incorporating chirality. They inserted a methyl group to reduce the number of chiral centres to one and incorporated benzyl groups for strong intermolecular π - π stacking interactions.^[70,71] Further investigations revealed a spring-like motion caused by the flexible benzyl rings and their intermolecular interactions, which is accompanied by a hysteresis profile for the *SCO*, as reported by Deng et al.^[72] Using the NCBH₃ co-ligand led to both enantiopure complexes (**31**) crystallizing in a polar space group, exhibiting an incomplete gradual spin transition at $T_{1/2} = 98$ K, which is represented in **Figure 6**. Desolvation of the sample (**31**) caused an overall high-spin state due to the reduction of hydrogen bonding in intermolecular interactions. Reversible *LIESST* measurements showed 75% metastable high-spin state

for solvated complexes (**31**), while the desolvated samples exhibited a rare reversible reverse *LIESST* photoconversion by 34%.

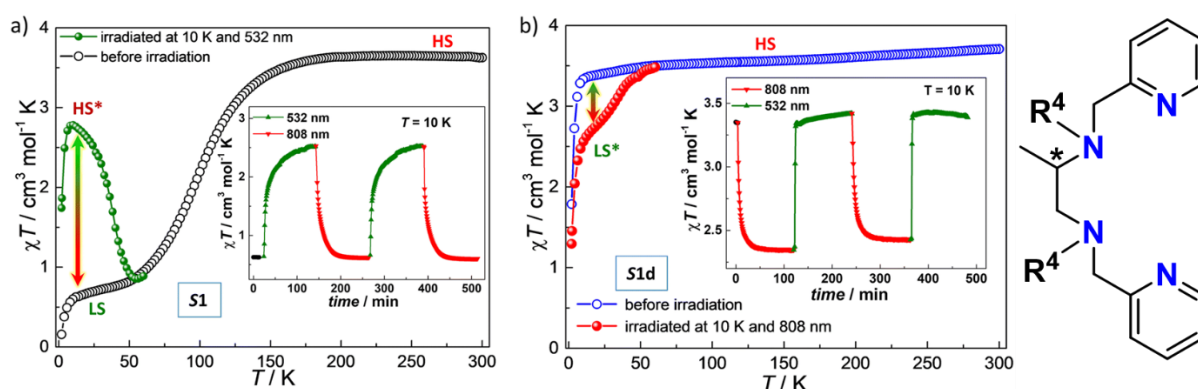


Figure 6: $\chi_M T$ vs T measured plot of the complexes (**31**) solvated (a) and (**31**) desolvated (b) as well as reported *LIESST* measurements for both complexes and enantiomers and the schematic representation of the ligand design featuring the ethylenediamine motive (right).^[71] Reprinted from literature with permission.

Increasing the ligand field strength of NCE co-ligands by improving interlinking between complexes via NC-Au-CN bridges has been reported in the literature and was uniquely applied in a follow-up study by Zhao et al.^[73] The benzyl spring-like motion combined with elastic Au-Au intermolecular interactions leads to two hysteresis profiles for the desolvated enantiopure complexes (**33**) (**Figure 7**). The first hysteresis occurs between 360 K and 380 K and is explained as a non-spin magnetic transition with $\Delta T = 32 \text{ K}$ ($T_{1/2}^\uparrow = 362 \text{ K}$, $T_{1/2}^\downarrow = 330 \text{ K}$), linked to a phase change driven by the movement of the benzylic units.^[72,74] Between 160 K and 280 K, an asymmetric hysteresis was observed, accompanied by a symmetry breaking to a polar space group due to the formation of strong Au-Au intermolecular interactions ($\Delta T = 42 \text{ K}$, $T_{1/2}^\uparrow = 220 \text{ K}$, $T_{1/2}^\downarrow = 178 \text{ K}$). The rotation of the benzylic units and the elasticity of the Au-Au interactions impart anisotropic “breathing” behaviour to the structure. The solvated complexes (**32**) show a gradual hysteresis profile with a two-step cooling profile ($\Delta T = 26 \text{ K}$, $T_{1/2}^\uparrow = 214 \text{ K}$, $T_{1/2}^\downarrow = 178 \text{ K}$ and $T_{1/2}^\downarrow = 210 \text{ K}$). The racemic complex (**34**) contains interacting Λ - and Δ -isomers linked via Au-Au, hydrogen bonding, and C-H \cdots π interactions, forming a 3D framework. These cooperative interactions result in a gradual transition profile for the solvated complex (**34**) ($T_{1/2} = 146 \text{ K}$) and the desolvated complex (**34**) ($T_{1/2} = 214 \text{ K}$), distinct from the enantiopure complexes.

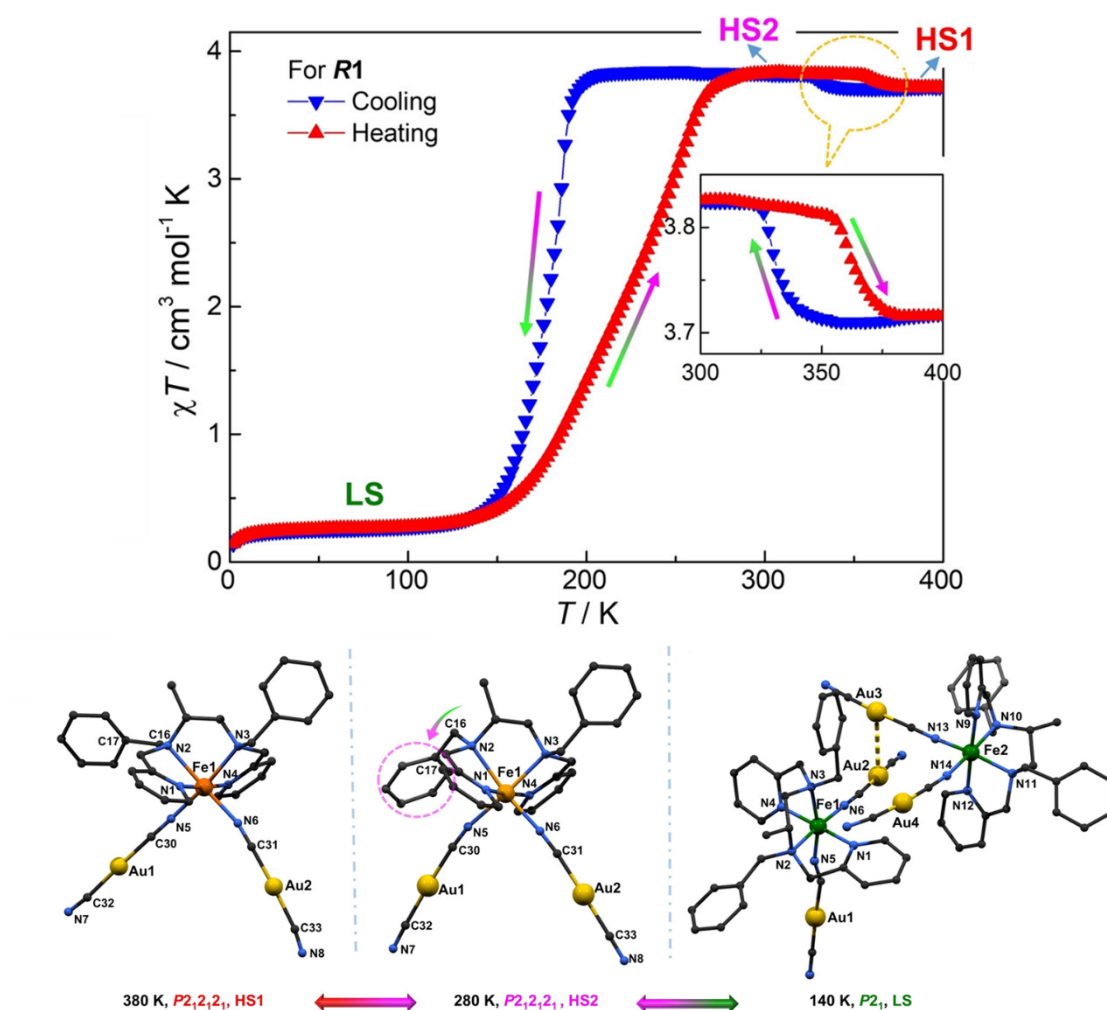


Figure 7: Molecular structure and intermolecular interactions of complex (33) for each crystallographic phase and $\chi_M T$ vs T measured plot of the complexes (33) solvated.^[73] Reprinted from literature with permission.

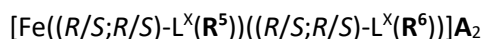
Both presented studies nicely show the tunability of the iron(II) complexes by variations of the coligands – not only for the ligand field strength but also for the difference in intermolecular interactions. Further, these examples show the potential of ligand modification with flexible groups (benzylic group) with small chiral influence (methyl group) for further ligand designs and interesting properties useful for potential applications. Further chiral diamine based on the ethylenediamine motif can be explored in the future.

Table 2: List of the chiral complexes based on the symmetric diamine ligand design.

Nr.	Stereoisomer	Basis	R ⁴	NCE	Profil	T _{1/2} / K	Citation
25	<i>RR/SS</i>	cyclohexyl		NCS	gradual	162	[63]
26	<i>RR/SS</i>	cyclohexyl		NCSe	gradual	146	
27	<i>Rac</i>	cyclohexyl		NCS		HS	
28	<i>Rac</i>	cyclohexyl		NCSe		HS	
29	<i>RR-S/SS-R</i>	cyclohexyl		NCS	gradual incomplete	110	[65]
30	<i>RR-S/SS-R</i>	cyclohexyl		NCSe	gradual	260	
31	<i>R/S</i>	diamine	benzyl	NCBH ₃	incomplete gradual	98	[71]
32	<i>R/S</i>	diamine	benzyl	NCBH ₃		HS	[73]
	<i>R/S</i>	diamine	benzyl	NCAuCN	1) Hysteresis (26K)	1) 214↑ 210↓ 2) 178	
33	<i>R/S</i>	diamine	benzyl	NCAuCN	After Desolvation	1) 362↑	[73]
					1) Hysteresis (32K)	330↓ 2) 220↑	
34	<i>Rac</i>	diamine	benzyl	NCAuCN	gradual	146	
					After Desolvation	214	

3. Tridentate Ligands Incorporating a Pybox Motif

One of the most extensively studied groups of chiral ligand systems for iron(II) *SCO* complexes is the substituted *pybox* = pyridine-2,6-bis(oxazoline) motif, which is also well-known in the field of asymmetric catalysis. Chirality can be introduced for example by using reduced amino acids in cyclization reactions, allowing for a wide range of easily implemented substitutions.^[75,76] In the following discussion, we will adopt a defined terminology to distinguish between the investigated complexes, using the general formula:



Here, *R/S* denotes the stereochemistry at the chiral centers of the substituent $\text{R}^{5/6}$ - since each ligand contains two stereocenters, both configurations must be specified. **X** represents the heteroatom within the chalcogenazole ring, $\text{R}^{5/6}$ is the ligand substituent, and **A** denotes the counterion (shown in **Figure 8**).

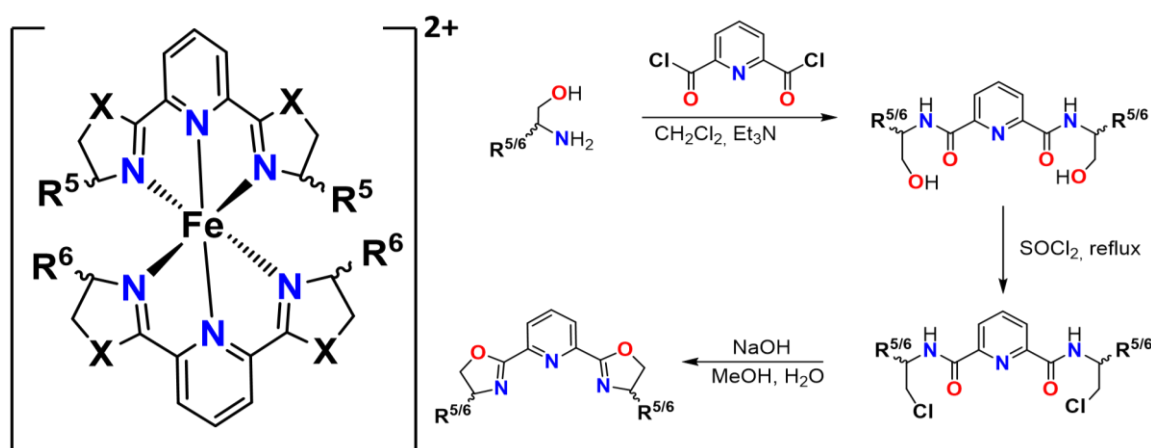


Figure 8: Schematic representation of the octahedral coordinated iron(II) complexes based on the reported *pybox* ligands (left) and the literature known synthesis route of these ligands based on the chosen amino alcohol.^[75,76]

The first investigation of chiral *pybox* ligand systems for iron(II) *SCO* compounds was reported by Burrows *et al.* in 2017. They examined the steric impact of the substituent $\text{R}^{5/6}$ by varying $\text{R}^{5/6}$ from Hydrogen, through methyl (Me) and phenyl (Ph) to isopropyl (ⁱPr), and analysed the influence of chirality by comparing the enantiopure $[\text{Fe}((R)\text{-L}^{\text{O}}(\text{R}^5)(R)\text{-L}^{\text{O}}(\text{R}^6))]^{2+}$ complex with the racemic $[\text{Fe}((R)\text{-L}^{\text{O}}(\text{R}^5)(S)\text{-L}^{\text{O}}(\text{R}^6))]^{2+}$ complex and perchlorate as anion **A**.^[77]

In the solid state, no clear trend was observed with regard to the steric effect on the spin transition. For the enantiopure *R*-enantiomers with $\text{R}^{5/6}$ = Me, Ph, and ⁱPr, only the Phenyl substitution (**42**) resulted in a gradual *SCO* at $T_{1/2}$ = 350 K, while the other complexes (**41**) and (**43**) remained in the high-spin state from 3 K to 350 K. Similar results were reported for the racemic mixture (**39**), which contains Phenyl substituent ($T_{1/2}$ > 400 K), whereas the complex with the isopropyl derivative (**40**) remained in

the high-spin state. It must be noted that the Phenyl groups promote intermolecular π - π interactions, and solvent molecules were identified in the crystal packing, contributing to differences in intermolecular interactions between these complexes.

Intramolecular interactions were explored by comparing the racemic and enantiopure complexes, as the orientation of the substituents $R^{5/6}$ interferes more in the enantiopure complex, resulting in a more twisted coordination sphere (shown in **Figure 9**). This leads to a more stabilized high-spin state, reflected in the lower critical temperature observed for the enantiopure complex.

To investigate the steric influence of the substituent $R^{5/6}$, Burrow *et al.* performed *Evans NMR* measurements, considering the redistribution of heterochiral to homochiral complexes.^[77] These measurements together with the solid state *SQUID* magnetometry measurements. Increasing the steric bulkiness of substituent $R^{5/6}$ caused an increase in $T_{1/2}$ from 192 K for **(35)** $R^{5/6}$ = Methyl to the complex **(43)** remaining in the high-spin state for $R^{5/6}$ = isopropyl in deuterated acetone. Since the solvent affects the spin transition in solution, $R^{5/6}$ = H and Phenyl, which both exhibit gradual *SCO* at $T_{1/2}$ = 245 K and 244 K in deuterated acetonitrile due to solubility issues, could not be fully compared.^[77] For $R^{5/6}$ = Phenyl, both enantiopure *R*-enantiomers **(42)** and the racemic complex **(39)** were measured in deuterated acetonitrile, confirming the gradual spin transition observed in the solid state. The steric interactions in the enantiopure complex **(38)** stabilize the high-spin state, shown by $T_{1/2}$ = 244 K, compared to 278 K for the racemic complex **(39)**.

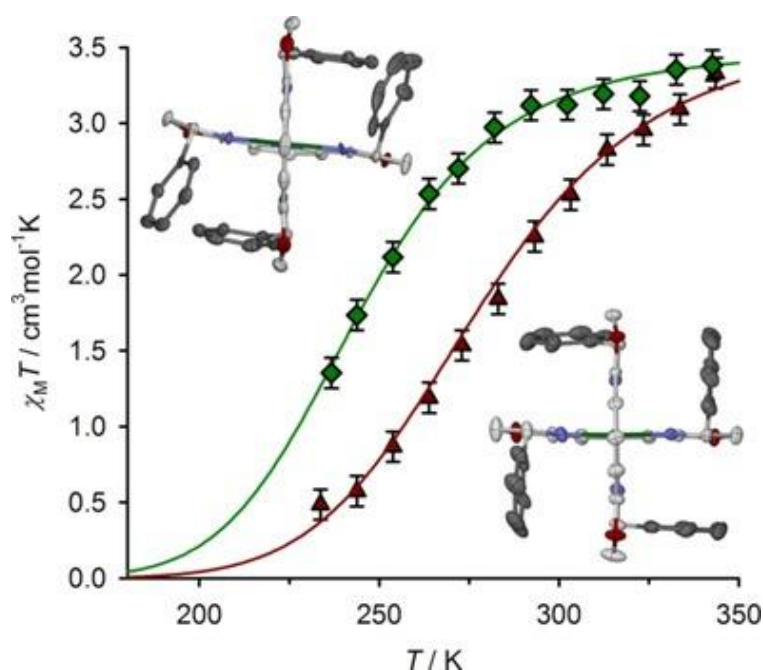


Figure 9: Representation of the impact of the intramolecular interactions in case of the enantiopure complexes and the racemic complex, leading to steric impact and χ_{MT} vs T measured plot of the complexes **(38)** (green) and **(39)** (red) for the *VT-NMR* measurements in solution.^[77] Reprinted from literature with permission.

R.-G. Wang *et al.* investigated the effect of the ligand symmetry by comparing the complexes $[\text{Fe}((R)\text{-L}^{\text{O}}(\mathbf{R}^5)(R)\text{-L}^{\text{O}}(\mathbf{R}^6)))]^{2+}$ (enantiopure), $[\text{Fe}((R)\text{-L}^{\text{O}}(\mathbf{R}^5)(S)\text{-L}^{\text{O}}(\mathbf{R}^6)))]^{2+}$ (racemic), and $[\text{Fe}((RS)\text{-L}^{\text{O}}(\mathbf{R}^5)(RS)\text{-L}^{\text{O}}(\mathbf{R}^6)))]^{2+}$ (meso) with $\mathbf{R}^{5/6} = \text{Phenyl}$ and $\mathbf{A} = \text{ClO}_4^-$, along with the influence of counter anion variations $\mathbf{A} = \text{BF}_4^-, \text{ClO}_4^-, \text{B}(\text{Ph})_4^-$ for the meso complex. They used data of the VT NMR solution study and the solid state magnetic measurements, which are shown in **Figure 9**.^[78] They could observe, that the anion plays a significant role in cooperativity known from the literature before.^[54–56]

The meso complex (**47**) with $\mathbf{A} = \text{ClO}_4^-$ shows a gradual spin transition reaching $2.05 \text{ cm}^3 \cdot \text{mol}^{-1} \cdot \text{K}$ at 400 K. Complex (**48**) with $\mathbf{A} = \text{BF}_4^-$ displays incomplete SCO ($\chi_M T = 0.7 \text{ cm}^3 \cdot \text{mol}^{-1} \cdot \text{K}$). In contrast, (**49**) with $\mathbf{A} = \text{PF}_6^-$ exhibits an abrupt SCO from 300 K, likely due to solvent loss; the desolvated form shows a two-step transition ($T_{1/2} = 360 \text{ K}$) with hysteresis $\Delta T = 20 \text{ K}$ ($T_{1/2}^{\uparrow} = 280 \text{ K}$, $T_{1/2}^{\downarrow} = 260 \text{ K}$). With $\mathbf{A} = \text{BPh}_4^-$, complex (**50**) undergoes a gradual, incomplete transition between 72 - 300 K.

To isolate the influence of packing and investigate symmetry effects, *Evans NMR* measurements combined with theoretical calculations of energy differences between optimized high-spin and low-spin geometries were performed. The enantiopure complex (**44**) exhibits two intramolecular interactions causing the strongest octahedral distortion and thus the most stabilized high-spin state with $T_{1/2} = 247 \text{ K}$, as well as the highest energy for both $S = 0$ and $S = 2$ states. The meso complex shows one intramolecular interaction, while the racemic complex has none, resulting in stabilization of the high-spin state with $T_{1/2} = 260 \text{ K}$ (meso/(**46**)) and $T_{1/2} = 281 \text{ K}$ (racemic/(**45**)), consistent with energy difference calculations.

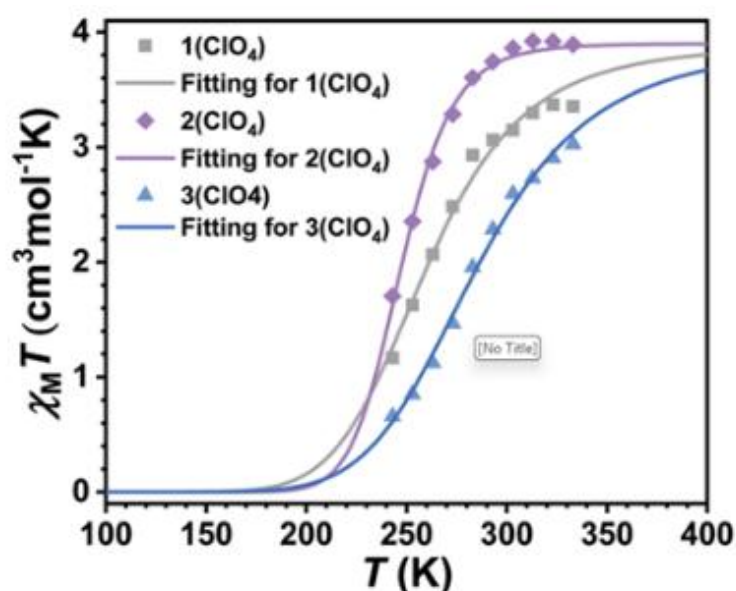


Figure 10: $\chi_M T$ vs T measured plot of the complexes (**44**) (= Nr. 2), (**45**) (= Nr. 3) and (**46**) (= Nr. 1) in case of VT-NMR measurements in solution.^[78] Reprinted from literature with permission.

To stabilize the low-spin state, electron-withdrawing and electron-donating groups, alongside steric effects, are considered crucial.^[79] Substituting the oxygen atom (**X**) with sulfur is expected to provide a stronger σ -donor effect, stabilizing the low-spin state. Shahid et al. introduced sulfur into ligands with $R^{5/6}$ = phenyl, isopropyl, and tert-butyl using perchlorate as the counteranion. To compare counteranion effects, tetrafluoroborate was used with $R^{5/6}$ = phenyl and **X** = S, in addition to **X** = O and $R^{5/6}$ = tert-butyl.^[80]

The anion's impact on the temperature-dependent solid-state magnetization was minor; both complexes with $R^{5/6}$ = phenyl and **X** = S and enantiopure ligands, comparing **A** = BF_4^- (**51**) and ClO_4^- (**53**), showed an abrupt *SCO* at $T_{1/2} = 330 \pm 2$ K with 50% conversion, followed by a gradual incomplete spin transition at 370 K. The racemic mixture (**55**) remained in the low-spin state up to 300 K, with a gradual increase in χ_{MT} indicating incomplete *SCO*.

For ligand $R^{5/6}$ = isopropyl the low-spin state is more stabilized for **X** = S (**59**), showing a gradual incomplete *SCO* at $T_{1/2} = 215$ K with 50% conversion, while the racemic complex (**60**) undergoes a 30% spin transition at 370 K. Complexes (**61**) and (**62**) containing oxygen (**X** = O) remain in the high-spin state over the entire temperature range.^[77] Consistent with previous studies, enantiopure complexes show stronger stabilization of the high-spin state and greater octahedral distortion compared to racemic mixtures.^[78] Due to the strong influence of packing on *SCO* behaviour, *Evans NMR* measurements were used to investigate heteroatom substitution effects.^[81]

Substitution of oxygen by sulfur results in stronger low-spin stabilization relative to oxygen derivatives, evidenced by an overall increase in $T_{1/2}$ in solution, or complexes remaining in the low-spin state throughout the measured temperature range. For example, with $R^{5/6}$ = Phenyl, the critical temperature in solution shifts by 100 K ($T_{1/2}^{(57)} = 344$ K vs. $T_{1/2}^{(54)} = 244$ K).^[77]

This effect was supported by *DFT* calculations in the gas phase, although the stronger σ -basicity of the sulfur derivative was not fully reflected in case of or exemplary for $R^{5/6}$ = isopropyl, likely due to the neglecting of intermolecular dispersion interactions by the B86PW91 functional used.

Since the steric and symmetry effects on homoleptic complexes are well-studied, Shahid et al. investigated heteroleptic complexes containing various achiral ligands (bimpy, bpp, and terpy) coordinated to the central iron(II) and one 2-thiazoline or 2-oxazoline ligand with different $R^{5/6}$ substituents.^[82] For the heteroleptic complex with R^5 = Phenyl, the effect of heteroatom substitution was confirmed: racemic complexes (**67**) exhibited spin transitions at $T_{1/2} = 344$ K ($T_{1/2}^{(56)} = 278$ K; $T_{1/2}^{(58)}$ remains low spin).^[77,80] Similar trends were observed for the heteroleptic racemic complex (**68**) with R^5 = isopropyl, which shows a *SCO* at $T_{1/2} = 241$ K. The oxygen-containing complex (**60**) remains high spin, while the sulfur-containing complex (**62**) remains low spin.^[77,80]

Heteroleptic complexes with achiral ligands offer opportunities to modulate the ligand field, with intramolecular interactions between the ligands also playing a significant role. Single crystal *XRD*, solid-state *SQUID* magnetometry, and *Evans NMR* revealed the following $T_{1/2}$ trend for heteroleptic complexes containing one bipy ligand: $L_{iPrO} > L_{PhO} > L_{iPrS} > L_{PhS}$. This trend was not perfectly matched in complexes containing *bpp*: $L_{iPrO} > L_{iPrS} > L_{PhO} > L_{PhS}$, which was not easily explained by the structures. *DFT* calculations suggested that differences arise from the interplay of σ -donor and π -acceptor properties among *bpp*, *bimpy*, and *terpy* ligands, resulting in a ligand field more sensitive to ligand sphere variations for *bimpy* and *terpy* due to stronger π -bonding.

Since intramolecular interactions impact spin transition properties, further π -interactions were considered by Li *et al.* by introducing additional phenyl groups to the ligand.^[83] Both enantiomers were synthesized, and solvated complexes remained in the high-spin state over the complete measured temperature range. Instead desolvated samples (**79**) and (**80**) showed stronger high-spin stabilization with $T_{1/2} = 197$ K and 194 K, compared to the mono-phenyl substituted complex ($T_{1/2} = 350$ K), indicating the importance of changes in intermolecular interactions, as the temperature dependent magnetisation measurements show in **Figure 11**.^[77] Further second harmonic generation (*SHG*) experiments revealed relatively strong nonlinear optical activity due to the chirality of the complexes, suggesting potential optically active applications.

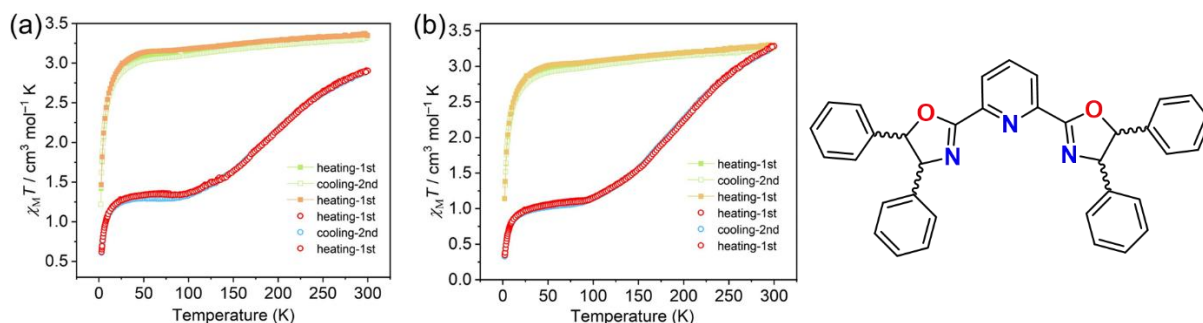


Figure 11: Schematic representation of the ligand used by Lu *et al.* and $\chi_M T$ vs T measured plot of the complexes (**79**) (a) and (**80**) (b).^[83] Reprinted from literature with permission.

To summarize, investigations on chiral *pybox* systems demonstrate a high potential for modulating the ligand field through sterically demanding groups and choice of chalcogen atom in the heterocycle. The observed trends, supported by *Evans NMR* measurements, show that larger steric groups stabilize the high-spin state more strongly. Symmetry affects intramolecular interactions, playing a major role in spin state stabilization, with $T_{1/2}^{\text{Enantiopure}} > T_{1/2}^{\text{Meso}} > T_{1/2}^{\text{Racemate}}$.^[78] Lastly, the chalcogen atom exerts an electronic influence on the ligand field, as the σ -basicity increases from oxygen to sulfur, leading to enhanced low-spin stabilization and increased critical temperature $T_{1/2}$.^[80]

Table 3: List of the chiral complexes based on the *pybox* based ligand design.

Nr.	Stereo-isomer L1	R ⁵ L1	X	Stereo-isomer L2	R ⁶ L2	X	A	Profile /solvent	T _{1/2} /K	measured system	Citation
35	<i>R</i>	Me	O	<i>R</i>	Me	O	ClO ₄	Aceton	192	solution	[77]
36	<i>R</i>	Ph	O	<i>R</i>	Ph	O	ClO ₄	Aceton	HS	solution	
37	<i>R</i>	iPr	O	<i>R</i>	iPr	O	ClO ₄	Aceton	HS	solution	
38	<i>R</i>	Ph	O	<i>R</i>	Ph	O	ClO ₄	Acetonitrile	244	solution	
39	<i>R</i>	Ph	O	<i>S</i>	Ph	O	ClO ₄	Acetonitrile	278	solution	
40	<i>R</i>	iPr	O	<i>S</i>	iPr	O	ClO ₄	Aceton	HS	solution	
41	<i>R</i>	Me	O	<i>R</i>	Me	O	ClO ₄		HS	solidstate	
42	<i>R</i>	Ph	O	<i>R</i>	Ph	O	ClO ₄	gradual	350	solidstate	
43	<i>R</i>	iPr	O	<i>R</i>	iPr	O	ClO ₄		HS	solidstate	
44	<i>R</i>	Ph	O	<i>R</i>	Ph	O	ClO ₄	Acetonitrile	247	solution	[78]
45	<i>R</i>	Ph	O	<i>S</i>	Ph	O	ClO ₄	Acetonitrile	281	solution	
46	<i>RS</i>	Ph	O	<i>RS</i>	Ph	O	ClO ₄	Acetonitrile	260	solution	
47	<i>RS</i>	Ph	O	<i>RS</i>	Ph	O	ClO ₄	gradual incomplete		solid state	
48	<i>RS</i>	Ph	O	<i>RS</i>	Ph	O	BF ₄	gradual incomplete		solid state	
49	<i>RS</i>	Ph	O	<i>RS</i>	Ph	O	PF ₆	abrupt After Desolvation, Hysteresis (20 K)	360 280↑ 260↓	solid state	
50	<i>RS</i>	Ph	O	<i>RS</i>	Ph	O	B(Ph) ₄	gradual incomplete		solid state	
51	<i>R</i>	Ph	S	<i>R</i>	Ph	S	BF ₄	incomplete gradual	330	solid state	[80]
52	<i>R</i>	Ph	S	<i>S</i>	Ph	S	BF ₄	incomplete	LS	solid state	
53	<i>R</i>	Ph	S	<i>R</i>	Ph	S	ClO ₄	incomplete gradual	330	solid state	
54	<i>R</i>	Ph	S	<i>R</i>	Ph	S	ClO ₄	Acetonitrile	244	solution	
55	<i>R</i>	Ph	S	<i>S</i>	Ph	S	ClO ₄	incomplete	LS	solid state	
56	<i>R</i>	Ph	O	<i>S</i>	Ph	O	ClO ₄	Acetonitrile	278	solution	
57	<i>R</i>	Ph	S	<i>R</i>	Ph	S	ClO ₄	Acetonitrile	344	solution	
58	<i>R</i>	Ph	S	<i>S</i>	Ph	S	ClO ₄	Acetonitrile	LS	solution	
59	<i>R</i>	iPr	S	<i>R</i>	iPr	S	ClO ₄	Acetonitrile	HS	solid state	
60	<i>R</i>	iPr	S	<i>S</i>	iPr	S	ClO ₄	Acetonitrile	HS	solution	
61	<i>R</i>	iPr	O	<i>R</i>	iPr	O	ClO ₄	Acetonitrile	277	solid state	
62	<i>R</i>	iPr	O	<i>S</i>	iPr	O	ClO ₄	Acetonitrile	LS	solution	
63	<i>R</i>	tert-Butyl	S	<i>R</i>	tert-Butyl	S	ClO ₄	Acetonitrile	HS	solution	
64	<i>R</i>	tert-Butyl	S	<i>S</i>	tert-Butyl	S	ClO ₄	Acetonitrile	-	solution	
65	<i>R</i>	tert-Butyl	O	<i>R</i>	tert-Butyl	O	ClO ₄	Acetonitrile	HS	solution	
66	<i>R</i>	tert-Butyl	O	<i>S</i>	tert-Butyl	O	ClO ₄	Acetonitrile	-	solution	
67	<i>R</i>	Ph	O	<i>S</i>	Ph	S	ClO ₄	Acetonitrile	344	solution	[82]
68	<i>R</i>	iPr	O	<i>S</i>	iPr	S	ClO ₄	Acetonitrile	241	solution	
69	<i>R</i>	Ph	O		bimpy		ClO ₄	Acetonitrile	292	solution	
70	<i>R</i>	Ph	S		bimpy		ClO ₄	Acetonitrile	>380	solution	
71	<i>R</i>	iPr	O		bimpy		ClO ₄	Acetonitrile	221	solution	
72	<i>R</i>	iPr	S		bimpy		ClO ₄	Acetonitrile	330	solution	
73	<i>R</i>	Ph	O		bpp		ClO ₄	Acetonitrile	285	solution	
74	<i>R</i>	Ph	S		bpp		ClO ₄	Acetonitrile	364	solution	

Ligand design of chiral Spin crossover complexes

Nr.	Stereo-isomer L1	R ⁵ L1	X	Stereo-isomer L2	R ⁶ L2	X	A	Profil /solvent	T _{1/2} /K	measured system	Citation
75	<i>R</i>	iPr	O		bpp		ClO ₄	Acetonitrile	232	solution	
76	<i>R</i>	iPr	S		bpp		ClO ₄	Acetonitrile	266	solution	
77	<i>R</i>	Ph	O		terpy		ClO ₄	Acetonitrile	LS	solution	
78	<i>R</i>	iPr	S		terpy		ClO ₄	Acetonitrile	LS	solution	
79	<i>RS</i>	Ph-Ph	O	<i>RS</i>	Ph-Ph	O	ClO ₄		197	solid state	[83]
80	<i>SR</i>	Ph-Ph	O	<i>SR</i>	Ph-Ph	O	ClO ₄		194	solid state	

4. Additional Ligand Designs Beyond these Categories

Within this chapter we will present mononuclear iron complexes, which do not include the previously discussed ligand classes. Heptacoordinated ligands with chiral groups for iron(II) *SCO* complexes were developed by Acha *et al.* (2015) and Wang *et al.* (2015) based on the (2*E*,12*E*)-2,13-dimethyl-6,9-dioxo-3,12-diaza-1(2,6)-pyridinacyclotridecaphane-2,12-diene core unit, substituted at positions 7 and 8 with 1) two phenyl groups^[84] and 2) two benzyloxy groups^[85] (shown in **Figure 12**). The enantiopure complexes (**81**) exhibit an incomplete spin transition with $T_{1/2} = 250$ K, and the *LIESST* effect was observed, whereas the racemic mixture (**82**) remains in the low spin state. The *SCO* is accompanied by a change in coordination geometry, as the asymmetric unit contains one macrocycle with coordination number 5 and an overall coordination numbers of 6 and 7. This phenomenon was previously reported in the literature as a possible strategy to stabilize the low spin state with a smaller coordination number, by Guionnen *et al.*^[86] To improve ligand flexibility, substitution with the benzyloxy group was performed, resulting in a gradual spin transition between 0 K and 150.^[85]

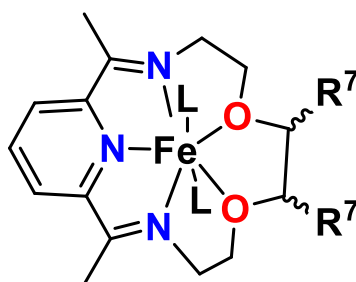


Figure 12: Schematic representation of the iron(II) complex reported by Quiang *et al.* and Acha *et al.* (**81**) ($R^7 = \text{Ph}$), and complex (**83**) ($R^7 = \text{CH}_2\text{OCH}_2\text{Ph}$).^[84,85] Reprinted from literature with permission.

An intriguing example of introducing chirality into the ligand system for iron(II) *SCO* complexes was reported by Ru *et al.*^[31] They designed (*R*)/(*S*)-4,5-pinenepyridyl-2-pyrazine and (*R*)/(*S*)-4,5-pinenepyridyl-2-pyridine ligands by introducing chirality via a pinene group and synthesized enantiopure complexes $[\text{Fe}((R/S)\text{-L})(\text{bpz})_2]$ using two achiral bis(1-pyrazolyl)borohydride ligands to saturate the coordination sphere. Complexes (**84**) containing the pyridine unit remain in the high spin state over the measured temperature range in the solid state, whereas those (**85**) with the pyrazine group undergo an abrupt *SCO* with a hysteresis of $\Delta T = 2$ K ($T_{1/2}^\uparrow = 189$ K and $T_{1/2}^\downarrow = 187$ K) (shown in **Figure 13**), attributed to differences in ligand field strength. The *SCO* is accompanied by a change in the dielectric constant, a rare observation in chiral *SCO* complexes, explained by the chirality of the ligand and the spin transition. These findings open the opportunity for multifunctional material build by introduction of chiral and polar elements.

This chapter aims to broaden the reader's perspective on the versatility of introducing chirality through ligand design.

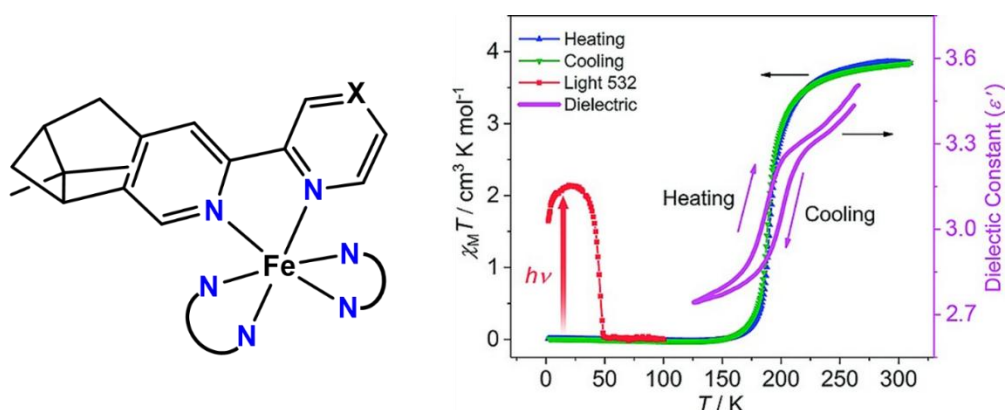


Figure 13: Schematic representation of the iron(II) complex reported by Jing *et al.* (left) and $\chi_M T$ vs T measured plot of the complexes (**84**) (right) as well as the LIESST measurement in solid state and the temperature dependent dielectric constant measurement.^[31] Reprinted from literature with permission.

Table 4: List of the chiral complexes based on different ligand design.

Nr.	Enantiomer	R ⁷	X	Profile	T _{1/2} / K	Citation
81	RR/SS	Ph		incomplete	250	[84]
82	RS	Ph		incomplete	LS	
83	SS	CH ₂ OCH ₂ Ph			HS	[85]
84	R/S		CH		HS	[31]
85	R/S		N	Hysteresis (2K)	187↑ 189↓	

Conclusion

This review provides a concise summary of chiral iron(II) *SCO* complexes, focusing on the introduction of chirality through ligand design. It presents an overview of studies on ligand design and structure-property relationships involving chiral ligands, as well as how these properties can be modulated by substituent variations. The correlation between stereoisomers and *SCO* behaviour - particularly between enantiopure complexes and racemic mixtures - is highlighted, emphasizing the role of intermolecular interactions in the solid state and intramolecular interactions in solution. Several examples of well-designed complexes demonstrate the advantages of incorporating chirality into ligand design for multifunctional materials such as optical switches and ferroelectric materials. The increasing interest in chirality and the use of polarization as a means of information storage is driven by advances in spectroscopy techniques, including ultrafast circular dichroism (*CD*) spectroscopy.^[23] Future research leveraging polarization for information processing is expected to explore phenomena such as the *CD-LIESST* effect and switchable *CISS* effect, with important implications for molecular spintronics. A thorough understanding of chirality's impact will be essential for these investigations.

References

- [1] A. Enriquez-Cabrera, A. Rapakousiou, M. P. Bello, G. Molnár, L. Salmon, A. Bousseksou, *Coord. Chem. Rev.* **2020**, *419*, 213396.
- [2] K. S. Kumar, M. Ruben, *Coord. Chem. Rev.* **2017**, *346*, 176–205.
- [3] G. Molnár, S. Rat, L. Salmon, W. Nicolazzi, A. Bousseksou, *Adv. Mater.* **2018**, *30*, 1703862.
- [4] P. Gütllich, A. B. Gaspar, Y. Garcia, *Beilstein J. Org. Chem.* **2013**, *9*, 342–391.
- [5] V. Ksenofontov, A. B. Gaspar, P. Gütllich, in *Spin Crossover in Transition Metal Compounds III*, Springer, Berlin Heidelberg, **2004**, pp. 23–64.
- [6] P. O. Ribeiro, B. P. Alho, R. M. Ribas, E. P. Nóbrega, V. S. R. de Sousa, P. J. von Ranke, *J. Magn. Magn. Mater.* **2019**, *489*, 165340.
- [7] G. Chastanet, C. Desplanches, C. Baldé, P. Rosa, M. Marchivie, P. Guionneau, *Chem. Sq.* **2018**, *2*, 2.
- [8] P. Gütllich, A. Hauser, *Coord. Chem. Rev.* **1990**, *97*, 1–22.
- [9] S. M. Kamel, L. Daróczy, L. Z. Tóth, D. L. Beke, G. G. Juárez, S. Cobo, L. Salmon, G. Molnár, A. Bousseksou, *J. Mater. Chem.* **2024**, *12*, 5757–5765.
- [10] O. A. Qamar, F. Jamil, M. Hussain, M. Mustafa, R. U. Rehman, A. Inayat, M. S. Habib, M. Sajid, *Chem. Pap.* **2023**, *77*, 7331–7359.
- [11] E. Ruiz, *Phys. Chem. Chem. Phys.* **2014**, *16*, 14–22.
- [12] S. Yuan, N. Natt, B. J. Powell, *Inorg. Chem.* **2025**, *64*, 7182–7193.
- [13] A. B. Gaspar, M. Seredyuk, P. Gütllich, *J. Mol. Struct.* **2009**, *924–926*, 9–19.
- [14] Y. Zhang, S. E. Alavi, I. Soroceanu, D. W. Kamau, A. Rotaru, I. Séguy, L. Salmon, G. Molnár, A. Bousseksou, *Adv. Electron. Mater.* **2025**, *11*, 2400590.
- [15] F. Devínsky, *Symmetry* **2021**, *13*, 2277.
- [16] A. Banreti, S. Bhattacharya, F. Wien, K. Matsuo, M. Réfrégiers, C. Meinert, U. Meierhenrich, B. Hudry, D. Thompson, S. Noselli, *Nat. Commun.* **2022**, *13*, 7059.
- [17] J. Byron, J. Kreuzwieser, G. Purser, J. van Haren, S. N. Ladd, L. K. Meredith, C. Werner, J. Williams, *Nature* **2022**, *609*, 307–312.
- [18] Y. Liu, Z. Wu, D. W. Armstrong, H. Wolosker, Y. Zheng, *Nat. Rev. Chem.* **2023**, *7*, 355–373.
- [19] Y. Zheng, K. Mao, S. Chen, H. Zhu, *Front. Bioeng. Biotechnol.* **2021**, *9*, 703004.
- [20] M. Kataria, S. Seki, *Chem. Eur. J.* **2025**, *31*, e202403460.
- [21] H. Dong, S. Hua, S. Li, *J. Phys. Chem. A* **2009**, *113*, 1335–1342.
- [22] C. Durukan, J. Faierson, I. van der Wal, J. L. Pérez, S. Hennig, T. N. Grossmann, *J. Pept. Sci.* **2025**, *31*, e70024.

- [23] Z. A. VanOrman, W. R. Kitzmann, A.-P. M. Reponen, T. Deshpande, H. J. Jöbbsis, S. Feldmann, *Nat. Rev. Chem.* **2025**, *9*, 208–223.
- [24] R. U. McVicker, N. M. O’Boyle, *J. Med. Chem.* **2024**, *67*, 2305–2320.
- [25] P. S. Steinlandt, L. Zhang, E. Meggers, *Chem. Rev.* **2023**, *123*, 4764–4794.
- [26] B. P. Bloom, Y. Paltiel, R. Naaman, D. H. Waldeck, *Chem. Rev.* **2024**, *124*, 1950–1991.
- [27] M. Oppermann, F. Zinna, J. Lacour, M. Chergui, *Nat. Chem.* **2022**, *14*, 739–745.
- [28] S. Ohkoshi, S. Takano, K. Imoto, M. Yoshikiyo, A. Namai, H. Tokoro, *Nat. Photon.* **2014**, *8*, 65–71.
- [29] A. Iazzolino, A. O. Hamouda, A. Naïm, O. Stefánczyk, P. Rosa, E. Freysz, *Appl. Phys. Lett.* **2017**, *110*, 161908.
- [30] W.-K. Han, Z.-H. Li, W. Zhu, T. Li, Z. Li, X. Ren, Z.-G. Gu, *Dalton Trans.* **2017**, *46*, 4218–4224.
- [31] J. Ru, F. Yu, P. Shi, C. Jiao, C. Li, R. Xiong, T. Liu, M. Kurmoo, J. Zuo, *Eur. J. Inorg. Chem.* **2017**, *2017*, 3144–3149.
- [32] C. Bartual-Murgui, L. Piñeiro-López, F. J. Valverde-Muñoz, M. C. Muñoz, M. Seredyuk, J. A. Real, *Inorg. Chem.* **2017**, *56*, 13535–13546.
- [33] I. A. Kühne, A. Ozarowski, A. Sultan, K. Esien, A. B. Carter, P. Wix, A. Casey, M. Heerah-Boo luck, T. D. Keene, H. Müller-Bunz, S. Felton, S. Hill, G. G. Morgan, *Inorg. Chem.* **2022**, *61*, 3458–3471.
- [34] C. T. Kelly, R. Jordan, S. Felton, H. Müller-Bunz, G. G. Morgan, *Chem. Eur. J.* **2023**, *29*, e202300275.
- [35] I. A. Gural’skiy, V. A. Reshetnikov, A. Szebesczyk, E. Gumienna-Kontecka, A. I. Marynin, S. I. Shylin, V. Ksenofontov, I. O. Fritsky, *J. Mater. Chem. C* **2015**, *3*, 4737–4741.
- [36] V. B. Jakobsen, L. O’Brien, G. Novitchi, H. Müller-Bunz, A. Barra, G. G. Morgan, *Eur. J. Inorg. Chem.* **2019**, *2019*, 4405–4411.
- [37] M. Fujiki, *Symmetry* **2014**, *6*, 677–703.
- [38] I. A. Gural’skiy, O. I. Kucheriv, S. I. Shylin, V. Ksenofontov, R. A. Polunin, I. O. Fritsky, *Chem. Eur. J.* **2015**, *21*, 18076–18079.
- [39] L.-F. Qin, C.-Y. Pang, W.-K. Han, F.-L. Zhang, L. Tian, Z.-G. Gu, X. Ren, Z. Li, *CrystEngComm* **2015**, *17*, 7956–7963.
- [40] X. Zhang, H. Sun, D. Chen, X. Li, J. Xiao, Y. Meng, T. Liu, *Eur. J. Inorg. Chem.* **2024**, e202400201.
- [41] S. E. Howson, L. E. N. Allan, N. P. Chmel, G. J. Clarkson, R. J. Deeth, A. D. Faulkner, D. H. Simpson, P. Scott, *Dalton Trans.* **2011**, *40*, 10416.
- [42] T. J. Ward, K. D. Ward, *Anal. Chem.* **2012**, *84*, 626–635.
- [43] J. Sui, N. Wang, J. Wang, X. Huang, T. Wang, L. Zhou, H. Hao, *Chem. Sci.* **2023**, *14*, 11955–12003.
- [44] V. Maliuzhenko, M. Weselski, J. Gregoliński, M. Książek, J. Kusz, R. Bronisz, *Inorg. Chem.* **2024**, *63*, 17762–17773.
- [45] S. Kawabata, K. Nakabayashi, K. Imoto, S. Klimke, F. Renz, S. Ohkoshi, *Dalton Trans.* **2021**, *50*, 8524–8532.

- [46] J. P. Flood, M. J. Wallis, J. Tadros, Y. Nakashima, D. J. Fanna, J. R. Aldrich-Wright, L. F. Lindoy, S. Hayami, F. Li, *Inorg. Chem.* **2025**, *64*, 8100–8108.
- [47] D.-H. Ren, D. Qiu, C.-Y. Pang, Z. Li, Z.-G. Gu, *Chem. Commun.* **2015**, *51*, 788–791.
- [48] K. S. Kumar, Y. Bayeh, T. Gebretsadik, F. Elemo, M. Gebrezgiabher, M. Thomas, M. Ruben, *Dalton Trans.* **2019**, *48*, 15321–15337.
- [49] D.-H. Ren, X.-L. Sun, L. Gu, D. Qiu, Z. Li, Z.-G. Gu, *Inorg. Chem. Commun.* **2015**, *51*, 50–54.
- [50] L. Tian, C.-Y. Pang, F.-L. Zhang, L.-F. Qin, Z.-G. Gu, Z. Li, *Inorg. Chem. Commun.* **2015**, *53*, 55–59.
- [51] S. E. Howson, L. E. N. Allan, N. P. Chmel, G. J. Clarkson, R. van Gorkum, P. Scott, *Chem. Commun.* **2009**, 1727.
- [52] T. Hashibe, T. Fujinami, D. Furusho, N. Matsumoto, Y. Sunatsuki, *Inorg. Chim. Acta* **2011**, *375*, 338–342.
- [53] Z.-G. Gu, C.-Y. Pang, D. Qiu, J. Zhang, J.-L. Huang, L.-F. Qin, A.-Q. Sun, Z. Li, *Inorg. Chem. Commun.* **2013**, *35*, 164–168.
- [54] S. Zhao, H. Zhou, C. Qin, H. Zhang, Y. Li, M. Yamashita, S. Wang, *Chem. Eur. J.* **2023**, *29*, e202300554.
- [55] C. Köhler, E. Rentschler, *Eur. J. Inorg. Chem.* **2016**, *2016*, 1955–1960.
- [56] C. F. Herold, S. I. Shylin, E. Rentschler, *Inorg. Chem.* **2016**, *55*, 6414–6419.
- [57] A. B. Gaspar, M. Seredyuk, *Coord. Chem. Rev.* **2014**, *268*, 41–58.
- [58] L.-F. Qin, C.-Y. Pang, W.-K. Han, F.-L. Zhang, L. Tian, Z.-G. Gu, X. Ren, Z. Li, *Dalton Trans.* **2016**, *45*, 7340–7348.
- [59] C. P. Brock, W. B. Schweizer, J. D. Dunitz, *J. Am. Chem. Soc.* **1991**, *113*, 9811–9820.
- [60] W.-K. Han, L.-F. Qin, C.-Y. Pang, C.-K. Cheng, W. Zhu, Z.-H. Li, Z. Li, X. Ren, Z.-G. Gu, *Dalton Trans.* **2017**, *46*, 8004–8008.
- [61] Y. Sekimoto, M. R. Karim, N. Saigo, R. Ohtani, M. Nakamura, S. Hayami, *Eur. J. Inorg. Chem.* **2017**, *2017*, 1049–1053.
- [62] H. Petzold, P. Djomgoue, G. Hörner, J. M. Speck, T. Ruffer, D. Schaarschmidt, *Dalton Trans.* **2016**, *45*, 13798–13809.
- [63] T.-T. Ma, X.-P. Sun, Z.-S. Yao, J. Tao, *Inorg. Chem. Front.* **2020**, *7*, 1196–1204.
- [64] M. M. Khusniyarov, *Chem. Eur. J.* **2016**, *22*, 15178–15191.
- [65] A. Regueiro, V. García-López, A. Forment-Aliaga, M. Clemente-León, *Dalton Trans.* **2024**, *53*, 10637–10643.
- [66] B. Eftekhari-Sis, A. Abdollahifar, M. M. Hashemi, M. Zirak, *Eur. J. Org. Chem.* **2006**, *2006*, 5152–5157.
- [67] H. Wu, Y. Shen, L. Fan, Y. Wan, P. Zhang, C. Chen, W. Wang, *Tetrahedron* **2007**, *63*, 2404–2408.
- [68] S. Sundaresan, S. Brooker, *Inorg. Chem.* **2023**, *62*, 12192–12202.

-
- [69] S. Sundaresan, J. Eppelsheimer, L. M. Carrella, E. Rentschler, *Eur. J. Inorg. Chem.* **2025**, *28*, e202400690.
- [70] X.-Q. Chen, Y.-D. Cai, Y.-S. Ye, M.-L. Tong, X. Bao, *Inorg. Chem. Front.* **2019**, *6*, 2194–2199.
- [71] X.-H. Zhao, Y.-F. Deng, J.-Q. Huang, M. Liu, Y.-Z. Zhang, *Inorg. Chem. Front.* **2024**, *11*, 808–816.
- [72] Y.-F. Deng, Y.-N. Wang, X.-H. Zhao, Y.-Z. Zhang, *CCS Chem.* **2022**, *4*, 3064–3075
- [73] X. Zhao, Y. Deng, J. Xi, J. Huang, Y. Zhang, *Angew. Chem. Int. Ed.* **2025**, *64*, e202414826.
- [74] X.-H. Zhao, D. Shao, J.-T. Chen, D.-X. Gan, J. Yang, Y.-Z. Zhang, *Sci. China Chem.* **2022**, *65*, 532–538.
- [75] G. Desimoni, G. Faita, P. Quadrelli, *Chem. Rev.* **2003**, *103*, 3119–3154.
- [76] B. D. Ward, L. H. Gade, *Chem. Commun.* **2012**, *48*, 10587.
- [77] K. E. Burrows, S. E. McGrath, R. Kulmaczewski, O. Cespedes, S. A. Barrett, M. A. Halcrow, *Chem. Eur. J.* **2017**, *23*, 9067–9075.
- [78] R.-G. Wang, Y.-S. Meng, F.-F. Gao, W.-Q. Gao, C.-H. Liu, A. Li, T. Liu, Y.-Y. Zhu, *Dalton Trans.* **2021**, *50*, 3369–3378.
- [79] M. G. Robb, S. V. Chong, S. Brooker, *Dalton Trans.* **2024**, *53*, 10974–10981.
- [80] N. Shahid, K. E. Burrows, M. J. Howard, C. M. Pask, O. Cespedes, P. C. McGowan, M. A. Halcrow, *Inorg. Chem.* **2021**, *60*, 14336–14348.
- [81] B. Weber, F. A. Walker, *Inorg. Chem.* **2007**, *46*, 6794–6803.
- [82] N. Shahid, K. E. Burrows, C. M. Pask, O. Cespedes, M. J. Howard, P. C. McGowan, M. A. Halcrow, *Dalton Trans.* **2022**, *51*, 4262–4274.
- [83] L. Li, J.-P. Luo, X.-F. Li, Z. Shao, D.-Y. Chen, Q. Shi, L. Zhao, Y.-S. Meng, T. Liu, *Inorg. Chem. Commun.* **2025**, *162*, 114382.
- [84] Q. Wang, S. Venneri, N. Zarrabi, H. Wang, C. Desplanches, J.-F. Létard, T. Seda, M. Pilkington, *Dalton Trans.* **2015**, *44*, 6711–6714.
- [85] R. T. Acha, M. Pilkington, *CrystEngComm* **2015**, *17*, 8897–8905.
- [86] P. Guionneau, F. Le Gac, A. Kaiba, J. S. Costa, D. Chasseau, J.-F. Létard, *Chem. Commun.* **2007**, 3723.

Motivation

A key advancement in SCO research is the pursuit of multifunctional materials for real-world applications such as sensors^[1], memory devices^[2], and quantum technologies. The milestones of introducing chirality into ligand systems for spin crossover (SCO) complexes, which we discussed in the last chapter, highlight the growing importance of chirality and the opportunities it creates for the development of multifunctional materials.

Chirality in particular opens new avenues by combining the molecular switchable nature of SCO with other phenomena like ferroelectricity^[3], circular dichroism^[4,5], and chiral recognition^[6]. This includes promising directions like light-induced excited spin state trapping (LIESST) in chiral systems, as well as potential applications in spintronics *via* the CISS effect (chiral-induced spin selectivity). In racemic mixture the coupling of LIESST-effect with the CD-Effect would enable two more states – one per enantiomer – as the left enantiomer would be mayor switched by the corresponding circular polarized light. This is first reported by Naaman and co-workers due to the spin polarization of electrons passing through chiral molecules on surfaces, which opens the opportunity to use switchable chiral molecules for spin filters in spintronics.^[7,8] The CISS effect, already observed in fully organic *Feringa* molecular motors, could be more feasibly harnessed in spin crossover systems through rational ligand design - especially using helical or stereogenic frameworks.^[9]

It is worth noting that chirality provides a huge opportunity to investigate and understand the impact of packing on the spin transition. This is because enantiopure complexes are likely to be packed differently in a crystal lattice than racemic mixtures, due to the different intermolecular and intramolecular interactions reported by Burrows *et al.*^[10]

The introducing of chirality, as discussed in the chapter “Ligand design for chiral iron(II) SCO complexes”, can be achieved for example by chiral anions or guests.^[11–13] However, this limits the possibility of modification to the list of chiral guests, and often these are difficult to modify and to perform the enantiopure crystallization, which is not controllable.^[14,15] Further chiral SCO complexes are built up with chiral ligands, which are based on affordable building blocks.^[10,16,17] However, imparting chirality into SCO-active ligand systems remains a synthetic challenge. Enantiomer separation often requires financially costly techniques such as chiral HPLC or separation of diastereomers, unless enantiomerically pure starting materials are used. A novel ligand synthesis approach for asymmetric 1,3,4-chalcogendiazole-based ligands enables the use of amino acids as starting materials, providing inherent chirality combined with a high degree of structural versatility. Introducing different amino acids with various alcylic and bulky groups (alanine to valine) can be used to investigate the steric impact of the substituent on the intramolecular and the intermolecular interactions.

Within the Rentschler group, 1,3,4-oxadiazole- and 1,3,4-thiadiazole-based ligands have been thoroughly investigated to better understand the role of intermolecular interactions, such as hydrogen bonding, solvents^[18,19] and counterions effects^[20,21], and π - π stacking^[22,23], affect spin crossover properties. The influence of these interactions can be observed in the variation of critical transition temperatures T_c and the abruptness of the spin transition.^[24,25] Interestingly, some of these alterations even locks the complexes in one spin state.^[3,16,26] Over the years the Rentschler group has collected knowledge in structure-function correlations within a family of complexes, leading to an understanding of the role of subtle changes in ligand environments as well as crystal packing. These factors can have a significant impact on the cooperative behaviour of *SCO* molecular materials.

Symmetric dinuclear 1,3,4-thiadiazoles have led to fascinating phase trapping and ordering effects dependent on the cooling rate, as shown by Fürmeyer *et al.* for $[\text{Fe}_2(\text{L}^{\text{TA-TDA-TA}})_2(\text{BF}_4)_4]$ (**Figure 1**; left).^[20] Mononuclear complexes such as $[\text{Fe}(\text{L}^{\text{Naph-TDA-py}})_2(\text{NCBH}_3)_2]$ (**Figure 1**; middle), featuring asymmetric substitutions with extended aromatic systems, exhibit strong π - π interactions and cooling-rate-dependent high-spin/low-spin fractions.^[22] The complex $[\text{Fe}(\text{L}^{\text{Naph-ODA}})(\text{NCBH}_3)_2]$ (**Figure 1**; right), featuring an asymmetric oxadiazole ligand, shows temperature-dependent synergism between naphthyl fluorescence and the spin transition, clearly demonstrating the potential for a synergetic response coupling spin switching with optical response.^[27]

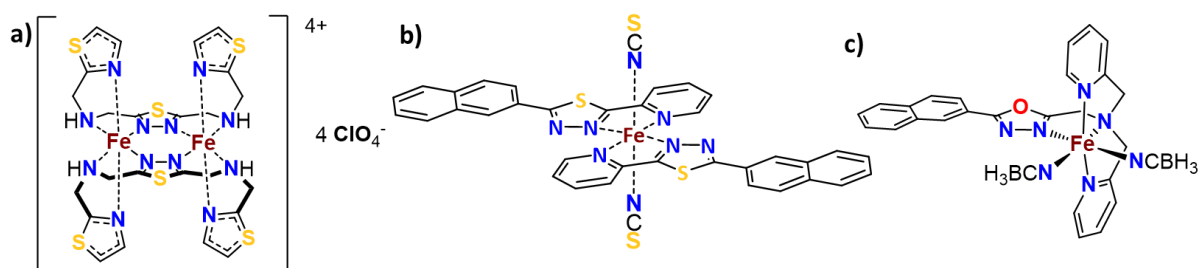


Figure 1: SCO Complex systems previously investigated by the Rentschler group: a) dinuclear 1,3,4-thiadiazole based complexes reported by Fürmeyer *et al.* showing phase trapping and spin state ordering^[20] b) mononuclear symmetric 1,3,4-thiadiazole based complex with naphthyl groups leading to strong intermolecular interaction and exhibiting speed depending high/low spin state fraction by Kiehl *et al.*^[22] c) asymmetric 1,3,4-oxadiazole based complex investigated for synergism between spin crossover and temperature dependent emission by Eppelsheimer *et al.*^[27]

The aim of the present study was to investigate the substitution of the chalcogen atom in the 1,3,4-chalcogendiazole ring, moving from oxygen to sulfur, and its effect on SCO properties by comparing $[\text{Fe}(\text{L}^{\text{Ph-TDA}})(\text{NCBH}_3)_2]$ to the well-established $[\text{Fe}(\text{L}^{\text{Ph-ODA}})(\text{NCBH}_3)_2]$.^[18,19] This substitution impacts both the coordination geometry and electronic environment of the complex, influencing the spin state equilibrium. While 1,3,4-thiadiazoles often require high temperatures for synthesis, which favors racemization, the milder conditions required for 1,3,4-oxadiazole formation help preserve stereochemical integrity, making them particularly attractive for chiral *SCO* research.^[28,29] Further

project aims of using chiral spin crossover complexes for switchable spin valves requires complexes, which could be applied on surface. Neutral complexes provide the possibility for surface deposition *via* sublimation, a crucial requirement for spintronic applications such as investigating switchable *CISS* (chiral-induced spin selectivity) effects.^[30]

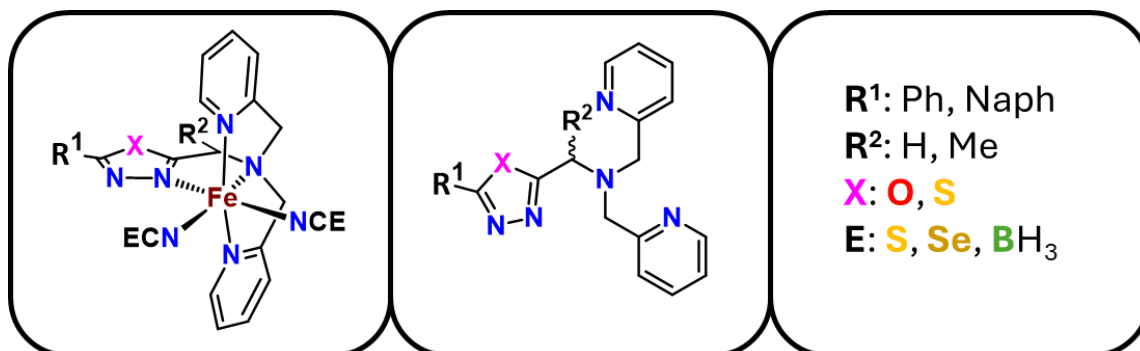


Figure 2: Ligand design approaches for investigations on 1) the influence of the impact substituting the oxygen in the 1,2,3-chalcogendiazole heterocycle with sulfur ($R^1 = \text{Ph}$, $X = \text{S}$), 2) the interplay of polymorph using chirality in 1,3,4-thiadiazole based complexes ($R^1 = \text{Ph}$, $X = \text{S}$, $E = \text{BH}_3$), 3) a systematic model complex for investigations of stereocenter dependency of spin crossover properties ($R^1 = \text{Naph}$, $X = \text{O}$, $E = \text{BH}_3$) and 4) the solvent dependency of coordination isomers and molecular motion on the spin crossover profile ($R^1 = \text{Naph}$, $X = \text{S}$, $E = \text{BH}_3$).

Based on previous findings by Eppelsheimer *et al.*, which revealed a synergy between *SCO* and luminescence via antenna effects, the objective is to design asymmetric and chiral 1,3,4-oxadiazole-based ligands, which enable optical readouts of the spin state.^[27] The mild reaction conditions for oxadiazole-based systems make this approach feasible, as they ensure the retention of chirality during synthesis.^[29] In parallel, modifications to bispyridylmethylamine (*BPA*)-type ligands are being explored to control coordination isomerism, based on the relative position of the pyridyl-units, which may influence *SCO* properties but has not yet been fully characterized in the literature.^[31,32]

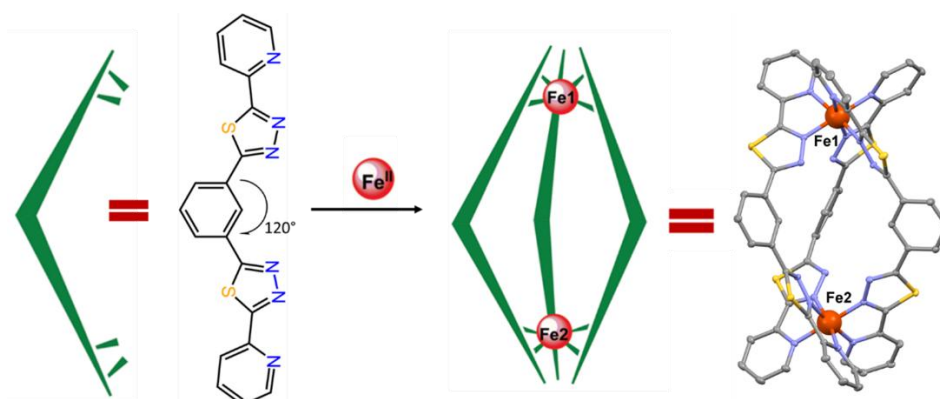


Figure 3: Ligand design for dinuclear 1,3,4-thiadiazole helical complexes for investigations of chiral supramolecular spin crossover complexes and host guest chemistry.^[33]

The imparting of the helical motif in polynuclear complexes allows the system to undergo a multi-step spin crossover. In the case of a dinuclear system, three steps can be exhibited: $[\text{HS}][\text{HS}] \rightarrow [\text{HS}][\text{LS}] \rightarrow$

[LS][LS].^[34] The design is based on three symmetric ligands with two bidentate coordination pockets, bridging two iron(II) centers.^[35,36] This can be achieved by using 1,2,4-triazole-pyridine coordination pockets, where the 5-position of the heterocycle is connected to the pyridine unit and the 3-position of the heterocycle is bond to an aryl unit (e.g. isophthalic unit) bridging both coordination pockets. As the N4-atom of the 1,3,4-Triazole-unit can modify by different attached alkyl groups, the spin crossover properties is highly dependent on these substituent, which was shown by Kitchen *et al.*, due to the intramolecular interactions between these substituent and the heterocycle.^[37] In case of 1,2-diazole-units on of the nitrogen can be protonated, where this proton is pointing inside the cavity of the helical complex. This allows to stabiles the intercalation of anions, which is a promising tool to adjust the spin crossover and to use this complexes as small guest sensor material.^[35] Helicates are promising supramolecular architecture appearing in P- and M-enantiomers based on the rotation of the helical structure along the vector between both centres.^[38] Finally, the introduction of chirality by helical motif gives rises to new possibilities for creating helically chiral systems that exhibit Λ/Δ isomerism stepwise spin transitions^[20,21], and host-guest functionality^[6], with potential for encapsulating chiral or achiral molecules^[39].

References

- [1] J. Linares, E. Codjovi, Y. Garcia, *Sensors* **2012**, *12*, 4479-4492.
- [2] K. S. Woo, A. Zhang, A. Arabelo, T. D. Brown, M. Park, A. A. Talin, E. J. Fuller, R. S. Bisht, X. Qian, R. Arroyave, S. Ramanathan, L. Thomas, R. S. Williams, S. Kumar, *Nat. Commun.* **2024**, *15*, 4656.
- [3] W.-K. Han, L.-F. Qin, C.-Y. Pang, C.-K. Cheng, W. Zhu, Z.-H. Li, Z. Li, X. Ren, Z.-G. Gu, *Dalton Trans.* **2017**, *46*, 8004-8008.
- [4] A. Iazzolino, A. Ould Hamouda, A. Naïm, O. Stefánczyk, P. Rosa, E. Freysz, *Appl. Phys. Lett.* **2017**, *110*, 161908.
- [5] T. Verbiest, S. V. Elshocht, M. Kauranen, L. Helleman, J. Snauwaert, C. Nuckolls, T. J. Katz, A. Persoons, *Science* **1998**, *282*, 913-915.
- [6] L. A. Barrios, R. Diego, M. Darawsheh, J. I. Martínez, O. Roubeau, G. Aromí, *Chem. Commun.* **2022**, *58*, 5375-5378.
- [7] K. Ray, S. P. Ananthavel, D. H. Waldeck, R. Naaman, *Science* **1999**, *283*, 814-816.
- [8] T. N. H. Nguyen, G. Salvan, O. Hellwig, Y. Paltiel, L. T. Baczewski, C. Tegenkamp *Chem. Sci.* **2024**, *15*, 14905–14912.
- [9] R. Malatong, T. Sato, J. Kumsampao, T. Minato, M. Suda, V. Promarak, H. M. Yamamoto *Small* **2023**, *19*, 2302714.

- [10] K. E. Burrows, S. E. McGrath, R. Kulmaczewski, O. Cespedes, S. A. Barrett, M. A. Halcrow, *Chem. Eur. J.* **2017**, *23*, 9067-9075.
- [11] I. A. Gural'skiy, V. A. Reshetnikov, A. Szebesczyk, E. Gumienna-Kontecka, A. I. Marynin, S. I. Shylin, V. Ksenofontov, I. O. Fritsky, *J. Mater. Chem. C* **2015**, *3*, 4737-4741.
- [12] V. B. Jakobsen, L. O'Brien, G. Novitchi, H. Müller-Bunz, A. Barra, G. G. Morgan, *Eur. J. Inorg. Chem.* **2019**, *2019*, 4405-4411.
- [13] L.-F. Qin, C.-Y. Pang, W.-K. Han, F.-L. Zhang, L. Tian, Z.-G. Gu, X. Ren, Z. Li, *Cryst. Eng. Comm.* **2015**, *17*, 7956-7963.
- [14] C. Bartual-Murgui, L. Piñeiro-López, F. J. Valverde-Muñoz, M. C. Muñoz, M. Seredyuk, J. A. Real *Inorg. Chem.* **2017**, *56*, 13535-13546.
- [15] C. T. Kelly, R. Jordan, S. Felton, H. Müller-Bunz, G. G. Morgan, *Chem. Eur. J.* **2023**, *29*, e202300275.
- [16] L.-F. Qin, C.-Y. Pang, W.-K. Han, F.-L. Zhang, L. Tian, Z.-G. Gu, X. Ren, Z. Li *Dalton Trans.* **2016**, *45*, 7340–7348.
- [17] X. Zhao, Y. Deng, J. Xi, J. Huang, Y. Zhang, *Angew. Chem. Int. Ed.* **2025**, *137*, e202414826.
- [18] S. Sundaresan, J. Eppelsheimer, E. Gera, L. Wiener, L. M. Carrella, K. R. Vignesh, E. Rentschler, *Dalton Trans.* **2024**, *53*, 10303-10317.
- [19] S. Sundaresan, J. Eppelsheimer, L. M. Carrella, E. Rentschler, *Eur. J. Inorg. Chem.* **2025**, *28*, e202400690.
- [20] F. Fürmeyer, L. M. Carrella, V. Ksenofontov, A. Möller, E. Rentschler, *Inorg. Chem.* **2020**, *59*, 2843-2852.
- [21] C. F. Herold, S. I. Shylin, E. Rentschler, *Inorg. Chem.* **2016**, *55*, 6414-6419.
- [22] J. Kiehl, T. Hochdörffer, L. M. Carrella, V. Schünemann, M. H. Nygaard, J. Overgaard, E. Rentschler, *Inorg. Chem.* **2022**, *61*, 3141-3151.
- [23] S. Sundaresan, J. Kiehl, L. M. Carrella, E. Rentschler, *Cryst. Growth Des.* **2023**, *23*, 1648-1655.
- [24] P. Gütlich, *Eur. J Inorg. Chem.* **2013**, *2013*, 581-591.
- [25] J. A. Wolny, K. Gröpl, J. Kiehl, E. Rentschler, V. Schünemann, *Dalton Trans.* **2024**, *53*, 8391-8397.
- [26] X.-H. Zhao, Y.-F. Deng, J.-Q. Huang, M. Liu, Y.-Z. Zhang, *Inorg. Chem. Front.* **2024**, *11*, 808-816.
- [27] S. Sundaresan, J.-G. Becker, J. Eppelsheimer, A. E. Sedykh, L. M. Carrella, K. Müller-Buschbaum, E. Rentschler, *Dalton Trans.* **2023**, *52*, 13181-13189.
- [28] G. Nagendra, R. S. Lamani, N. Narendra, V. V. Sureshbabu, *Tetrahedron Lett.* **2010**, *51*, 6338-6341.
- [29] H. A. Rajapakse, H. Zhu, M. B. Young, B. T. Mott, *Tetrahedron Lett.* **2006**, *47*, 4827-4830.
- [30] K. S. Kumar, M. Ruben, *Angew. Chem. Int. Ed.* **2021**, *60*, 7502-7521.

- [31] G. S. Matouzenko, E. Jeanneau, A. Yu. Verat, A. Bousseksou, *Dalton Trans.* **2011**, 40, 9608.
- [32] G. S. Matouzenko, A. Bousseksou, S. Lecocq, P. J. Van Koningsbruggen, M. Perrin, O. Kahn, A. Collet, *Inorg. Chem.* **1997**, 36, 2975-2981.
- [33] J.-G. Becker, J. F. Nüsing, S. Sundaresan, R. Diego, M. Mondeshki, L. M. Carrella, E. Rentschler, *Cryst. Growth Des.* **2024**, 24, 7662-7669.
- [34] R. W. Hogue, S. Singh, S. Brooker *Chem. Soc. Rev.* **2018**, 47, 7303-7338.
- [35] M. Darawsheh, L. A. Barrios, O. Roubeau, S. J. Teat, G. Aromí, *Chem. Eur. J.* **2016**, 22, 8635-8645.
- [36] S. Singh, R. W. Hogue, H. L. C. Feltham, S. Brooker, *Dalton Trans.* **2019**, 48, 15435-15444.
- [37] J. A. Kitchen, J. Olguín, R. Kulmaczewski, N. G. White, V. A. Milway, G. N. L. Jameson, J. L. Tallon, S. Brooker, *Inorg. Chem.* **2013**, 52, 11185-11199.
- [38] Q. Huang, Y.-P. Tang, C.-G. Zhang, Z. Wang, L. Dai, *ACS Catal.* **2024**, 14, 16256-16265.
- [39] M. Darawsheh, L. A. Barrios, O. Roubeau, S. J. Teat, G. Aromí, *Angew. Chem. Int. Ed.* **2018**, 57, 13509-13513.

Outline of the Thesis

Navigation through this work is facilitated by the following outline. Based on the insights into symmetric 1,3,4-thiadiazole-based iron(II) spin-crossover complexes like $[\text{Fe}(\text{L}^{\text{Naph-TDA-py}})_2(\text{NCBH}_3)_2]$ reported by Jonathan Kiehl, the molecular symmetry is reduced by incorporating an N,N-bis(methylpyridyl) functionality instead of the pyridine motive (shown in **Figure 1**).

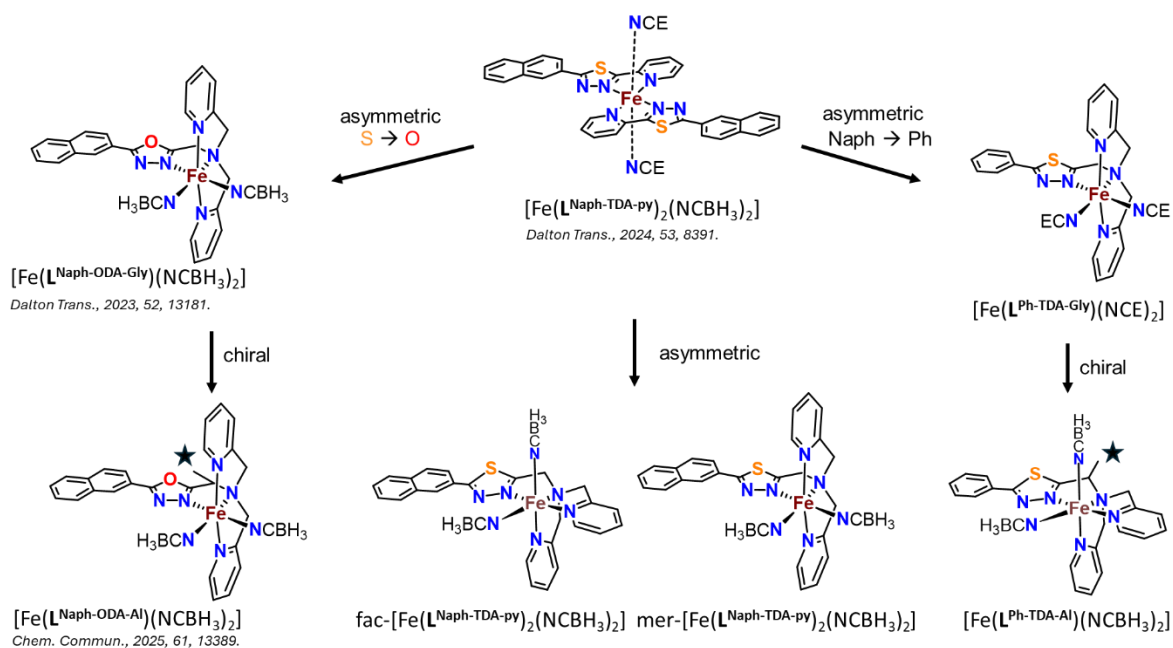


Figure 1: Scheme of synthesized, characterized and investigated complexes and the incorporated modifications discussed in the following chapters.

In Chapter 1, we first discuss the substitution of the naphthyl group in the symmetric 1,3,4-thiadiazole ligand by a phenyl group, leading to an asymmetric achiral 1,3,4-thiadiazole ligand and the complex $[\text{Fe}(\text{L}^{\text{Ph-TDA-Gly}})(\text{NCE})_2]$ with $\text{E} = \text{S}, \text{Se},$ and BH_3 . The influence of varying NCE co-ligands ($\text{E} = \text{S}, \text{Se},$ and BH_3) on the spin-crossover properties are investigated.

The introduction of chirality through the use of enantiopure alanine instead of glycine as the starting amino acid in the ligand synthesis is presented in Chapter 2, along with the impact of the intermolecular interactions on the *SCO* properties arising from different polymorphs formed by enantiopure and racemic mixtures of the complex $[\text{Fe}(\text{L}^{\text{Ph-TDA-Al}})(\text{NCBH}_3)_2]$. The formation of these polymorphs was traced to the non-equal coordination mode – in the achiral complex a meridional coordination mode can be observed, while in the chiral a facial coordination is present.

Besides than modifying the aryl system, we retained the naphthyl group and alter the heteroatom in the 1,3,4-chalcogendiazole ring from sulfur to oxygen. Julian Eppelsheimer shows an intriguing synergistic effect between the naphthyl emission and the spin-crossover behaviour in the solid state of

$[\text{Fe}(\text{L}^{\text{Naph-ODA-Gly}})(\text{NCBH}_3)_2]$. Further the Spin crossover in solution could be investigated by *EVANS-NMR* technique. These findings are presented in Chapter 3.

Using alanine as the starting material in the improved ligand synthesis yielded a stereoconservatively formed 1,3,4-oxadiazole-based complex $[\text{Fe}(\text{L}^{\text{Naph-ODA-Al}})(\text{NCBH}_3)_2]$. This compound exhibits a meridional coordination mode and is described in Chapter 4. Moreover, the subtle steric effect of the methyl group was found to have no influence on crystal packing, as all three complexes (R-enantiomer, S-enantiomer, and the racemic mixture) display identical packing motifs and temperature-dependent magnetic behavior.

To examine the facial and meridional isomers, two solvatomorphs of the asymmetric 1,3,4-thiadiazole complex $[\text{Fe}(\text{L}^{\text{Naph-TDA-py}})_2(\text{NCBH}_3)_2]$ bearing a naphthyl aryl system were synthesised and investigate. The detailed studies can be found in Chapter 5.

The final Chapter 6 comprise the discussion of the 1,3,4-oxadiazole- and 1,3,4-thiadiazole-based helical complexes and examines the influence of the bite angle, resulting from substitution of the chalcogen atom in the 1,3,4-chalcogendiazole ligand. Additionally, the intercalation behavior of small guest species, such as Li^+ ions, was examined.

Chapter 1: Achiral 1,3,4-Thiadiazole complexes for quantitative Packing analysis

This chapter presents the improved synthesis of the tetradentate ligand $L^{\text{Ph-TDA}}$ and its application in the design of three novel iron(II) complexes: $[\text{Fe}(L^{\text{Ph-TDA}})(\text{NCE})_2]$ ($E = \text{S, Se, BH}_3$). The complexes were structurally and magnetically characterized, by various methods including *ESI-MS*-spectrometry, elemental analysis, *IR*-spectroscopy, variable temperature *XRD*-measurement and *Mössbauer*-spectroscopy and *SQUID*-magnetometry. Structural and magnetic characterisation reveal that the complexes with the co-ligand NCSe remain in the *HS* state over the complete measured temperature range, while the co-ligand NCBH_3 lead to an abrupt *SCO*, attributed to the stronger ligand field strengths. The influence of the sulfur atom in the 1,3,4-thiadiazole core, in comparison to its isomorphous 1,3,4-oxadiazole analogues, was found to be minor. On the other hand, the NCS -containing complex shows unusual ordering phenomena, resulting in a $[\text{HS}][\text{LS}]$ spin state-ordered phase without a phase transition. This can be attributed to the presence of two individual iron complexes in the asymmetric unit with different distortion parameters. An DFT Model was used to investigate the packing energy and the impact on the spin state ordering phenomena.

The results are presented as a scientific article planned to publish.

Author contribution:

The general synthesis of the ligand system and the complexes was developed by [REDACTED], while the laboratory work on the ligand was performed by [REDACTED] and the complex synthesis was performed by [REDACTED] and [REDACTED]. The *IR*-spectroscopy was collected by [REDACTED] as well as the sample preparation for elemental analysis, *NMR*-spectroscopy and *ESI-MS*-spectrometry. Solid state absorption spectroscopy was performed in cooperation with [REDACTED], who performed the measurements while [REDACTED] prepared the samples. [REDACTED] collected the single crystal *XRD* data and refined the structure. The evaluation of the magnetic and structural data was done by [REDACTED]. *Mössbauer* spectroscopy data were collected by [REDACTED] as well as computational calculations supervised by [REDACTED] from *RPTU* Kaiserslautern. The Manuscript was written by [REDACTED], with input from [REDACTED] and [REDACTED]. [REDACTED] had the supervision during the manuscript process. All Authors have read and agreed to the submitted version of the manuscript.

Manuscript: Sub Lattice Driven Spin State Ordering and Coordination Elasticity in Fe(II) 1,3,4-Thiadiazole Complexes

Jens-Georg Becker,¹ Sriram Sundaresan², Tim Hochdörffer³, Juliusz A. Wolny³, Luca M. Carrella,¹ Volker Schünemann³ and Eva Rentschler^{1*}

¹Department Chemie, Johannes-Gutenberg-Universität Mainz, Duesbergweg 10–14, 55128 Mainz, Germany. Email: rentschl@uni-mainz.de

²Institute of Physics, Czech Academy of Sciences, Cukrovarnická 10, 162 00 Prague, Czech Republic.

³Department of Physics, University of Kaiserslautern-Landau, Erwin-Schrödinger-Str. 46, 67663 Kaiserslautern, Germany.

Abstract:

We report novel synthesis of 1-(5-phenyl-1,3,4-thiadiazol-2-yl)-N,N-bis(pyridin-2-ylmethyl)methanamine ($L^{\text{Ph-TDA}}$) ligand along with three complexes: $[\text{Fe}(L^{\text{Ph-TDA}})(\text{NCE})_2] \cdot \text{H}_2\text{O}$, where E = S (**C1**), Se (**C2**), and BH_3 (**C3**). All complexes were fully characterized by variable-temperature single-crystal X-ray diffraction and *SQUID* magnetometry. Notably, **C1** exhibits sublattice spin-state ordering at low temperatures, with one iron center in the asymmetric unit adopting a low-spin (LS) state, whereas a second one is locked in high-spin (HS). Light-induced spin state trapping (*LIESST*) successfully generated the high-spin (HS-HS) state at low temperatures, whereas the hidden LS-LS state could not be accessed *via* reverse-*LIESST*. Complex **C2** remained in the HS state across the entire temperature range studied. In contrast, complex **C3** displayed a complete, one-step spin crossover with a transition temperature ($T_{1/2}$) of 153 K. The spin state ordering at low temperatures for **C1** was further probed by *VT-Mössbauer* spectroscopy. Density functional theory (*DFT*) calculations quantify the energetic contributions underpinning the ordered LS-HS state in **C1** and further rationalize the ligand-field and co-ligand effects governing the spin crossover in the series. Comparison with the previously reported 1,3,4-oxadiazole analogs highlights the critical role of heteroatom substitution and NCE co-ligand variation in tuning the magnetic bistability.

Introduction:

Molecular materials often exhibit fascinating ordering phenomena, in which the arrangement of molecules within a crystal lattice dictates their electronic, magnetic, and optical properties.^[1–10] These effects are particularly pronounced in molecular solids, where the balance between intramolecular electronic structure and intermolecular packing interactions governs properties such as magnetism, conductivity, and optical response. The interplay between electronic configuration, lattice distortions, and intermolecular interactions often gives rise to cooperative behavior in molecular frameworks. Subtle perturbations at the molecular scale can propagate through the lattice, leading to stepwise spin

transitions, phase coexistence, or partial ordering of spin states. These phenomena are particularly relevant in materials exhibiting spin-crossover (*SCO*) behavior.

Spin-state ordering is commonly observed in *SCO* compounds, where the cooperative interconversion between high-spin (HS) and low-spin (LS) states produces correlated arrangements of spin centers within the lattice.^[11–14] In classical *SCO* systems, non-symmetry-breaking transitions result in gradual changes in the HS/LS population with temperature. A change in molecular volume accompanies each transition, and when the lattice cannot accommodate the strain, symmetry breaking may occur.^[14–16]

Theoretical approaches, including Landau theory^[15] and elastic models^[15,17–20], have been used to rationalize complex *SCO* profiles, such as multi-step or incomplete transitions. These frameworks highlight the role of lattice elasticity and two distinct order parameters: the non-symmetry-breaking parameter q , which describes the electronic instability, and the symmetry-breaking parameter η , which captures structural rearrangements, both of which govern the *SCO* pathway. Stepwise, non-symmetry-breaking transitions have been reported in mononuclear Fe(II) complexes with two inequivalent sublattices in the asymmetric unit.^[21] Each sublattice exhibits a distinct ligand-field environment and can be described by an independent order parameter (q_1, q_2).^[15] Although chemically identical, these sublattices may undergo spin transitions at different temperatures, resulting in a global stepped response.^[22–25]

Previous studies from our group have reported various *SCO* phenomena, including phase trapping, magnetic bistability, and spin-state ordering in 1,3,4-thiadiazole-based complexes, as well as mono- and dinuclear *SCO* complexes incorporating 1,3,4-oxadiazole ligands. In some cases, *SCO* is coupled with other functional properties, such as luminescence.^[26–28]

Though the spin state of $3d^4$ – $3d^7$ complexes is primarily determined by ligand-field strength, ligand-field effects alone do not fully account for observed *SCO* behavior of Fe(II) complexes. Intermolecular interactions and crystal packing also play decisive roles.^[29,30]

Herein, we report the synthesis of a tetradentate 1,3,4-thiadiazole-based ligand and its Fe(II) complexes with three different monodentate pseudohalide co-ligands (NCS^- , NCSe^- , and NCBH_3^-), providing a systematic platform to tune the ligand-field strength.^[31–35] This series enables a direct correlation between molecular structure, crystal packing, and spin-state behavior. Notably, the NCS^- complex exhibits spin-state ordering at low temperature, highlighting the cooperative interplay between lattice packing and ligand-field effects. Comprehensive structural, magnetic, and spectroscopic analyses, complemented by *DFT* calculations, reveal how phase transitions govern the emergence of ordered spin states and provide fundamental insight into controlling *SCO* behavior in molecular materials.

Results and discussion:

Synthesis:

The ligand was synthesized according to the reaction scheme given in Figure 1, with slight modifications to our previously reported ligand synthesis.^[36] 1-(5-phenyl-1,3,4-thiadiazole-2-yl)-N,N-bis(pyridin-2-ylmethyl)methanamine ($L^{\text{Ph-TDA}}$) was synthesised in two steps. Starting from glycine, reductive amination with pyridinecarboxyaldehyde and sodium trisacetoxyborhydride in dichloromethane was performed to obtain bis(pyridine-2-yl)glycine (**I**) in low yields (30%).^[37,38] The obtained product (**I**) was then further reacted with N,N'-Carbonyldiimidazole (CDI) as coupling agent in dichloromethane coupled with benzohydrazide in a peptide-like coupling reaction *in situ* to obtain N'-(bis(pyridin-2-ylmethyl)glycyl)benzohydrazide.^[39,40] Without any further purification or isolation, this was again further reacted *in situ* with Lawesson's reagent in dry tetrahydrofuran to obtain the desired 1-(5-phenyl-1,3,4-thiadiazol-2-yl)-N,N-bis(pyridin-2-ylmethyl)methanamine ($L^{\text{Ph-TDA}}$) in high yields (85%).^[41] The obtained Ligand $L^{\text{Ph-TDA}}$ was fully characterized by a range of techniques including $^1\text{H-NMR}$ -, $^{13}\text{C-NMR}$ -, 2D-NMR-, IR-spectroscopy and mass spectrometry.

The synthesis of the complexes was carried out under a nitrogen atmosphere and in dry acetonitrile by using the literature-reported precursor complexes $[\text{Fe}(\text{py})_4(\text{NCE})_2]$, with E = S, Se, and BH_3 .^[28] The desired complexes $[\text{Fe}(L^{\text{Ph-TDA}})(\text{NCE})_2]$ with E = S (**C1**), Se (**C2**) and BH_3 (**C3**) were obtained in moderate yields. In all three cases, the complexes obtained are air-stable and fully characterized using a range of techniques, including IR spectroscopy, which shows a principal peak at 2047 cm^{-1} and 2061 cm^{-1} , clearly confirming the formation of the complexes **C1** and **C2** by the characteristic C-N triple-bond stretching mode. Additionally, in the case of **C1**, the presence of a small shoulder close to 2047 cm^{-1} from the C-N triple bond suggests that the NCS co-ligands are bound to iron centers within two distinct coordination environments. For complex **C3**, the principal peak from the C-N triple bond is very close to the CO_2 peak around 2300 cm^{-1} ; therefore, it is difficult to identify. However, it can still be observed in the CO_2 -corrected spectrum at 2182 cm^{-1} . The reported values are consistent with those in the literature for Fe(II) complexes with NCE co-ligands.^[31,35] The formation of the complex is also confirmed by shifts of the C-N vibrations of the 1,3,4-thiadiazole core, which are 1587 cm^{-1} and 1567 cm^{-1} compared to **C1** (1600 cm^{-1} and 1570 cm^{-1}), **C2** (1603 cm^{-1} and 1570 cm^{-1}) and **C3** (1604 cm^{-1} and 1571 cm^{-1}). These shifts indicate a change in electron density due to coordination, as reported for similar complexes with a 1,3,4-oxadiazole core (**Figure S8 - S10**).^[32] The X-ray data for all three complexes were collected from single crystals carefully picked from the mother liquor, whereas magnetic data were collected from the pure bulk powder, which was filtered and dried in air unless otherwise indicated. Wherever possible, variable-temperature X-ray data were collected to investigate changes in bond lengths and other structural parameters associated with spin crossover. The bulk purity of the sample

is confirmed by elemental analysis and mass spectrometry, which indicate that, compared to the single-crystal *XRD* Data, the lattice solvent is exchanged from acetonitrile to water upon exposure to air. So, in all three cases, the powder samples of the complexes are obtained as a monohydrate. For better readability in the following sections, **C1-C3** refers to the bulk complex as monohydrates $\text{CX}\cdot\text{H}_2\text{O}$ ($X = 1, 2$ and 3). In the *HRES* mass spectrometry analysis of the complexes, the principal peak $[\text{Fe}(\text{L}^{\text{Ph-TDA}})(\text{NCE})]^+$ was found in all three cases, with $\text{E} = \text{S}$ (**C1**), Se (**C2**) and BH_3 (**C3**) confirmed by their corresponding isotopic patterns (**Figure S13 - S18**).

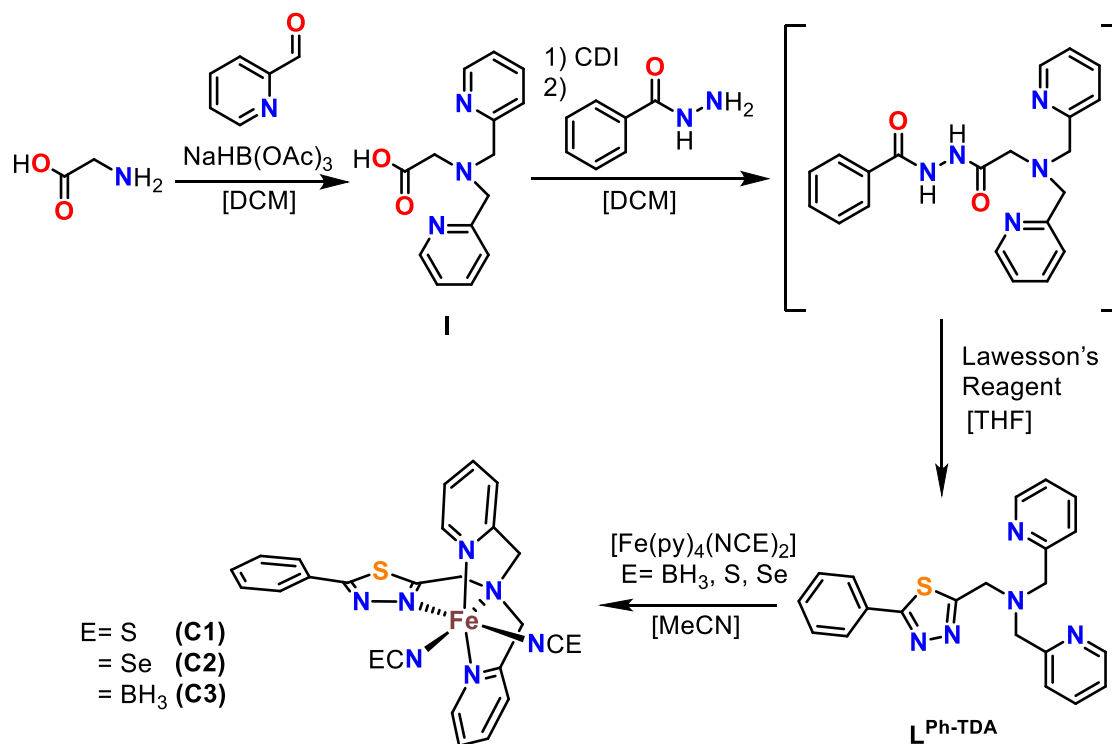


Figure 1: Multi step synthetic scheme for synthesis of 1-(5-phenyl-1,3,4-thiadiazol-2-yl)-N,N-bis(pyridin-2-ylmethyl)methanamine ($\text{L}^{\text{Ph-TDA}}$).

Temperature dependent magnetic properties:

To evaluate the impact of variation in the NCE auxiliary ligand on the ligand field strength of the $\text{Fe}(\text{II})$ center, and consequently on the spin crossover (*SCO*) properties, the temperature dependence of the magnetic moments was examined for all three complexes (**C1 - C3**). Temperature-dependent magnetic susceptibility (χ_{MT}) was measured on pure microcrystalline samples in the range of 10 - 300 K under heating and cooling conditions.

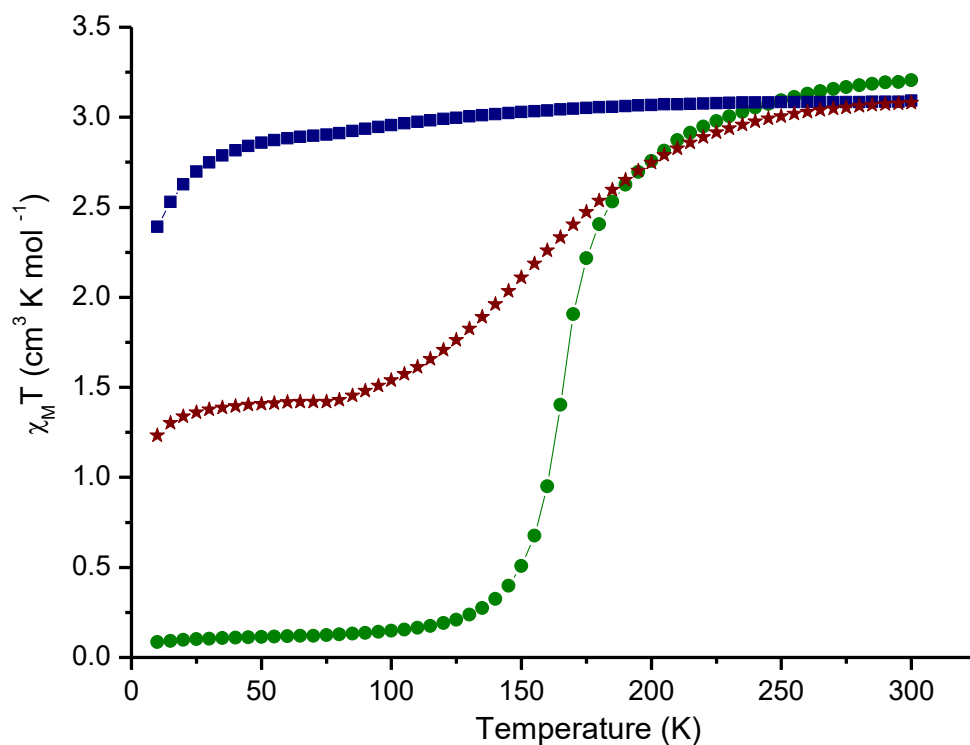


Figure 2: Temperature dependence of the molar susceptibility based on one $[\text{Fe}(\text{L}^{\text{Ph-TDA}})(\text{NCE})_2]$ unit with $E = \text{S}$ (**C1**; red), Se (**C2**; blue) and BH_3 (**C3**; green) depicted in $\chi_M T$ vs. T . The magnetic susceptibilities were determined between 300-10 K and 10-300 K and the additional data are shown in the *ESI* (**Figure S52 - S55**). The circle, square and stars represent the data, while the lines are just guides for the eye.

A $\chi_M T$ value of 3.09 at room temperature and $2.87 \text{ cm}^3 \cdot \text{K} \cdot \text{mol}^{-1}$ at 50 K confirms that the **C2** complex remains in the high-spin state across the entire temperature range (see **Figure 2**, blue curve). These values are in excellent agreement with literature data for mononuclear high-spin (HS) Fe(II) complexes, which typically exhibit magnetic moments in the range of $3\text{-}4 \text{ cm}^3 \cdot \text{K} \cdot \text{mol}^{-1}$.^[29,42] The slight decrease in the $\chi_M T$ value below 50 K can be attributed to a combination of weak intermolecular dipolar interactions and the zero-field splitting effects of the Fe(II) center.

In contrast, complex **C3** undergoes a complete one-step spin transition centered around 170 K ($T_{1/2}^{\text{down}} = T_{1/2}^{\text{up}} = 170 \text{ K}$). This is clearly reflected in the change in $\chi_M T$ from $0.08 \text{ cm}^3 \cdot \text{K} \cdot \text{mol}^{-1}$ at low temperatures to $2.96 \text{ cm}^3 \cdot \text{K} \cdot \text{mol}^{-1}$ at higher temperatures. When this SCO behavior is compared to that of the related 1,3,4-oxadiazole analog, $[\text{Fe}(\text{L}^{\text{Ph-ODA}})(\text{NCBH}_3)_2] \cdot 0.8 \text{ H}_2\text{O} \cdot 0.5 \text{ CH}_3\text{OH}$, it is worth noting that the spin transition in **C3** occurs more gradually over a 50 K range, likely due to lattice and solvent effects, as well as differences in crystal packing, which will be discussed in detail later.^[33] However, the slight shift in $T_{1/2}$ from 166 K, for the oxadiazole-based complex, to 170 K, for the thiadiazole-based analog, indicates only a small increase in ligand field strength upon replacing the 1,3,4-oxadiazole moiety with a 1,3,4-thiadiazole unit.^[33] A more pronounced effect seems to arise from the change in the ligand field strength imposed by the NCSe^- co-ligands. While **C2**, which contains NCSe^- co-ligands, remains in the

HS state throughout the 10 - 300 K range, **C3**, which contains stronger NCBH_3^- co-ligands, exhibits a well-defined spin transition at 170 K.

Based on this trend, it was expected that **C1**, with the weakest co-ligand (NCS^-), would remain in the HS state throughout the temperature range, as would **C2**. At room temperature, the observed $\chi_{\text{M}}T$ value of $3.08 \text{ cm}^3 \cdot \text{K} \cdot \text{mol}^{-1}$ for one $[\text{Fe}(\text{L}^{\text{Ph-TDA}})(\text{NCS})_2]$ unit closely matches the values reported in the literature for HS Fe(II) species, and is in good agreement with those of **C2** and **C3**. However, upon cooling, the $\chi_{\text{M}}T$ value gradually decreases to $1.41 \text{ cm}^3 \cdot \text{K} \cdot \text{mol}^{-1}$ and reaches a plateau between 30 and 85 K, with a $T_{1/2}$ value of 153 K. The spin switch occurs at higher temperatures than for **C2** with NCSe and at lower temperatures than for **C3** with NCBH_3 . This behavior deviates from the expected trend based solely on ligand field strength. The observation of an incomplete spin crossover in **C1** can be attributed to several structural and lattice-related factors commonly encountered in Fe(II) *SCO* systems. Partial conversion from the *HS* to the *LS* state is often the result of crystal packing constraints, which leave a fraction of the molecules in the *HS* configuration. Additionally, kinetic trapping of the *HS* species during cooling cannot be excluded a priori. Assuming negligible contribution to the magnetic moment from the low-spin (LS) Fe(II) state ($^1\text{A}_{1\text{g}}$, $S = 0$), the plateau value of $1.41 \text{ cm}^3 \cdot \text{K} \cdot \text{mol}^{-1}$ at 50 K indicates that 46% of the Fe(II) centers are trapped in the HS state. To further substantiate the partial *SCO* behavior observed for **C1**, variable-temperature *Mössbauer* spectroscopy (vide infra) and a thorough analysis of the structural data were performed.

Structural Characterization and Spin Crossover Behavior of Complexes C1–C3

Single crystals of the three complexes $[\text{Fe}(\text{L}^{\text{Ph-TDA}})(\text{NCE})_2] \cdot \text{solvent}$ ($\text{E} = \text{SCN}$ (**C1**), SeCN (**C2**), BH_3CN (**C3**)) were investigated by variable-temperature single-crystal X-ray diffraction (*SC-XRD*) at 120 K and 240 K (**C1**) or 230 K (**C3**). Complex **C1** $[\text{Fe}(\text{L}^{\text{Ph-TDA}})(\text{NCS})_2] \cdot 0.5 \text{ MeCN}$ crystallizes in the triclinic space group $\text{P}\bar{1}$, containing two independent $[\text{Fe}(\text{L}^{\text{Ph-TDA}})(\text{NCS})_2]$ units and one solvent molecule in the asymmetric unit. Both complexes **C2** and **C3** $([\text{Fe}(\text{L}^{\text{Ph-TDA}})(\text{NCE})_2] \cdot \text{MeCN}, \text{E} = \text{Se}, \text{BH}_3)$ crystallize in the monoclinic $\text{C2}/c$ space group. Each has one crystallographically independent complex and two and a half acetonitrile molecules in the asymmetric unit. Key crystallographic parameters are provided in **Tables S3 – S7**.

Each Fe(II) center in all three complexes is octahedrally coordinated by one tetradentate $\text{L}^{\text{Ph-TDA}}$ ligand and two cis-positioned pseudohalide co-ligands (NCS^- , NCSe^- , or NCBH_3^-). Depending on the co-ligand and temperature, the resulting FeN_6 cores display varying degrees of angular and bond-length distortion. At 120 K, **C1** exhibits two distinct iron sites: Fe1 and Fe2 (**Figure 3**). At 240 K, both are in the HS state with an average Fe-N distance of 2.18 Å (Fe1) and 2.16 Å (Fe2). Upon cooling to 120 K, Fe1 remains in the HS state with an average Fe-N distance of 2.17 Å, while Fe2 contracts to 1.98 Å. This

indicates that only Fe2 undergoes an HS \rightarrow LS transition.^[33,34] This is also reflected in the trigonal twist angle, which decreases from 92.8° at 240 K to 43.9° at 120 K for Fe2, but changes only slightly for Fe1 (109.3° \rightarrow 108.1°).^[43]

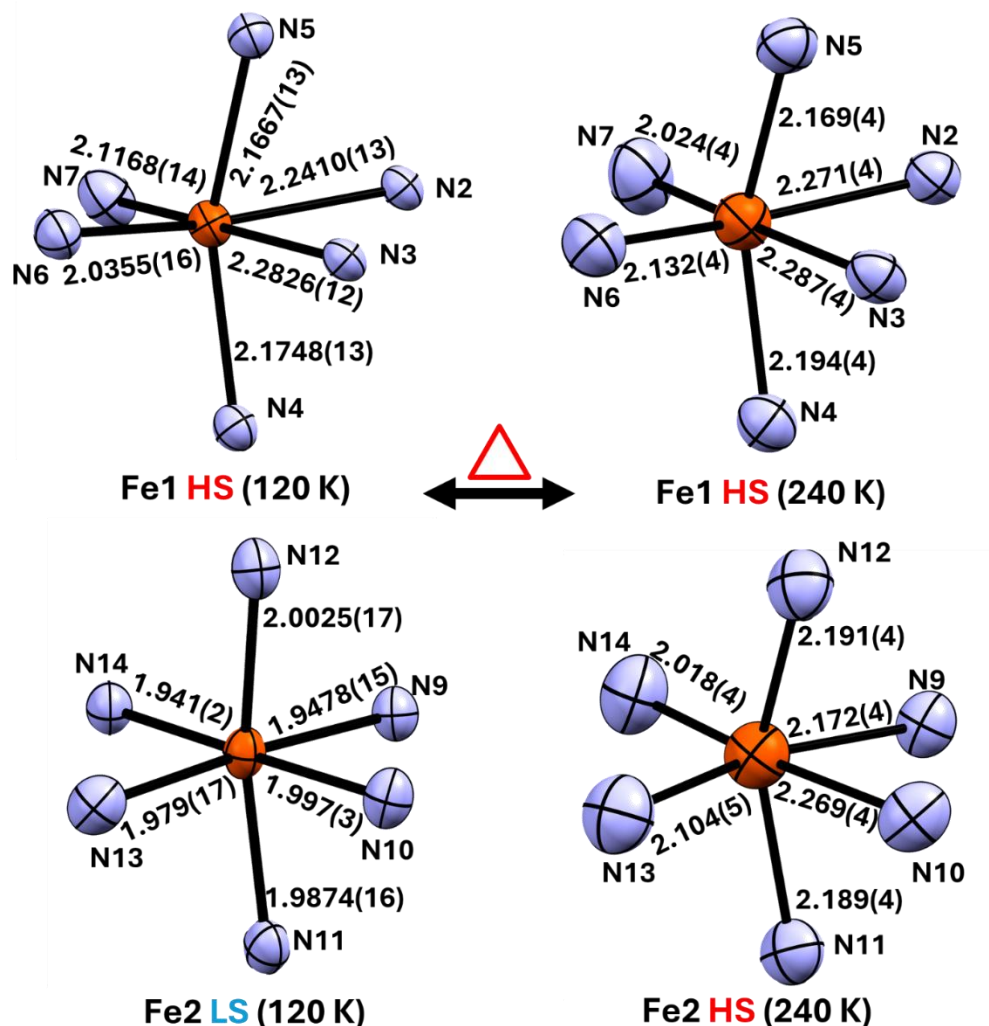


Figure 3: Iron(II)-nitrogen bond lengths for the two crystallographically independent, Fe1 and Fe2, iron(II) centers, in **C1** at 120 K and 240 K.

For **C2**, the Fe atom is disordered over two positions (85:15 ratio) with average Fe-N bond distances of 2.17 ± 0.08 Å and 2.06 ± 0.11 Å, and corresponding distortion parameters of 101.7° and 49.6°.^[33,43] These values are consistent with the high-spin configuration. Finally, in **C3**, no Fe-site disorder is observed. The average Fe-N distance at 120 K is 1.97 ± 0.02 Å, characteristic of the LS state, whereas at 230 K it increases to 2.15 ± 0.05 Å, indicative of a HS state.^[33,43] The distortion parameter rises from 49.6° to 86.9°, confirming a reversible, thermally induced spin crossover (SCO) (**Figure 4**).

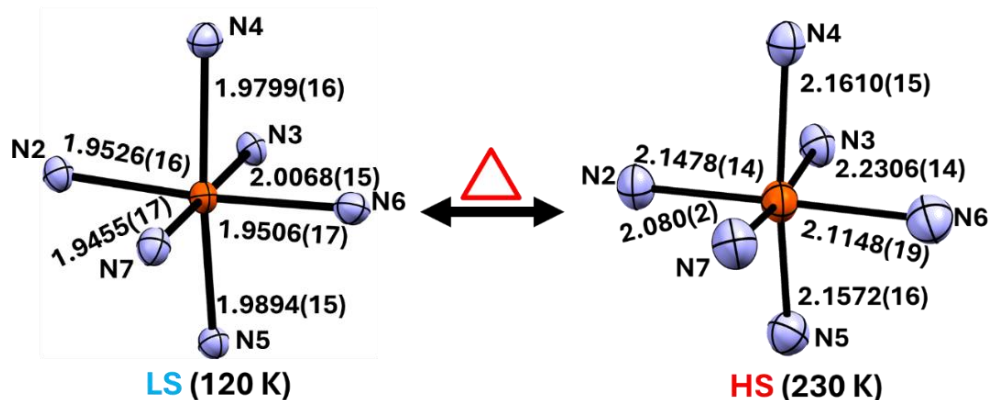


Figure 4: Metal donor bond distances at 120 and 230 K for $[\text{Fe}(\text{L}^{\text{Ph-TDA}})(\text{NCBH}_3)_2] \cdot \text{H}_2\text{O}$ (**C3**).

Comparison of **C2** and **C3** cell parameters according to the relation

$$\Pi = \frac{(a + b + c)}{(a' + b' + c')} - 1 = 0.008$$

(*B. Ribar et al.*^[44]) indicates that both are isostructural and isomorphous, despite differing co-ligands.^[31,32,45] Their nearly identical cell volumes (**C2**: 6508 Å³; **C3**: 6439 Å³ at 120 K) support this conclusion. At 230 K, the cell volume of **C3** increases by about 4%, consistent with a spin-state change from *LS* to *HS*. In contrast, **C2** remains essentially unchanged, confirming a locked HS configuration.

Packing motifs play an important role in modulating the *SCO* behavior of complexes.^[46] Thus, the intermolecular interactions of the complexes **C1** - **C3** are discussed in more detail here. In **C2** and **C3**, adjacent $[\text{Fe}(\text{L}^{\text{Ph-TDA}})(\text{NCE})_2]$ molecules form dimers via strong π - π interactions between the 5-phenyl-1,3,4-thiadiazole rings, with plane-to-atom distances of 3.558 Å (**C2** at 120 K), 3.377 Å (**C3** at 120 K), and 3.523 Å (**C3** at 230 K). Beyond these dimers, only weak π - π interactions are present between the tilted pyridyl rings (**Figures S39, S40, S45 - S46, S50-S51**). Solvent molecules occupy channels along the *c*-axis, where the sulfur atoms of the thiadiazole rings and the Se or BH₃ atoms/groups of the co-ligands point toward the interior (**Figures S38, S44, S49**). The complexes therefore behave as isolated π - π -linked dimers, with limited long-range cooperativity.

In **C1**, the packing arrangement is distinctly different. Two types of $[\text{Fe}(\text{L}^{\text{Ph-TDA}})(\text{NCS})_2]$ units (Fe1 and Fe2) are present, forming homologous pairs (Fe1-Fe1, Fe2-Fe2) separated by confined solvent molecules rather than channels. The Fe1-Fe1 dimers exhibit strong π - π stacking between the thiadiazole and phenyl groups, with plane-to-atom distances of 3.309 Å at 120 K and 3.376 Å at 240 K. These distances are even shorter than those in **C2** and **C3**, indicating particularly strong π - π coupling. No additional hydrogen bonds or π - π interactions are observed.^[46] The Fe2-Fe2 pairs, in contrast, are more weakly connected: the 5-phenyl-1,3,4-thiadiazole rings are co-planar but laterally shifted,

reducing the orbital overlap. Weak π - π interactions between pyridyl moieties connect these pairs into zig-zag chains, creating a more flexible lattice environment. This structural softness enables partial *SCO* in **C1**, localized to the Fe2 sublattice.

Changes in the Fe-N bond length and the resulting change in the unit cell volume clearly demonstrate the distinct *SCO* behavior throughout the series. For complex **C1**, only the Fe2 sites undergo conversion to the low-spin (LS) state upon cooling, while the Fe1 sites remain in the high-spin (HS) configuration. The coexistence of HS and LS centers within the same lattice gives rise to spin-state ordering. The unit-cell volume changes only slightly, from 2515 Å³ at low temperature to 2620 Å³ at high temperature, consistent with approximately 50% of the Fe(II) centers switching. In the case of **C2**, all structural parameters confirm a stable HS configuration throughout the entire temperature range investigated. By contrast, complex **C3** exhibits a complete and gradual *SCO*, as evidenced by both *SC-XRD* and magnetic measurements. Upon warming, the average Fe-N bond lengths increase from 1.97 Å to 2.15 Å, accompanied by a rise in the distortion parameter from 49.6° to 86.9°, and an expansion of the unit-cell volume by about 4%.^[46]

Overall, the combination of structural rigidity, π - π coupling, and ligand-field strength dictates the degree and cooperativity of spin crossover in these Fe(II) complexes. The three derivatives [Fe(L^{Ph-TDA})(NCE)₂] (E = S, Se, BH₃) display markedly different behaviors: **C1** exhibits sublattice spin-state ordering at low temperatures, **C2** remains locked in the HS state, and **C3** undergoes a complete, one-step *SCO* with $T_{1/2} = 153$ K.

Variable-temperature Mössbauer spectroscopy:

As illustrated in **Figure 5** and **Table 1**, the Mössbauer spectrum at 77 K was analyzed using two components, each with a 50% relative contribution, that can be assigned to two different iron centers in **C1**. Component 1 shows an isomer shift $\delta = 1.08$ mm · s⁻¹ and a quadrupole splitting $\Delta E_Q = 2.62$ mm · s⁻¹. These parameters are characteristic of an HS iron(II) in an octahedral ligand field and are assigned to the HS state of Fe1.^[47] Component 2, on the other hand, exhibits $\delta = 0.45$ mm · s⁻¹ and $\Delta E_Q = 0.25$ mm · s⁻¹. Such low values of the isomer shift and quadrupole splitting can be attributed to an LS iron(II) ion in an octahedral field and are assigned to the *LS* state of Fe2.^[47]

With increasing temperature, component 3 emerges showing $\delta = 1.04$ mm · s⁻¹ and $\Delta E_Q = 2.71$ mm · s⁻¹ and a relative contribution of 19% at the cost of component 2 at 150 K (**Figure 5b**). These parameters are typical of HS iron(II). Therefore, component 3 is assigned to the HS state of Fe2. This shows that a thermal spin transition from the *LS* to the *HS* state occurs in Fe2. In contrast, increasing the temperature results in nearly constant values of the isomer shift and quadrupole splitting for Fe1 (component 1). Only δ is slightly reduced due to the second order Doppler shift. This means that Fe1 is in the HS state

at all experimentally accessible temperatures, which is consistent with the magnetic susceptibility measurements and supports the structural analysis's conclusions. Further increase of the temperature to 270 K leads to the complete spin transition to the *HS* state of Fe2 (**Figure 5d**) in perfect agreement with the magnetic measurements and the crystal structure.

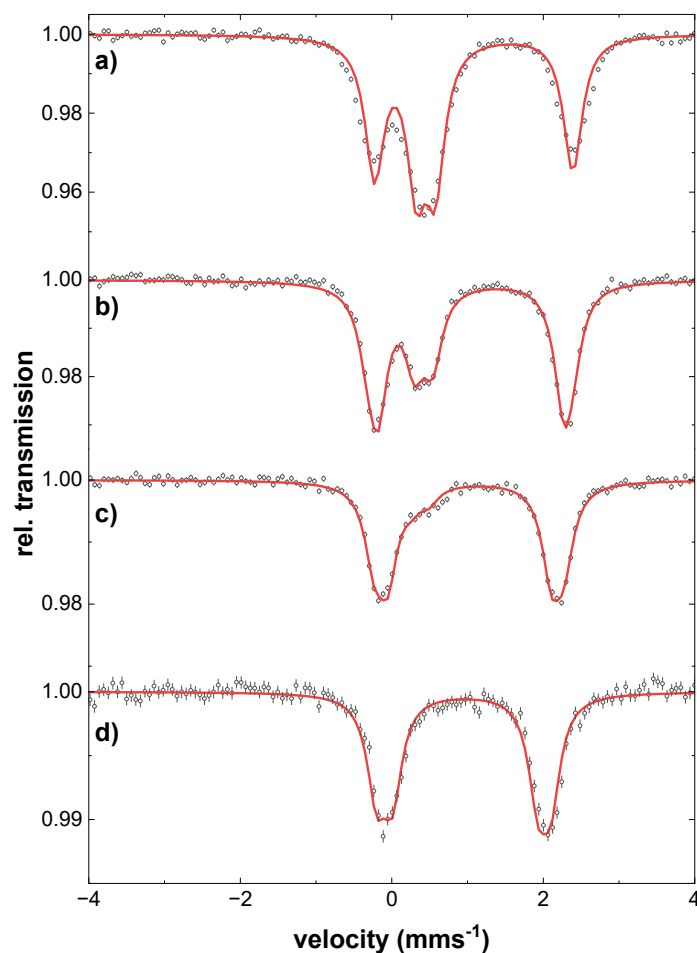


Figure 5: Mössbauer spectra of compound **C1** at a) 90 K, b) 150 K, c) 210 K and d) 270 K. The open circles show the experimental data obtained at the respective temperatures, the red solid lines represent simulations based on Lorentzian line shapes. The simulation parameters are listed in **Table 1**.

Table 1: Mössbauer parameters of Fe1 and Fe2 of the complex **C1** as obtained from the analysis of the experimental data displayed in **Fig. 5**. The line width Γ is 0.30(2) mms⁻¹ for all components.

T [K]	Fe1			Fe2					
	component 1			component 2			component 3		
	δ [mms ⁻¹]	ΔE_Q [mms ⁻¹]	area [%]	δ [mms ⁻¹]	ΔE_Q [mms ⁻¹]	area [%]	δ [mms ⁻¹]	ΔE_Q [mms ⁻¹]	area [%]
90	1.08(2)	2.62(3)	50	0.45(3)	0.25(4)	50			
150	1.05(2)	2.46(3)	50	0.42(3)	0.24(4)	31(3)	1.04(2)	2.71(3)	19(3)
210	1.03(2)	2.16(3)	50	0.38(3)	0.23(4)	9(3)	1.02(2)	2.51(3)	41(3)
270	0.97(2)	1.92(3)	50				0.95(2)	2.30(3)	50

DFT modelling

Clearly in the $[\text{Fe}(\text{L}^{\text{Ph-TDA}})(\text{NCE})_2]$ with E = S (**C1**), Se (**C2**) and BH₃ (**C3**) complexes, the packing effects play just a significant role as the ligand field strength. In the isomorphous structures of **C2** and **C3** the ligand field strength is the crucial factor to observe spin transition or not. With a weaker ligand field induced by the NCS⁻ ligands no spin transition can be observed (**C2**), while the stronger ligand field of NCBH₃⁻ leads to a spin crossover at 170 K. In case of **C1** obviously the packing plays the main factor. Although the coordination environments of $[\text{Fe1}(\text{L}^{\text{Ph-TDA}})(\text{NCS})_2]$ and $[\text{Fe2}(\text{L}^{\text{Ph-TDA}})(\text{NCS})_2]$ are nearly identical, they behave completely different on cooling. Thus, we looked at the elastic effects of the packing via *DFT* calculations.

First, we calculated the ground state energies of the HS (E_{HS}) and the LS (E_{LS}) states for the isolated molecules **C1** - **C3**. This yields the electronic spin transition energies $E_{\text{el}}^{\text{iso}} = E_{\text{HS}} - E_{\text{LS}}$. Next, for compound **C1** we estimated the effect of the lattice which has a spin occupation of HS:LS = 1:1 at low temperatures on the spin transition energies of the sites Fe1 and Fe2. For this purpose, we used the method recently proposed by us.^[48]

Within this approach, one performs calculations of spin transition energy in the model crystal $E_{\text{el}}^{\text{cryst}}$ by optimizing the geometry of the LS and HS states of the molecules in the environment of their neighbors, with coordinates taken from the crystal structure. The geometry of the neighbors remains fixed. For **C1** a model containing 22 complex molecules and 11 molecules of MeCN, present in the crystal lattice, was used. As in previous paper the high-spin molecules that were not optimised were replaced by the diamagnetic Zn(II) analogues in order to minimise the computational effort.^[48] The observed disorder arising from the deviation of the 5-phenyl-1,3,4-thiadiazole moieties at the Fe1 pairs of the single-crystal structure of **C1** was neglected in the model, as it has no influence. Since the

inversion center lies between the moieties, both isomers are present in equal amounts and thus have the same intermolecular interactions. Furthermore, the disorder associated with Fe2 and the NCS coligand was also disregarded, as it corresponds to partially unswitched high-spin Fe(II). At temperatures below 85 K, the system exhibits a 50:50 distribution of high-spin (*HS*) and low-spin (*LS*) Fe(II). Since the crystal structure was measured at 120 K, the disorder was not explicitly modelled. The used model is depicted schematically in **Figure 6**. The optimised structures are given as *pdb* and *xyz* files in Supplementary Materials.

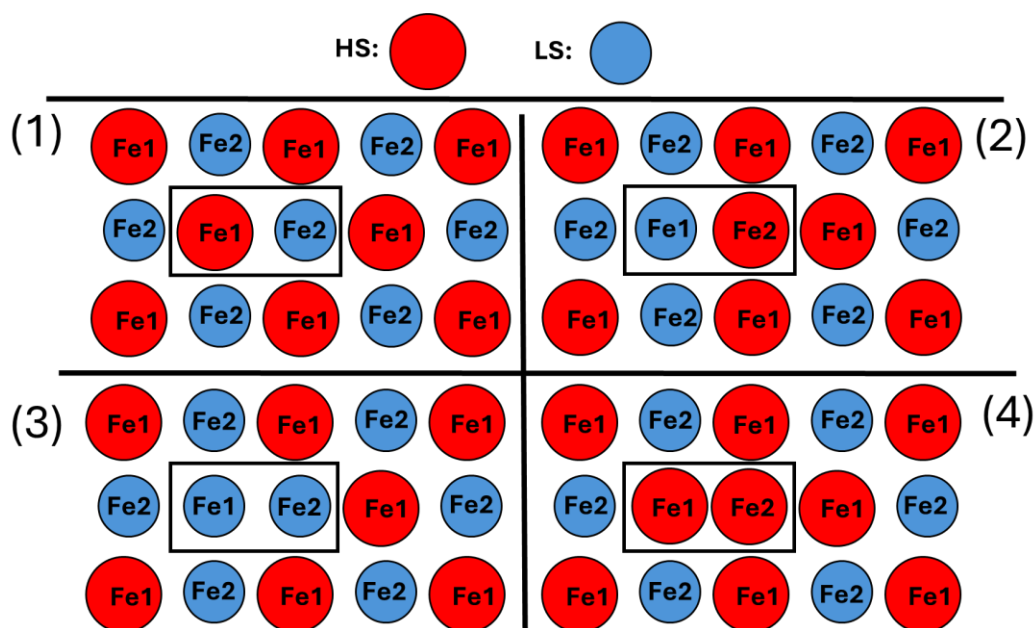


Figure 6: Graphic representation of the model of the low-temperature crystal structure of **C1** used for the DFT calculations for the four cases considered: (1) HS-Fe1-LS-Fe2 (as observed in the crystal structure), (2) LS-Fe1-HS-Fe2 (inverse to the situation observed in the crystal structure), (3) LS-LS and (4) HS-HS. The complexes are simplified by circles (red = high spin state iron(II)) and blue circle (low spin state state). The molecules in the black box were optimized. The molecules out of the box, as well as MeCN, were kept frozen during optimization. To reduce the computational time the frozen Fe2 molecules were modeled as the Zn(II) analogs.

Two molecules at the centre of the model assembly were optimised for four possible spin states: both in the LS state (LS-Fe1-LS-Fe2) (3); both in the HS state (HS-Fe1-HS-Fe2) (4); Fe1 in the HS state and Fe2 in the LS state (HS-Fe1-LS-Fe2, corresponding to the crystal structure at low temperatures) (1); and Fe1 in the LS state and Fe2 in the HS state (LS-Fe1-HS-Fe2) (contrary to what is observed in the crystal structure) (2). Details of how the particular spin distributions were achieved can be found in the Computational Methods section in the SI. The geometry of the other thirteen complex molecules and the solvated acetonitrile molecules was frozen. The optimized systems are provided as *PDB* files in the *ESI*. The combined results are given in **Table 2**.

Table 2: First column: DFT (CAM-B3LYP/CEP-31G/D3) calculated values of E_{el}^{iso} in (kJ·mol⁻¹) for **C1**, **C2** and **C3**. Second column: Electronic energies of the three different spin isomers of the **C1** crystal model taken relative to the HS-Fe1-HS-Fe2 spin isomer model. Third column: Spin transition energies to the 2HS isomer. Fourth column: Calculated values of $H_{elastic}$.

Isolated molecule/ E_{el}^{iso}		Models of crystal of C1 /relative electronic energies		E_{el}^{cryst}		$H_{elastic}$
C1	-34	LS-Fe1-LS-Fe2	37 ^a	[2LS -> 2HS] ^a	-37	-31 ^a
C2	-28	HS-Fe1-LS-Fe2	19	[Fe1 ^{HS} Fe2 ^{LS} -> 2HS]	-19	-15
C3	-21	LS-Fe1-HS-Fe2	29	[Fe1 ^{LS} Fe2 ^{HS} -> 2HS]	-29	-5
		HS-Fe1-HS-Fe2	0			
[Fe(L ^{npdtz}) ₂ (NCS) ₂] ^b	-18			[LS->HS] LS matrix	-9	-9
				[LS->HS] HS matrix	-20	2

^afor two switching centres. ^b [48]

The absolute values of the obtained electronic spin transition energies E_{el} are highly dependent on the applied exchange-correlation functional.^[48,49] Therefore, it is important to compare the obtained values within a series of related molecules/molecular assemblies. In this respect, the calculated values for the isolated complex molecules **C1** - **C3** suggest that **C3** ($E_{el}^{iso} = -21$ kJ·mol⁻¹) is the molecule with the lowest stabilization of the HS state. This is the only one of the three systems displaying the full HS-to-LS transition in the 300 - 10 K range. The calculated energies of the isolated molecules are in perfect agreement with the increase in ligand field strength from NCS⁻ < NCS^{e-} < NCBH₃⁻. Stronger ligand field strength stabilizes the LS versus the HS i.e. destabilize the HS versus the LS in the order **C3** > **C2** > **C1**. Complex **C1** with the lowest value of $E_{el}^{iso} = -34$ kJ·mol⁻¹ show partial switching of the iron(II). This leads to the conclusion that packing effects present in the crystal lattice of **C1** allow the LS state for 50% of the molecules at low temperatures.

Modeling four **C1** structures using a 22-molecule assembly reveals the relative energies of four different spin-state distributions in Fe1 and Fe2, while keeping the matrix identical to that of the crystal structure of the low-temperature phase of **C1**.

(i) The HS-Fe1-HS-Fe2 spin isomer has the lowest energy, while the LS-Fe1-LS-Fe2 spin isomer has the highest energy.

(ii) The HS-Fe1-LS-Fe2 spin isomer, which corresponds to that observed at low temperatures, is 19 kJ·mol⁻¹ higher in energy than the HS-Fe1-HS-Fe2 isomer and 10 kJ·mol⁻¹ lower than the LS-Fe1-HS-Fe2 isomer, i.e., the isomer with the inverted spin distribution of the Fe1 and Fe2 centers. This result indicates the influence of the crystal lattice of the low-temperature phase, in which the LS-Fe1-HS-Fe2 spin isomer is a double-center defect. To quantify the effect of the lattice on the spin transition energies compared to that calculated for the isolated molecules we now introduce the parameter $H_{elastic}$, which we define as the difference between the spin transition energy calculated for the isolated molecule

E_{el}^{iso} and the spin transition energy obtained for the model crystal E_{el}^{cryst} . It is well known that E_{el}^{iso} reflects the effects of the ligand field differences between spin isomers that may be tuned by the ligand strain effects.^[51] In addition to the ligand field differences, E_{el}^{cryst} also contains contributions from intermolecular interactions in the crystal and hence reflects the elastic interaction between lattice and the center of a given spin.

In our model system there are three possible spin transitions: (i) LS Fe1 and LS Fe2 undergo spin transition: [2LS \rightarrow 2HS], (ii) Fe1 remains HS and only Fe2 undergoes spin transition: [Fe1^{HS}Fe2^{LS} \rightarrow 2HS], and (iii) Fe2 remains HS and only Fe1 undergoes spin transition: [Fe1^{LS}Fe2^{HS} \rightarrow 2HS].

For (i) [2LS \rightarrow 2HS] we have calculated $H_{elastic} = -31 \text{ kJ}\cdot\text{mol}^{-1}$ ($2 \times -34 + 37$) which amounts to $-15.5 \text{ kJ}\cdot\text{mol}^{-1}$ per Fe(II) centre. That suggests an average stabilization of the LS-pair with one LS-defect compared to the isolated molecules. For (ii) [Fe1^{HS}Fe2^{LS} \rightarrow 2HS] we obtain $H_{elastic} = -15 \text{ kJ}\cdot\text{mol}^{-1}$, pointing to a similar stabilization of the LS-state in the lattice, compared to the isolated molecule. For (iii) [Fe1^{LS}Fe2^{HS} \rightarrow 2HS] we get $H_{elastic} = -5 \text{ kJ}\cdot\text{mol}^{-1}$, indicating a low effect of the lattice on the LS \rightarrow HS spin transition in the matrix corresponding to the low-temperature structure. Hence, the results imply generally the stabilisation of the low-spin state by the 1:1 HS-LS lattice compared to the isolated molecule, the effect being the lowest when the observed occupation of sites Fe(1) and Fe(2) by the high-spin and low-spins molecules, respectively is reversed. The calculated spin transition values for the related [Fe(L^{npdtz})₂(NCS)₂] complex we give the $H_{elastic}$ values of -9 and $2 \text{ kJ}\cdot\text{mol}^{-1}$ for the LS- and HS-lattice model, respectively^[48] pointing to a stabilisation of the low-spin state by the low-spin matrix.

A further insight into the effects of 1:1 LS:HS matrix on the energy and geometry of the “defects” may be obtained by comparing the structures of the optimised low-spin and high-spin molecules for all four patterns of occupation of the Fe(1) and Fe(2) sites. For this purpose we performed the point-energy calculations for the optimised molecules in (LS-Fe1-LS-Fe2), (HS-Fe1-HS-Fe2), (HS-Fe1-LS-Fe2) and (LS-Fe1-HS-Fe2) pairs. The results are given in **Table 3**.

Table 3: Calculated relative energies (point energies of the isolated molecules) of the low-spin and high-spin molecules for the Fe(1)-Fe(2) pair optimised with the 22-molecule models of the different spin distributions. The lowest value of four obtained was taken to be zero. The energies of the “defects” in the LS:HS matrix are given in italics.

	HS-Fe1-LS-Fe2	LS-Fe1-HS-Fe2	LS-Fe1-LS-Fe2 Fe(1)	LS-Fe1-LS-Fe2 Fe(2)	HS-Fe1-HS-Fe2 Fe(1)	HS-Fe1-HS-Fe2 Fe(2)
$E_{LS} / \text{kJ}\cdot\text{mol}^{-1}$	0	6	6	0		
$E_{HS} / \text{kJ}\cdot\text{mol}^{-1}$	1	5			0	4

It seems that the LS centre has two possible structures, corresponding to the “regular” one, observed in *X-ray* for Fe(2) and the “defect” one differing at 6 kJ·mol⁻¹ in energy.

Table 4: Calculated low-spin Fe-N distances (in Å) for the “regular” (low-spin Fe(2) and “defect” ones (low-spin Fe(1)) structures for the optimised models of three spin distributions of the low-spin state. The values for the “defect” are given in italics.

	HS-Fe1-LS-Fe2	LS-Fe1-HS-Fe2	LS-Fe1-LS-Fe2	
			Fe(1)	Fe(2)
Fe-N _{thiazole}	1.968	<i>2.004</i>	<i>2.006</i>	1.969
Fe-N _{Nsp3}	2.051	<i>2.048</i>	<i>2.047</i>	2.052
Fe-N _{py}	1.996, 1.996	<i>1.990, 2.006</i>	<i>1.990, 2.006</i>	1.995, 1.996
Fe-N _{NCS}	1.958, 1.967	<i>1.952, 1.971</i>	<i>1.952, 1.973</i>	1.959, 1.969

In **Table 4** we compare the calculated bond lengths for three possible distributions of the low-spin state between Fe(1) and Fe(2) sites, i.e. two LS/HS systems and the LS/LS one. It is evident that the low-spin Fe(2) in HS-Fe1-LS-Fe2 and LS-Fe1-LS-Fe2 models are the same, with the largest difference to be 0.002 Å for one of the Fe-N_{py} bond. Similar consistency occurs for the two structures bearing a low-spin defect in Fe(1) site. The main structural difference between the “regular” and “defect” geometry is the average 0.0365 Å elongation of the Fe-N_{thiazole} bond for the latter. No other bond reveals a particular distance difference for both structures. Hence, solely the above-mentioned elongation in the “defect” structures brings about the 6 kJ·mol⁻¹ increase in its energy.

Table 5: Calculated high-spin Fe-N distances (in Å) for the “regular” high-spin structure of the regular (high-spin Fe(1) and “defect” ones (high-spin Fe(2)) for the optimised models of three spin distributions of the high-spin state. The values for the “defect” are given in italics.

	HS-Fe1-LS-Fe2	LS-Fe1-HS-Fe2	HS-Fe1-HS-Fe2	
			Fe(1)	Fe(2)
Fe-N _{thiazole}	2.192	<i>2.146</i>	<i>2.144</i>	2.191
Fe-N _{Nsp3}	2.305	<i>2.311</i>	<i>2.312</i>	2.306
Fe-N _{py}	2.142, 2.142	<i>2.138, 2.161</i>	<i>2.139, 2.162</i>	2.143
Fe-N _{NCS}	2.141, 2.040	<i>2.113, 2.067</i>	<i>2.109, 2.063</i>	2.136, 2.039

The obtained results for the high-spin bond lengths are collected in **Table 5**. Again, it seems that both “regular” HS structures are nearly identical, the largest differences concerning one of the Fe-N_{NCS} bonds (0.005 Å), while the “defect” ones match equally well with the largest differences concerning again one of the Fe-N_{NCS} bonds (0.004 Å). Similarly, the only pronounced change on going from the “regular” and “defect” structures concerns the Fe-N_{thiazole} which is on average 0.0465 Å shorter for the “defect”

structures. This pattern, together with a bit lower energetic effect of distortion effect for the high-spin isomers resembles the general pattern of elongation of the low-spin bonds and shortening of the high-spin upon distortion by lattice.^[48,49]

Conclusions:

In summary, we have introduced a new 1,3,4-thiadiazole-based tetradentate ligand, $L^{\text{Ph-TDA}}$, and demonstrated its ability to stabilize distinct spin states in a family of iron(II) complexes, $[\text{Fe}(L^{\text{Ph-TDA}})(\text{NCE})_2]$ ($E = \text{S, Se, BH}_3$). The series of complexes, **C1-C3**, reveals a clear dependence of spin-crossover (SCO) behavior on the ligand-field strength of the coordinated pseudohalides, following the order $\text{NCS}^- < \text{NCSe}^- < \text{NCBH}_3^-$. In **C1**, the weaker NCS^- co-ligand generates a small ligand-field splitting and a distorted coordination environment, giving rise to sublattice spin-state ordering at low temperature: π - π -stacked Fe1 dimers remain locked in the high-spin (HS) state, while more flexible Fe2 sites undergo partial SCO. In **C2**, substitution by the slightly stronger NCSe^- co-ligand enhances the ligand field, but due to packing effects, **C2** remains locked in the HS state throughout the measured temperature range. By contrast, **C3**, containing the strongest-field NCBH_3^- co-ligand, stabilizes the low-spin (LS) state at low temperature and undergoes a complete SCO centered around $T_{1/2} \approx 150$ K.

The observation of ordered LS-HS sublattices in **C1** underscores the delicate balance between electronic and cooperative effects that dictates bistability. Complementary DFT calculations provide quantitative insight into the energetics of the spin states, clarifying how ligand-field strength, coordination geometry, and the choice of co-ligand collectively determine SCO behavior. Together, these results position the $(L^{\text{Ph-TDA}})\text{-Fe(II)-NCE}$ framework as a versatile platform for engineering spin-state ordering and controllable SCO phenomena, advancing design principles for multifunctional molecular switches and enabling the rational exploitation of ordered spin states and photoinduced phase transitions in responsive magnetic materials.

Experimental:

All chemicals were purchased from Deutero, Fisher Chemicals, TCI, Sigma-Aldrich BLD Pharma and Carbolution used without further purification. Solvents were dried according to the literature known procedures and used freshly distilled. NMR spectra were recorded at room temperature with a Bruker Avance DSX 400 and analyzed with the program MestReNova.^[50] Magnetic susceptibility measurements were performed on a Quantum Design SQUID magnetometer MPMSXL in a temperature range between 5 and 300 K with an applied field of 1 kOe. The ATR-IR spectra was recorded at room temperature on a Bruker ALPHAII ATR-IR, analysed with the software OPUS and plotted in Origin 7.5 V5. HRes ESI mass spectra were recorded on Agilent 6200 series TOF/6500 series G-TOF (11.0.203.0) at Johannes Gutenberg-University Mainz in acetonitrile. Elemental analysis

(Elementar vario EL Cube: C, H, and N) were measured at the microanalytical laboratories of the Johannes Gutenberg University Mainz. Solid State UV-Vis measurement were done with following setup: Synchronous scans of the solid sample and the reference (PTFE plate) were measured with a FLS1000 spectrometer from *Edinburgh Instruments* equipped with a cooled photomultiplier detector PMT-980 and BaSO₄ was used as matrix. A xenon arc lamp Xe2 (450 W) was used for excitation. The measurements were carried out using a liquid nitrogen cooled MicrostatN from *Oxford Instruments* combined with the Cryosphere from *Edinburgh Instruments*. X-ray diffraction data were collected with STOE STADIVARI at the Johannes Gutenberg University Mainz. The structures were solved with ShelXT and refined with ShelXL implemented in the program Olex2.^[51-53] The X-ray cif file data are deposited on the Cambridge CCDC database with identification numbers 2480291-2480295.

Mössbauer spectroscopy

Mössbauer experiments were performed in transmission geometry in time-scale mode in conjunction with a 512-channel analyzer (WissEl GmbH, Starnberg, Germany). Variable temperature measurements were performed using a continuous flow cryostat (Optistat^{DN}, Oxford Instruments, Abingdon, UK). The radioactive source consisted of ⁵⁷Co diffused in Rh with an activity of 1.67 GBq. The calibration of the spectrometer was carried out against α -iron at room temperature. The analysis of the spectral data was accomplished using least-squares fits and Lorentzian line shapes employing the public domain program Vinda running on Excel 2003[®] platform.^[54]

DFT-calculations

DFT calculations were performed with Gaussian 16^[55] using the CAM-B3LYP^[56] functional and the cep-31g basis^[57-59] set with Grimme D3 dispersion correction^[60]. Further details of calculations are given in ESI.

Ligand Synthesis:**Bis(pyridine-2-yl)glycine (I)**

Glycine (3.00 g, 79.93 mmol, 1.0 eq.) was suspended in 80 mL DCM under nitrogen atmosphere. Under cooling with ice sodium trisacetoxyborohydride (21.18 g, 99.91 mmol, 2.5 eq.) was added and stirred. After 10 minutes a solution of 2-Pyridinecarbaldehyd (7.60 mL, 79.93 mmol, 2.0 eq.) in 20 mL dichloromethane was added. The cooling was replaced, and the yellowish suspension was allowed to warm up overnight. 70 ml saturated sodium bicarbonate solution was added and after 30 minutes the two phases were extracted, and the aqueous phase was extracted twice with 150 mL DCM. The organic phase was dried over sodium sulphate and the solvent was removed under reduced pressure. The crude product was purified via column chromatography (dichloromethane: methanol; 90:10). The product was isolated as brown powder (3.113 g, 12.10 mmol, 30 %). ¹H-NMR (400 MHz, Chloroform-*d* δ(ppm)): 8.59 – 8.53 (m, 2H), 7.67 (td, *J* = 7.7, 1.8 Hz, 1H), 7.33 – 7.29 (m, 1H), 7.23 (ddd, *J* = 7.6, 4.9, 1.2 Hz, 1H), 4.11 (s, 2H), 3.61 (s, 1H).

1-(5-phenyl-1,3,4-thiadiazol-2-yl)-N,N-bis(pyridin-2-ylmethyl)methanamine (L^{Ph-TDA})

Bis(pyridin-2-ylmethyl)glycine (3.00 g, 11.66 mmol, 1 eq.) was solved in 80 mL dichloromethane under nitrogen atmosphere and ice cooling. Carbonyldiimidazol (1.89, 11.66 mmol, 1eq.) was added to the solution and stirred for 1h. Afterwards benzohydrazide (1.59, 11.66 mmol, 1eq.) added and the suspension was stirred overnight. The solvent was removed under reduced pressure and the residue was solved in 100 ml dry THF under nitrogen atmosphere. Lawesson's reagent (5.16 g, 12.76 mmol, 1.1 eq) was added and the yellow solution was stirred under reflux overnight. The solvent was removed under reduced pressure. The residue was mixed with 300 mL DCM and 75 mL saturated bicarbonate solution and extracted. The organic phase was twice washed with 75 mL saturated bicarbonate solution, dried over sodium sulphate and the solvent was removed under reduced pressure. The crude product was purified via column chromatography (dichloromethane: methanol; 95:5). The product was isolated as brown powder (3.69 g, 9.87 mmol, 85 %) ¹H-NMR (400 MHz, Chloroform-*d* δ(ppm)): 8.60 (ddd, *J* = 4.9, 1.9, 0.9 Hz, 2H), 8.00 – 7.95 (m, 2H), 7.71 (td, *J* = 7.7, 1.8 Hz, 2H), 7.55 (dt, *J* = 7.8, 1.1 Hz, 2H), 7.51 – 7.47 (m, 3H), 7.21 (ddd, *J* = 7.5, 4.9, 1.2 Hz, 2H), 4.23 (s, 2H), 3.98 (s, 4H). ¹³C NMR (101 MHz, Chloroform-*d* δ(ppm)): 170, 169, 158, 149, 137, 131, 130, 129, 128, 123.17, 122, 60, 53. FT-IR: $\tilde{\nu}$ (cm⁻¹) = 2935, 2820, 1587, 1567, 1474, 1456, 1431, 1358, 1309, 1240, 1181, 1143, 1110, 1085, 1064, 1043, 1026, 995, 975, 961, 914, 889, 875, 835, 773, 756, 684, 625, 608, 577, 519, 507, 402; ESI-MS (m/z): calc. for [C₂₂H₂₂N₅S₁]⁺ expected: 374.14 (100.00 %); found: 374.143 (100.00 %); Elemental Analysis calculated for L^{Ph-TDA} H₂O 0.7 CH₃OH (C_{23.7} H_{25.8} N₅O_{1.7}S): C, 63.54, H, 4.90, N, 16.45. found: C, 63.71, H, 4.08, N, 16.36.

Complex Synthesis:

The Precursor complex $[\text{Fe}(\text{py})_4(\text{NCS})_2]$, $[\text{Fe}(\text{py})_4(\text{NCSe})_2]$ and $[\text{Fe}(\text{py})_4(\text{NCBH}_3)_2]$ were synthesised accordingly to literature known procedure.^[14]

 $[\text{Fe}(\text{L}^{\text{Ph-TDA}})(\text{NCS})_2]$ (C1)

The following reaction was carried out in a glovebox under an inert atmosphere. $[\text{Fe}(\text{py})_4(\text{NCS})_2]$ (231.0 mg, 0.3143 mmol, 1 eq.) was suspended in 16 mL dry acetonitrile and stirred for 30 minutes. The suspension was added to a solution of $\text{L}^{\text{Ph-TDA}}$ (174.5 mg, 0.4672 mmol, 1 eq.) in 2 mL of acetonitrile and the resulting orange mixture was stirred for 1 h. The orange precipitate was obtained in moderate yields (173 mg, 0.4672 mmol, 67 %), was filtered and dried under Nitrogen atmosphere. Orange crystals suitable for X-ray diffraction were obtained after four days of slow evaporation out of the filtrated solution. FT-IR: $\tilde{\nu}$ (cm^{-1}) 2914, 2047, 1600, 1570, 1459, 1432, 1348, 1307, 1250, 1148, 1097, 1048, 1017, 988, 954, 874, 823, 795, 762, 733, 688, 641, 511, 492, 471; ESI-MS (m/z): calc. for $[\text{C}_{22}\text{H}_{19}\text{FeN}_6\text{S}_2]^+$ expected: 487.05 (100.00 %); found: 487.05 (100.00 %); Elemental Analysis calculated for $[\text{Fe}(\text{L}^{\text{Ph-TDA}})(\text{NCS})_2] \cdot \text{H}_2\text{O}$ ($\text{C}_{23}\text{H}_{21}\text{FeN}_7\text{OS}_3$): C, 49.21, H, 3.86, N, 17.15. found: C, 49.03, H, 3.76, N, 17.40.

 $[\text{Fe}(\text{L}^{\text{Ph-TDA}})(\text{NCSe})_2]$ (C2)

The following reaction was carried out in a glovebox under an inert atmosphere. $[\text{Fe}(\text{py})_4(\text{NCSe})_2]$ (231.0 mg, 0.4672 mmol, 1 eq.) was suspended in 16 mL dry acetonitrile and stirred for 30 minutes. The suspension was added to a solution of $\text{L}^{\text{Ph-TDA}}$ (174.5 mg, 0.4672 mmol, 1 eq.) in 2 mL of acetonitrile and the resulting yellow mixture was stirred for 1 h. The yellow precipitate was obtained in moderate yields (179 mg, 0.2781 mmol, 60 %), was filtered and dried under Nitrogen atmosphere. Yellow crystals suitable for X-ray diffraction were obtained after four days of slow evaporation out of the filtrated solution. FT-IR: $\tilde{\nu}$ (cm^{-1}) 2905, 2061, 1763, 1603, 1570, 1476, 1458, 1438, 1349, 1304, 1282, 1254, 1171, 1153, 1097, 1073, 1048, 1017, 998, 969, 955, 940, 896, 874, 823, 759, 732, 690, 640, 618, 581, 511, 496, 476, 447, 423; ESI-MS (m/z): calc. for $[\text{C}_{22}\text{H}_{19}\text{FeN}_6\text{SSe}]^+$ expected: 535.0 (100.00 %); found: 535.0 (100 %); Elemental Analysis calculated for $[\text{Fe}(\text{L}^{\text{Ph-TDA}})(\text{NCSe})_2] \cdot \text{H}_2\text{O}$ ($\text{C}_{23}\text{H}_{21}\text{FeN}_7\text{O}_1\text{SSe}_2$): C, 42.10, H, 3.28, N, 13.64. found: C, 42.03, H, 3.22, N, 14.92.

 $[\text{Fe}(\text{L}^{\text{Ph-TDA}})(\text{NCBH}_3)_2]$ (C3)

The following reaction was carried out in a glovebox under an inert atmosphere. $[\text{Fe}(\text{py})_4(\text{NCBH}_3)_2]$ (107.0 mg, 0.2336 mmol, 1 eq.) was suspended in 8 mL dry acetonitrile and stirred for 30 minutes. The suspension was added to a solution of $\text{L}^{\text{Ph-TDA}}$ (87.25 mg, 0.2336 mmol, 1 eq.) in 1 mL of acetonitrile and the resulting mixture was stirred for 1 h and the solution was filtered. The product was obtained in moderate yields as brown crystals suitable for X-ray diffraction after four days of slow evaporation (29.75 mg, 0.05845 mmol, 25 %). FT-IR: $\tilde{\nu}$ (cm^{-1}) = 2916, 2338, 2182, 1626, 1604, 1571, 1479, 1460,

1441, 1351, 1316, 1287, 1252, 1115, 1050, 1020, 989, 956, 880, 805, 760, 733, 689, 642, 578, 511, 493, 454, 417; ESI-MS (m/z): calc. for $[\text{C}_{23}\text{H}_{24}\text{BFeN}_6\text{S}]^+$ expected: 469.11 (100.00 %); found: 469.11 (100.00 %); Elemental Analysis calculated for $[\text{Fe}(\text{L}^{\text{Ph-TDA}})(\text{NCBH}_3)_2] \cdot \text{H}_2\text{O}$ ($\text{C}_{24}\text{H}_{29}\text{B}_2\text{FeN}_7\text{OS}$): C, 52.27, H, 4.91, N, 19.24. found: C, 52.42, H, 5.16, N, 18.60.

Acknowledgements:

The authors thank Dr. Robert Naumann and Prof. Heinze (JGU) for the solid state UV-Vis measurements and evaluation of the data. JGB, JAW, VS and ER acknowledge funding from the Deutsche Forschungsgemeinschaft (DFG, German Research Foundation)-TRR 173-268565370 Spin+X (Project No. A04). J. A. W. and V. S. are grateful to Allianz für Hochleistungsrechnen Rheinland-Pfalz (AHRP) for providing CPU-time within the project RPTU-SPINPLUSXA4.

Conflicts of interest

There are no conflicts to declare

References:

- [1] J. S. Miller *Chem. Soc. Rev.* **2011**, *40*, 3266.
- [2] E. Collet, H. Watanabe, N. Bréfuel, L. Palatinus, L. Roudaut, L. Toupet, K. Tanaka, J.-P. Tuchagues, P. Fertey, S. Ravy, B. Toudic, H. Cailleau *Phys. Rev. Lett.* **2012**, *109*, 257206.
- [3] S. Kamilya, S. Mehta, M. Semwal, R. Lescouëzec, Y. Li, J. Pechousek, V. R. Reddy, E. Rivière, M. Rouzières, A. Mondal *Inorg. Chem.* **2023**, *62*, 8794–8802.
- [4] J. E. Clements, J. R. Price, S. M. Neville, C. J. Kepert *Angew. Chem. Int. Ed.* **2016**, *55*, 15105 - 15109.
- [5] J. Cruddas, B. J. Powell *J. Am. Chem. Soc.* **2019**, *141*, 19790 - 19799.
- [6] A. Rotaru, I. A. Gural'skiy, G. Molnár, L. Salmon, P. Demont, A. Bousseksou *Chem. Commun.* **2012**, *48*, 4163 - 4165.
- [7] Z.-B. Hu, X. Yang, J. Zhang, L.-A. Gui, Y.-F. Zhang, X.-D. Liu, Z.-H. Zhou, Y. Jiang, Y. Zhang, S. Dong, Y. Song *Nat. Comm.* **2024**, *15*, 4702.
- [8] Z. Zhang, C. Duan, S. Wang, T. Xie, F. Zou, Y. Luo, R. Tang, K. Guo, L. Yuan, K. Zhang, Y. Wang, J. Qiu, K. Yan *Angew. Chem. Int. Ed.* **2024**, *136*, e202412042.
- [9] Q. Li, Z. Li *Acc. Chem. Res.* **2020**, *53*, 962 - 973.
- [10] J. J. Zakrzewski, M. Liberka, J. Wang, S. Chorazy, S. Ohkoshi *Chem. Rev.* **2024**, *124*, 5930 - 6050.
- [11] P. Gütllich, A. Hauser, H. Spiering *Angew. Chem. Int. Ed. Engl.* **1994**, *33*, 2024 - 2054.
- [12] P. Gutlich, V. Ksenofontov, A. Gaspar *Coor. Chem. Rev.* **2005**, *249*, 1811 - 1829.
- [13] G. D. Harzmann, R. Frisenda, H. S. J. Van Der Zant, M. Mayor *Angew. Chem. Int. Ed.* **2015**, *54*, 13425 - 13430.
- [14] R. G. Torres Ramírez, E. Trzop, E. Collet *Dalton Trans.* **2024**, *53*, 10159 - 10167.
- [15] G. Azzolina, R. Bertoni, E. Collet *J. Appl. Phys.* **2021**, *129*, 085106.
- [16] M. Shatruck, H. Phan, B. A. Chrisostomo, A. Suleimenova *Coord. Chem. Rev.* **2015**, *289 - 290*, 62 - 73.
- [17] A.-I. Popa, L. Stoleriu, C. Enachescu *J. Appl. Phys.* **2021**, *129*, 131101.
- [18] M. Nishino, Y. Singh, K. Boukheddaden, S. Miyashita *J. Appl. Phys.* **2021**, *130*, 141102.
- [19] E. Collet, G. Azzolina *Phys. Rev. Mat.* **2021**, *5*, 044401.
- [20] J. Pavlik, R. Boča *Eur. J. Inorg. Chem.* **2013**, *2013*, 697 - 709.
- [21] K. D. Murnaghan, C. Carbonera, L. Toupet, M. Griffin, M. M. Dîrtu, C. Desplanches, Y. Garcia, E. Collet, J. Létard, G. G. Morgan *Chem. Eur. J.* **2014**, *20*, 5613 - 5618.
- [22] Y. Garcia, O. Kahn, L. Rabardel, B. Chansou, L. Salmon, J. P. Tuchagues *Inorg. Chem.* **1999**, *38*, 4663 - 4670.
- [23] E. Milin, V. Patinec, S. Triki, E.-E. Bendeif, S. Pillet, M. Marchivie, G. Chastanet, K. Boukheddaden *Inorg. Chem.* **2016**, *55*, 11652 - 11661.

- [24] T. Boonprab, S. J. Lee, S. G. Telfer, K. S. Murray, W. Phonsri, G. Chastanet, E. Collet, E. Trzop, G. N. L. Jameson, P. Harding, D. J. Harding *Angew. Chem. Int. Ed.* **2019**, *131*, 11937 - 11941.
- [25] G. Li, O. Stefanczyk, K. Kumar, L. Guérin, K. Okuzono, K. Tran, M. Seydi Kilic, K. Nakabayashi, K. Imoto, A. Namai, Y. Nakamura, S. Ranjan Maity, F. Renz, G. Chastanet, S. Ohkoshi *Angew. Chem. Int. Ed.* **2025**, *64*, e202423095.
- [26] J. Kiehl, T. Hochdörffer, L. M. Carrella, V. Schünemann, M. H. Nygaard, J. Overgaard, E. Rentschler *Inorg. Chem.* **2022**, *61*, 3141 - 3151.
- [27] C. Köhler, E. Rentschler *Eur. J. Inorg. Chem.* **2016**, *2016*, 1955 - 1960.
- [28] S. Sundaresan, J.-G. Becker, J. Eppelsheimer, A. E. Sedykh, L. M. Carrella, K. Müller-Buschbaum, E. Rentschler *Dalton Trans.* **2023**, *52*, 13181 - 13189.
- [29] P. Gütlich, Y. Garcia, H. A. Goodwin *Chem. Soc. Rev.* **2000**, *29*, 419 - 427.
- [30] D. J. Harding, P. Harding, W. Phonsri *Coordination Chemistry Reviews* **2016**, *313*, 38 - 61.
- [31] M. You, G. T. Nguyen, D. Shao, T. Wang, X.-Y. Chang, L. Ungur, Y.-Z. Zhang *Dalton Trans.* **2022**, *51*, 5596 - 5602.
- [32] S. Sundaresan, S. Brooker *Inorg. Chem.* **2023**, *62*, 12192 - 12202.
- [33] S. Sundaresan, J. Eppelsheimer, E. Gera, L. Wiener, L. M. Carrella, K. R. Vignesh, E. Rentschler *Dalton Trans.* **2024**, *53*, 10303 - 10317.
- [34] R. W. Hogue, R. G. Miller, N. G. White, H. L. C. Feltham, G. N. L. Jameson, S. Brooker *Chem. Commun.* **2014**, *50*, 1435 - 1437.
- [35] A. Arroyave, A. Lennartson, A. Dragulescu-Andrasi, K. S. Pedersen, S. Piligkos, S. A. Stoian, S. M. Greer, C. Pak, O. Hietsoi, H. Phan, S. Hill, C. J. McKenzie, M. Shatruk *Inorg. Chem.* **2016**, *55*, 5904 - 5913.
- [36] J.-G. Becker, S. Sundaresan, Luca. M. Carrella, E. Rentschler *Chem. Commun.* **2025**, *61*, 13389 - 13392.
- [37] P. N. Basa, C. A. Barr, K. M. Oakley, X. Liang, S. C. Burdette *J. Am. Chem. Soc.* **2019**, *141*, 12100 - 12108.
- [38] Sm. K. Levalada, S. R. Banerjee, K. P. Maresca, J. W. Babich, J. Zubieta *Synthesis* **2004**, *11*, 1759 - 1766
- [39] A. A. Pund, S. S. Saboo, G. M. Sonawane, A. C. Dukale, B. K. Magare *Synth. Commun.* **2020**, *50*, 3854 - 3864.
- [40] A. A. Pund, M. H. Shaikh, B. G. Chandak, V. N. Bhosale, B. K. Magare *Polycyclic Aromatic Compounds* **2023**, *43*, 1247 - 1262.
- [41] G. Nagendra, R. S. Lamani, N. Narendra, V. V. Sureshbabu *Tetrahedron Letters* **2010**, *51*, 6338 - 6341.
- [42] H. S. Scott, R. W. Staniland, P. E. Kruger *Coord. Chem. Rev.* **2018**, *362*, 24–43.

- [43] S. Yuan, N. Natt, B. J. Powell *Inorg. Chem.* **2025**, *64*, 7182 - 7193.
- [44] A. Kálmán, G. Argay, D. Scharfenberg-Pfeiffer, E. Höhne, B. Ribár *Acta Crystallogr., Sect. B: Struct. Sci.* **1991**, *47*, 68 - 77.
- [45] S. Ranjan, R. Devarapalli, S. Kundu, S. Saha, S. Deolka, V. R. Vangala, C. M. Reddy *IUCrJ* **2020**, *7*, 173 - 183.
- [46] P. Guionneau *Dalton Trans.* **2014**, *43*, 382 - 393.
- [47] E. Kuzmann, Z. Homonnay, Z. Klencsár, R. Szalay *Molecules* **2021**, *26*, 1062.
- [48] J. A. Wolny, K. Gröpl, J. Kiehl, E. Rentschler, V. Schünemann *Dalton Trans.* **2024**, *53*, 8391 - 8397.
- [49] J. A. Wolny, X. Li, M. Dîrtu, K. Gröpl, T. Hochdörffer, H. Paulsen, Y. Garcia, V. Schünemann *RSC Adv.* **2025**, *15*, 32009 - 32030.
- [50] J. C. Cobas, F. J. Sardina *Concepts Magnetic Resonance* **2003**, *19A*, 80 - 96.
- [51] G. M. Sheldrick *Acta Crystallogr. A. Found. Adv.* **2015**, *71*, 3 - 8.
- [52] G. M. Sheldrick *Acta Crystallogr. A. Found. Crystallogr.* **2008**, *64*, 112 - 122.
- [53] G. M. Sheldrick, T. R. Schneider in *Methods in Enzymology*, Elsevier, **1997**, pp. 319 - 343.
- [54] H. P. Gunnlaugsson *Hyperfine Interact* **2016**, *237*, 79.
- [55] M. J. Frisch, G. W. Trucks, H. B. Schlegel, G. E. Scuseria, M. A. Robb, J. R. Cheeseman, G. Scalmani, V. Barone, G. A. Petersson, H. Nakatsuji, X. Li, M. Caricato, A. V. Marenich, J. Bloino, B. G. Janesko, R. Gomperts, B. Mennucci, H. P. Hratchian, J. V. Ortiz, A. F. Izmaylov, J. L. Sonnenberg, D. Williams-Young, F. Ding, F. Lipparini, F. Egidi, J. Goings, B. Peng, A. Petrone, T. Henderson, D. Ranasinghe, V. G. Zakrzewski, J. Gao, N. Rega, G. Zheng, W. Liang, M. Hada, M. Ehara, K. Toyota, R. Fukuda, J. Hasegawa, M. Ishida, T. Nakajima, Y. Honda, O. Kitao, H. Nakai, T. Vreven, K. Throssell, J. A. Montgomery Jr., J. E. Peralta, F. Ogliaro, M. J. Bearpark, J. J. Heyd, E. N. Brothers, K. N. Kudin, V. N. Staroverov, T. A. Keith, R. Kobayashi, J. Normand, K. Raghavachari, A. P. Rendell, J. C. Burant, S. S. Iyengar, J. Tomasi, M. Cossi, J. M. Millam, M. Klene, C. Adamo, R. Cammi, J. W. Ochterski, R. L. Martin, K. Morokuma, O. Farkas, J. B. Foresman, D. J. Fox **2016**.
- [56] T. Yanai, D. P. Tew, N. C. Handy *Chem. Phys. Lett.* **2004**, *393*, 51 - 57.
- [57] W. J. Stevens, H. Basch, M. Krauss *J. Chem. Phys.* **1984**, *81*, 6026 - 6033.
- [58] W. J. Stevens, M. Krauss, H. Basch, P. G. Jasien *Can. J. Chem.* **1992**, *70*, 612 - 630.
- [59] T. R. Cundari, W. J. Stevens *J. Chem. Phys.* **1993**, *98*, 5555 - 5565.
- [60] S. Grimme, J. Antony, S. Ehrlich, H. Krieg *J. Chem. Phys.* **2010**, *132*, 154104.

ESI: Sub Lattice Driven Spin State Ordering and Coordination Elasticity in Fe(II) 1,3,4-Thiadiazole Complexes

Jens-Georg Becker,¹ Sriram Sundaresan^{1,2}, Tim Hochdörffer³, Juliusz A. Wolny³, Luca M. Carrella¹, Volker Schünemann³ and Eva Rentschler^{1*}

¹Department Chemie, Johannes-Gutenberg-Universität Mainz, Duesbergweg 10–14, 55128 Mainz, Germany.
Email: rentschl@uni-mainz.de

²Institute of Physics, Czech Academy of Sciences, Cukrovarnická 10, 162 00 Prague, Czech Republic.

³Department of Physics, University of Kaiserslautern-Landau, Erwin-Schrödinger-Str. 46, 67663 Kaiserslautern, Germany.

Table of Contents

1. <i>NMR</i> -Spectra:	97
2. <i>IR</i> -spectra:.....	100
3. <i>HRES ESI</i> Mass spectra:.....	102
4. Crystal structure description	106
5. Crystallographic Data.....	124
6. Magnetic data.....	133
7. Light-induced excited spin state trapping:	134
8. Solid state <i>UV-Vis</i> measurement.....	136
9. <i>DFT</i> data and methods	139

1. NMR-spectra:

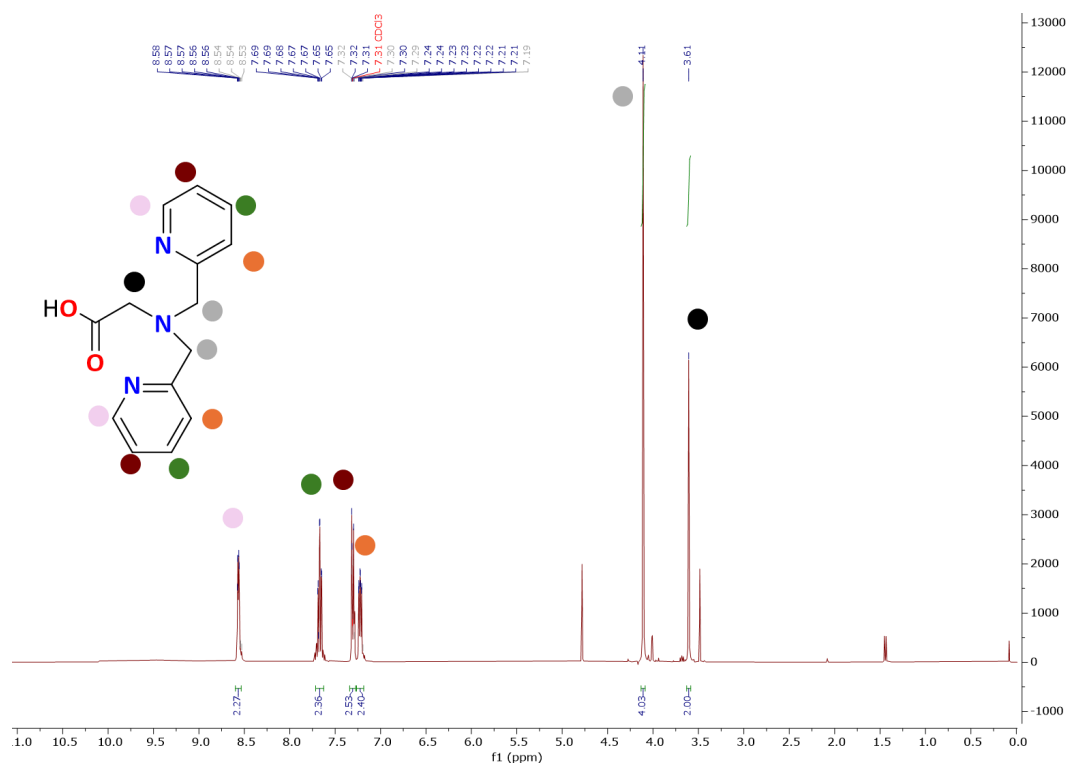


Figure S1: $^1\text{H-NMR}$ spectrum of the tert-butyl bis(pyridin-2-ylmethyl)glycine (I) in CDCl_3 [400 MHz]. The peak at 4.78 ppm could be assigned to impurity, which could be dichloromethane. The peak at 3.49 can be assigned to methanol and the peak at 1.44 could be assigned to water.^[1]

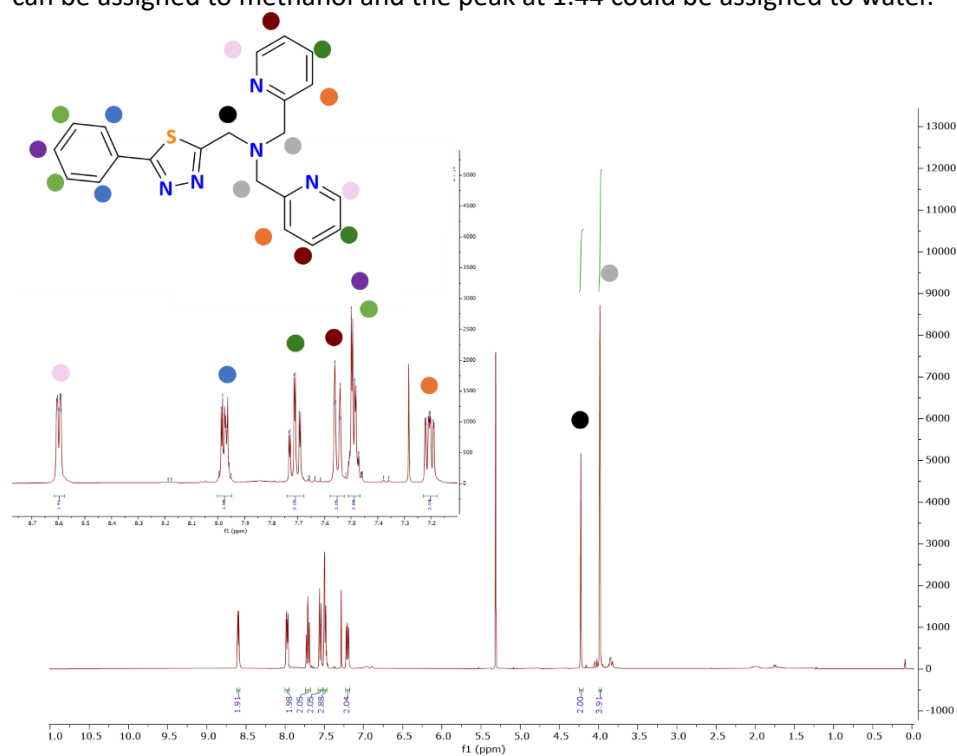


Figure S2: $^1\text{H-NMR}$ spectrum of the 1-(5-phenyl-1,3,4-thiadiazol-2-yl)-N,N-bis(pyridin-2-ylmethyl)methanamine ($\text{L}^{\text{Ph-TDA}}$) in CDCl_3 [400 MHz]. The peak at 5.31 ppm could be assigned to dichloromethane.^[1]

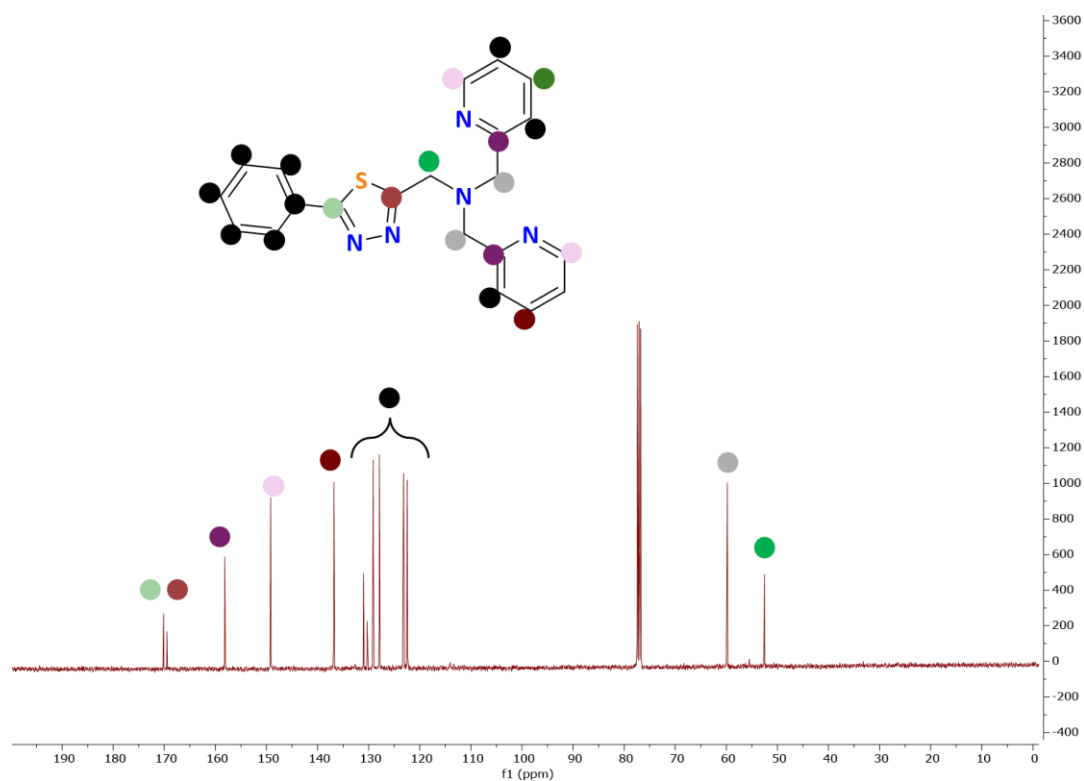


Figure S3: ^{13}C -NMR spectrum of the1-(5-phenyl-1,3,4-thiadiazol-2-yl)-N,N-bis(pyridin-2-ylmethyl)methanamine ($\text{L}^{\text{Ph-TDA}}$) in CDCl_3 [400 MHz].

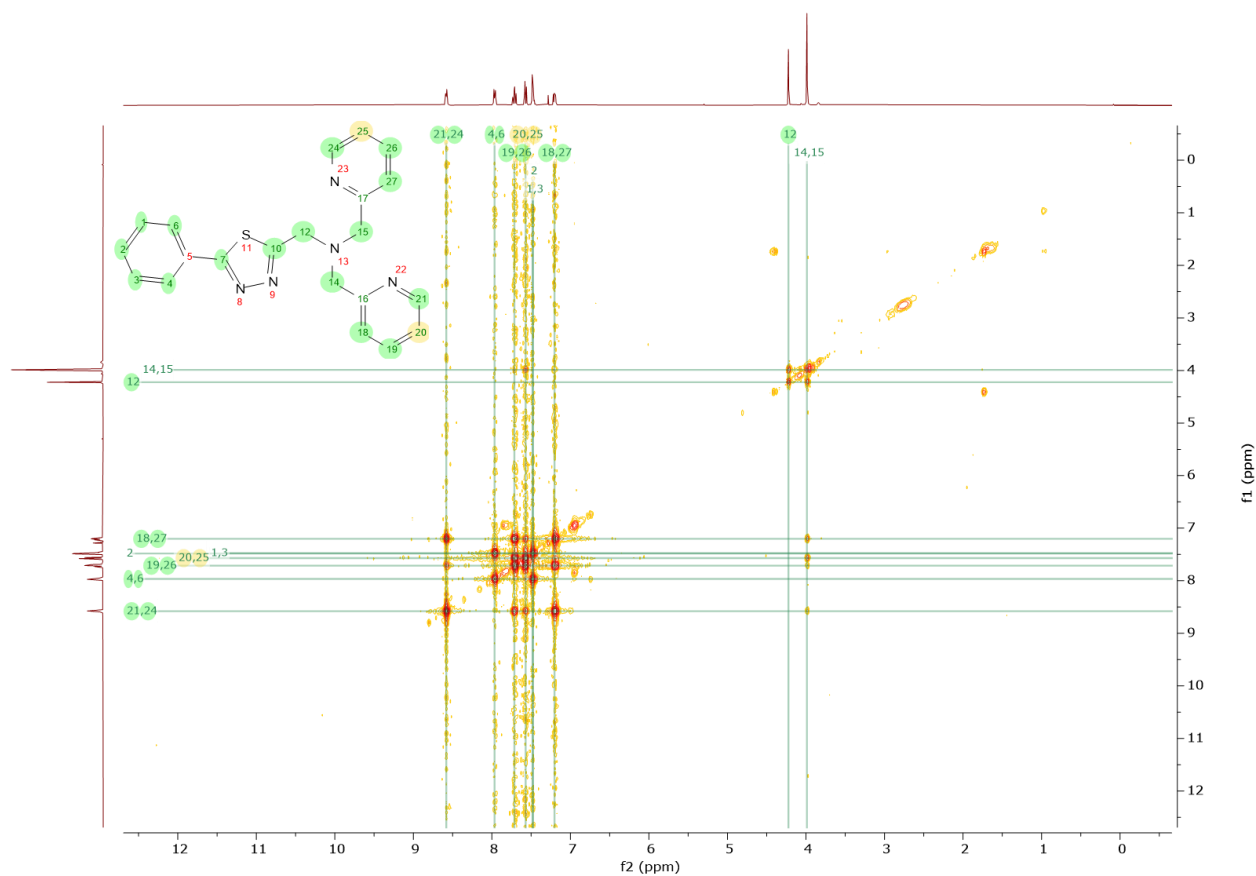


Figure S4: COSY spectrum of the1-(5-phenyl-1,3,4-thiadiazol-2-yl)-N,N-bis(pyridin-2-ylmethyl)methanamine ($\text{L}^{\text{Ph-TDA}}$) in CDCl_3 [400 MHz].

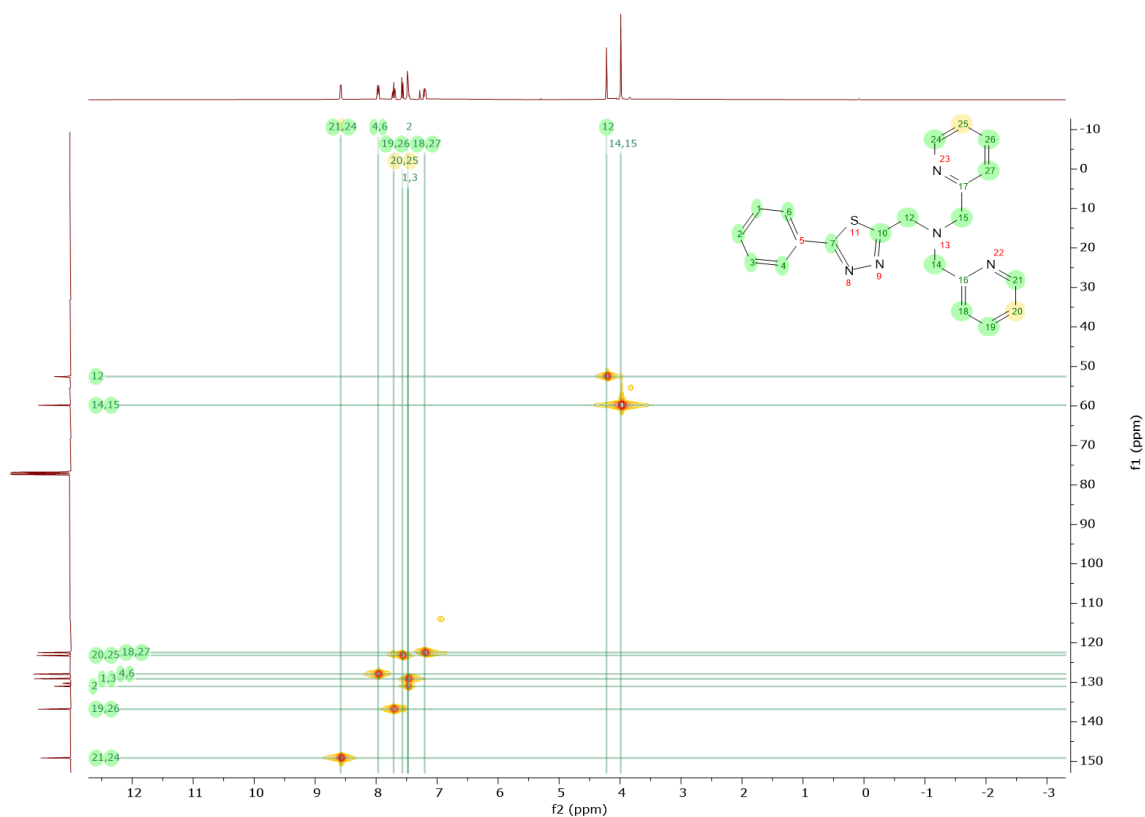


Figure S5: *HSCQ* spectrum of the1-(5-phenyl-1,3,4-thiadiazol-2-yl)-N,N-bis(pyridin-2-ylmethyl)methanamine ($\text{L}^{\text{Ph-TDA}}$) in CDCl_3 [400 MHz].

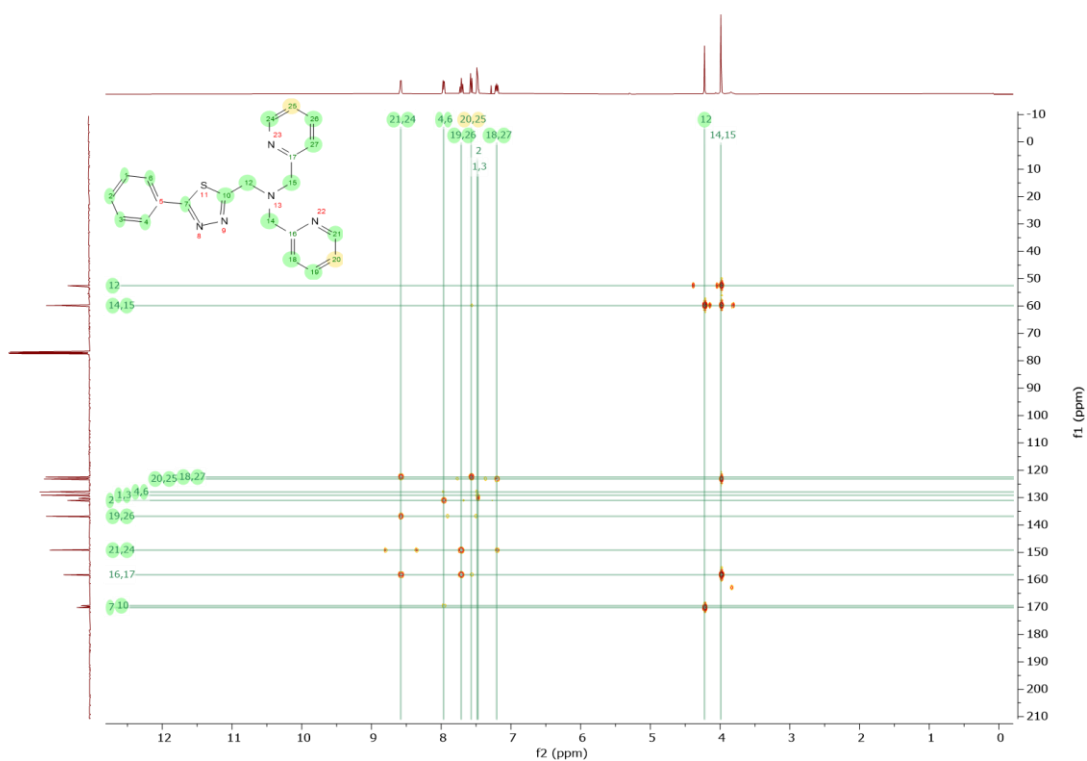


Figure S6: *HMBC* spectrum of the1-(5-phenyl-1,3,4-thiadiazol-2-yl)-N,N-bis(pyridin-2-ylmethyl)methanamine ($\text{L}^{\text{Ph-TDA}}$) in CDCl_3 [400 MHz].

2. IR-spectra:

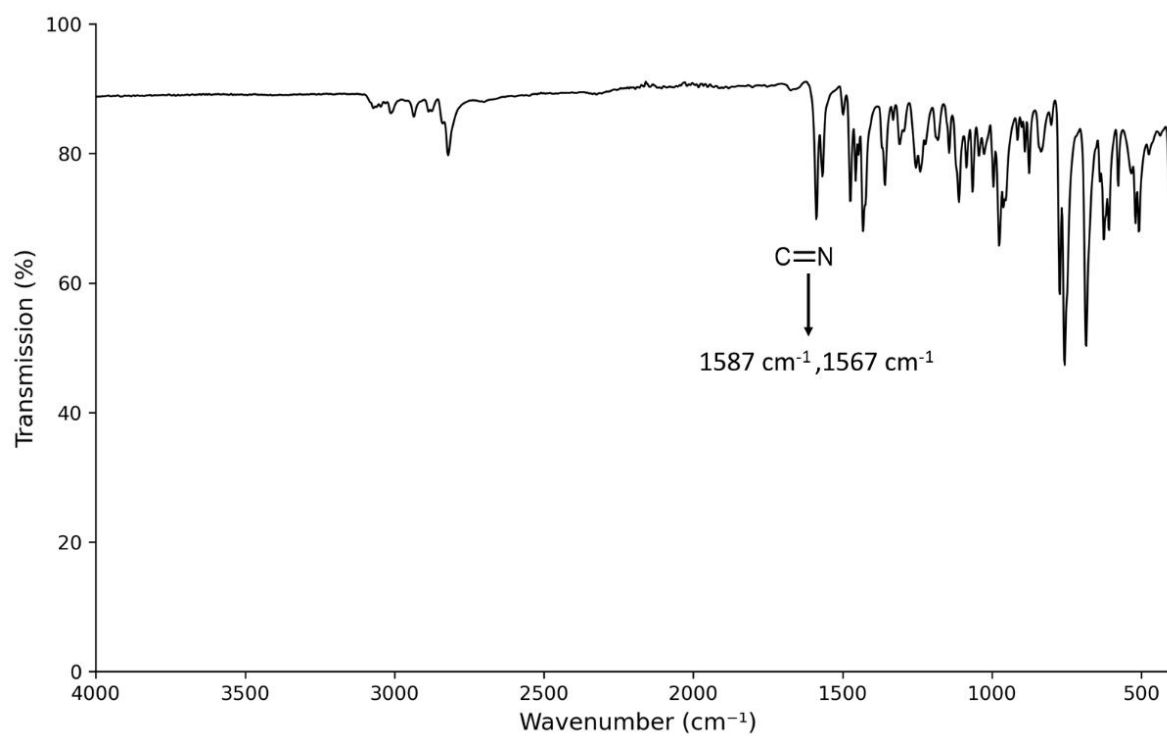


Figure S7: IR-spectrum of the Ligand $L^{\text{Ph-TDA}}$.

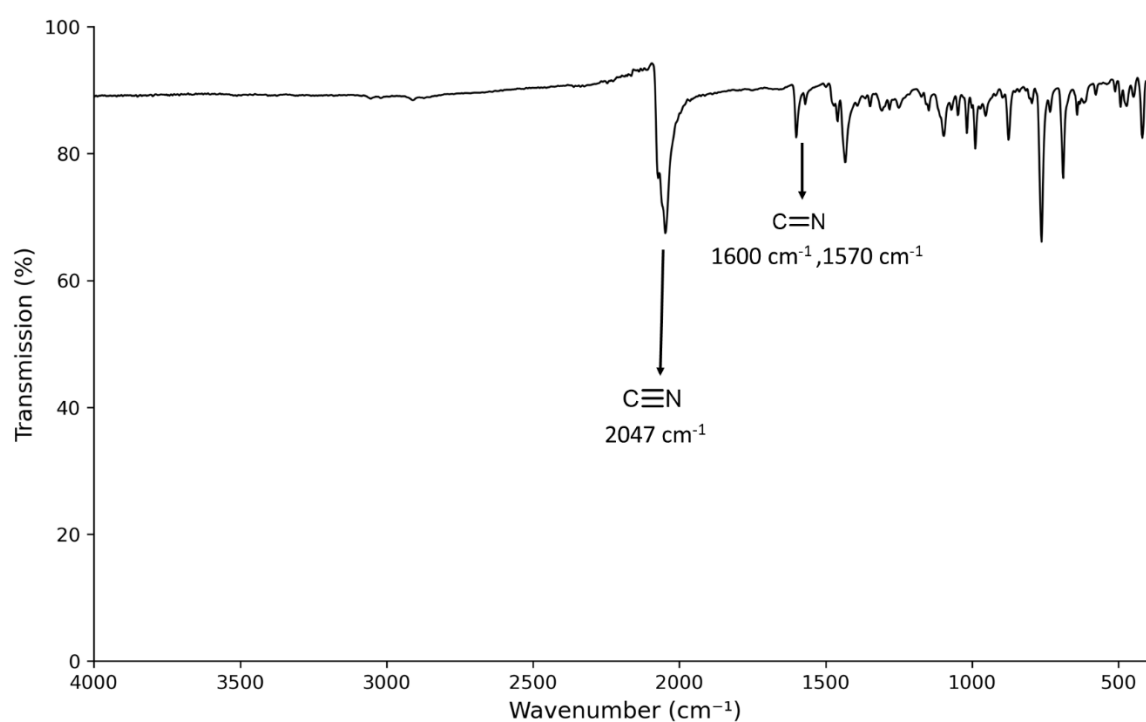


Figure S8: IR-spectrum of $[\text{Fe}(\text{L}^{\text{Ph-TDA}})(\text{NCS})_2] \cdot \text{H}_2\text{O}$ (**C1**).

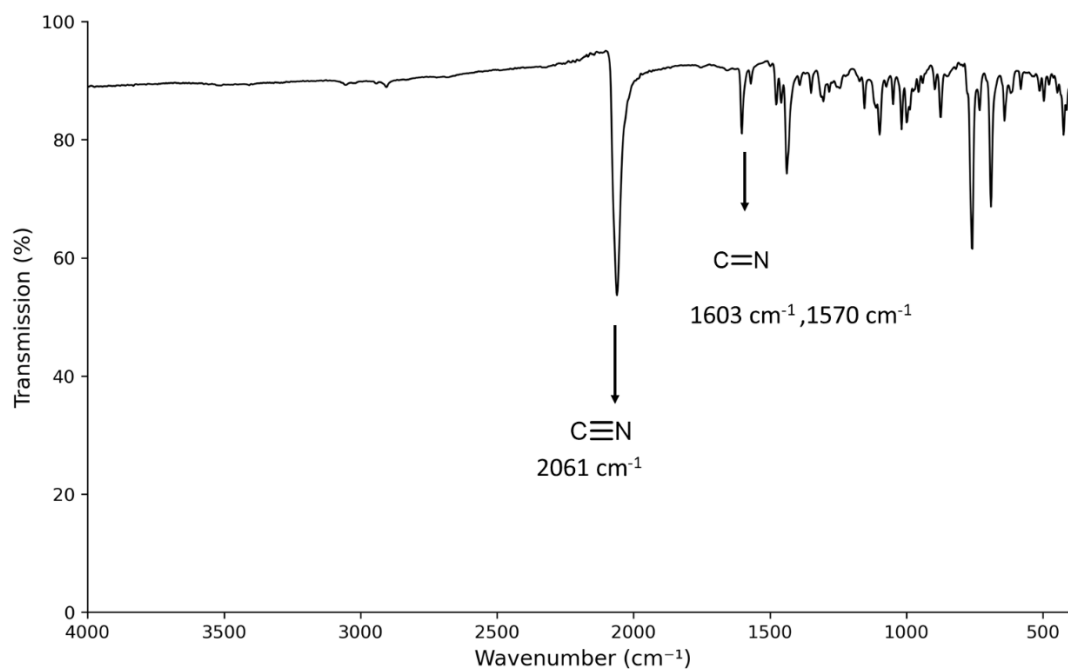


Figure S9: IR-spectrum of $[\text{Fe}(\text{L}^{\text{Ph-TDA}})(\text{NCSe})_2] \cdot \text{H}_2\text{O}$ (C2).

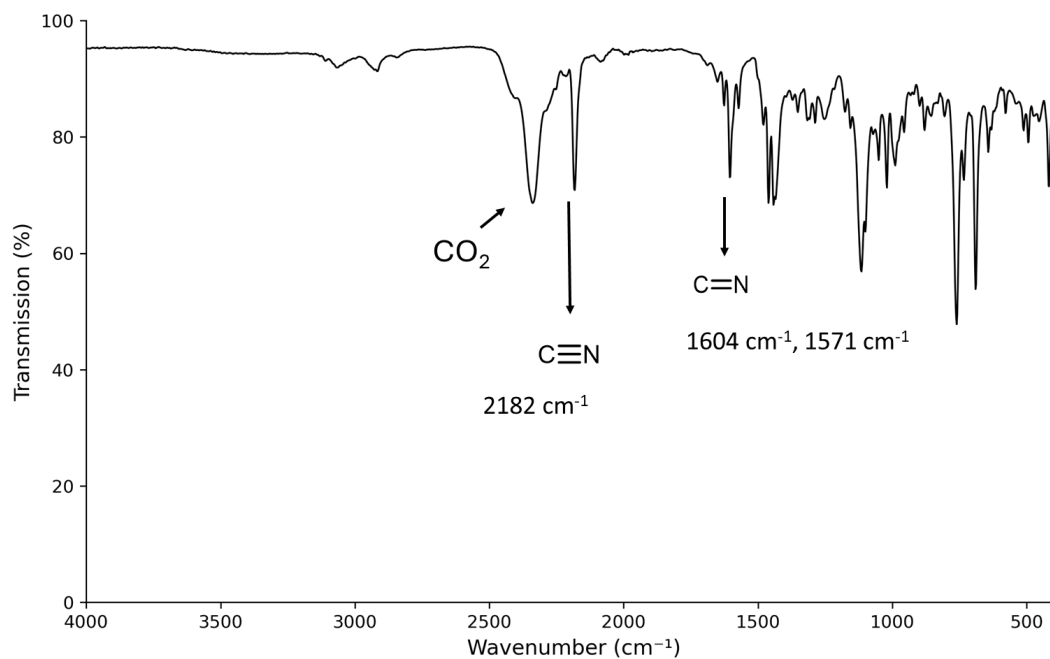


Figure S10: IR- spectrum of $[\text{Fe}(\text{L}^{\text{Ph-TDA}})(\text{NCBH}_3)_2] \cdot \text{H}_2\text{O}$ (C3).

3. HRES ESI Mass spectra:

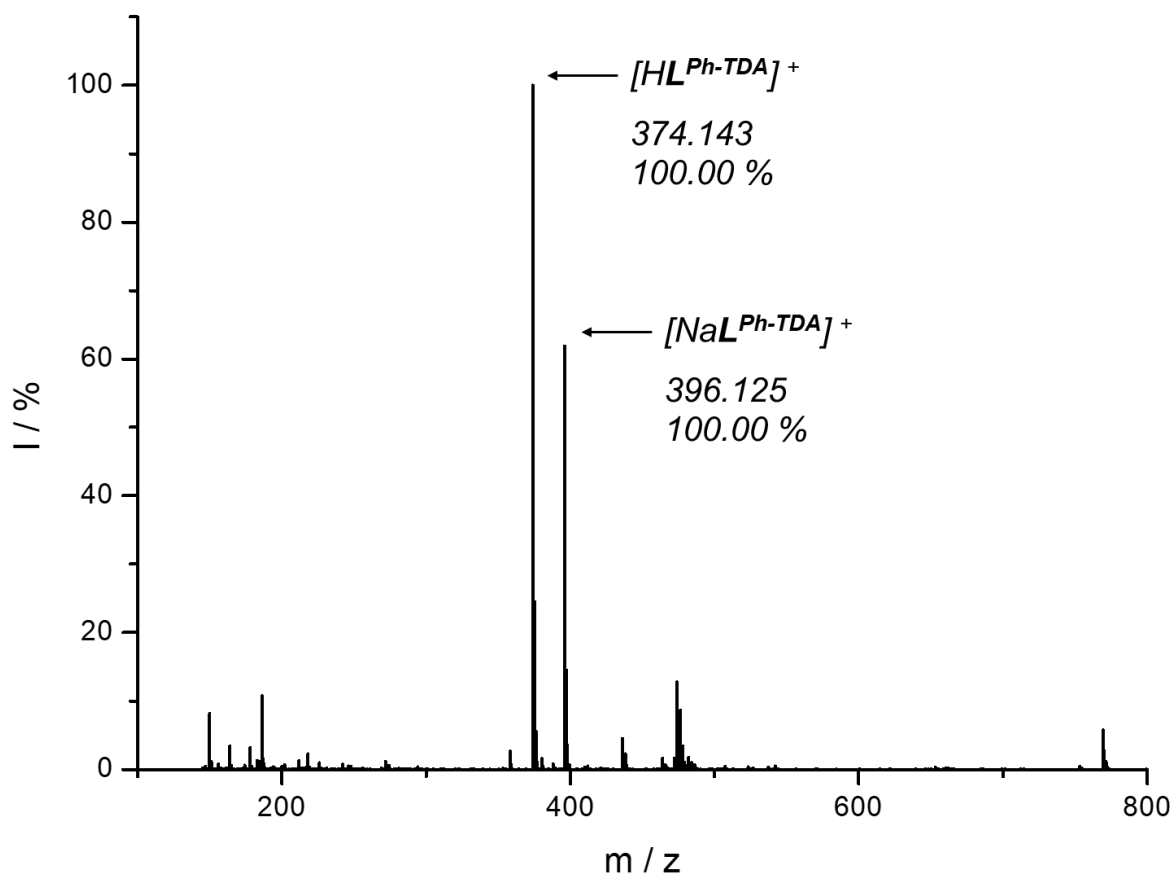


Figure S11: Mass spectrum (ESI positive) of the Ligand $L^{\text{Ph-TDA}}$.

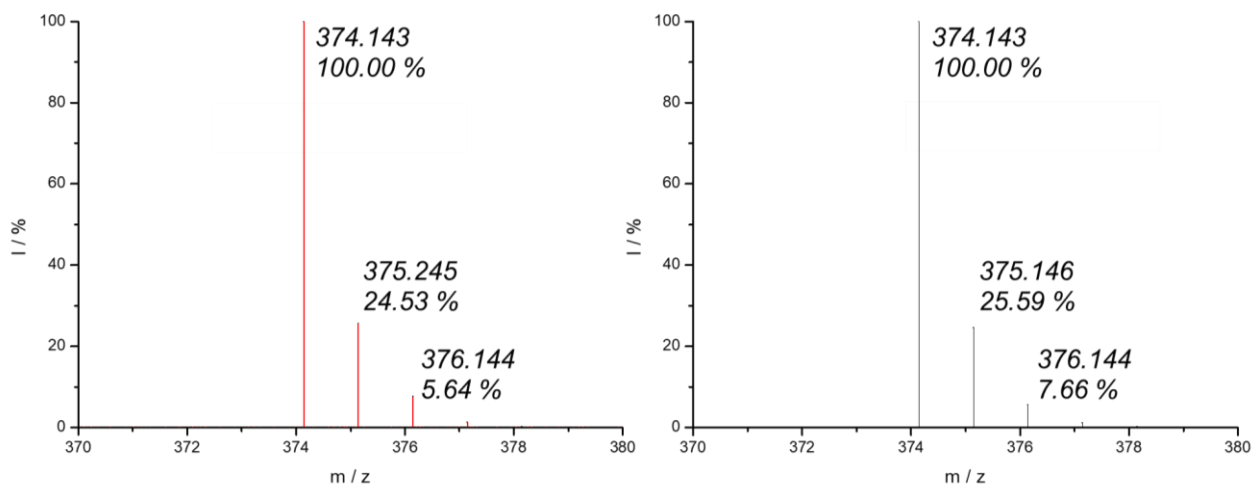


Figure S12: Isotopic pattern of ESI mass spectrum of Ligand $L^{\text{Ph-TDA}}$ measured (left; red marked overlap of the isotopic pattern) and predicted (right).

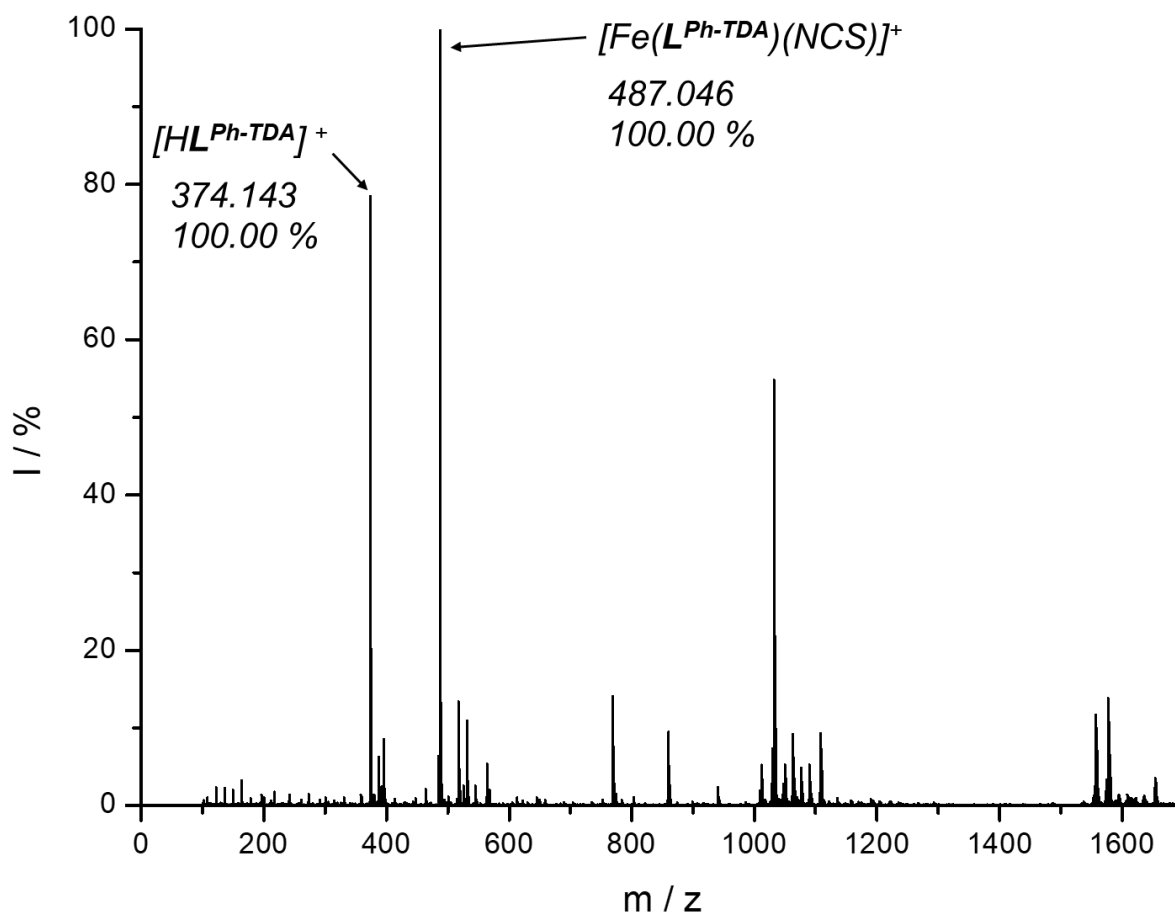


Figure S13: Mass spectrum (ESI positive) of the complex $[\text{Fe}(\text{L}^{\text{Ph-TDA}})(\text{NCS})_2] \cdot \text{H}_2\text{O}$ (**C1**).

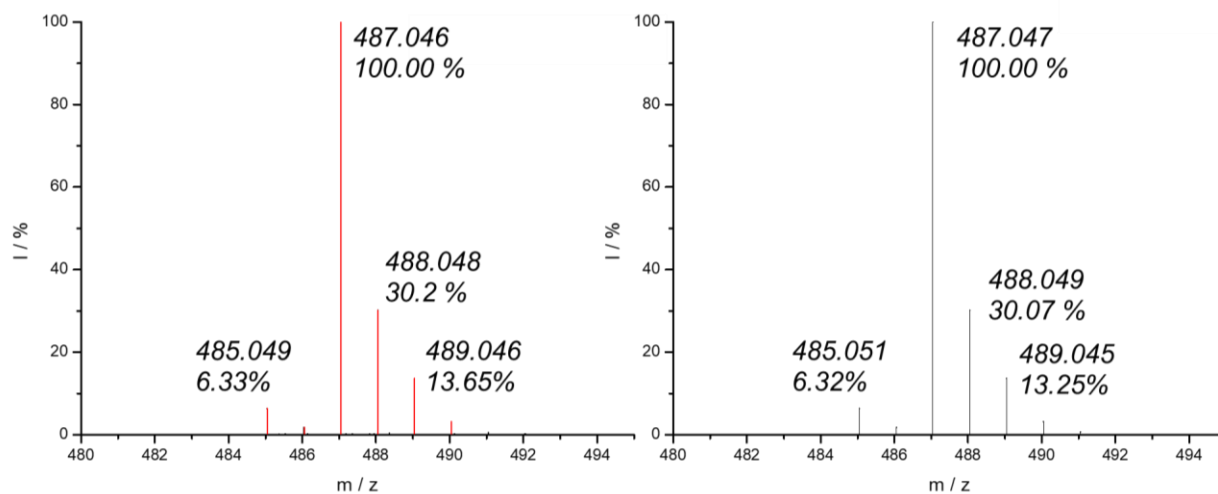


Figure S14: Isotopic pattern of ESI mass spectrum of $[\text{Fe}(\text{L}^{\text{Ph-TDA}})(\text{NCS})_2] \cdot \text{H}_2\text{O}$ (**C1**) measured (left; red marked overlap of the isotopic pattern) and predicted (right).

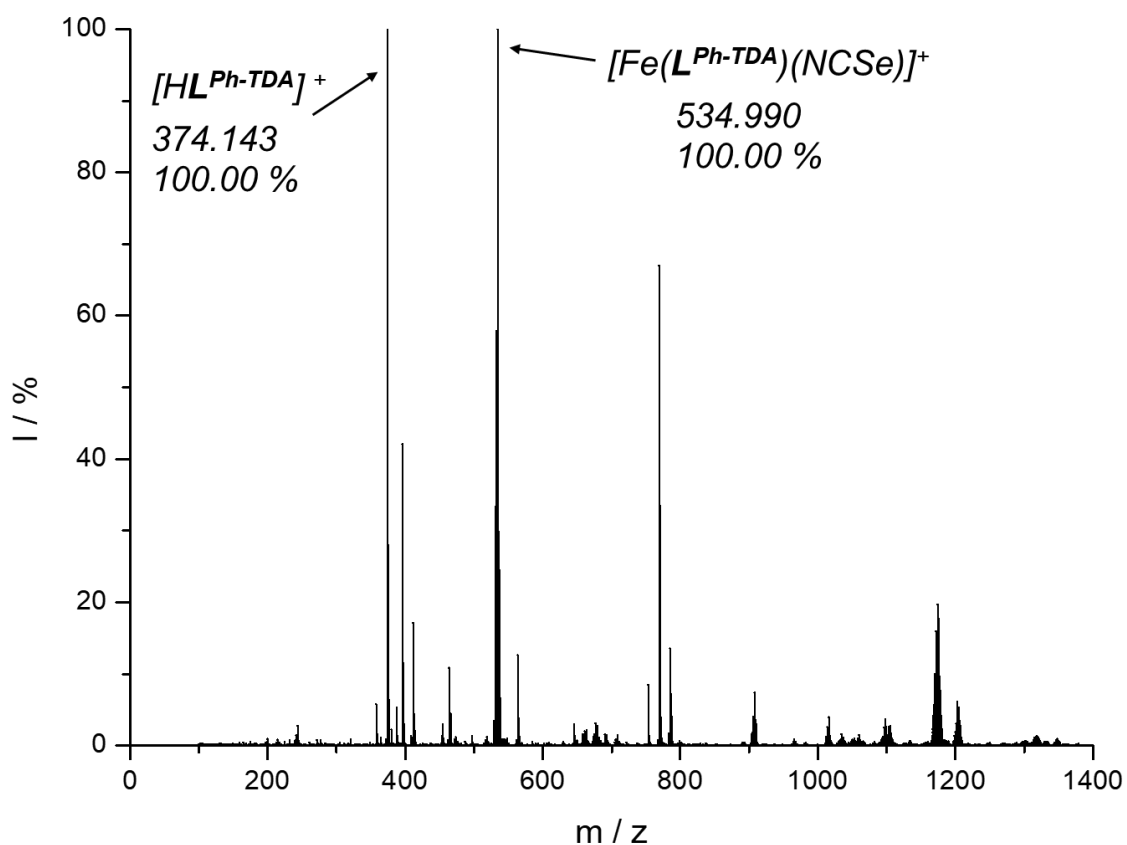


Figure S15: Mass spectrum (ESI positive) of the $[Fe(L^{Ph-TDA})(NCSe)_2] \cdot H_2O$ (C2).

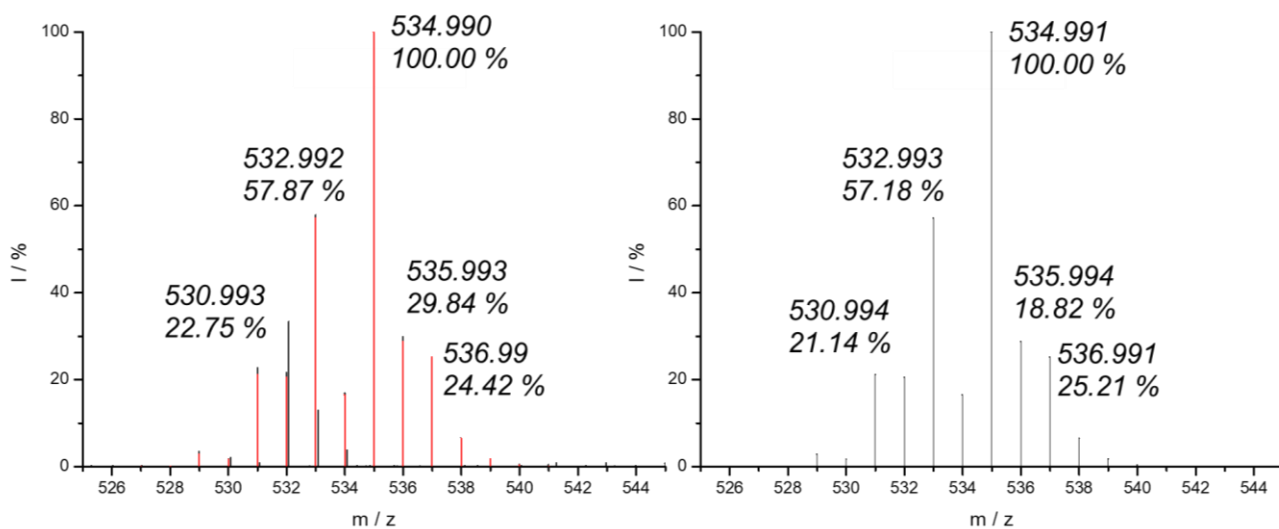


Figure S16: Isotopic pattern of ESI mass spectrum of $[Fe(L^{Ph-TDA})(NCSe)_2] \cdot H_2O$ (C2) measured (left; red marked overlap of the isotopic pattern) and predicted (right).

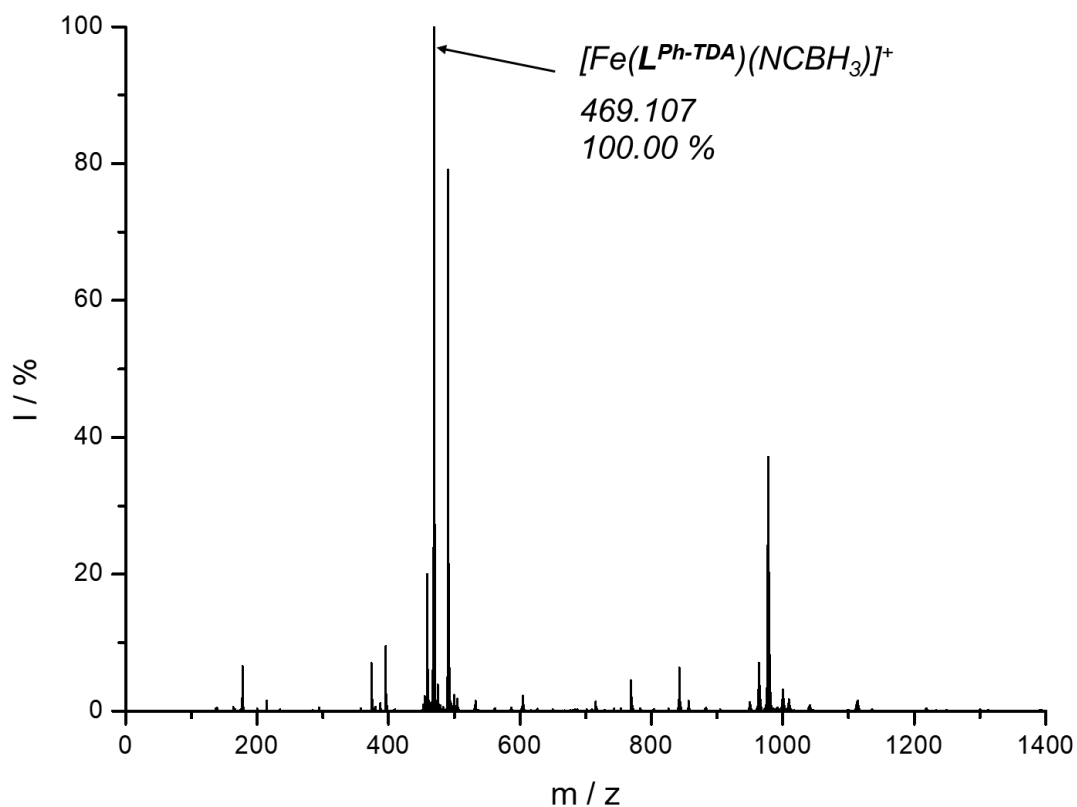


Figure S17: Mass spectrum (ESI positive) of the Complex $[\text{Fe}(\text{L}^{\text{Ph-TDA}})(\text{NCBH}_3)_2] \cdot \text{H}_2\text{O}$ (**C3**).

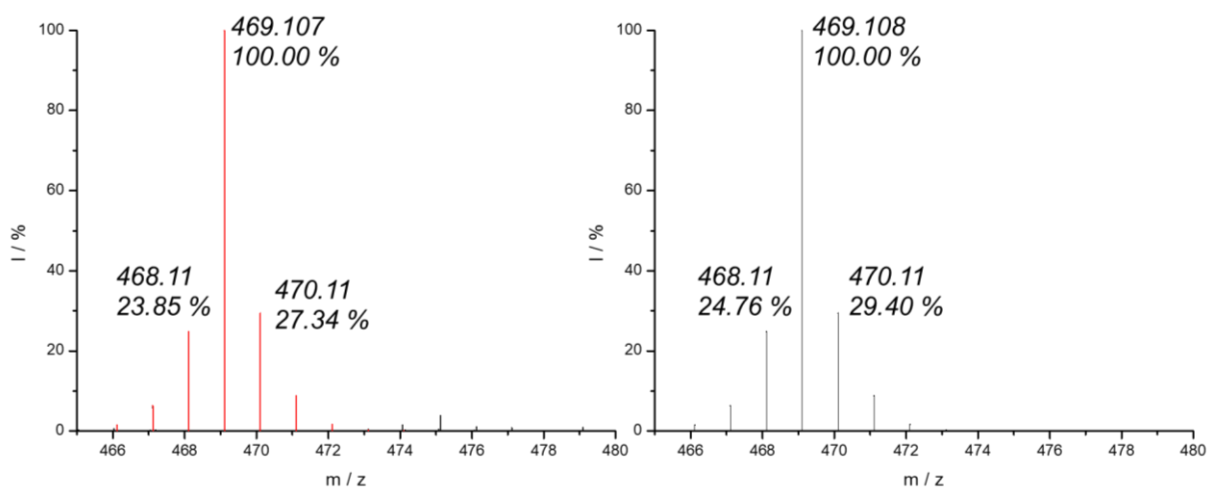


Figure S18: Isotopic pattern of ESI mass spectrum of $[\text{Fe}(\text{L}^{\text{Ph-TDA}})(\text{NCBH}_3)_2] \cdot \text{H}_2\text{O}$ (**C3**) measured (left; red marked overlap of the isotopic pattern) and predicted (right).

4. Crystal structure description:

As mentioned in the crystallographic section, **C2** and **C3** are isostructural, both have similar in packing as well. Along the *a*-axis the ground plane of the unit cell is represented by *b*- and *c*-axis as a rectangle, showing two kinds of empty channels between complexes, in which all sulfur and selenium atoms are pointing inside (**Figure S33**). Based on slightly different cell parameters for *b*- and *c*-axis compared to **C2** the channels are less asymmetric in case of **C3**. The differences are represented as well for the position of the iron atoms which are oriented along the *a*-axis in case of **C2** with smaller overlap compared to the complex **C3**. Along the *b*-axis the complexes are orientated as stairs with interplanar interactions between Phenyl and 1,3,4-Thiadiazole units in the centre of the unit cell followed by network formation due to pyridine-pyridine-unit interactions. Between these 1D networks intermolecular interaction could not be observed. Parallel to the *c*-axis channels of solvent molecules could be determined **Figure S19**. One solvent channel is observed per unit cell. The sulfur atoms of the 1,3,4-Thiadiazole unit pointing towards the solvent channels in every direction. The stacked Phenyl-1,3,4-Thiadiazole units are oriented along the *c* axis as well on the corner and the centre of the unit cell.

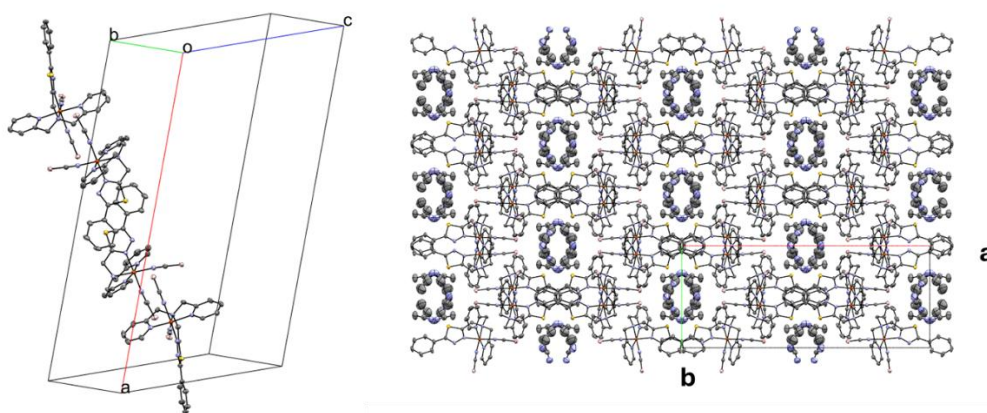


Figure S19: Visualization of formed 1D-chain of π - π -interactions between the Phenyl-1,3,4-Thiadiazole-units and Pyridine-units of Complexes **C2** and **C3** (left) and view of the packing along the *c*-axis to show the solvent channels (right). Hydrogen atoms were removed for better overview.

C3 and previously reported 1,3,4-Oxadiazole analogue complex $[\text{Fe}(\text{L}^{\text{Ph-ODA}})(\text{NCBH}_3)_2] \cdot 0.8 \text{ H}_2\text{O} \cdot 0.5 \text{ CH}_3\text{OH}$ crystallized from acetonitrile in the same space group $C2/c$. The cell volume differs between both complexes and the unit-cell similarity index \mathcal{I} is 0.1 for 120 K and 0.098 for 240 K indicate that both complexes are not isomorphous.^[2] Due to the structural similarity of the complexes the packing is similar as well leading to channel of solvent along *c* axis and π - π -interaction between the 1,3,4-

heterocycles and phenyl units responsible for cooperative interaction.^[2] Since the packing and the space group are quite similar between these two complexes, the change in the magnetic behaviour arises mainly from the change in the geometry around the iron(II) centres. Detailed investigations around are in the crystallographic section of the main manuscript.

Table S1: Extracted parameter of interplanar angle, centroid-centroid distance and the off-set for **C1** to **C3** for the π - π -interaction between 1,3,4-Thiadiazole- and Phenyl-unit at 120 K.

	Interplanare angle / °	centroid-centroid distance / Å	Off-set / Å
[Fe(L ^{Ph-TDA})(NCS) ₂] · MeCN			
Fe1	6.115	3.566	1.119
Fe2	6.634	4.477	3.002
[Fe(L ^{Ph-TDA})(NCSe) ₂] · MeCN	8.263	3.699	1.145
[Fe(L ^{Ph-TDA})(NCBH ₃) ₂] · MeCN	5.859	3.735	1.412

As the packing of **C1** differs to **C2** and **C3** the comparison must be done with caution. Based on the values, the packing has an influence on the off-set for **C1** compared to **C2** and **C3**. As the off-set is smaller for **C2** and **C3** compared to **C1** and for **C1** the offset is on the limit suggested by B. K. Saha et al. the π - π -interaction for **C1** should be less strong.^[3] Only in case of **C2** and **C3** π - π -interaction between two pyridine-units could be seen, which results in the building of the networks. These values are shown in **Table S2**. The values suggest a contribution of the π - π -interaction of the Pyridine-units to the intermolecular interactions.

Table S2: Extracted parameter of the interplanar angle, centroid-centroid distance and the off-set for **C1** to **C3** for the intermolecular π - π -interaction between the Pyridine-units.

	Interplanar angle / °	centroid-centroid distance / Å	Off-set / Å
[Fe(L ^{Ph-TDA})(NCSe) ₂] · MeCN	20.363	4.422	2.434
[Fe(L ^{Ph-TDA})(NCBH ₃) ₂] · MeCN	23.533	4.277	1.506

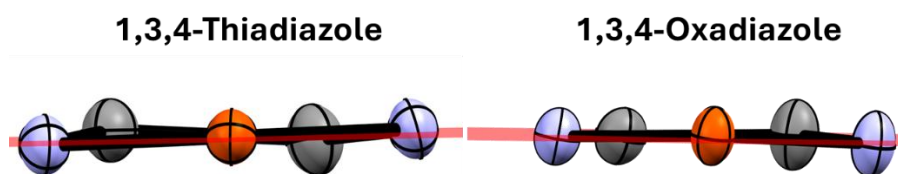


Figure S20: Visualization of the distortion differences in the coordination pocket of 1,3,4-thiadiazole (left) and 1,3,4-oxadiazole (right), based on the five-membered ring (C8–N2–Fe1–N3–C9). A plane was placed through all ring atoms to illustrate the atomic displacements, which can be attributed to the different bite angles (N2–C8–C9).

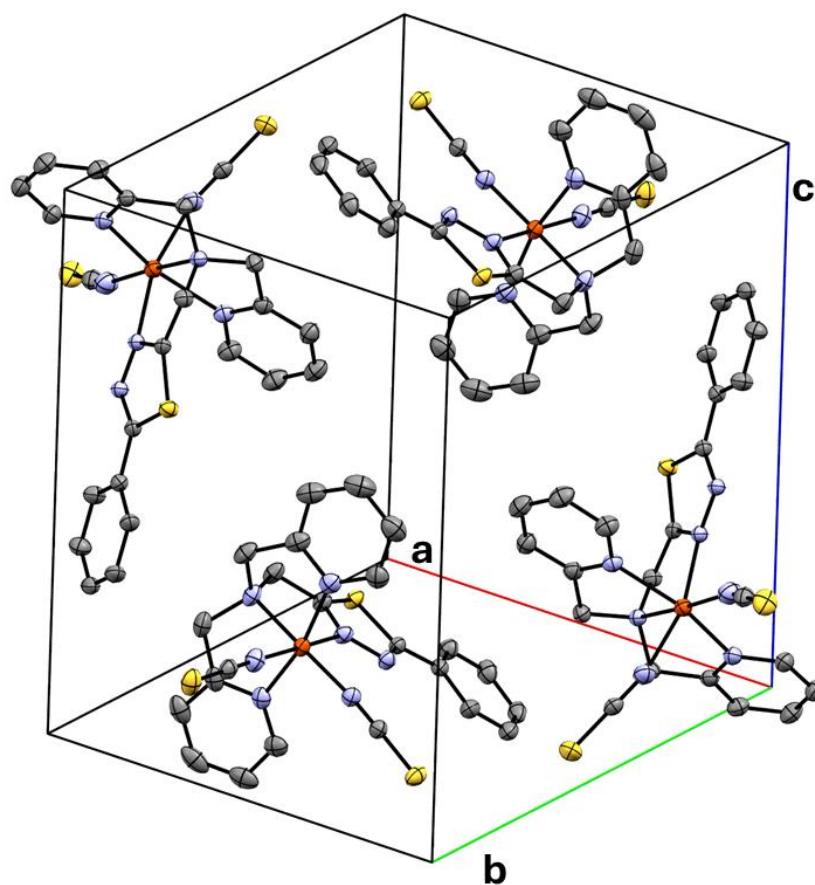


Figure S21: Unit cell of $[\text{Fe}(\text{L}^{\text{Ph-TDA}})(\text{NCS})_2] \cdot \text{MeCN}$ (**C1**) at 120 K. Solvent molecules and Hydrogen atoms were removed for better overview.

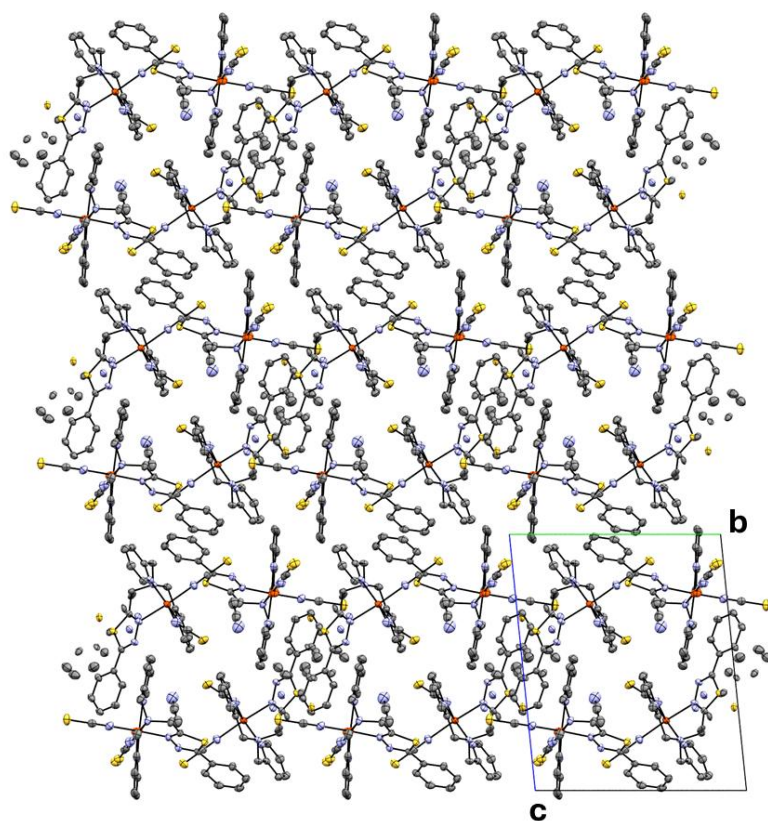


Figure S22: Visualisation of the packing for complex $[\text{Fe}(\text{L}^{\text{Ph-TDA}})(\text{NCS})_2] \cdot \text{MeCN}$ (**C1**) along a -axis at 120 K. Solvent molecules and Hydrogen atoms were removed for better overview.

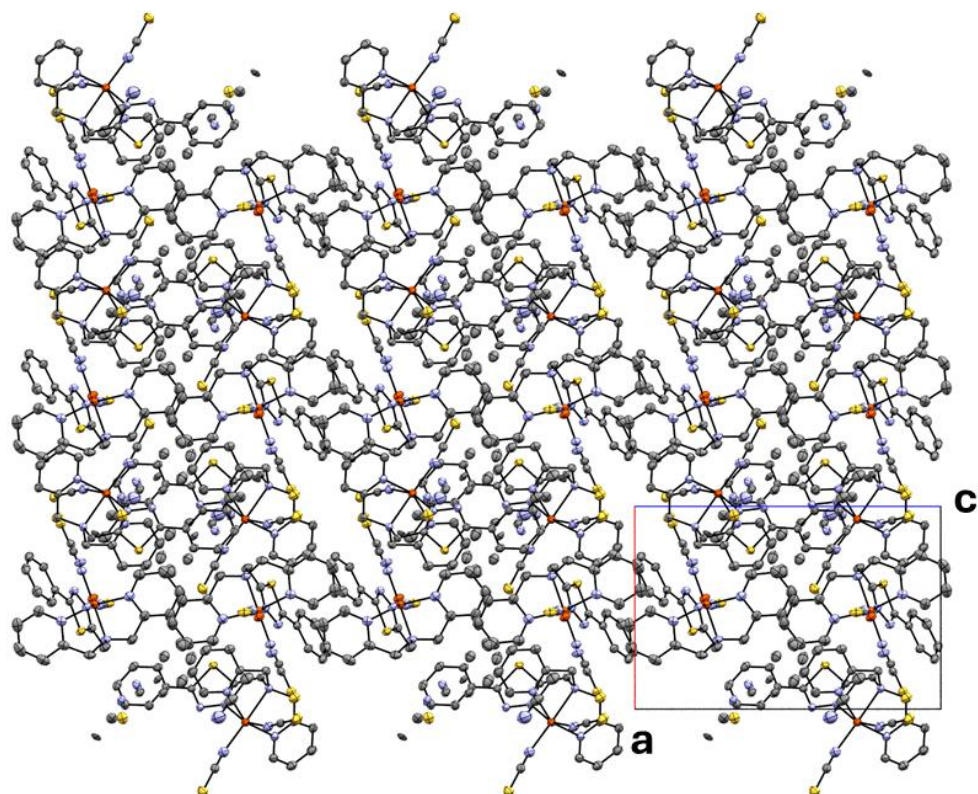


Figure S23: Visualisation of the packing for complex $[\text{Fe}(\text{L}^{\text{Ph-TDA}})(\text{NCS})_2] \cdot \text{MeCN}$ (**C1**) b -axis (right) at 120 K. Solvent molecules and Hydrogen atoms were removed for better overview.

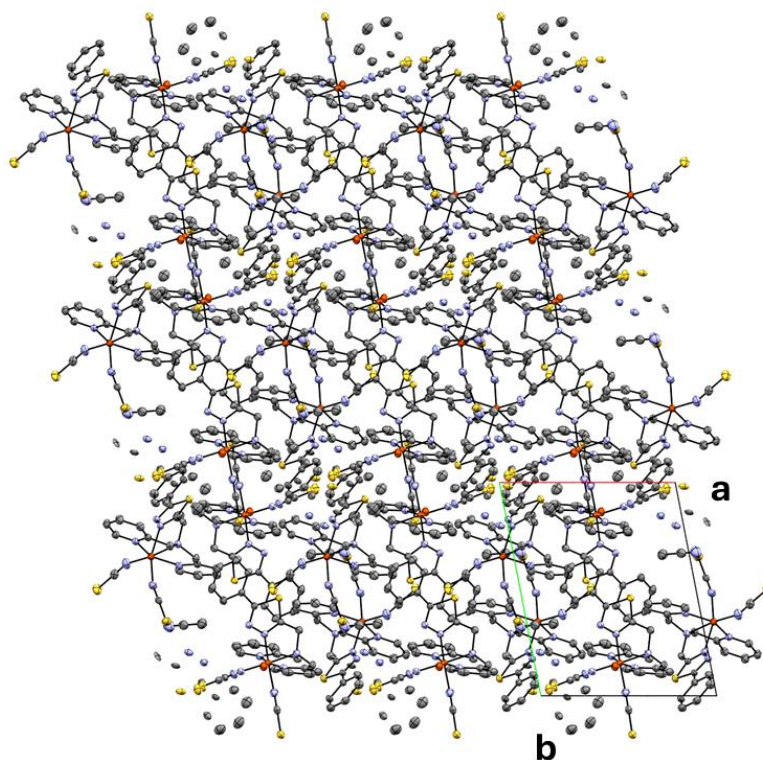


Figure S24: Visualisation of the packing for complex $[\text{Fe}(\text{L}^{\text{Ph-TDA}})(\text{NCS})_2] \cdot \text{MeCN}$ (**C1**) along *c*-axis at 120 K. Solvent molecules and Hydrogen atoms were removed for better overview.

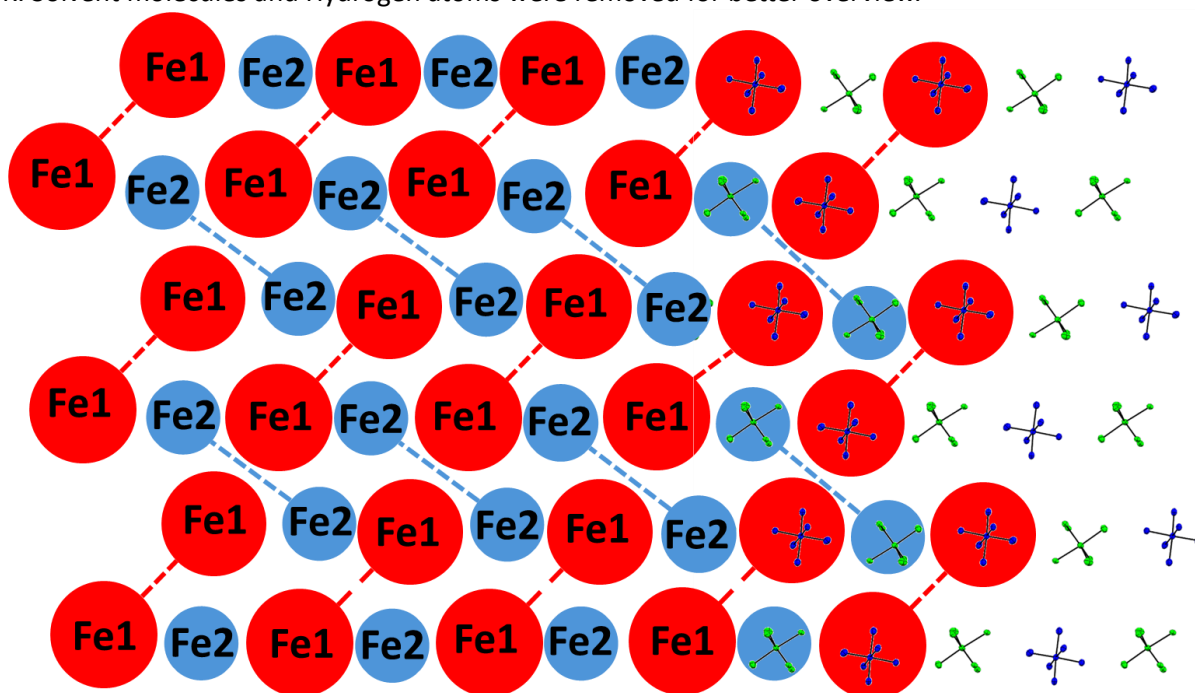


Figure S25: Visualisation of the order of the two complexes (**red**: high Spin; **blue**: low Spin) and the phenyl-1,3,4-Thiadiazole π - π -interaction (dashed line) for Complex $[\text{Fe}(\text{L}^{\text{Ph-TDA}})(\text{NCS})_2] \cdot \text{MeCN}$ (**C1**) along *a*-axis at 120 K.

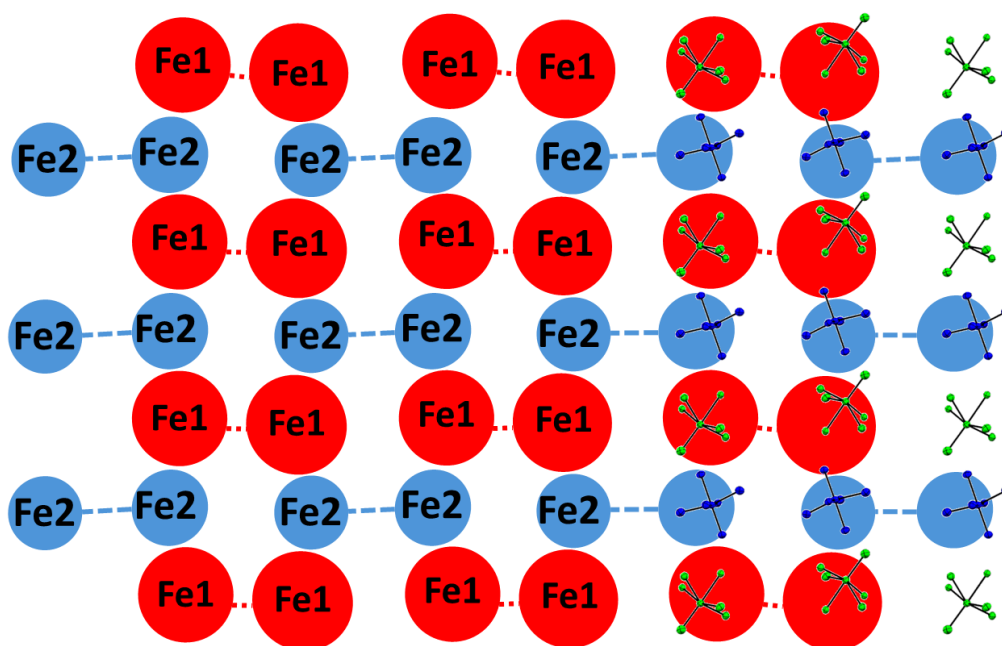


Figure S26: Visualisation of the order of the two complexes (**red**: high Spin; **blue**: low Spin) and the phenyl-1,3,4-Thiadiazole π - π -interaction (dashed line) for complex $[\text{Fe}(\text{L}^{\text{Ph-TDA}})(\text{NCS})_2] \cdot \text{MeCN}$ (**C1**) along *b*-axis at 120 K.

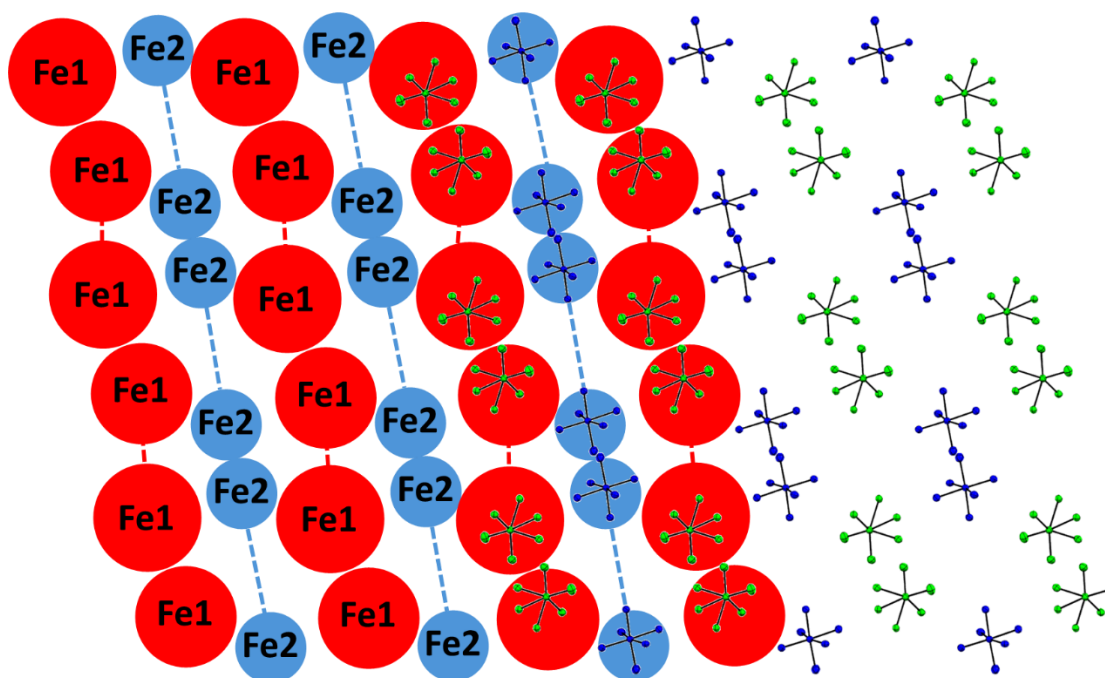


Figure S27: Visualisation of the order of the two complexes (**red**: high Spin; **blue**: low Spin) and the phenyl-1,3,4-Thiadiazole π - π -interaction (dashed line) for complex $[\text{Fe}(\text{L}^{\text{Ph-TDA}})(\text{NCS})_2] \cdot \text{MeCN}$ (**C1**) along *c*-axis at 120 K.

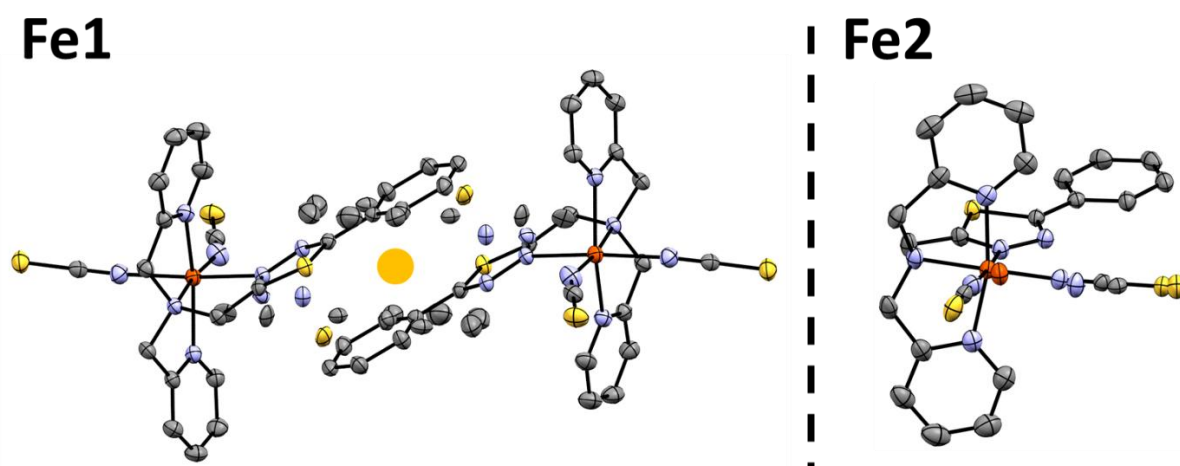


Figure S28: Visualisation of the disorder in $[\text{Fe}(\text{L}^{\text{Ph-TDA}})(\text{NCS})_2] \cdot \text{MeCN}$ (**C1**) at 120 K: deflection of the Phenyl-1,3,4-thiadiazole unit around the inversion centre (orange) for Fe1 pairs (left), and disorder of the Fe–NCS unit arising from incomplete spin transition of Fe2 and elongated Fe–N bonds in the high-spin state (right).

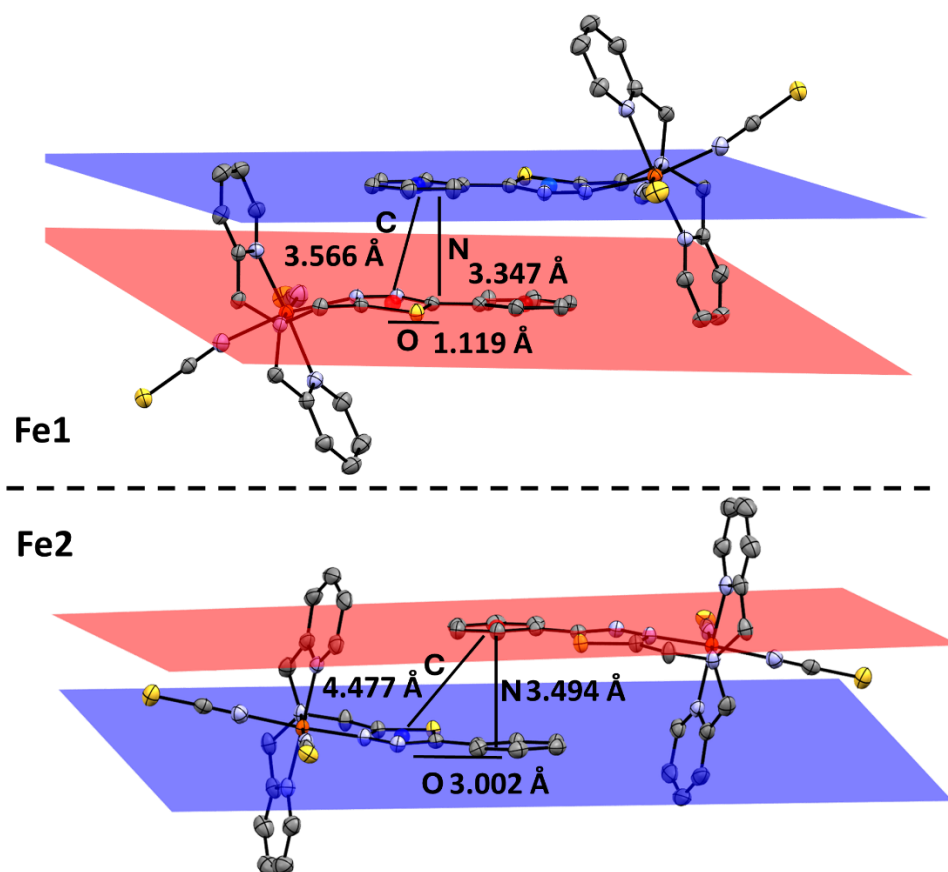


Figure S29: Visualisation of the π - π -interaction between Phenyl- and 1,3,4-Thiadiazole-unit with Offset (O), Normal vector (N) and centroid-centroid-distance (C) for Complex $[\text{Fe}(\text{L}^{\text{Ph-TDA}})(\text{NCS})_2] \cdot \text{MeCN}$ (**C1**) for the Fe1 and Fe2 pairs at 120 K.

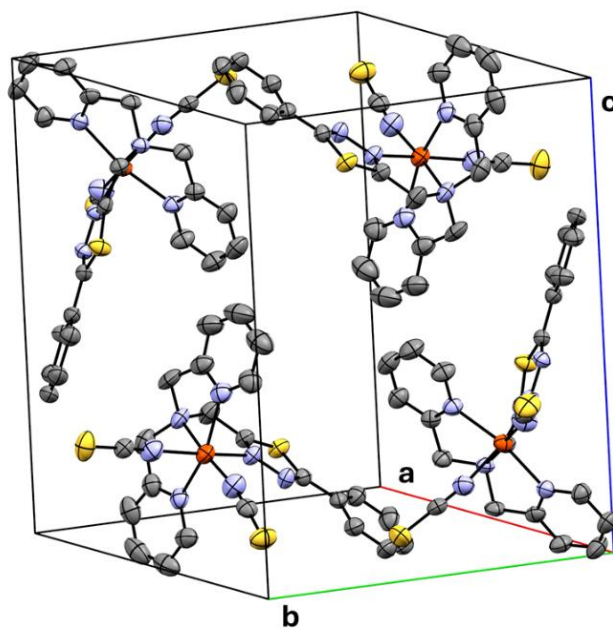


Figure S30: Unit cell of $[\text{Fe}(\text{L}^{\text{Ph-TDA}})(\text{NCS})_2] \cdot \text{MeCN}$ (**C1**) at 240 K. Solvent molecules and Hydrogen atoms were removed for better overview.

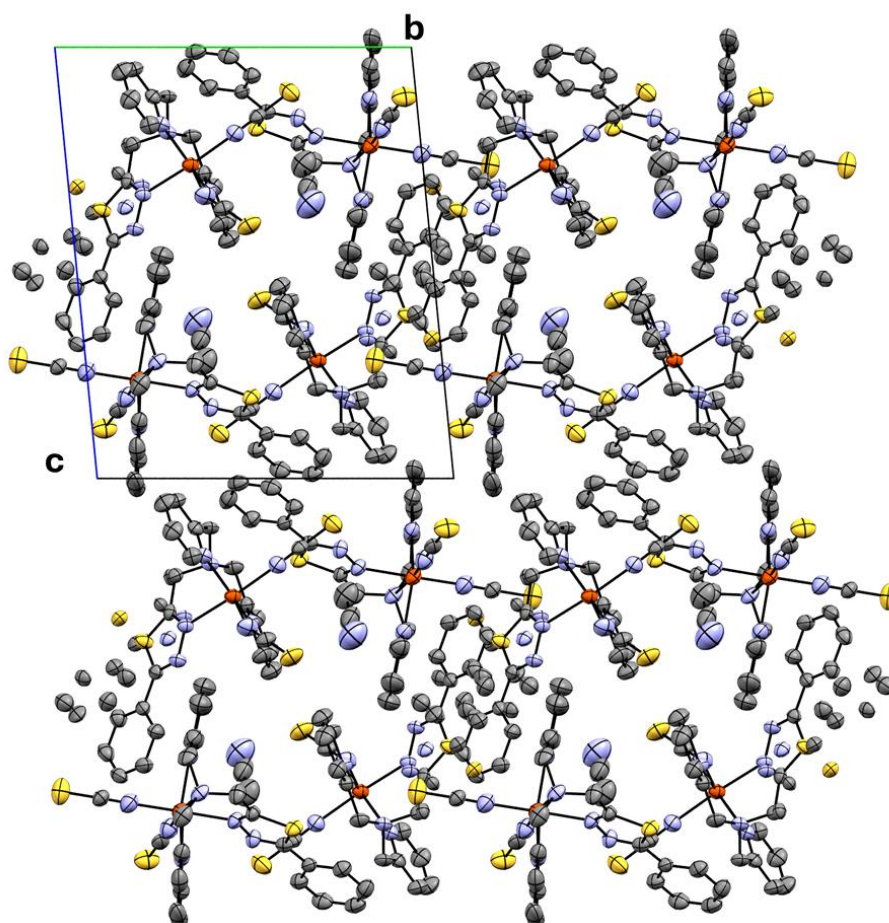


Figure S31: Visualisation of the packing for complex $[\text{Fe}(\text{L}^{\text{Ph-TDA}})(\text{NCS})_2] \cdot \text{MeCN}$ (**C1**) along a -axis at 240 K. Hydrogen atoms were removed for better overview.

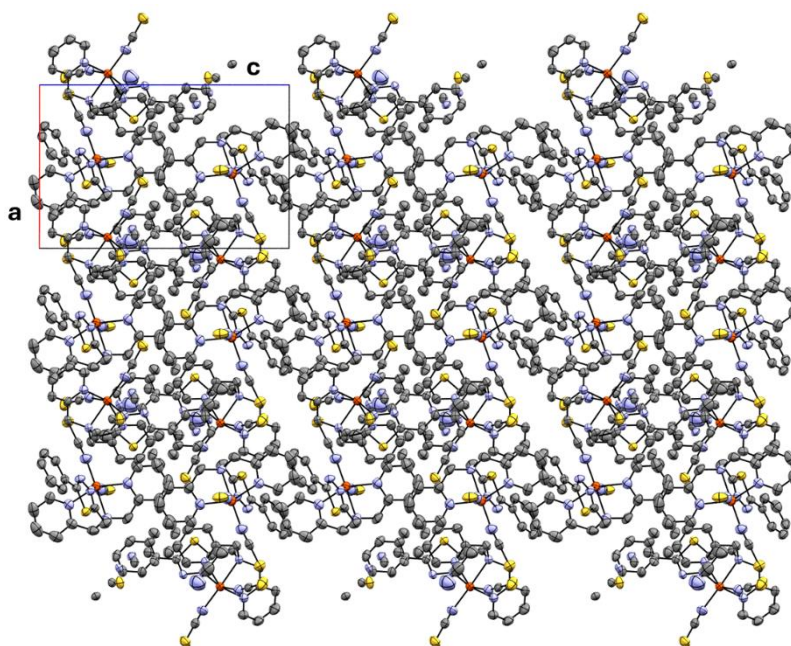


Figure S32: Visualisation of the packing for complex $[\text{Fe}(\text{L}^{\text{Ph-TDA}})(\text{NCS})_2] \cdot \text{MeCN}$ (**C1**) along *b*-axis at 240 K. Hydrogen atoms were removed for better overview.

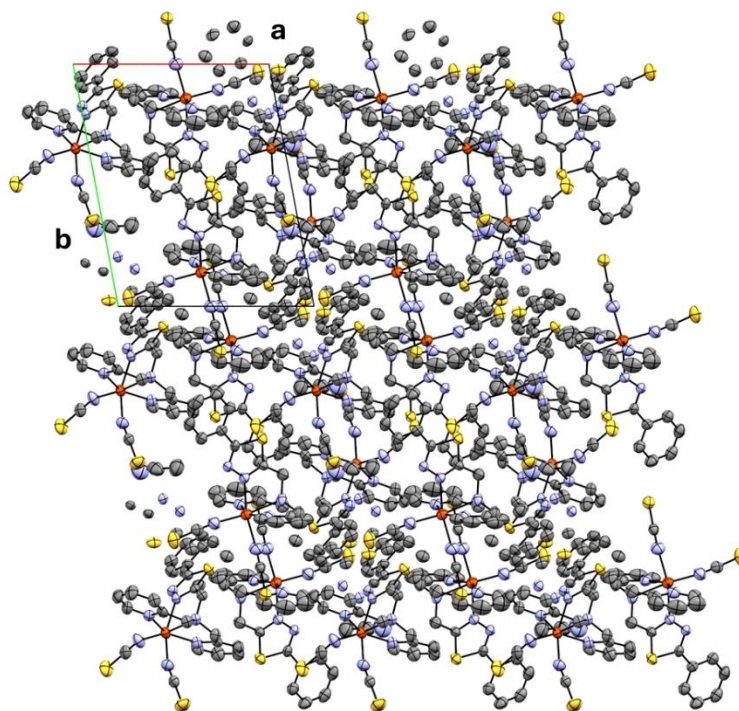


Figure S33: Visualisation of the packing for complex $[\text{Fe}(\text{L}^{\text{Ph-TDA}})(\text{NCS})_2] \cdot \text{MeCN}$ (**C1**) along *c*-axis at 240 K. Hydrogen atoms were removed for better overview.

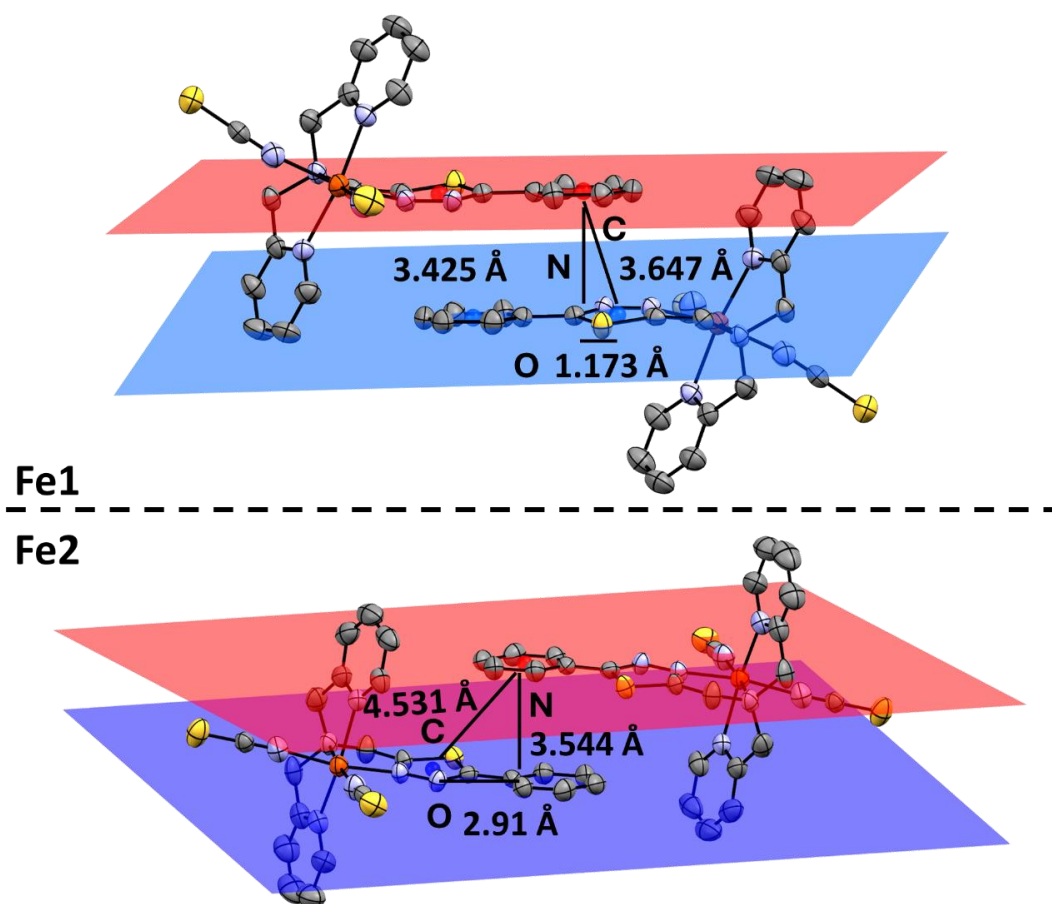


Figure S34: Visualisation of the π - π -interaction between Phenyl- and 1,3,4-Thiadiazole-unit with off-set (O), Normal vector (N) and centroid-centroid-distance (C) for Complex $[\text{Fe}(\text{L}^{\text{Ph-TDA}})(\text{NCS})_2] \cdot \text{MeCN}$ (C1) for the Fe1 and Fe2 pairs at 240 K.

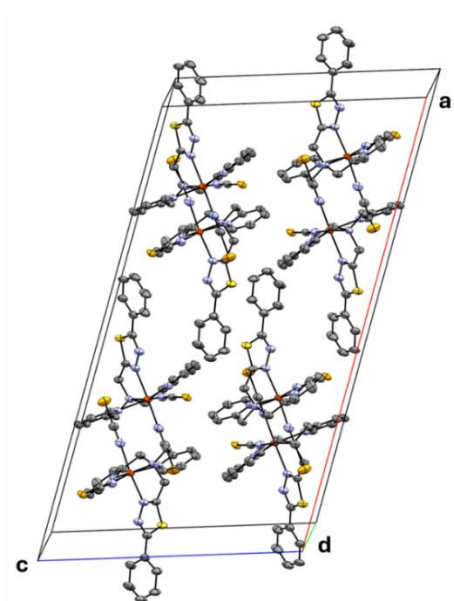


Figure S35: Unit cell of $[\text{Fe}(\text{L}^{\text{Ph-TDA}})(\text{NCS})_2] \cdot 2.5 \text{ MeCN}$ (C2). Solvent molecules and Hydrogen atoms were removed for better overview.

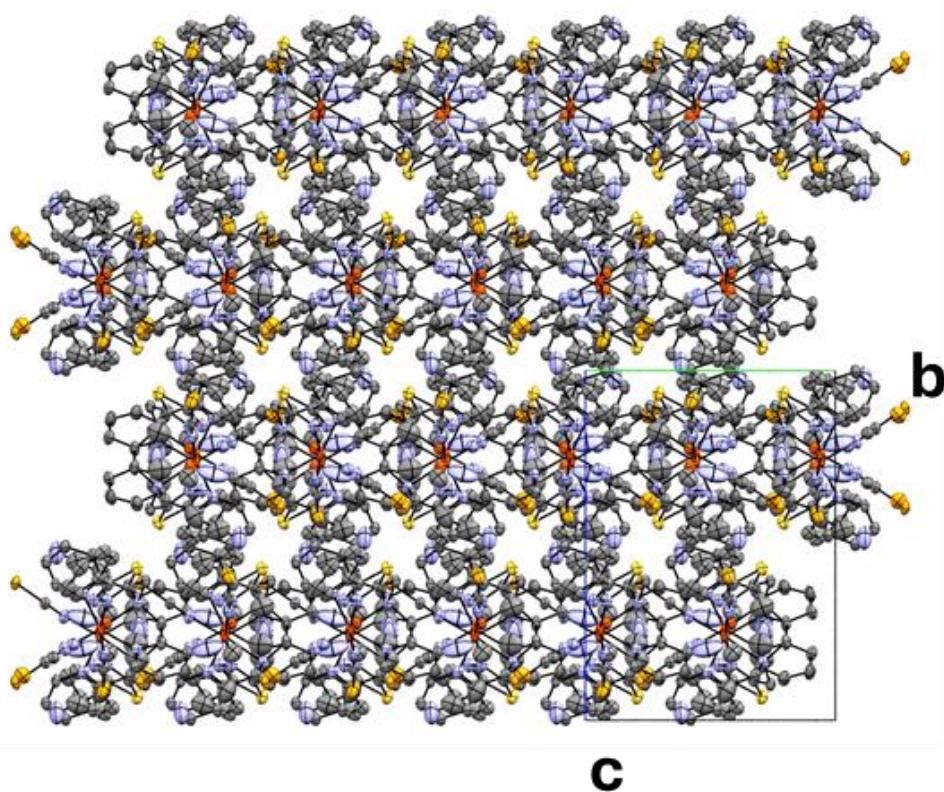


Figure S36: Visualisation of the packing for complex $[\text{Fe}(\text{L}^{\text{Ph-TDA}})(\text{NCSe})_2] \cdot 2.5 \text{ MeCN}$ (**C2**) *a*-axis. Hydrogen atoms were removed for better overview.

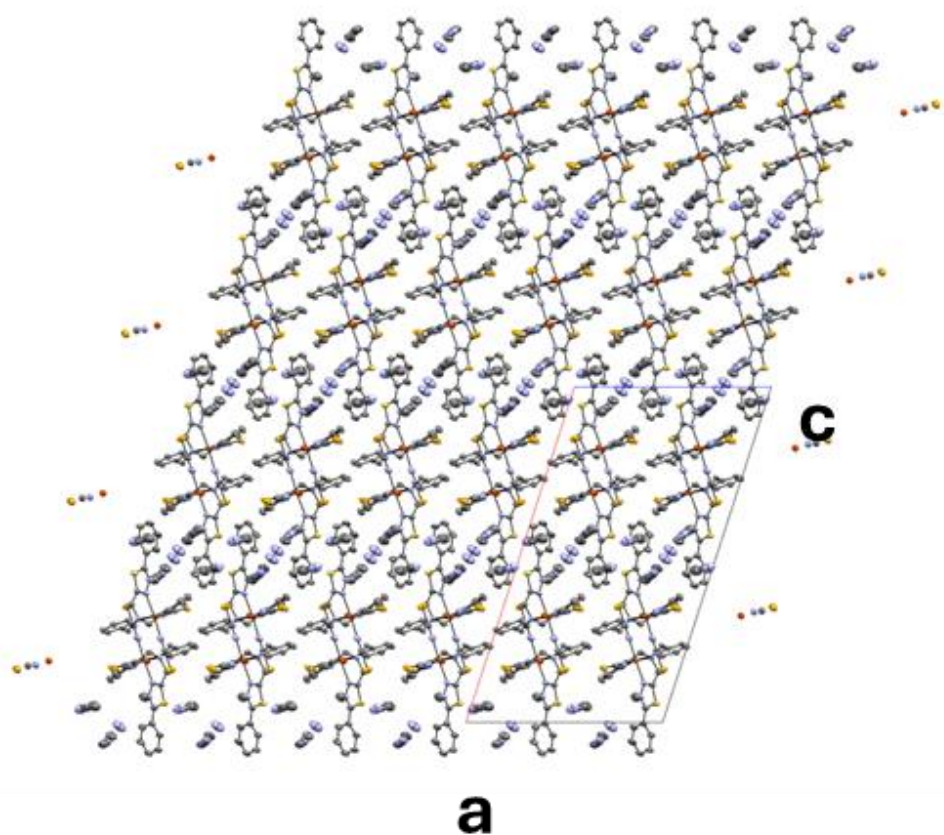


Figure S37: Visualization of the packing for complex $[\text{Fe}(\text{L}^{\text{Ph-TDA}})(\text{NCSe})_2] \cdot 2.5 \text{ MeCN}$ (**C2**) along *b*-axis. Hydrogen atoms were removed for better overview.

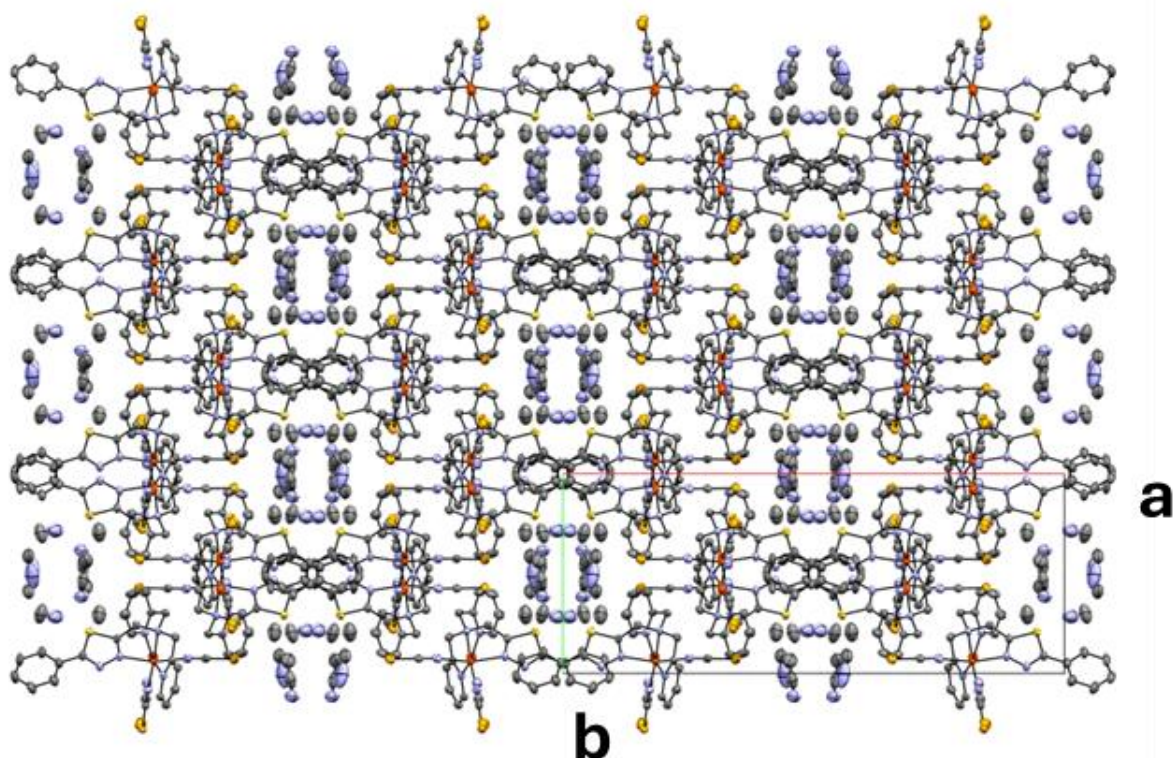


Figure S38: Visualization of the packing for complex $[\text{Fe}(\text{L}^{\text{Ph-TDA}})(\text{NCSe})_2] \cdot 2.5 \text{ MeCN}$ (**C2**) *c*-axis. Hydrogen atoms were removed for better overview.

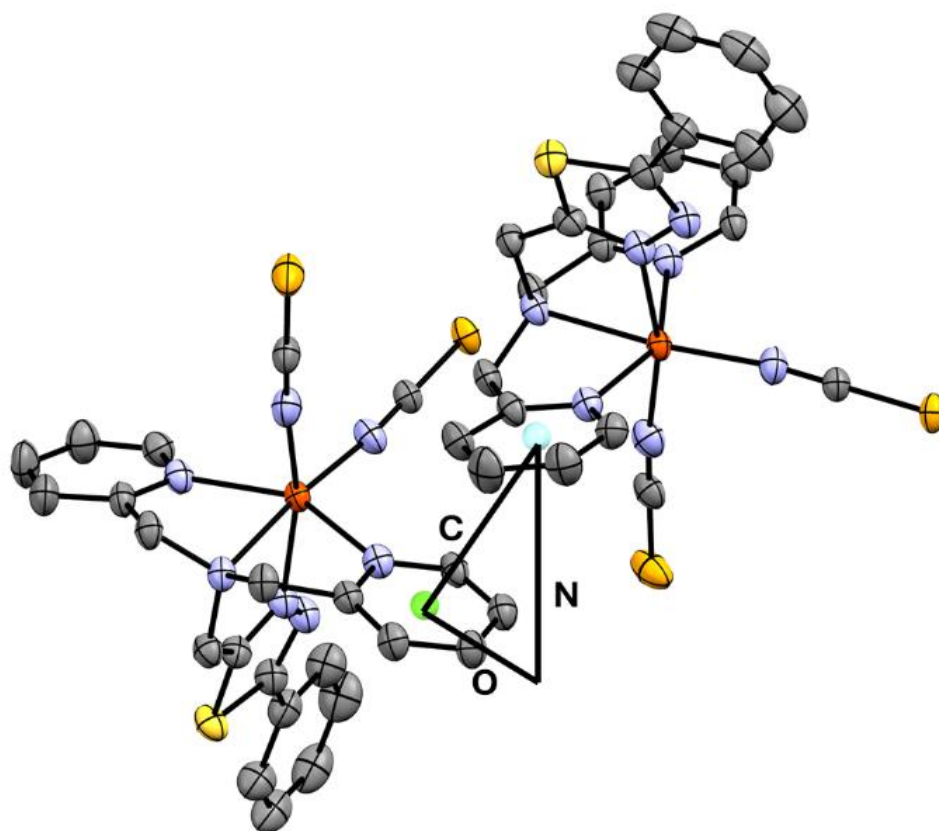


Figure S39: Visualisation of the π - π -interaction between Pyridine-units with offset (O: 2.434 Å), Normal vector (N: 2.963 Å) and centroid-centroid-distance (C: 4.42 Å) for complex $[\text{Fe}(\text{L}^{\text{Ph-TDA}})(\text{NCSe})_2] \cdot 2.5 \text{ MeCN}$ (**C2**).

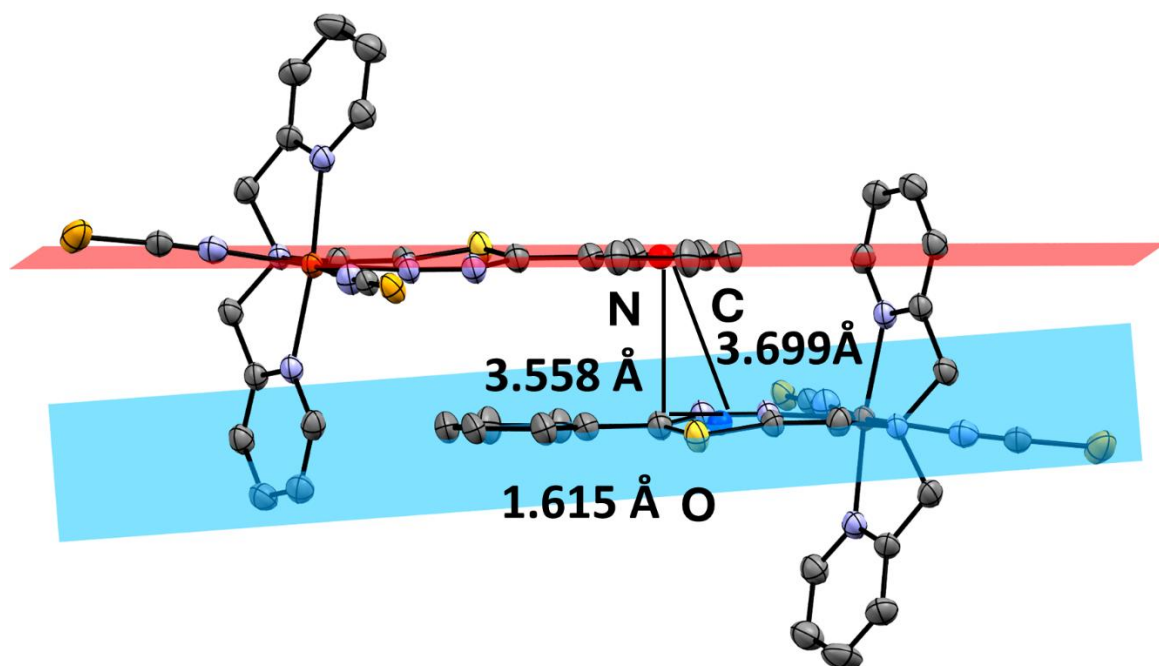


Figure S40: Visualisation of the π - π -interaction between Phenyl- and 1,3,4-Thiadiazole-unit with off-set (O), Normal vector (N) and centroid-centroid-distance (C) for complex $[\text{Fe}(\text{L}^{\text{Ph-TDA}})(\text{NCSe})_2] \cdot 2.5 \text{ MeCN}$ (C2).

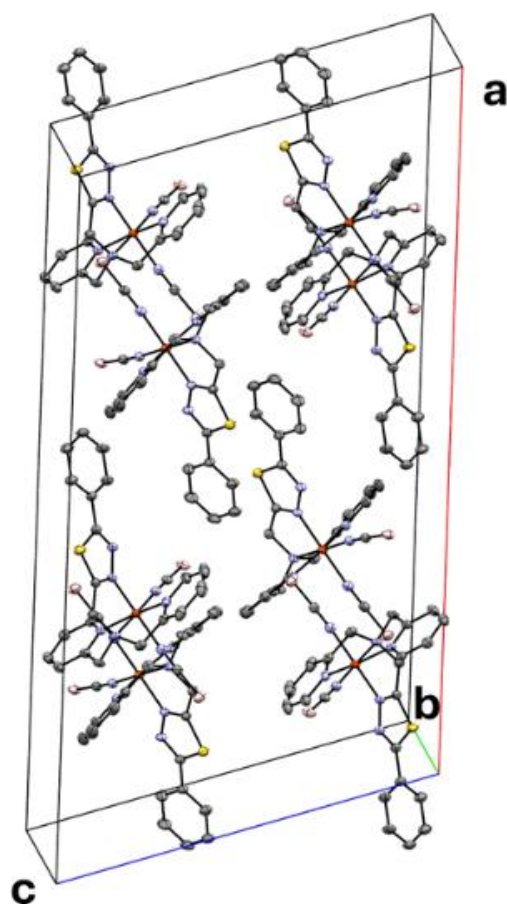


Figure S41: Unit cell of $[\text{Fe}(\text{L}^{\text{Ph-TDA}})(\text{NCBH}_3)_2] \cdot 2.5 \text{ MeCN}$ (C3) at 120 K. Solvent molecules and Hydrogen atoms were removed for better overview.

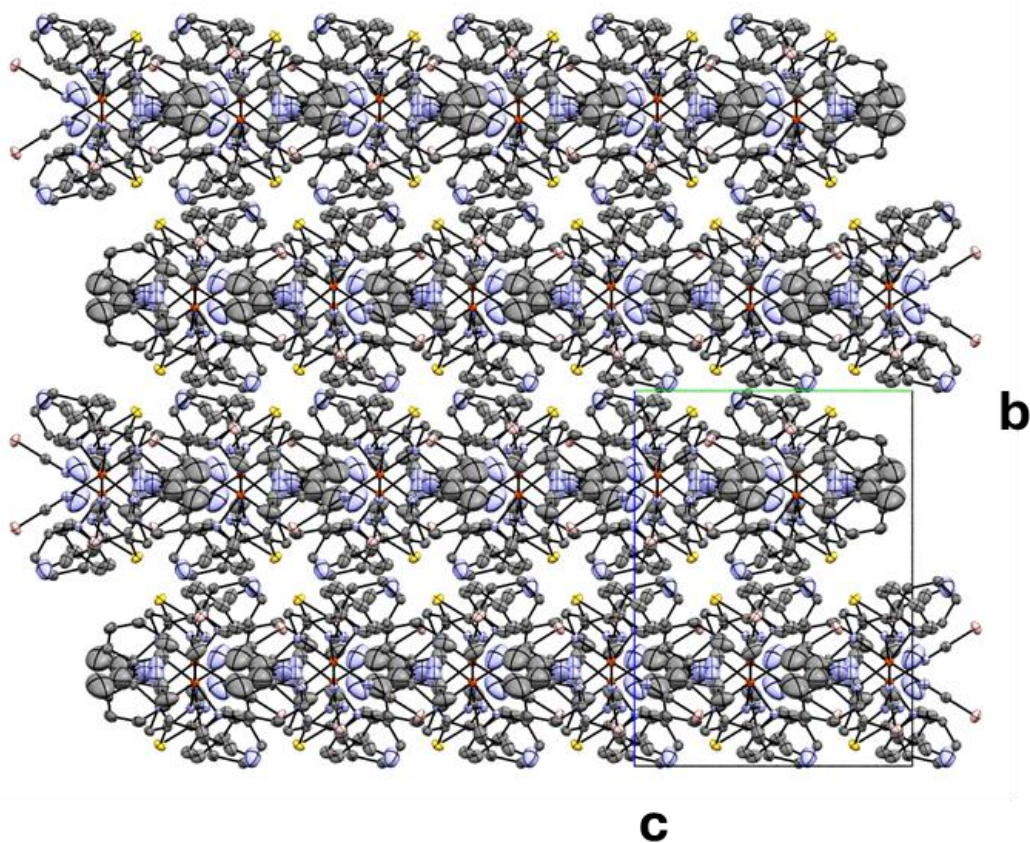


Figure S42: Visualisation of the packing for complex $[\text{Fe}(\text{L}^{\text{Ph-TDA}})(\text{NCBH}_3)_2] \cdot 2.5 \text{ MeCN}$ (**C3**) at 120 K along a -axis. Hydrogen atoms were removed for better overview.

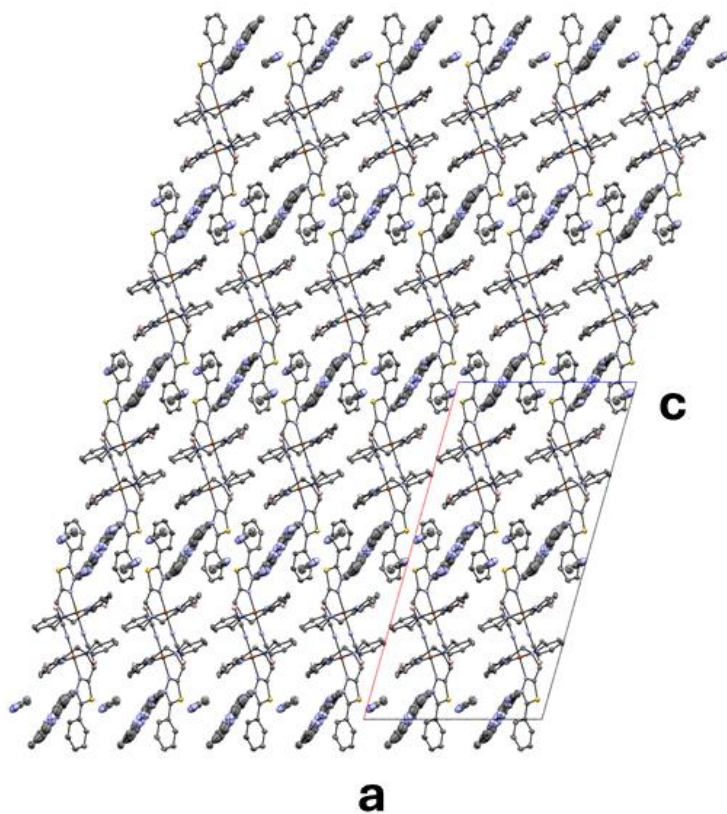


Figure S43: Visualisation of the packing for complex $[\text{Fe}(\text{L}^{\text{Ph-TDA}})(\text{NCBH}_3)_2] \cdot 2.5 \text{ MeCN}$ (**C3**) at 120 K along b -axis. Hydrogen atoms were removed for better overview.

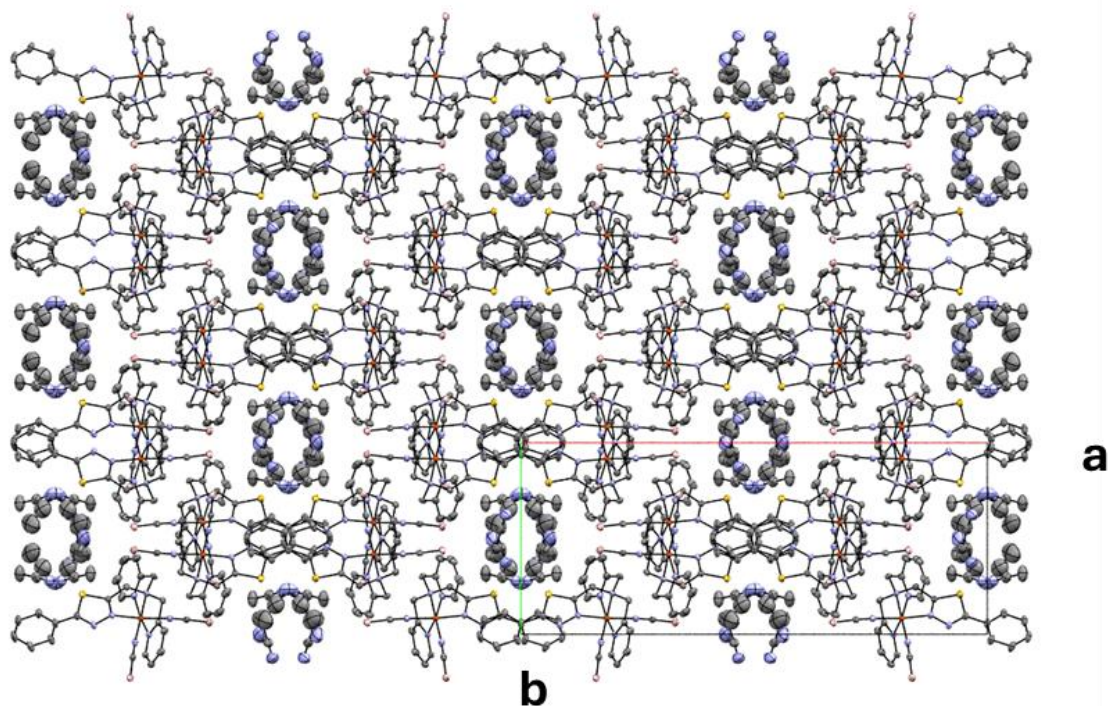


Figure S44: Visualization of the packing for complex $[\text{Fe}(\text{L}^{\text{Ph-TDA}})(\text{NCBH}_3)_2] \cdot 2.5 \text{ MeCN}$ (**C3**) at 120 K *c*-axis. Hydrogen atoms were removed for better overview.

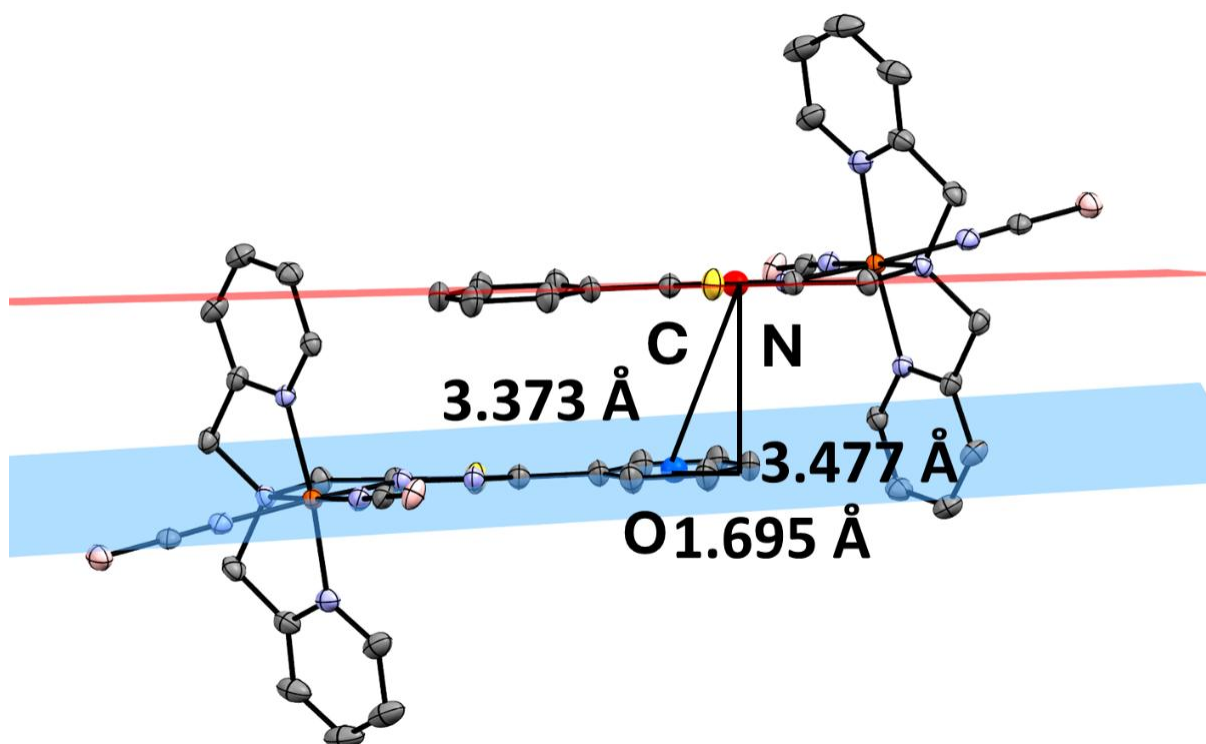


Figure S45: Visualisation of the π - π -interaction between Phenyl- and 1,3,4-Thiadiazole-unit with off-set (O), Normal vector (N) and centroid-centroid-distance (C) for complex $[\text{Fe}(\text{L}^{\text{Ph-TDA}})(\text{NCBH}_3)_2] \cdot 2.5 \text{ MeCN}$ (**C3**) at 120 K.

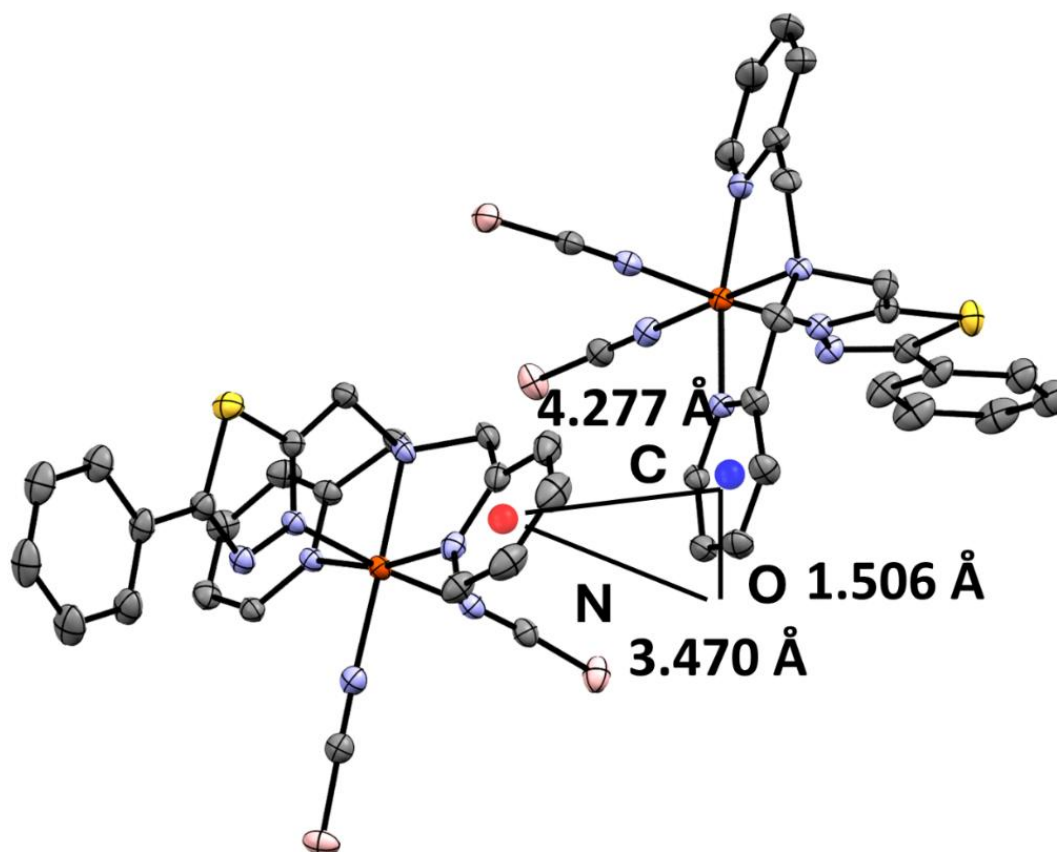


Figure S46: Visualisation of the π - π -interaction between pyridine-units with offset (O), Normal vector (N) and centroid-centroid-distance (C) for complex $[\text{Fe}(\text{L}^{\text{Ph-TDA}})(\text{NCBH}_3)_2] \cdot 2.5 \text{ MeCN}$ (**C3**) at 120 K.

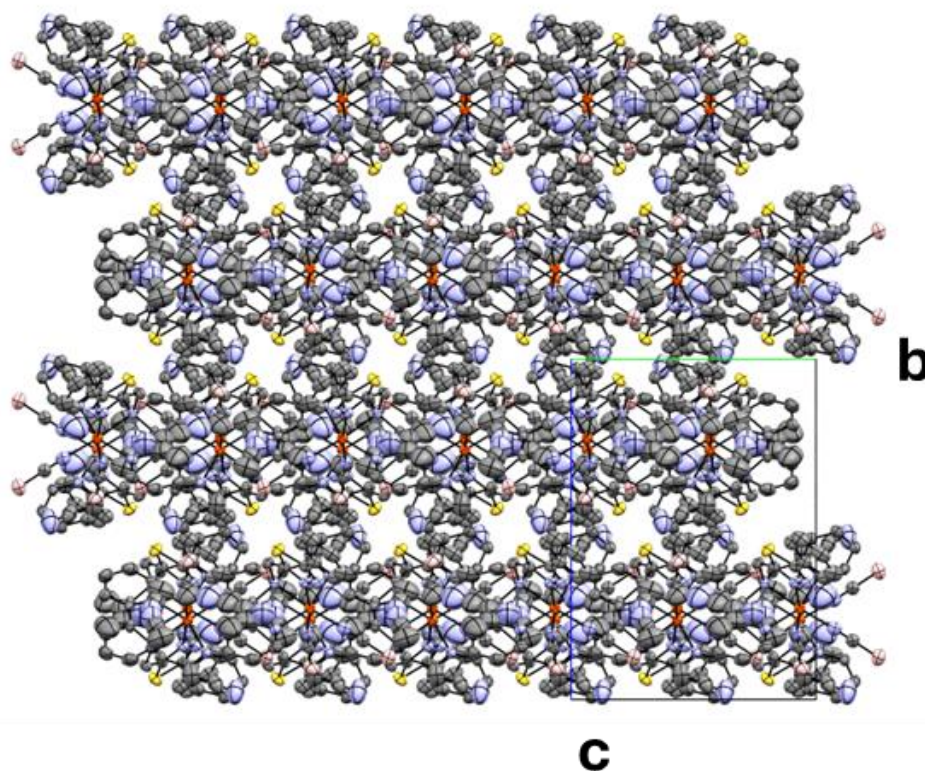


Figure S47: Visualisation of the packing for complex $[\text{Fe}(\text{L}^{\text{Ph-TDA}})(\text{NCBH}_3)_2] \cdot 2.5 \text{ MeCN}$ (**C3**) at 230 K along a -axis. Hydrogen atoms were removed for better overview.

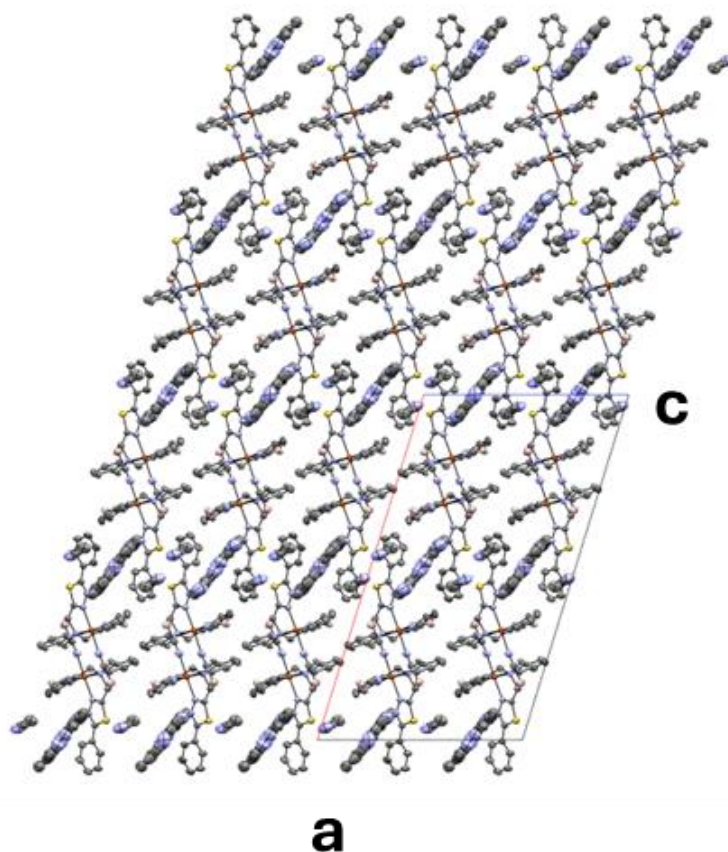


Figure S48: Visualisation of the packing for complex $[\text{Fe}(\text{L}^{\text{Ph-TDA}})(\text{NCBH}_3)_2] \cdot 2.5 \text{ MeCN}$ (**C3**) at 230 K along *b*-axis. Hydrogen atoms were removed for better overview.

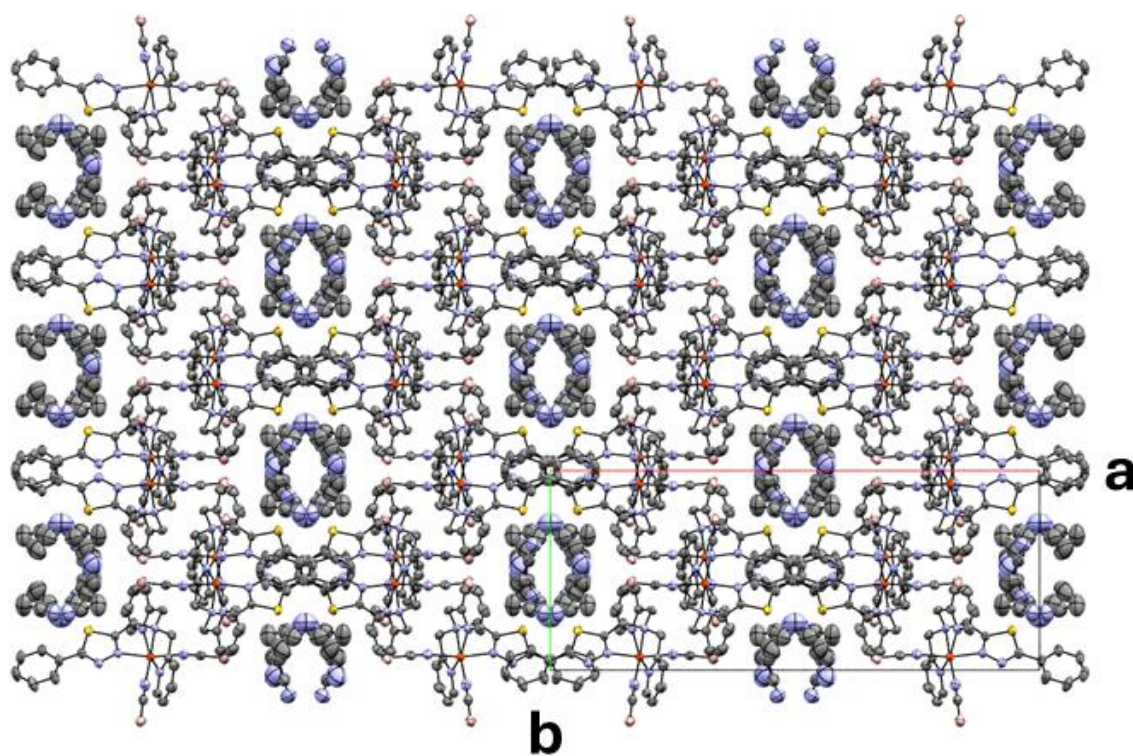


Figure S49: Visualisation of the packing for complex $[\text{Fe}(\text{L}^{\text{Ph-TDA}})(\text{NCBH}_3)_2] \cdot 2.5 \text{ MeCN}$ (**C3**) at 230 K along *c*-axis. Hydrogen atoms were removed for better overview.

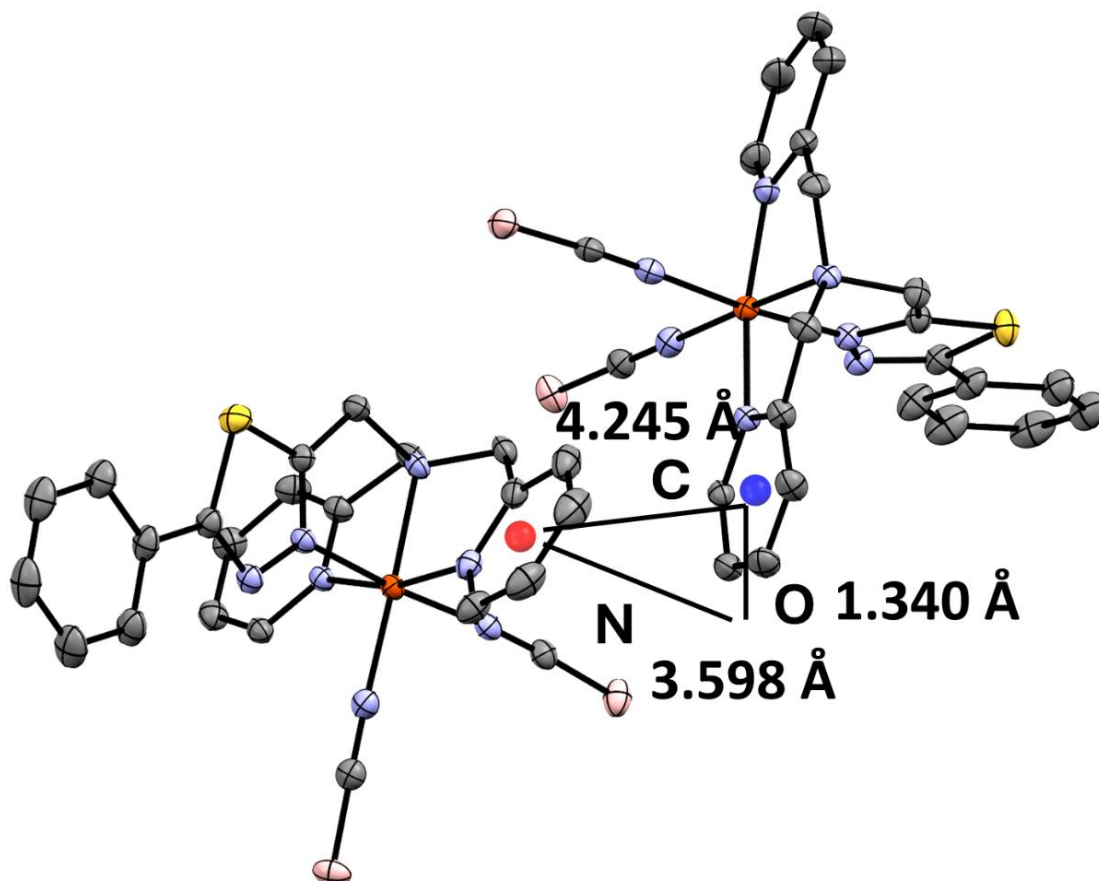


Figure S50: Visualisation of the π - π -interaction between pyridine-units with offset (O), normal vector (N) and centroid-centroid-distance (C) for complex $[\text{Fe}(\text{L}^{\text{Ph-TDA}})(\text{NCBH}_3)_2] \cdot 2.5 \text{ MeCN}$ (**C3**) at 230 K.

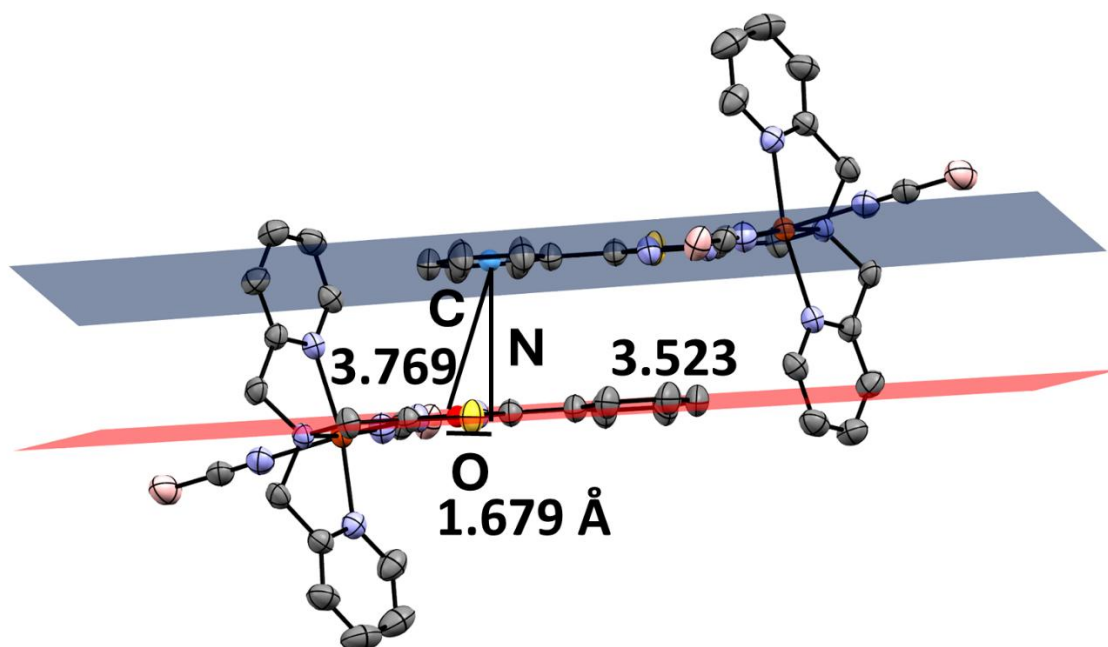


Figure S51 Visualisation of the π - π -interaction between Phenyl- and 1,3,4-Thiadiazole-unit with off-set (O), normal vector (N) and centroid-centroid-distance (C) for complex $[\text{Fe}(\text{L}^{\text{Ph-TDA}})(\text{NCBH}_3)_2] \cdot 2.5 \text{ MeCN}$ (**C3**) at 230 K.

5. Crystallographic Data:

Table S3: Measurement parameters for $[\text{Fe}(\text{L}^{\text{Ph-TDA}})(\text{NCS})_2] \cdot \text{MeCN}$ (**C1**) at 120 K.

Parameter	Result
Empirical formula	$\text{C}_{23}\text{H}_{19}\text{FeN}_7\text{S}_3 \cdot \text{C}_2\text{H}_3\text{N}$
Formula weight	1132.02
Temperature/K	120
Crystal system	triclinic
Space group	P-1
a/Å	11.1571(2)
b/Å	13.8853(3)
c/Å	16.6309(3)
$\alpha/^\circ$	84.104(2)
$\beta/^\circ$	88.812(2)
$\gamma/^\circ$	78.965(2)
Volume/Å ³	2515.44(9)
Z	2
$\rho_{\text{calc}}/\text{g}/\text{cm}^3$	1.495
μ/mm^{-1}	0.878
F(000)	1164
Radiation	Mo-K α ($\lambda = 0.71073$)
2 θ range for data collection/ $^\circ$	2.157 to 33.800
Index ranges	$-16 \leq h \leq 16, -19 \leq k \leq 21, -23 \leq l \leq 25$
Reflections collected	57581
Independent reflections	17266 [$R_{\text{int}} = 0.0154, R_{\text{sigma}} = 0.0184$]
Data/restraints/parameters	17266/185/787
Goodness-of-fit on F^2	1.025
Final R indexes [$I \geq 2\sigma(I)$]	$R_1 = 0.0381, wR_2 = 0.0917$
Final R indexes [all data]	$R_1 = 0.0461, wR_2 = 0.0970$

Table S4: Measurement parameters for $[\text{Fe}(\text{L}^{\text{Ph-TDA}})(\text{NCS})_2] \cdot \text{MeCN}$ (**C1**) at 240 K.

Parameter	Result
Empirical formula	$\text{C}_{23}\text{H}_{19}\text{FeN}_7\text{S}_3 \cdot \text{C}_2\text{H}_3\text{N}$
Formula weight	1132.02
Temperature/K	240 K
Crystal system	triclinic
Space group	P-1
a/Å	11.203 (7)
b/Å	14.143(11)
c/Å	16.910(13)
$\alpha/^\circ$	84.30(6)
$\beta/^\circ$	89.04(6)
$\gamma/^\circ$	79.39(6))
Volume/Å³	2620(3)
Z	2
$\rho_{\text{calc}}/\text{g}/\text{cm}^3$	1.435
μ/mm^{-1}	0.843
F(000)	1164
Radiation	Mo-K α ($\lambda = 0.71073$)
2θ range for data collection/$^\circ$	2.209 to 33.950
Index ranges	$-10 \leq h \leq 16, -11 \leq k \leq 20, -25 \leq l \leq 23$
Reflections collected	15053
Independent reflections	10872 [$R_{\text{int}} = 0.0372, R_{\text{sigma}} = 0.1223$]
Data/restraints/parameters	17266/252/750
Goodness-of-fit on F^2	0.862
Final R indexes [$I \geq 2\sigma(I)$]	$R_1 = 0.0540, wR_2 = 0.1225$
Final R indexes [all data]	$R_1 = 0.1551, wR_2 = 0.1507$

Table S5: Measurement parameters for [Fe(L^{Ph-TDA})(NCSe)₂] · 2.5 MeCN (**C2**) at 120 K.

Parameter	Result
Empirical formula	C ₂₃ H ₁₉ FeN ₇ SSe ₂ · 2.5 C ₂ H ₃ N
Formula weight	741.92
Temperature/K	120.0
Crystal system	monoclinic
Space group	C2/c
a/Å	31.3953 (13)
b/Å	11.8669(5)
c/Å	17.4680(6)
α/°	90
β/°	107.895(3)
γ/°	90
Volume/Å³	6193.1(4)
Z	8
ρ_{calc} g/cm³	1.591
μ/mm⁻¹	2.941
F(000)	2968
Crystal size/mm³	0.22 × 0.187 × 0.14
Radiation	MoKα (λ = 0.71073)
2θ range for data collection/°	2.097 to 32.761
Index ranges	-43 ≤ h ≤ 43, -16 ≤ k ≤ 16, -26 ≤ l ≤ 24
Reflections collected	41065
Independent reflections	9842[R _{int} = 0.0275, R _{sigma} = 0.0277]
Data/restraints/parameters	9842/73/417
Goodness-of-fit on F²	1.084
Final R indexes [I ≥ 2σ (I)]	R ₁ = 0.0620, wR ₂ = 0.1552
Final R indexes [all data]	R ₁ = 0.0829, wR ₂ = 0.1678

Table S6: Measurement parameters for $[\text{Fe}(\text{L}^{\text{Ph-TDA}})(\text{NCBH}_3)_2] \cdot 2.5 \text{ MeCN}$ (**C3**) at 120 K.

Parameter	Result
Empirical formula	$\text{C}_{23}\text{H}_{25}\text{B}_2\text{FeN}_7\text{S} \cdot 2.5 \text{ C}_2\text{H}_3\text{N}$
Formula weight	625.18
Temperature/K	120
Crystal system	monoclinic
Space group	C2/c
a/Å	30.9617(7)
b/Å	12.1406(2)
c/Å	17.1318(4)
$\alpha/^\circ$	90
$\beta/^\circ$	107.055(2)
$\gamma/^\circ$	90
Volume/Å ³	6156.5(2)
Z	8
$\rho_{\text{calc}}/\text{g}/\text{cm}^3$	1.349
μ/mm^{-1}	0.595
F(000)	2612
Radiation	Mo K α ($\lambda = 0.71073$)
2 θ range for data collection/ $^\circ$	2.081 to 32.76
Index ranges	$-45 \leq h \leq 46, -15 \leq k \leq 18, -24 \leq l \leq 26$
Reflections collected	37958
Independent reflections	9183 [$R_{\text{int}} = 0.0399, R_{\text{sigma}} = 0.0237$]
Data/restraints/parameters	9808/18/406
Goodness-of-fit on F ²	1.114
Final R indexes [$I \geq 2\sigma(I)$]	$R_1 = 0.0573, wR_2 = 0.1661$
Final R indexes [all data]	$R_1 = 0.0595, wR_2 = 0.1679$

Table S7: Measurement parameters for $[\text{Fe}(\text{L}^{\text{Ph-TDA}})(\text{NCBH}_3)_2] \cdot 2.5 \text{ MeCN}$ (**C3**) at 230 K.

Parameter	Result
Empirical formula	$\text{C}_{23}\text{H}_{25}\text{B}_2\text{FeN}_7\text{S} \cdot 2.5 \text{ C}_2\text{H}_3\text{N}$
Formula weight	625.18
Temperature/K	230
Crystal system	monoclinic
Space group	$C2/c$
$a/\text{\AA}$	31.237(2)
$b/\text{\AA}$	12.1599(6)
$c/\text{\AA}$	17.6916(12)
$\alpha/^\circ$	90
$\beta/^\circ$	107.101(2)
$\gamma/^\circ$	90
Volume/ \AA^3	6422.9(7)
Z	8
$\rho_{\text{calc}}/\text{g/cm}^3$	1.265
μ/mm^{-1}	0.568
F(000)	2552
Radiation	Mo $K\alpha$ ($\lambda = 0.71073$)
2 θ range for data collection/ $^\circ$	2.059 to 32.742
Index ranges	$-44 \leq h \leq 45, -15 \leq k \leq 18, -24 \leq l \leq 26$
Reflections collected	40853
Independent reflections	10231 [$R_{\text{int}} = 0.0445, R_{\text{sigma}} = 0.0253$]
Data/restraints/parameters	10231/48/407
Goodness-of-fit on F^2	1.047
Final R indexes [$I \geq 2\sigma(I)$]	$R_1 = 0.0558, wR_2 = 0.1610$
Final R indexes [all data]	$R_1 = 0.0616, wR_2 = 0.1675$

Table S8: cis-N-Fe-N bond angles of Fe1 and Fe2 for the complex $[\text{Fe}(\text{L}^{\text{Ph-TDA}})(\text{NCS})_2] \cdot \text{MeCN}$ (**C1**) at 120 K and 240 K.

Fe1	120 K	240 K	Fe2	120 K	240 K
N2-Fe1-N3	75.63(4)	76.01(14)	N9-Fe2-N10	85.05(9)	76.82(14)
N2-Fe1-N4	93.90(5)	93.73(15)	N9-Fe2-N11	86.71(6)	82.27(14)
N2-Fe1-N5	78.03(5)	77.50(15)	N9-Fe2-N12	92.19(7)	89.54(15)
N2-Fe1-N7	98.35(6)	97.94(16)	N10-Fe2-N11	83.49(9)	76.01(14)
N3-Fe1-N4	74.72(5)	74.12(13)	N10-Fe2-N12	83.98(9)	76.00(15)
N3-Fe1-N5	76.54(5)	76.41(13)	N10-Fe2-N13	92.44(8)	91.57(16)
N3-Fe1-N6	88.44(5)	88.05(14)	N11-Fe2-N13	90.05(7)	89.98(16)
N4-Fe1-N6	91.43(5)	91.41(14)	N11-Fe2-N14	96.34(12)	103.77(16)
N4-Fe1-N7	102.81(6)	103.64(15)	N12-Fe2-N13	90.45(7)	92.68(16)
N5-Fe1-N6	88.68(5)	89.19(14)	N12-Fe2-N14	97.18(10)	103.78(16)
N5-Fe1-N7	105.64(6)	105.46(15)	N13-Fe2-N14	89.53(11)	95.38(17)
N6-Fe1-N7	98.04(6)	98.41(17)	N14-Fe2-N9	92.98(11)	96.24(16)

Table S9: cis N-Fe-N bond angles for the complex $[\text{Fe}(\text{L}^{\text{Ph-TDA}})(\text{NCSe})_2] \cdot 2.5 \text{ MeCN}$ (**C2**) at 120 K.

	Bond angle / °		Bond angle / °		Bond angle / °
N2-Fe1-N7	97.87(16)	N4-Fe1-N6	92.66(13)	N5-Fe1-N7	107.83(17)
N2-Fe1-N5	81.11(12)	N4-Fe1-N7	102.86(16)	N6-Fe1-N5	90.50(12)
N2-Fe1-N4	88.76(12)	N6-Fe1-N7	95.55(17)	N3-Fe1-N6	89.81(13)
N2-Fe1-N3	77.00(12)	N4-Fe1-N3	74.40(12)	N3-Fe1-N5	74.46(12)

Table S10: cis-N-Fe-N bond angles for the complex $[\text{Fe}(\text{L}^{\text{Ph-TDA}})(\text{NCBH}_3)_2] \cdot 2.5 \text{ MeCN}$ (**C3**) at 120 K and 230 K.

	120 K	230 K
N2-Fe1-N5	92.26(6)	84.32(6)
N2-Fe1-N4	86.19(7)	89.66(6)
N2-Fe1-N3	84.34(6)	78.87(5)
N2-Fe1-N7	94.58(7)	97.44(7)
N3-Fe1-N4	82.67(7)	76.44(5)
N3-Fe1-N5	82.55(6)	76.18(6)
N3-Fe1-N6	92.10(6)	91.53(6)
N4-Fe1-N6	89.95(7)	92.61(6)
N4-Fe1-N7	98.41(7)	99.92(7)
N5-Fe1-N6	90.69(6)	88.91(6)
N5-Fe1-N7	96.36(6)	107.35(7)
N6-Fe1-N7	89.05(7)	92.43(7)

Table S11: Iron(II)-Nitrogen bond length for Fe1 and Fe2 Complex $[\text{Fe}(\text{L}^{\text{Ph-TDA}})(\text{NCS})_2] \cdot \text{MeCN}$ (**C1**) at 120 K and 240 K.

	120 K Bond length / Å	240 K Bond length / Å
Fe1 N2	2.2410(13)	2.024(4)
Fe1 N3	2.2826(12)	2.132(4)
Fe1 N4	2.1748(13)	2.194(4)
Fe1 N5	2.1667(13)	2.169(4)
Fe1 N6	2.1168(14)	2.271(4)
Fe1 N7	2.0355(16)	2.024(4)
Spin State	HS	HS
Fe2 N9	1.9478(15)	2.172(4)
Fe2 N10	1.997(3)	2.269(4)
Fe2 N11	1.9874(16)	2.189(4)
Fe2 N12	2.0025(17)	2.191(4)
Fe2 N13	1.9792(17)	2.104(5)
Fe2 N14	1.941(2)	2.018(4)
Spin State	LS	HS

Table S12: Iron(II)-Nitrogen bond length for Complex $[\text{Fe}(\text{L}^{\text{Ph-TDA}})(\text{NCSe})_2] \cdot 2.5 \text{ MeCN}$ (**C2**).

	Bond length / Å		Bond length / Å
Fe1 N2	2.199(3)	Fe1 N5	2.184(3)
Fe1 N3	2.289(3)	Fe1 N6	2.086(4)
Fe1 N4	2.197(3)	Fe1 N7	2.062(5)

Table S13: Iron(II)-Nitrogen bond length for Complex [Fe(L^{Ph-TDA})(NCBH₃)₂] · 2.5 MeCN (**C3**) at 120 K and 230 K.

	120 K Bond length / Å	230 K Bond length / Å
Fe1 N2	1.9526(16)	2.1478(14)
Fe1 N3	2.0068(15)	2.2306(14)
Fe1 N4	1.9799(16)	2.1610(15)
Fe1 N5	1.9894(15)	2.1572(16)
Fe1 N6	1.9506(17)	2.1148(19)
Fe1 N7	1.9455(17)	2.080(2)
	LS	HS

Table S14: Distortion parameter and average Iron(II)-Nitrogen bond length of the Iron(II) center in **C1**, **C2** and **C3** Iron(II) at 120 K and 230 K.

	Distortion Parameter / °	Average Fe-N bondlength / Å
C1 (Fe1) 120 K LS	108.13	2.17 ± 0.09
C1 (Fe2) 120 K HS	43.87	1.98 ± 0.03
C1 (Fe1) 240 K HS	109.31	2.2 ± 0.1
C1 (Fe2) 240 K HS	92.80	2.16 ± 0.09
C2 120 K HS	101.73	2.17 ± 0.08
C3 120 K LS	49.65	1.97± 0.03
C3 230 K HS	86.90	2.15 ± 0.05

6. Magnetic data:

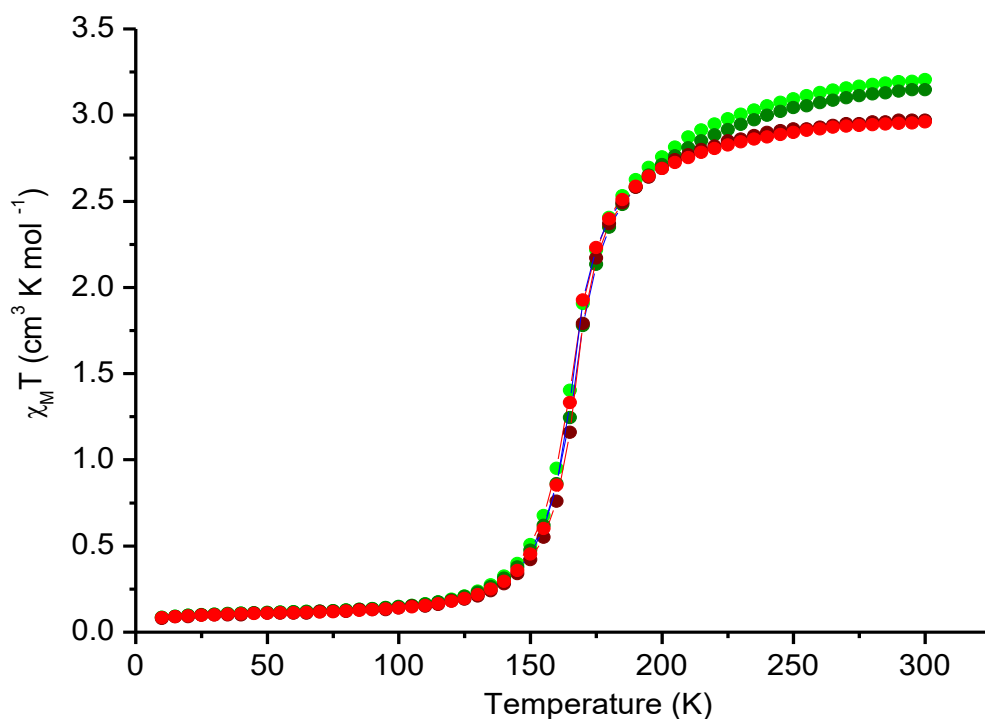


Figure S52: χ_M vs T measured of microcrystalline product of $[\text{Fe}(\text{L}^{\text{Ph-TDA}})(\text{NCBH}_3)_2] \cdot \text{H}_2\text{O}$ (**C3**) in the form of the resulting $\chi_M T$ vs T plot. Magnetic susceptibility was determined between 300-10 K (dark red) and 10-300 K (red circle), waiting at 300 K for 30 minutes and 300-10 K (dark green circle) and 10-300 K (green circle).

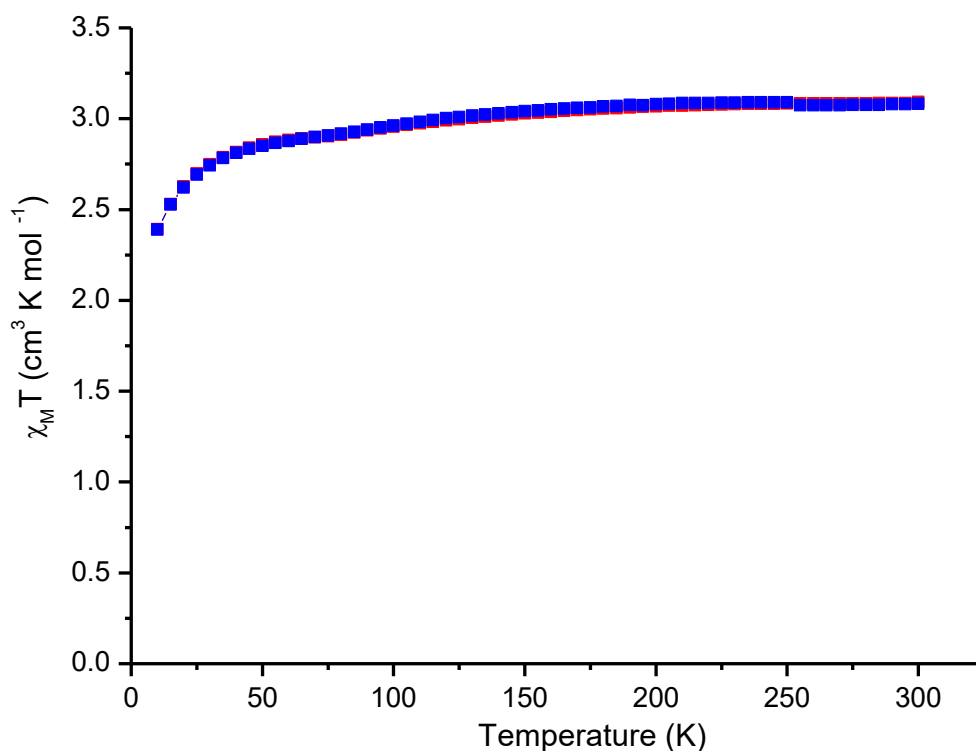


Figure S53: χ_M vs T measured of microcrystalline product of $[\text{Fe}(\text{L}^{\text{Ph-TDA}})(\text{NCSe})_2] \cdot \text{H}_2\text{O}$ (**C2**) in the form of the resulting $\chi_M T$ vs T plot. Magnetic susceptibility was determined between 300-10 K (blue squares) and 10-300 K (red squares).

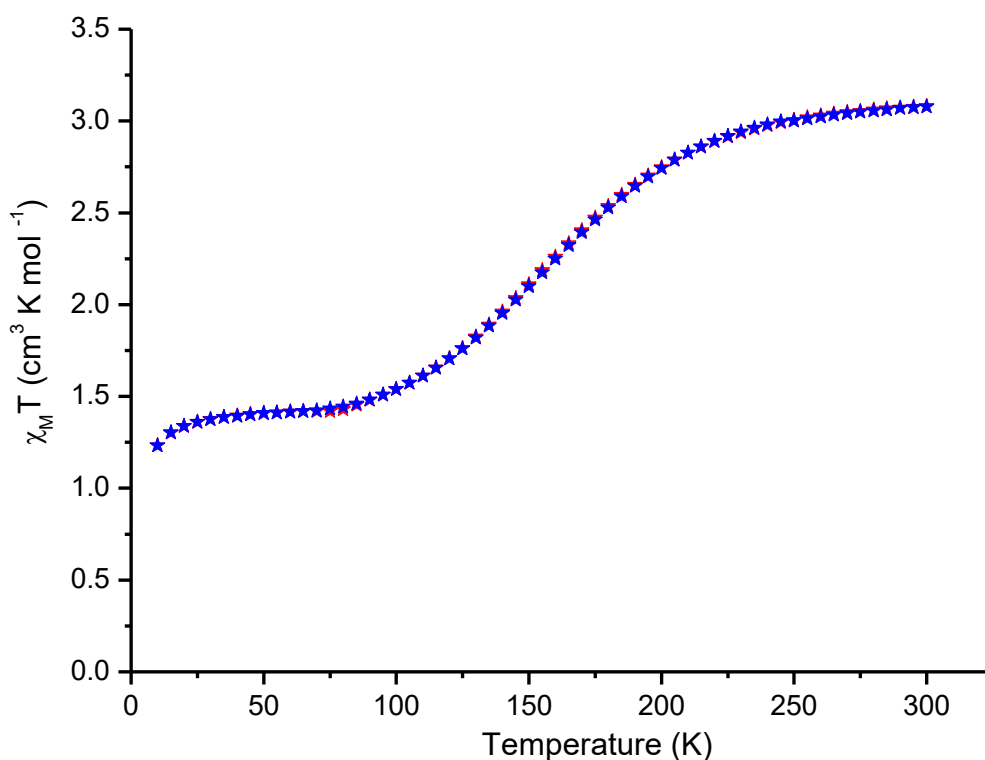


Figure S54: $\chi_M T$ vs T measured of microcrystalline product of $[\text{Fe}(\text{L}^{\text{Ph-TDA}})(\text{NCS})_2] \cdot \text{H}_2\text{O}$ (**C1**) in the form of the resulting $\chi_M T$ vs T plot. Magnetic susceptibility was determined between 300-10 K (blue stars) and 10-300 K (red stars).

7. Light-induced excited spin state trapping:

Magnetic measurements indicate that in complex **C1** only Fe2 undergo spin crossover at low temperature and Fe1 remains in the high-spin state. The drop of the $\chi_M T$ -values at very low temperatures (< 35 K) can be either attributed to the switch of Fe1, so that all iron(II) are in the *LS*, or to the combination of weak intermolecular dipolar interaction and weak zero-field splitting of the Fe(II) center. To probe the potential for complete spin state conversion, we performed light-induced excited spin state trapping (*LIESST*) experiments. The aim was twofold: first, to determine whether selective light irradiation could drive the low-spin Fe(II) centres (Fe2) into a fully high-spin at low temperatures; and second, to explore the “*reverse-LIESST*” effect, assessing whether the high-spin population at low temperatures could be pushed to a fully low-spin state.

To investigate the *reverse-LIESST* and *LIESST*-effect, knowledge about the absorption properties is essential to find the right absorption band for exciting the complexes. Solid state absorption spectra at room temperature and 77 K were measured on a powder sample for **C1** between 350 nm and 900 nm and are shown in **Figure S56-S69**. At room temperature, two transition regions are distinguishable. The high energy absorption between 350 nm and 550 nm can most probably be assigned to *MLCT* or *LMCT*, where the low energy absorption from 700 nm to 900 nm is attributed to either a d-d-transition or a

charge transfer between the iron(II) and the NCS co-ligand.^[88] At lower temperature, an absorption next to the ligand-based transition occurs between 520 nm and 650 nm, which is related to the metal-to-ligand-charge transfer (*MLCT*) of the low spin fraction attributed to partial spin crossover, observed by single crystal *XRD* and *SQUID* measurements.^[88] Over 680 nm periodic signals are observed in the signals, which are assigned to artifacts based on the set up for the reference (holder) and the sample. Both wavelengths for the *LIESST* and reverse *LIESST* were chosen based on the solid-state *UV-Vis* data obtained on **C1**.

The *LIESST*-effect was observed by exciting the sample at 5 K with $\lambda = 520$ nm for 2 h, as at this wavelength the absorption of the relevant *MLCT* band was determined. Then the light source was switched off and the sample was warmed to room temperature while continuously measuring the magnetic moment. The *LIESST*-effect results in a plateau reaching a $\chi_M T$ -value of $2.20 \text{ cm}^3 \cdot \text{K} \cdot \text{mol}^{-1}$, which implies that around 50% of the low spin centers were switched. The characteristics of the experimental setup do not allow observation of the complete switching process. Because the penetration depth of the excitation light is limited, only a fraction of the molecules within the bulk sample are irradiated. Preparing an ultrathin film to ensure uniform irradiation would, however, lead to an unacceptably low magnetic signal, preventing reliable detection of the spin-state change.

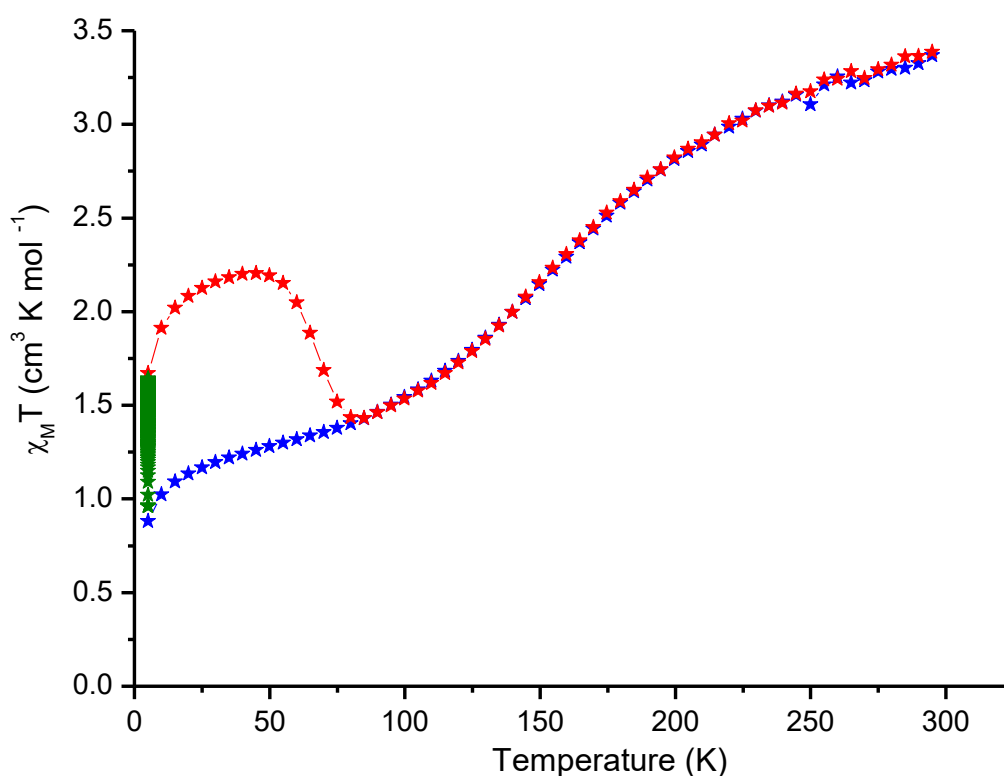


Figure S1: χ_M vs. T measured of microcrystalline product of $[\text{Fe}(\text{L}^{\text{Ph-TDA}})(\text{NCS})_2] \cdot \text{H}_2\text{O}$ (**C1**) in the form of the resulting $\chi_M T$ vs. T plot. Magnetic susceptibility was determined between 300-10 K (blue), during exciting the sample with $\lambda = 550$ nm (green) and 10-300 K (red).

In complex **C1**, attempts to drive the system fully into the *LS-LS* state using *reverse-LIESST* (at 850 nm) were unsuccessful. This behaviour could be rationalized in light of the mechanistic framework proposed by Sakaki *et al.*^[89] If the minimum of potential energy surface of the excited state is above the minimum of potential energy surface of the E_g -state, the relaxation to this state is favoured above the path to the $^1A_{1g}$ (*reverse-LIESST*).

8. Solid state *UV-Vis* measurement:

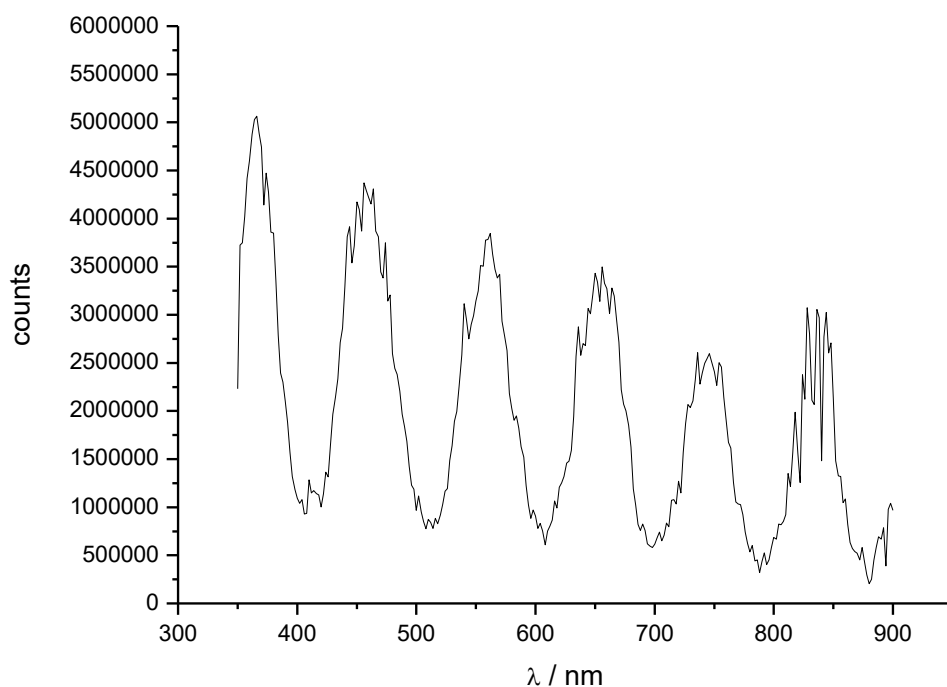


Figure S56: Solid state *UV-Vis* measurement of the reference at 293 K.

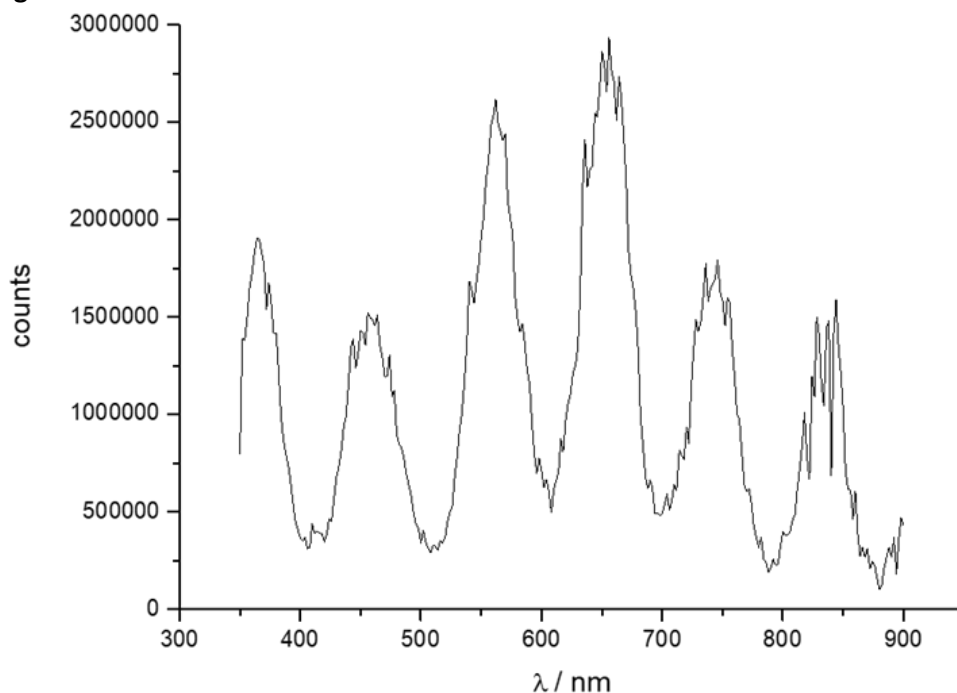


Figure S57: Solid state *UV-Vis* measurement of $[\text{Fe}(\text{L}^{\text{Ph-TDA}})(\text{NCS})_2] \cdot \text{H}_2\text{O}$ (**C1**) at 293 K.

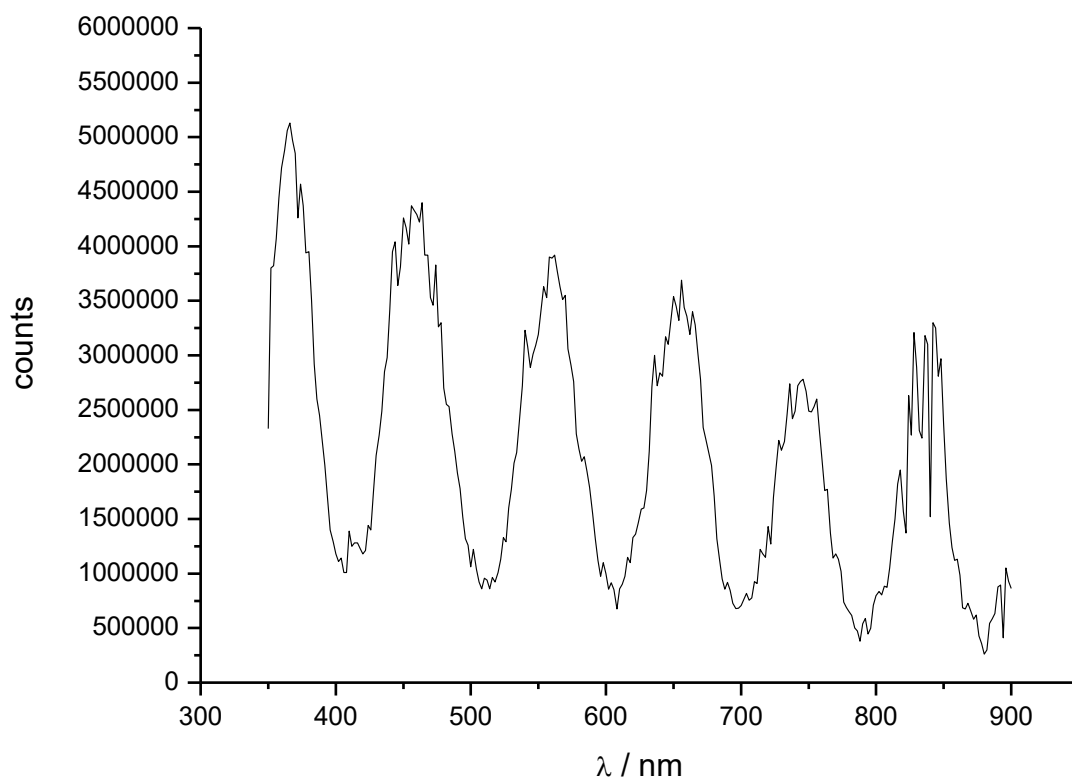


Figure S58: Solid state *UV-Vis* measurement of the reference at 77 K.

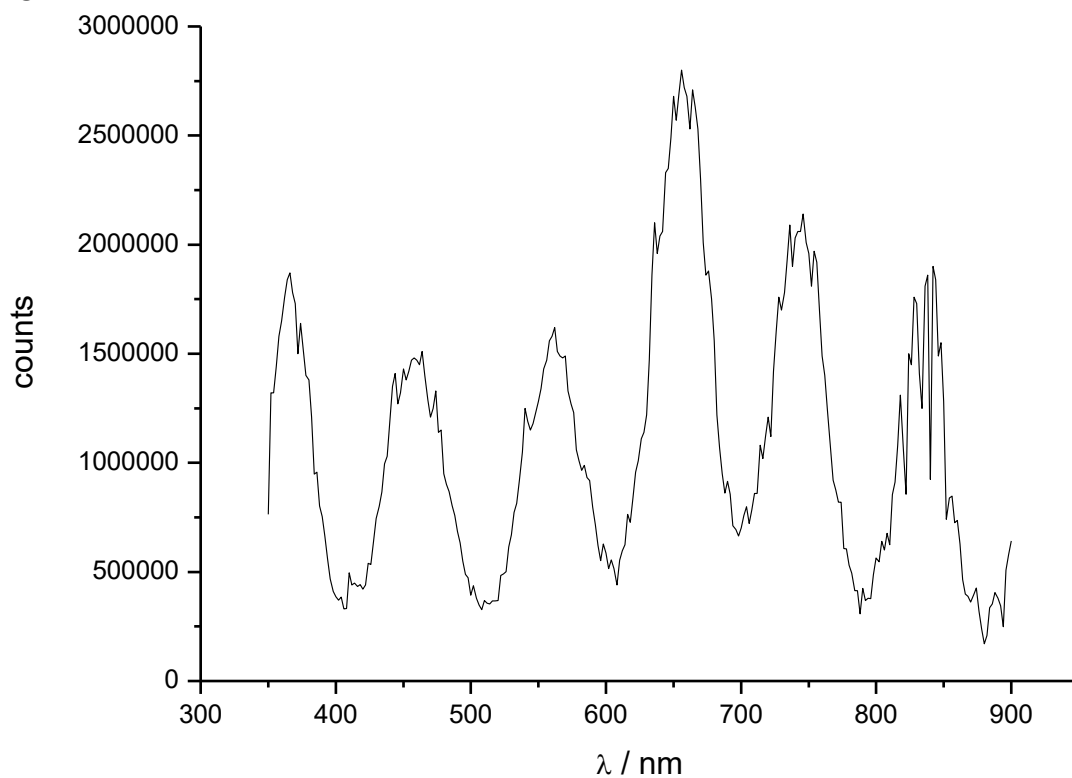


Figure S59: Solid state *UV-Vis* measurement of $[\text{Fe}(\text{L}^{\text{Ph-TDA}})(\text{NCS})_2] \cdot \text{H}_2\text{O}$ (C1) at 77 K.

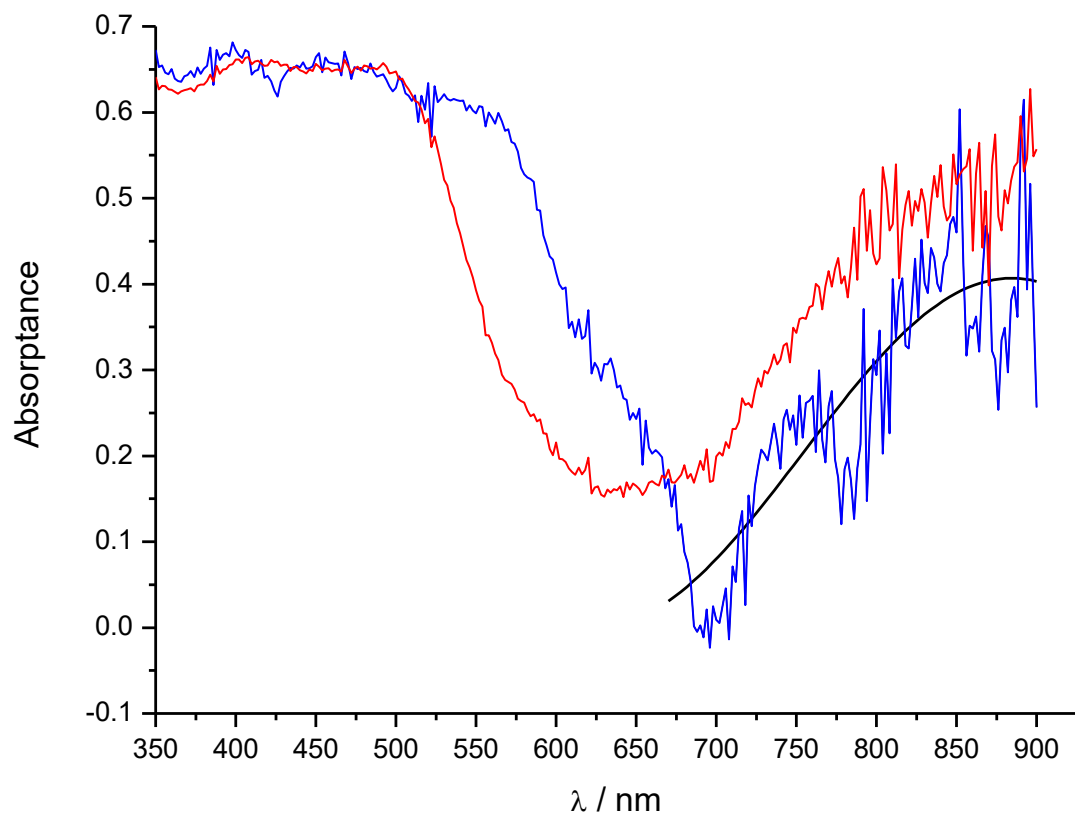


Figure S60: Solid state absorbance measurement plotted as Absorbance vs λ of $[\text{Fe}(\text{L}^{\text{Ph-TDA}})(\text{NCS})_2] \cdot \text{H}_2\text{O}$ (C1) at 77 K (blue) and 293 K (red), with the fit (black) of Absorbance between 680 nm and 900 nm to visualize the transition band.

9. DFT-Methods and Model

Assigning the proper spin distribution in the models of the crystal.

For the modelling of the crystal with the method applied in this report it is essential that one obtains the proper spin density distribution in the initial guess for the wave function. This could be done with applying of the Atomic Groups option of Gaussian package. In the following part we illustrate this approach for the example of *LS-Fe1-HS-Fe2* spin isomer, i.e. the one in which the spin states of Fe1 and Fe2 are reversed in comparison with the crystal structure. First, we cut 15 molecules out of the crystal structure, 8 low-spin Fe2 and 7 high-spin Fe1.

The model is schematically shown below. The molecules that are subsequently optimised are marked with the thicker rim. The geometry of the others is frozen in all further calculations

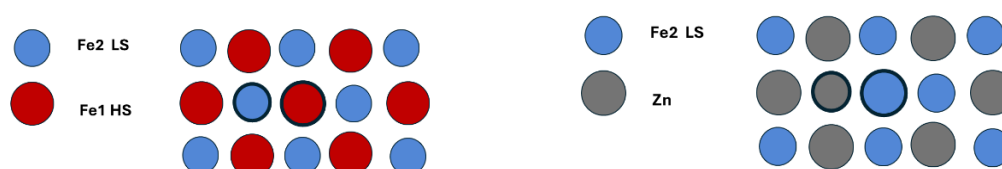


Figure S61: Left: Schematic representation of the initial cut from the crystal structure of the low-temperature phase of **C1** used in *DFT* modelling. Note that the actual geometry of the model does not correspond to the 2D sheet. Right: the model in the iron atoms in the *HS* molecules were replaced with zinc atoms (Model 1). The molecules that are subsequently optimised are marked with the thicker rim.

In the further calculations all *HS* molecules are replaced with zinc analogues. Although Model 1 has the multiplicity of 1 the economy of calculation suggests the application of Atomic Groups of *Gaussian*. Thus, with help of the *GaussView* utility the atoms in the model were divided into 16 groups. 15 each correspond to the complex *LS* molecules and one to six *MeCN* molecules present in the model cut from the crystal structure. The latter are not shown in the Schemes. The corresponding input file is given as *Zn_model_AG.gjf* in the document *Input_Files.txt*.

Note that the two molecules that's geometries are subsequently optimised are respectively denoted as Fragment = 5 (*LS-Fe1*) and Fragment =1 3 (*Zn2*). The following calculations yields the initial guesses for each fragment separately. In the next calculations the guess for the entire model is computed. The corresponding input file is given as *Zn_model_SCF.gjf* in the *Input_Files.txt*.

With the so obtained initial guess for the wave function the geometry of Model 1 was optimised to give Model 2 by optimising only Fragments 5 and 13 (see **Figure S61**).



Figure S62: Optimisation of the Model 1 (left) to Model 2 (right). Note that considering the size of the optimised molecules Model 2 represents the double-site defect in the lattice. For the further calculations the Zn molecule in position 2 must be changed to the HS-Fe1 one. The corresponding Model 3 is shown in **Figure S60**. The molecules that are subsequently optimised are marked with the thicker rim.

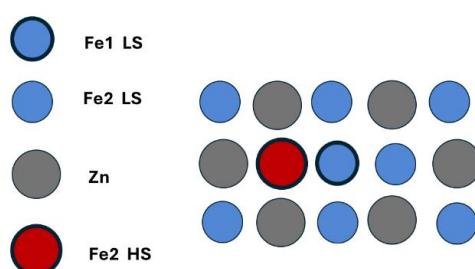


Figure S63: Schematic representation of Model 3 used for final geometry optimisation. The optimised molecules are marked with the thicker rim.

At this point the problem of the proper initial guess arises, namely one need the one with a proper spin density due to four unpaired electrons for the molecule marked red in **Figure S60**.

To obtain it the following procedure was applied. For each molecular fragment including the six molecules of MeCN the point calculations were performed. The corresponding input files for the further optimised low-spin Fragment 5 and high-spin Fragment 13 molecules (denoted blue and red with thicker rim in **Figure S60**) are given as frag_5.gjf and frag_13.gjf in the Input_Files.txt document. The corresponding input file for the MeCN molecule group and the examples for frozen LS-Fe(II) molecules and Zn(II) molecules are given as frag_2.gjf, frag_7.gjf and frag_1.gjf respectively in the Input_Files.txt document. It is crucial to use the keyword *nosymm* in these calculations. This series of calculations produces 16 checkpoint files that are then used in the subsequent Atomic Group calculations. The corresponding input file is given as model_3_AG.gjf data in the Input_Files.txt document. Note the difference between details of the Zn_model_AG.gjf and model_3_AG.gjf input files (keyword *guess=(input,fragment=16,nottranslate)*). In the next step again the initial guess of the wave function is calculated, see the input data model_3_SCF.gjf. The inspection of the spin density distribution confirmed the spin density due to four unpaired electrons on the Fe(II) of the Fragment 13 (marked red in **Figure S60**). Having the proper initial guess the geometry optimisation of the Fragments 5 and 13 may be performed.

10. Reference:

- [1] G. R. Fulmer, A. J. M. Miller, N. H. Sherden, H. E. Gottlieb, A. Nudelman, B. M. Stoltz, J. E. Bercaw, K. I. Goldberg, *Organometallics* **2010**, 29, 2176–2179.
- [2] S. Sundaresan, J. Eppelsheimer, E. Gera, L. Wiener, L. M. Carrella, K. R. Vignesh, E. Rentschler, *Dalton Trans.* **2024**, 53, 10303–10317.
- [3] A. Banerjee, A. Saha, B. K. Saha, *Crystal Growth & Design* **2019**, 19, 2245–2252.
- [4] G. Li, O. Stefanczyk, K. Kumar, L. Guérin, K. Okuzono, K. Tran, M. Seydi Kilic, K. Nakabayashi, K. Imoto, A. Namai, Y. Nakamura, S. Ranjan Maity, F. Renz, G. Chastanet, S. Ohkoshi, *Angew. Chem. Int. Ed.* **2025**, 64, e202423095.
- [5] H. Ando, Y. Nakao, H. Sato, S. Sakaki, *Dalton Trans.* **2010**, 39, 1836–1845.

Chapter 2: Chiral 1,3,4-Thiadiazole Complexes for Packing analysis

The synthesis and enantioselective separation of $L^{Ph-TDA-Al}$ via chiral *HPLC* are described, along with the synthesis and structural analysis of the enantiopure complexes $[Fe(L^{Ph-TDA-(R/S)-Al})(NCBH_3)_2]$ and the racemic mixture $[Fe(L^{Ph-TDA-(Rac)-Al})(NCBH_3)_2]$ will be presented in this chapter. Variable-temperature single-crystal *X-ray* diffraction measurements reveal alternating R- and S-enantiomers in the crystal packing of the racemic complex. Magnetic investigations showed that the racemic mixture remains in the high-spin state, while the enantiopure complexes exhibit an abrupt spin transition. This behavior was correlated with structural insights from crystal packing, highlighting enhanced cooperativity due to π - π stacking interactions. Additionally, nuclear inelastic scattering (*NIS*) experiments performed at the synchrotron further support this correlation.

The results are presented as a scientific article planned to publish.

Author contribution:

The general synthesis of the ligand system and the complexes was developed by [REDACTED], while the laboratory work on the ligand was performed by [REDACTED] and [REDACTED] and the complex synthesis was performed by [REDACTED]. The *IR*-spectroscopy and CD spectroscopy was collected by [REDACTED] as well as the sample preparation for elemental analysis, *NMR*-spectroscopy and *ESI-MS*-spectrometry. The separation of the enantiomers of the ligand was achieved by chiral *HPLC* performed by [REDACTED] under the supervision and the *HPLC* from [REDACTED]. [REDACTED] collected the single crystal *XRD* data and refined the structure. The evaluation of the magnetic and structural data was done by [REDACTED]. *Mössbauer* data as well as *NIS*-experiments data at *BESY* were collected by [REDACTED] supervised [REDACTED] from *RPTU* Kaiserslautern.

The Manuscript was written by [REDACTED], with input from [REDACTED] and [REDACTED]. [REDACTED] had the supervision during the manuscript process. All Authors have read and agreed to the submitted version of the manuscript.

Manuscript: Understanding Polymorphism and Spin Crossover in Chiral Iron(II) Complexes: Structure–Property Insights

Jens-Georg Becker¹, Sriram Sundaresan¹, Tim Hochdörffer², Juliusz A. Wolny², Marco A. M. Tummeley², Alexander Friesen¹, Luca M. Carrella¹, Volker Schünemann² and Eva Rentschler^{1*}

¹Department Chemie, Johannes-Gutenberg-Universität Mainz, Duesbergweg 10–14, 55128 Mainz, Germany. Email: rentschl@uni-mainz.de

²Department of Physics, University of Kaiserslautern-Landau, Erwin-Schrödinger-Str. 46, 67663 Kaiserslautern, Germany

Abstract:

The influence of crystal packing polymorphism on the spin crossover behaviour of iron(II) complexes incorporating the chiral ligand 1-(5-phenyl-1,3,4-thiadiazol-2-yl)-N,N-bis(pyridin-2-ylmethyl)ethan-1-amine ($L^{\text{Ph-TDA-Al}}$) has been investigated. The ligand was synthesized and employed to prepare two enantiopure and one racemic complex, $[\text{Fe}(L^{\text{Ph-TDA-(X)-Al}})(\text{NCBH}_3)_2]$, where X = S (**C1**), R (**C2**), and racemic (**C3**). Both enantiopure complexes (**C1** and **C2**) undergo an abrupt spin crossover centered at $T_c = 195$ K, while the racemic analogue (**C3**) remains locked in the high-spin state across the measured temperature range. Single-crystal *X-ray* diffraction of **C1** and **C3**, combined with variable-temperature magnetic susceptibility measurements, establishes a clear structure-property relationship, underscoring the role of crystal packing in governing spin crossover bistability.

Introduction:

Spin crossover (*SCO*) complexes are promising molecular switches with potential in sensing, data storage, and molecular devices.^[1,2] In iron(II) systems, reversible switching between low- and high-spin states can be triggered by temperature, light, or pressure.^[3,4] The critical transition temperature (T_c) depends sensitively on both the molecular structure, governed by ligand field strength, and the solid-state packing, which controls cooperativity. Subtle variations in intermolecular interactions can therefore profoundly alter *SCO* behaviour, making control of crystal packing a key design parameter for applications.^[5,6] Understanding and controlling the next-nearest neighbour interaction is therefore crucial, especially given the growing interest in integrating *SCO* complexes into soft matter^[7], thin films^[8] or in nanoparticles^[9], such as sensors^[10], or devices for data storage and processing^[11].

Incorporating chirality through ligand design adds further functionality: chiral complexes can display optical activity, crystallize in polar space groups, and support polymorphism between enantiopure and racemic forms despite identical molecular structures.^[12–15] Since enantiopure and racemic complexes often adopt distinct crystal packing arrangements, differences in intermolecular interactions can lead

to divergent *SCO* behaviour. These features expand the design space toward multifunctional materials, including switchable nonlinear optical^[16,17] systems and ferroelectric systems.^[13]

Information on the impact of different polymorphs of specific complexes on their spin crossover behavior is a key element for understanding and applying spin crossover materials.^[18,19] Conventional Mössbauer spectroscopy is used to identify the spin state of iron - element-specific - and further provides information about the coordination environment around the metal center.^[20] Another frequently discussed technique, which uses γ -quanta from synchrotron irradiation, is nuclear inelastic scattering (*NIS*).^[21] *NIS* offers element-specific insights into the phonon density of states (*pDOS*), supporting a deeper understanding of phonon-driven relaxation processes and lattice dynamics.^[22,23] Density functional theory (*DFT*) calculations related to molecular packing and interaction effects can be refined with *NIS* measurements, as the obtained *pDOS* serves as a valuable benchmark and model validation tool.^[22]

In this work, we introduce chirality to a mononuclear spin crossover (*SCO*) complex based on 1,3,4-thiadiazole using alanine, the smallest chiral molecule in nature, as a building block. Building on previous 1,3,4-oxadiazole and 1,3,4-thiadiazole ligands, we incorporated a methyl group as a steric-dictating substituent (**Figure 1**).^[24,25] The resulting ligand 1-(5-phenyl-1,3,4-thiadiazol-2-yl)-N,N-bis(pyridin-2-ylmethyl)ethan-1-amine (**L^{Ph-TDA-Al}**), was designed to investigate the influence of chirality and crystal packing on the *SCO* behaviour.^[24–26] The enantiomers of this ligand were separated using semi-preparative chiral high-performance liquid chromatography (*HPLC*) and were then used to synthesis three novel complexes: the *S*- and *R*-enantiomers, and the racemate. Comprehensive characterization was performed using a combination of analytical techniques and circular dichroism (*CD*) spectroscopy. Structure–property relationships were explored by correlating crystal packing, determined by single-crystal *X-ray* diffraction, with high-spin to low-spin transitions measured via *SQUID* magnetometry, enabling a detailed correlation between molecular packing and *SCO* behavior. Further temperature dependent *Mössbauer* measurements were used to confirm the spin state transition and investigations by *NIS* spectroscopy opens the opportunity to use packing model for the packing analysis.

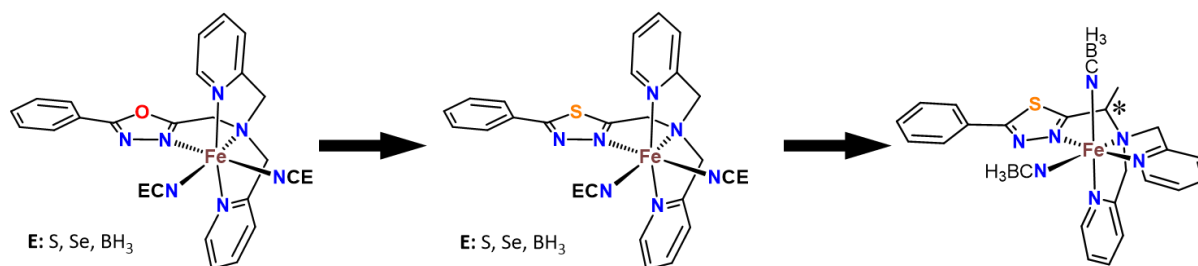


Figure 1: Evolution of the of mononuclear 1,3,4-thiadiazole- and 1,3,4-oxadiazole complexes previously reported to the newest chiral 1,3,4-thiadiazole-Iron(II)-complex.^[24,25]

Results and discussion:

Synthesis:

The Ligands R- and S-1-(5-phenyl-1,3,4-thiadiazol-2-yl)-N,N-bis(pyridin-2-ylmethyl)ethan-1-amine ($L^{\text{Ph-TDA-(S)-Al}}$ and $L^{\text{Ph-TDA-(R)-Al}}$) were synthesized using the similar of synthesis procedure as our recently published two-step synthesis, by using D-Alanine as amino acid (**Figure 2**).^[27] D-Alanine was used as starting reagent for the reductive amination with pyridine carbaldehyde and sodium trisacetoxyborohydride in dichloromethane. After purification by column chromatography the intermediate product, Bis(pyridin-2-ylmethyl)-alanine (**I**), was obtained in moderate yield (54 %) and characterised by $^1\text{H-NMR}$.^[28,29] Lastly, the intermediate product (**I**) was reacted with the coupling agent carbonyldiimidazole (CDI) and benzohydrazide in dry dichloromethane. After evaporating the solvent and dissolving the residue in dry tetrahydrofuran, the desired product, 1-(5-phenyl-1,3,4-thiadiazol-2-yl)-N,N-bis(pyridin-2-ylmethyl)ethan-1-amine ($L^{\text{Ph-TDA-(Rac)-Al}}$), was synthesized with Lawesson's reagent as the cyclisation agent. The product was obtained in a moderate yield as racemic mixture, as proven by chiral *HPLC* (high performance liquid chromatography) (54 %).^[30] The enantiopure products $L^{\text{Ph-TDA-(R)-Al}}$ and $L^{\text{Ph-TDA-(S)-Al}}$ were obtained via semi-preparative chiral column purification. The ligand $L^{\text{Ph-TDA-(Rac)-Al}}$ was fully characterised by multiple methods, including $^1\text{H-}$, $^{13}\text{C-}$, 2D-NMR and IR-spectroscopy, elemental analyses and mass spectrometry. The given synthesis procedure demonstrates the potential of two-step synthesis for an amino acid based tetradentate ligand with variations based on different modifications of the chosen amino acid.

Complexation reactions of the enantiopure Ligands $L^{\text{Ph-TDA-(R)-Al}}$ and $L^{\text{Ph-TDA-(S)-Al}}$ with $[\text{Fe}(\text{py})_4(\text{NCBH}_3)_2]$ in dry acetonitrile yielded the two enantiopure and the racemic complex, $[\text{Fe}(L^{\text{Ph-TDA-(X)-Al}})(\text{NCBH}_3)_2]$, where X = S (**C1**), R (**C2**), and racemic (**C3**). All targeted complexes were obtained in moderate yield and characterized by using a range of techniques such as IR-, CD (circular dichroism)- and UV-Vis-spectroscopy, elemental analysis and ESI-mass spectrometry.

The presence of the characteristic C-N triple bond stretching mode at 2177 cm^{-1} confirms the coordination of the NCBH_3 Co-Ligand. The formation of the desired complexes was supported by the observed shift in the C–N stretching vibrations of the 1,3,4-thiadiazole unit. Upon coordination, changes in electron density causes the characteristic bands to shift from 1587 cm^{-1} and 1567 cm^{-1} (free ligand) to 1602 cm^{-1} and 1574 cm^{-1} in all complexes (**Figure S8 – S10**). In the following we will discuss the bulk samples using the solvatomorph based on the elemental analysis with **C1** · 0.5 H_2O , **C2** · 0.5 H_2O and **C3** and in case of the structural environment and packing we will use the solvatomorph based on the single crystal XRD (**C1** · 1.5 MeCN and **C3** · 2 MeCN). X-ray single crystal measurement were performed for complex $[\text{Fe}(L^{\text{Ph-TDA-(S)-Al}})(\text{NCBH}_3)_2] \cdot 1.5\text{ MeCN}$ (**C1** · 1.5 MeCN) and $[\text{Fe}(L^{\text{Ph-TDA-(Rac)-Al}})(\text{NCBH}_3)_2] \cdot 2\text{ MeCN}$ (**C3** · 2 MeCN) to investigate the intermolecular interactions via packing and the

coordination environment around the iron(II). As we wanted to investigate the difference in packing and intermolecular interactions, we used the single crystal structure *XRD* analysis for the racemic complex **C3** · 2 MeCN and exemplary the enantiopure and *S*-enantiomeric complexes **C1** · 1.5 MeCN. For complex **C1** · 1.5 MeCN, single-crystal *X-ray* diffraction was performed at variable temperatures to examine the spin crossover behaviour as for **C3** · 2 MeCN the bond lengths at 120 K suggest already the locked high spin state.

The purity of the bulk samples used for *SQUID* measurements was confirmed by elemental analysis and mass spectrometry. Elemental analysis revealed the substitution of lattice solvent acetonitrile with water molecules upon solvent evaporation, resulting in monohydrated forms for the enantiopure complexes **C1** · 0.5 H₂O and **C2** · 0.5 H₂O. In contrast, no lattice solvent was detected by elemental analysis in the bulk sample of the racemic complex **C3**. The positive ESI-mass spectroscopy reveals the base peak as the complex fragment [Fe(L^{Ph-TDA-Al})(NCBH₃)⁺ (*m/z* = 483.12) for the enantiopure complexes, with the exception of **C3** · 0.5 H₂O which was synthesized based on ⁵⁷Fe enriched precursor (*m/z* = 484.12) (**Figure S13 – S18**). The isotopic pattern confirms the complex formation (**Figure S13 – S18**). Temperature-dependent magnetic data for all three complexes were collected by using *SQUID* magnetometry between 10 K and 300 K and the bulk sample was dried under a nitrogen atmosphere. *CD*-spectra in acetonitrile were used to confirm the stability of the complex's chirality and to assess the influence of chirality on the absorption bands.

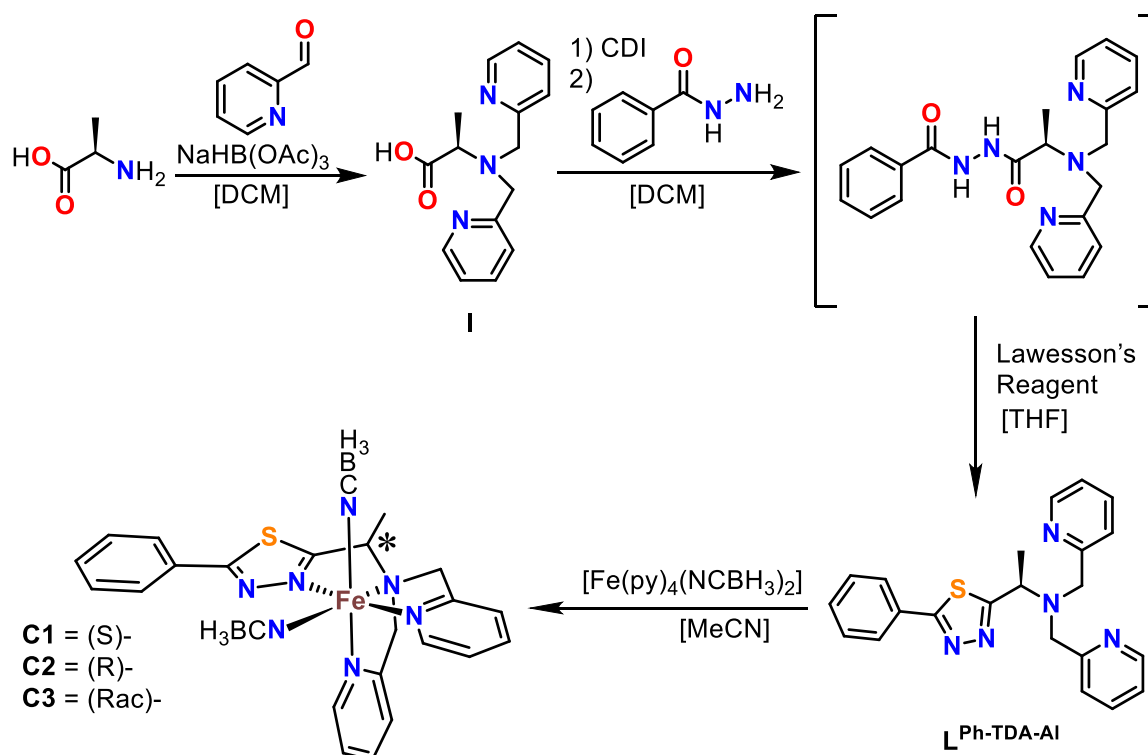


Figure 2: Synthesis of the ligand 1-(5-phenyl-1,3,4-thiadiazol-2-yl)-*N,N*-bis(pyridin-2-ylmethyl)ethan-1-amine (L^{Ph-TDA-Al}) and the complexes **C1** · 0.5 H₂O - **C3**.

Structural determination of complex C1 and C3

For complexes **C1** · 1.5 MeCN and **C3** · 2 MeCN single crystals suitable for single Crystal XRD measurement were obtained from acetonitrile. **C1** · 1.5 MeCN crystallizes as brown crystals in the chiral monoclinic space group C2, **C3** · 2 MeCN, as the racemic mixture of the ligand, is forming yellow greenish crystals of the triclinic centrosymmetric space group P-1. X-ray structural data for both complexes were collected at 120 K, and the key crystallographic parameters are summarized in **Tables S2** and **S3**, as we aimed for a comparison between the packing and intermolecular interactions between the enantiopure exemplary seen by **C1** · 1.5 MeCN and racemic mixture **C3** · 2 MeCN. In case of **C1** · 1.5 MeCN at 120 K the iron(II)-nitrogen bond lengths suggest the low spin state (**Table S8**) and to investigate the spin crossover we further measured the single crystal XRD at 220 K.^[26]

C1 · 1.5 MeCN contains four complex units along with six molecules of acetonitrile, whereas **C3** · 2 MeCN, the racemic mixture, consists of two complex units and four molecules of acetonitrile. The molecular structure of **C1** · 1.5 MeCN and **C3** · 2 MeCN is similar, with the only difference being the chiral carbon. In **C3** · 2 MeCN, the R- and S-enantiomers of the complex alternate.

In contrast to the recently published achiral $[\text{Fe}(\text{L}^{\text{Ph-TDA}})(\text{NCBH}_3)_2]$, which adopts a meridional coordination geometry, where the coordinating pyridine nitrogen-atoms N4 and N5 placed in trans position the given complex $[\text{Fe}(\text{L}^{\text{Ph-TDA-Al}})(\text{NCBH}_3)_2]$, is forming the facial coordination due to the cis position of the pyridine nitrogen-atoms N4 and N5, shown in **Figure 3**.

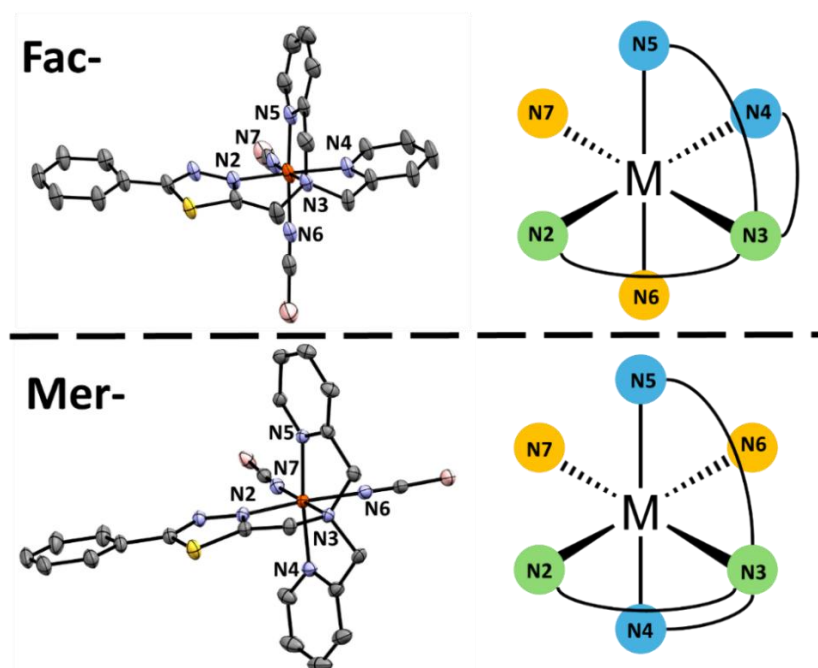


Figure 3: Visualization of the coordination mode difference between the the fac-shaped $[\text{Fe}(\text{L}^{\text{Ph-TDA-(S-Al)}})(\text{NCBH}_3)_2] \cdot 1.5 \text{ MeCN}$ (**C1** · 1.5 MeCN) (down) and mer-shaped $[\text{Fe}(\text{L}^{\text{Ph-TDA}})(\text{NCBH}_3)_2] \cdot 1.5 \text{ MeCN}$ (above) and at 120 K with the coordinating nitrogen-atoms colored in: **orange** NCBH_3 , **light blue** Pyridine-units, **green** bridging nitrogen and the N2 in the 1,3,4-thiadiazole unit.

This results from a bending of the bite pocket of the 1,3,4-thiadiazole ring involving the coordinating bridging nitrogen, caused by the steric and geometric influence of the methyl group at the carbon atom C3. Notably, the bite angle differs between the two complexes, though the variation in the octahedral distortion parameters $\Sigma_0(\text{FeN}_6)$ at 120 K - 49.65 for $[\text{Fe}(\text{L}^{\text{Ph-TDA}})(\text{NCBH}_3)_2] \cdot \text{H}_2\text{O}$ and 53.72 for $[\text{Fe}(\text{L}^{\text{Ph-TDA-(S-Al)}})(\text{NCBH}_3)_2] \cdot 1.5 \text{ MeCN}$ - is minor, indicating a similar geometric influence exerted by the isomer. The difference between these two coordination shapes and the reason for forming both based on an similar coordination environment was described by Collet and Kahn *et al.*^[31,32] Due to the substitution of an ethyl chain ((2-Aminoethyl)bis(2-pyridylmethyl)amine DPEA) to an propyl chain ((3-Aminopropyl)bis(2-pyridylmethyl)amine (DPPA)) the coordination sphere was switched from meridional to facial, underlining the influence of the substitution to the bite pocket.^[31] A similar observation was made in a series of tris(pyridin-2-ylmethyl)amine (tmpa) ligands, where substitution at the coordinating nitrogen with sterically demanding groups favoured the formation of the fac-isomer (3-tetramethyl-guanidine substitution) in contrast to mer -isomer (N,N-dimethyl substitution).^[33]

A slight colour change in the crystal of enantiopure $[\text{Fe}(\text{L}^{\text{Ph-TDA-(S-Al)}})(\text{NCBH}_3)_2] \cdot 1.5 \text{ MeCN}$ (**C1**) was observed by cooling down, indicating thermal driven spin crossover (SCO). To further investigate this, single-crystal X-ray diffraction (XRD) measurements were conducted at 220 K. Changes in bond lengths at different temperatures are frequently used in the literature to support varying populations of the anti-bonding e_g^* -orbitals, which are indicative of spin-state transitions.^[34] As shown in **Figure 4** the Fe-N bond lengths increase with temperature, supporting the occurrence of a spin crossover in the range of 120 K to 220 K.

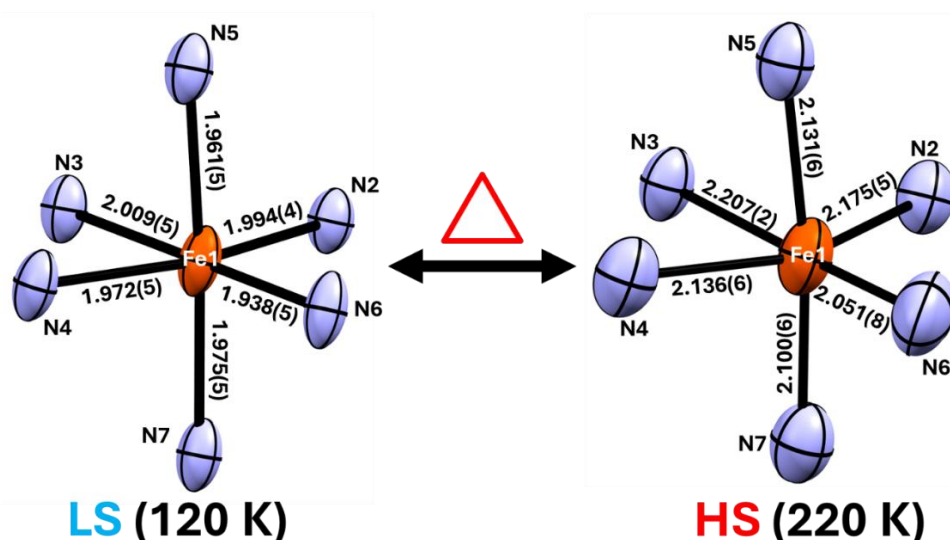


Figure 4: Fe-N bond length changing of the complex $[\text{Fe}(\text{L}^{\text{Ph-TDA-(S-Al)}})(\text{NCBH}_3)_2] \cdot 1.5 \text{ MeCN}$ (**C1**). by visualization of the first coordination environment around the Fe(II) at 120 K and 220 K temperature.

An average increase in Fe-N bond lengths of 0.159 Å (approximately 7%) is consistent with values reported in the literature, where the most significant change is observed for the bridging nitrogen-iron

bond (Fe1-N3), while the smallest changes occur for the NCBH_3 co-ligands (Fe1-N6 and Fe1-N7).^[34,35] This structural expansion affects the entire coordination environment, leading to an increase in unit cell volume of about 5% from 120 K to 220 K.^[35] Additionally, the distortion parameter defined by Hendrickson *et al.* serves as a useful tool for characterizing spin crossover transitions.^[36] For complex **C1** · 1.5 MeCN, the distortion parameter increases from 53.72° at 120 K to 88.49° at 220 K, supporting the occurrence of a spin transition within this temperature range. In contrast, complex **C3** · 2 MeCN exhibits a distortion parameter of 95.51° and an average Fe-N bond length of 2.181 \AA , indicative of a high-spin state at 120 K, which suggest that **C3** · 2 MeCN is locked in high spin.^[25]

Although each complex exhibits the same molecular structure, only the enantiopure complex **C1** · 1.5 MeCN displays spin crossover behaviour, suggesting that crystal packing plays a significant role in influencing the spin state. Since no hydrogen bonding interactions were observed in either crystal structure, π - π stacking appears to be the predominant intermolecular interaction contributing to the packing arrangement.^[37] Visualization of the packing along the cell axes *a*, *b* and *c* is given in the appendix (**Figure S19 - S33**).

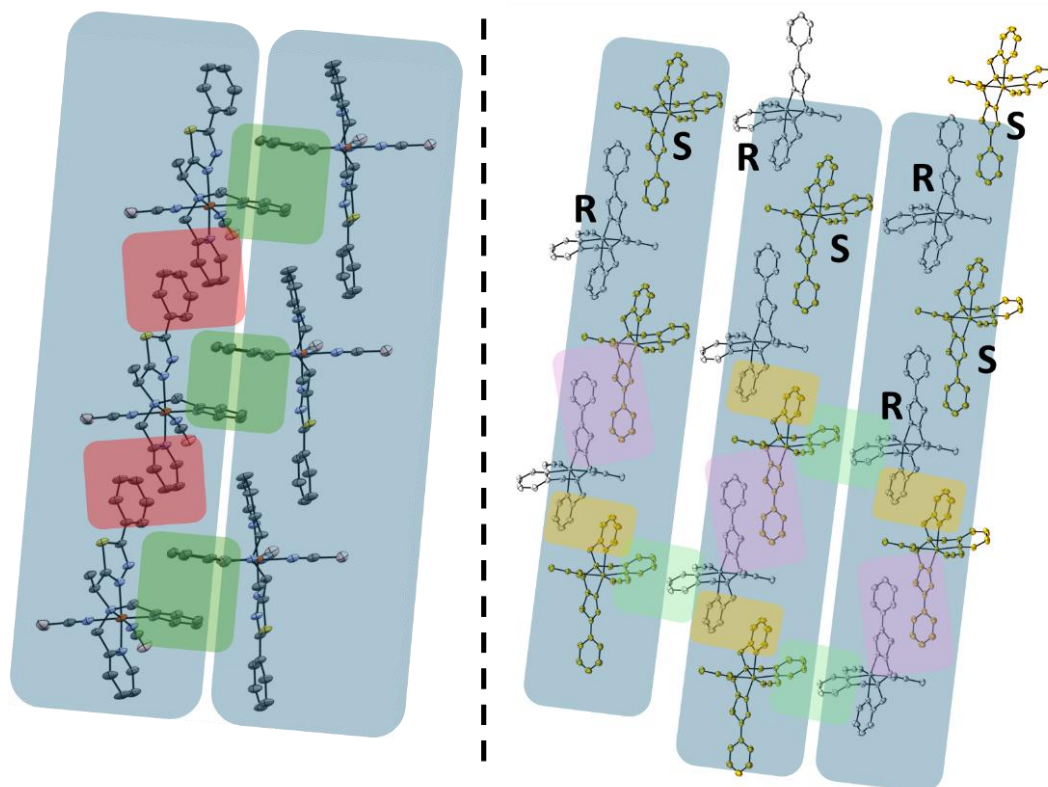


Figure 5: Visualization of the different π - π -interaction (red: phenyl-trans-pyridine; green: cis-pyridine; yellow: trans-pyridine; pink: phenyl-1,3,4-thiadiazole) inside the crystal structure of **C1** · 1.5 MeCN (left) and **C3** · 2 MeCN (right) leading to the formation of 1D double chains (left) and 2D layer network (right).

In the case of complex **C1** · 1.5 MeCN, π - π interactions between the trans-oriented pyridine units (positioned opposite to the 1,3,4-thiadiazole moiety) and the phenyl groups result in a stair-like chain along the *c*-axis. The key parameters - centroid - centroid distance (c-c distance), offset, and interplanar angle - were calculated using the same methodology we recently reported and are given in **Figure S24** and **S27** in the ESI. The measured offset and c-c distance support the presence of significant π - π interactions between these units.^[38] Two of these stair-like chains in complex **C1** · 1.5 MeCN associate to form a double chain via π - π interactions between the cis-oriented pyridine units. The small offset observed here indicates a strong overlap between the cis-pyridine rings (as shown in **Figure S24** and **S27**). Between these double chains, solvent-accessible channels extend along the *c*-axis - similar to those in complex **C3** · 2 MeCN, where the solvent channels are oriented along the *a*-axis. At 220 K, the centroid-centroid distances and offsets for the trans- and phenyl-based π - π interactions increase, while the offset for the cis-pyridine interactions remains comparatively low. This contrast suggests dynamic motion in the packing structure as a consequence of the spin crossover.^[39,40] In racemic complex **C3** · 2 MeCN, chains are formed through alternating R- and S-enantiomers, stabilized by π - π interactions between the phenyl and 1,3,4-thiadiazole moieties of adjacent complexes. Additional π - π stacking between trans-pyridine units occurs along the space diagonal and forming the chain (illustrated in **Figure S33** and **Table S1**). The values presented indicate moderate interactions between the aryl units.^[38]

The π - π -interactions of the cis-pyridine-units for **C3** · 2 MeCN located between the chains lead to an 2D-network (layer), which could be the reason for the strong packing, which results in the overall stabilization of the high spin state (**Figure 5**).^[37,41]

Temperature dependent magnetization:

The investigation of the temperature dependent magnetization was done by *SQUID* magnetometry in cooling mode 300 K to 10 K and heating mode 10 K to 300 K and are shown in **Figure 6** as $\chi_M T$ vs. T plot.

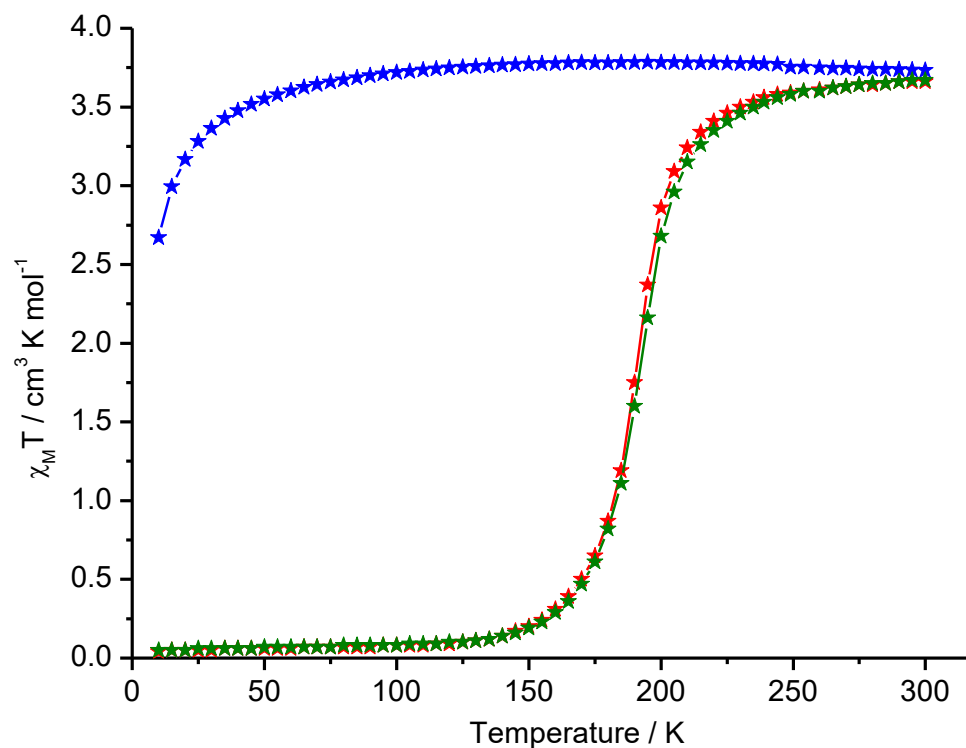


Figure 6: χ_M vs. T measured of microcrystalline product of $[\text{Fe}(\text{L}^{\text{Ph-TDA-(S)-Al}})(\text{NCBH}_3)_2] \cdot 0.5 \text{ H}_2\text{O}$ (**C1** · 0.5 H_2O) (green), $[\text{Fe}(\text{L}^{\text{Ph-TDA-(R)-Al}})(\text{NCBH}_3)_2] \cdot 0.5 \text{ H}_2\text{O}$ (**C2** · 0.5 H_2O) (red) and $[\text{Fe}(\text{L}^{\text{Ph-TDA-(Rac)-Al}})(\text{NCBH}_3)_2]$ (**C3**) (blue) in the form of the resulting $\chi_M T$ vs. T plot. Magnetic susceptibility was determined between 300 K - 10 K.

At higher temperatures the complexes **C1** · 0.5 H_2O and **C2** · 0.5 H_2O converge to a value of 3.66 $\text{cm}^3 \cdot \text{mol}^{-1} \cdot \text{K}$ for the product of $\chi_M T$ which is attributed to an $^5\text{T}_{2g}$ with an estimated g value of 2 reported by the literature.^[34,35,42] Upon cooling at a rate of 10 $\text{K} \cdot \text{min}^{-1}$, an abrupt spin crossover is observed, as indicated by a sharp drop in $\chi_M T$ to 0.05 $\text{cm}^3 \cdot \text{mol}^{-1} \cdot \text{K}$. This value is consistent with the low-spin $^1\text{A}_{1g}$ state and is further supported by the shortened Fe-N bond lengths observed in the crystal structure at 120 K.^[34,35,42] The T_C was determined by the first derivate of $\chi_M T$ in respect to T and yields to $T^{\uparrow}_C = T^{\downarrow}_C = 195 \text{ K}$ (**Figure S40 - S42**). Given the well-documented influence of solvent molecules on crystal packing, the sample of the S-enantiomer complex **C1** · 0.5 H_2O was remeasured after maintaining it at 300 K for 30 minutes, using the same measurement routine as previously applied. (**Figure S37 and S41**).^[43,44]

The observed decrease in the saturation value of $\chi_M T$ to 3.55 $\text{cm}^3 \cdot \text{mol}^{-1} \cdot \text{K}$ is attributed to a change in the molar mass, while no shift in the transition temperature ($T^{\uparrow}_C = T^{\downarrow}_C = 195 \text{ K}$) or loss of abruptness in the spin crossover was detected. Combined with the absence of hydrogen bonding interactions - both within the crystal packing and between the solvent channels and the double chains - these

findings suggest that the abrupt nature of the transition is primarily driven by the π - π stacking interactions between aryl groups linking units inside and between chains. As discussed above in case of **C3** the packing results in a stronger 3d-network due to the higher – in contrast to **C1** · 0.5 H₂O - connected chains, which results to a plateau of $\chi_{MT} = 3.78 \text{ cm}^3 \cdot \text{mol}^{-1} \cdot \text{K}$ attributed to the $^5T_{2g}$ high spin state and decreasing χ_{MT} from 50 K to an maxima with $3.67 \text{ cm}^3 \cdot \text{mol}^{-1} \cdot \text{K}$ at 10 K which is assigned to zero field splitting.^[34,35,42]

In comparison to the recently published $[\text{Fe}(\text{L}^{\text{Ph-TDA}})(\text{NCBH}_3)_2] \cdot \text{H}_2\text{O}$ the substitution and the resulting mer-fac-isomerisation lead to an increase to a higher T_c of 42 K. The observed minimal change of the bite angle (**Figure S34**) suggest that the T_c difference is primarily explained by packing effects, particularly the π - π interactions between the aryl units.

The lower degree of intermolecular connectivity in **C1** · 0.5 H₂O, which forms 1D double chains with reduced symmetry, compared to the more extensively interlinked 2D network observed in **C3**, is proposed to be the primary reason for the abrupt spin crossover in **C1** · 0.5 H₂O. In contrast, the racemic mixture in **C3** stays in high spin, emphasizing the significant role of crystal packing and polymorphism, despite the identical molecular structure. The influence of different packing motifs between enantiopure and racemic forms on the critical temperature of spin crossover complexes is well documented in the literature:

Similar investigations had been done by Ma et al. on the tetradentate ligand N¹,N²-bis(pyridin-2-ylmethyl)cyclohexane-1,2-diamine) with iron(II) as coordination center and two selenocyanate as co ligands.^[45] The π - π -, H- π - and Se- π -interactions lead to the formation of the packing which results in the overall high spin in case of the racemic complex. The enantiopure complexes were found to exhibit an abrupt spin crossover at $T_c = 146 \text{ K}$ highlighting the significant influence of chirality on the spin crossover behaviour. Further Zhang et al. observed results in agreement for an N₆ coordinated cobalt(II) complex with (1E,1'E)-1,1'-(pyridine-2,6-diyl)bis(N-((R/S)-1-(naphthalen-1-yl)ethyl)methanimine) as tridentate ligand, where mainly the naphthyl groups are responsible for the interactions between the complexes.^[15]

Mössbauer spectroscopy

In addition to the *SQUID* experiments, *Mössbauer* experiments were performed on compound **C1** · 0.5 H₂O to characterize the *SCO* behavior. The results are shown in **Figure 7** and **Table 1**. The *Mössbauer* spectrum at 240 K was analyzed using two components. Component 1 displays an isomer shift $\delta = 0.44 \text{ mm} \cdot \text{s}^{-1}$ and a quadrupole splitting $\Delta E_Q = 0.31 \text{ mm} \cdot \text{s}^{-1}$ with a relative contribution of 22%. Such low values for isomer shift and quadrupole splitting are characteristic of a low-spin iron(II) embedded in an octahedral field.^[20] On the other hand, component 2 shows $\delta = 1.00 \text{ mm} \cdot \text{s}^{-1}$ and $\Delta E_Q = 1.42 \text{ mm} \cdot \text{s}^{-1}$

which a relative contribution of 78%. These parameters are typical for high-spin iron(II).^[20] Therefore, the compound **C1** · 0.5 H₂O is in a mixed spin state at 240 K. Upon cooling the sample to 200 K, the relative contributions change to 60% for component 1 and 40% for component 2 revealing a spin transition from high-spin state to low-spin state. The increase of the values for the quadrupole splitting and isomer shift can be attributed to the second order Doppler shift. In contrast, the *Mössbauer* spectrum at 77 K reveals one component with $\delta = 0.46 \text{ mm}\cdot\text{s}^{-1}$ and $\Delta E_Q = 0.35 \text{ mm}\cdot\text{s}^{-1}$. Thus, the experiment identifies a complete LS state at 77 K. Overall, the results of *Mössbauer* spectroscopy are in good agreement with the results obtained from the *SQUID* experiments.

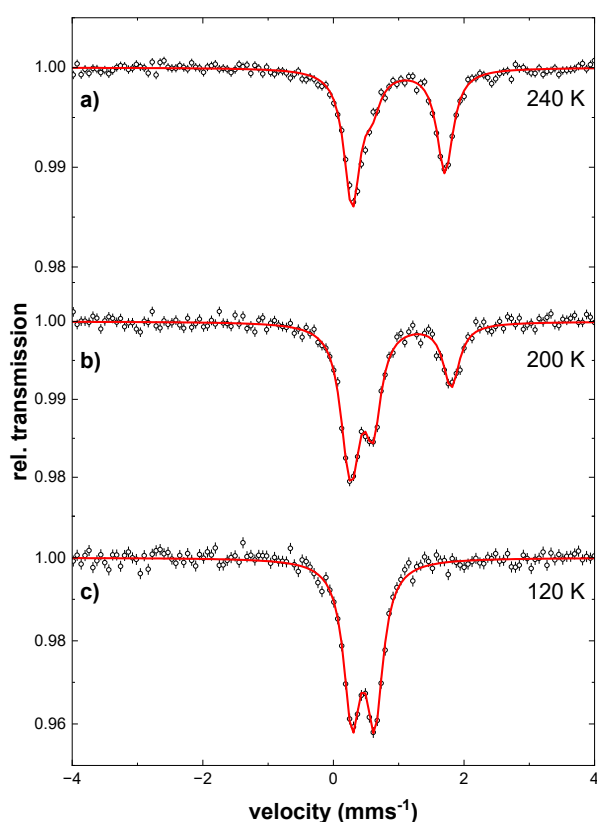


Figure 7: Mössbauer spectra of compound **C1** · 0.5 H₂O recorded at a) 240 K, b) 200 K and c) 120 K. The open circles show the experimental data obtained at the respective temperatures and the red solid lines represent simulations based on Lorentzian line shapes. The parameters of the simulations are listed in **Table 1**.

Table 1: Mössbauer parameters of the complex $\mathbf{C1} \cdot 0.5 \text{ H}_2\text{O}$ as obtained from the analysis of the experimental data displayed in **Figure 7**. The line width Γ is $0.30(2) \text{ mm}\cdot\text{s}^{-1}$ for all components.

T [K]	component 1			component 2		
	δ [$\text{mm}\cdot\text{s}^{-1}$]	ΔE_Q [$\text{mm}\cdot\text{s}^{-1}$]	Area [%]	δ [$\text{mm}\cdot\text{s}^{-1}$]	ΔE_Q [$\text{mm}\cdot\text{s}^{-1}$]	Area [%]
120	0.46(3)	0.35(2)	100	-	-	-
200	0.45(3)	0.32(2)	60(3)	1.00(3)	1.60(3)	40(3)
240	0.44(3)	0.31(2)	22(3)	1.00(3)	1.42(3)	78(3)

CD- and UV-Vis spectra

To confirm the enantiopure character of the complexes $\mathbf{C1} \cdot 0.5 \text{ H}_2\text{O}$ and $\mathbf{C2} \cdot 0.5 \text{ H}_2\text{O}$ circular dichroism (CD)-spectra were recorded in acetonitrile across a concentration range, covering the wavelength region from 200 to 500 nm. The composed CD-spectra of $\mathbf{C1} \cdot 0.5 \text{ H}_2\text{O}$ (blue) and $\mathbf{C2} \cdot 0.5 \text{ H}_2\text{O}$ (red) are shown in **Figure 8** combined with the absorption spectra plotted as molar extinction coefficient. This combined representation allows for a detailed investigation of the electronic transitions and band structure associated with the chiral complexes in solution.

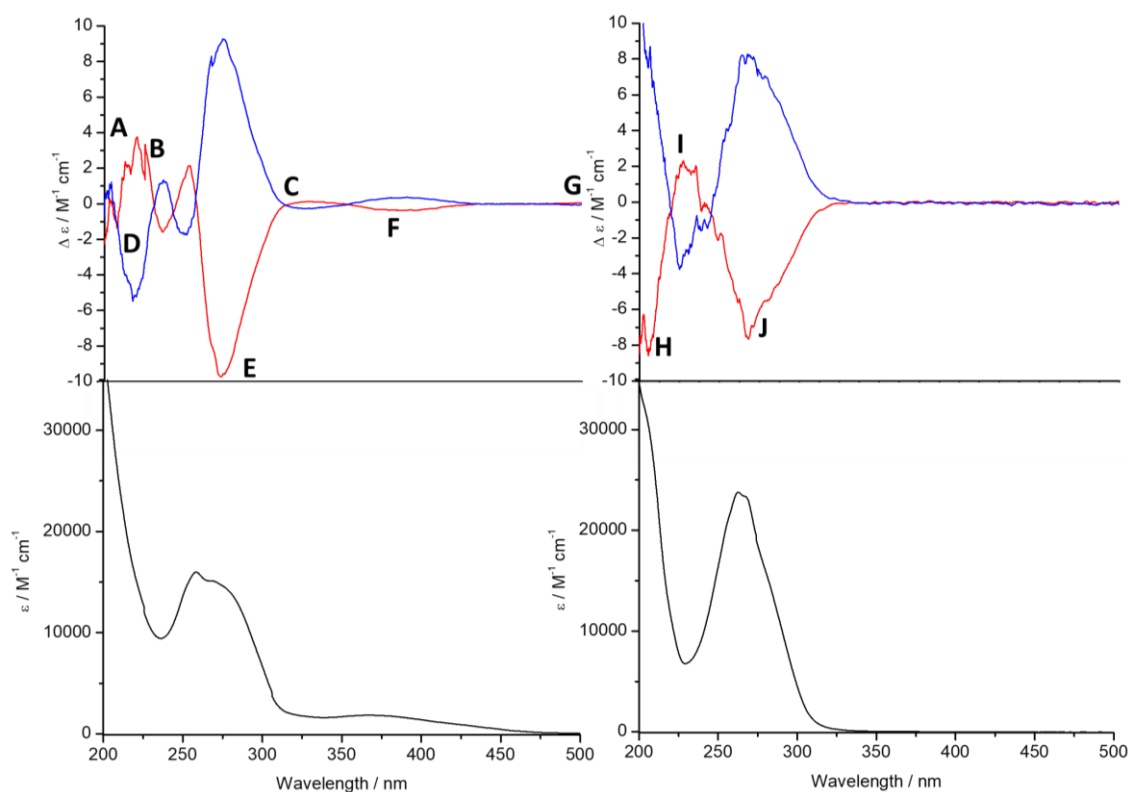


Figure 8: CD-spectra of left: $[\text{Fe}(\text{L}^{\text{Ph-TDA-(S)-Al}})(\text{NCBH}_3)_2] \cdot 0.5 \text{ H}_2\text{O}$ ($\mathbf{C1} \cdot 0.5 \text{ H}_2\text{O}$) (blue), $[\text{Fe}(\text{L}^{\text{Ph-TDA-(R)-Al}})(\text{NCBH}_3)_2] \cdot 0.5 \text{ H}_2\text{O}$ ($\mathbf{C2} \cdot 0.5 \text{ H}_2\text{O}$) (red) and UV-Vis absorption spectra $[\text{Fe}(\text{L}^{\text{Ph-TDA-(S)-Al}})(\text{NCBH}_3)_2] \cdot 0.5 \text{ H}_2\text{O}$ ($\mathbf{C1} \cdot 0.5 \text{ H}_2\text{O}$) (black) between 200 nm and 500 nm; right: $\text{L}^{\text{Ph-TDA-(S)-Al}}$ (blue), $\text{L}^{\text{Ph-TDA-(R)-Al}}$ (red) and UV-Vis absorption spectra $\text{L}^{\text{Ph-TDA-(S)-Al}}$ (black) between 200 nm and 500 nm.

For **C1** · 0.5 H₂O a positive cotton effect could be observed for 209 nm – 230 nm (**A**), 245 nm – 257 nm (**B**) and 314 nm – 348 nm (**C**) and a negative cotton effect between 230 nm – 242 nm (**D**), 257 nm- 314 nm (**E**) and 355 nm – 430 nm (**F**). The artifacts for the transition for 209 nm – 230 nm (**A**) can be attributed to solvent effects. From 470 nm starting a negative cotton effect could be observed with 0.06 meg at 500 nm suggesting a transition (**G**). Unfortunately, due to the lamp further measurement could not be done. **C2** · 0.5 H₂O as the other enantiomer shows a mirrored identical *CD*-spectra, which proves by the symmetry of the spectra that both complexes are enantiopure. The dip for **C2** · 0.5 H₂O at 267 nm is explained by concentration issues of the measured solution.

The transitions between 209 nm and 314 nm can be assigned to ligand based π - π^* -transitions by comparing with the absorption spectra of the ligands. For the ligand three absorption bands were observed (**Figure 8**). A negative cotton effect is shown for the absorption between 200 nm to 220 nm (**H**) and 245 nm to 320 nm (**J**), whereas a positive cotton effect is observed for the transition from 220 nm to 245 nm (**I**). The transition between 355 nm and 430 nm (**F**) can be attributed to an *MLCT* from the iron(II) to the NCBH₃ seen by similar complex with other NCE complexes and similar iron(II) high spin complexes.^[46,47]

Packing analysis of both Polymorphs by Nuclear vibrational spectroscopy

The powdered sample of **C2** · 0.5 H₂O was inserted in a He-bath cryostat and measured before and after laser irradiation. The starting temperature was set at the variable temperature insert to 10 K which is reflected by the temperature obtained by the calculated temperature of the *pDOS* of 14.2 ± 0.3 K. The temperature was determined by comparing the Stokes and anti-Stokes bands of the vibrations close to the resonance of the nuclear inelastic scattering spectra.^[48] With a 150 mW and 532 nm continuous laser the sample was irradiated for 30 minutes. The resulting intensity at the sample was 15 ± 5 mW due to loss of intensity inside the used fiber optics. All measurements taken after the laser irradiation were with no additional laser irradiation. After the irradiation the *pDOS* showed a calculated temperature of 12.8 ± 0.3 K for the sample. By increasing the temperature at the deviation between the set temperature and the calculated temperature decreases as shown in **Table 2**.

Table 2: Temperature comparison of the experimental set temperature and the calculated temperature of the Stokes and anti-Stokes pairs in the nuclear inelastic spectra.

Set Temperature	10 K	10 K after irradiation	20 K	40 K	60 K
Calculated Temperature	14.2 ± 0.3 K	12.8 ± 0.3 K	22.4 ± 0.5 K	42.1 ± 0.3 K	60.7 ± 0.7 K

It can be noted that a transition took place since the intensity of the vibrational bands at 10 K dropped by 81% (shown in **Table 3**) while bands were generated at the region between 130 - 310 cm^{-1} after the irradiation with the laser as shown in **Figure 9**. Some *LS* modes are still present in the vibrational spectrum which show an incomplete transition of states as presented in **Table 3**.^[49] With the comparison of the calculated *LS* state data and the experimental data at 10 K without laser irradiation are congruent if the calculated data would be shifted by 9.5 cm^{-1} to lower energies. The most dominant modes in the *LS* area from 320 to 500 cm^{-1} are at 329, 353, 371, 382, 430 and 441 cm^{-1} . The *HS* calculation has already the most overlap with the experimental data clearly visible at the band at 292 cm^{-1} . The other vibrations have a broader structure in the vibrational spectrum. Which is a result of the fewer taken scans, but the bands are comparable with the calculated data of the high-spin state. The methods to calculate the vibrational spectra are described in the following chapter.

Before laser illumination the sample is mostly in the *LS* state as indicated by the vibrational modes located in the region of 320 - 560 cm^{-1} .^[49] Some residue *HS* state was trapped and is still present due to the fast cooling of the sample. With the irradiation of the laser the sample switches dominantly into the *HS* state due to the *LIESST* effect.^[50] As the temperature rises the decay of the *LIESST* effect is visible as shown in **Figure 11**. With continuous heating the *HS* state decays and the relative contribution of the *LS* state increases until the spectra of 10 K without laser irradiation and at 60 K are comparably the same.

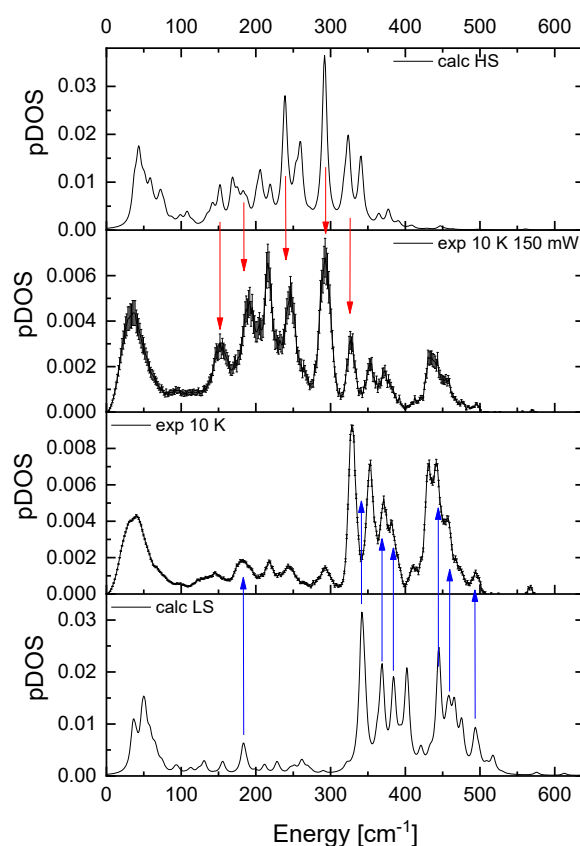


Figure 9: Comparison of the experimental data and the calculation of the spin states. The arrows indicate the positions of the most dominant regions of the calculated spectra displayed in the experimental data.

Table 3: The relative contribution of the calculated spin state spectra in the experimental data in **Figure 9** obtained by fitting the experimental data with the calculated data.

Spin-state contribution	10 K	10 K after laser	20 K after laser	40 K after laser	60 K after laser
HS	19%	85%	73%	46%	15%
LS	81%	15%	27%	54%	85%

At 10 K the lamb *Mössbauer* factor, the heat capacity and the vibrational entropy are unaffected by the irradiation with the 150 mW laser the force constant and the internal energy show a significant decrease respectively $2.42 \text{ N}\cdot\text{m}^{-1} / \text{a.u.}$ and 12.15 meV as shown in **Figure 10**. Due to the temperature dependency of the lamb *Mössbauer* factor the parameter decreases with an increase in temperature.^[51] This behavior is contrary to the parameters of the vibrational entropy, heat capacity, force constant and internal energy in the system increase with a higher temperature. The thermodynamic parameters were calculated according to reference.^[48]

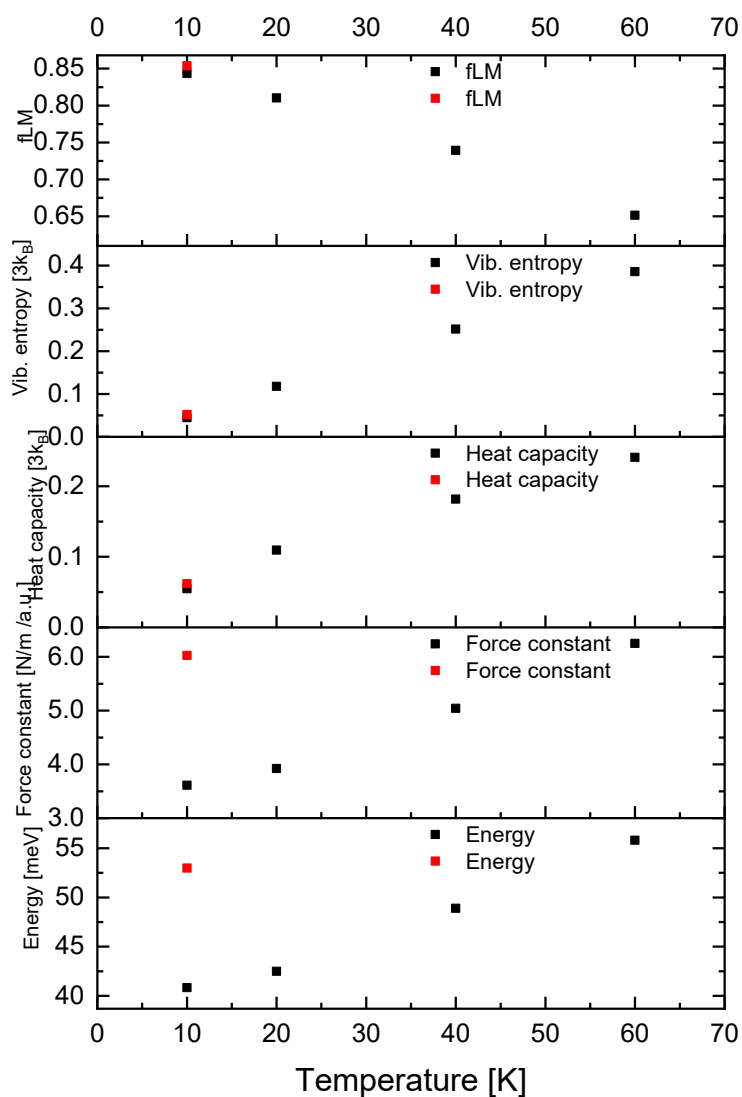


Figure 10: Thermodynamic parameters of the ρDOS at given temperature the red point is the sample without laser irradiation of 150 mW at 520 nm right polarized light. After irradiation of 30 min the laser was turned off and the temperature was increased without additional irradiation. The measurement without laser is marked red.

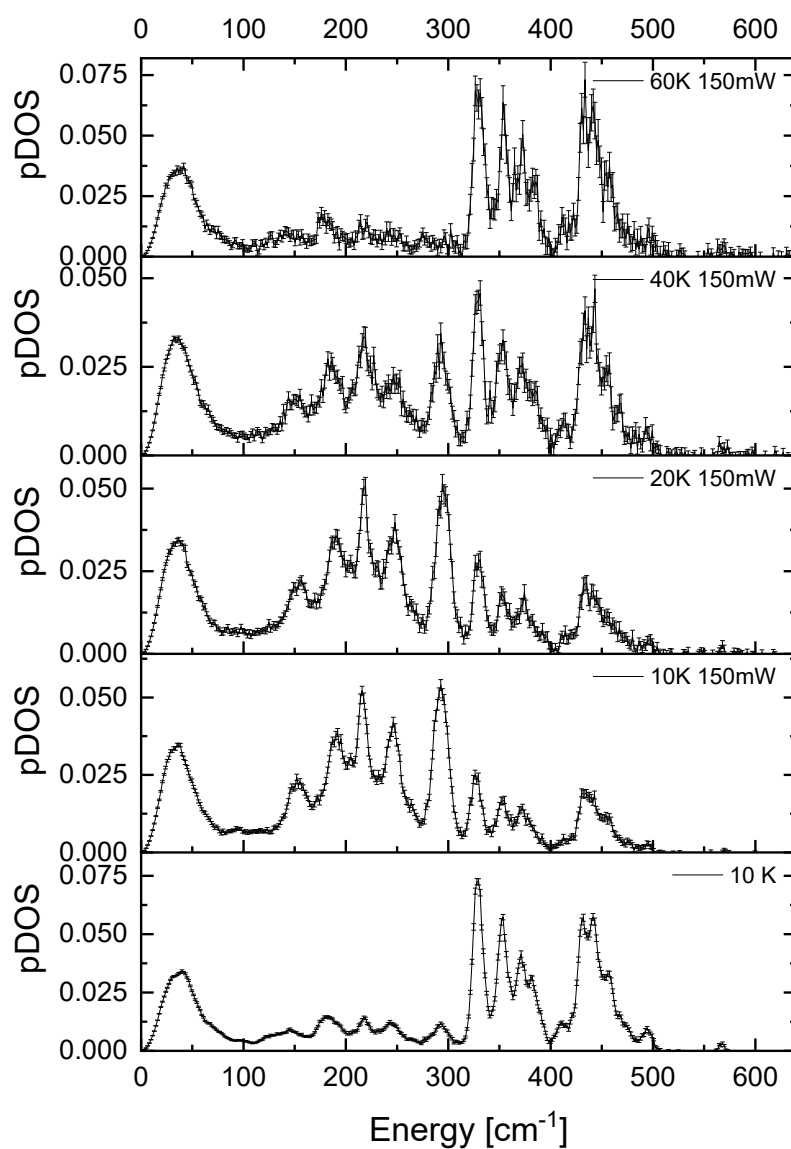


Figure 11: Stacked plot of the powdered sample $C2 \cdot 0.5 H_2O$ *pDOS* before and after the illumination with the laser of 150 mW. After irradiation of 30 min the laser was turned off and the temperature was increased without additional irradiation. The decay of the *LIESST* effect is visible. Due to the irradiation high spin modes are exited and with increasing temperature the intensity of these bands decreases.

Conclusions:

These studies underline the reported significance of structure-property relationship of ligand based chiral spin crossover coordination molecules.^[15,45,47,52–56] In essence, we synthesized an amino acid based chiral ligand in a novel synthesis approach using chiral semi-preparative *HPLC* for enantiomer separation. Three iron(II) complexes of both enantiomers and the racemic mixture with NCBH_3 as co ligand were characterized through a range of analytic methods. The enantiopure complexes **C1** · 0.5 H_2O and **C2** · 0.5 H_2O occurring in chiral space group C2 exhibit a sharp transition at $T_c = 195$ K.

In contrast, the racemic complex **C3** crystallizes in the achiral space group P-1 and remains in the high-spin state across the entire measured temperature range. These findings highlight the pronounced effect of intermolecular interactions and crystal packing - arising from polymorphism - despite the molecular structures being identical across all complexes. Combined with single crystal structure, *SQUID* Magnetometry and *Mössbauer* spectroscopy the major contribution of the π - π -interactions between the aryl-groups could be determined for the enantiopure complexes. The stabilization of the high spin state of the racemic mixture is attributed to the higher amount of linking π - π -interactions. Further insights into the intermolecular interaction were found by performing *NIS* spectroscopy and the *pDOS*. *DFT* models could give an opportunity to give more insights into the impact of intermolecular interactions. The influence of the optical activity in these design complexes on light induced spin crossover with polarized light (so called *CD-LIESST*) will be part of further investigations.

Experimental:

All chemicals were purchased from Deutero, Fisher Chemicals, TCI, Sigma-Aldrich, BLD Pharma and Carbolution used without further purification. Chiral *HPLC* were performed on the racemic mixture to separate both enantiomers. To separate the enantiomers in preparative scale following system was used: Knauer WellChrom Preparative Pump K-1800 connected to the *HPLC* column, a Knauer Variable Wavelength Monitor at $\lambda = 254$ nm and a differential Refraktometer with Nucleosil (50 Å to 5 μ ; size: 32 nm x 250 nm) and 20 % EtOH/n-Hexan and 20 mL/min and 50 mbar. Analytics were performed by Knauer Pump 64 connected to the *HPLC* column, a Knauer Variable Wavelength Monitor at $\lambda = 254$ nm and a differential Refraktometer with Nucleosil (50 Å to 5 μ ; size: 4.6 nm x 250 nm) and 20 % EtOH/n-Hexan and 2 mL/min and 35 mbar. NMR spectra were recorded at room temperature with a Bruker Avance DSX 400 and analyzed with the program MestReNova.^[57] Magnetic susceptibility measurements were performed on a Quantum Design *SQUID* magnetometer MPMS XL-7 *SQUID* in a temperature range between 5 and 300 K with an applied field of 1 kOe. All mass spectra (Advion expression-L CMS) as well as elemental analysis (Elementar vario EL Cube: C, H, and N) were measured at the microanalytical laboratories of the Johannes Gutenberg University Mainz. CD spectroscopy was performed on a J-815 spectrometer (JASCO, Easton, MD). Samples were baseline corrected and

measured using 1000 QS (HELLMA) quartz glass cuvettes with a path length of 1 mm or 10 mm at varying temperatures, controlled by a PTC-423S/15 Peltier element at 20°C. Each measurement was repeated twice to minimize errors. X-ray diffraction data were collected with STOE STADIVARI at the Johannes Gutenberg University Mainz. The structures were solved with ShelXT^[58] and refined with ShelXL^[59,60] implemented in the program Olex2.^[61]

The Mössbauer experiments were performed at RPTU Kaiserslautern with a 512-channel analyzer in time-scale mode and transmission geometry (WissEl GmbH, Starnberg, Germany). A continuous flow cryostat (Optistat^{DN}, Oxford Instruments, Abingdon, UK) was utilized to perform variable temperature measurements. The nuclear source consisted of ⁵⁷Co diffused in Rh with an activity of 1.67 GBq and the calibration of the spectrometer was carried out against α -iron at room temperature. The analysis of the spectral data was completed employing the public domain program Vinda running on Excel 2003[®] platform using least-squares fits and Lorentzian line shapes.^[62]

At the beamline P01 at the synchrotron “Deutsche Elektronen Synchrotron” DESY the nuclear inelastic scattering experiments were performed. The operation mode had a bunch spacing of 192 ns. Two sets of monochromators were used to tune the energy of the beam to the nuclear resonance energy of ⁵⁷Fe first excited state. The used He-bath cryostat SVT-400 SPECIAL CRYOSTAT was manufactured by Janis Reseach Company. A distance of 8 mm was achieved between the sample and the avalanche photo diode. The intensity of the irradiation at the sample from the laser was 15 ± 5 mW. The measured energy range started at -20 and finished at 80 meV with the transition energy set as 0 meV. The time spent per point was 7 seconds and an energy step size of 0.2 meV. When multiple scans of the same conditions were taken the spectra were summed for a better statistical result. The measurement at 10 K without laser irradiation was performed 8 times, at the 10 K measurement after laser irradiation was performed twice. The other results shown were singular measurements. The resulting spectra were converted into partial density of state (*pDOS*) spectra for comparison with density functional theory calculated vibrational spectra. The laser used for the irradiation was the model RLTMGL-532 1-450 mW from Roithner Lasertechnik GmbH.

Ligand Synthesis:

The Ligand was synthesised based on the same procedure as we described in our recent work, whether we started the synthesis by using D-Alanine.

Bis(pyridin-2-ylmethyl)-D-alanine (I)

D-Alanine (3.00 g, 33.67 mmol, 1.0 eq.) was suspended in 80 mL dichloromethane under nitrogen atmosphere. 2-Pyridinecarbaldehyde (6.75 mL, 70.96 mmol, 2.1 eq.) was added to the white solid containing suspension, resulting in a brown suspension. After 30 minutes under cooling with ice sodium triacetoxyborohydride (17.84 g, 84.18 mmol, 2.5 eq.) was added and stirred. The cooling was replaced and the yellowish suspension was allowed to warm up overnight. 70 ml saturated sodium bicarbonate solution was added and after 30 minutes the two phases were extracted and the aqueous phase was extracted twice with 150 mL dichloromethane. The organic phase was dried over sodium sulphate and the solvent was removed under reduced pressure. The crude product was purified via column chromatography (dichloromethane: methanol; 90:10). The product was isolated as brown oil (4.962 g, 18.29 mmol, 54 %). ^1H NMR (400 MHz, Chloroform-*d* δ (ppm)): 8.53 (ddd, $J = 5.0, 1.8, 0.9$ Hz, 2H), 7.63 (td, $J = 7.7, 1.8$ Hz, 2H), 7.29 (dd, $J = 7.5, 1.2$ Hz, 3H), 7.19 (ddd, $J = 7.6, 5.0, 1.2$ Hz, 2H), 4.00 (d, $J = 2.6$ Hz, 4H), 3.68 (q, $J = 7.1$ Hz, 1H), 1.44 (d, $J = 7.1$ Hz, 3H).

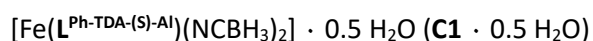
1-(5-phenyl-1,3,4-thiadiazol-2-yl)-N,N-bis(pyridin-2-ylmethyl)ethan-1-amine ($\text{L}^{\text{Ph-TDA-(Rac)-Al}}$)

Bis(pyridin-2-ylmethyl)-D-alanine (I) (4.500 g, 16.59 mmol, 1 eq.) was solved in 80 mL dichloromethane under nitrogen atmosphere and ice cooling. Carbonyldiimidazole (2.958 g, 18.24 mmol, 1.1 eq.) was added to the solution and stirred for 1h. Afterwards benzohydrazide (2.484 g, 18.24 mmol, 1.1 eq.) was added and the suspension was stirred overnight. The solvent was removed under reduced pressure and the residue was solved in 100 ml dry tetrahydrofuran under nitrogen atmosphere. Lawesson's reagent (8.050 g, 19.90 mmol, 1.2 eq) was added and the yellow solution was stirred under reflux overnight. The solvent was removed under reduced pressure. The residue was mixed with 300 mL dichloromethane and 75 mL saturated bicarbonate solution and extracted. The organic phase was twice washed with 75 mL saturated bicarbonate solution, dried over sodium sulphate and the solvent was removed under reduced pressure. The crude product was purified via column chromatography (dichloromethane: methanol; 95:5). The product was isolated as brown powder (3.458 g, 8.924 mmol, 54 %). The enantiomers were separated via HPLC (Nucleosil 50-5, EtOH/hexane 20:80, 20 mL/min, 50 bar) to afford $\text{L}^{\text{Ph-TDA-(S)-Al}}$ (446 mg, 1.203 mmol) and $\text{L}^{\text{Ph-TDA-(R)-Al}}$ (264 mg, 0.6813 mmol) as enantiopure products. ^1H NMR (400 MHz, Chloroform-*d* δ (ppm)): 8.55 (ddd, $J = 4.9, 1.8, 0.9$ Hz, 2H), 8.01 – 7.92 (m, 2H), 7.71 (td, $J = 7.6, 1.8$ Hz, 2H), 7.64 (dt, $J = 8.0, 1.1$ Hz, 2H), 7.58 – 7.42 (m, 3H), 7.22 – 7.10 (m, 2H), 4.41 (q, $J = 6.7$ Hz, 1H), 4.13 – 3.89 (m, 4H), 1.75 (d, $J = 6.7$ Hz, 3H). ^{13}C NMR (101 MHz, Chloroform-*d*

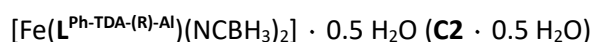
δ (ppm): 159.14, 149.17, 136.75, 130.95, 130.40, 129.08, 127.91, 122.59, 122.30, 56.26, 55.78, 12.64.
 FT-IR: $\tilde{\nu}$ (cm^{-1}) = 2978, 1587, 1567, 1472, 1455, 1427, 1380, 1364, 1302, 1238, 1143, 1044, 978, 944, 848, 760, 719, 687, 654, 628, 611, 573, 531, 499, 403. ESI-MS (m/z): calc. for $[\text{C}_{22}\text{H}_{22}\text{N}_5\text{S}_1]^+$ expected: 387.16 (100.00 %); found: 387.16 (100.00 %); Elemental Analysis calculated for $\text{L}^{\text{Ph-TDA-Al}} \text{H}_2\text{O} \cdot 0.7 \text{CH}_3\text{OH}$ ($\text{C}_{23.7}\text{H}_{25.8}\text{N}_5\text{O}_{1.7}\text{S}$): C, 63.54, H, 4.90, N, 16.45. found: C, 63.71, H, 4.08, N, 16.36.

Complex Synthesis:

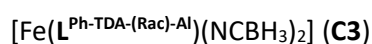
The Precursor complex $[\text{Fe}(\text{py})_4(\text{NCBH}_3)_2]$ was synthesised accordingly to literature known procedure.^[26]



The following reaction was carried out in a glovebox under an inert atmosphere. $[\text{Fe}(\text{py})_4(\text{NCBH}_3)_2]$ (107.0 mg, 0.2336 mmol, 1 eq.) was suspended in 8 mL dry acetonitrile and stirred for 30 minutes. The suspension was added to a solution of $\text{L}^{\text{Ph-TDA-(S)-Al}}$ (87.25 mg, 0.2336 mmol, 1 eq.) in 1 mL of acetonitrile and the resulting mixture was stirred for 1 h and the solution was filtered. The product was obtained in moderate yields as brown microcrystalline material. Crystals suitable for X-ray diffraction were achieved after four days of slow evaporation (47 mg, 0.236 mmol, 38 %). FT-IR: $\tilde{\nu}$ (cm^{-1}) = 2985, 2333, 2177, 1602, 1574, 1481, 1460, 1443, 1430, 1393, 1340, 1284, 1250, 1155, 1113, 1067, 1055, 1038, 1016, 1001, 926, 899, 873, 841, 813, 763, 731, 686, 670, 636, 581, 552, 507, 492, 405; ESI-MS (m/z): calc. for $[\text{C}_{23}\text{H}_{24}\text{BFeN}_6\text{S}]^+$ expected: 483.12 (100.00 %); found: 483.12 (100.00 %); Elemental Analysis calculated for $[\text{Fe}(\text{L}^{\text{Ph-TDA-(S)-Al}})(\text{NCBH}_3)_2] \cdot 0.5 \cdot \text{H}_2\text{O}$ ($\text{C}_{24}\text{H}_{28}\text{B}_2\text{FeN}_7\text{O}_{0.5}\text{S}$): C, 54.18, H, 5.30, N, 18.43. found: C, 53.64, H, 5.07, N, 18.65.



Same procedure for as **C1** with the R-enantiomer of the ligand $\text{L}^{\text{Ph-TDA-(R)-Al}}$ was used to prepare Complex **C2**. Brown microcrystalline material (71 mg, 0.1357 mmol, 58 %). FT-IR: $\tilde{\nu}$ (cm^{-1}) = 2985, 2333, 2177, 1602, 1574, 1481, 1460, 1443, 1430, 1393, 1340, 1284, 1250, 1155, 1113, 1067, 1055, 1038, 1016, 1001, 926, 899, 873, 841, 813, 763, 731, 686, 670, 636, 581, 552, 507, 492, 405; ESI-MS (m/z): calc. for $[\text{C}_{23}\text{H}_{24}\text{BFeN}_6\text{S}]^+$ expected: 483.12 (100.00 %); found: 483.12 (100.00 %); Elemental Analysis calculated for $[\text{Fe}(\text{L}^{\text{Ph-TDA-(R)-Al}})(\text{NCBH}_3)_2] \cdot 0.5 \cdot \text{H}_2\text{O}$ ($\text{C}_{24}\text{H}_{28}\text{B}_2\text{FeN}_7\text{O}_{0.5}\text{S}$): C, 54.18, H, 5.30, N, 18.43. found: C, 53.76, H, 5.17, N, 18.94.



Same procedure as for **C1** with the 1:1 ratio of S- and R-enantiomer of the ligand $\text{L}^{\text{Ph-TDA-(S/R)-Al}}$ was used to prepare complex **C3**. Yellow greenish microcrystalline material and yellow greenish crystals suitable for X-ray diffraction were achieved after four days of slow evaporation (49 mg, 0.09368 mmol, 40 %).

FT-IR: $\tilde{\nu}$ (cm⁻¹) = 2333, 2177, 1602, 1574, 1481, 1460, 1443, 1429, 1393, 1340, 1284, 1250, 1155, 1113, 1067, 1055, 1039, 1016, 1001, 927, 900, 873, 813, 763, 731, 687, 670, 636, 581, 552, 507, 492, 476, 416, 405; ESI-MS (m/z): calc. for [C₂₃H₂₄BFe⁵⁷N₆S]⁺ expected: 484.12 (100.00 %); found: 484.12 (100.00 %); Elemental Analysis calculated for [Fe(L^{Ph-TDA-(Rac)-Al})(NCBH₃)₂] (C₂₄H₂₇B₂FeN₇S): C, 55.11, H, 5.20, N, 18.75. found: C, 54.65, H, 5.06, N, 18.75.

References:

- [1] G. Molnár, S. Rat, L. Salmon, W. Nicolazzi, A. Bousseksou *Adv. Mater.* **2018**, *30*, 1703862.
- [2] K. S. Kumar, M. Ruben *Angew. Chem. Int. Ed.* **2021**, *60*, 7502–7521.
- [3] J. Linares, E. Codjovi, Y. Garcia *Sensors* **2012**, *12*, 4479–4492.
- [4] G. Chastanet, M. Lorenc, R. Bertoni, C. Desplanches *Comptes Rendus. Chimie* **2018**, *21*, 1075–1094.
- [5] A. Dürrmann, G. Hörner, D. Baabe, F. W. Heinemann, M. A. C. De Melo, B. Weber *Nat. Commun.* **2024**, *15*, 7321.
- [6] K. Ridier, G. Molnár, L. Salmon, W. Nicolazzi, A. Bousseksou *Solid State Sciences* **2017**, *74*, A1–A22.
- [7] A. B. Gaspar, M. Seredyuk *Coord. Chem. Rev.* **2014**, *268*, 41–58.
- [8] N. Konstantinov, A. Tauzin, U. N. Noubé, D. Dragoe, B. Kundys, H. Majjad, A. Brosseau, M. Lenertz, A. Singh, S. Berciaud, M.-L. Boillot, B. Doudin, T. Mallah, J.-F. Dayen *J. Mater. Chem. C* **2021**, *9*, 2712–2720.
- [9] I. A. Gural'skiy, V. A. Reshetnikov, A. Szebesczyk, E. Gumienna-Kontecka, A. I. Marynin, S. I. Shylin, V. Ksenofontov, I. O. Fritsky *J. Mater. Chem. C* **2015**, *3*, 4737–4741.
- [10] V. Maliuzhenko, M. Weselski, J. Gregoliński, M. Książek, J. Kusz, R. Bronisz *Inorg. Chem.* **2024**, *63*, 17762–17773.
- [11] K. S. Woo, A. Zhang, A. Arabelo, T. D. Brown, M. Park, A. A. Talin, E. J. Fuller, R. S. Bisht, X. Qian, R. Arroyave, S. Ramanathan, L. Thomas, R. S. Williams, S. Kumar *Nat. Commun.* **2024**, *15*, 4656.
- [12] N. Suryadevara, A. Pausch, E. Moreno-Pineda, A. Mizuno, J. Bürck, A. Baksi, T. Hochdörffer, I. Šalitroš, A. S. Ulrich, M. M. Kappes, V. Schünemann, W. Kloppe, M. Ruben *Chemistry A European J* **2021**, *27*, 15172–15180.
- [13] J. Ru, F. Yu, P. Shi, C. Jiao, C. Li, R. Xiong, T. Liu, M. Kurmoo, J. Zuo *Eur J Inorg Chem* **2017**, *2017*, 3144–3149.
- [14] J. Tao, R.-J. Wei, R.-B. Huang, L.-S. Zheng *Chem. Soc. Rev.* **2012**, *41*, 703–737.
- [15] X. Zhang, H. Sun, D. Chen, X. Li, J. Xiao, Y. Meng, T. Liu *Eur J Inorg Chem* **2024**, e202400201.
- [16] S. Ohkoshi, S. Takano, K. Imoto, M. Yoshikiyo, A. Namai, H. Tokoro *Nature Photon* **2014**, *8*, 65–71.

- [17] T. Verbiest, S. V. Elshocht, M. Kauranen, L. Hellemans, J. Snauwaert, C. Nuckolls, T. J. Katz, A. Persoons *Science* **1998**, *282*, 913–915.
- [18] F.-L. Yang, W.-H. Wu, Y.-Q. Wang, X. Chen, B.-B. Liang, H.-L. Mi, G.-L. Zhang, X.-Y. Chen, Y. Shi *Crystal Growth & Design* **2021**, *21*, 6671–6683.
- [19] S. Vela, J. J. Novoa, J. Ribas-Arino *Phys. Chem. Chem. Phys.* **2014**, *16*, 27012–27024.
- [20] E. Kuzmann, Z. Homonnay, Z. Klencsár, R. Szalay *Molecules* **2021**, *26*, 1062.
- [21] P. Gütllich, E. Bill, A. X. Trautwein, Springer Berlin Heidelberg, Berlin, Heidelberg, **2011**.
- [22] S. Rackwitz, J. A. Wolny, K. Muffler, K. Achterhold, R. Ruffer, Y. Garcia, R. Diller, V. Schünemann *Phys. Chem. Chem. Phys.* **2012**, *14*, 14650.
- [23] G. Félix, M. Mikolasek, H. Peng, W. Nicolazzi, G. Molnár, A. I. Chumakov, L. Salmon, A. Bousseksou *Phys. Rev. B* **2015**, *91*, 024422.
- [24] S. Sundaresan, J. Eppelsheimer, E. Gera, L. Wiener, L. M. Carrella, K. R. Vignesh, E. Rentschler *Dalton Trans.* **2024**, *53*, 10303–10317.
- [25] S. Sundaresan, J. Eppelsheimer, L. M. Carrella, E. Rentschler *Eur. J. Inorg. Chem.* **2025**, *28*, e202400690.
- [26] S. Sundaresan, J.-G. Becker, J. Eppelsheimer, A. E. Sedykh, L. M. Carrella, K. Müller-Buschbaum, E. Rentschler *Dalton Trans.* **2023**, *52*, 13181–13189.
- [27] J.-G. Becker, S. Sundaresan, Luca. M. Carrella, E. Rentschler *Chem. Commun.* **2025**, 10.1039.D5CC03779D.
- [28] Sm. K. Levalada, S. R. Banerjee, K. P. Maresca, J. W. Babich, J. Zubieta *Synthesis* **2004**.
- [29] P. N. Basa, C. A. Barr, K. M. Oakley, X. Liang, S. C. Burdette *J. Am. Chem. Soc.* **2019**, *141*, 12100–12108.
- [30] G. Nagendra, R. S. Lamani, N. Narendra, V. V. Sureshbabu *Tetrahedron Letters* **2010**, *51*, 6338–6341.
- [31] G. S. Matouzenko, A. Bousseksou, S. Lecocq, P. J. Van Koningsbruggen, M. Perrin, O. Kahn, A. Collet *Inorg. Chem.* **1997**, *36*, 5869–5879.
- [32] G. S. Matouzenko, A. Bousseksou, S. Lecocq, P. J. Van Koningsbruggen, M. Perrin, O. Kahn, A. Collet *Inorg. Chem.* **1997**, *36*, 2975–2981.
- [33] S. Kisslinger, H. Kelm, S. Zheng, A. Beitat, C. Würtele, R. Wortmann, S. Bonnet, S. Herres-Pawlis, H. Krüger, S. Schindler *Zeitschrift anorg. allge. chemie* **2012**, *638*, 2069–2077.
- [34] P. Gütllich, Y. Garcia, H. A. Goodwin *Chem. Soc. Rev.* **2000**, *29*, 419–427.
- [35] H. L. C. Feltham, A. S. Barltrop, S. Brooker *Coord. Chem. Rev.* **2017**, *344*, 26–53.
- [36] J. K. McCusker, A. L. Rheingold, D. N. Hendrickson *J. Am. Chem. Soc.* **2000**, *122*, 17, 4092–4097
- [37] J. Kiehl, T. Hochdörffer, L. M. Carrella, V. Schünemann, M. H. Nygaard, J. Overgaard, E. Rentschler *Inorg. Chem.* **2022**, *61*, 3141–3151.

- [38] A. Banerjee, A. Saha, B. K. Saha *Crystal Growth & Design* **2019**, *19*, 2245–2252.
- [39] J. E. Angulo-Cervera, M. Piedrahita-Bello, B. Martin, S. E. Alavi, W. Nicolazzi, L. Salmon, G. Molnár, A. Bousseksou *Mater. Adv.* **2022**, *3*, 5131–5137.
- [40] P. Guionneau *Dalton Trans.* **2014**, *43*, 382–393.
- [41] S. Sundaresan, J. Kiehl, L. M. Carrella, E. Rentschler *Crystal Growth & Design* **2023**, *23*, 1648–1655.
- [42] M. A. Halcrow, Ed. , *Wiley*, **2013**.
- [43] C. F. Herold, S. I. Shylin, E. Rentschler *Inorg. Chem.* **2016**, *55*, 6414–6419.
- [44] U. Habarakada, T. Boonprab, P. Harding, K. S. Murray, W. Phonsri, S. M. Neville, M. Ahmed, D. J. Harding *Crystal Growth & Design* **2022**, *22*, 4895–4905.
- [45] T.-T. Ma, X.-P. Sun, Z.-S. Yao, J. Tao *Inorg. Chem. Front.* **2020**, *7*, 1196–1204.
- [46] N. Ortega-Villar, V. M. Ugalde-Saldívar, M. C. Muñoz, L. A. Ortiz-Frade, J. G. Alvarado-Rodríguez, J. A. Real, R. Moreno-Esparza *Inorg. Chem.* **2007**, *46*, 7285–7293.
- [47] A. Regueiro, V. García-López, A. Forment-Aliaga, M. Clemente-León *Dalton Trans.* **2024**, *53*, 10637–10643.
- [48] W. Sturhahn *J. Phys.: Condens. Matter* **2004**, *16*, S497–S530.
- [49] J.-P. Tuchagues, A. Bousseksou, G. Molnár, J. J. McGarvey, F. Varret in *Spin Crossover in Transition Metal Compounds III*, Springer-Verlag, Berlin/Heidelberg, **2004**, pp. 84–103.
- [50] J. A. Wolny, R. Diller, V. Schünemann *Eur. J. Inorg. Chem.* **2012**, *2012*, 2635–2648.
- [51] V. Schünemann, H. Winkler *Rep. Prog. Phys.* **2000**, *63*, 263–353.
- [52] L.-F. Qin, C.-Y. Pang, W.-K. Han, F.-L. Zhang, L. Tian, Z.-G. Gu, X. Ren, Z. Li *Dalton Trans.* **2016**, *45*, 7340–7348.
- [53] Y. Sekimoto, M. R. Karim, N. Saigo, R. Ohtani, M. Nakamura, S. Hayami *Eur. J. Inorg. Chem.* **2017**, *2017*, 1049–1053.
- [54] R.-G. Wang, Y.-S. Meng, F.-F. Gao, W.-Q. Gao, C.-H. Liu, A. Li, T. Liu, Y.-Y. Zhu *Dalton Trans.* **2021**, *50*, 3369–3378.
- [55] K. E. Burrows, S. E. McGrath, R. Kulmaczewski, O. Cespedes, S. A. Barrett, M. A. Halcrow *Chem. A. Eur. J.* **2017**, *23*, 9067–9075.
- [56] L. Li, J.-P. Luo, X.-F. Li, Z. Shao, D.-Y. Chen, Q. Shi, L. Zhao, Y.-S. Meng, T. Liu *Inorg. Chem. Comm.* **2025**, 114382.
- [57] J. C. Cobas, F. J. Sardina *Concepts Magnetic Resonance* **2003**, *19A*, 80–96.
- [58] G. M. Sheldrick *Acta Crystallogr. A. Found. Adv.* **2015**, *71*, 3–8.
- [59] G. M. Sheldrick *Acta Crystallogr. A. Found. Crystallogr.* **2008**, *64*, 112–122.
- [60] G. M. Sheldrick, T. R. Schneider in *Methods in Enzymology*, Elsevier, **1997**, pp. 319–343.

- [61] O. V. Dolomanov, L. J. Bourhis, R. J. Gildea, J. A. K. Howard, H. Puschmann *J. Appl. Crystallogr.* **2009**, *42*, 339–341.
- [62] H. P. Gunnlaugsson *Hyperfine Interact* **2016**, *237*, 79.

ESI: Understanding Polymorphism and Spin Crossover in Chiral Iron(II) Complexes: Structure-Property Insights

Jens-Georg Becker¹, Sriram Sundaresan², Tim Hochdörffer³, Juliusz A. Wolny³, Marco A. M. Tummeley³, Alexander Friesen¹, Luca M. Carrella¹, Volker Schünemann³ and Eva Rentschler^{1*}

¹Department Chemie, Johannes-Gutenberg-Universität Mainz, Duesbergweg 10–14, 55128 Mainz, Germany.
Email: rentschl@uni-mainz.de

²Institute of Physics, Czech Academy of Sciences, Cukrovarnická 10, 162 00 Prague, Czech Republic.

³Department of Physics, University of Kaiserslautern-Landau, Erwin-Schrödinger-Str. 46, 67663 Kaiserslautern, Germany

Table of Contents

1. NMR-Spectra:	169
2. IR-spectra:.....	172
3. Mass spectra:.....	174
4. Crystallographic Data.....	178
5. Temperature dependent magnetization measurement	190
6. CD-Spectra and chiral HPLC	195

1. NMR-Spectra:

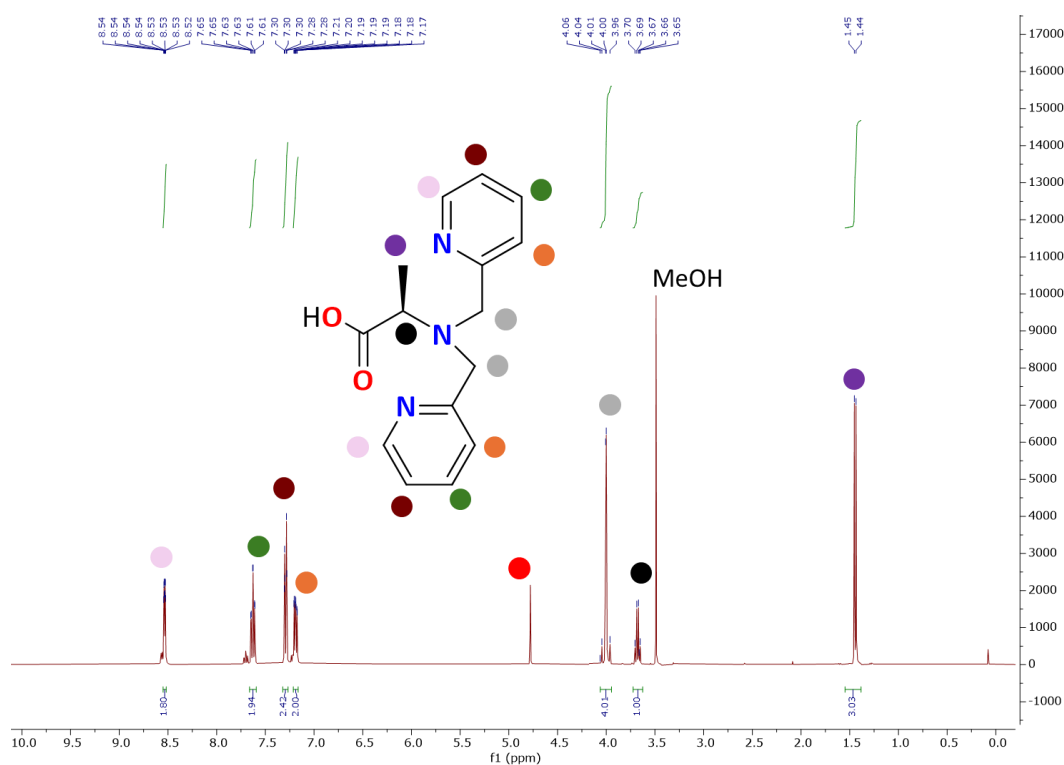


Figure S1: $^1\text{H-NMR}$ spectrum of the Bis(pyridin-2-ylmethyl)-D-alanine (I) in CDCl_3 [400 MHz]. All signals can be assigned. The signal at 4.78 ppm (red) can be assigned to pyridin-2-ylmethanol. And the signal at 3.49 ppm can be assigned to methanol.^[1]

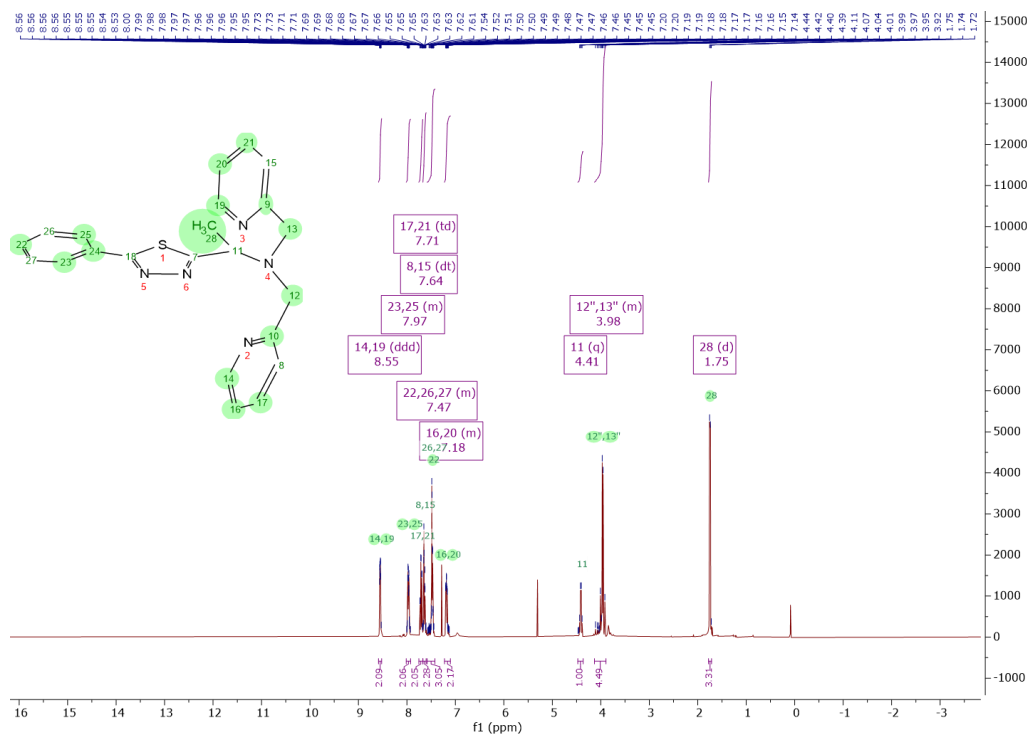


Figure S2: $^1\text{H-NMR}$ spectrum of the (R)-1-(5-phenyl-1,3,4-thiadiazol-2-yl)-N,N-bis(pyridin-2-ylmethyl)ethan-1-amine ($\text{L}^{\text{Ph-TDA-(Rac)-Al}}$) in CDCl_3 [400 MHz]. All signals can be assigned. The aliphatic peaks are due to grease and solvent residues of dichloromethane.^[1]

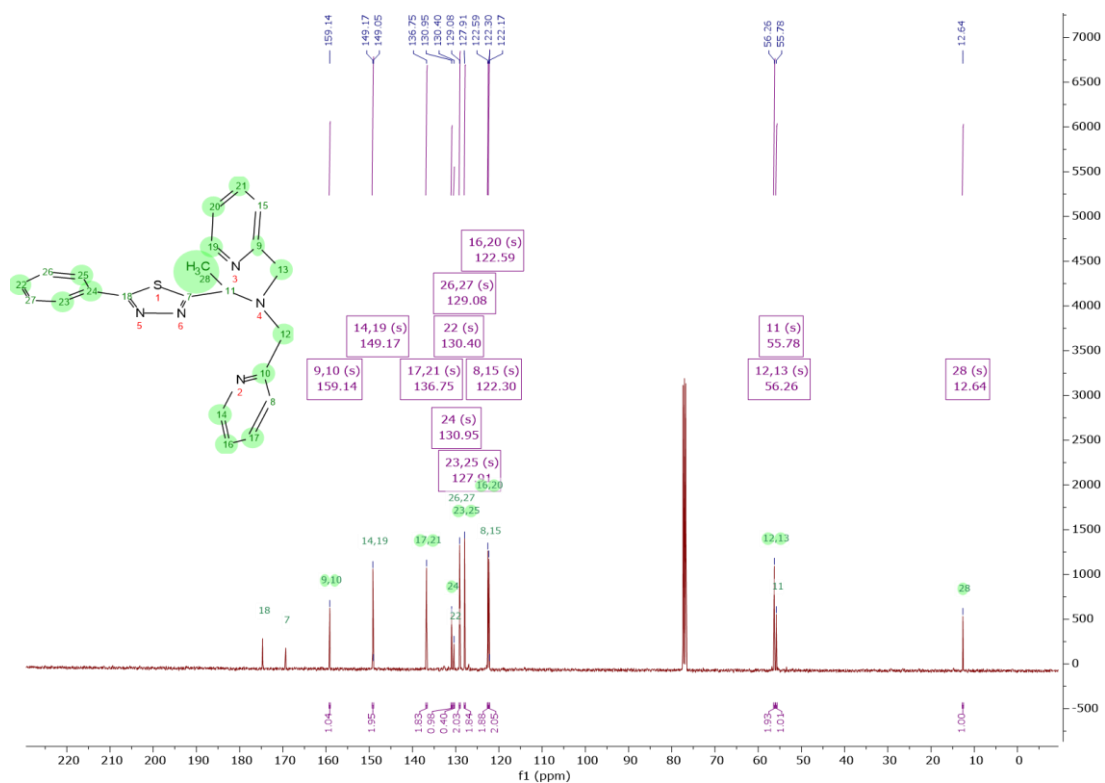


Figure S3: ^{13}C -NMR spectrum of the ligand $\text{L}^{\text{Ph-TDA-(Rac)-Al}}$ measured in CDCl_3 [101MHz].

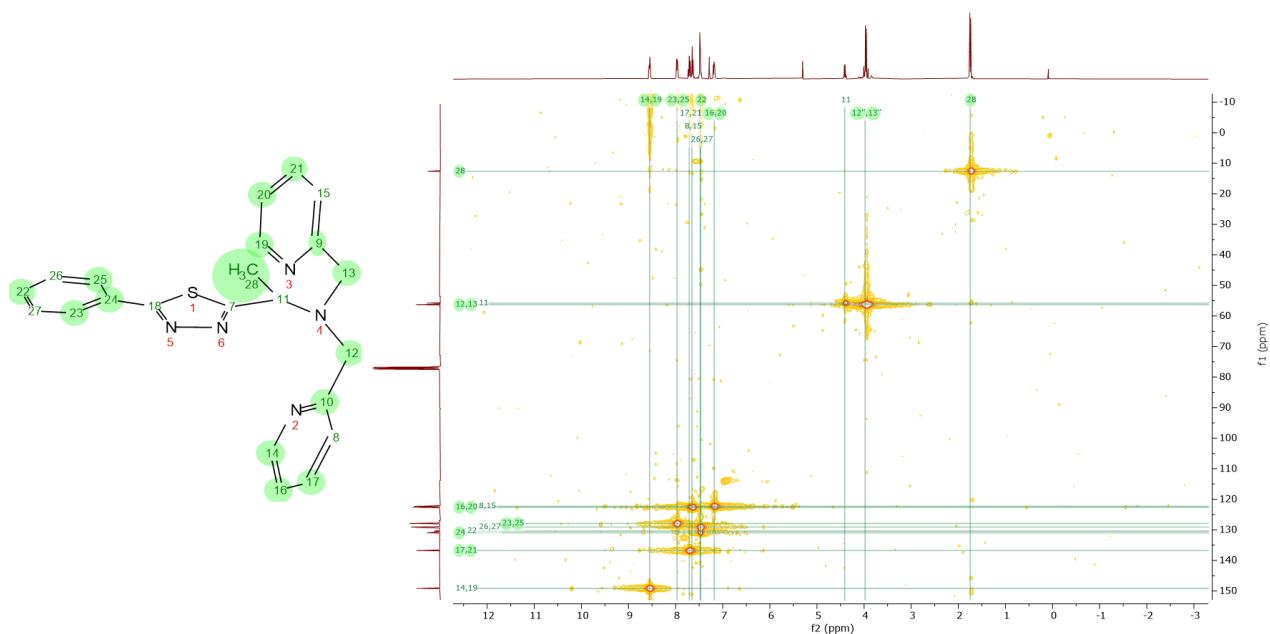


Figure S4: HSQC-NMR spectrum of ligand $\text{L}^{\text{Ph-TDA-(Rac)-Al}}$ measured in CDCl_3 .

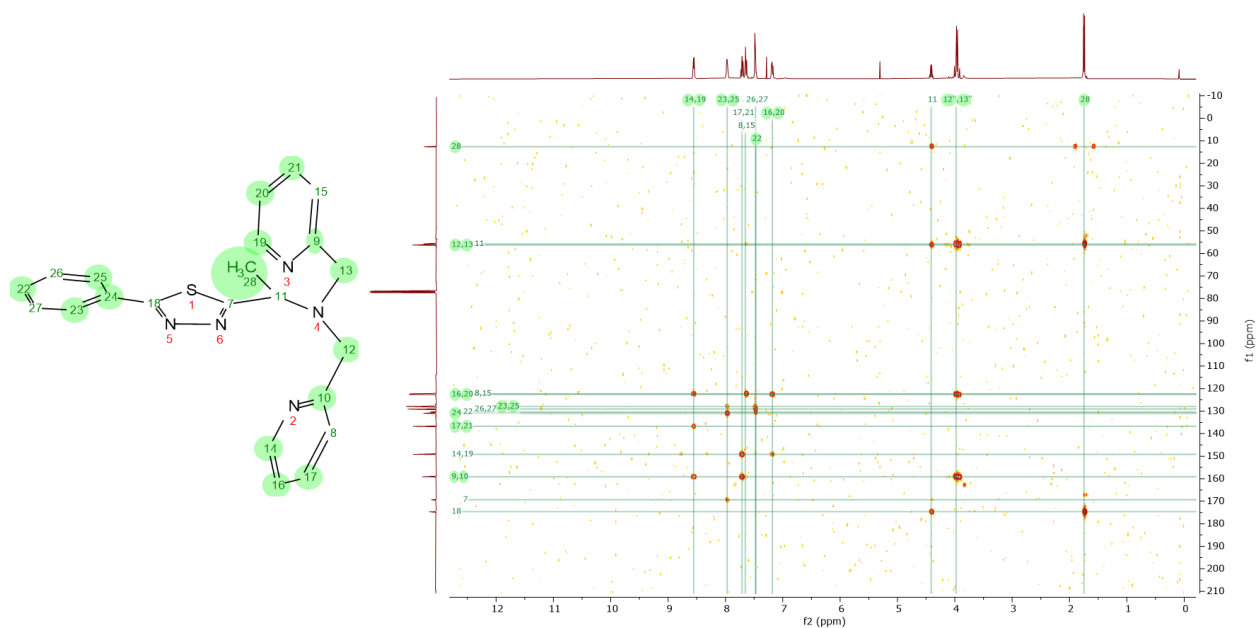


Figure S5: HMBC-NMR spectrum of ligand $L^{\text{Ph-TDA-(Rac)-Al}}$ measured in CDCl_3 .

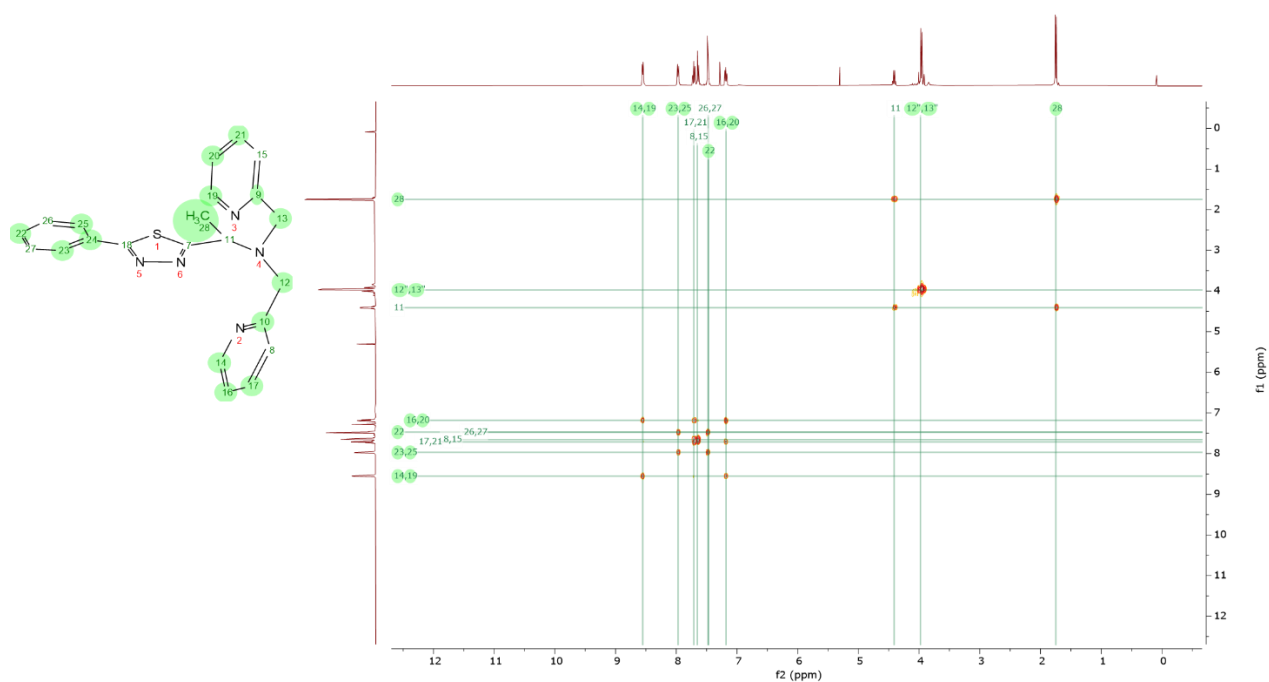
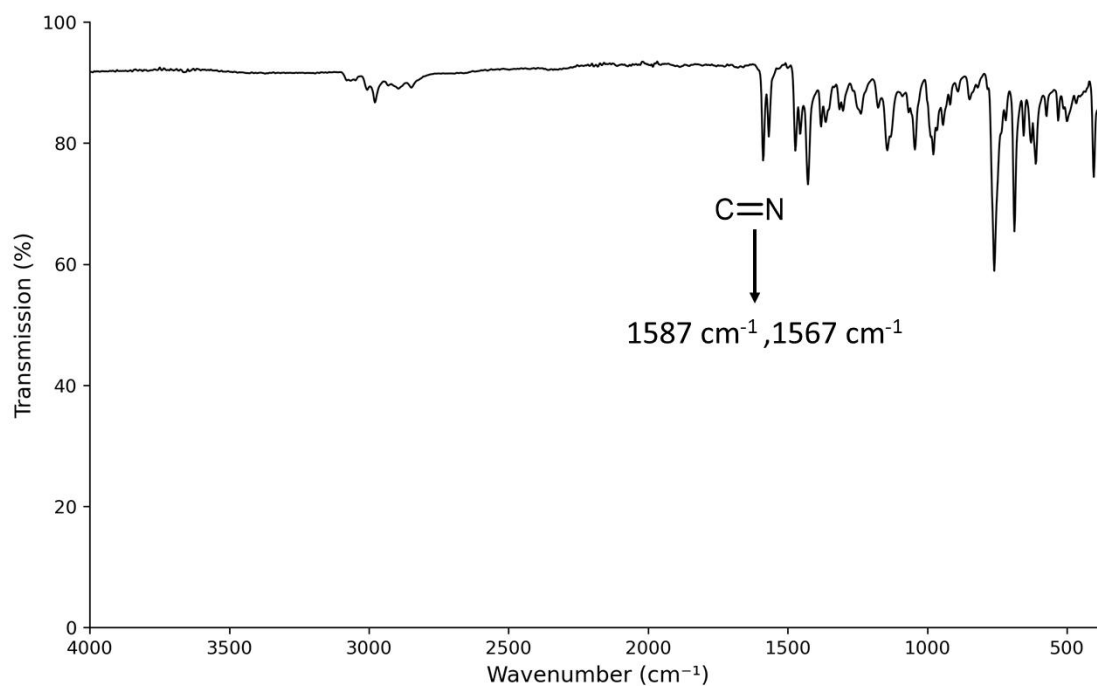
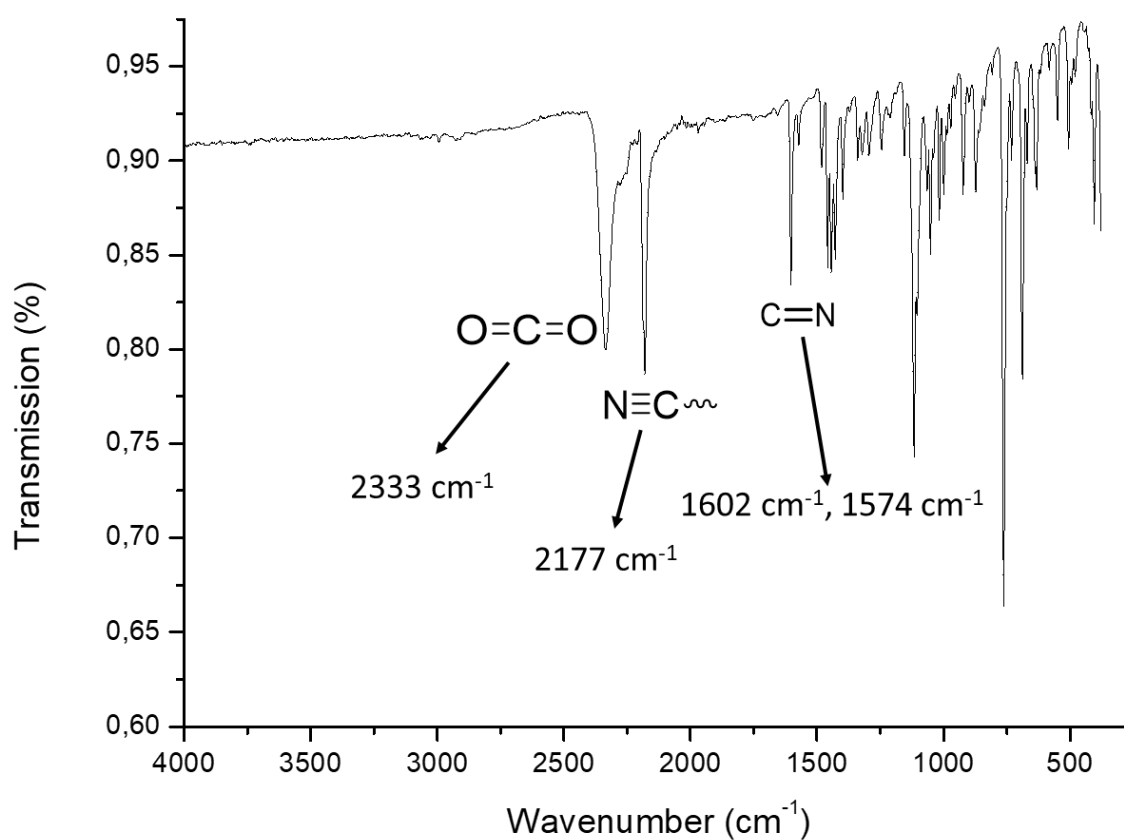


Figure S6: COSY-NMR spectrum of ligand $L^{\text{Ph-TDA-(Rac)-Al}}$ measured in CDCl_3 [400 MHz].

2. IR-spectra:**Figure S7:** IR spectrum of the Ligand $L^{\text{Ph-TDA-(Rac)-Al}}$.**Figure S8:** IR spectrum of $[\text{Fe}(L^{\text{Ph-TDA-(S)-Al}})(\text{NCBH}_3)_2] \cdot 0.5 \text{H}_2\text{O}$ (**C1** · 0.5 H₂O).

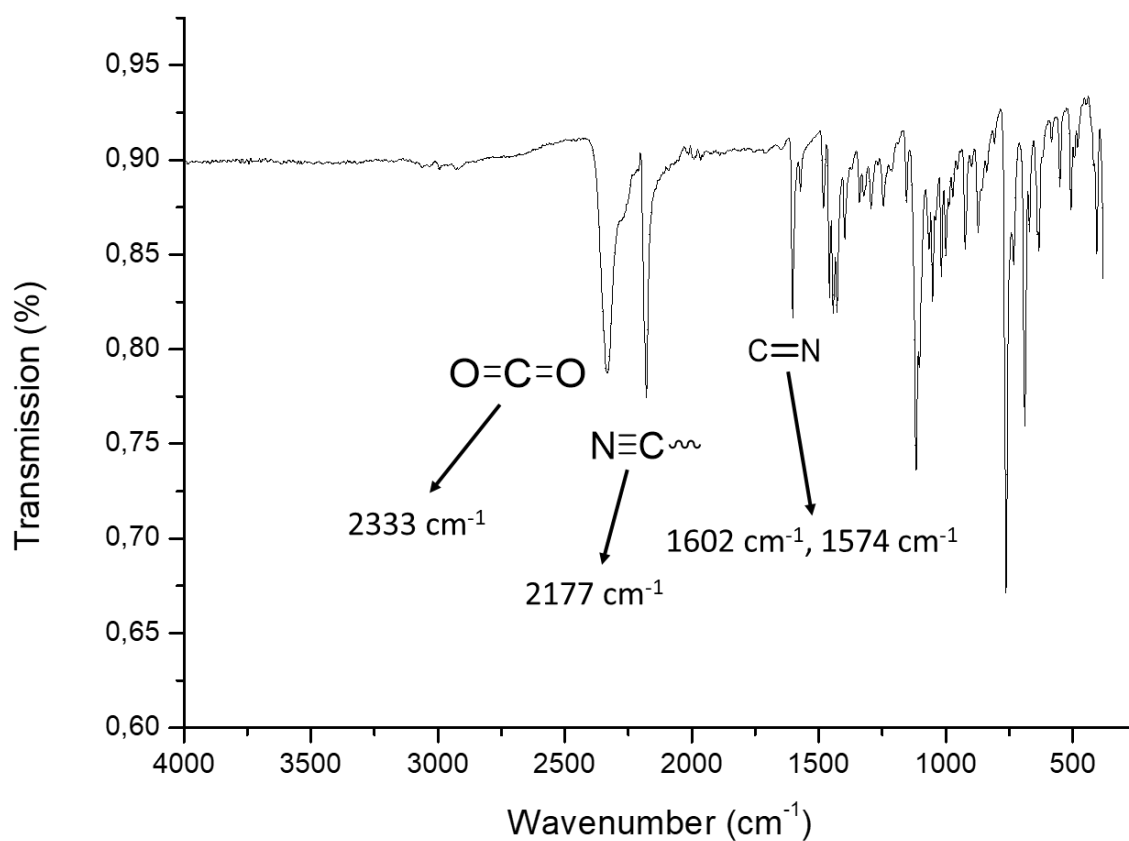


Figure S9: IR spectrum of $[\text{Fe}(\text{L}^{\text{Ph-TDA-(R)-Al})(\text{NCBH}_3)_2] \cdot 0.5 \text{H}_2\text{O}$ ($\text{C2} \cdot 0.5 \text{H}_2\text{O}$).

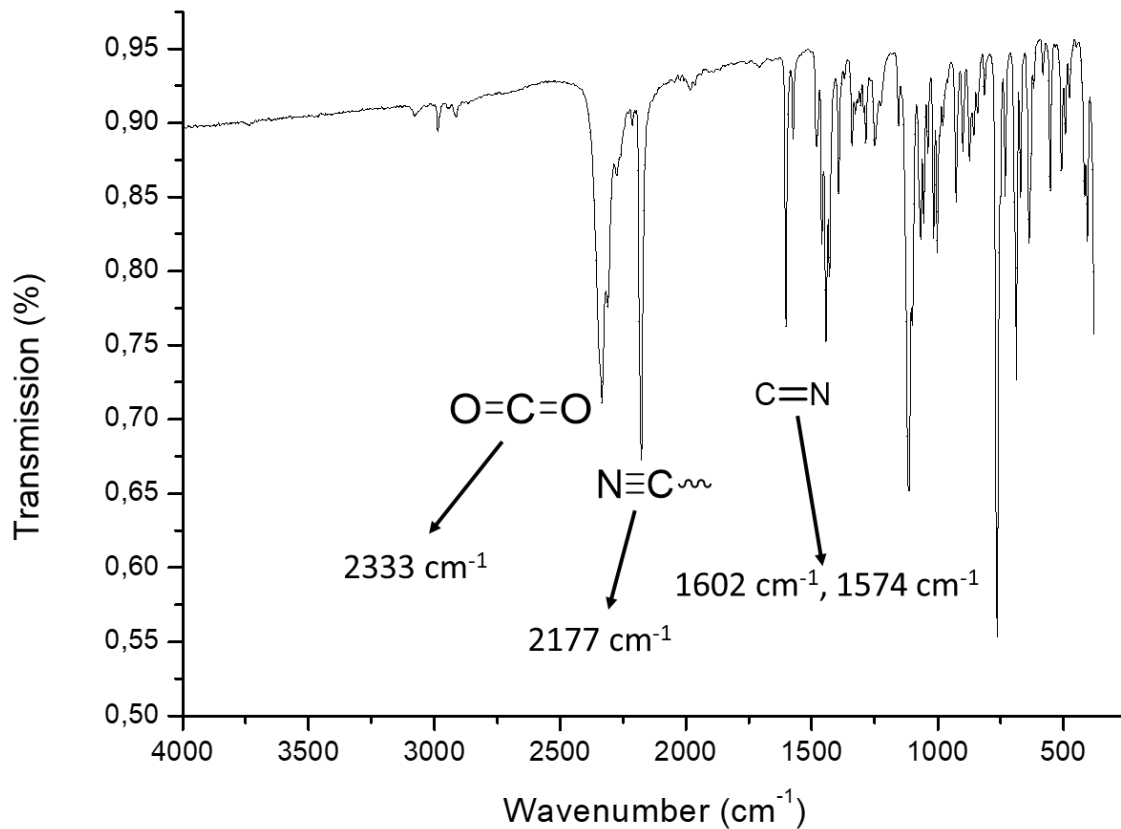


Figure S10: IR spectrum of $[\text{Fe}(\text{L}^{\text{Ph-TDA-(Rac)-Al})(\text{NCBH}_3)_2] (\text{C3} \cdot 0.5 \text{H}_2\text{O})$.

3. Mass spectra:

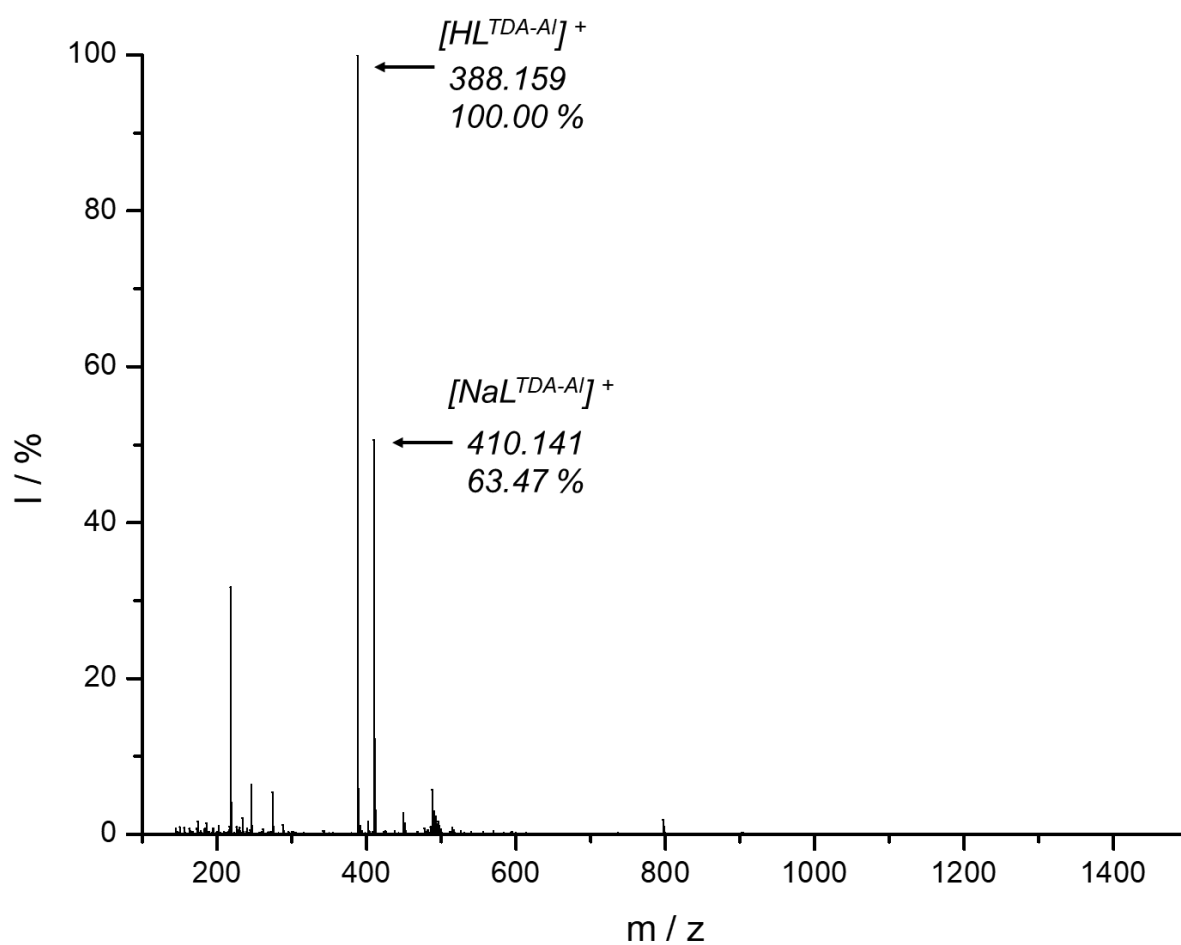


Figure S11: Mass spectrum (ESI positive) of the Ligand $L^{\text{Ph-TDA-(Rac)-Al}}$.

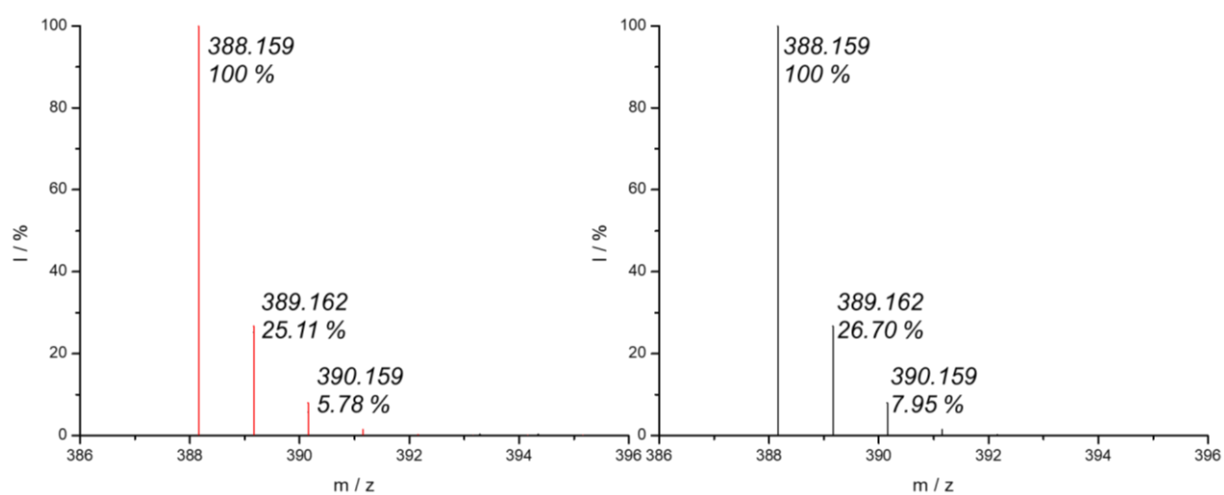


Figure S12: Isotopic pattern of ESI mass spectra of $L^{\text{Ph-TDA-(Rac)-Al}}$ measured (left with red overlap of the isotopic pattern) predicted (right).

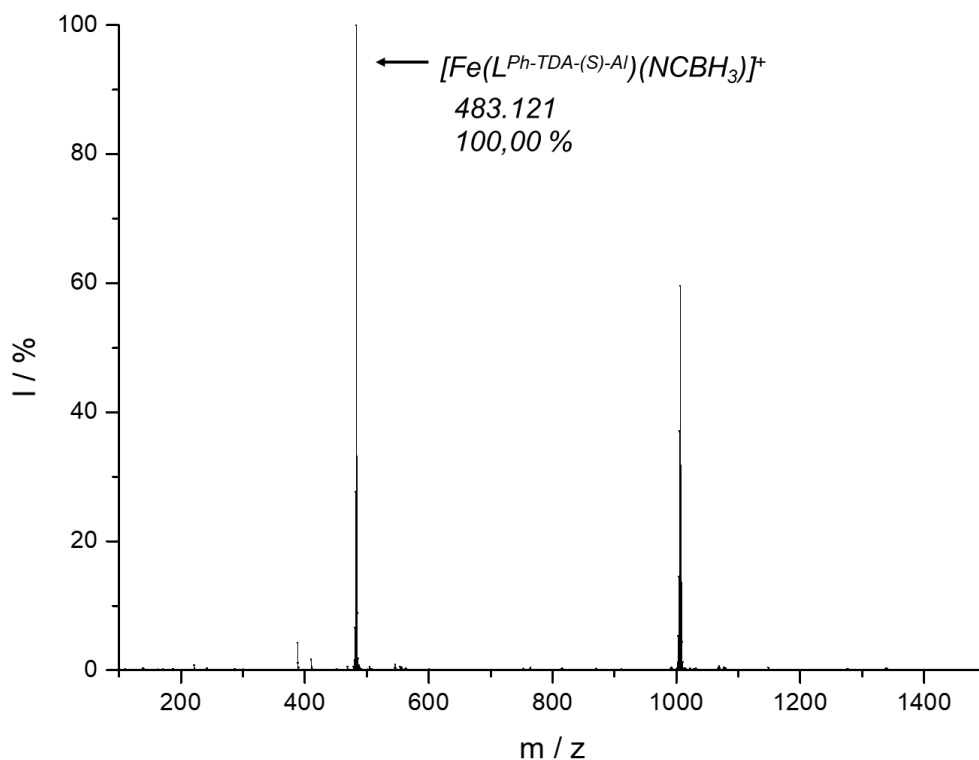


Figure S13: Mass spectrum (ESI positive) of the complex $[\text{Fe}(\text{L}^{\text{Ph-TDA-(S)-Al}})(\text{NCBH}_3)_2] \cdot 0.5 \text{H}_2\text{O}$ (**C1** · 0.5 H_2O).

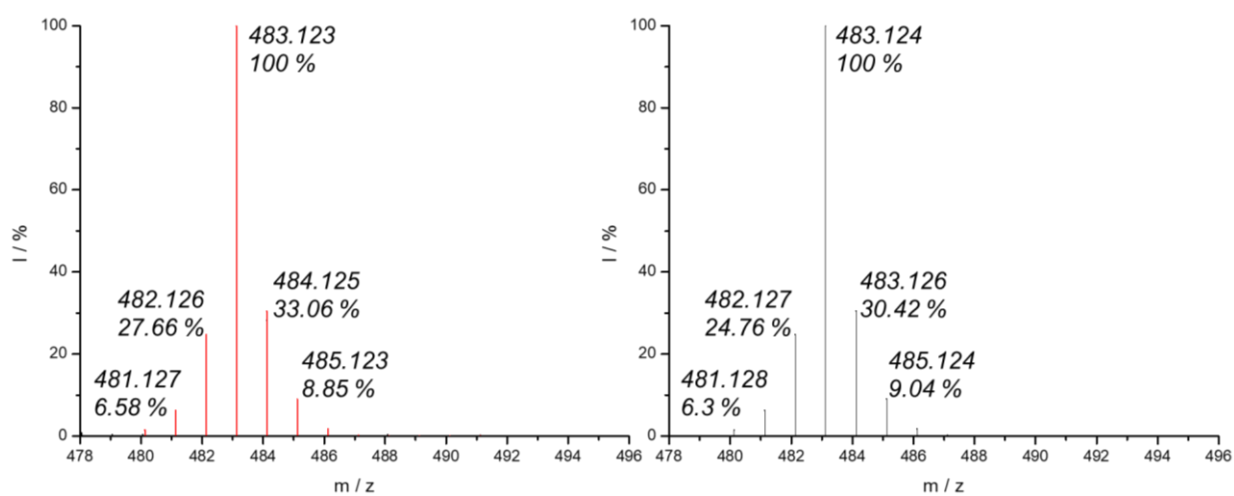


Figure S14: Isotopic pattern of ESI mass spectra of $[\text{Fe}(\text{L}^{\text{Ph-TDA-(S)-Al}})(\text{NCBH}_3)_2] \cdot 0.5 \text{H}_2\text{O}$ (**C1** · 0.5 H_2O) measured (left with red overlap of the isotopic pattern) predicted (right).

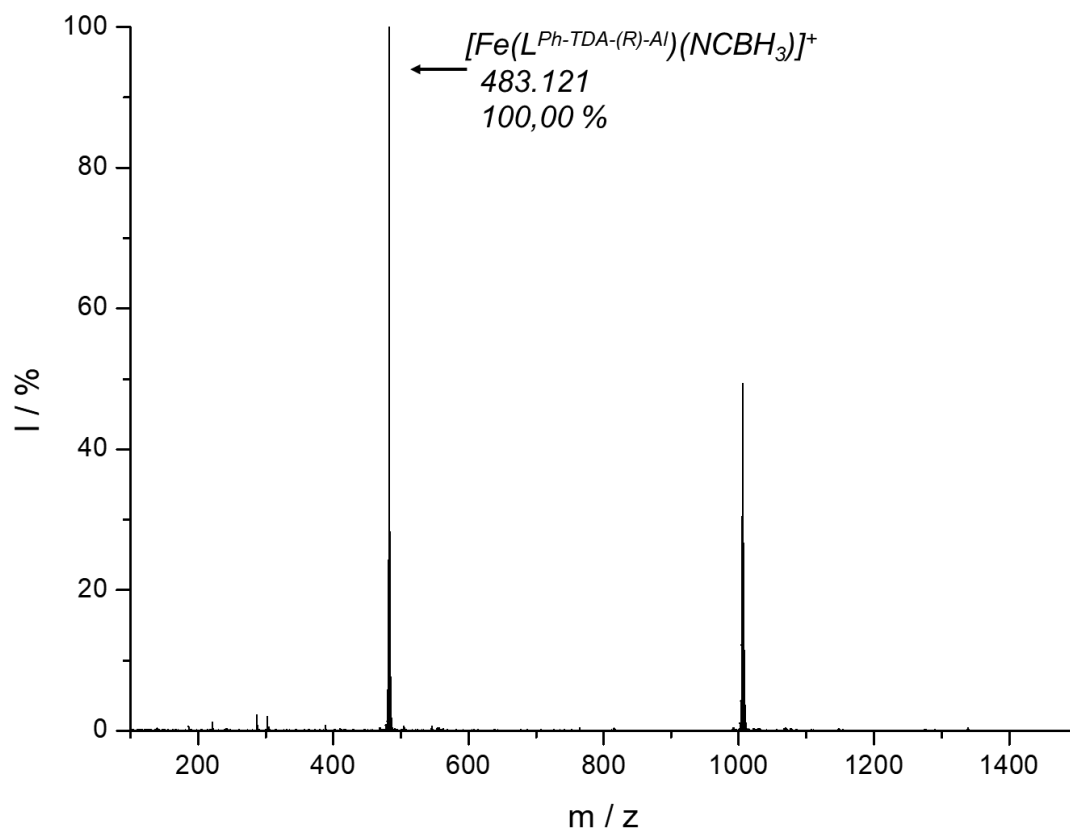


Figure S15: Mass spectrum (ESI positive) of the complex $[\text{Fe}(\text{L}^{\text{Ph-TDA-(R)-Al}})(\text{NCBH}_3)_2] \cdot 0.5 \text{H}_2\text{O}$ (**C2** · 0.5 H_2O).

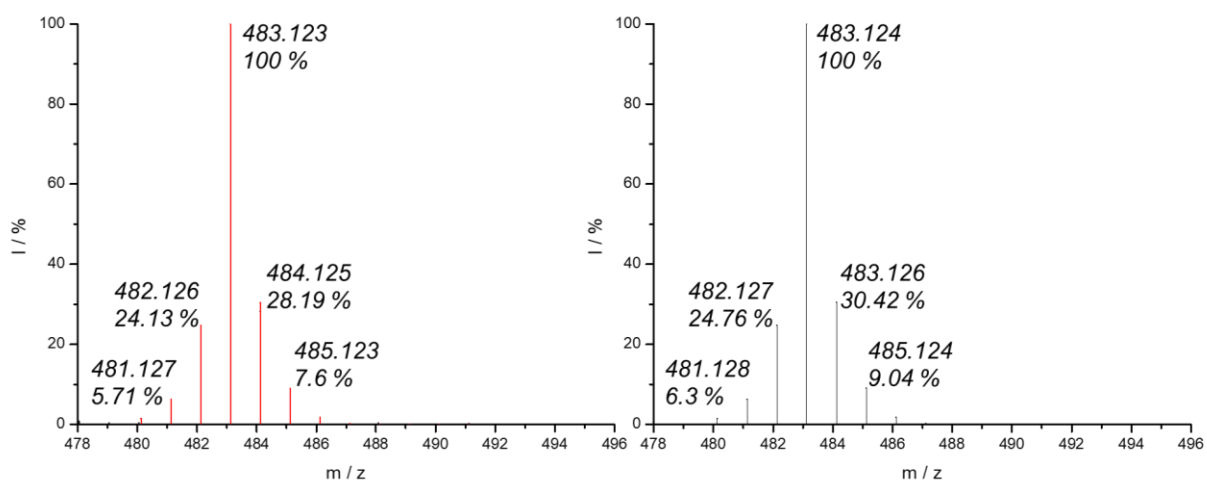


Figure S16: Isotopic pattern of ESI mass spectra of $[\text{Fe}(\text{L}^{\text{Ph-TDA-(R)-Al}})(\text{NCBH}_3)_2] \cdot 0.5 \text{H}_2\text{O}$ (**C2** · 0.5 H_2O) measured (left with red overlap of the isotopic pattern) predicted (right).

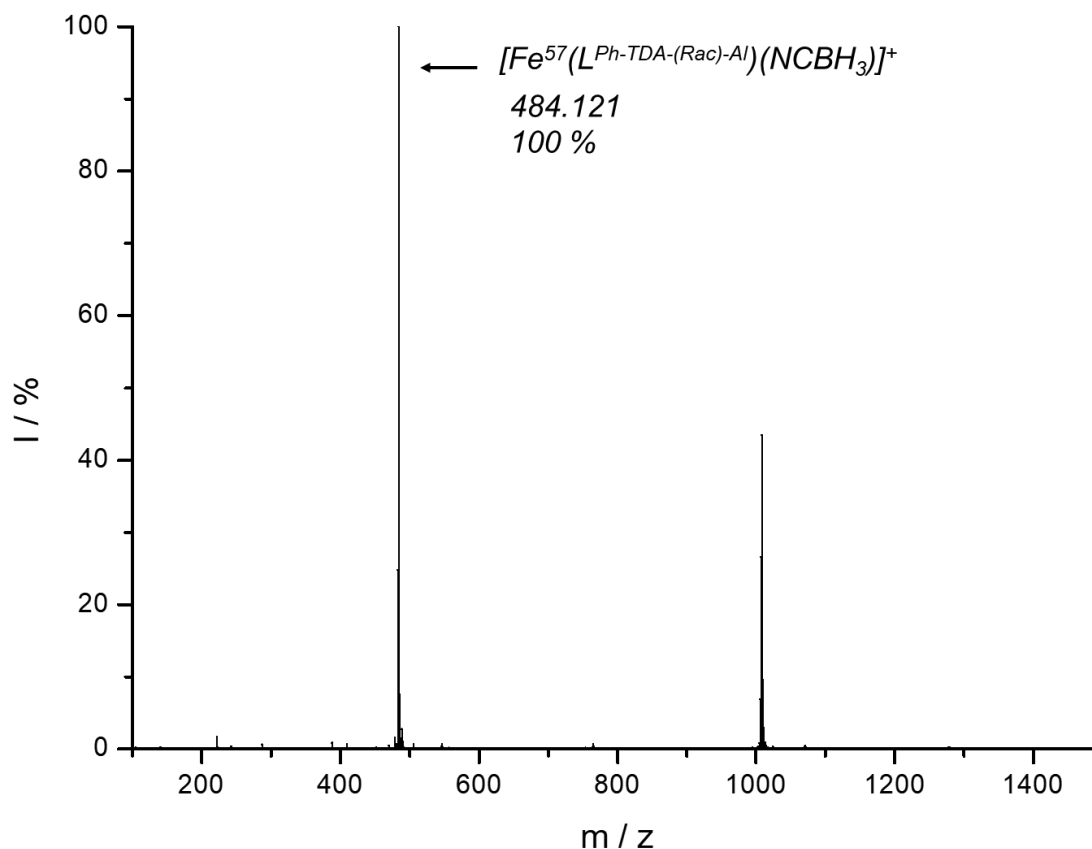


Figure S17: Mass spectrum (ESI positive) of the complex $[\text{Fe}(\text{L}^{\text{Ph-TDA-(Rac)-Al}})(\text{NCBH}_3)_2]$ (**C3**).

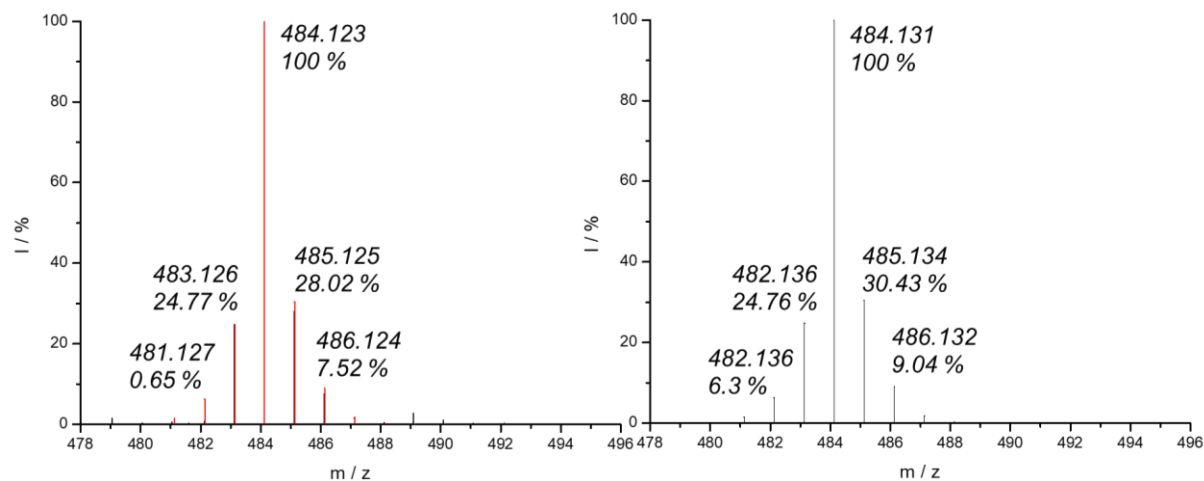


Figure S18: Isotopic pattern of ESI mass spectra of $[\text{Fe}(\text{L}^{\text{Ph-TDA-(Rac)-Al}})(\text{NCBH}_3)_2]$ (**C3**) measured (left with red overlap of the isotopic pattern) predicted (right).

4. Crystallographic Data

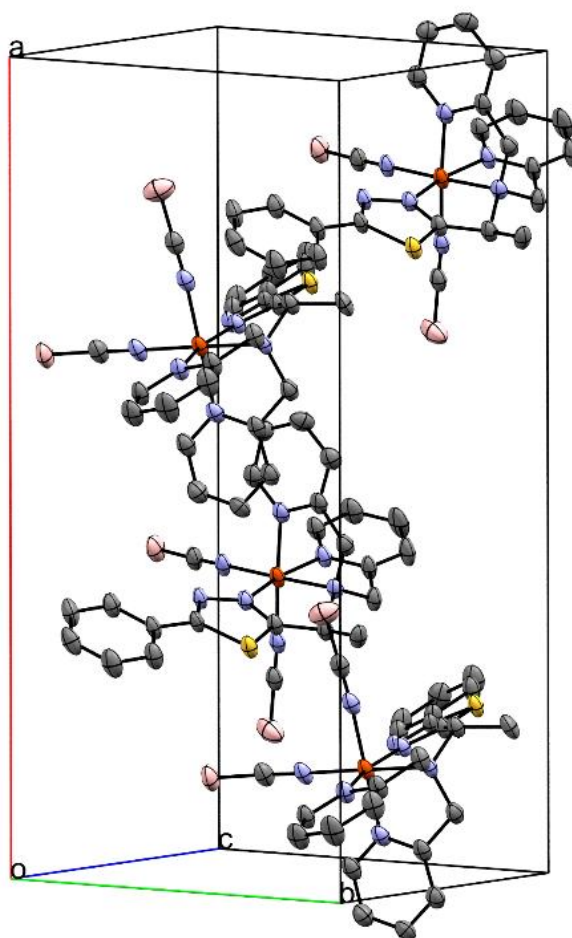


Figure S19: Unit cell of $[\text{Fe}(\text{L}^{\text{Ph-TDA-(S)-Al}})(\text{NCBH}_3)_2] \cdot 1.5 \text{ MeCN}$ (**C1** · 1.5 MeCN) at 120 K. Solvent molecules and Hydrogen atoms were removed for better overview.

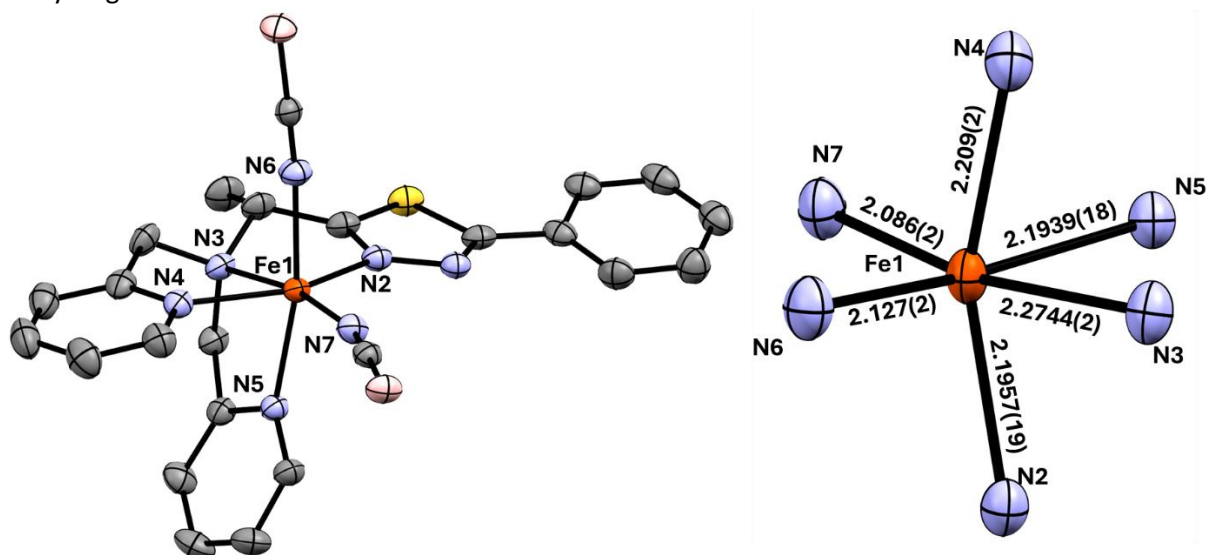


Figure S20: Fe-N-bond length of the complex $[\text{Fe}(\text{L}^{\text{Ph-TDA-(Rac)-Al}})(\text{NCBH}_3)_2] \cdot 1.5 \text{ MeCN}$ (**C3** · 1.5 MeCN) of the first coordination sphere, visualizing the high spin character of the Iron(II).

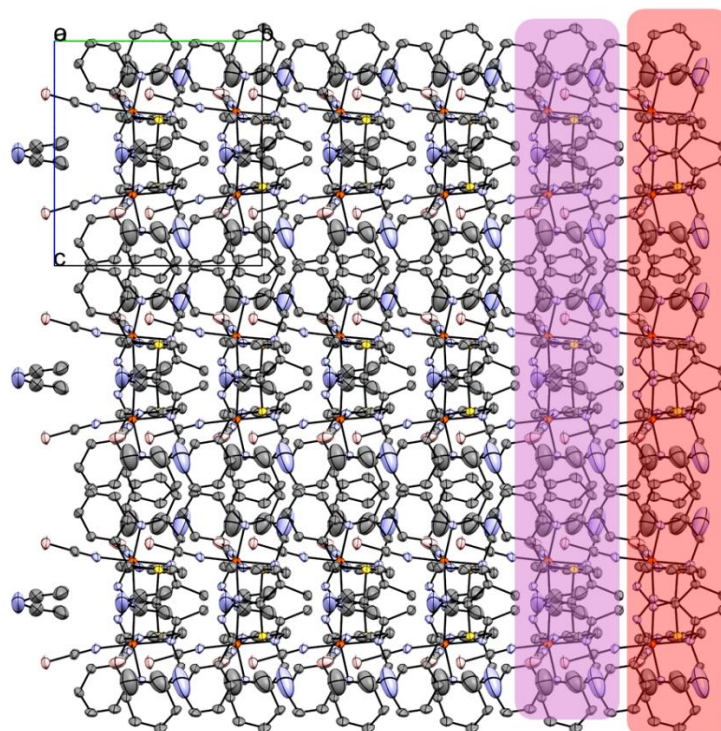


Figure S21: Visualisation of the packing for $[\text{Fe}(\text{L}^{\text{Ph-TDA-(S)-Al}})(\text{NCBH}_3)_2] \cdot 1.5 \text{ MeCN}$ ($\text{C1} \cdot 1.5 \text{ MeCN}$) along a-axis at 120 K. **Pink:** solvent channel; **Red** and **Blue:** chains due to trans-Pyridine-Pyridine-Stacking and Phenyl-1,3,4-Thiadiazole-Stacking; **Green:** cis-Pyridine-Pyridine-Stacking. Hydrogen atoms were removed for better overview.

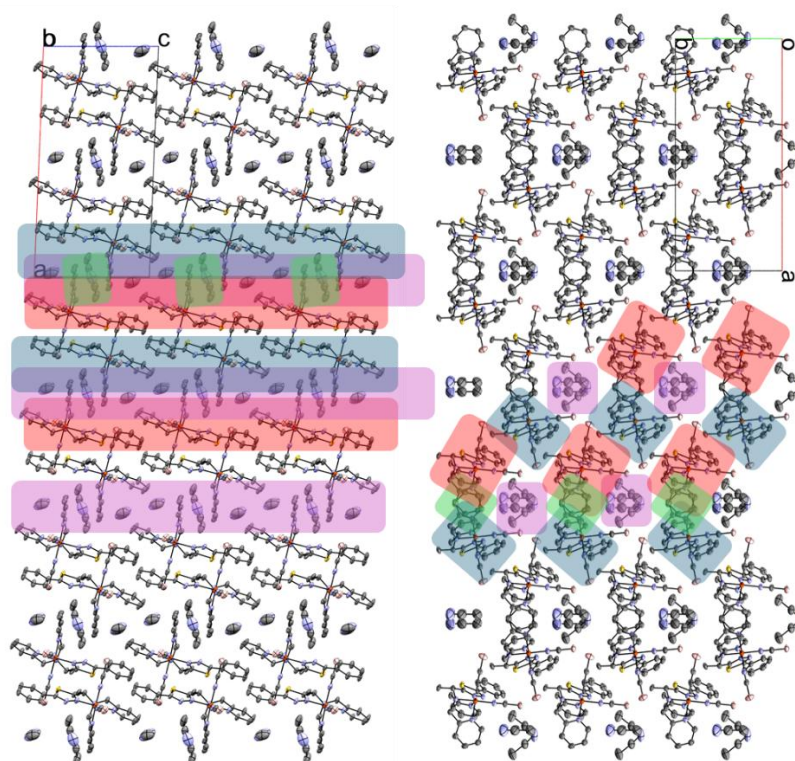


Figure S22: Visualisation of the packing for $[\text{Fe}(\text{L}^{\text{Ph-TDA-(S)-Al}})(\text{NCBH}_3)_2] \cdot 1.5 \text{ MeCN}$ ($\text{C1} \cdot 1.5 \text{ MeCN}$) along b-axis (left) and c-axis (right) at 120 K. **Pink:** solvent channel; **Red** and **Blue:** chains due to trans-Pyridine-Pyridine-Stacking and Phenyl-1,3,4-Thiadiazole-Stacking; **Green:** cis-Pyridine-Pyridine-Stacking. Hydrogen atoms were removed for better overview.

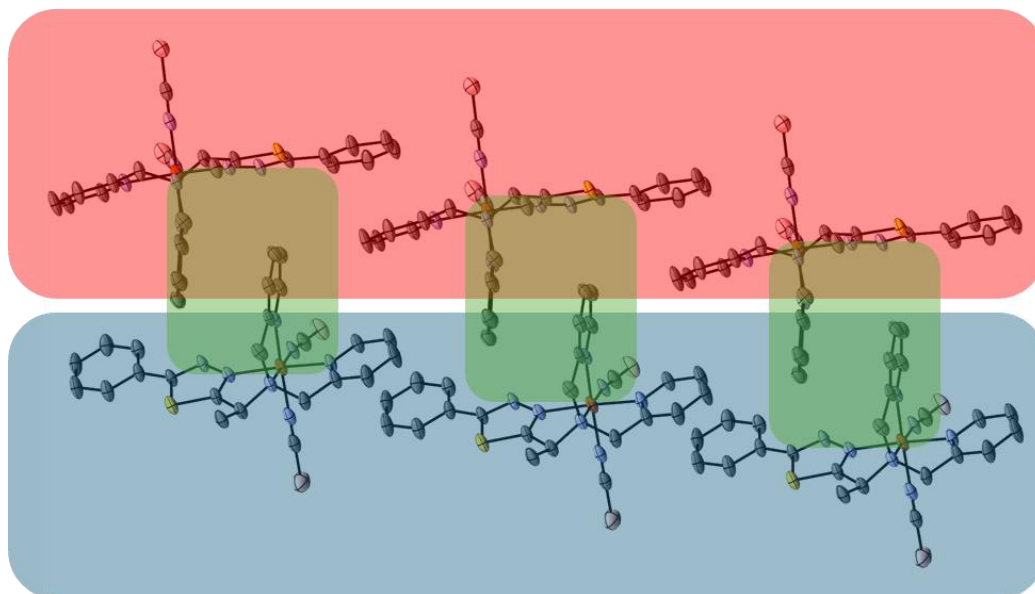


Figure S23: Visualisation of the stacking for $[\text{Fe}(\text{L}^{\text{Ph-TDA-(S)-Al}})(\text{NCBH}_3)_2] \cdot 1.5 \text{ MeCN}$ (**C1** · 1.5 MeCN) along the chains with Pyridine-Phenyl-Stacking (blue), cis-Pyridine-Pyridine-Stacking (green) and Pyridine-Pyridine-Stacking (red) at 120 K.

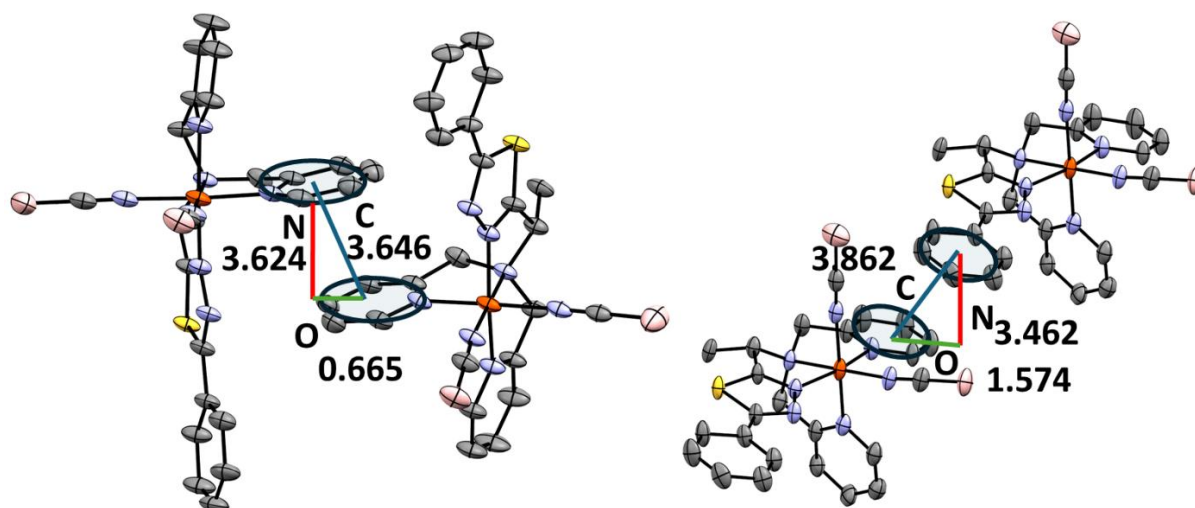


Figure S24: Visualisation of the π - π -interaction between Pyridine- and Pyridine-units (left) and Pyridine- and Phenyl-units (right) with Off-set (green), Normalvector (red) and Centroid-Centroid-distance (blue) and their values in Å for Complex $[\text{Fe}(\text{L}^{\text{Ph-TDA-(S)-Al}})(\text{NCBH}_3)_2] \cdot 1.5 \text{ MeCN}$ (**C1** · 1.5 MeCN) at 120 K.

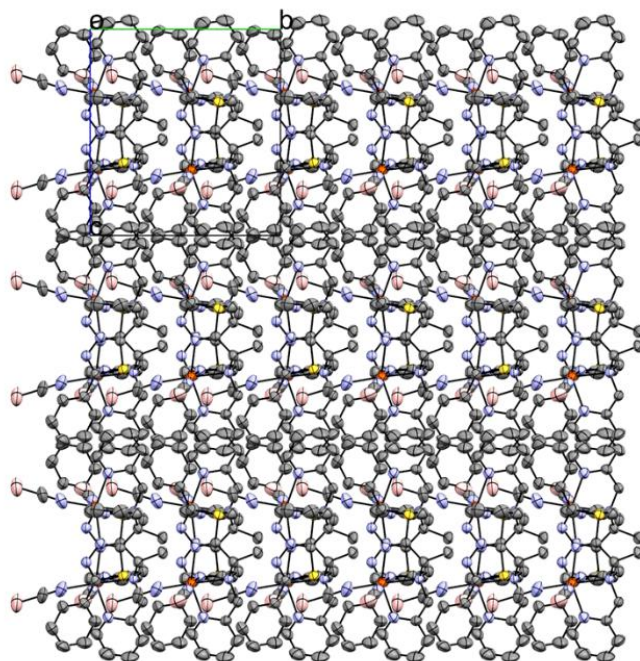


Figure S25: Visualisation of the packing for $[\text{Fe}(\text{L}^{\text{Ph-TDA-(S)-Al}})(\text{NCBH}_3)_2] \cdot 1.5 \text{ MeCN}$ (**C1** · 1.5 MeCN) along a-axis at 220 K. Solvent molecules and Hydrogen atoms were removed for better overview.

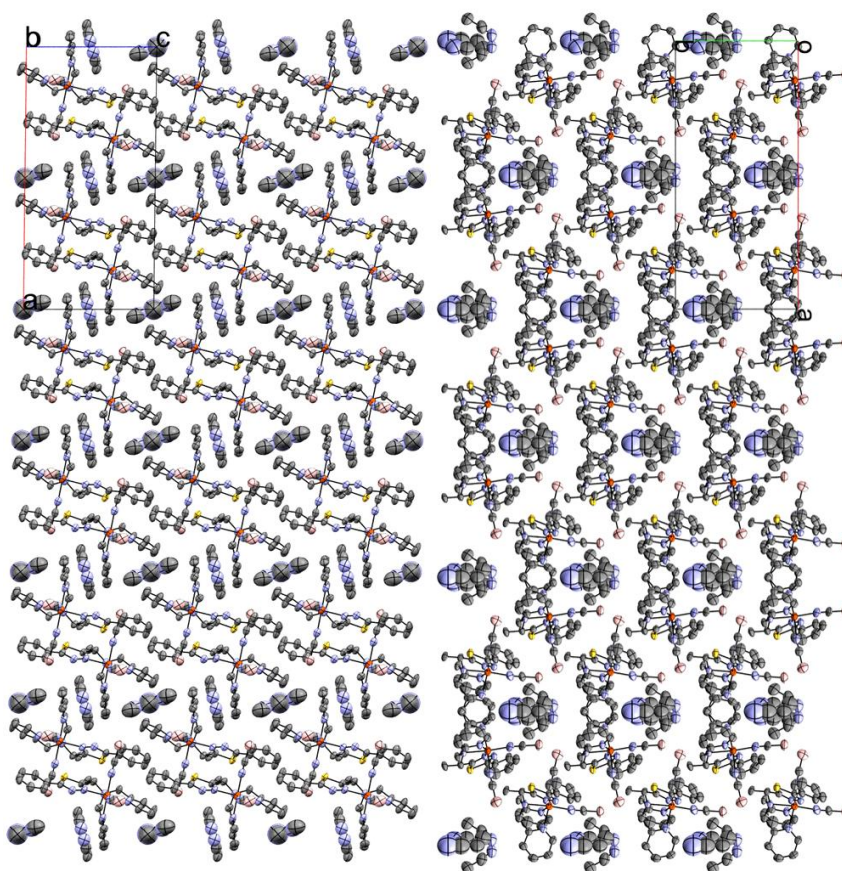


Figure S26: Visualisation of the packing for $[\text{Fe}(\text{L}^{\text{Ph-TDA-(S)-Al}})(\text{NCBH}_3)_2] \cdot 1.5 \text{ MeCN}$ (**C1** · 1.5 MeCN) along b-axis (left) and c-axis (right) at 220 K. Hydrogen atoms were removed for better overview.

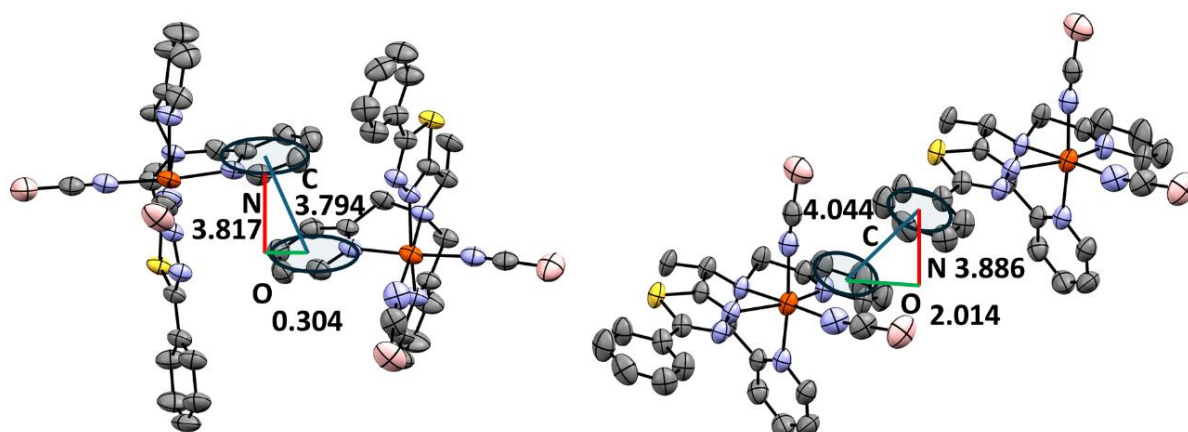


Figure S27: Visualisation of the π - π -interaction between Pyridine- and Pyridine-units (left) and Pyridine- and Phenyl-units (right) with Off-set (green), Normalvector (red) and Centroid-Centroid-distance (blue) and their values in Å for Complex $[\text{Fe}(\text{L}^{\text{Ph-TDA-(S)-Al}})(\text{NCBH}_3)_2] \cdot 1.5 \text{ MeCN}$ (**C1** · 1.5 MeCN) at 220 K.

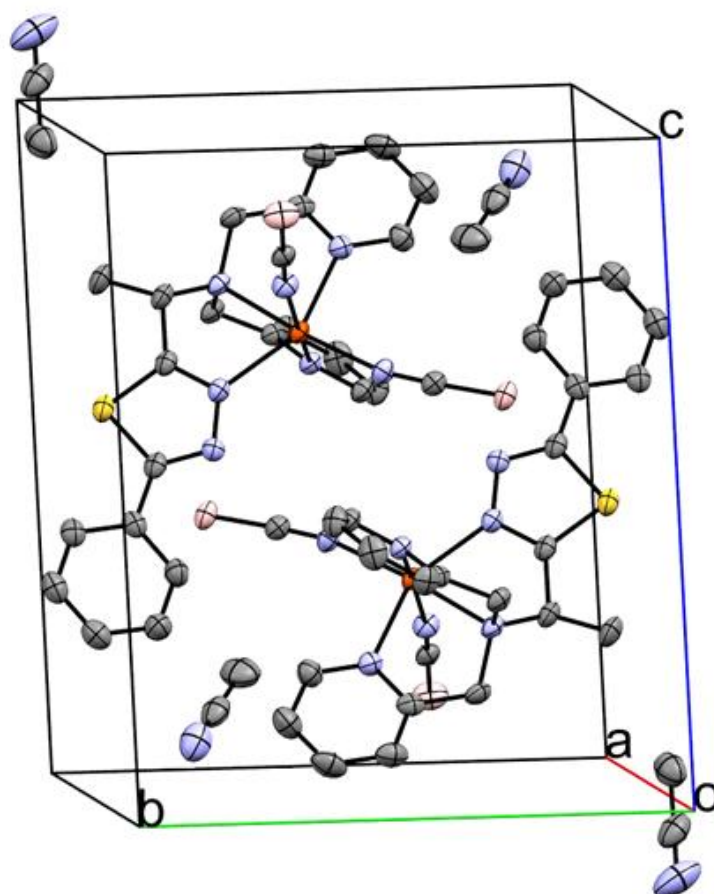


Figure S28: Unit cell of $[\text{Fe}(\text{L}^{\text{Ph-TDA-(Rac)-Al}})(\text{NCBH}_3)_2] \cdot 2 \text{ MeCN}$ (**C3** · 2 MeCN) at 120 K. Hydrogen atoms were removed for better overview.

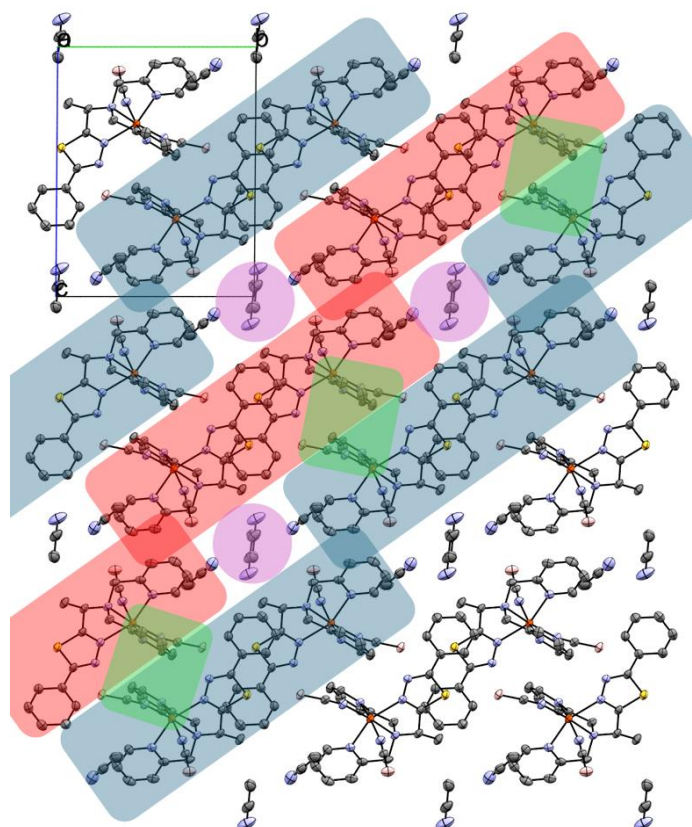


Figure S29: Visualisation of the packing for $[\text{Fe}(\text{L}^{\text{Ph-TDA-(Rac)-Al}})(\text{NCBH}_3)_2] \cdot 2 \text{ MeCN}$ ($\text{C3} \cdot 2 \text{ MeCN}$) along a-axis at 120 K. **Pink:** solvent channel; **Red and Blue:** chains due to trans-Pyridine-Pyridine-Stacking and Phenyl-1,3,4-Thiadiazole-Stacking; **Green:** cis-Pyridine-Pyridine-Stacking. Hydrogen atoms were removed for better overview.

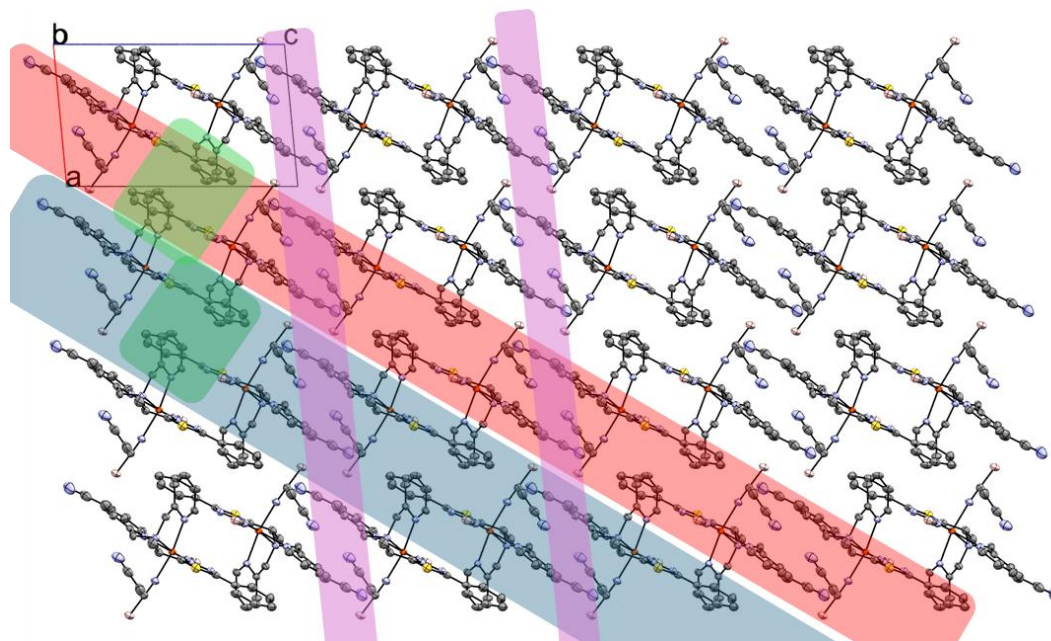


Figure S30: Visualisation of the packing for $[\text{Fe}(\text{L}^{\text{Ph-TDA-(Rac)-Al}})(\text{NCBH}_3)_2] \cdot 2 \text{ MeCN}$ ($\text{C3} \cdot 2 \text{ MeCN}$) along b-axis at 120 K. **Pink:** solvent channel; **Red and Blue:** chains due to trans-Pyridine-Pyridine-Stacking and Phenyl-1,3,4-Thiadiazole-Stacking; **Green:** cis-Pyridine-Pyridine-Stacking. Hydrogen atoms were removed for better overview.

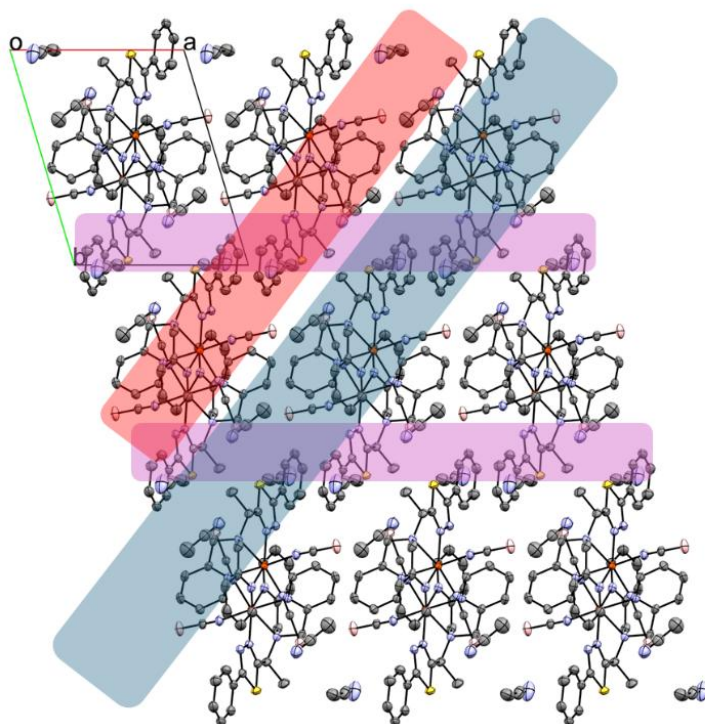


Figure S31: Visualisation of the packing for $[\text{Fe}(\text{L}^{\text{Ph-TDA-(Rac)-Al}})(\text{NCBH}_3)_2] \cdot 2 \text{ MeCN}$ ($\text{C3} \cdot 2 \text{ MeCN}$) along c -axis at 120 K. **Pink:** solvent channel; **Red and Blue:** chains due to *trans*-Pyridine-Pyridine-Stacking and Phenyl-1,3,4-Thiadiazole-Stacking; **Green:** *cis*-Pyridine-Pyridine-Stacking. Hydrogen atoms were removed for better overview.

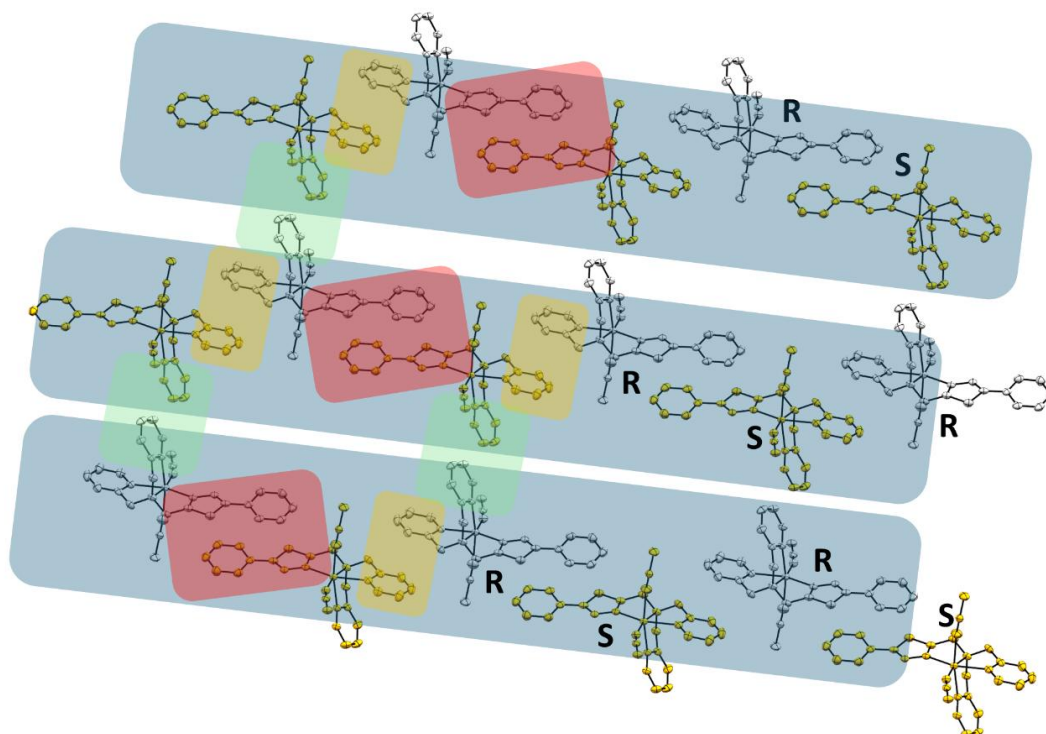


Figure S32: Visualisation of the stacking for $[\text{Fe}(\text{L}^{\text{Ph-TDA-(Rac)-Al}})(\text{NCBH}_3)_2] \cdot 2 \text{ MeCN}$ ($\text{C3} \cdot 2 \text{ MeCN}$) along the chains (**Blue**) with Phenyl-1,3,4-Thiadiazole-units (**Red**) and Pyridine-Pyridine-units stacking (**Yellow**) and Pyridine-Pyridine-units stacking (**Green**) forming the linked 2D network with alternating R/S-enantiomers.

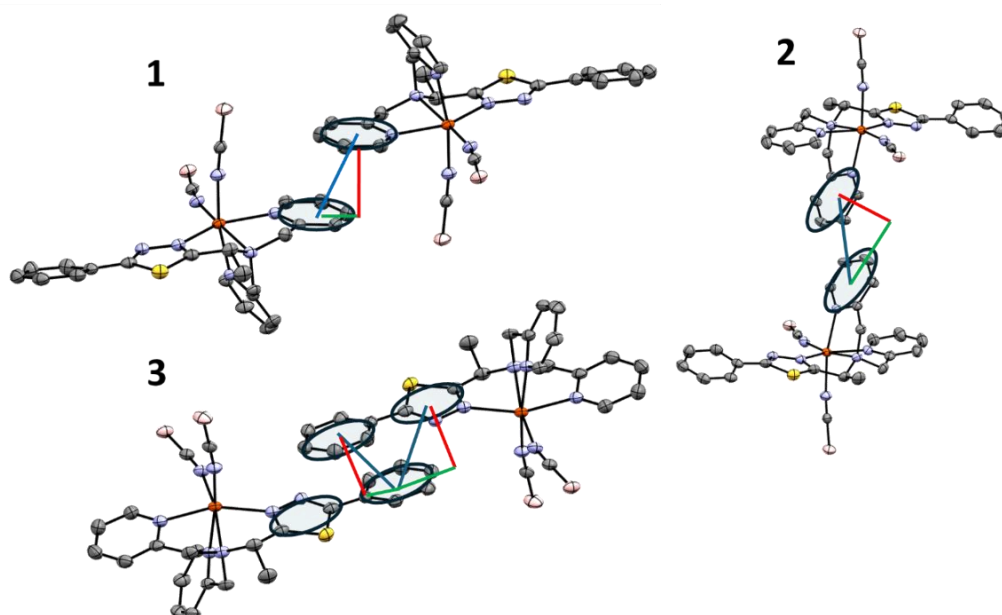


Figure S33: Visualisation of the π - π -interaction between Pyridine- and Pyridine-units (1) and Pyridine- and Pyridine-units (2), Phenyl-1,3,4-Thiadiazole-units (3) with off-set (green), normal vector (red) and centroid-centroid-distance (blue) for complex $[[\text{Fe}(\text{L}^{\text{Ph-TDA-Rac-Al}})(\text{NCBH}_3)_2] \cdot 2 \text{ MeCN}$ (**C3** \cdot 2 MeCN) at 120 K. The values are given in **Table S1**.

Table S1: Values of the π - π -interaction centroid-centroid-distance, off-set and normal vector for Complex $[\text{Fe}(\text{L}^{\text{Ph-TDA-Rac-Al}})(\text{NCBH}_3)_2] \cdot 2 \text{ MeCN}$ (**C3** \cdot 2 MeCN) at 120 K.

Interactions	centroid-centroid distance / Å	off-set / Å	normal vector / Å
trans-Pyridine-Pyridine (1)	4.239	1.940	3.768
Cis-Pyridine-Pyridine (2)	4.677	3.223	3.392
Phenyl-1,3,4-Thiadiazole (3)	3.959	2.120	3.824
Phenyl-Phenyl (3)	4.514	2.756	3.574

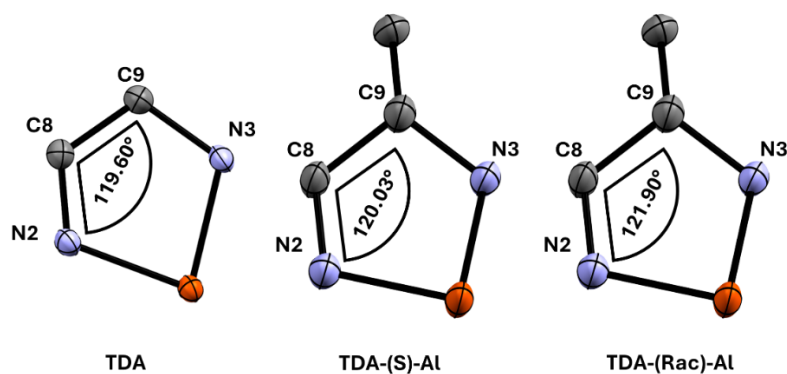


Figure S34: Visualisation of bite angle for the reported complex $[\text{Fe}(\text{L}^{\text{Ph-TDA}})(\text{NCBH}_3)_2] \cdot \text{H}_2\text{O}$ (left), $[\text{Fe}(\text{L}^{\text{Ph-TDA-(S)-Al}})(\text{NCBH}_3)_2] \cdot 1.5 \text{ MeCN}$ (**C1** \cdot 1.5 MeCN) (middle) and $[\text{Fe}(\text{L}^{\text{Ph-TDA-(Rac)-Al}})(\text{NCBH}_3)_2] \cdot 2 \text{ MeCN}$ (**C3** \cdot 2 MeCN) (right).

Table S2: Measurement parameters for $[\text{Fe}(\text{L}^{\text{Ph-TDA-(S-Al)}})(\text{NCBH}_3)_2] \cdot 1.5 \text{ MeCN}$ (**C1** · 1.5 MeCN) at 120 K.

Parameter	Results
Empirical formula	$\text{C}_{27}\text{H}_{31.5}\text{B}_2\text{FeN}_{8.5}\text{S}$ ($\text{C}_{24}\text{H}_{27}\text{B}_2\text{FeN}_7\text{S}$ 1.5 $\text{C}_2\text{H}_3\text{N}$)
Formula weight	584.64
Temperature/K	120
Crystal system	monoclinic
Space group	C2
a/Å	23.5289(9)
b/Å	10.8092(3)
c/Å	11.7115(4)
$\alpha/^\circ$	90
$\beta/^\circ$	92.313(3)
$\gamma/^\circ$	90
Volume/Å³	2976.14(17)
Z	4
$\rho_{\text{calc}}/\text{g}/\text{cm}^3$	1.305
μ/mm^{-1}	0.609
F(000)	1220
Radiation	Mo K α ($\lambda = 0.71073$)
2θ range for data collection/$^\circ$	2.406 to 32.702
Index ranges	$-32 \leq h \leq 31$, $-15 \leq k \leq 14$, $-16 \leq l \leq 16$
Reflections collected	26318
Independent reflections	8370 [$R_{\text{int}} = 0.0401$, $R_{\text{sigma}} = 0.0337$]
Data/restraints/parameters	9179/61/371
Goodness-of-fit on F²	1.109
Final R indexes [$I \geq 2\sigma(I)$]	$R_1 = 0.0873$, $wR_2 = 0.2304$
Final R indexes [all data]	$R_1 = 0.0920$, $wR_2 = 0.2378$

Table S3: Measurement parameters for $[\text{Fe}(\text{L}^{\text{Ph-TDA-(S-Al)}})(\text{NCBH}_3)_2] \cdot 1.5 \text{ MeCN} (\text{C1} \cdot 1.5 \text{ MeCN})$ at 220 K.

Parameter	Results
Empirical formula	$\text{C}_{27}\text{H}_{31.5}\text{B}_2\text{FeN}_{8.5}\text{S}$ ($\text{C}_{24}\text{H}_{27}\text{B}_2\text{FeN}_7\text{S} \cdot 1.5 \text{ C}_2\text{H}_3\text{N}$)
Formula weight	584.64
Temperature/K	220
Crystal system	monoclinic
Space group	C2
a/Å	23.985(3)
b/Å	10.9860(8)
c/Å	11.9233(11)
$\alpha/^\circ$	90
$\beta/^\circ$	90.661(8)
$\gamma/^\circ$	90
Volume/Å ³	3141.5(5)
Z	4
$\rho_{\text{calc}} \text{ g/cm}^3$	1.236
μ/mm^{-1}	0.577
F(000)	1220
Radiation	Mo K α ($\lambda = 0.71073$)
2 θ range for data collection/ $^\circ$	2.395 to 32.899
Index ranges	$-32 \leq h \leq 32, -16 \leq k \leq 15, -16 \leq l \leq 16$
Reflections collected	28535
Independent reflections	7596 [$R_{\text{int}} = 0.0444, R_{\text{sigma}} = 0.0364$]
Data/restraints/parameters	9677/76/390
Goodness-of-fit on F ²	1.096
Final R indexes [$I \geq 2\sigma(I)$]	$R_1 = 0.0900, wR_2 = 0.2427$
Final R indexes [all data]	$R_1 = 0.1043, wR_2 = 0.2677$

Table S4: Measurement parameters for $[\text{Fe}(\text{L}^{\text{Ph-TDA-(Rac)-Al}})(\text{NCBH}_3)_2] \cdot 2 \text{ MeCN} (\mathbf{C3} \cdot 2 \text{ MeCN})$ at 120 K.

Parameter	Results
Empirical formula	$\text{C}_{27}\text{H}_{31.5}\text{B}_2\text{FeN}_{8.5}\text{S} (\text{C}_{24}\text{H}_{27}\text{B}_2\text{FeN}_7\text{S} 2 \text{ C}_2\text{H}_3\text{N})$
Formula weight	605.16
Temperature/K	120
Crystal system	triclinic
Space group	P-1
a/Å	9.3799(3)
b/Å	12.0599(3)
c/Å	14.5887(4)
$\alpha/^\circ$	88.851(2)
$\beta/^\circ$	84.528(2)
$\gamma/^\circ$	73.327(2)
Volume/Å³	1573.65(8)
Z	2
$\rho_{\text{calc}}/\text{g}/\text{cm}^3$	1.277
μ/mm^{-1}	4.721
F(000)	632
Radiation	Cu K α ($\lambda = 1.54186$)
2θ range for data collection/$^\circ$	5.317 to 68.515
Index ranges	$-11 \leq h \leq 11, -15 \leq k \leq 14, -16 \leq l \leq 14$
Reflections collected	33556
Independent reflections	5341 [$R_{\text{int}} = 0.0316, R_{\text{sigma}} = 0.0163$]
Data/restraints/parameters	5451/0/375
Goodness-of-fit on F²	1.075
Final R indexes [$I \geq 2\sigma(I)$]	$R_1 = 0.0562, wR_2 = 0.1576$
Final R indexes [all data]	$R_1 = 0.0567, wR_2 = 0.1587$

Table S5: Fe-N bond angles for the complex $[\text{Fe}(\text{L}^{\text{Ph-TDA-(S)-Al}})(\text{NCBH}_3)_2] \cdot 1.5 \text{ MeCN}$ (**C1** · 1.5 MeCN) 120 K.

	Bond angle / °		Bond angle / °		Bond angle / °
N2 Fe1 N3	81.7(2)	N5 Fe1 N3	85.1(2)	N7 Fe1 N5	94.1(2)
N4 Fe1 N3	83.4(2)	N5 Fe1 N4	85.3(2)	N7 Fe1 N6	87.8(2)
N4 Fe1 N6	91.9(2)	N7 Fe1 N2	100.2(2)	N6 Fe1 N2	89.52(19)
N5 Fe1 N2	92.74(19)	N7 Fe1 N4	94.7(2)	N6 Fe1 N3	92.9(2)

Table S6: Fe-N bond angles for the complex $[\text{Fe}(\text{L}^{\text{Ph-TDA-(S)-Al}})(\text{NCBH}_3)_2] \cdot 1.5 \text{ MeCN}$ (**C1** · 1.5 MeCN) 220 K.

	Bond angle / °		Bond angle / °		Bond angle / °
N2 Fe1 N3	75.70(18)	N5 Fe1 N4	82.1(2)	N7 Fe1 N6	92.3(3)
N4 Fe1 N3	78.24(19)	N7 Fe1 N2	108.6(3)	N6 Fe1 N2	88.0(2)
N5 Fe1 N2	91.33(19)	N7 Fe1 N4	97.3(3)	N6 Fe1 N3	91.9(2)
N5 Fe1 N3	79.7(2)	N7 Fe1 N5	96.0(3)	N6 Fe1 N4	94.8(2)

Table S7: Fe-N bond angles for the complex $[\text{Fe}(\text{L}^{\text{Ph-TDA-(Rac)-Al}})(\text{NCBH}_3)_2] \cdot 2 \text{ MeCN}$ (**C3** · 2 MeCN) 120 K.

	Bond angle / °		Bond angle / °		Bond angle / °
N5 Fe1 N2	95.77(7)	N4 Fe1 N3	76.30(7)	N7 Fe1 N5	92.98(7)
N5 Fe1 N4	81.50(7)	N6 Fe1 N2	89.05(7)	N7 Fe1 N2	113.22(8)
N5 Fe1 N3	78.45(7)	N6 Fe1 N4	89.49(8)	N7 Fe1 N4	95.72(8)
N2 Fe1 N3	74.93(7)	N6 Fe1 N3	93.32(7)	N7 Fe1 N6	94.22(8)

Table S8: Iron(II) -Nitrogen bond length and average bond length for $[\text{Fe}(\text{L}^{\text{Ph-TDA-(S)-Al}})(\text{NCBH}_3)_2] \cdot 1.5 \text{ MeCN}$ (**C1** · 1.5 MeCN) at 120 K and 220 K and complex $[\text{Fe}(\text{L}^{\text{Ph-TDA-(Rac)-Al}})(\text{NCBH}_3)_2] \cdot 2 \text{ MeCN}$ (**C3** · 2 MeCN) at 120 K.

	C1 at 120 K	C1 at 220 K	C3 at 120 K
Average	1.975	2.133	2.181
Fe1 N2	1.994(4)	2.175(5)	2.1939(18)
Fe1 N3	2.009(5)	2.207(4)	2.1957(19)
Fe1 N4	1.972(5)	2.136(6)	2.209(2)
Fe1 N5	1.961(5)	2.131(6)	2.2744(19)
Fe1 N6	1.975(5)	2.100(6)	2.127(2)
Fe1 N7	1.938(5)	2.051(8)	2.086(2)
Spin state iron(II)	LS	HS	HS

5. Temperature dependent magnetization measurement

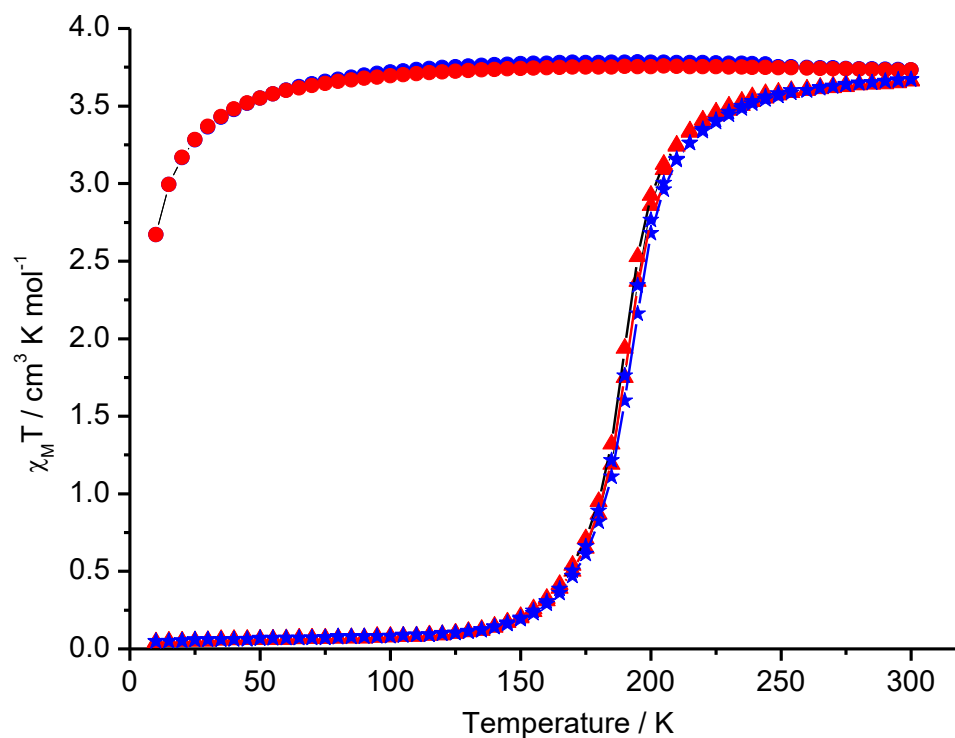


Figure S35: $\chi_M T$ vs. T measured of microcrystalline product of $[\text{Fe}(\text{L}^{\text{Ph-TDA-(S-Al)}})(\text{NCBH}_3)_2] \cdot 0.5 \text{H}_2\text{O}$ (**C1** · 0.5 H₂O) (**Star**), $[\text{Fe}(\text{L}^{\text{Ph-TDA-(R-Al)}})(\text{NCBH}_3)_2] \cdot 0.5 \text{H}_2\text{O}$ (**C2** · 0.5 H₂O) (**Triangle**) and $[\text{Fe}(\text{L}^{\text{Ph-TDA-(Rac-Al)}})(\text{NCBH}_3)_2]$ (**C3**) (**Sphere**) in the form of the resulting $\chi_M T$ vs. T plot. Magnetic susceptibility was determined between 300 - 10 K (blue) and 10-300 K (red).

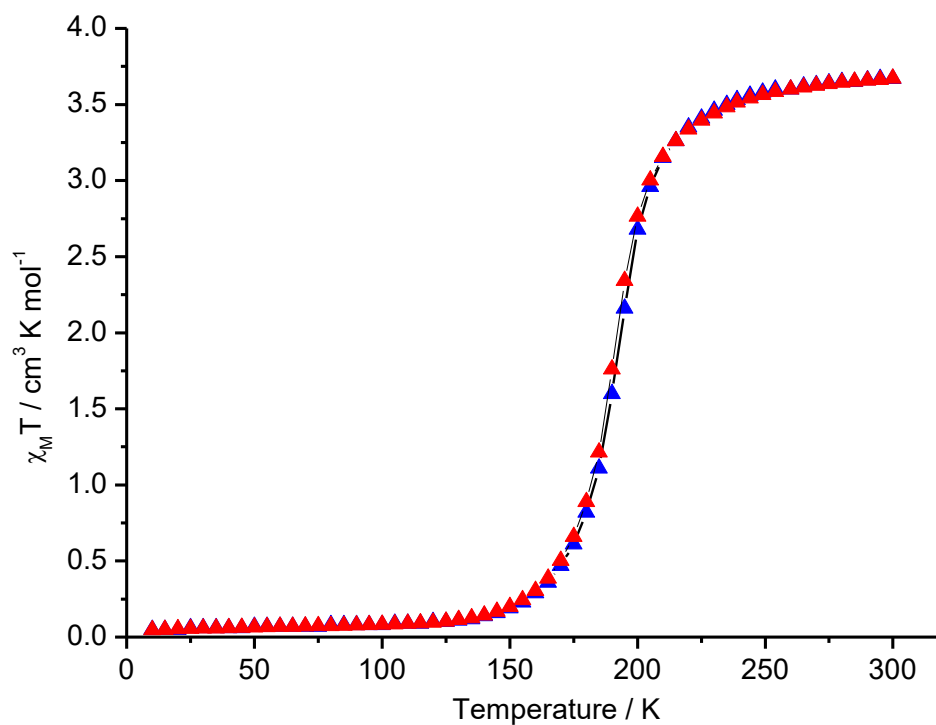


Figure S36: χ_M vs. T measured of microcrystalline product of $[\text{Fe}(\text{L}^{\text{Ph-TDA-(S)-Al}})(\text{NCBH}_3)_2] \cdot 0.5 \text{H}_2\text{O}$ (**C1** · 0.5 H₂O) in the form of the resulting $\chi_M T$ vs. T plot. Magnetic susceptibility was determined between 300 - 10 K (blue) and 10 - 300 K (red).

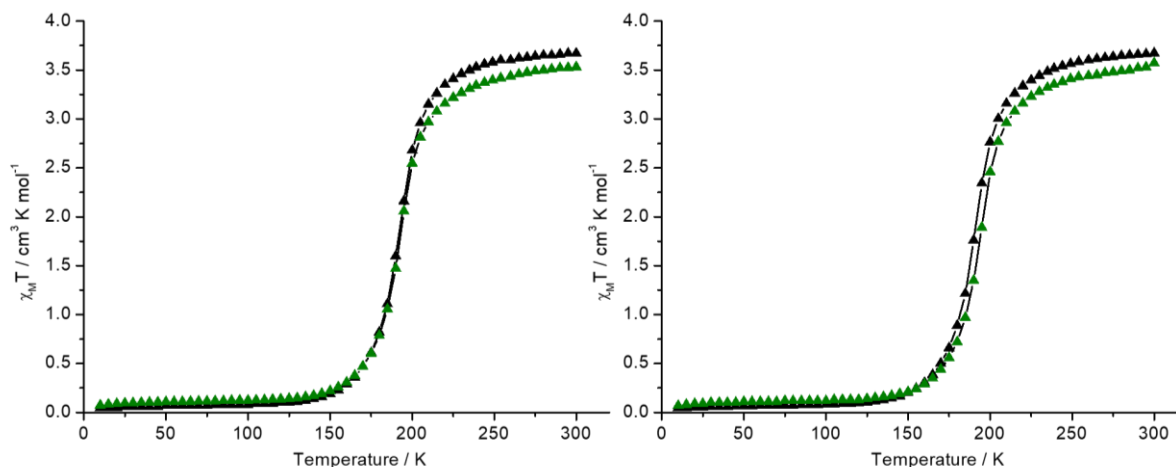


Figure S37: χ_M vs. T measured of microcrystalline product of $[\text{Fe}(\text{L}^{\text{Ph-TDA-(S)-Al}})(\text{NCBH}_3)_2] \cdot 0.5 \text{H}_2\text{O}$ (**C1** · 0.5 H₂O) in the form of the resulting $\chi_M T$ vs. T plot. Magnetic susceptibility was determined between 300 - 10 K (left) and 10 - 300 K (right) for the first cycle (black) and the second cycle (green) after 30 minutes on plateau at 300 K.

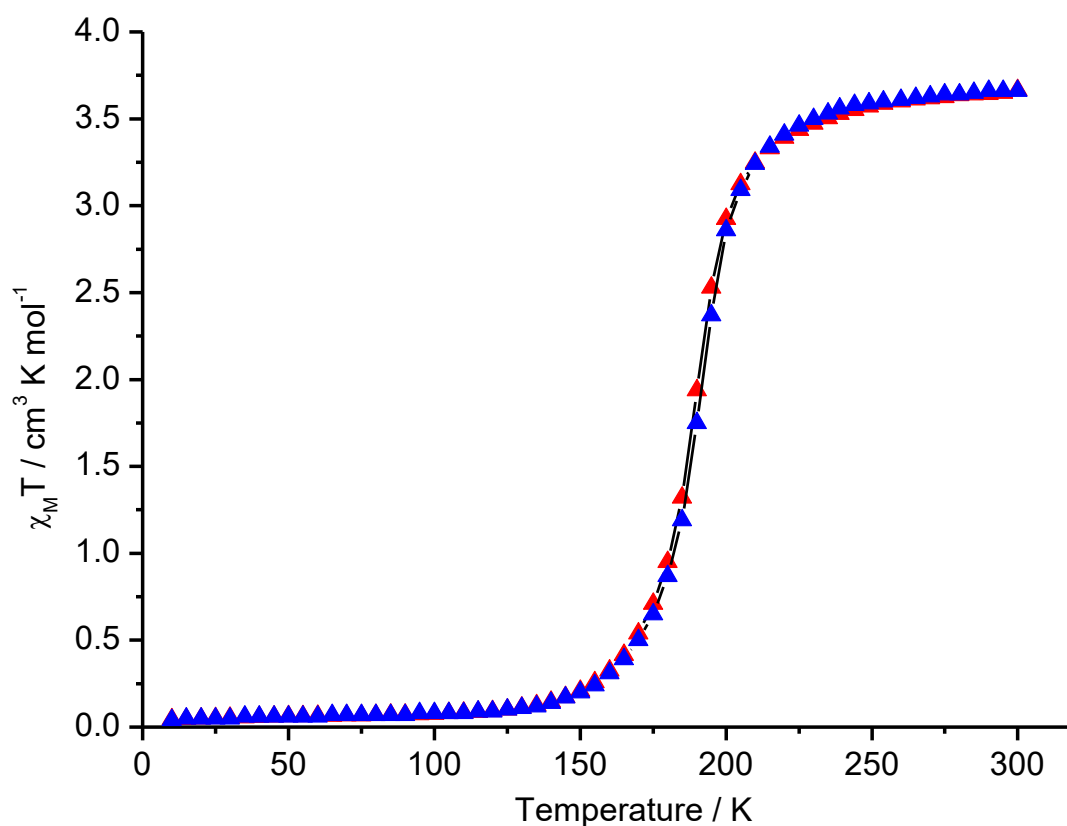


Figure S38: χ_M vs. T measured of microcrystalline product of $[\text{Fe}(\text{L}^{\text{Ph-TDA-(R)-Al}})(\text{NCBH}_3)_2] \cdot 0.5 \text{H}_2\text{O}$ (**C2** · 0.5 H₂O) in the form of the resulting $\chi_M T$ vs. T plot. Magnetic susceptibility was determined between 300 - 10 K (blue) and 10-300 K (red).

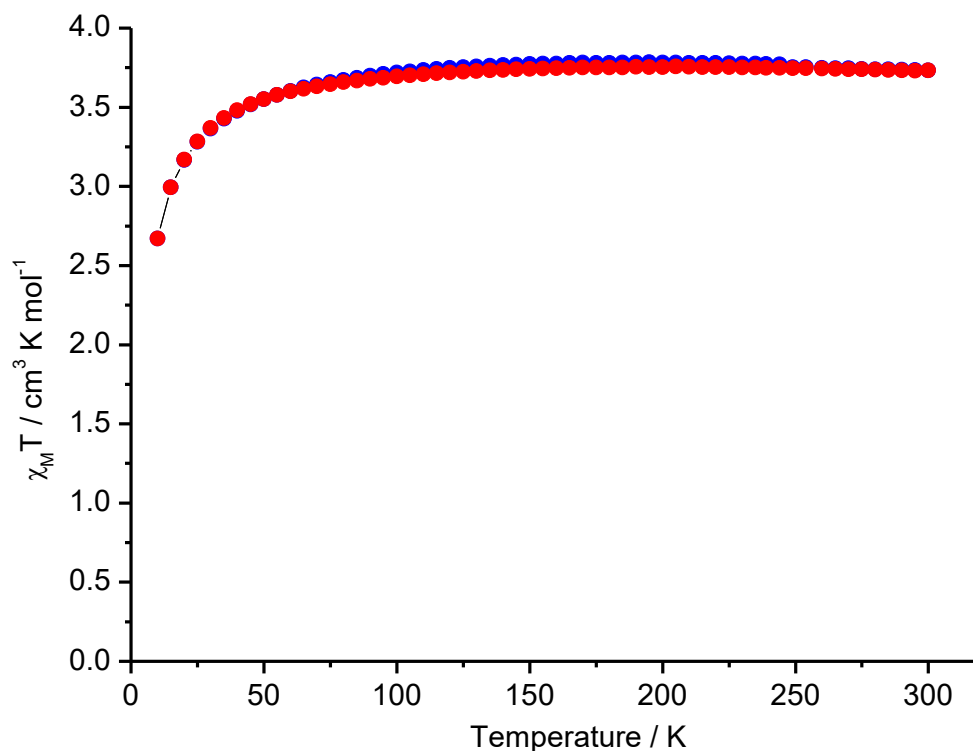


Figure S39: χ_M vs. T measured of microcrystalline product of $[\text{Fe}(\text{L}^{\text{Ph-TDA-Rac-Al}})(\text{NCBH}_3)_2]$ (**C3**) in the form of the resulting $\chi_M T$ vs. T plot. Magnetic susceptibility was determined between 300-10 K (blue) and 10 - 300 K (red).

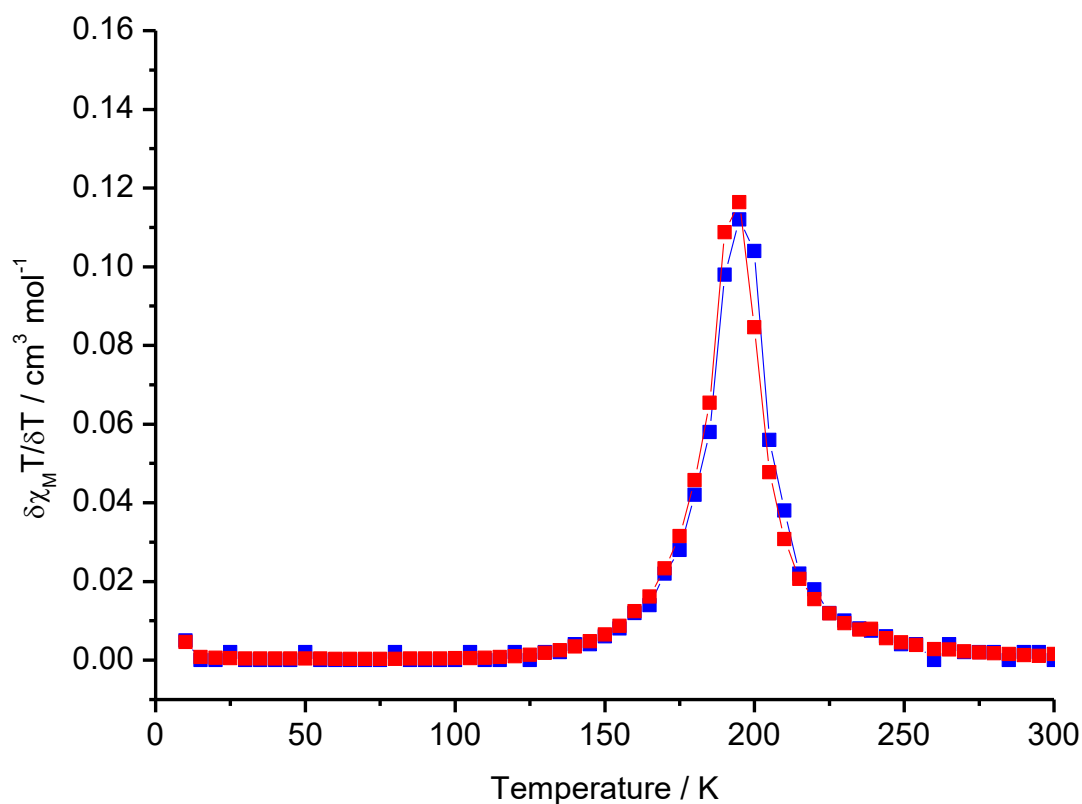


Figure S40: First derivative of $\frac{\delta\chi_M T}{\delta T}$ with respect to T for $[\text{Fe}(\text{L}^{\text{Ph-TDA-S-Al}})(\text{NCBH}_3)_2] \cdot 0.5 \text{H}_2\text{O}$ (**C1** · 0.5 H₂O) in the form of the resulting of $\frac{\delta\chi_M T}{\delta T}$ vs. T plot. Magnetic susceptibility was determined between 300 - 10 K (blue) and 10 - 300 K (red).

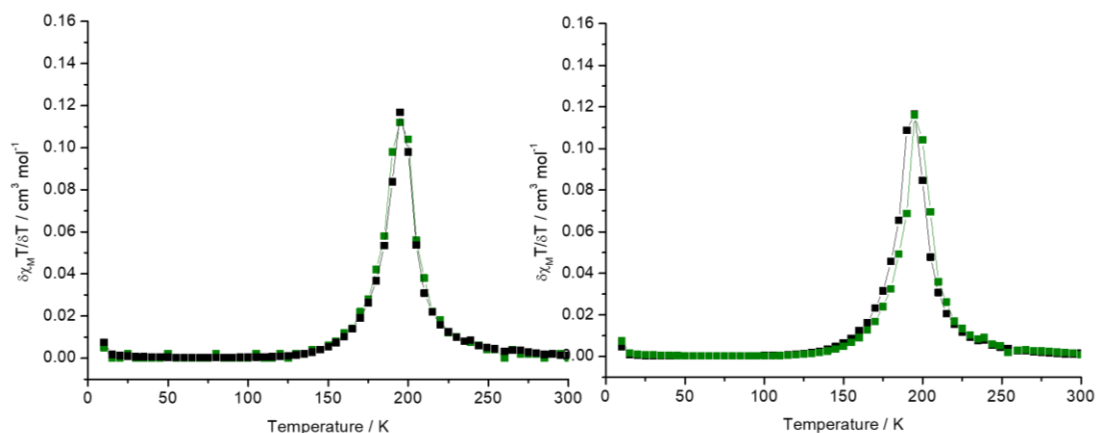


Figure S41: First derivative of $\frac{\delta\chi_M T}{\delta T}$ with respect to T for $[\text{Fe}(\text{L}^{\text{Ph-TDA-(S)-Al}})(\text{NCBH}_3)_2] \cdot 0.5 \text{H}_2\text{O}$ (**C1** · 0.5 H₂O) in the form of the resulting $\frac{\delta\chi_M T}{\delta T}$ vs. T plot. Magnetic susceptibility was determined between 300 - 10 K (**left**) and 10 - 300 K (**right**) for the first cycle (**black**) and the second cycle (**green**) after 30 minutes on plateau at 300 K.

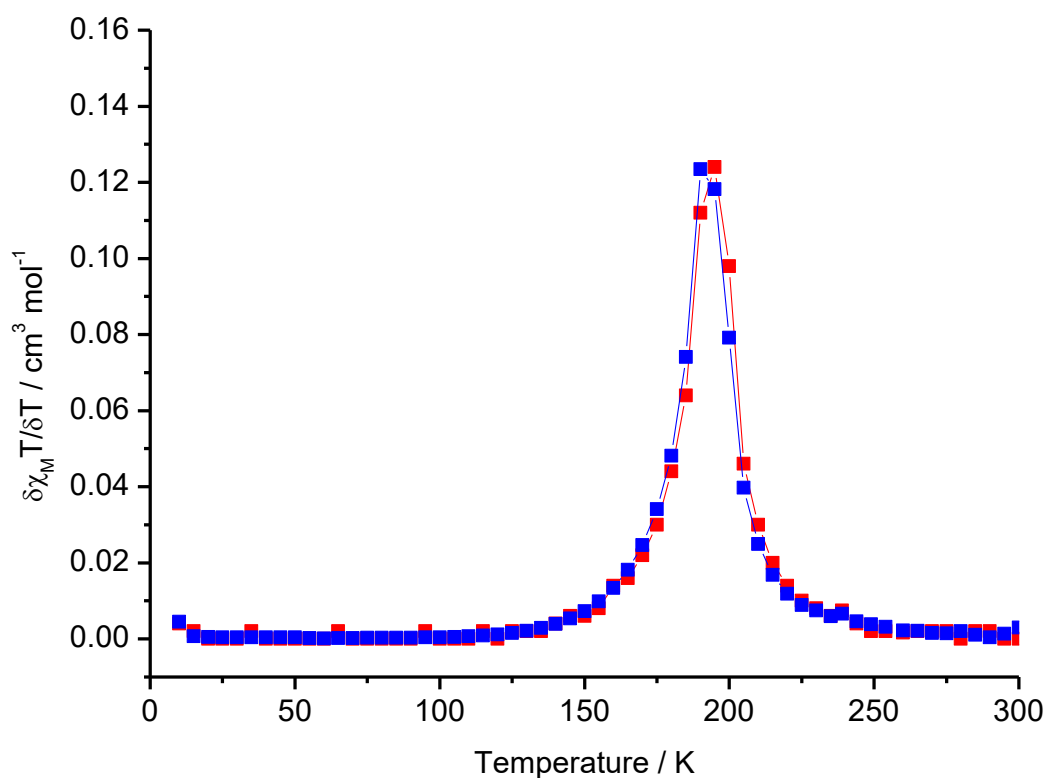


Figure S42: First derivative of $\frac{\delta\chi_M T}{\delta T}$ with respect to T for $[\text{Fe}(\text{L}^{\text{Ph-TDA-(R)-Al}})(\text{NCBH}_3)_2] \cdot 0.5 \text{H}_2\text{O}$ (**C2** · 0.5 H₂O) in the form of the resulting $\frac{\delta\chi_M T}{\delta T}$ vs. T plot. Magnetic susceptibility was determined between 300 - 10 K (**blue**) and 10 - 300 K (**red**).

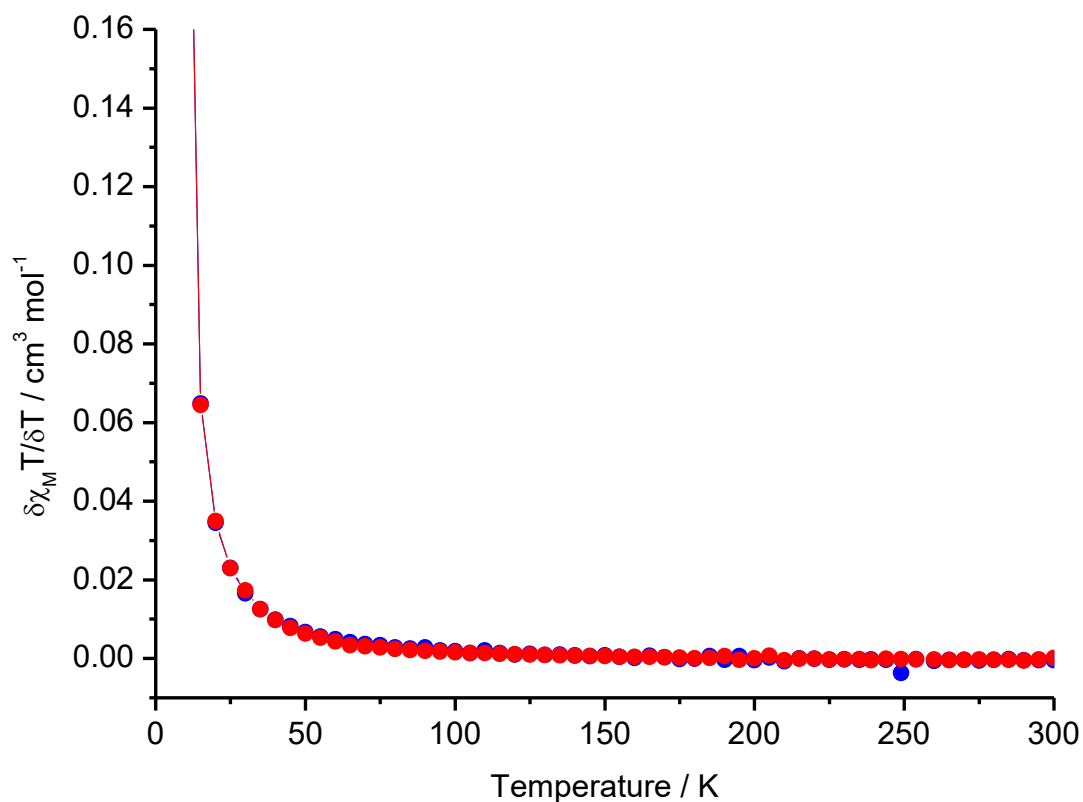


Figure S43: First derivative of $\frac{\delta\chi_M T}{\delta T}$ with respect to T for $[\text{Fe}(\text{L}^{\text{Ph-TDA-(Rac-Al)}})(\text{NCBH}_3)_2]$ (**C3**) in the form of the resulting $\frac{\delta\chi_M T}{\delta T}$ vs. T plot. Magnetic susceptibility was determined between 300 - 10 K (blue) and 10 - 300 K (red).

6. CD-Spectra and chiral HPLC

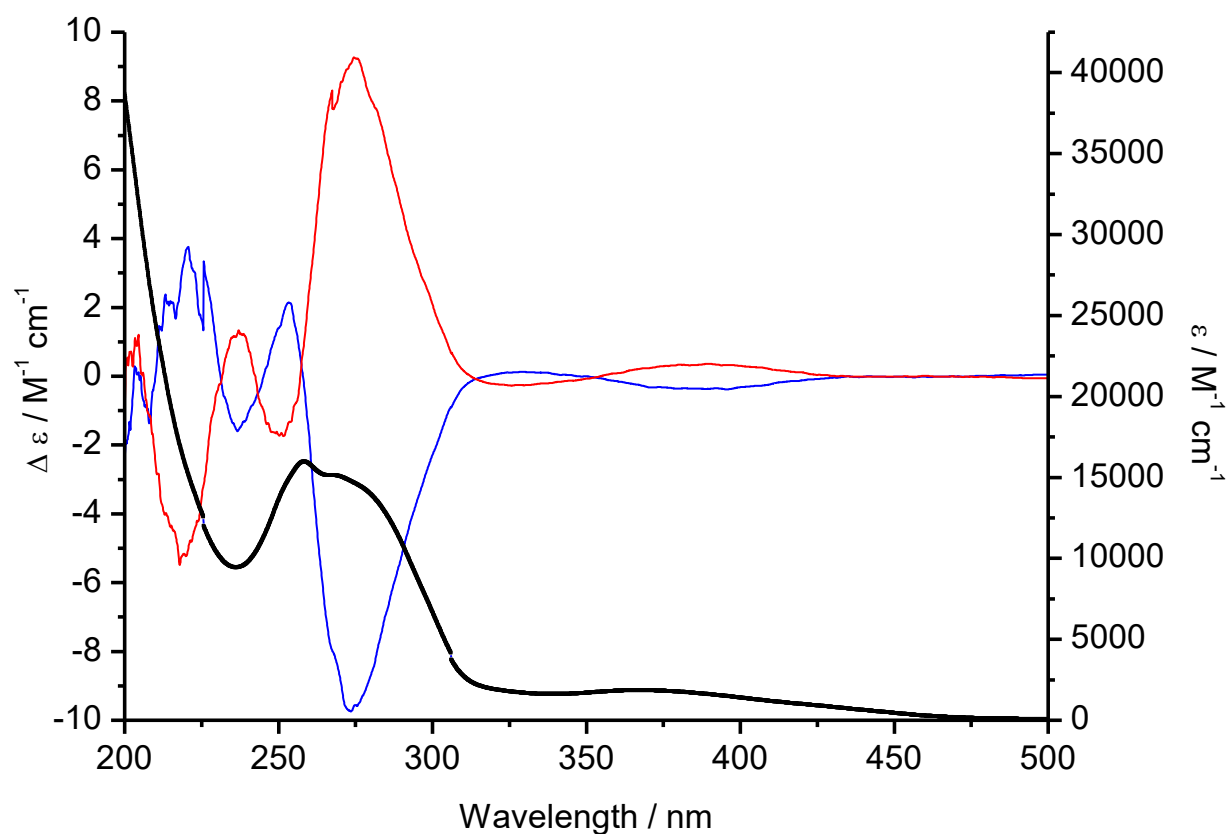


Figure S44: CD-spectra of $[\text{Fe}(\text{L}^{\text{Ph-TDA-(S-Al)}})(\text{NCBH}_3)_2] \cdot 0.5 \text{ H}_2\text{O}$ (**C1** · 0.5 H₂O) (**blue**), $[\text{Fe}(\text{L}^{\text{Ph-TDA-(R-Al)}})(\text{NCBH}_3)_2] \cdot 0.5 \text{ H}_2\text{O}$ (**C2** · 0.5 H₂O) (**red**) and UV-Vis absorption spectrum $[\text{Fe}(\text{L}^{\text{Ph-TDA-(S-Al)}})(\text{NCBH}_3)_2] \cdot 0.5 \text{ H}_2\text{O}$ (**C1**) (**black**).

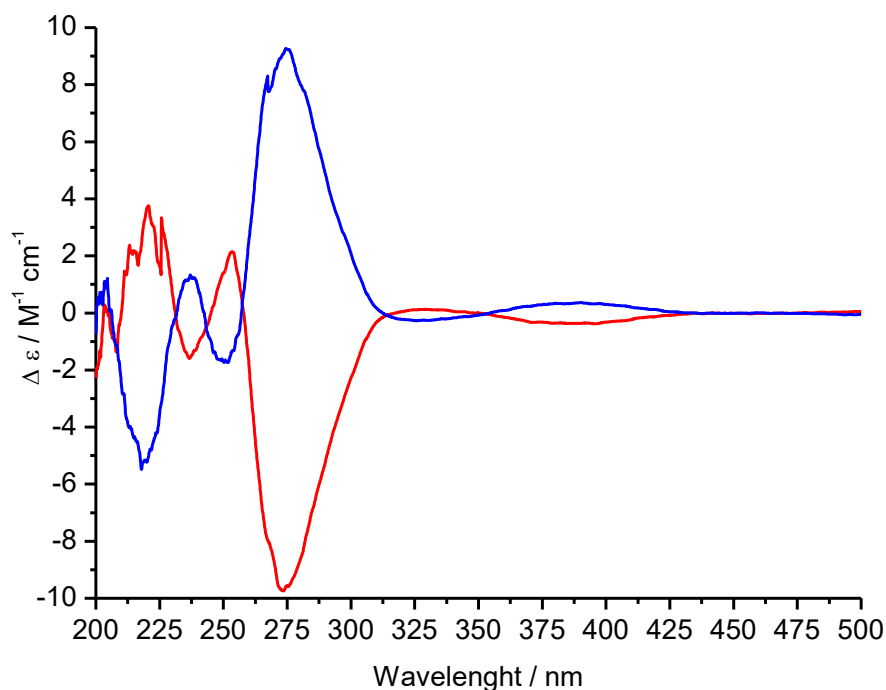


Figure S45: CD-spectra of $[\text{Fe}(\text{L}^{\text{Ph-TDA-(S-Al)}})(\text{NCBH}_3)_2] \cdot 0.5 \text{ H}_2\text{O}$ (**C1** · 0.5 H₂O) (**blue**), $[\text{Fe}(\text{L}^{\text{Ph-TDA-(R-Al)}})(\text{NCBH}_3)_2] \cdot 0.5 \text{ H}_2\text{O}$ (**C2** · 0.5 H₂O) (**red**).

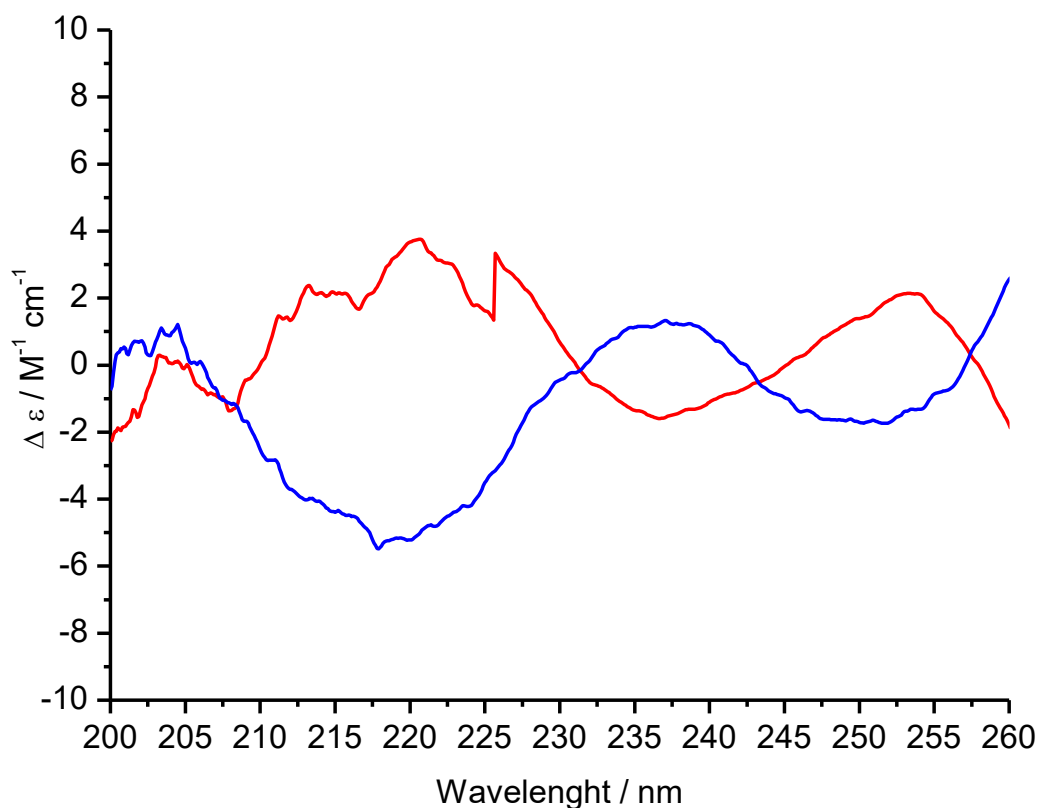


Figure S46: CD-spectra of $[\text{Fe}(\text{L}^{\text{Ph-TDA-(S)-Al}})(\text{NCBH}_3)_2] \cdot 0.5 \text{ H}_2\text{O}$ (**C1** · 0.5 H_2O) (**blue**), $[\text{Fe}(\text{L}^{\text{Ph-TDA-(R)-Al}})(\text{NCBH}_3)_2] \cdot 0.5 \text{ H}_2\text{O}$ (**C2** · 0.5 H_2O) (**red**) from 200 nm to 260 nm.

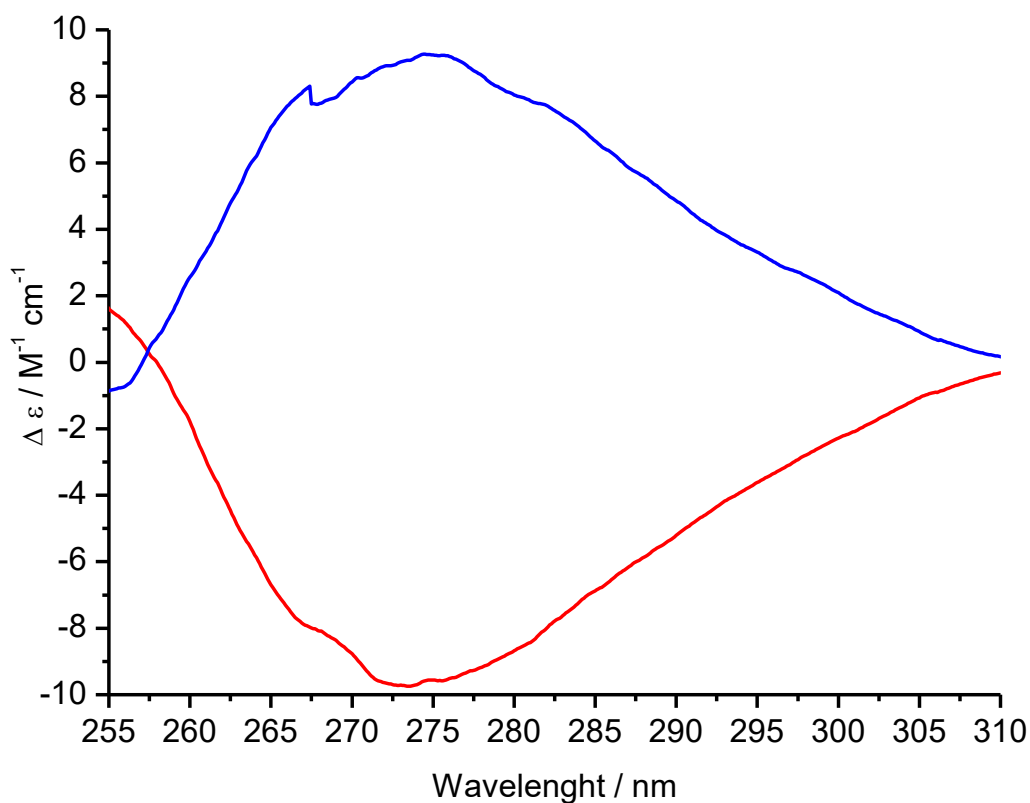


Figure S47: CD-spectra of $[\text{Fe}(\text{L}^{\text{Ph-TDA-(S)-Al}})(\text{NCBH}_3)_2] \cdot 0.5\text{H}_2\text{O}$ (**C1** · 0.5 H_2O) (**blue**), $[\text{Fe}(\text{L}^{\text{Ph-TDA-(R)-Al}})(\text{NCBH}_3)_2] \cdot 0.5 \text{ H}_2\text{O}$ (**C2** · 0.5 H_2O) (**red**) from 255 nm to 310 nm.

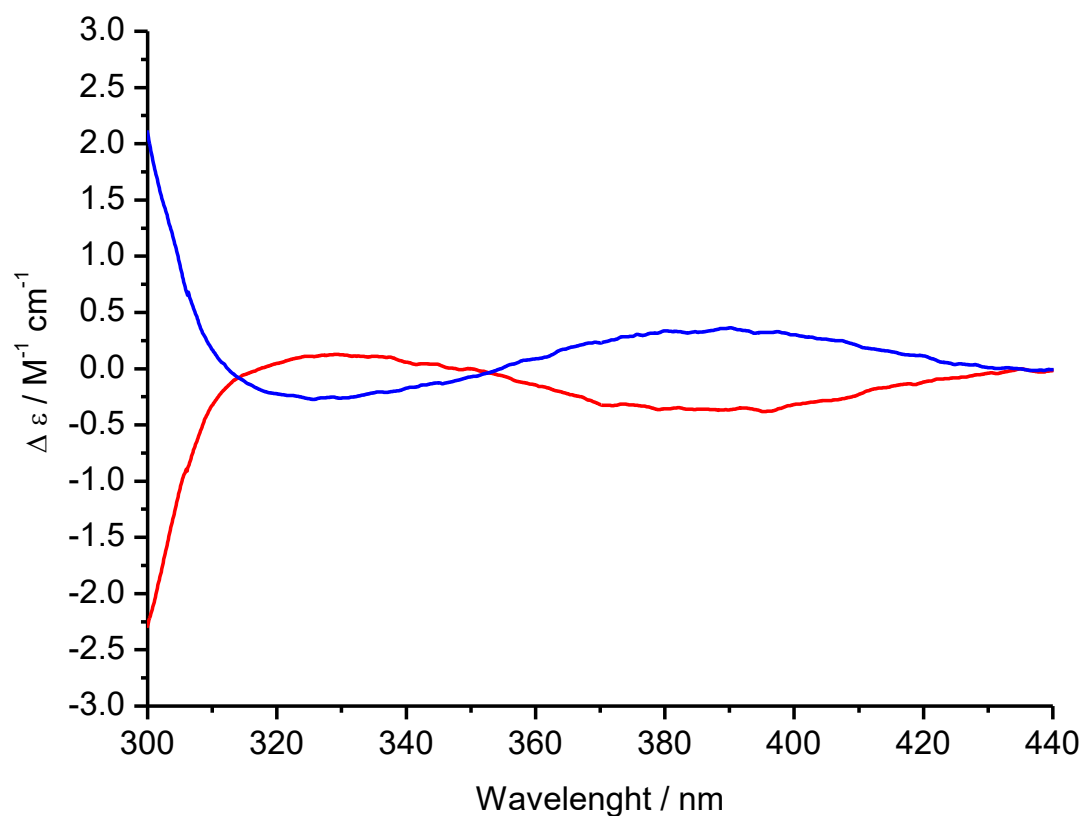


Figure S48: CD-spectra of $[\text{Fe}(\text{L}^{\text{Ph-TDA-(S)-Al}})(\text{NCBH}_3)_2] \cdot 0.5 \text{ H}_2\text{O}$ (**C1** · 0.5 H₂O) (**blue**), $[\text{Fe}(\text{L}^{\text{Ph-TDA-(R)-Al}})(\text{NCBH}_3)_2] \cdot 0.5 \text{ H}_2\text{O}$ (**C2** · 0.5 H₂O) (**red**) from 300 nm to 440 nm.

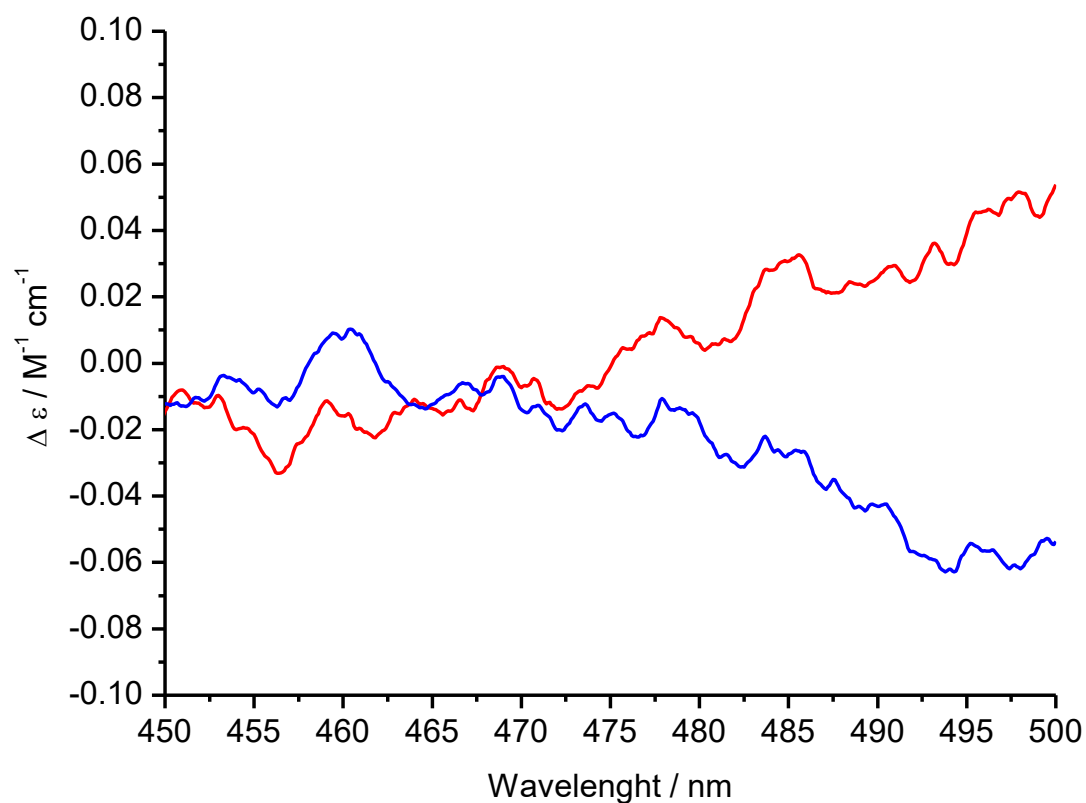


Figure S49: CD-spectra of $[\text{Fe}(\text{L}^{\text{Ph-TDA-(S)-Al}})(\text{NCBH}_3)_2] \cdot 0.5 \text{ H}_2\text{O}$ (**C1** · 0.5 H₂O) (**blue**), $[\text{Fe}(\text{L}^{\text{Ph-TDA-(R)-Al}})(\text{NCBH}_3)_2] \cdot 0.5 \text{ H}_2\text{O}$ (**C2** · 0.5 H₂O) (**red**) from 450 nm to 500 nm.

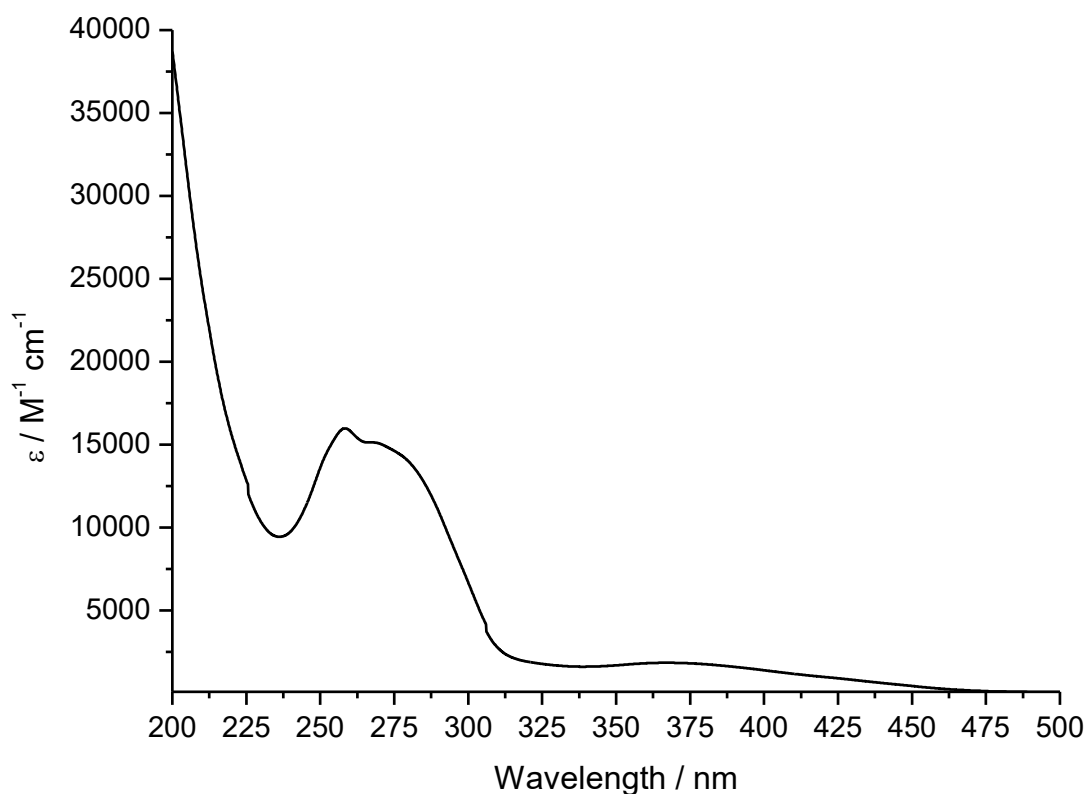


Figure S50: UV-Vis absorption spectrum $[\text{Fe}(\text{L}^{\text{Ph-TDA-(S)-Al}})(\text{NCBH}_3)_2] \cdot 0.5 \text{H}_2\text{O}$ (**C1** · 0.5 H_2O) (**black**) between 200 nm and 500 nm.

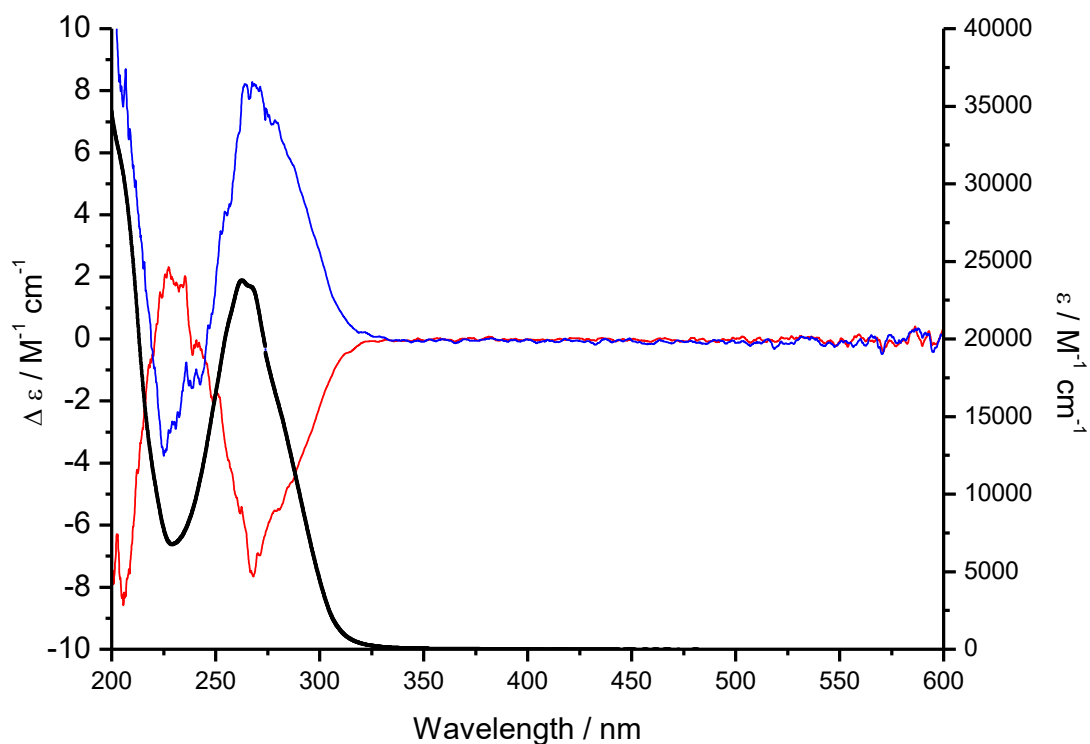


Figure S51: CD-spectra of $\text{L}^{\text{Ph-TDA-(S)-Al}}$ (**blue**) and $\text{L}^{\text{Ph-TDA-(R)-Al}}$ (**red**) and UV-Vis absorption spectrum $\text{L}^{\text{Ph-TDA-(R)-Al}}$ (**black**).

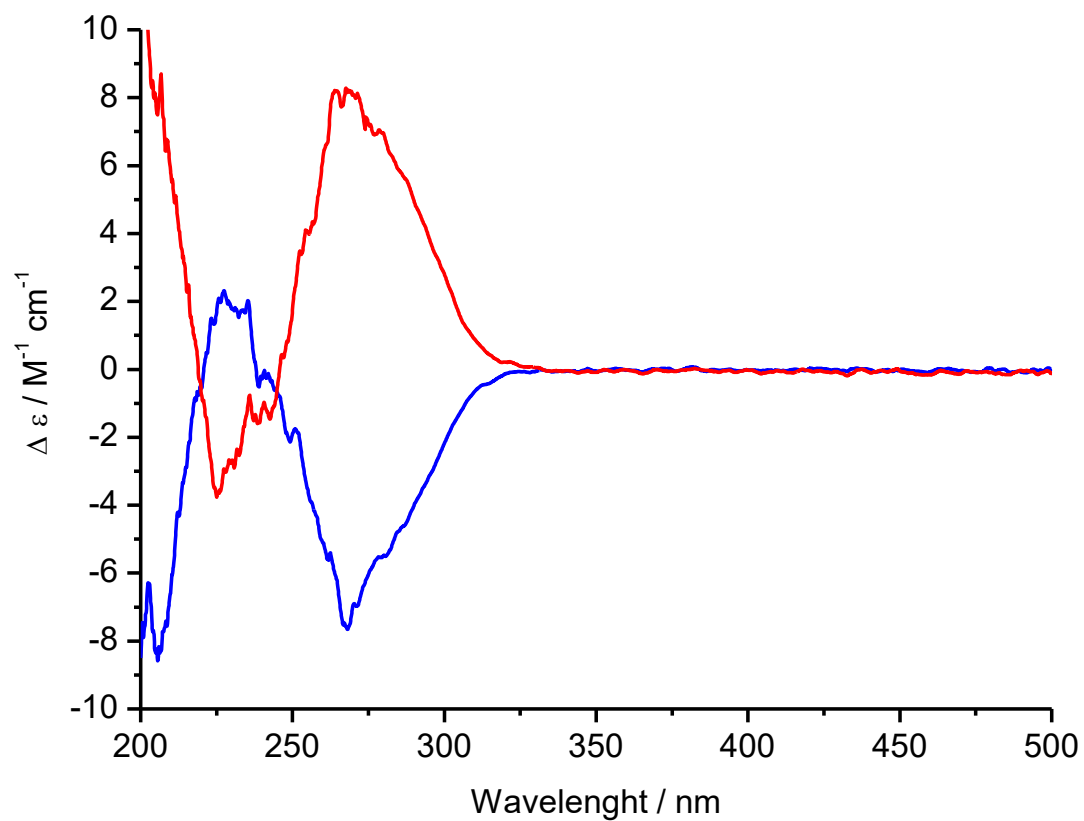


Figure S52: CD-spectra of $\text{L}^{\text{Ph-TDA-(S)-Al}}$ (blue) and $\text{L}^{\text{Ph-TDA-(R)-Al}}$ (red).

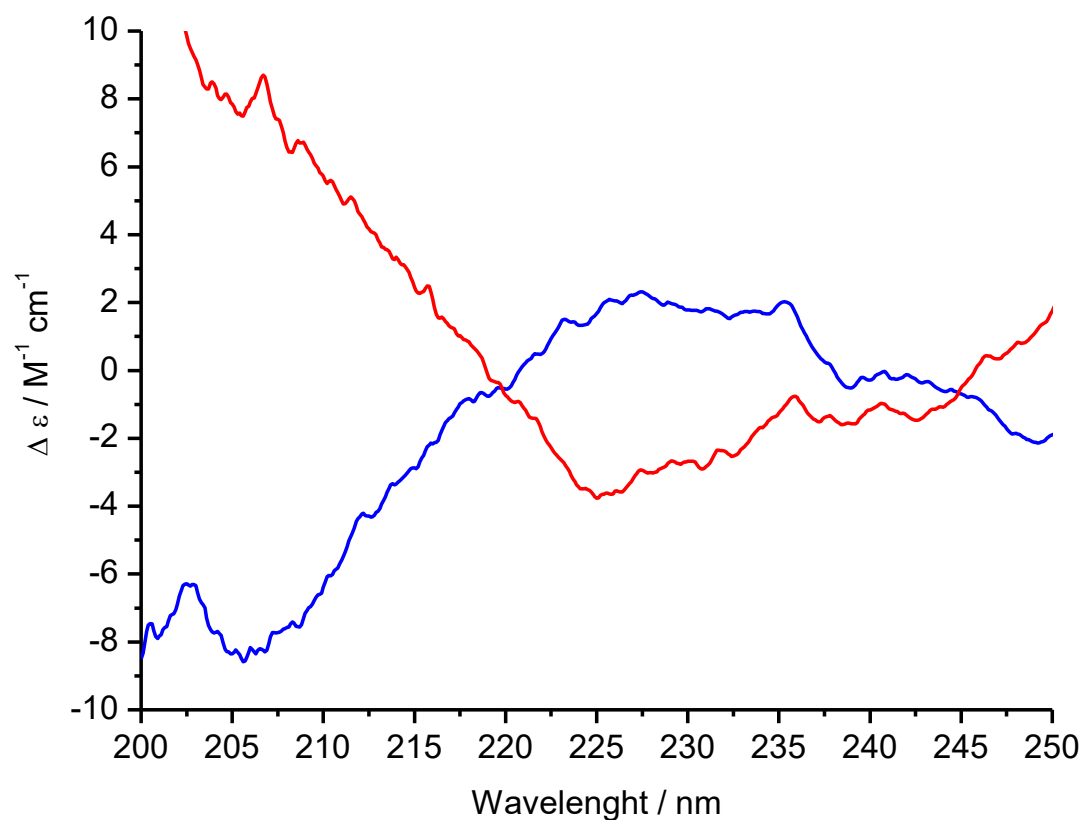


Figure S53: CD-spectra of $\text{L}^{\text{Ph-TDA-(S)-Al}}$ (blue), $\text{L}^{\text{Ph-TDA-(R)-Al}}$ (red) between 200 nm and 250 nm.

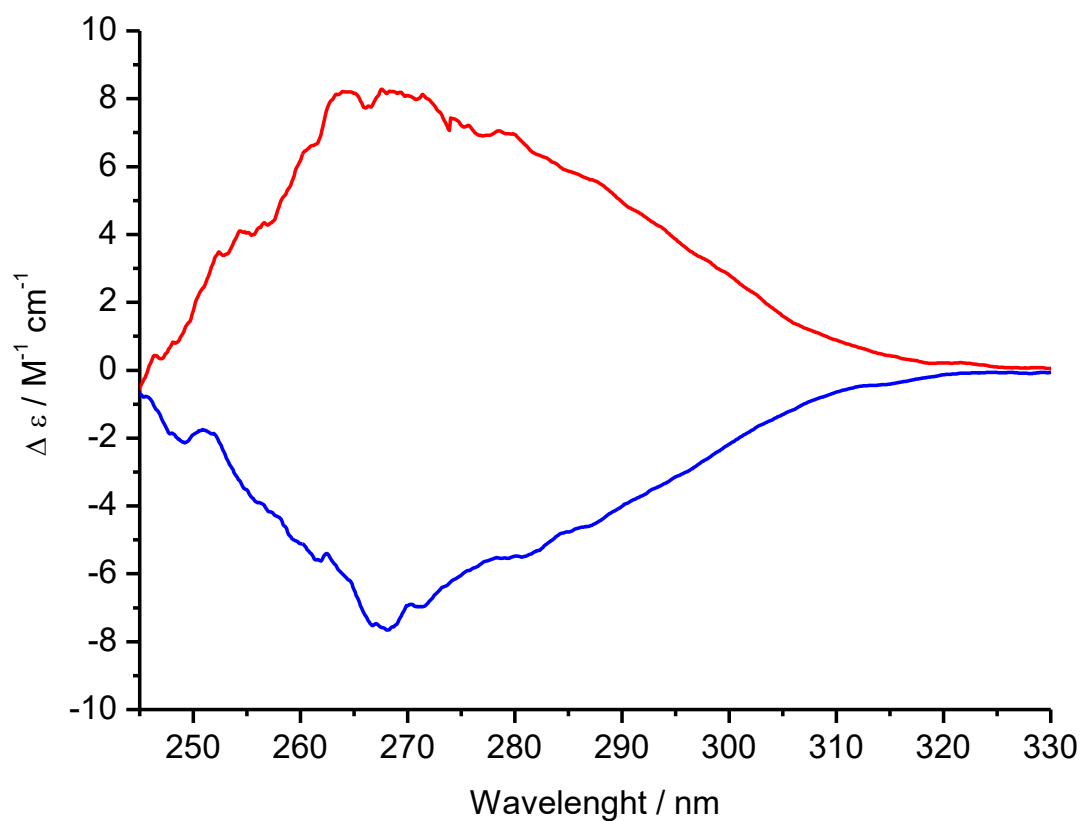


Figure S54: CD-spectra of $L^{\text{Ph-TDA-(S)-Al}}$ (blue), $L^{\text{Ph-TDA-(R)-Al}}$ (red) between 245 nm and 325 nm.

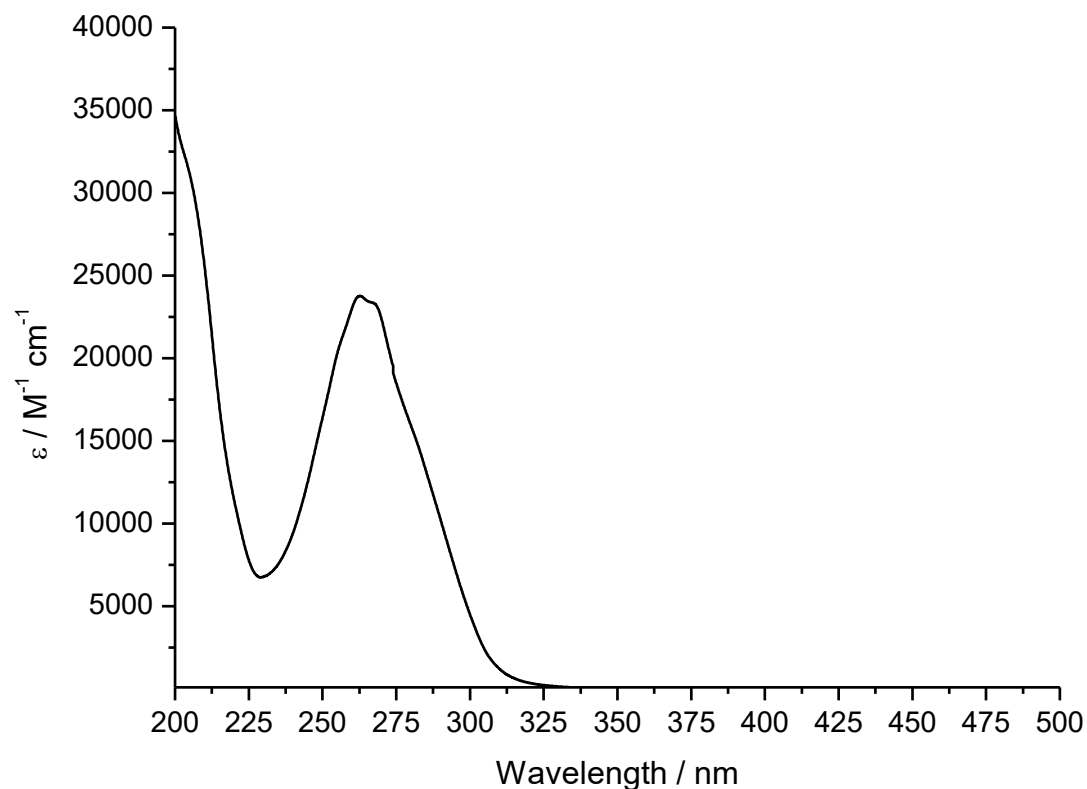


Figure S55: UV-Vis absorption spectrum $L^{\text{Ph-TDA-(R)-Al}}$ (black) between 200 nm and 500 nm.

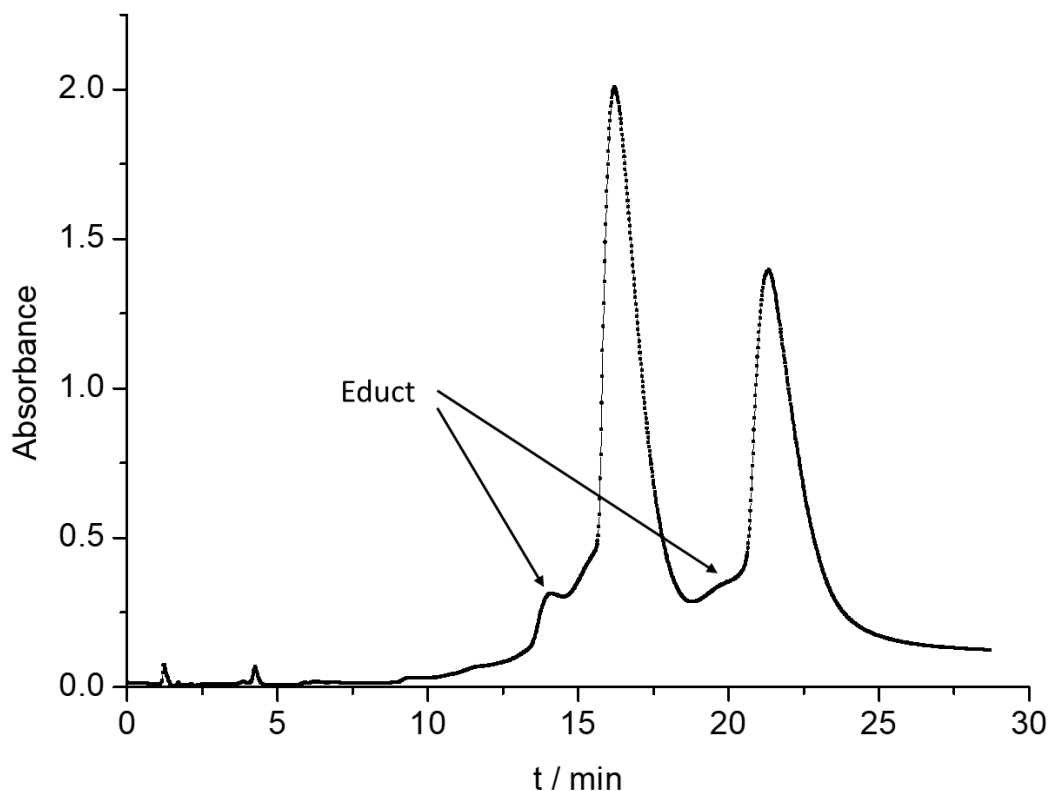


Figure S56: Analytic chiral HPLC chromatogram of the racemic mixture of $L^{\text{Ph-TDA-Al}}$ before the purification with the semi-preparable chiral HPLC. The peaks with retention time 14 min and 20 min are assigned to the educt (**I**) due to difficult separation of both by column purification.

7. References:

- [1] G. R. Fulmer, A. J. M. Miller, N. H. Sherden, H. E. Gottlieb, A. Nudelman, B. M. Stoltz, J. E. Bercaw, K. I. Goldberg, *Organometallics* **2010**, *29*, 2176–2179.

Chapter 3: Synergism between the Luminescence of Sensor and Spin Crossover

This chapter focuses on the synthesis and characterization of the tetradentate ligand $L^{\text{Naph-ODA}}$, by various *NMR* and *IR*-spectroscopy and *ESI-MS*-spectrometry. Further the ligand was used for the design, synthesis, and characterization of a diamagnetic model complex $[\text{Zn}(L^{\text{Naph-ODA}})(\text{NCBH}_3)_2]$ and a spin-crossover iron(II) complex $[\text{Fe}(L^{\text{Naph-ODA}})(\text{NCBH}_3)_2]$. Both complexes were characterized by *NMR*-, *IR*- and emission spectroscopy as well as the iron(II) complex by *SQUID* magnetometry. Further the complexes were used to investigate the temperature dependence of the naphthyl emission in the solid state, in correlation with *SQUID* magnetometry and variable-temperature single-crystal *X-ray* diffraction to study the synergetic between the emission and the *SCO* in solid state. Additionally, the spin-state transition in the absence of packing effects was examined using *Evans NMR* magnetometry.

The results are presented as scientific article published in Dalton Transaction (DOI: <https://doi.org/10.1039/D3DT02420B>).

Reprinted with the permission from:

Copyright 2023 Royal Society of Chemistry

Author contribution:

██████████ designed the ligand and complexes synthesis, where the ligand synthesis was performed by ██████████ as well as the crystallisation of the complexes. The *IR*-spectroscopy was performed by ██████████ as well as the sample preparation of elemental analysis, *NMR*-spectroscopy and *ESI-MS*-spectrometry. ██████████ collected the single crystal *XRD* data and refined the structure. The evaluation of the magnetic and structural data was done by ██████████. The temperature dependent solid state emission spectroscopy was performed in supervision of ██████████ from Gießen. The *Evans NMR* measurements were performed by ██████████.

The Manuscript was written by ██████████, with input from ██████████ and ██████████. ██████████ had the supervision during the manuscript process. All Authors have read and agreed to the published version of the manuscript.

Manuscript: Synergetic Spin Singlet-Quintet Switching and Luminescence in mononuclear Fe(II) 1,3,4-Oxadiazole Tetradentate Chelates with NCBH₃ Co-ligand.

Sriram Sundaresan,^a Jens-Georg Becker,^a Julian Eppelsheimer,^a Alexander E. Sedykh,^b Luca. M. Carrella,^a Klaus Müller-Buschbaum^b and Eva Rentschler^{a*}

^aDepartment Chemie, Johannes-Gutenberg-Universität Mainz, Duesbergweg 10–14, 55128 Mainz, Germany. Email: rentschl@uni-mainz.de

^bInstitute of Inorganic and Analytical Chemistry, Justus-Liebig-University Giessen, Heinrich-Buff-Ring 17, 35392, Giessen, Germany.

Abstract:

We report the multi-step synthesis of tetradentate 2-(Naphthalen-2-yl)-5-[N,N-bis(2-pyridylmethyl)aminomethyl]-1,3,4-oxadiazole ($L^{\text{Tetra-ODA}}$) along with its corresponding $[\text{Fe}(L^{\text{Tetra-ODA}})(\text{NCBH}_3)_2] \cdot 1.5 \text{ CH}_3\text{OH}$ (**C1**) complex which is the first mononuclear 1,3,4-oxadiazole based Fe(II) spin crossover (SCO) complex and its zinc analogue $[\text{Zn}(L^{\text{Tetra-ODA}})(\text{NCBH}_3)_2] \cdot 0.5 \text{ H}_2\text{O}$ (**C2**). The spin transition is followed by VT-X-ray crystallography $[\text{Fe}(L^{\text{Tetra-ODA}})(\text{NCBH}_3)_2] \cdot 1.5 \text{ CH}_3\text{OH}$ (**C1**) at 120 and 220 K. The magnetic susceptibility measurements on bulk recorded from 2–300 K show the complex exhibits a complete abrupt reversible spin transition with a $T_{1/2}$ of 207 K. The loss of the lattice solvent methanol shifts the $T_{1/2}$ slightly to around 210 K. The spin transition in solution for $[\text{Fe}(L^{\text{Tetra-ODA}})(\text{NCBH}_3)_2] \cdot 1.5 \text{ CH}_3\text{OH}$ (**C1**) was followed using VT-¹H-NMR Evans method in CD₃CN, with a $T_{1/2}$ of 357 K. Solid state VT luminescence studies indicate some preliminary evidence of interplay of luminescence and spin transition in $[\text{Fe}(L^{\text{Tetra-ODA}})(\text{NCBH}_3)_2] \cdot 1.5 \text{ CH}_3\text{OH}$ (**C1**) complex.

Introduction:

The second most earth abundant transition metal in the periodic table, iron has a really rich chemistry because of its role and application in various fields of research, including medicine, catalysis, materials, and magnetism.^[1–4] The commonly stable oxidation states Fe(II) and Fe(III) are often extensively investigated in the field of magnetism as, interestingly, this metal ion has access to more than one way of populating the electrons in the 3d orbitals within one oxidation state. The electronic arrangement can be reversibly switched between the two states by external stimuli, making them ideal candidates for switches of molecular origin.^[5–10] This phenomenon is called spin crossover (SCO), which was first discovered by Cambi and co-workers in trivalent iron and is commonly studied in divalent iron.^[11,12] Other 3d metals with d⁴ - d⁷ electronic configuration also have the potential to switch between the

states.^[10,13–15] Commonly used perturbations are temperature, pressure, light, magnetic and electric fields.^[6,16–18] The vivid interest in investigating the phenomena in divalent iron is because the existence of paramagnetism in the metal centre can be switched on/off as the switch between the two states is from an isotropic fully paired diamagnetic low spin state ($S = 0$; maximum pairing) to a high spin state ($S = 2$; minimum pairing).^[12,19] These molecular switches make their potential application in various fields, including data storage, because of the binary states and also in displays and sensors, as the change between the states is often associated with changes in the physical properties, such as a change in colour and metal donor bond distances.^[7,20–22] The preferences over the chelating ligand donor atoms for the ferrous and ferric ion changes to aid the spin switch. Ferrous ion typically prefers $N6$ or an $N4S2$ donor set in general in comparison to the ferric ion, which mostly favours an $N4O2$ donor set to undergo spin transition.^[6,8,19]

For making the spin switchable molecules useful for the real-world application, one of the main hurdles faced by the material chemist are designing the complexes with appropriate ligand field that enables the spin switch close to ambient accessible temperature. In the process of tuning the ligand field strength by ligand design, three NCE co-ligands where $E = BH_3, Se$ and S are commonly studied to tune the ligand field strength are more commonly used in solid state^[23–26] and also used rarely in solution.^[27,28] Tuning of the $T_{1/2}$ in solid state is often governed by anions, lattice solvent effects and packing effects due to pi-pi interactions, hydrogen bonding interactions (also mediated by anions or lattice solvents) which makes it hard to enable predictable tuning.^[29–33] These effects can be both advantageous (increase in cooperativity, thus more abrupt and spin transition with hysteresis) or disadvantageous (SCO dependent on these interactions and locking the complex in one spin state) to the SCO phenomena in solid state.^[26,30,34,35] In solution packing effects are absent and the ligand field has the main influence and some nice linear correlations with different parameters such as the Hammett constants,^[36] solvent polarity index (P'),^[37,38] alkyl chain lengths,^[37] choice of NCEs, coordination ability parameter (σ^{TM}) are achieved.^[28] The main drawback with the solution spin crossover studies is the speciation. The ligand systems most commonly studied in the SCO literature are bidentate and tend to speciate. Moving to more robust ligands with higher denticity (chelate effect) might aid to reduce the speciation problem, but can never be ruled out as known from some recent solution studies.^[28]

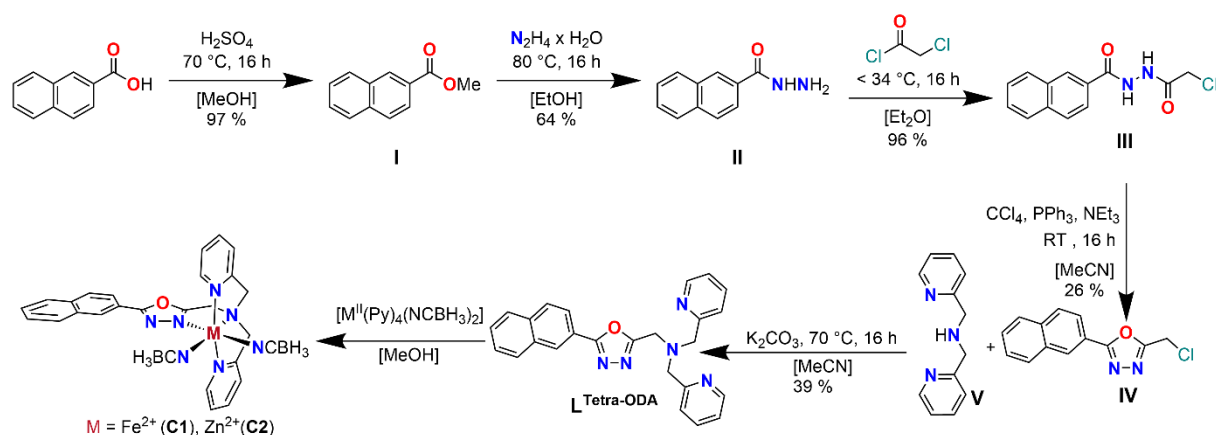
In the design of molecular switches over the last decade, the material chemist also, over the recent years, made attempts to bundle up other functionalities to the system, such as luminescence and ferroelectric properties.^[39] The luminescence coupled with the switchable property in the metal ion is really fascinating because of its various applications in the field of optical sensors such as optical thermometers and chemical sensors etc.^[40–42] Luminescence can be used to monitor or read out the

spin switch without any spectroscopic or sophisticated magnetic measurements.^[39,43] The potential applications of these advanced multifunctional materials include magneto-optical switches or the new generation of multi-sensors.^[7,39,43] Mononuclear complexes based on 1,3,4-thiadiazole with a luminophore such as naphthalene in the ligand design have been recently reported by some of us.^[26,29] The extended aromatic ring also aids cooperativity between the metal centres to induce an abrupt spin transition with a wide hysteresis up to 58 K.^[29] Ligand systems based on other bis bidentate ligands such as triazole are also commonly studied for SCO investigation in Fe(II),^[19,26,32,44,45] whereas Fe(II) complexes based on 1,3,4-oxadiazole is seldom reported in the literature. Some of us reported the first dinuclear Fe(II) 1,3,4-oxadiazole complex with a wide hysteresis of 26 K.^[33] The role of counterion in tuning the spin transition in solid state was also investigated.^[33] Attempts made to further tune the ligand field by choice of a five-membered thiazole ring in comparison to the six-membered pyridine ring were not successful, and the compounds stayed in *HS* over the measured temperature range irrespective of the three different counterions used.^[46] Other attempts to synthesise mononuclear Fe(II) SCO complexes described in literature have, to the best of our knowledge, also not been successful so far. Klingele, Letard and co-workers in 2013 have reported a mono nuclear Fe(II) complex based on bis bidentate oxadiazole ligand and NCS co-ligand, the complex stayed in *HS* over the measured temperature window.^[18] More recently Herchel and co-workers have made modification to the ligand design from Letard group with a 5-membered furan and thiophene group substituted bis bidentate ligand where in this case too the complex stayed in *HS* state over the measured temperature window.^[47] We report the synthesis and characterisation of the first mononuclear spin crossover Fe(II) complex based on 1,3,4-oxadiazole ligand with NCBH₃ co-ligands and a luminophore to generate multifunctional spin switchable Fe(II) complex. The NCBH₃ co-ligand was mainly chosen in comparison to the other two NCE (S and Se) for the current study because of its strong ligand field (*LF*). As ligands based on 1,3,4-oxadiazole in combination with the NCE were always yielding *HS* complexes^[18, 47] the strongest *LF* contributing NCE was chosen to investigate its influence on the spin state.

Results and Discussion:

Synthesis:

2-(Naphthalen-2-yl)-5-[N,N-bis(2-pyridylmethyl)aminomethyl]-1,3,4-oxadiazole ($L^{\text{Tetra-ODA}}$) was synthesized in five steps (**Scheme 1**). In the first step, 2-naphthoic acid was converted to methyl naphthalene-2-carboxylate (**I**) by Fischer esterification in high yields.^[26,29] 2-Naphthohydrazide (**II**) was synthesized in a subsequent nucleophilic reaction of methyl naphthalene-2-carboxylate with hydrazine monohydrate in moderate yields.^[26,29] The following condensation reaction with chloroacetyl chloride yielded N'-(2-chloroacetyl) naphthalene-2-carbohydrazide (**III**) in high yields. Ring-closing was achieved by the use of the three-component system triphenylphosphine, carbon tetrachloride and triethylamine to yield 2-(Chloromethyl)-5-(naphthalen-2-yl)-1,3,4-oxadiazole (**IV**) in low yields.^[33,46] In the fifth and final step, $L^{\text{Tetra-ODA}}$ was successfully isolated after a nucleophilic reaction of **IV** and bis(pyridine-2-ylmethyl) amine (**V**) in moderate yields, using potassium carbonate as base. The obtained $L^{\text{Tetra-ODA}}$ was fully characterized using a range of techniques, including $^1\text{H-NMR}$, $^{13}\text{C-NMR}$, 2D-NMR , IR , mass spectrometry and elemental analysis (**Figure S1-10**, **S15** and **S18**). The complexation reaction **C1** and **C2** in methanol with tetradentate $L^{\text{Tetra-ODA}}$ ligand with $[\text{Fe}(\text{py})_4(\text{NCBH}_3)_2] \cdot 2.5 \text{H}_2\text{O}$ and $[\text{Zn}(\text{py})_4(\text{NCBH}_3)_2] \cdot 0.5 \text{H}_2\text{O}$ precursors in methanol yielded $[\text{Fe}(L^{\text{Tetra-ODA}})(\text{NCBH}_3)_2] \cdot 1.5 \text{CH}_3\text{OH}$ (**C1**) and $[\text{Zn}(L^{\text{Tetra-ODA}})(\text{NCBH}_3)_2] \cdot 0.5 \text{H}_2\text{O}$ (**C2**) respectively in moderate yields. Complex (**C1**) was characterized by variable temperature X-ray crystallography (120 and 220 K), SQUID magnetometry (2 - 400 K), ESI mass spec (Principal peak for both complexes which corresponds to $[\text{M}^{\text{II}}(L^{\text{Tetra-ODA}})(\text{NCBH}_3)_2]^+$ (**Figure S18-19**), IR (**Figure S16-17**) and elemental analysis. Complex **C2** was characterized by $^1\text{H-NMR}$, $^{13}\text{C-NMR}$ (**Figure S11-12**), elemental analysis and HRes mass spectrometry with isotopic pattern matches for the principal peak (**Figure S19-22**).



Scheme 1: Multistep ligand synthesis of $L^{\text{Tetra-ODA}}$ along with complex synthesis of **C1** and **C2**.

Solid Magnetic data:

The temperature dependent magnetic behavior of $[\text{Fe}(\text{L}^{\text{Tetra-ODA}})(\text{NCBH}_3)_2] \cdot 1.5 \text{ CH}_3\text{OH}$ (**C1**) was measured in pure orange microcrystalline powder in the temperature range between 300 K and 2 K in both cooling and heating mode (**Figure 1** and **Figure S37-S38**). As the sample was air stable as described in the experimental section, the sample preparation for the SQUID magnetometry measurement were carried out under normal aerobic condition. At 300 K, a $\chi_M T$ product of $3.45 \text{ cm}^3 \cdot \text{mol}^{-1} \cdot \text{K}$ ($g = 2$) can be observed, which is agreement with the literature for $^5\text{T}_{2g}$ HS ground state.^[8,19] Cooling of the sample leads to an abrupt and complete spin crossover to the diamagnetic $^1\text{A}_{1g}$ low-spin state,^[5,8,19] as indicated by the change in bond length from the VT-Xray data obtained at 120 and 220 K. The first derivative of $\chi_M T$ with respect to T yields a transition temperature of $T_c^\uparrow = T_c^\downarrow = 207 \text{ K}$ (**Figure S39**).

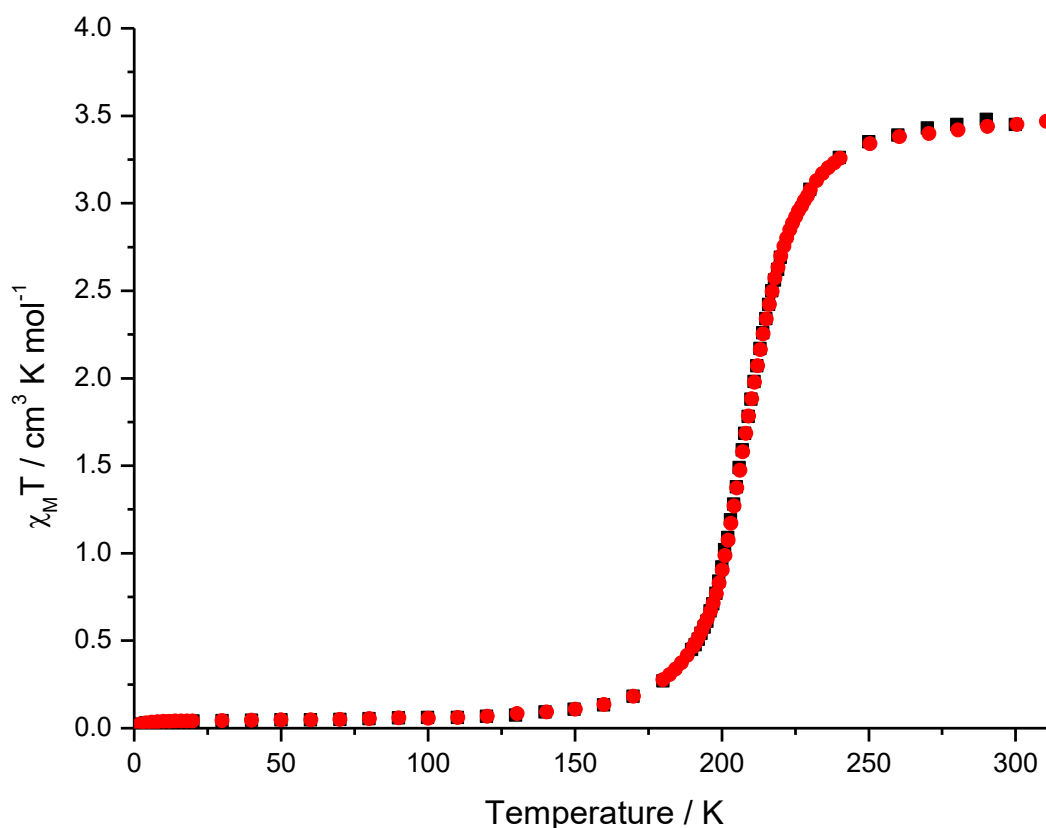


Figure 1: $\chi_M T$ vs T measured from 300 \rightarrow 2 K (black), 2 K \rightarrow 300 K (red) of $[\text{Fe}(\text{L}^{\text{Tetra-ODA}})(\text{NCBH}_3)_2] \cdot 1.5 \text{ CH}_3\text{OH}$ (**C1**).

As we know from the SCO literature, in many cases, the spin transition is influenced by the lattice solvents in the solid state.^[30,32] The measured sample was exposed to air for five days. This finding suggests the absence of solvent loss. Furthermore, there was no colour change of the orange microcrystals, indicating chemical inertness to atmospheric oxygen. Magnetic data collection after five days over the temperature range of 300 \rightarrow 100 K in multiple cycles (five cycles) clearly indicates that there is no significant change of $\chi_M T$ observable compared to the first measurement (**Figure S38**).

Thus, the *SCO* property in $[\text{Fe}(\text{L}^{\text{Tetra-ODA}})(\text{NCBH}_3)_2] \cdot 1.5 \text{ CH}_3\text{OH}$ is stable after exposure to air. When the sample was heated upto 400 K there is a slight shift in the $T_{1/2}$ was observed to 210 K due to the loss of the lattice solvent methanol as indicated from a small bump 335 K in the heating mode (**Figure S37**). The magnetic behavior changes associated with the lattice solvent removal is well established in the *SCO* literature.^[26,30,32]

The spin transition in solution was measured using variable temperature $^1\text{H-NMR}$ using *Evans* method in CD_3CN at a concentration of $5.06 \times 10^{-3} \text{ M}$ from 298 to 343 K (at 5 K intervals) in heating mode. Each data set was modelled as a gradual and complete *SCO* using the regular solution model (**Equation S1** and **Table S4**), assuming the $\chi_M T_{max} = 4.00 \text{ cm}^3 \cdot \text{mol}^{-1} \cdot \text{K}$ with a good fit of $R^2 = 0.98$ obtained. The *Evans* method has a relative error of 5-10%. $T_{1/2}$ was calculated by dividing ΔH by ΔS . The $[\text{Fe}(\text{L}^{\text{Tetra-ODA}})(\text{NCBH}_3)_2] \cdot 1.5 \text{ CH}_3\text{OH}$ (**C1**) shows a $T_{1/2}$ of 357 K. As mentioned in the introduction speciation is the key problem in solution. The use of ligands with higher denticity was employed to reduce the impact of speciation, as a tetradentate ligand is more stable than a bidentate or a tridentate ligand (chelating effect) commonly used in the literature. It should be noted that the possibility of speciation should not be entirely ruled out. Molar conductivity measurements were performed, as this is one of the few ways to investigate the speciation issue in a paramagnetic sample. In the current study as the complex **C1** prepared was neutral molar conductivity measurements should ideally give a zero as a value. Perfect zero values are very rarely obtained. The value obtained was just $53 \text{ S} \cdot \text{cm}^2 \cdot \text{mol}^{-1}$ which shows the complex slightly dissociates in solution but is far less than a 2:1 conductor in acetonitrile when the NCBH_3 anion is dissociated completely (2:1 conductor in MeCN literature range is from 230-250 $\text{S} \cdot \text{cm}^2 \cdot \text{mol}^{-1}$). The $T_{1/2}$ obtained should therefore be taken with caution.

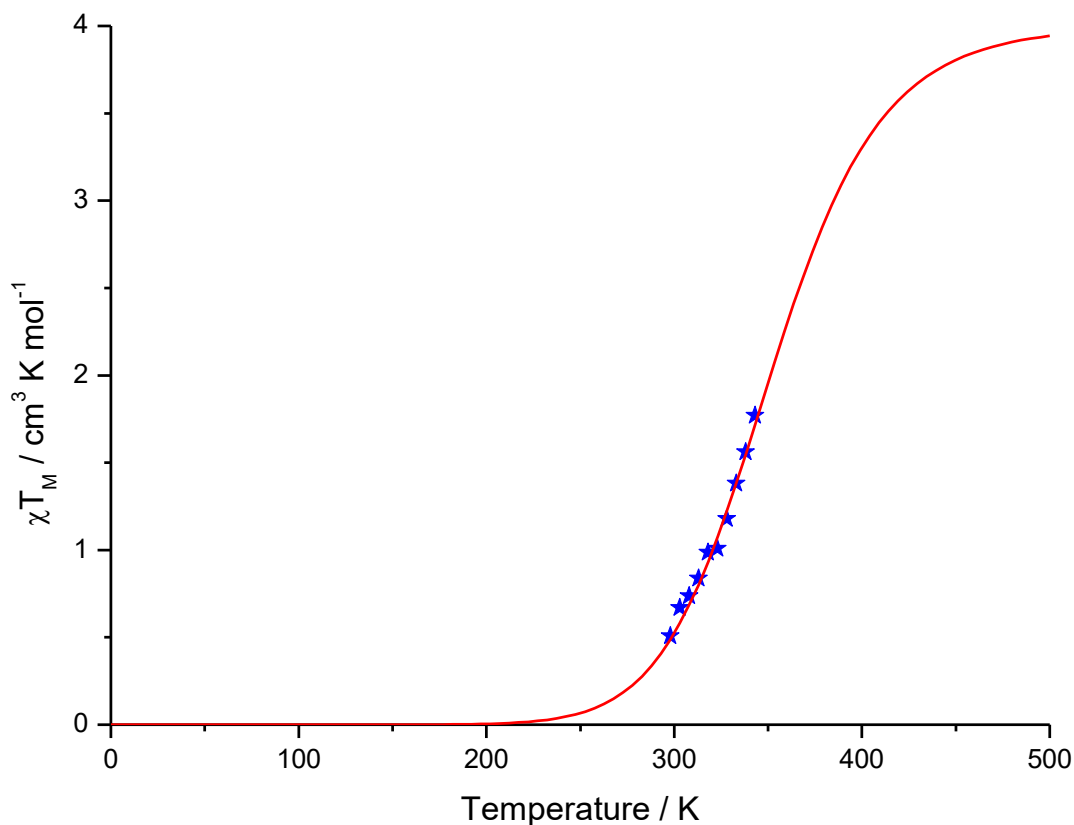


Figure 2: $\chi_M T$ vs T measured from 298 to 343 K (at 5 K intervals) in heating mode in CD_3CN for $[\text{Fe}(\text{L}^{\text{Tetra-ODA}})(\text{NCBH}_3)_2] \cdot 1.5\text{CH}_3\text{OH}$ (**C1**).

Structural determination:

Orange block shaped single crystals of $[\text{Fe}(\text{L}^{\text{Tetra-ODA}})(\text{NCBH}_3)_2] \cdot 1.5 \text{CH}_3\text{OH}$ (**C1**) were obtained from methanol after two days of slow evaporation. The X-ray data was collected at 220 K (**Table S1**). The complex crystallizes in the monoclinic space group $C2/c$ with eight formula units in the unit cell. The coordination sphere of the complex **C1** can be described as one $\text{L}^{\text{Tetra-ODA}}$ ligand molecule coordinates via its tetradentate binding pocket and the coordination sphere is saturated by two monodentate NCBH_3 co-ligands (**Figure S23**). One nitrogen of the oxadiazole ring shapes, together with the amine function and the two co-ligands, the equatorial base of the coordination octahedron. Thus, the pseudohalides NCBH_3 exhibits a *cis*-configuration. The apical positions of the octahedron are occupied by the trans-coordinating pyridyl moieties. At 220 K, a mean metal-ligand distance of $\bar{d}(\text{Fe-N}) = 2.17 \text{ \AA}$ can be found, representing a high-spin iron(II) center. This spin state is further confirmed by the present distortion of the octahedral coordination sphere with $\Sigma_0(\text{FeN}_6) = 94.0^\circ$. The largest deviation from the ideal coordination sphere is caused by the apical pyridine moieties, forming a trans-angle of 152.7° .

In the case of **C1**, three different types of π - π interactions are present in the crystalline phase. The first intermolecular non-classical C-H \cdots π -hydrogen bond can be found between the C-H function of a pyridyl group and the π -system of the naphthyl group. The least-squares mean plane A is formed by the atoms

C2-C7, while the interacting C-H function is labeled as C18-H18. Next to an interaction distance of $d_{QH} = 2.94 \text{ \AA}$, an offset of $r = 1.26 \text{ \AA}$ can be found. The relevant geometrical angles are $\alpha = 159.5^\circ$ and $\beta = 64.6^\circ$ (**Figure S24**). Thus, this C-H $\cdots\pi$ hydrogen bond causes a one-dimensional chain-like arrangement of complex molecules along the c-axis (**Figure S26**). Two neighboring chains are crosslinked via two additional π - π interactions. Firstly, a parallel stacking between the naphthalene rings of two complex molecules can be observed. The interplanar angle ϑ is equal to 1.8° . Next to that, an interplanar distance of $d_{AB} = 3.40 \text{ \AA}$ and an offset of $r = 2.14 \text{ \AA}$ can be found. In addition, a second intermolecular T-shape π - π interaction is present between the same two complex molecules. Therefore, the naphthyl group exhibits a non-classical C-H $\cdots\pi$ hydrogen bond to a pyridine ring. The involved plane A includes N5, C16, C17, C18, C19 and C20, while the interacting C-H fragment is labeled as C5-H5. The interaction distance is equal to $d_{QH} = 2.96 \text{ \AA}$ with an offset of $r = 0.93 \text{ \AA}$. The involved angles are $\alpha = 152.3^\circ$ and $\beta = 71.7^\circ$. Due to these three unique intermolecular interactions, one-dimensional chain of dimers is formed along the c-axis (**Figure S25** and **S28**).

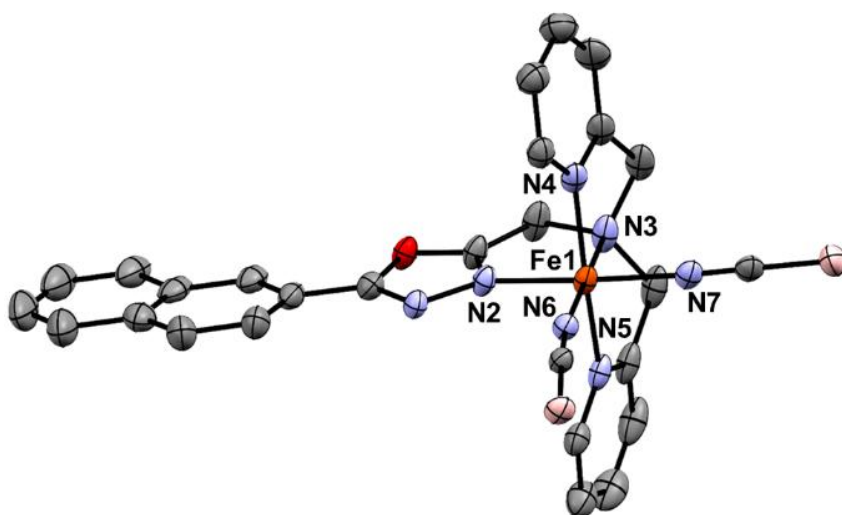


Figure 3: Representative crystal structure of $[\text{Fe}(\text{L}^{\text{Tetra-ODA}})(\text{NCBH}_3)_2] \cdot 1.5 \text{ CH}_3\text{OH}$ (**C1**) collected at 220 K. The donor atoms and the Iron atoms are labeled. Hydrogen atoms are omitted for clarity. Colour code: grey-C, blue-N, orange-Fe, red-O, Spanish pink-B. ORTEP representation with atomic displacement parameters at the 50% level of probability.

To investigate the change in bond length associated with the spin state change. X-ray data was collected at 120 K. At the given temperature, the compound still crystallized in the same monoclinic space group $C2/c$ with eight formula units in the unit cell (**Table S1**). But it is important to note that the colour of the crystal changed from orange to dark red at 120 K. As anticipated, the cell volume decreased from $6164.9(3) \text{ \AA}^3$ to $5835.1(3) \text{ \AA}^3$, which displays a reduction of the cell volume of about 5 %. This can be attributed to the fact that the octahedral coordination sphere of low-spin iron(II) ions is smaller compared to high-spin iron(II) ions since there is no occupation of antibonding e_g^* -orbitals.^[8,19] Furthermore, since the occupation of the bonding t_{2g} -orbitals in *LS* Fe(II) is perfectly isotropic, indeed,

a lower distortion of the N_6 -coordination sphere was found in the low-spin state at 120 K. The octahedral distortion parameter is equal to $\Sigma_O(FeN_6) = 47.0^\circ$. **Figure S27** shows that the major difference arises from the position of the apical coordinated pyridyl groups. Thus, the embedded *trans*-angle increases from $152.75(5)^\circ$ at 220 K to $166.83(6)^\circ$ at 120 K. A detailed summary of structural parameters of **C1** for both temperatures are tabulated in **Table S1**. The average metal-ligand distance is equal to 1.97 \AA , which is 9% shorter than the average distance in the *HS* state **Figure 4**. This reduction of the FeN_6 coordination sphere is in good agreement with the literature.^[8,12,19] The change in the bond length is in agreement with the magnetic data. The abruptness of the spin transition can be attributed to the intermolecular π - π interactions, which result in the *chain-like* ordering of complex molecules along the *c*-axis. Thus, structural changes associated with the *SCO* (primarily the contraction of the octahedral coordination sphere) can be transferred to neighboring molecules quite easily.

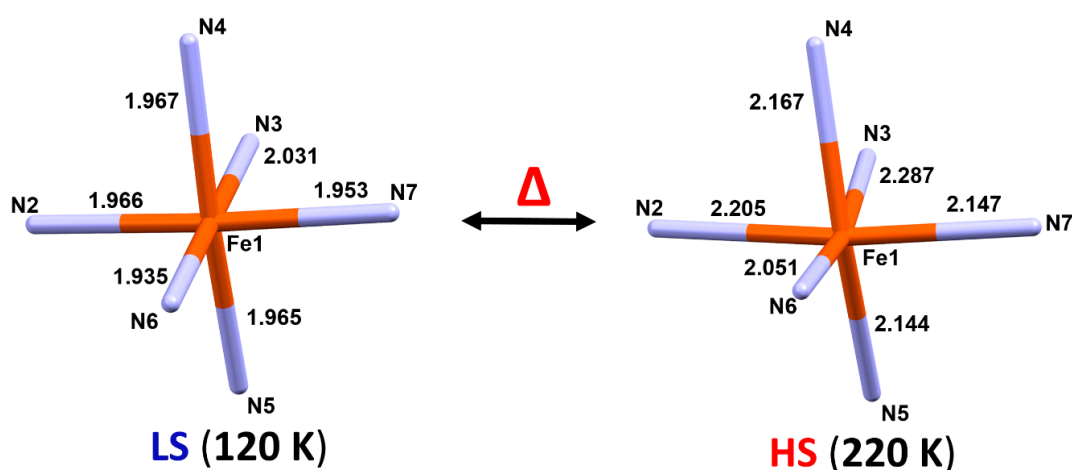


Figure 4: Metal donor bond distances at 120 and 220 K for $[Fe(L^{\text{Tetra-ODA}})(NCBH_3)_2] \cdot 1.5 CH_3OH$ (**C1**).

Photoluminescence spectroscopy:

The tetradentate $L^{\text{Tetra-ODA}}$ ligand was designed to have a *SCO* suitable tetradentate binding pocket as well as the naphthyl group, acting as luminophore. Firstly, the photoluminescence of both complexes **C1** and **C2** was investigated on crystalline samples at room temperature and at 77 K (**Figure S32-33**) regarding excitation and emission. The *UV-Vis* spectra of the ligand and both the complexes were measured in *n*-butyronitrile (**Figure S29**). Absorption takes place around 200 - 350 nm and no absorbance above 350 nm. Due to the presence of few aromatic rings in the ligand backbone, the absorbance is attributed to mixture of $\pi \rightarrow \pi^*$ transitions. The *UV-Vis* spectra were also recorded in few different concentrations as shown in **Figure S30-31**. Both samples were irradiated with light of the wavelength of 300 nm. The emission spectrum of **C1** at 77 K is very close to naphthalene and its emission wavelengths (around 330 - 450 nm) reported in the literature.^[48,49] This was also confirmed by comparison of the free ligand emission data in *n*-butyronitrile (**Figure S36**) which appears slightly

shifted in comparison the metal complex. Two well-resolved emission maxima at $\lambda_{em,1} = 343$ nm and $\lambda_{em,2} = 359$ nm can be observed (**Figure 5**), next to one shoulder-like maximum at $\lambda_{em,3} = 378$ nm. Measuring the same sample at room temperature slightly shifts $\lambda_{em,1}$ and $\lambda_{em,2}$ to 348 nm and 359 nm, respectively (**Figure S32**). The shoulder-like emission band is not resolved anymore. Similar to **C1**, the emission spectrum of **C2** at 77 K resembles the luminescence of naphthalene. However, emission band shifts are more pronounced. Thus, three well-resolved emission maxima at $\lambda_{em,1} = 354$ nm, $\lambda_{em,2} = 373$ nm and $\lambda_{em,3} = 392$ nm can be found. In addition to that, a fourth shoulder-like band at $\lambda_{em,4} = 414$ nm becomes apparent. Measuring the same sample at room temperature reveals a different shape of the emission band. The emission maxima $\lambda_{em,2}$ and $\lambda_{em,3}$ shift to 369 nm and 387 nm, respectively, while $\lambda_{em,1}$ and $\lambda_{em,4}$ remain unchanged. However, the relative intensity of $\lambda_{em,1}$ drastically decreases, whereas that of $\lambda_{em,4}$ increases (**Figure S32**).

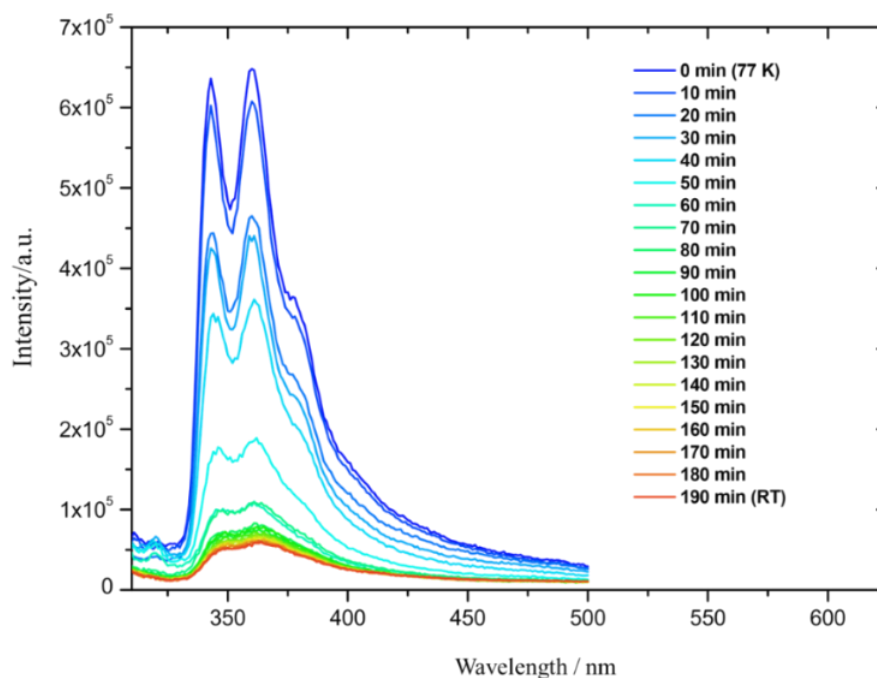


Figure 5: Temperature dependent emission spectra of $[\text{Fe}(\text{L}^{\text{Tetra-ODA}})(\text{NCBH}_3)_2] \cdot 1.5 \text{CH}_3\text{OH}$ (**C1**) between 310 nm and 625 nm for a series of time-related measurements. Within 190 min, liquid nitrogen was allowed to evaporate, which results in a heating of the sample to room temperature.

To further investigate the dependency of emission intensity from temperature, two additional series of measurements were carried out. Therefore, the cuvettes containing either **C1** and **C2**, were adjusted in a Dewar assembly half-filled with liquid nitrogen. Subsequently, emission spectra were recorded for the same parameters with a delay of 10 min between each measurement. Altogether, 20 spectra were recorded for each compound covering the temperature range from 77 K to room temperature (**Figure 5**, **Figure S34-35**). However, the exact sample temperature could not be controlled in a linear way during that time. Considering the shape and intensity of emission bands in both samples, it can be assumed that the major spectroscopical changes are complete after 60 min, approximately. After this

time, the spectra do not significantly differ anymore. For both samples, the overall intensity of emission decreases with increasing temperature. For **C2**, this can be ascribed to the typical thermal quenching of the luminescence intensity.^[50] In the case of **C1**, however, this effect may also be assigned to a potential interplay between the *SCO* and luminescence.^[39,51,52] Over the time in the case **C1** closer to room temperature, the *HS* character of the complex would have increased which will also lead to quenching of the luminescence.^[39,51,52]

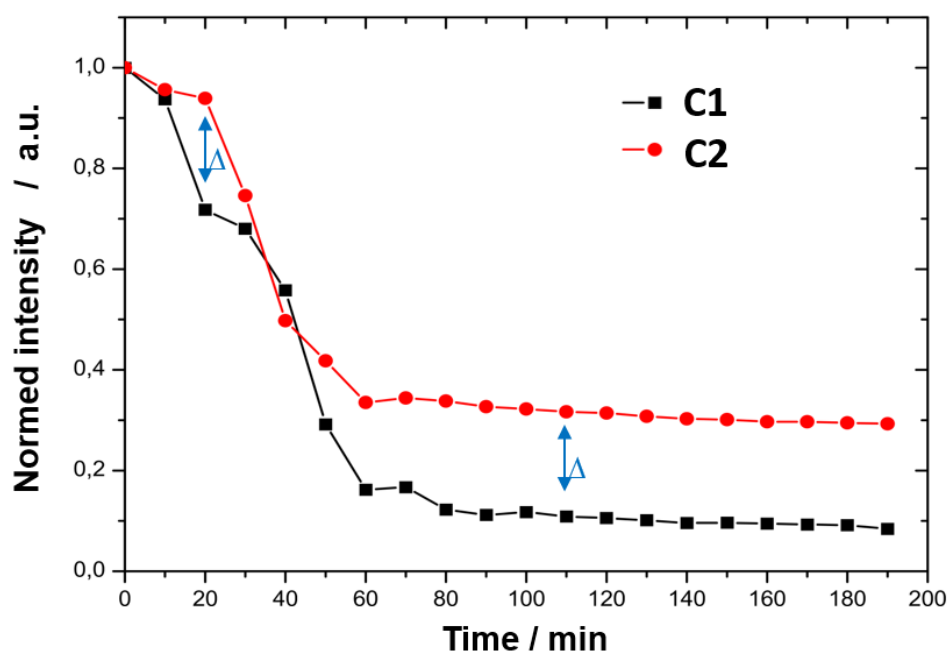


Figure 6: Normalized intensity of $\lambda_{em,2}$ vs. time for $[\text{Fe}(\text{L}^{\text{Tetra-ODA}})(\text{NCBH}_3)_2] \cdot 1.5 \text{ CH}_3\text{OH}$ (**C1**) ($\lambda_{em,2} = 359 \text{ nm}$, black squares) and $[\text{Zn}(\text{L}^{\text{Tetra-ODA}})(\text{NCBH}_3)_2] \cdot 0.5 \text{ H}_2\text{O}$ (**C2**) ($\lambda_{em,2} = 359 \text{ nm}$, red circles). The offset Δ is attributed to the present *SCO* in **C1**.

To compare the progression of luminescence quenching, the normalized intensity of the most pronounced emission maxima $\lambda_{em,2}$ (359 nm in **C1** and 373 nm in **C2**) were plotted vs. time for both compounds (**Figure 6**).^[51,52] The normalized intensity of $\lambda_{em,2}$ in $[\text{Zn}(\text{L}^{\text{Tetra-ODA}})(\text{NCBH}_3)_2] \cdot 0.5 \text{ H}_2\text{O}$ (**C2**) decreases only slightly in the first 20 min, as the warming up process needs to initiate and become linear. The maximum intensity then decreases continuously to a value of 35% after 60 minutes. After this time, no significant changes in intensity can be observed, indicating that the experimental system is at room temperature, as is known also from the emission spectra. In contrast, the behavior of $[\text{Fe}(\text{L}^{\text{Tetra-ODA}})(\text{NCBH}_3)_2] \cdot 1.5 \text{ CH}_3\text{OH}$ (**C1**) is somewhat different. While the percentage of intensity after 10 min is approximately the same as for **C2**, the value drops pronouncedly to about 70% at 20 min. This displays a difference of $\Delta = 20\%$ to the value of **C2** at that same time. After that, the normalized intensity decreases progressively until it plateaus at about 60 min, showing the same behavior as **C2**. However, it results in a plateau at around 10% intensity, which is lower compared to the analogous zinc(II) complex. Interestingly, this gap between the plateaus

of both compounds (marked as Δ in **Figure 6**) is exactly the offset of emission intensity between the two complexes at 20 min. This preliminary evidence clearly indicates an interplay between the SCO and luminescence in complex **C1** until 20 mins. After 30 min, the progression of intensity is analogous to **C2** (vertically shifted by Δ), which can be attributed to thermal quenching.

Conclusion:

We report the multi-step synthesis of a new novel tetradentate 1,3,4-oxadiazole based ligand $L^{\text{Tetra-ODA}}$ along with its corresponding $[\text{Fe}(L^{\text{Tetra-ODA}})(\text{NCBH}_3)_2] \cdot 1.5 \text{ CH}_3\text{OH}$ (**C1**) and $[\text{Zn}(L^{\text{Tetra-ODA}})(\text{NCBH}_3)_2] \cdot 0.5 \text{ H}_2\text{O}$ (**C2**) complexes. The spin transition in complex **C1** was followed by variable temperature X-ray crystallographic data collected at 120 and 220 K, along with the SQUID magnetometry. Complex **C1** shows an abrupt spin transition centered around 207 K in solid state with a slight shift in $T_{1/2}$ with a solvent loss to 210 K when heated up to 400 K and with a $T_{1/2}$ of 357 K in solution in CD_3CN . Both complexes **C1** and **C2** also show luminescence properties. Preliminary investigations also show an interplay between SCO and luminescence for complex **C1**. A more detailed study on temperature dependent luminescence behaviour along with the role of the NCE co-ligand and the effect of lattice solvent is currently underway.

Experimental:

All chemicals were purchased from Alfa Aesar, Deutero, Fisher Chemicals, TCI, Sigma-Aldrich, and Acros Organics and used without further purification. Solvents were dried according to the literature known procedures and used freshly distilled.^[53] Dry DMF was purchased from Sigma Aldrich. NMR spectra were recorded at room temperature with a Bruker Avance DSX 400 and analyzed with the program MestReNova.^[54] Magnetic susceptibility measurements were performed on a Quantum Design SQUID magnetometer MPMSXL in a temperature range between 2 and 400 K with an applied field of 1 kOe. All mass spectra (Advion expression-L CMS), as well as elemental analysis (Elementar vario EL Cube: C, H, and N), were measured at the microanalytical laboratories of the Johannes Gutenberg University Mainz. Luminescence spectra were recorded on a spectrophotometer Fluorolog 3 (HORIBA) at the Justus-Liebig-University of Giessen; measurements at 77 K and time-resolved measurements were performed using a Dewar assembly (FL-1013, HORIBA) filled with liquid nitrogen. X-ray diffraction data were collected with STOE STADIVARI at the Johannes Gutenberg University Mainz. The structures were solved with ShelXT^[55] and refined with ShelXL^[56,57] implemented in the program Olex2.^[58] The X-ray cif file data are deposited on the Cambridge CCDC database with identification numbers 2264782-2264783.

Ligand synthesis:**Methyl-2-naphthoate (I)**

This was prepared according to previously reported literature.^[26,29] To a solution of 2-naphthoic acid (25.83 g, 150.00 mmol, 1.0 equiv.) in methanol (150 ml) was added sulfuric acid (conc., 7.5 ml). The reaction was refluxed for 16 hours at 80 °C. Afterwards, the solvent was removed under reduced pressure, water (200 ml) was added, and the pH value was set to 9 with sodium bicarbonate. The aqueous phase was extracted four times with dichloromethane. The combined organic extracts were dried over magnesium sulfate, and the solvent was removed under reduced pressure to afford Methyl-2-naphthoate (I) as a colourless solid (27.07 g, 145.30 mmol, 97 %). ¹H-NMR (400 MHz, DMSO, δ (ppm)): 8.63 (s, 1H, NaphCH), 8.13 (d, 1H, NaphCH), 8.04 - 7.96 (m, 3H, NaphCH), 7.68 - 7.59 (m, 2H, NaphCH), 3.91 (s, 3H, CH₃).

2-Naphthohydrazide (II)

This was prepared according to previously reported literature.^[26,29] To a solution of Methyl-2-naphthoate (I) (27.07 g, 145.30 mmol, 1.0 equiv.) in 250 ml ethanol was added hydrazine monohydrate (50.00 ml, 41.20 g, 0.82 mol, 5.6 equiv.). The reaction was stirred for 16 hours at 80 °C. Afterwards, the mixture was concentrated under reduced pressure to 75 % of its volume. The resulting solid was filtered and washed with cold diethyl ether to yield 2-Naphthohydrazide (II) as a white powder (17.56 g, 94.33 mmol, 64 %). ¹H-NMR (400 MHz, DMSO, δ (ppm)): 9.94 (s, 1H, NH), 8.43 (s, 1H, NaphCH), 8.02 - 7.90 (m, 4H, NaphCH), 7.62 - 7.56 (m, 2H, NaphCH), 4.58 (s, 2H, NH₂).

N'-(2-chloroacetyl)-2-naphthohydrazide (III)

2-Naphthohydrazide (II) (17.56 g, 94.33 mmol, 1 equiv.) was suspended in diethyl ether (600 ml) and cooled to 0 °C. To this solution was added chloroacetylchloride (12.78 g, 9.00 ml, 113.18 mmol, 1.2 equiv.), dissolved in diethyl ether (150 ml), dropwise, keeping the temperature below 34 °C. The reaction mixture was stirred for 16 hours at room temperature. The colourless solid was filtered and washed with cold diethyl ether to yield N'-(2-chloroacetyl)-2-naphthohydrazide (III) as a colourless solid (23.72 g, 90.29 mmol, 96 %). ¹H-NMR (400 MHz, DMSO, δ (ppm)): 10.71 (s, 1H, NH), 10.48 (s, 1H, NH), 8.52 (s, 1H, NaphCH), 8.11 - 7.93 (m, 4H, NaphCH), 7.66 - 7.59 (m, 2H, NaphCH), 4.24 (s, 2H, CH₂).

2-(Chloromethyl)-5-(naphthalen-2-yl)-1,3,4-oxadiazole (IV)

N'-(2-chloroacetyl)-2-naphthohydrazide (III) (23.72 g, 90.29 mmol, 1 equiv.) was dissolved in acetonitrile (500 ml) under an inert atmosphere. To this solution triphenylphosphine (47.36 g, 180.58 mmol, 2 equiv.), triethylamine (18.27 g, 25.03 ml, 180.58 mmol, 2 equiv) and carbon tetrachloride (55.56 g, 34.94 ml, 361.16 mmol, 4 equiv.) were added simultaneously. The reaction was

stirred for 16 hours. The solvent was removed under reduced pressure to yield a black solid as a crude product. Column chromatography (SiO₂, chloroform) afforded 2-(Chloromethyl)-5-(naphthalen-2-yl)-1,3,4-oxadiazole (**IV**) (1.88 g, 7.68 mmol, 8.50 %) as a pale red solid in low yields. A second fraction obtained was further columned under same condition to yield pure product. The overall yield of this cyclisation step is (5.81 g, 23.745 mmol, 26%). ¹H-NMR (400 MHz, CDCl₃, δ (ppm)): 8.59 (s, 1H, NaphCH), 8.16 - 8.13 (m, 1H, NaphCH), 7.99 - 7.90 (m, 3H, NaphCH), 7.64 - 7.57 (m, 2H, NaphCH), 4.83 (s, 2H, CH₂).

Bis[(2-pyridyl)methyl]amine (V)

Pyridine-2-carboxaldehyde (3.21 g, 30.00 mmol, 1.0 equiv.) and 2-aminomethylpyridine (3.24 g, 30.00 mmol, 1.0 equiv.) were dissolved in methanol (200 ml) and stirred at room temperature for 4 hours. After cooling the mixture to 0 °C, sodium borohydride (3.03 g, 80.10 mmol, 2.67 equiv.) was added portion-wise, and the reaction mixture was stirred for 16 hours at room temperature. The solvent was removed under reduced pressure. The residue was taken up in 100 ml of water and extracted four times with chloroform (60 ml). The combined organic extracts were dried over magnesium sulfate and taken to dryness to afford Bis[(2-pyridyl)methyl]amine (**V**) as an orange oil (5.85 g, 29.34 mmol, 98 %). ¹H-NMR (400 MHz, CDCl₃, δ (ppm)): 8.54 (d, 2H, pyCH), 7.65 - 7.61 (m, 2H, pyCH), 7.34 (d, 2H, pyCH), 7.16 - 7.13 (m, 2H, pyCH), 3.97 (s, 4H, CH₂).

2-(Naphthalen-2-yl)-5-[N,N-bis(2-pyridylmethyl)aminomethyl]-1,3,4-oxadiazole (L^{Tetra-ODA})

Bis[(2-pyridyl)methyl]amine (**V**) (7.13 g, 35.79 mmol, 1.5 equiv.) and potassium carbonate (8.25 g, 59.65 mmol, 2.5 equiv.) were suspended in acetonitrile (250 ml) under an inert atmosphere and heated to 70 °C. To this solution was added 2-(Chloromethyl)-5-(naphthalen-2-yl)-1,3,4-oxadiazole (**IV**) (5.83 g, 23.86 mmol, 1 equiv.), together with its side product, triphenylphosphine oxide (13.10 g, 47.08 mmol), dissolved in acetonitrile (400 ml). The reaction mixture was stirred vigorously at 70 °C for 16 hours. The solid was filtered, and the solvent from the filtrate was removed under reduced pressure to afford a brown solid as a crude product. Column chromatography (SiO₂, chloroform/ methanol (39:1)) yielded 2-(Naphthalen-2-yl)-5-[N,N-bis(2-pyridylmethyl)aminomethyl]-1,3,4-oxadiazole (L^{Tetra-ODA}) as bright brown oil which crystallizes after several days (3.82 g, 9.37 mmol, 39 %). ¹H-NMR (400 MHz, CDCl₃, δ (ppm)): 8.56 - 8.51 (m, 3H), 8.11 - 8.08 (m, 1H), 7.96 - 7.93 (m, 2H), 7.89 - 7.86 (m, 1H), 7.69 - 7.65 (m, 2H), 7.59 - 7.54 (m, 4H), 7.17 - 7.14 (m, 2H), 4.18 (s, 2H, ODA-CH₂), 4.07 (s, 4H, Py-CH₂) ¹³C-NMR (101 MHz, CDCl₃, δ (ppm)): 165.42, 164.17, 158.22, 149.18, 136.81, 134.71, 132.80, 129.05, 128.89, 128.00, 127.44, 127.13, 123.38, 123.23, 122.41, 121.03, 59.97 (CH₂), 48.12 (CH₂). FT-IR: $\tilde{\nu}$ (cm⁻¹) = 3076, 3057, 3002, 2951, 2929, 2899, 2849, 1607, 1588, 1563, 1544, 1509, 1469, 1447, 1430, 1409, 1392, 1368, 1360, 1325, 1309, 1282, 1271, 1242, 1218, 1187, 1147, 1125, 1088, 1071,

1044, 1018, 987, 975, 962, 945, 908, 894, 879, 867, 846, 818, 767, 750, 721, 655, 630, 613, 593, 552, 540, 507, 473, 456, 425, 404. ESI-MS (m/z): calc. for $[\text{C}_{25}\text{H}_{22}\text{N}_5\text{O}]^+$ expected: 408.18 (100.00 %); found: 408.185 (100.00 %). Elemental analysis calculated for $\text{L}^{\text{Tetra-ODA}}$ ($\text{C}_{25}\text{H}_{21}\text{N}_5\text{O}$): C, 73.69, H, 5.19, N, 17.19. Found, C, 73.31, H, 5.21, N, 16.98.

Complex synthesis:

$[\text{Fe}(\text{L}^{\text{Tetra-ODA}})(\text{NCBH}_3)_2] \cdot 1.5 \text{CH}_3\text{OH}$ (C1)

The following reaction was carried out in a glovebox under an inert atmosphere. $[\text{Fe}(\text{py})_4(\text{NCBH}_3)_2]$ (45 mg, 0.1 mmol, 1 equiv.) was dissolved in methanol (3 ml) and stirred for 15 minutes. The solution was filtered with a syringe filter to remove unsolved particles. The filtrate was added to a solution of 2-(Naphthalen-2-yl)-5-[N,N-bis(2-pyridylmethyl)aminomethyl]-1,3,4-oxadiazole ($\text{L}^{\text{Tetra-ODA}}$) (41 mg, 0.1 mmol, 1 equiv.) in methanol (2 ml). The solution was kept undisturbed and set for slow evaporation of the solvent. After two days, orange block shaped crystals had formed that were suitable for X-ray structure analysis. The crystals were collected by filtration, washed with diethyl ether and dried at atmospheric pressure to afford $[\text{Fe}(\text{L}^{\text{Tetra-ODA}})(\text{NCBH}_3)_2] \cdot 1.1\text{CH}_3\text{OH}$ (C1) (38.00 mg, 0.070 mmol, 70 %). The complex once filtered is air stable for several days and stored in bench under normal ambient aerobic conditions. FT-IR: $\tilde{\nu}$ (cm^{-1}) = 2974, 2928, 2916, 2861, 2356, 2340, 2194, 2177, 1970, 1634, 1604, 1574, 1549, 1445, 1426, 1387, 1361, 1350, 1316, 1306, 1256, 1230, 1193, 1155, 1125, 1111, 1096, 1044, 1055, 1020, 994, 984, 977, 963, 940, 902, 892, 863, 849, 821, 754, 738, 718, 683, 669, 660, 645, 596, 540, 508, 477, 456, 418. ESI-MS (m/z): calc. for $[\text{C}_{26}\text{H}_{24}\text{BFeN}_6\text{O}]^+$ expected: 503.15 (100.00 %); found: 503.146 (100.00 %). Elemental Analysis calculated for $[\text{Fe}(\text{L}^{\text{Tetra-ODA}})(\text{NCBH}_3)_2] \cdot 1.5 \text{CH}_3\text{OH}$: C, 57.91, H, 4.90, N, 17.34. Found: C, 57.79, H, 4.90, N, 17.34.

$[\text{Zn}(\text{L}^{\text{Tetra-ODA}})(\text{NCBH}_3)_2] \cdot 0.5 \text{H}_2\text{O}$ (C2)

$[\text{Zn}(\text{py})_4(\text{NCBH}_3)_2]$ (45 mg, 0.1 mmol, 1 equiv.) was dissolved in methanol (3 ml) and stirred for 15 minutes. The solution was filtered with a syringe filter to remove unsolved particles. The filtrate was added to a solution of 2-(Naphthalen-2-yl)-5-[N,N-bis(2-pyridylmethyl)aminomethyl]-1,3,4-oxadiazole ($\text{L}^{\text{Tetra-ODA}}$) (41 mg, 0.1 mmol, 1 equiv.) in acetonitrile (3 ml). The solution was kept undisturbed and set for slow evaporation of the solvent. After one day, colourless microcrystalline needles were formed. The crystals were collected by filtration, washed with diethyl ether and dried at atmospheric pressure to yield $[\text{Zn}(\text{L}^{\text{Tetra-ODA}})(\text{NCBH}_3)_2]$ (C2) (23.48 mg, 0.042 mmol, 42 %). $^1\text{H-NMR}$ (400 MHz, DMSO, δ (ppm)): 8.71 - 8.65 (m, 3H), 8.21 - 8.07 (m, 6H), 7.70 - 7.64 (m, 6H), 4.55 (d, 2H, ODA- CH_2), 4.27 - 4.23 (m, 4H, Py- CH_2), 0.56 - 0.05 (m, 6H, BH_3). FT-IR: $\tilde{\nu}$ (cm^{-1}) = 3056, 2941, 2867, 2353, 2340, 2200, 2190, 1607, 1573, 1559, 1539, 1508, 1489, 1481, 1455, 1443, 1389, 1371, 1338, 1312, 1292, 1270, 1222, 1159, 1145, 1123, 1114, 1096, 1075, 1055, 1026, 997, 987, 967, 954, 910, 864,

846, 823, 795, 767, 752, 733, 723, 683, 652, 632, 593, 529, 502, 492, 476, 458, 418; ESI-MS (m/z): calc. for $[\text{C}_{26}\text{H}_{24}\text{BZnN}_6\text{O}]^+$ expected: 511.14 (100.00 %); found: 511.140 (100.00 %). Elemental analysis calculated for $[\text{Zn}(\text{L}^{\text{Tetra-ODA}})(\text{NCBH}_3)_2] \cdot 0.5 \text{H}_2\text{O}$: C, 57.75, H, 5.03, N, 17.06. Found C 57.64, H, 4.93, N, 17.59.

Acknowledgment:

SUS, JGB, JE, L.M.C and ER sincerely thanks the JGU Mainz for the funding and support. We thank Dr. Mihail Mondeski for the *Evans NMR* measurement. We would also like to thank the referees very much for taking the time to provide constructive feedback, which enabled us to improve this manuscript significantly.

Literature:

- [1] J. M. Zadrozny, D. J. Xiao, M. Atanasov, G. J. Long, F. Grandjean, F. Neese and J. R. Long, *Nat. Chem.*, **2013**, 5, 577–581.
- [2] J. Paglione and R. L. Greene, *Nat. Phys.*, **2010**, 6, 645–658.
- [3] Kawakami, T., Tsujimoto, Y., Kageyama, H. *et al.* Spin transition in a four-coordinate iron oxide. *Nature Chem.*, **2009**, 1, 371–376
- [4] V. A. Larson, B. Battistella, K. Ray, N. Lehnert and W. Nam, *Nat. Rev. Chem.*, **2020**, 4, 404–419.
- [5] M. A. Halcrow, *Spin-Crossover Materials: Properties and Applications*, John Wiley and Sons, **2013**.
- [6] D. J. Harding, P. Harding and W. Phonsri, *Coord. Chem. Rev.*, **2016**, 313, 38–61.
- [7] A. B. Gaspar and M. Seredyuk, *Coord. Chem. Rev.*, **2014**, 268, 41–58.
- [8] P. Gütlich, Y. Garcia and H. A. Goodwin, *Chem. Soc. Rev.*, **2000**, 29, 419–427.
- [9] A. Enriquez-Cabrera, A. Rapakousiou, M. Piedrahita Bello, G. Molnár, L. Salmon and A. Bousseksou, *Coord. Chem. Rev.*, **2020**, 419, 213396.
- [10] S. Sundaresan, I. A. Kühne, C. Evesson, M. M. Harris, A. J. Fitzpatrick, A. Ahmed, H. Müller-Bunz and G. G. Morgan, *Polyhedron*, **2021**, 208, 115386.
- [11] L. Cambi and L. Szegő, *Berichte der deutschen chemischen Gesellschaft (A and B Series)*, **1931**, 64, 2591–2598.
- [12] R. W. Hogue, S. Singh and S. Brooker, *Chem.Soc.Rev.*, **2018**, 47, 7303–7338.

- [13] S. Hayami, Y. Komatsu, T. Shimizu, H. Kamihata and Y. H. Lee, *Coord. Chem. Rev.*, **2011**, 255, 1981–1990.
- [14] I. Krivokapic, M. Zerara, M. L. Daku, A. Vargas, C. Enachescu, C. Ambrus, P. Tregenna-Piggott, N. Amstutz, E. Krausz and A. Hauser, *Coord. Chem. Rev.*, **2007**, 251, 364–378.
- [15] J. Olguín, *Coord. Chem. Rev.*, **2020**, 407, 213148.
- [16] V. Gómez, C. Sáenz De Pipaón, P. Maldonado-Illescas, J. C. Waerenborgh, E. Martin, J. Benet-Buchholz and J. R. Galán-Mascarós, *J. Am. Chem. Soc.*, **2015**, 137, 11924–11927.
- [17] J. F. Létard, *J. Mater. Chem.*, **2006**, 16, 2550–2559.
- [18] J. Klingele, D. Kaase, M. Schmucker, Y. Lan, G. Chastanet and ois Le, *Inorg. Chem*, **2013**, 52, 6010.
- [19] H. L. C. Feltham, A. S. Barltrop and S. Brooker, *Coord. Chem. Rev.*, **2017**, 344, 26–53.
- [20] K. S. Kumar and M. Ruben, *Angewandte Chemie - International Edition*, **2021**, 60, 7502–7521.
- [21] K. Senthil Kumar and M. Ruben, *Coord. Chem. Rev.*, **2017**, 346, 176–205.
- [22] N. A. A. M. Amin, S. M. Said, M. F. M. Salleh, A. M. Afifi, N. M. J. N. Ibrahim, M. M. I. M. Hasnan, M. Tahir and N. Z. I. Hashim, *Inorganica Chim Acta*, **2023**, 544, 121168.
- [23] M. You, G. T. Nguyen, D. Shao, T. Wang, X.-Y. Chang, L. Ungur and Y.-Z. Zhang, *Dalton Trans.*, 2022, 51, 5602.
- [24] R. W. Hogue, R. G. Miller, N. G. White, H. L. C. Feltham, G. N. L. Jameson and S. Brooker, *Chem. Commun*, **2014**, 50, 1435–1437.
- [25] B. Fei, X. Q. Chen, Y. De Cai, J. K. Fang, M. L. Tong, J. Tucek and X. Bao, *Inorg. Chem. Front.*, **2018**, 5, 1671–1676.
- [26] S. Sundaresan, J. Kiehl, L. M. Carrella and E. Rentschler, *Cryst. Growth Des.*, **2023**, 23, 3, 1648-1655.
- [27] S. Rodríguez-Jiménezjiménez and S. Brooker, *Inorg. Chem.*, **2017**, 56, 13697–13708.
- [28] S. Sundaresan and S. Brooker, *Inorg. Chem.* **2023**, 62, 31, 12192–12202
- [29] J. Kiehl, T. Hochdörffer, L. M. Carrella, M. H. Nygaard, J. Overgaard and E. Rentschler, *Inorg. Chem*, **2022**, 61, 7, 3141-3151.

- [30] U. Habarakada, T. Boonprab, P. Harding, K. S. Murray, W. Phonsri, S. M. Neville, M. Ahmed and D. J. Harding, *Cryst. Growth. Des.*, **2022**, 22, 4895–4905.
- [31] S. Sundaresan, I. A. Kühne, C. T. Kelly, A. Barker, D. Salley, H. Müller-Bunz, A. K. Powell and G. G. Morgan, *Crystals*, **2019**, 9(1), 19.
- [32] C. F. Herold, S. I. Shylin and E. Rentschler, *Inorg. Chem.*, **2016**, 55, 6414–6419.
- [33] C. Köhler and E. Rentschler, *Eur. J. Inorg. Chem.*, **2016**, 1955–1960.
- [34] S. Thakur, E. Golias, I. Kumberg, K. Senthil Kumar, R. Hosseinifar, J. Torres-Rodríguez, L. Kipgen, C. Lotze, L. M. Arruda, C. Luo, F. Radu, M. Ruben and W. Kuch, *J. Phys. Chem. C*, **2021**, 125, 33.
- [35] L. A. Barrios, E. Peyrecave-Lleixà, G. A. Craig, O. Roubeau, S. J. Teat and G. Aromí, *Eur. J. Inorg. Chem.*, **2014**, 6013–6021.
- [36] L. J. Kershaw Cook, R. Kulmaczewski, R. Mohammed, S. Dudley, S. A. Barrett, M. A. Little, R. J. Deeth and M. A. Halcrow, *Angewandte Chemie*, **2016**, 128, 4399–4403.
- [37] S. Sundaresan, J. A. Kitchen and S. Brooker, *Inorg Chem Front*, **2020**, 7, 2050–2059.
- [38] S. Rodríguez-Jiménezjiménez, A. S. Barltrop, N. G. White, H. L. C. Feltham and S. Brooker, *Inorg. Chem.*, **2018**, 57, 10.
- [39] A. B. Gaspar, V. Ksenofontov, M. Seredyuk and P. Gütllich, *Coord. Chem. Rev.*, **2005**, 249, 2661–2676.
- [40] M. Schäferling, *Angew. Chem. Int. Ed.*, **2012**, 51, 3532–3554.
- [41] K. Kumar, O. Stefanczyk, S. Chorazy, K. Nakabayashi, S.-i. Ohkoshi *Angew. Chem. Int. Ed.*, **2022**, **61**, 20, e202201265.
- [42] A. K. Kabański, M. Ptak and D. S. Stefańska, *ACS Appl. Mater. Interfaces*, **2023**, 15, 51.
- [43] K. Senthil Kumar and M. Ruben, *Coord. Chem. Rev.*, **2017**, 346, 176–205.
- [44] C. F. Herold, L. M. Carrella and E. Rentschler, *Eur. J. Inorg. Chem.*, **2015**, 3632–3636.
- [45] S. Rodríguez-Jiménezjiménez, M. Yang, I. Stewart, A. L. Garden and S. Brooker, *J. Am. Chem. Soc.*, **2017**, 139, 44.
- [46] S. Sundaresan, J. Eppelsheimer, L. M. Carrella and E. Rentschler, *Crystals 2022, Vol. 12, Page 404*, **2022**, 12, 404.

- [47] P. Zoufalý, A. Kliuikov, E. Čížmár, I. Císařová and R. Herchel, *Eur. J. Inorg. Chem.*, **2021**, 1190–1199.
- [48] L. B. Picraux, B. T. Weldon and J. K. Mccusker, *Inorg. Chem.*, **2003**, 42, 2, 273-282.
- [49] M. Saito, H. Kubota, K. Yamasa, K. Suzuki, T. Majima and H. Tsuchida, *Phys. Rev. A (Coll Park)*, **2020**, 102, 12820.
- [50] M. A. Reshchikov, A. A. Kvasov, M. F. Bishop, T. McMullen, A. Usikov, V. Soukhoveev and V. A. Dmitriev, *Phys. Rev. B.*, **2011**, 84, 75212.
- [51] B. Benaicha, K. Van Do, A. Yangui, N. Pittala, A. Lusson, M. Sy, G. Bouchez, H. Fourati, C. J. G, S. Triki and K. Boukheddaden, *Chem. Sci.*, **2019**, 10, 6791-6798.
- [52] R. González-Prieto, B. Fleury, F. Schramm, G. Zoppellaro, R. Chandrasekar, O. Fuhr, S. Lebedkin, M. Kappes and M. Ruben, *Dalton Trans.*, **2011**, 40, 7564-7570.
- [53] W. L. F. Armarego, *Purification of laboratory chemicals*, **2017**.
- [54] J. C. Cobas and F. J. Sardina, *Concepts Magn Reson Part A Bridg Educ Res*, **2003**, 19, 80–96.
- [55] G. M. Sheldrick, *Acta Cryst*, **2015**, 71, 3–8.
- [56] G. M. Sheldrick, *Acta Cryst, A. Found Crystallogr.* **2008**, 64, 112–122.
- [57] G. M. Sheldrick and T. R. Schneider, *Methods Enzymol*, **1997**, 277, 319–343.
- [58] O. V Dolomanov, L. J. Bourhis, R. J. Gildea, J. A. K. Howard and H. Puschmann, *J. Appl. Cryst*, **2009**, 42, 339–341.

ESI: Synergetic Spin Singlet-Quintet Switching and Luminescence in mononuclear Fe(II) 1,3,4-Oxadiazole Tetradentate Chelates with NCBH₃ Co-ligand.

Sriram Sundaresan,^a Jens-Georg Becker,^a Julian Eppelsheimer,^a Alexander Sedykh,^b Luca. M. Carrella,^a Müller-Buschbaum^b and Eva Rentschler^{a*}

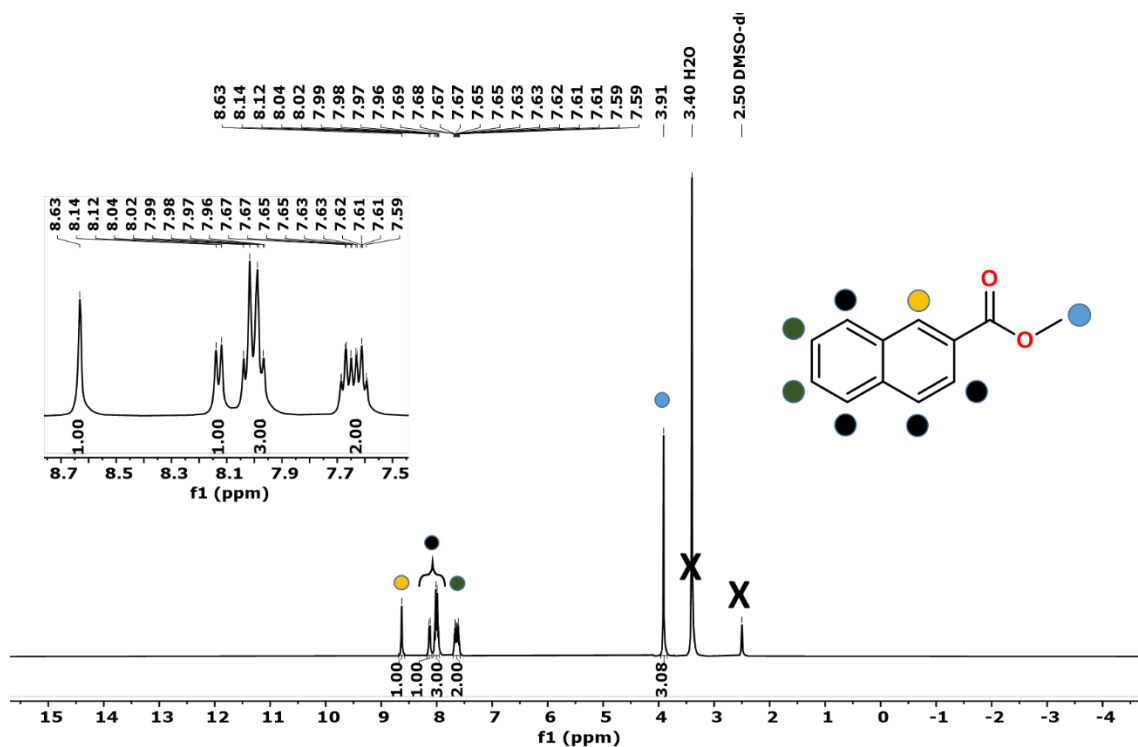
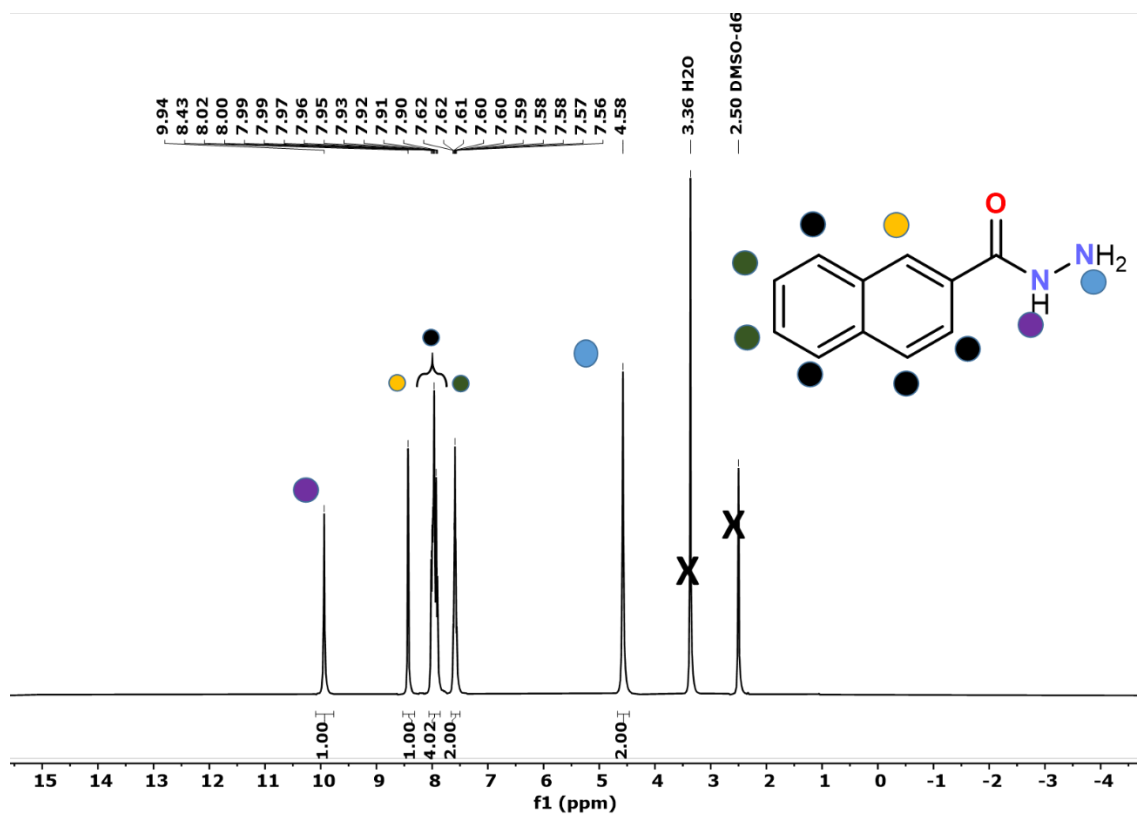
^aDepartment Chemie, Johannes-Gutenberg-Universität Mainz, Duesbergweg 10–14, 55128 Mainz, Germany.
Email: rentschl@uni-mainz.de

^bInstitute of Inorganic and Analytical Chemistry, Justus-Liebig-University Giessen, Heinrich-Buff-Ring 17, 35392, Giessen, Germany.

Table of Contents

1. <i>NMR</i> -spectra:.....	223
2. <i>IR</i> -spectra:.....	230
3. Mass spectra:.....	231
4. Crystal structures:.....	234
5. <i>UV-Vis</i> -Spectra:.....	238
6. Photoluminescence spectroscopy	240
7. Magnetic Data:	242

1. NMR-spectra:

Figure S1: $^1\text{H-NMR}$ -spectra of Methyl-2-naphthoate (I) in $\text{D}^6\text{-DMSO}$.Figure S2: $^1\text{H-NMR}$ -spectra of 2-Naphthohydrazide (II) in $\text{D}^6\text{-DMSO}$.

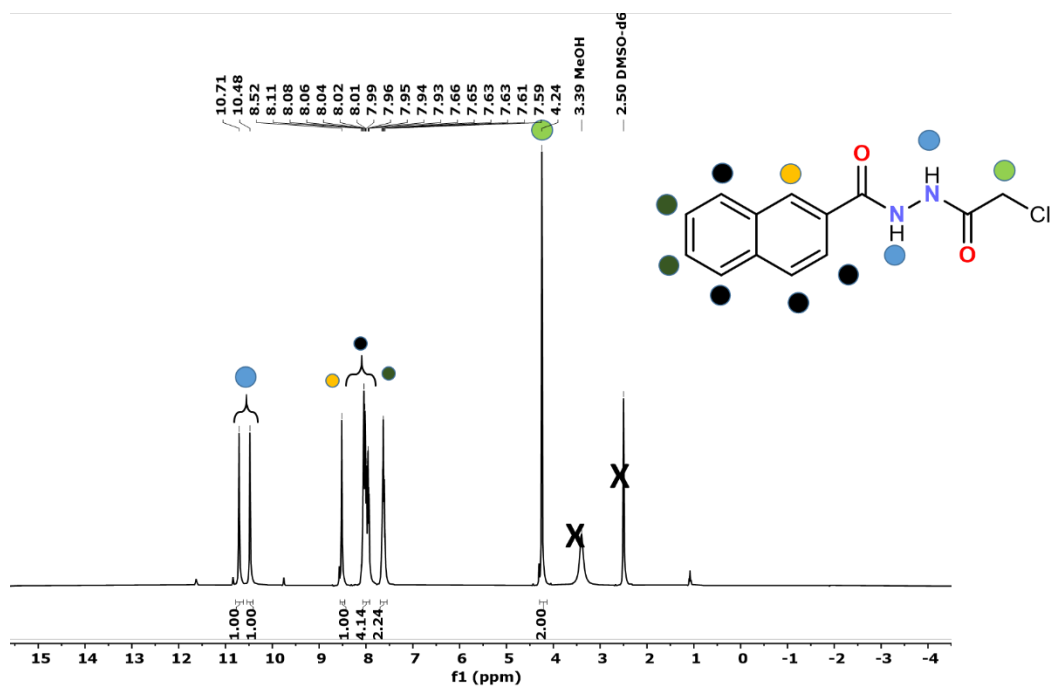


Figure S3: $^1\text{H-NMR}$ -spectra of N' -(2-chloroacetyl)-2-naphthohydrazide (III) in $\text{D}^6\text{-DMSO}$.

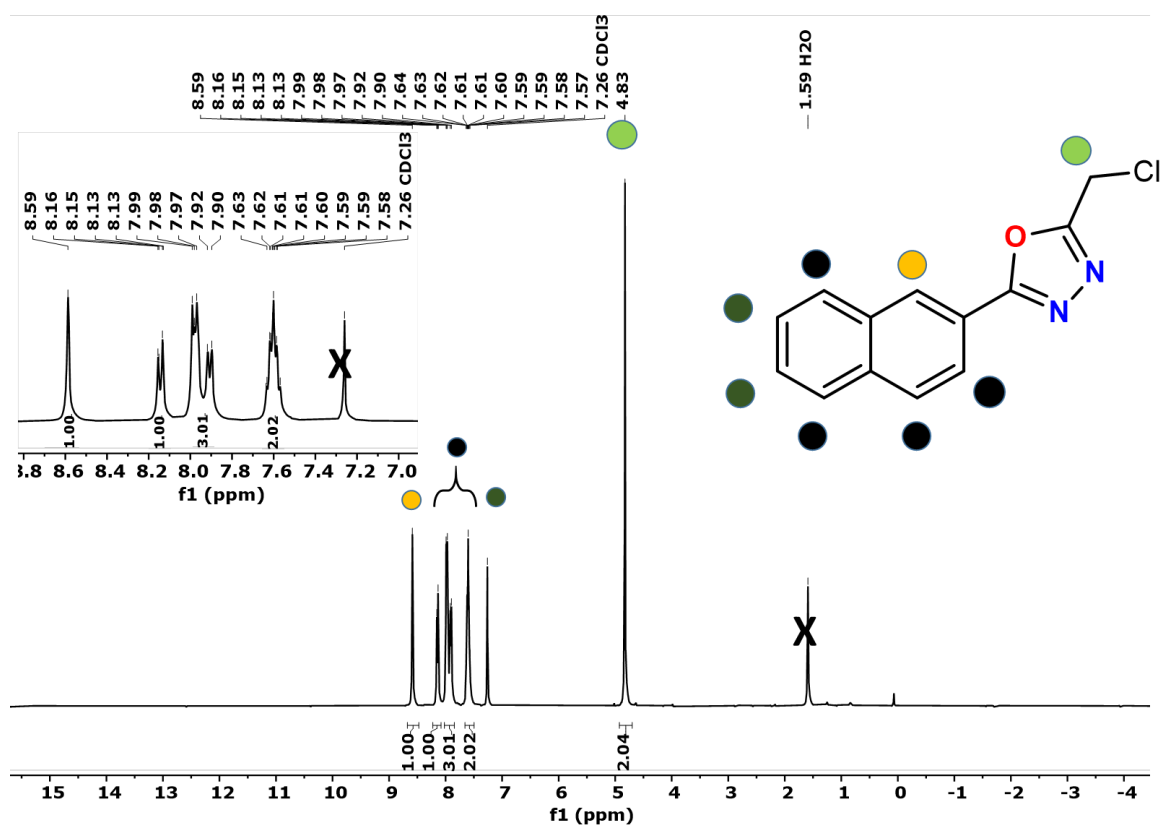


Figure S4: $^1\text{H-NMR}$ -spectra of 2-(Chloromethyl)-5-(naphthalen-2-yl)-1,3,4-oxadiazole (IV) in $\text{D}^6\text{-CDCl}_3$.

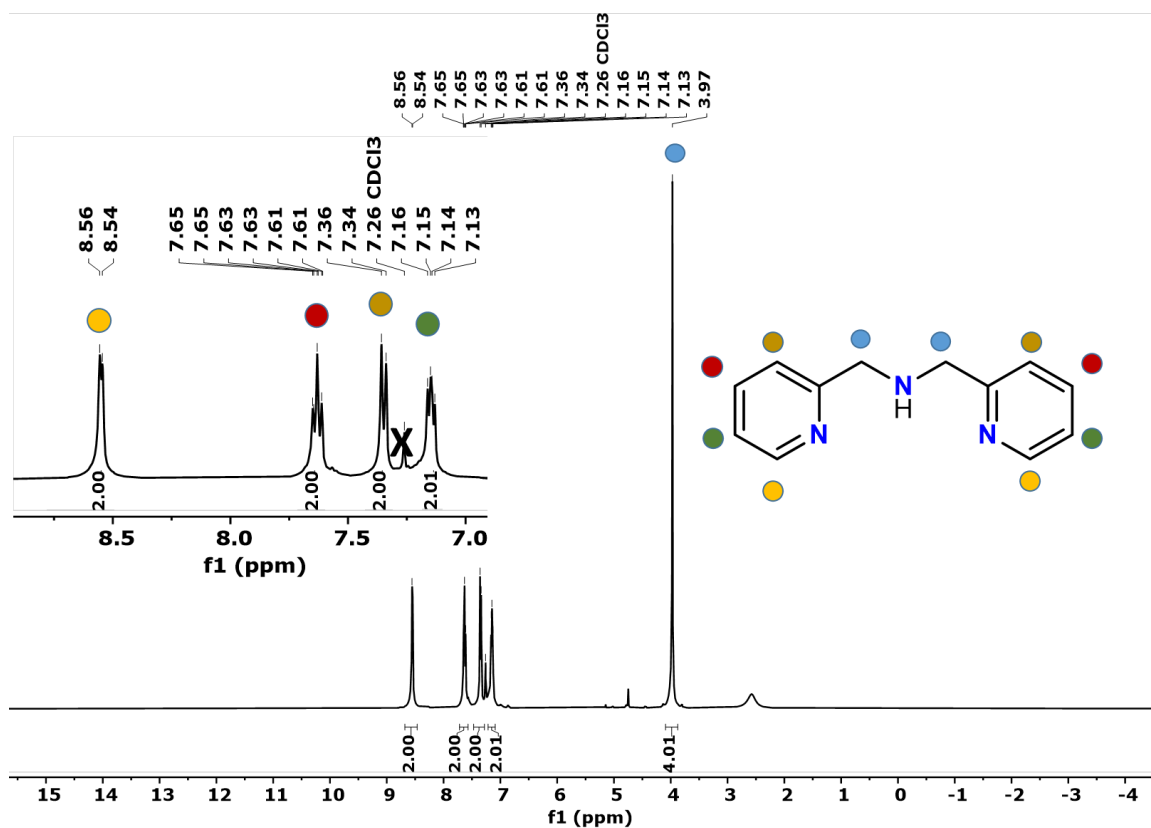


Figure S5: $^1\text{H-NMR}$ -spectra of Bis[(2-pyridyl)methyl]amine (**V**) in CDCl_3 .

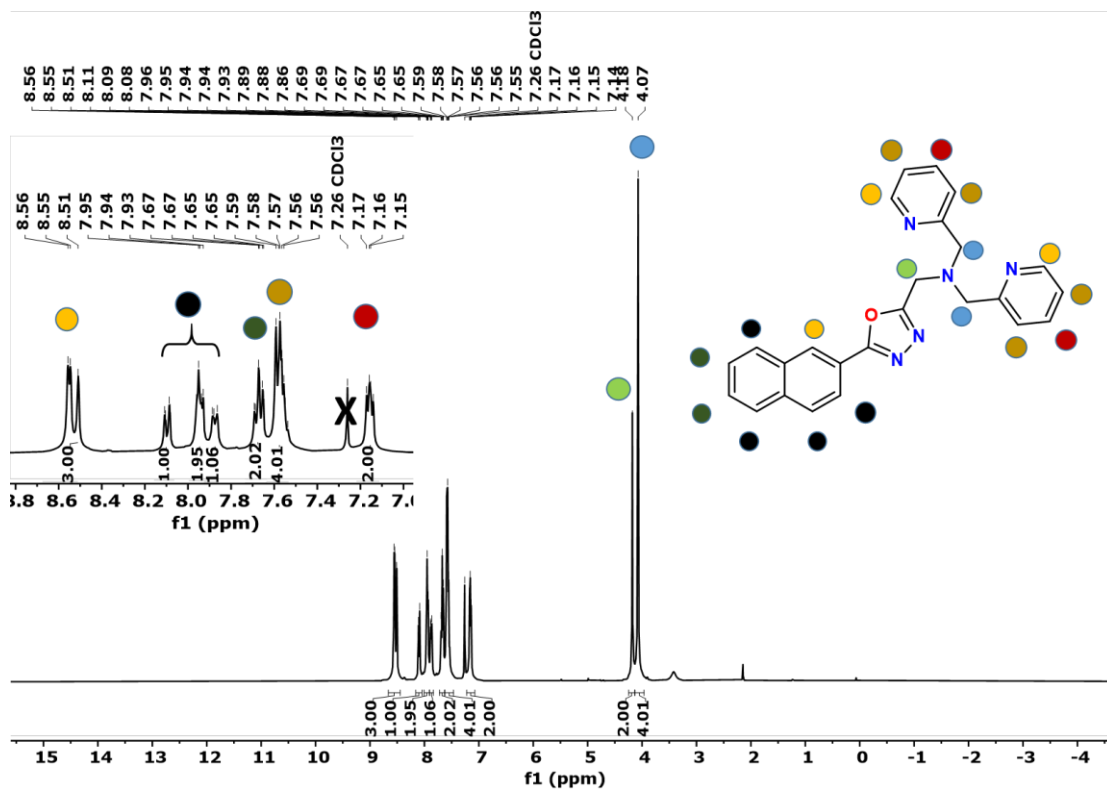


Figure S6: $^1\text{H-NMR}$ -spectra of 2-(Naphthalen-2-yl)-5-[N,N-bis(2-pyridylmethyl)aminomethyl]-1,3,4-oxadiazole (**L^{Tetra-ODA}**) in CDCl_3 .

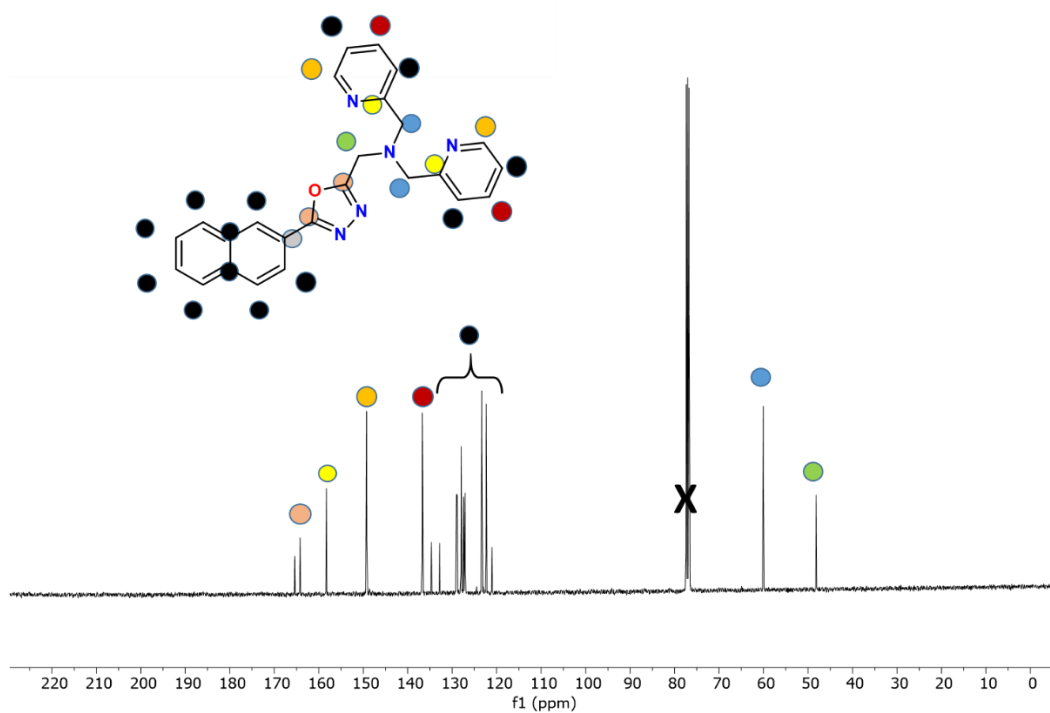


Figure S7: $^{13}\text{C-NMR}$ -spectra of 2-(Naphthalen-2-yl)-5-[N,N-bis(2-pyridylmethyl)aminomethyl]-1,3,4-oxadiazole ($L^{\text{Tetra-ODA}}$) in CDCl_3 .

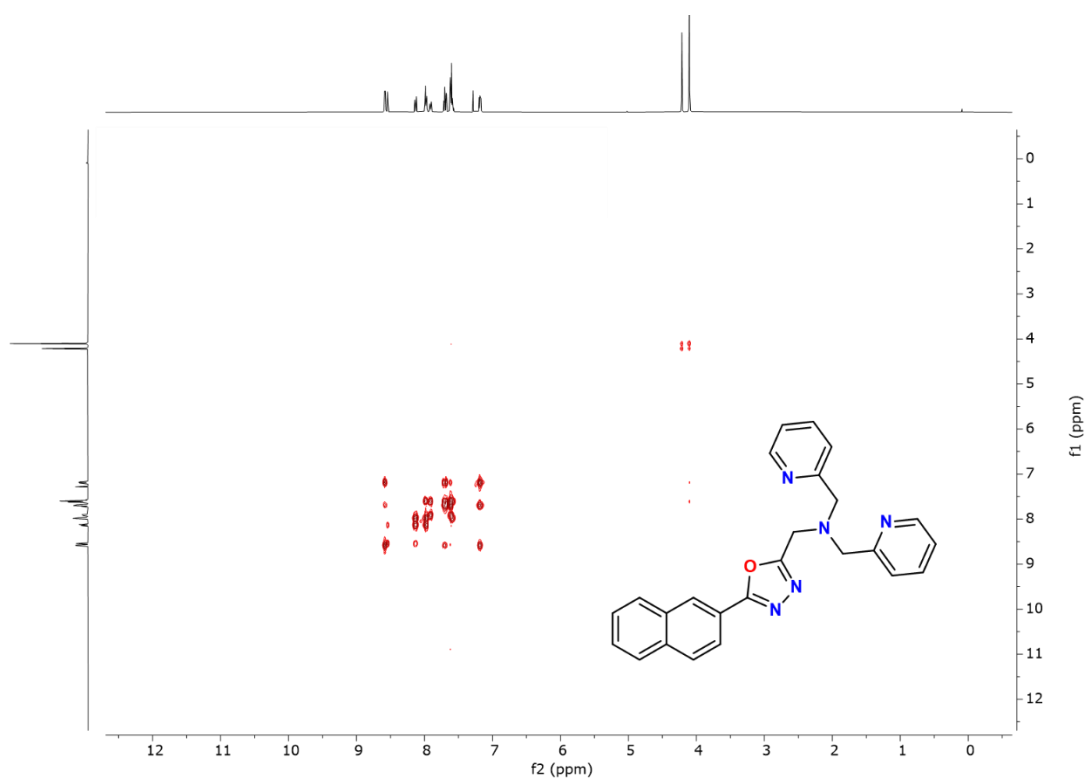


Figure S8: COSY-NMR-spectra of ($L^{\text{Tetra-ODA}}$) 2-(Naphthalen-2-yl)-5-[N,N-bis(2-pyridylmethyl)aminomethyl]-1,3,4-oxadiazole in CDCl_3 .

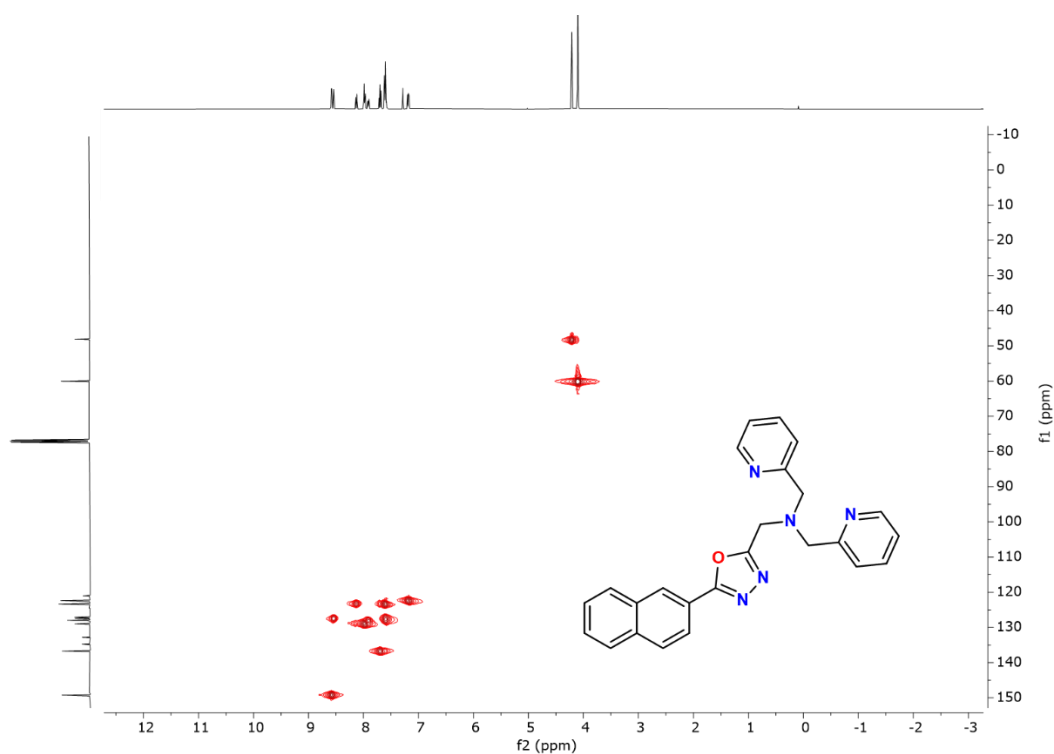


Figure S9: HSCQ-NMR-spectra of 2-(Naphthalen-2-yl)-5-[N,N-bis(2-pyridylmethyl)aminomethyl]-1,3,4-oxadiazole ($L^{\text{Tetra-ODA}}$) in $CDCl_3$.

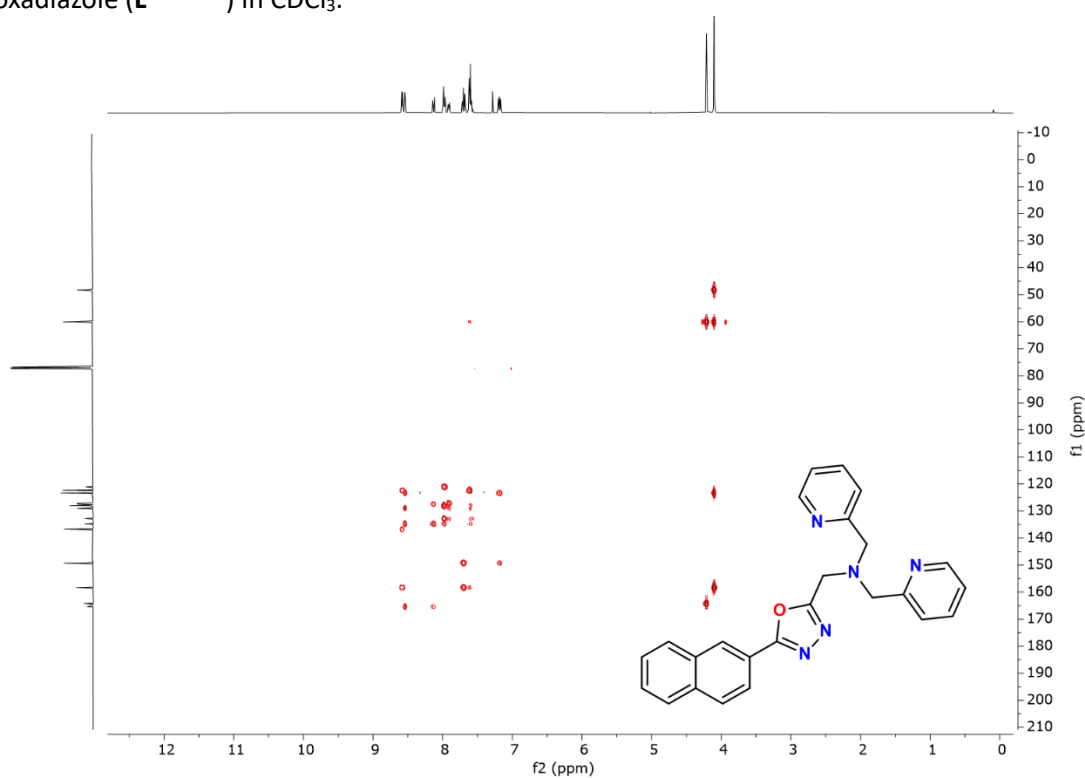
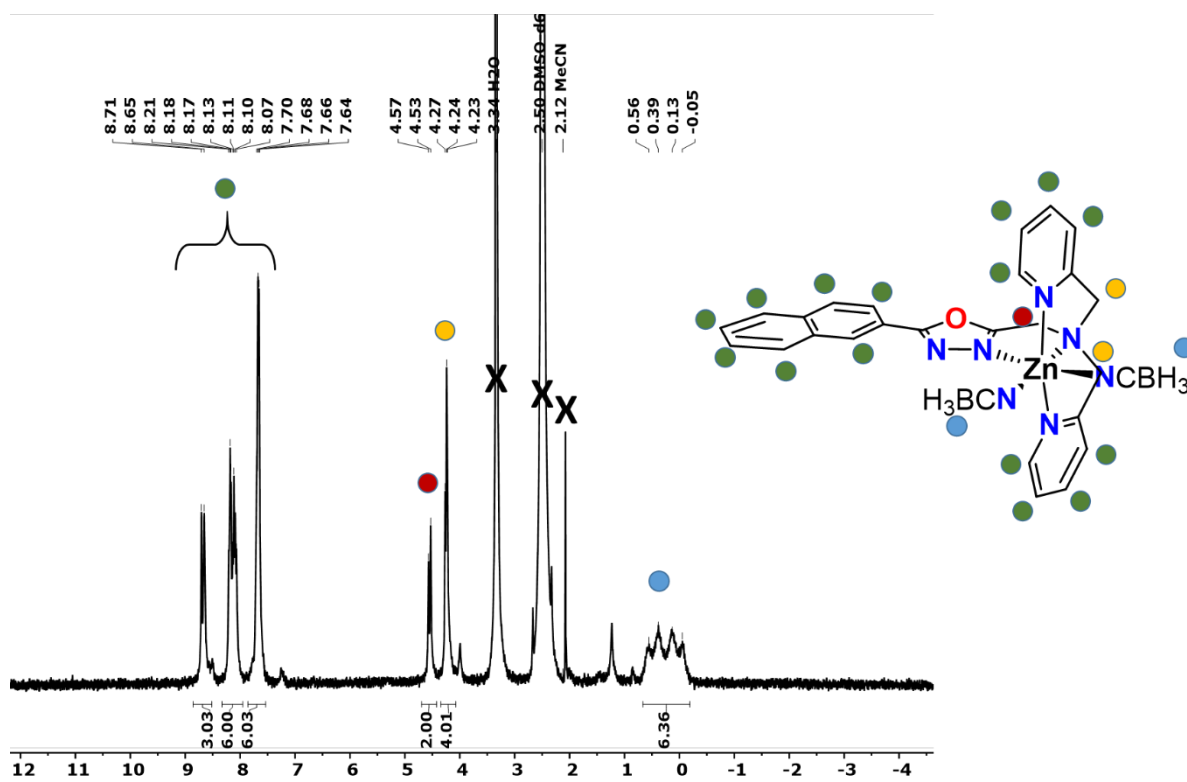
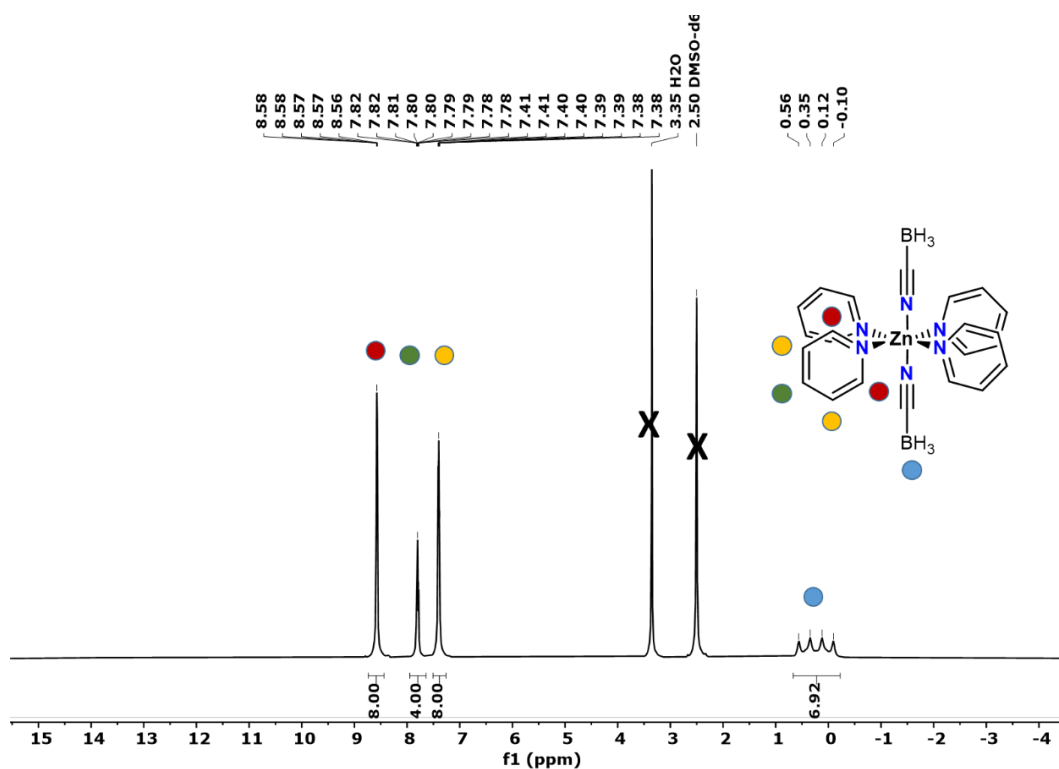


Figure S10: HMBC-NMR-spectra of 2-(Naphthalen-2-yl)-5-[N,N-bis(2-pyridylmethyl)aminomethyl]-1,3,4-oxadiazole ($L^{\text{Tetra-ODA}}$) in $CDCl_3$.



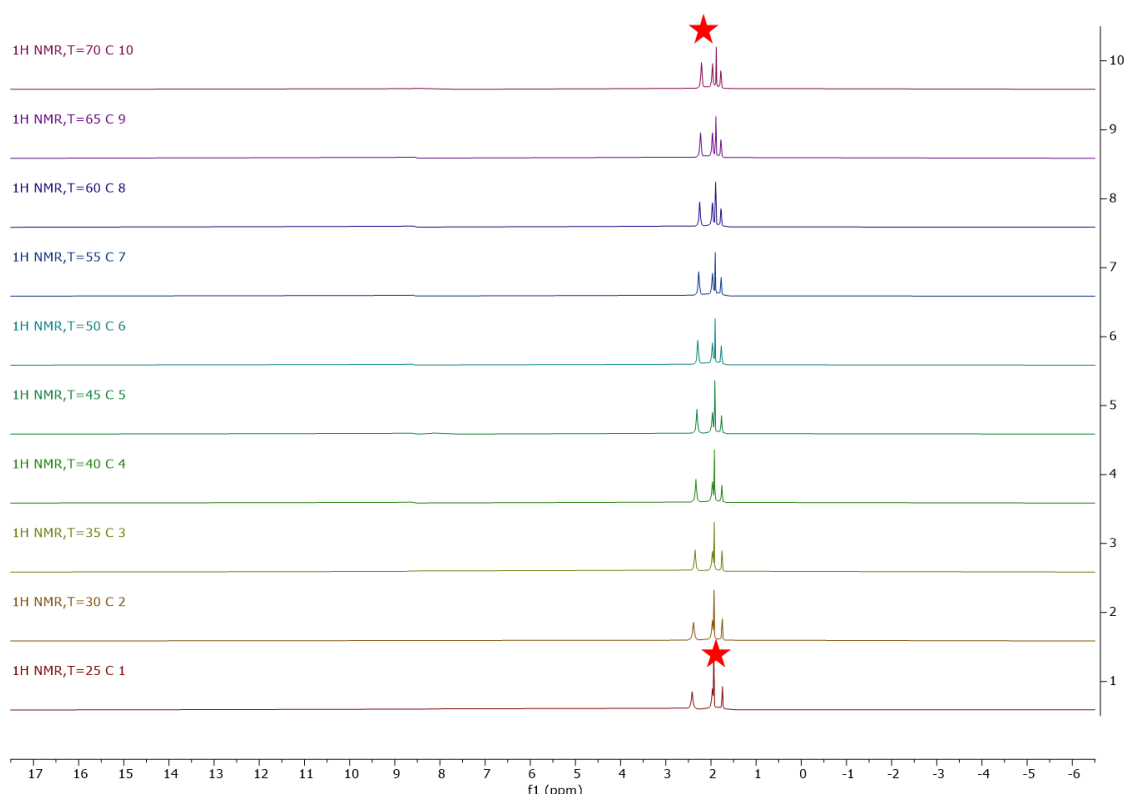


Figure S13: Temperature dependent *Evans*-measurement of $[\text{Fe}(\text{L}^{\text{Tetra-ODA}})(\text{NCBH}_3)_2] \cdot 1.5 \text{CH}_3\text{OH}$ in $\text{D}^3\text{-MeCN}$.

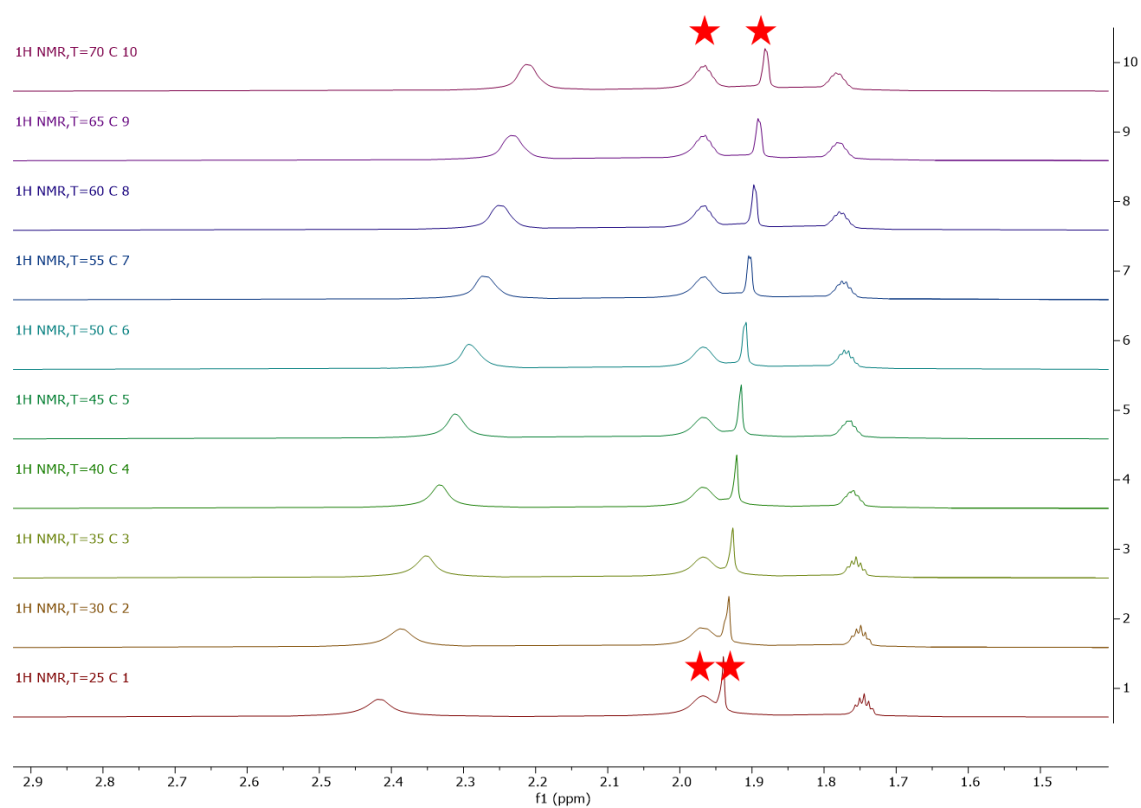


Figure S14: Temperature dependent *Evans*-measurement of $[\text{Fe}(\text{L}^{\text{Tetra-ODA}})(\text{NCBH}_3)_2] \cdot 1.5 \text{CH}_3\text{OH}$ in $\text{D}^3\text{-MeCN}$.

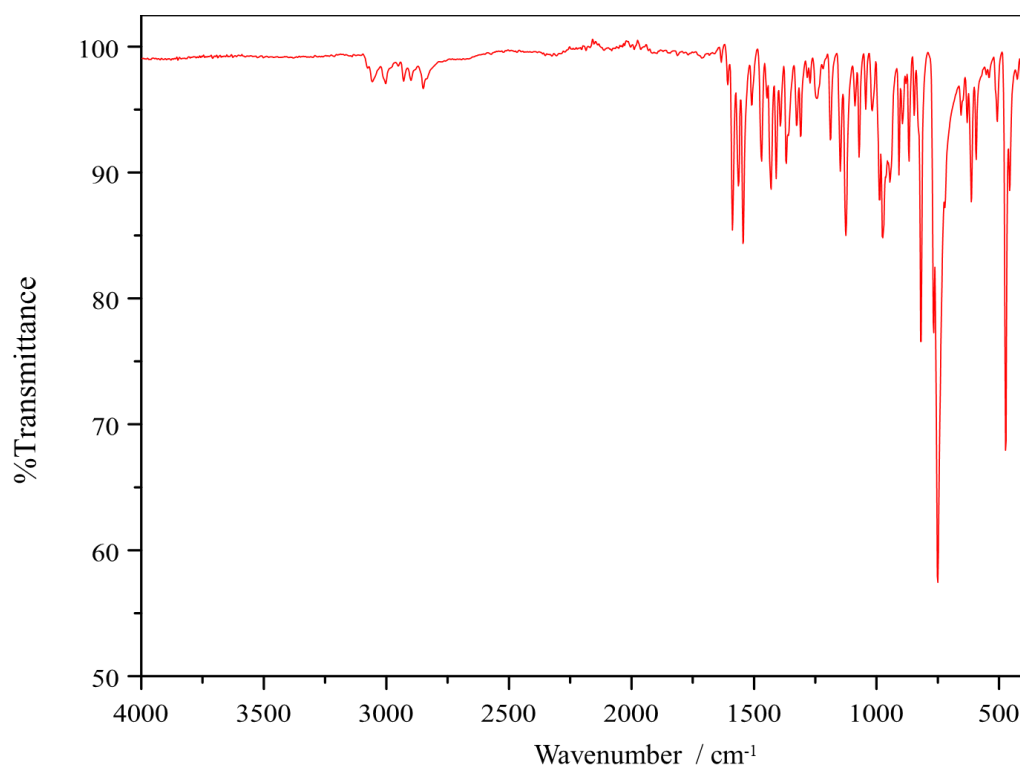
2. IR-spectra:

Figure S15: IR spectrum of 2-(Naphthalen-2-yl)-5-[N,N-bis(2-pyridylmethyl)aminomethyl]-1,3,4-oxadiazole ($L^{\text{Tetra-ODA}}$).

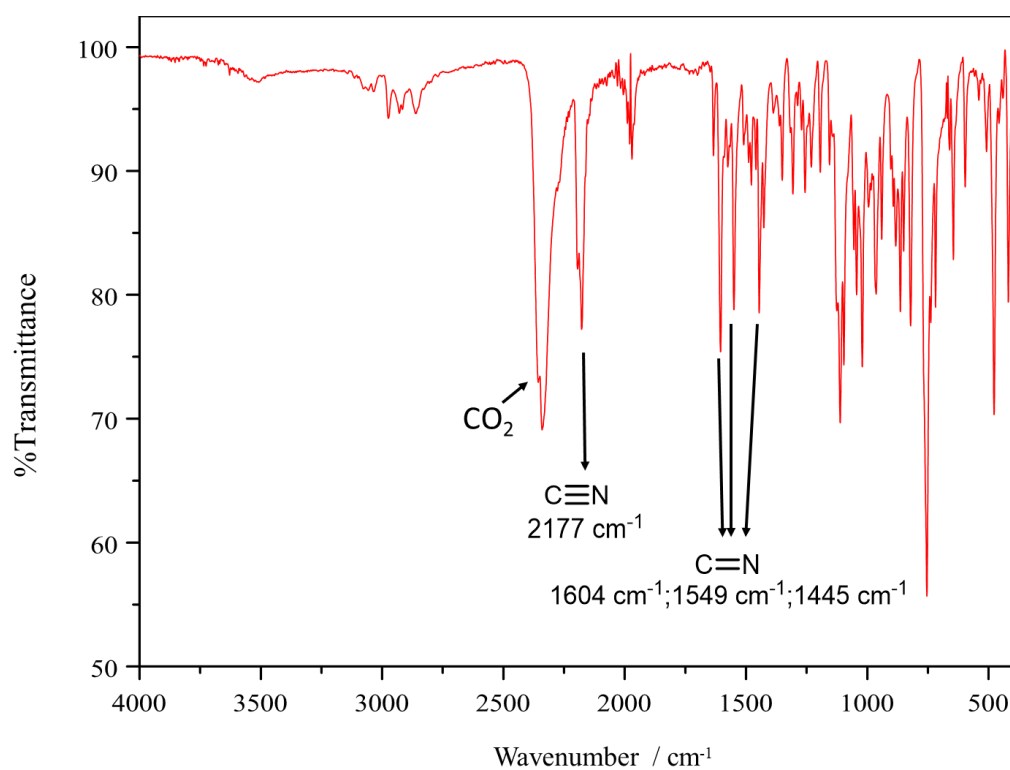


Figure S16: IR spectrum of $[\text{Fe}(L^{\text{Tetra-ODA}})(\text{NCBH}_3)_2] \cdot 1.5 \text{CH}_3\text{OH}$ (**C1**)

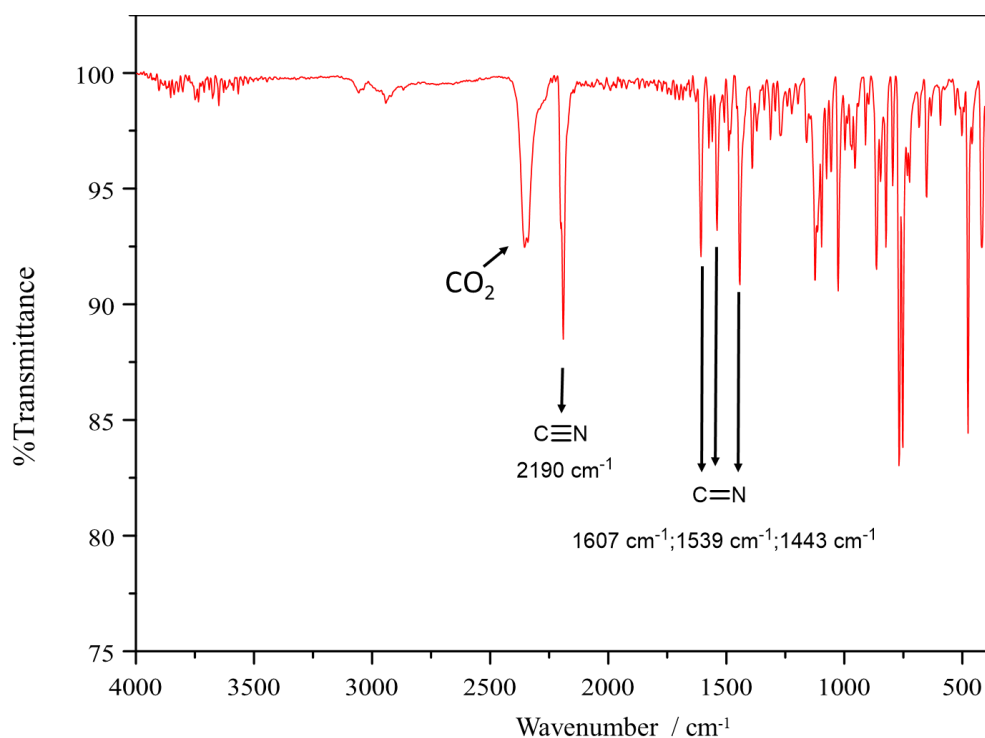


Figure S17: IR spectrum of $[Zn(L^{\text{Tetra-ODA}})(NCBH_3)_2] \cdot 0.5 H_2O$ (C2).

3. Mass spectra:

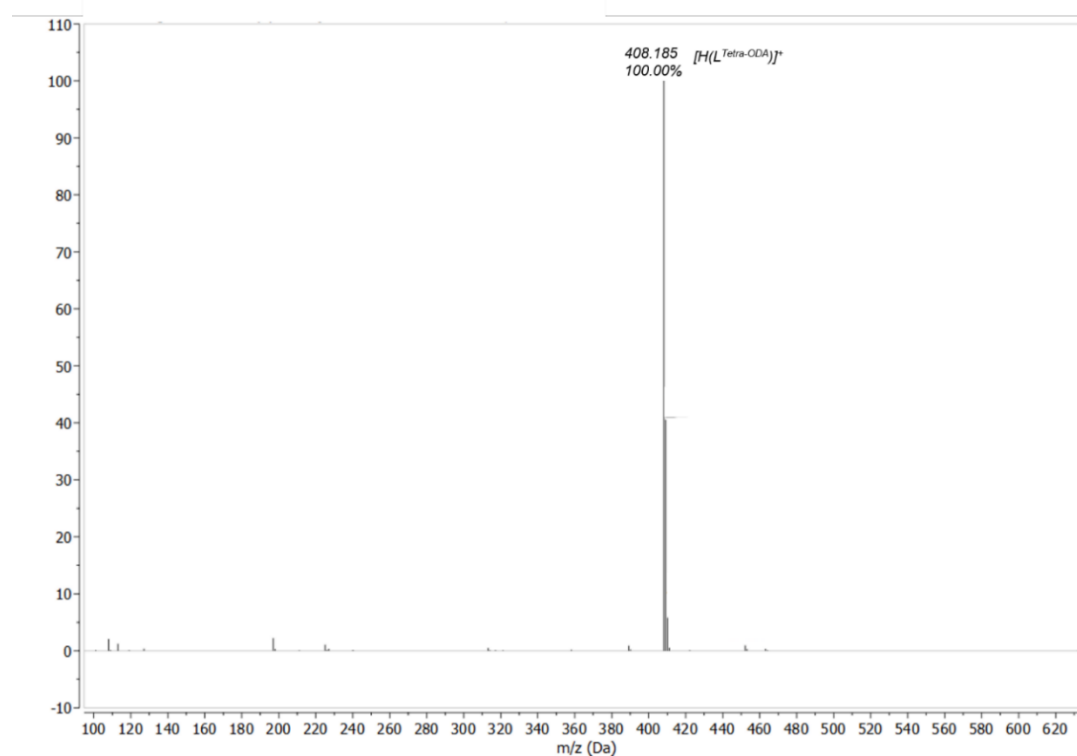


Figure S18: ESI mass spectrum of 2-(Naphthalen-2-yl)-5-[N,N-bis(2-pyridylmethyl)aminomethyl]-1,3,4-oxadiazole ($L^{\text{Tetra-ODA}}$).

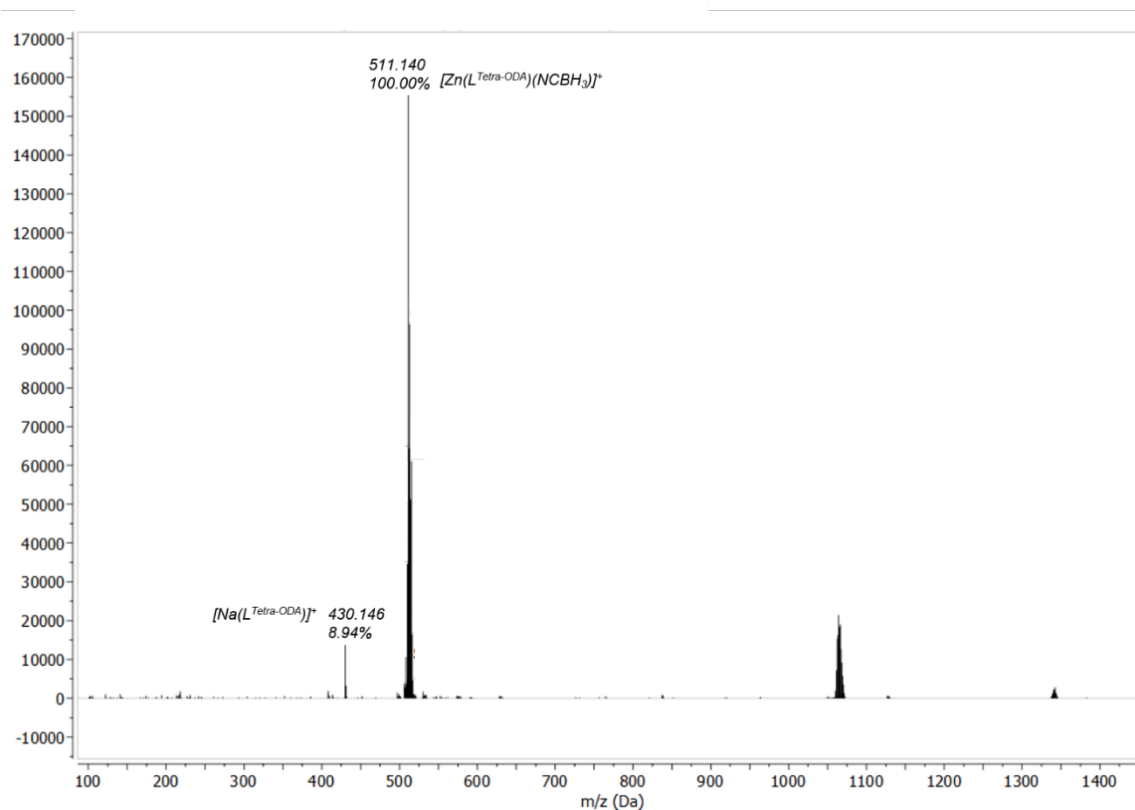


Figure S19: ESI mass spectrum of $[Zn(L^{Tetra-ODA})(NCBH_3)_2] \cdot 0.5 H_2O$.

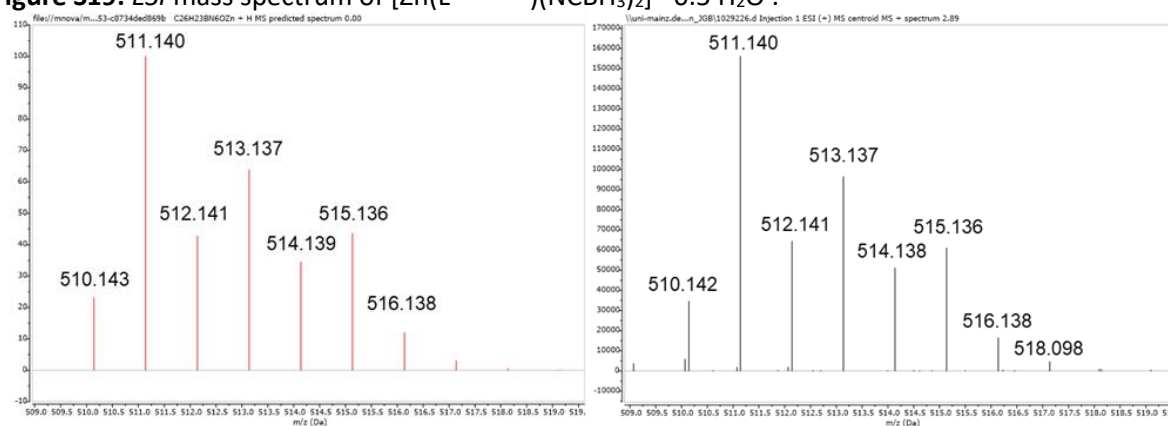


Figure S20: Isotopic pattern of ESI mass spectra of $[Zn(L^{Tetra-ODA})(NCBH_3)_2] \cdot 0.5 H_2O$: predicted (left) and measured (right).

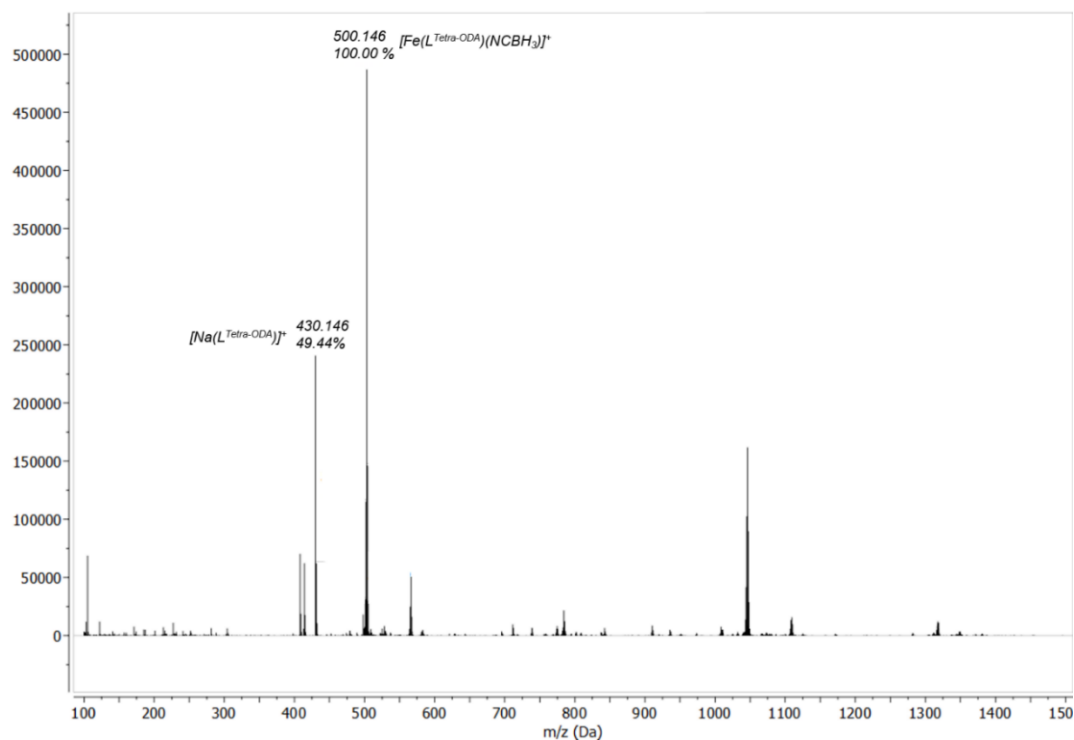


Figure S21: ESI mass spectrum of $[\text{Fe}(\text{L}^{\text{Tetra-ODA}})(\text{NCBH}_3)_2] \cdot 1.5 \text{CH}_3\text{OH}$ (**C1**)

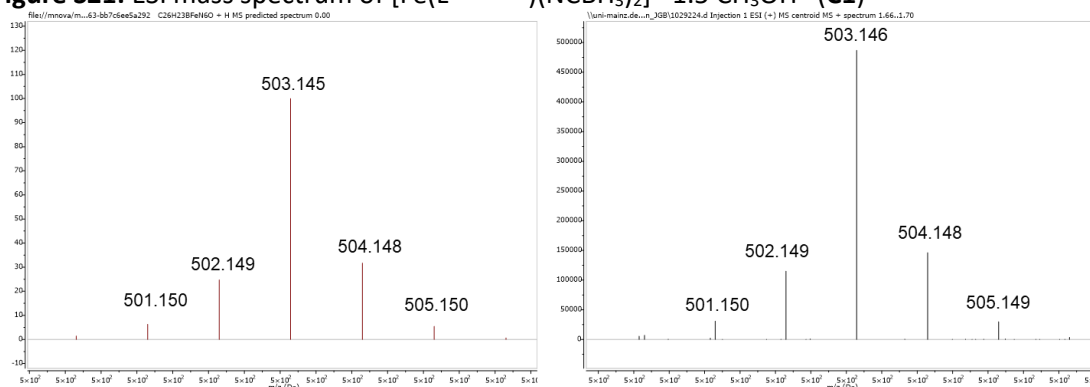


Figure S22: Isotopic pattern of ESI mass spectra of $[\text{Fe}(\text{L}^{\text{Tetra-ODA}})(\text{NCBH}_3)_2] \cdot 1.5 \text{CH}_3\text{OH}$ (**C1**): *predicted (left) and measured (right).*

4. Crystal structures:

Table S1: Crystallographic Data of $[\text{Fe}(\text{L}^{\text{Tetra-ODA}})(\text{NCBH}_3)_2] \cdot 1.5 \text{ CH}_3\text{OH}$ at 220 K and 120 K.

Compound	C1 (220 K)	C1 (120 K)
Empirical formula	(C ₂₇ H ₂₇ B ₂ FeN ₇ O) 1.5(CH ₄ O)	(C ₂₇ H ₂₇ B ₂ FeN ₇ O) 1.5(CH ₄ O)
Formula weight / g mol ⁻¹	591.09	591.09
Crystal size / mm	0.2 x 0.187 x 0.18	0.23 x 0.19 x 0.15
Crystal system	monoclinic	monoclinic
Space group	C2/c	C2/c
Unit cell dimensions		
a / Å	26.7229(7)	26.0632(7)
b / Å	10.9749(2)	10.5691(2)
c / Å	21.1290(6)	21.3067(6)
α / °	90	90
β / °	95.813(2)	96.182(2)
γ / °	90	90
Volume / Å ³	6164.9(3)	5835.1(3)
Z	8	8
ρ _{calc.} / g cm ⁻³	1.266	1.346
μ / mm ⁻¹	0.528	0.558
F(000)	2454	2472
Temperature / K	220	120
Diffractometer	STOE STADIVARI	STOE STADIVARI
Radiation	Mo-Kα	Mo-Kα
θ – range for data collection / °	1.938 < θ < 31.123	1.923 < θ < 30.771
Index ranges	-38 < h < 36 -15 < k < 15 -30 < l < 30	-36 < h < 37 -15 < k < 15 -30 < l < 30
Collected reflections	56550	51641
Independent reflections	58044	53070
Completeness	0.908	0.929
Max. and min. transmission	0.9893 and 0.4678	0.9090 and 0.2842
R _{int}	0.0364	0.0308
R _{sigma}	0.0318	0.0291
Data/ restraints/ parameters	9010 / 38 / 404	8470 / 31 / 403
Goodness-of-fit on F ²	0.977	1.078
Final R ₁ [I ≥ 2σ(I)]	0.0455	0.0444
Final wR ₂ [I ≥ 2σ(I)]	0.1354	0.1316
Final R ₁ [all data]	0.0638	0.0573
Final wR ₂ [all data]	0.1438	0.1369

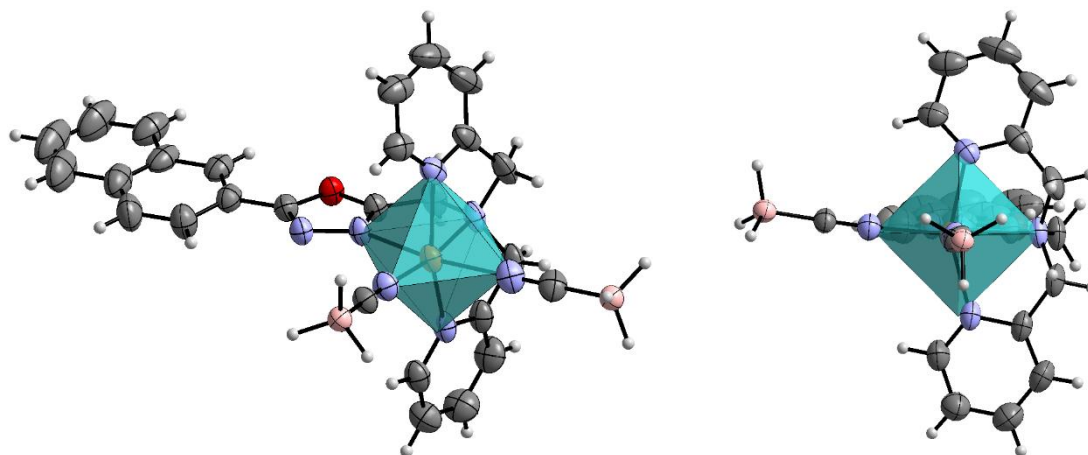


Figure S23: Molecular structure of $[\text{Fe}(\text{L}^{\text{Tetra-ODA}})(\text{NCBH}_3)_2] \cdot 1.5 \text{ CH}_3\text{OH}$ and its ideal coordination octahedron with front view (left) and view along the Fe-N5 axis (right), calculated with SHAPE. Colour scheme: dark grey – C, grey – H, violet – N, red – O, bright orange – Se, orange – Fe. ORTEP representation with atomic displacement parameters set to 50 % probability.

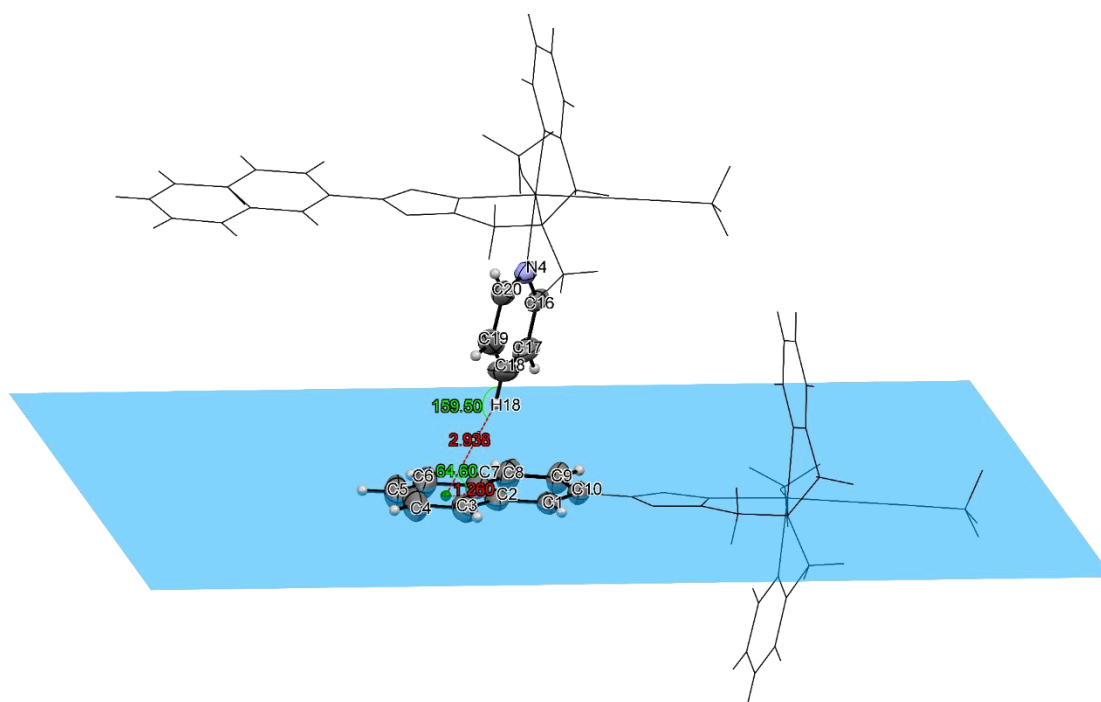


Figure S24: C-H... π interaction in $[\text{Fe}(\text{L}^{\text{Tetra-ODA}})(\text{NCBH}_3)_2] \cdot 1.5 \text{ CH}_3\text{OH}$ (240 K). Least-squares plane A is defined by C2, C3, C4, C5, C6 and C7. Interacting C-H fragment is labeled as C18-H18. Green point – center of the aromatic ring in A. Purple point – orthogonal intersection of H18 onto plane A. *Offset* $r = 1.26 \text{ \AA}$, *interaction distance* $d_{\text{QH}} = 2.94 \text{ \AA}$, $\alpha = 159.5^\circ$ and $\beta = 64.6^\circ$. ORTEP representation with atomic displacement parameters set to 50 % probability.

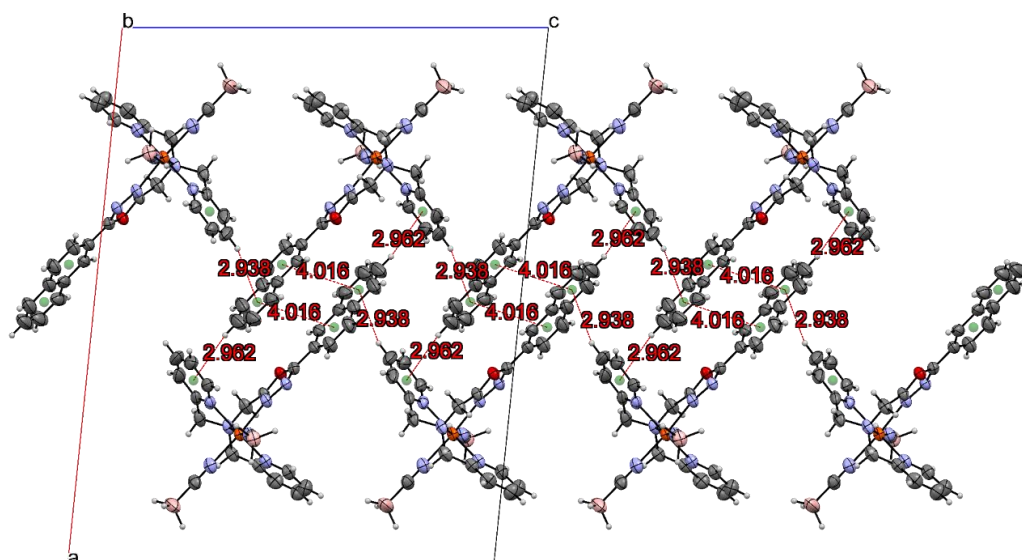


Figure S25: One-dimensional network of “complex dimers” in $[\text{Fe}(\text{L}^{\text{Tetra-ODA}})(\text{NCBH}_3)_2] \cdot 1.5 \text{CH}_3\text{OH}$. Red dashed lines represent intermolecular distances. Colour scheme: pink – B, dark grey – C, grey – H, violet – N, red – O, orange – Fe. ORTEP representation with atomic displacement parameters set to 50 % probability.

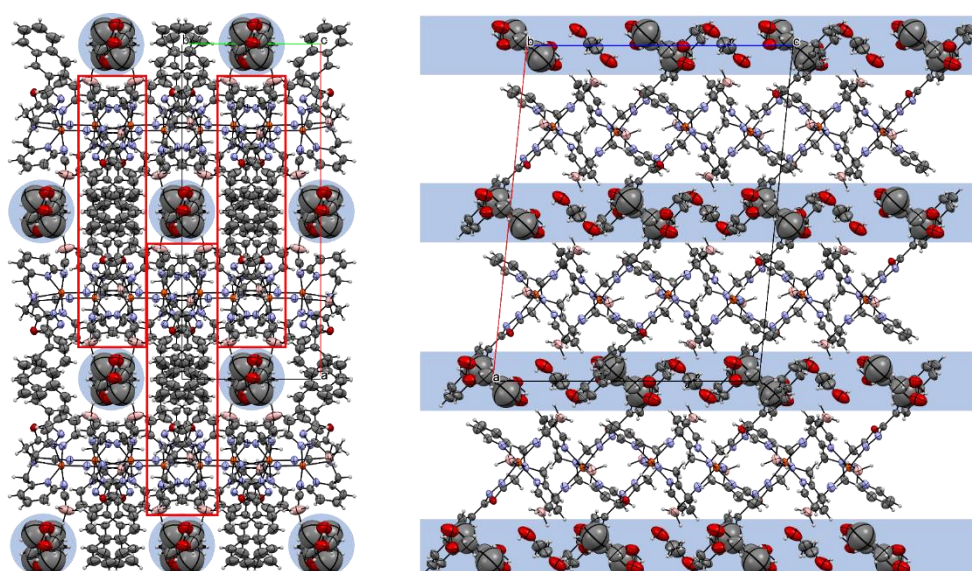


Figure S26: Packing of $[\text{Fe}(\text{L}^{\text{Tetra-ODA}})(\text{NCBH}_3)_2] \cdot 1.5 \text{CH}_3\text{OH}$ with view along the c-axis (left) and view along the b-axis (right). Red rectangles mark the one-dimensional chains of complex molecules along the c-axis. Blue areas illustrate the channel of solvent molecules. Colour scheme: pink – B, dark grey – C, grey – H, violet – N, red – O, orange – Fe. ORTEP representation with atomic displacement parameters set to 50 % probability.

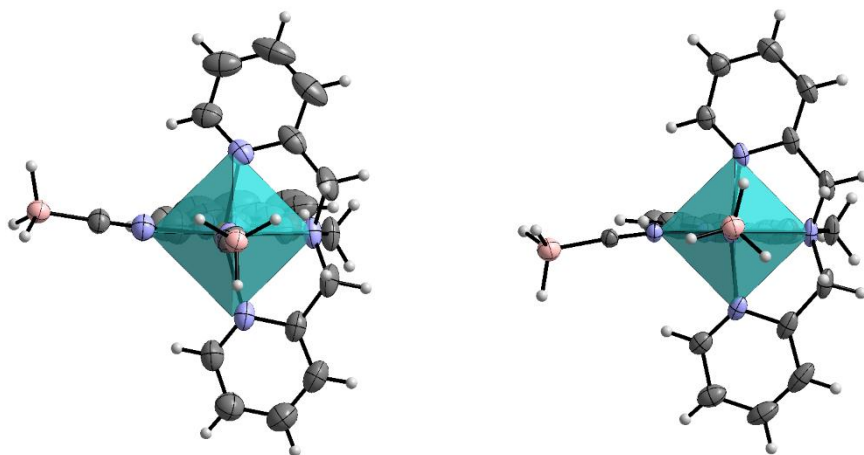


Figure S27: Molecular structure of $[\text{Fe}(\text{L}^{\text{Tetra-ODA}})(\text{NCBH}_3)_2] \cdot 1.5 \text{CH}_3\text{OH}$ and its ideal coordination octahedron with view along the Fe-N5 axis at 220 K (left) and 120 K (right), calculated with SHAPE. Colour scheme: pink – B, dark grey – C, grey – H, violet – N, red – O, orange – Fe. ORTEP representation with atomic displacement parameters set to 50 % probability.

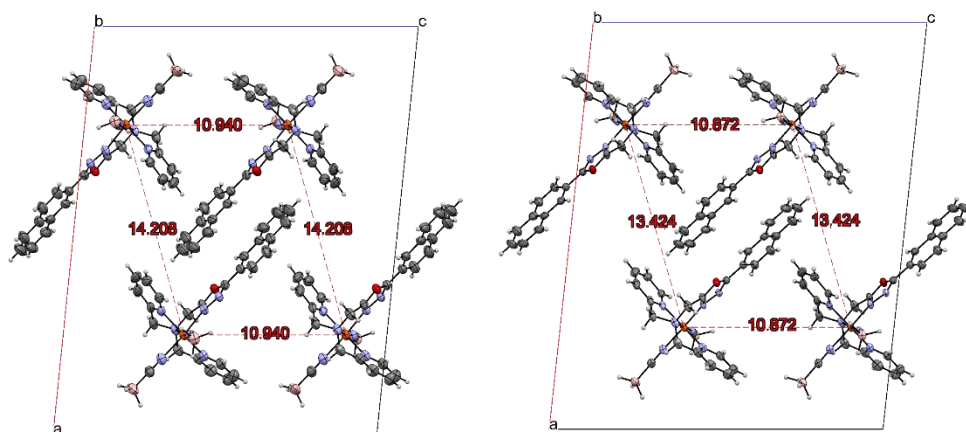


Figure S28: One-dimensional network of “complex dimers” in $[\text{Fe}(\text{L}^{\text{Tetra-ODA}})(\text{NCBH}_3)_2] \cdot 1.5 \text{CH}_3\text{OH}$ at 220 K (left) and 120 K (right). Unit cell changes are remarkably more pronounced along the a-axis, which corresponds to the interdimer short contacts. Red dashed lines represent intermolecular distances between iron(II) centers. Colour scheme: pink – B, dark grey – C, grey – H, violet – N, red – O, orange – Fe. ORTEP representation with atomic displacement parameters set to 50 % probability.

5. UV-Vis spectra:

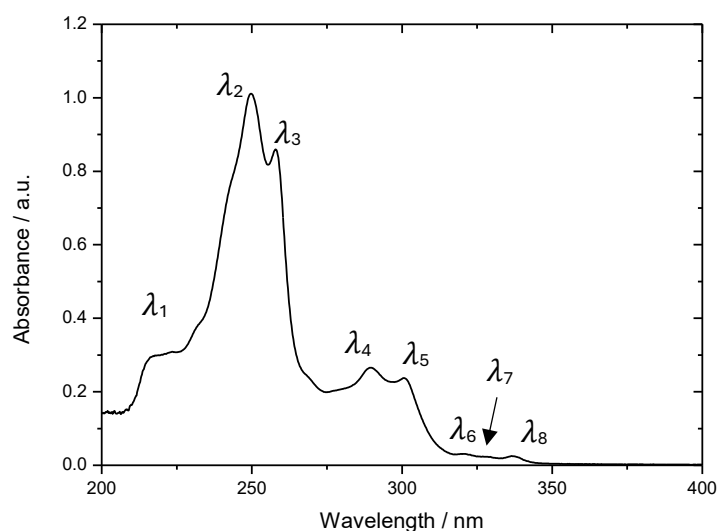


Figure S29: UV-Vis spectrum of $L^{\text{Tetra-ODA}}$ in n-butyronitril ($c = 0.03 \text{ mmol}\cdot\text{l}^{-1}$).

Table S2: Summary of the present absorption maxima λ_i in the UV-Vis spectrum of $L^{\text{Tetra-ODA}}$ in n-butyronitril with corresponding molar extinction coefficients (ϵ) in $\text{M}^{-1}\cdot\text{cm}^{-1}$.

	λ_1	λ_2	λ_3	λ_4	λ_5	λ_6	λ_7	λ_8
$\lambda_{\text{obs}} / \text{nm}$	216	249	258	289	300	320	328	337
$\epsilon / \text{M}^{-1}\text{cm}^{-1}$	15084	79001	67250	13506	11902	1068	775	850

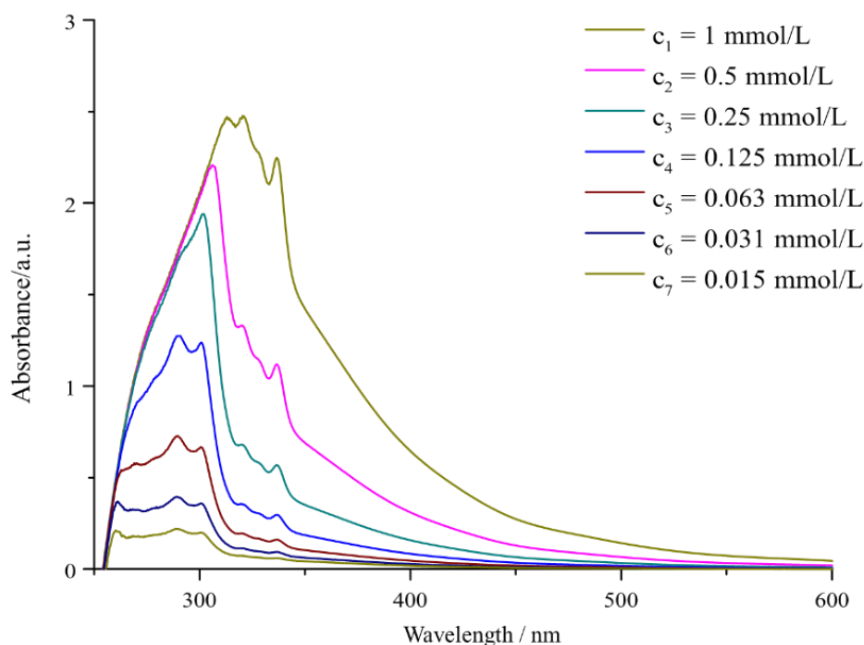
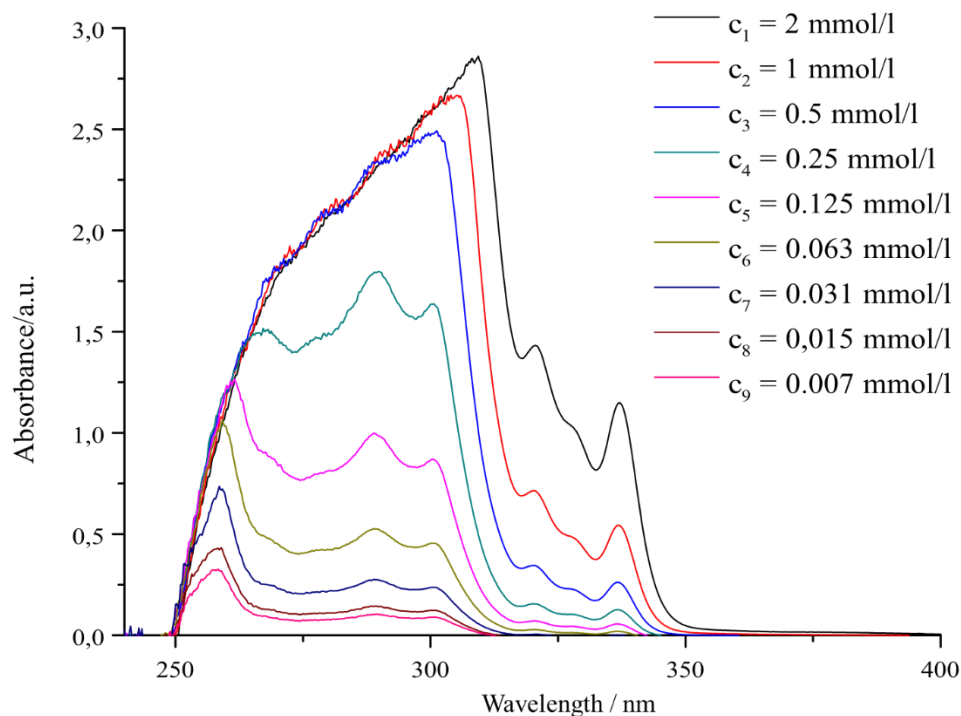


Figure 30: UV-Vis spectra of $[\text{Fe}(\text{L}^{\text{Tetra-ODA}})(\text{NCBH}_3)_2] \cdot 1.5 \text{ CH}_3\text{OH}$ in n-butyronitrile for different concentrations. From measurement to measurement, the concentration was halved by diluting the solution. There is no absorption observable between 600-1000 nm.

Table S3: Summary of the present absorption maxima λ_i in the UV-Vis spectra of $[\text{Fe}(\text{L}^{\text{Tetra-ODA}})(\text{NCBH}_3)_2] \cdot 1.5 \text{ CH}_3\text{OH}$ in n-butyronitrile with corresponding molar extinction coefficients ϵ in $\text{M}^{-1}\cdot\text{cm}^{-1}$.

	λ_1	λ_2	λ_3	λ_4	λ_5	λ_6
$\lambda_{\text{abs}} / \text{nm}$	258	289	301	320	328	337
$\epsilon / \text{M}^{-1}\text{cm}^{-1}$	2657	2729	3192	12488	13588	12890

**Figure S31:** UV-Vis spectra of $[\text{Zn}(\text{L}^{\text{Tetra-ODA}})(\text{NCBH}_3)_2] \cdot 0.5 \text{ H}_2\text{O}$ in n-butyronitrile for different concentrations. From measurement to measurement, the concentration was halved by diluting the solution. There is no absorption observable between 400-1000 nm.

6. Photoluminescence spectroscopy

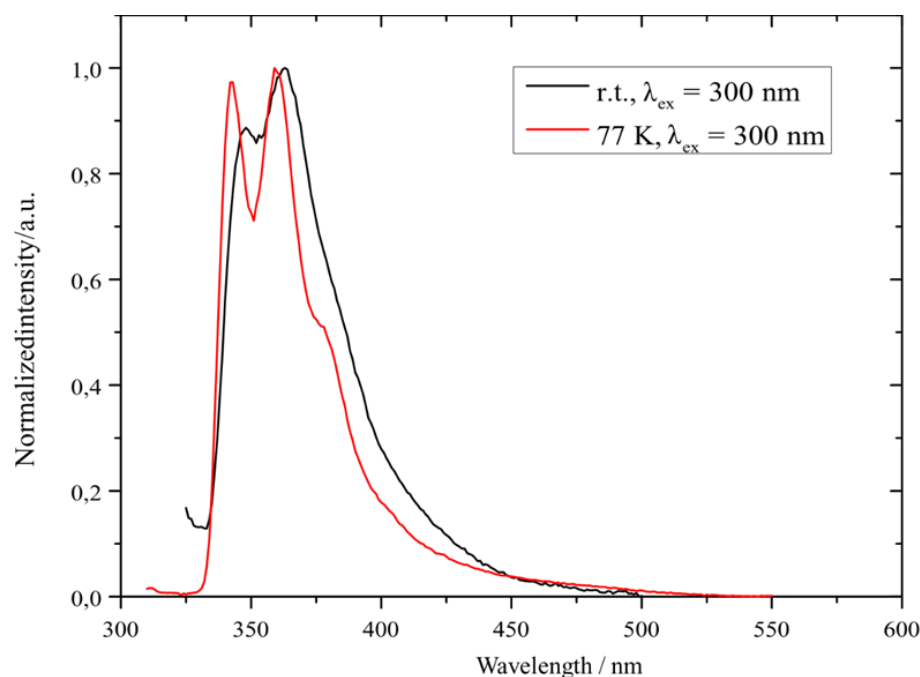


Figure S32: PL-spectra of $[\text{Fe}(\text{L}^{\text{Tetra-ODA}})(\text{NCBH}_3)_2] \cdot 1.5 \text{CH}_3\text{OH}$ in solid state. Samples were excited with $\lambda_{\text{ex}} = 300 \text{ nm}$. Measurements were done at 77 K (red solid lines) and at room temperature (black solid lines).

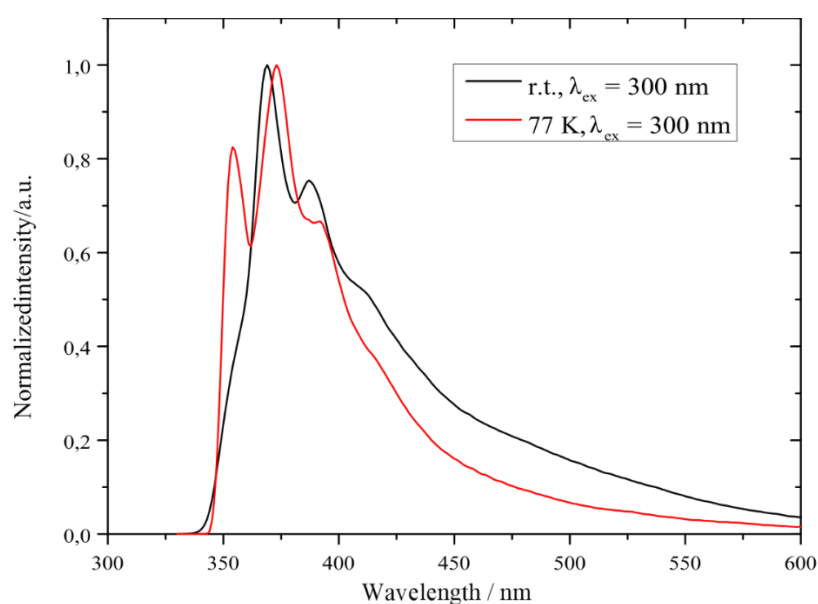


Figure S33: PL-spectra of $[\text{Zn}(\text{L}^{\text{Tetra-ODA}})(\text{NCBH}_3)_2] \cdot 0.5 \text{H}_2\text{O}$ in solid state. Samples were excited with $\lambda_{\text{ex}} = 300 \text{ nm}$. Measurements were done at 77 K (red solid lines) and at room temperature (black solid lines).

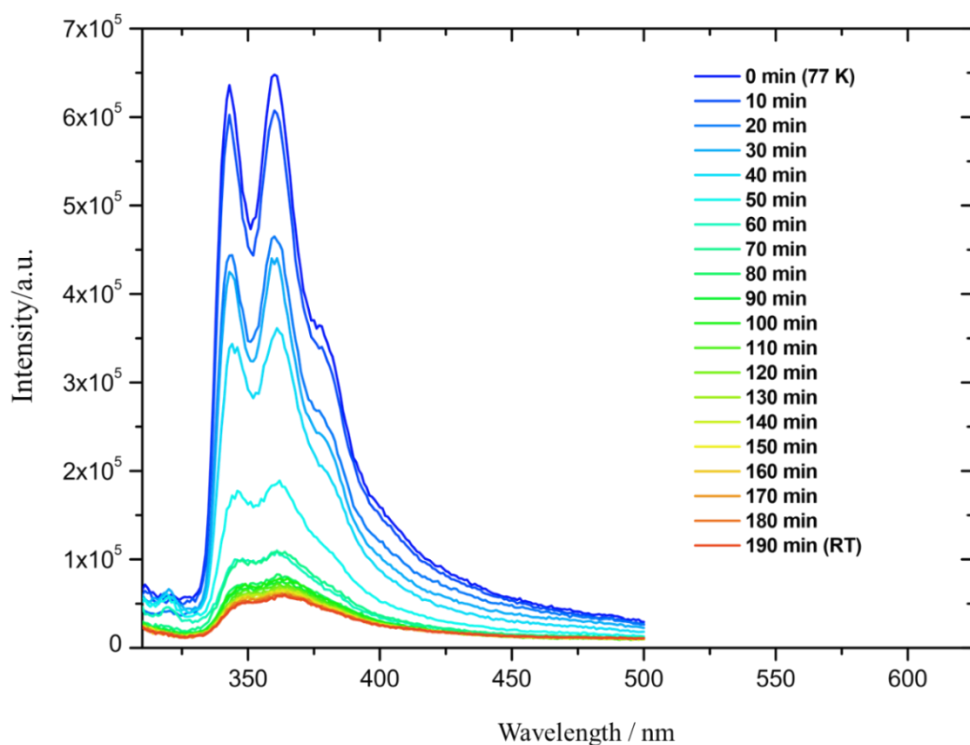


Figure S34: Emission spectra of $[\text{Fe}(\text{L}^{\text{Tetra-ODA}})(\text{NCBH}_3)_2] \cdot 1.5 \text{CH}_3\text{OH}$ between 310 nm and 500 nm for a series of time related measurements. During the measured 190 min, liquid nitrogen was allowed to evaporate, which results in a heating of the sample.

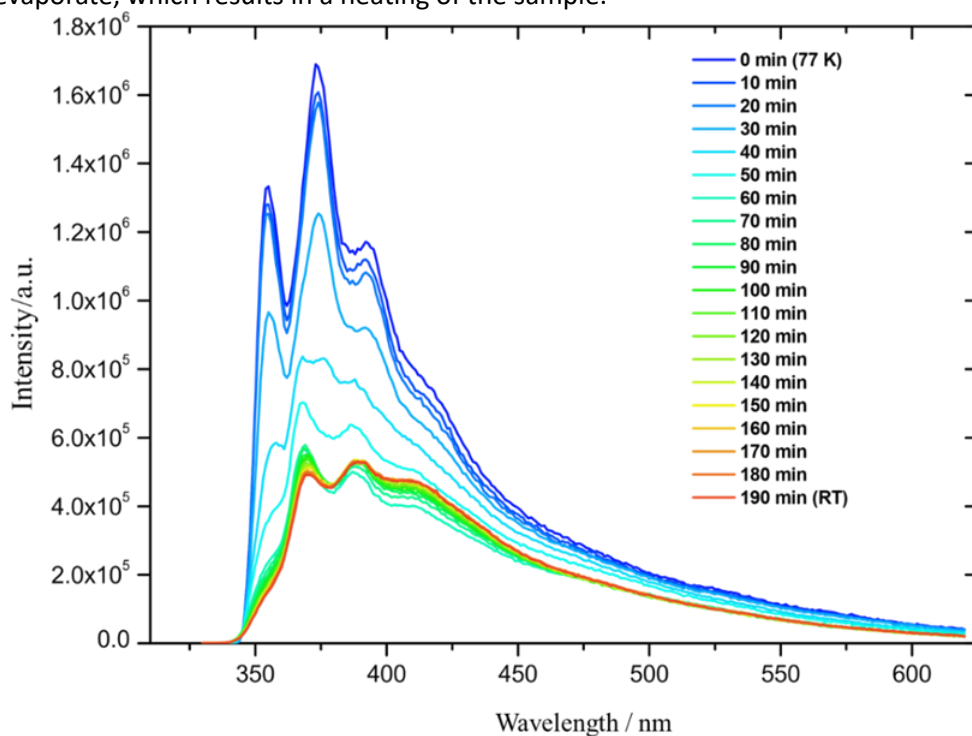


Figure S35: Emission spectra of $[\text{Zn}(\text{L}^{\text{Tetra-ODA}})(\text{NCBH}_3)_2] \cdot 0.5 \text{H}_2\text{O}$ between 310 nm and 625 nm for a series of time related measurements. During the measured 190 min, liquid nitrogen was allowed to evaporate, which results in a heating of the sample.

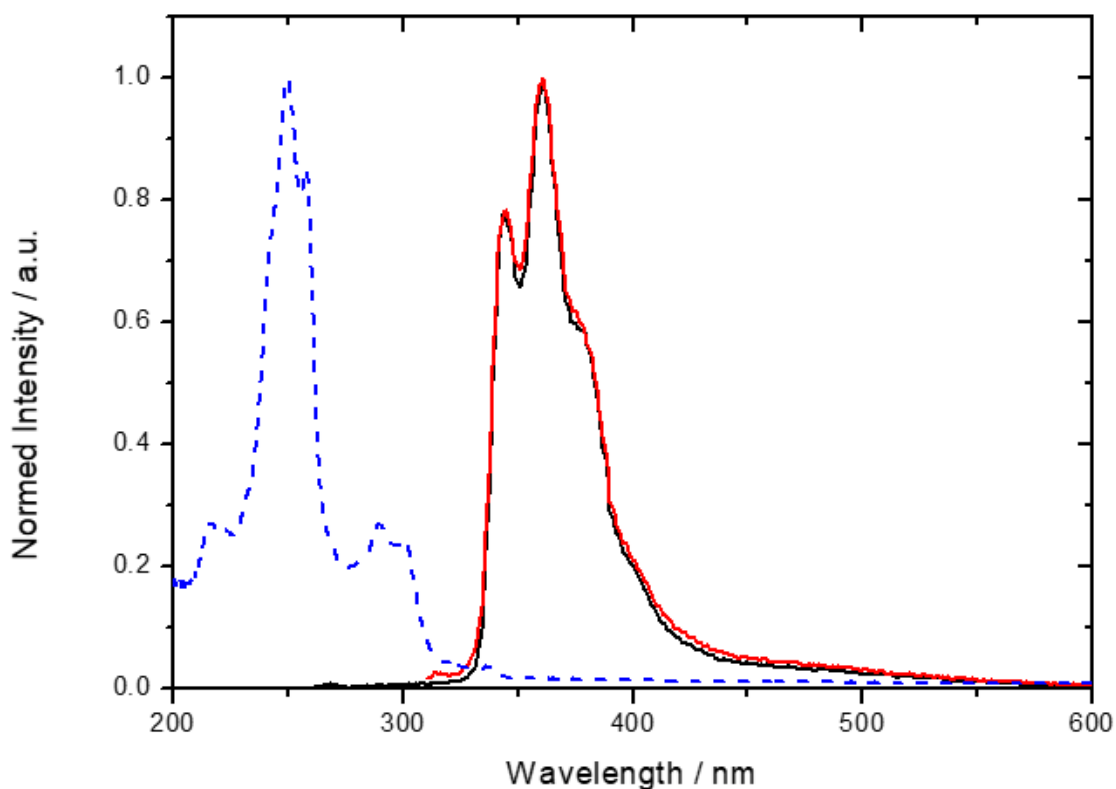


Figure S36: Combined intensity versus wavelength plot of absorption (blue dashed line) and emission spectra with excitation wavelengths of $\lambda_{\text{ex},1} = 249$ nm (black solid line) and $\lambda_{\text{ex},2} = 289$ nm (red solid line) of $\text{L}^{\text{Tetra-ODA}}$ in n-butyronitrile.

7. Magnetic Data:

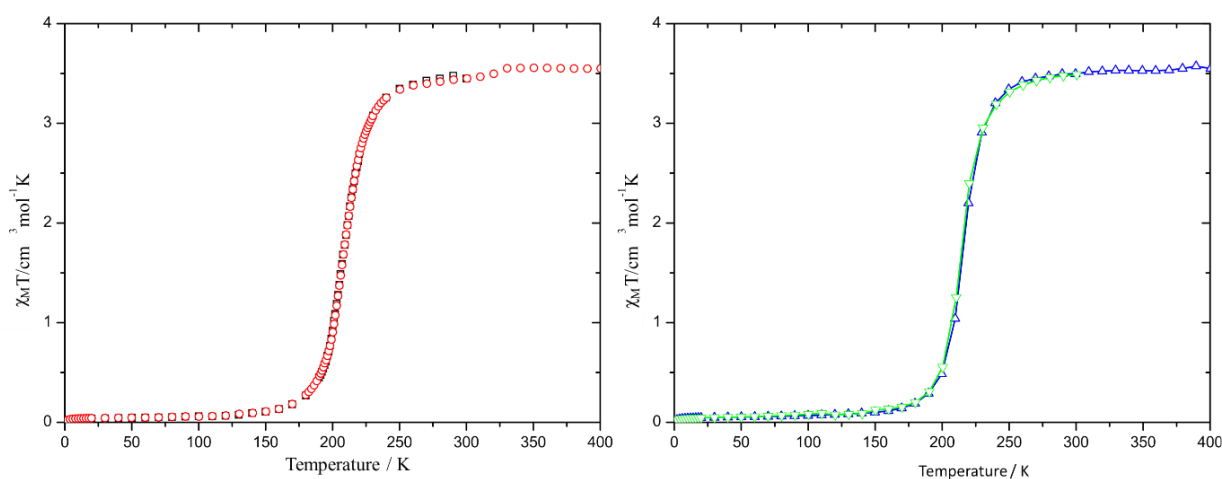


Figure S37: Temperature dependent magnetic behavior of single crystals of $[\text{Fe}(\text{L}^{\text{Tetra-ODA}})(\text{NCBH}_3)_2] \cdot 1.5 \text{CH}_3\text{OH}$ in the form of $\chi_M T$ vs. T plots. Left: Measurement between 300-2 K (black open squares) and 2-400 K (red open circles). Right: Subsequent measurement between 400-2 K (blue open triangles) and 2-300 K (green open triangles).

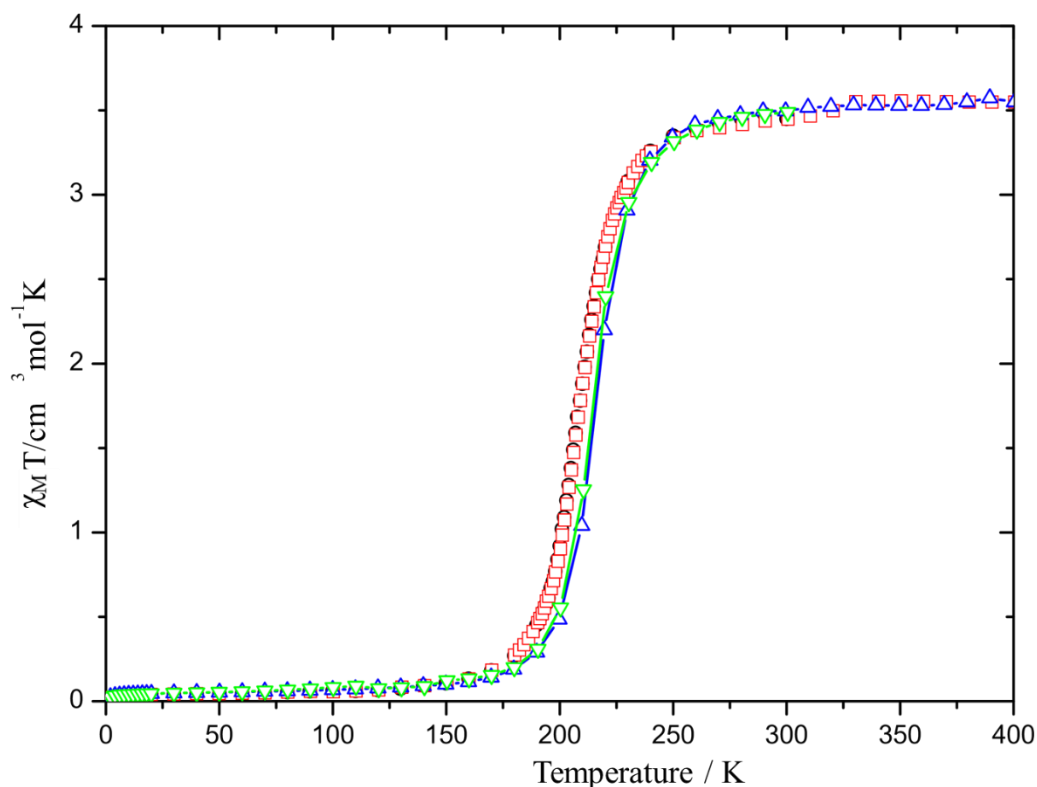


Figure S38: Temperature dependent magnetic behavior of single crystals of $[\text{Fe}(\text{L}^{\text{Tetra-ODA}})(\text{NCBH}_3)_2] \cdot 1.5 \text{CH}_3\text{OH}$ after five days under air in the form of the resulting $\chi_M T$ vs. T plot. Magnetic susceptibility was determined between 300-100 K (black open circles), 100-300 K (red open squares), 300-100 K (blue open squares) and 100-300 K (green open triangles).

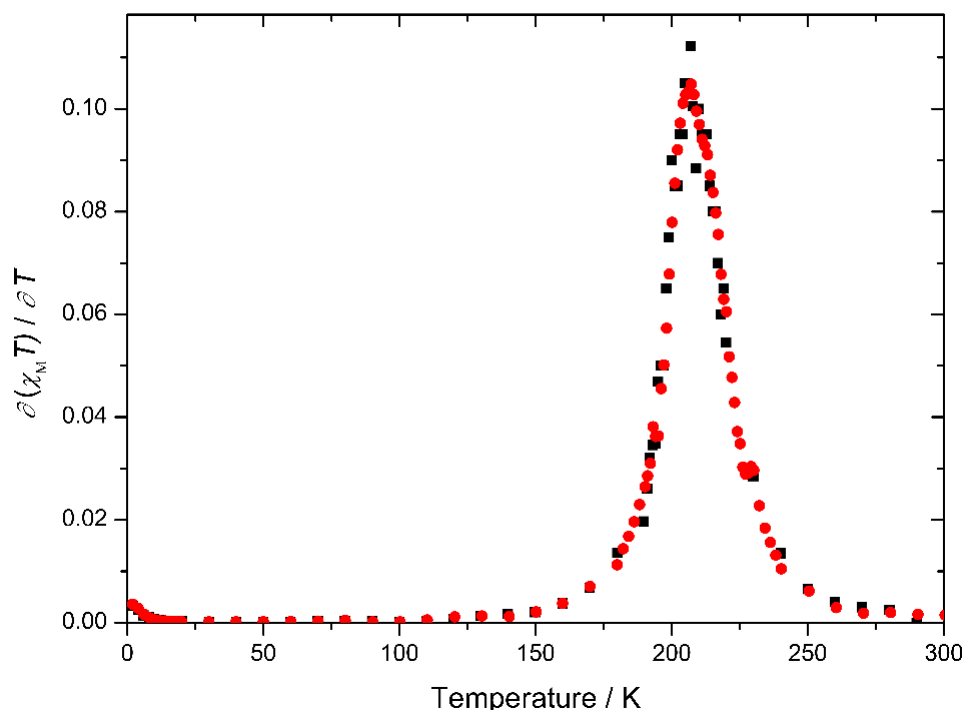


Figure S39: First derivative of $\chi_M T$ with respect to T for $[\text{Fe}(\text{L}^{\text{Tetra-ODA}})(\text{NCBH}_3)_2] \cdot 1.5 \text{CH}_3\text{OH}$. Susceptibility was measured from 300 K to 2 K (black open squares) and subsequently from 2 K to 400 K (red open circles).

The variable temperature *Evans NMR* data was measured in CD₃CN at a concentration of 5.06 X 10⁻³ M, from 298 to 343 K (at 5 K intervals) in heating mode [Fe(L^{Tetra-ODA})(NCBH₃)₂] · 1.5 CH₃OH. Once the temperature is reached the sample is stabilized at that temperature for two minutes at each step before measuring. The methodology to calculate $\chi_M T$ from *Evans* ¹H-NMR method data at a range of temperatures has been previously described.^[1-2]

The modelling of each dataset as a gradual and complete *SCO*, using the regular solution model, equation (1) below,^[3-4] resulted in good fits with $R^2 = 0.98$. For each data set, the fit gives ΔH and ΔS , the thermodynamic enthalpy and entropy values associated with the spin crossover. From these two values the $T_{1/2}$ value can be calculated, simply by dividing $\Delta H/\Delta S$, as $\Delta G = 0$ at $T_{1/2}$ (and $\Delta G = \Delta H - T\Delta S$). The derived parameters are reported in **Tables S1** and **S2**.

$$\chi_M T(T) = \chi_M T(\max) / 1 + e^{(-\Delta H/RT) + (\Delta S/R)} \quad (S1)^{[3-4]}$$

Where:

$\chi_M T(T)$ is $\chi_M T$ measured at temperature T ,

$\chi_M T(\max)$ is the maximum $\chi_M T$ value, which herein was set to 4.0 emu·K·mol⁻¹ as this value falls within the expected literature range for iron(II) complexes.^[5-6]

R is the ideal gas constant (8.314 J·mol⁻¹·K⁻¹)

Note:

The *Evans* method has a relative error of 5 - 10%,^[7] therefore significant errors are associated with the data fitting.

Table S4: Solution χT vs T data at 5.06 X 10⁻³ M in CD₃CN solutions of [Fe(L^{Tetra-ODA})(NCBH₃)₂] · 1.5 CH₃OH measured in the heating mode from 298 to 343 ± 1 K, at 5 K intervals.

Temperature (K)	χT (cm ³ ·K·mol ⁻¹)
298	0.5082
303	0.6703
308	0.7369
313	0.8375
318	0.9859
323	1.0078
328	1.1785
333	1.382
338	1.5611
343	1.7698

8. Synthesis of complex precursors

[Fe(Py)₄(NCBH₃)₂] · 2.5 H₂O

The precursor complex used for synthesis was prepared as reported in the literature.^[8] The following reaction was carried out under an inert atmosphere using Schlenk technique. Iron(II) tetrafluoroborate hexahydrate (2.00 g, 5.80 mmol, 1 eq.) and pyridine (1.82 g, 23.0 mmol, 4 eq.) were dissolved in degassed water (18 ml). To this solution sodium cyanoborohydride (0.72 g, 11.5 mmol, 2 equiv.) was added in portions. The resulting yellow suspension was stirred for one hour. The yellow solid was filtered and dried in vacuo to yield (3.288 g, 7.179 mmol Yield: 61 %) as yellow powder in moderate yields. FT-IR: $\tilde{\nu}$ (cm⁻¹) = 2341, 2184, 1599, 1440, 1216, 1120, 1068, 1038, 1008, 753, 697, 626, 421. Elemental analysis calculated C, 53.17, H, 6.19, N, 16.91. Found 52.85, H, 6.00, N, 16.69.

[Zn(Py)₄(NCBH₃)₂] · 0.5 H₂O

The precursor complex used for synthesis was prepared with slight modifications to the literature.^[8] Zinc(II) sulfate hydrate (2.00 g, 11.14 mmol, 1 equiv.), pyridine (3.52 g, 3.59 ml, 44.56 mmol, 4 equiv.) and sodium cyanoborohydride (1.40 g, 22.28 mmol, 2 equiv.) were suspended in water (50 ml). The reaction mixture was stirred for one hour, during which a colourless solid had formed. The solid was filtered and dried in vacuum to yield [Zn(py)₄(NCBH₃)₂] as colourless powder (1.79 g, 3.87 mmol, 35 %). ¹H-NMR (400 MHz, DMSO, δ (ppm)): 8.58 - 8.56 (m, 8H, pyCH), 7.82 - 7.78 (m, 4H, pyCH), 7.41 - 7.38 (m, 8H, pyCH), 0.56 - 0.10 (m, 6H, BH₃) FT-IR: $\tilde{\nu}$ (cm⁻¹) = 2980, 2341, 2184, 1598, 1575, 1558, 1541, 1520, 1507, 1487, 1457, 1440, 1397, 1216, 1153, 1120, 1068, 1038, 1008, 860, 765, 753, 697, 626, 420. Elemental analysis calculated C, 56.16, H, 5.78, N, 17.86. Found C, 55.82, H, 5.69, N, 17.66.

9. References:

- [1] D. F. Evans, *J. Chem. Soc.*, **1959**, 2003-2005.
- [2] C. Piguet, *J. Chem. Ed.*, **1997**, 74, 815-816.
- [3] O. Kahn, *Molecular Magnetism*, VCH Publishers Inc., New York, **1993**.
- [4] C. P. Slichter and H. G. Drickamer, *J. Chem. Phys.*, **1972**, 56, 2142-2160.
- [5] H. Toftlund and J. J. McGarvey, *Top. Curr. Chem.*, **2004**, 233, 151-166.
- [6] L. J. Kershaw Cook, R. Kulmaczewski, R. Mohammed, S. Dudley, S. A. Barrett, M. A. Little, R. J. Deeth and M. A. Halcrow, *Angew. Chem. Int. Ed.*, **2016**, 55, 4327-4331
- [7] L. A. Yatsunyk and F. A. Walker, *Inorg. Chem.*, **2004**, 43, 757-77.
- [8] K. Nakano, N Suemura, S Kawata, A Fuyuhiko, T Yagi, S Nasu, S Morimoto and S Kaizaki, *Dalton Trans.*, **2004**, 982-988.

Chapter 4: Unique packing properties of chiral 1,3,4-Oxadiazole Spin Crossover complexes

This chapter presents the stereo conservative synthesis of the two enantiomers of the ligand $L^{\text{Naph-ODA}}$ and their characterization by chiral *HPLC*, various *NMR*-, *IR*- and *CD*-spectroscopy as well as *ESI-MS*-spectrometry and elemental analysis. Both enantiomers of the ligand were used to synthesise three iron(II) complexes: $[\text{Fe}(L^{\text{Naph-ODA-Al}})(\text{NCBH}_3)_2]$, in both enantiomeric forms (R and S) as well as the racemic mixture. All complexes were characterised by *IR*-spectroscopy, *ESI-MS*-spectrometry and Elemental analysis. A unique structure-property correlation between the stereoisomers and crystal packing was observed, as all complexes exhibited similar packing motifs, despite the different symmetry of enantiomers and racemic mixtures, which was investigated by single-crystal *X-ray* diffraction and *SQUID* magnetometry. The stereochemical configuration of the complexes was further confirmed by circular dichroism (*CD*) spectroscopy.

The results are presented as scientific article published in *Chemical Communication* (DOI: <https://doi.org/10.1039/D5CC03779D>).

Reprinted with the permission from:

Copyright 2025 Royal Society of Chemistry

Author contribution:

The general synthesis of the ligand system and the complexes was developed by [REDACTED], while the laboratory work on the ligand was performed by [REDACTED] and [REDACTED] and the complex synthesis was performed by [REDACTED]. The *IR*-spectroscopy was collected by [REDACTED] as well as the sample preparation for elemental analysis, *NMR*-spectroscopy and *ESI-MS*-spectrometry. *CD* spectroscopy data were collected by [REDACTED] the *CD*-spectrometer of [REDACTED] and the evaluation of the data was performed by [REDACTED]. The stereo information of the enantiomers of the ligand was achieved by chiral *HPLC* performed by [REDACTED] under the supervision and the *HPLC* from [REDACTED]. [REDACTED] collected the single crystal *XRD* data and refined the structure. The evaluation of the magnetic and structural data was done by [REDACTED]. The Manuscript was written by [REDACTED], with input from [REDACTED] and [REDACTED]. [REDACTED] had the supervision during the manuscript process. All Authors have read and agreed to the submitted version of the manuscript.

Manuscript: Chirality Without Compromise: Identical Spin Crossover Behavior between the Racemate and the Enantiopure Fe(II) Complexes

Jens-Georg Becker,^a Sriram Sundaresan,^a Luca. M. Carrella,^a and Eva Rentschler^{a*}

The influence of chirality on the packing of solids, and consequently on the magnetic behavior of spin crossover (SCO) materials, is well documented. Here, we present an exceptional case involving three iron(II) complexes $[\text{Fe}(\text{L}^{\text{Naph-ODA-(X)-Al}})(\text{NCBH}_3)_2] \cdot 0.5 \text{CH}_3\text{CN}$ (X = racemic (C1), R (C2), and S (C3)), based on a new 1,3,4-oxadiazole ligand ($\text{L}^{\text{Naph-ODA-(X)}}$) with distinct stereocenters. These complexes have isostructural crystal lattices and identical incomplete thermal spin transitions with $T_{1/2} \approx 150 \text{ K}$, but unexpectedly, single-crystal X-ray diffraction reveals that the presence and configuration of the stereocenters do not quantifiably impact the solid-state structure or the spin crossover properties.

Molecular spin crossover (SCO) complexes have long been the subject of significant interest due to their potential application in memory devices, sensors and molecular switches, owing to their ability to reversibly switch between low spin state (LS) and high spin state (HS) in response to external stimuli, such as temperature, light, or pressure.^[1,2] Chirality, on the other hand, is serving as a powerful tool employed by nature both to store and to transmit information.^[3] This is vividly illustrated by the helical structures of biomolecules such as DNA and proteins, whose specific handedness is critical to their biological functions. The chirality of these molecules encodes structural and functional information, guiding processes such as molecular recognition and replication. Recently, the convergence of these two phenomena in molecular materials opened avenues for the development of multifunctional materials, particularly for next-generation applications in spintronics, quantum sensing, and molecular logic, where spin and stereochemical control are key.^[4,5]

Introducing a chiral element into a SCO active complex scaffold enables to impart enantioselective properties while, to the best of our knowledge, in all the cases known from the literature, this also modulates the magnetic behavior. Chirality can be introduced into SCO systems through chiral guests or anions,^[6,7] spontaneous resolution,^[8,9] supramolecular assembly,^[10,11] or enantiopure ligands.^[12–14] While ligand-based approaches offer precise stereochemical control, they are often limited by synthetic challenges and access to enantiopure precursors. It is well known from the literature that ligand chirality strongly influences coordination geometry, solid-state packing, and, ultimately, the SCO behavior such as transition temperature, abruptness, and hysteresis.^[12,15] All reported SCO systems

with inbuilt chirality in the ligand backbone usually show an enantiomer dependent magnetic response because of the packing effects caused by the introduction of chiral substituents.^[8,12]

A chirality independent spin switchable molecule enables these complexes to serve as experimental testbeds for a range of molecular spintronic phenomena, thereby providing a platform to investigate chiral-spin interactions in the absence of structural interference. In quantum devices dual encoding of spin state and molecular handedness enables multi-level read/write operations within a single molecule.

Building on our previous work with asymmetric 1,3,4-oxadiazole ligands,^[16–18] we now report a new synthetic strategy using chiral amino acids to access enantiopure ligands in fewer steps.

Both Enantiomers R- and S-1-(5-(naphthalen-2-yl)-1,3,4-oxadiazol-2-yl)-N,N-bis(pyridin-2-ylmethyl)ethan-1-amine were synthesized enantiopure by a two-step synthesis procedure (**Figure 1**), reacting the enantiopure aminoacids R- and S-alanine with pyridinecarboxyaldehyde and sodium trisacetoxyborohydride in dichloromethane according to a literature known reductive amination.^[19] The intermediate product Bis(pyridin-2-ylmethyl)-R-alanine (I-R) and Bis(pyridin-2-ylmethyl)-S-alanine (I-S) were obtained in moderate yield of 54% (I-R) and 30% (I-S) after purification by column chromatography. Both intermediate products were further reacted with carbonyldiimidazole as coupling reagent in dry dichloromethane following by nucleophilic substitution with naphthohydrazide.^[20] The dehydrative ring closure was successfully achieved by using carbon tetrabromide and triphenylphosphine in a one pot synthesis procedure.^[20]

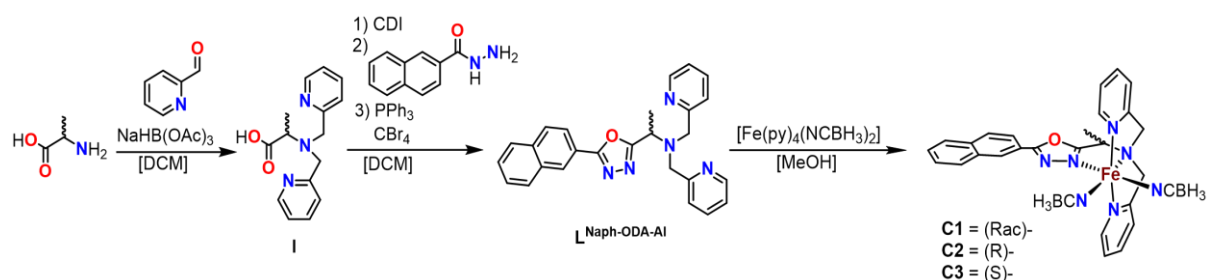


Figure 1: Multistep ligand synthesis of $L^{\text{Naph-ODA-Al}}$ along with complex synthesis of $[\text{Fe}(L^{\text{Naph-ODA-(X)-Al}})(\text{NCBH}_3)_2] \cdot 0.5 \text{CH}_3\text{CN}$ (**C1** X = Rac, **C2** X = R and **C3** X = S).

After purification by column chromatography both enantiopure products (R)-1-(5-(naphthalen-2-yl)-1,3,4-oxadiazol-2-yl)-N,N-bis(pyridin-2-ylmethyl)ethan-1-amine ($L^{\text{Naph-ODA-(R)-Al}}$) and (S)-1-(5-(naphthalen-2-yl)-1,3,4-oxadiazol-2-yl)-N,N-bis(pyridin-2-ylmethyl)ethan-1-amine ($L^{\text{Naph-ODA-(S)-Al}}$) were obtained in moderate yield 67% ($L^{\text{Naph-ODA-(R)-Al}}$) and 35% ($L^{\text{Naph-ODA-(S)-Al}}$). Both the ligands, $L^{\text{Naph-ODA-(R)-Al}}$ and $L^{\text{Naph-ODA-(S)-Al}}$, were fully characterized by different analytical methods, including $^1\text{H-NMR}$ -, $^{13}\text{C-NMR}$ -, 2D-NMR -, IR -spectroscopy, and mass spectrometry. Chiral $HPLC$ was employed to verify the

enantiomeric purity of the ligands (**Figure S74 and S75**). The two ligands were used in a nitrogen atmosphere for complexation reactions with the known precursor $[\text{Fe}(\text{py})_4(\text{NCBH}_3)_2]$ to obtain the three complexes $[\text{Fe}(\text{L}^{\text{Naph-ODA-(X)-Al}})(\text{NCBH}_3)_2] \cdot 0.5 \text{CH}_3\text{CN}$ (**C1** X = Rac, **C2** X = R, and **C3** X = S) in moderate yield as powders (detailed experimental in the ESI). **C1** was obtained using a racemic mixture of the enantiopure ligands.^[16] The bulk samples of the complexes were characterized *IR*-spectroscopy (**Figure S13 – S17**),^[21] *ESI-MS* (**Figure S18 - 27**), and elemental analysis. Phase purity was verified using *PXRD* (**Figure S68 - S70**). R- and S-chirality of the obtained complexes was confirmed by CD spectroscopy (**Figure S77**).

Single crystals suitable for *X-ray* diffraction (*XRD*) were obtained by recrystallization from acetonitrile. **C1** crystallizes in the monoclinic crystal system with the space group $P2_1/n$. In contrast, the enantiopure complexes **C2** and **C3** crystallize in the same monoclinic crystal system without the *n*-mirror plane, resulting in the chiral space group $P2_1$ (**Table S1-S6**). All complexes have identical unit cell sizes, parameters and the same molecule formula per unit cell ($Z = 4$). The coordination sphere of the iron(II) centers is completed by two NCBH_3 co-ligands that occupy *cis* positions relative to each other. *VT-SC-XRD* studies reveal that the average Fe-N bond lengths at 90 K is $2.026 \pm 0.010 \text{ \AA}$, consistent with intermediate or incomplete spin state. For comparison, a fully low spin (*LS*) configuration typically exhibits shorter Fe-N bonds, averaging around 1.97 \AA .^[16] The observed distortion parameters (Σ), range from 53.60° to 62.80° ($\pm 3.63^\circ$). These values are notably higher than that of the reference low-spin complex $[\text{Fe}(\text{L}^{\text{Naph-ODA}})(\text{NCBH}_3)] \cdot 1.5 \text{CH}_3\text{OH}$ $\Sigma_o(\text{FeN}_6) = 47.0^\circ$, confirming that all three complexes are in an incomplete low-spin state at low temperatures.^[16]

SC-XRD measurements at 220 K reveal a spin state transition, as indicated by a significant increase in Fe-N bond lengths compared to 90 K. The average Fe-N bond length at 220 K is $2.167 \pm 0.022 \text{ \AA}$ for all three complexes, consistent with a high-spin (*HS*) state.^[16] This assignment is further supported by an increased octahedral distortion, with values ranging between $\Sigma_o(\text{FeN}_6)$ 85.90° and 92.41° ($\bar{\Sigma}_o(\text{FeN}_6) = 89.78 \pm 3.30^\circ$).^[22] These values are similar to those reported in the literature for $[\text{Fe}(\text{L}^{\text{Naph-ODA}})(\text{NCBH}_3)] \cdot 1.5 \text{CH}_3\text{OH}$ ($\Sigma_o(\text{FeN}_6) = 94.0^\circ$; 2.17 \AA), confirming the full transition to the high-spin state.^[16] The spin transition is also confirmed by a 3.5% increase in the unit cell volume upon heating.

The enantiopure complexes **C2** and **C3** exhibit distinct point chirality due to the stereogenic methyl group, while the racemic complex **C1** features a distorted methyl group, indicating a random distribution of R- and S-enantiomers within the crystal lattice. In all three complexes **C1-C3**, the iron(II) center adopts a meridional coordination geometry with the ligand $\text{L}^{\text{Naph-ODA-Al}}$, which itself is achiral apart from the point chirality introduced by the methyl substitution, as previously noted.^[16,23]

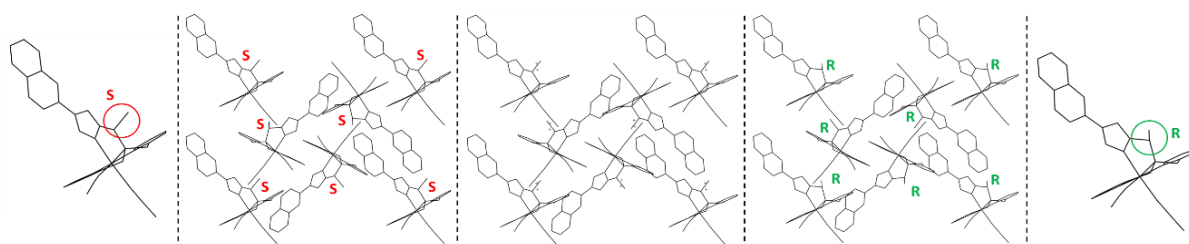


Figure 2: Packing diagrams to visualize the similarities in the packing of the complexes $[\text{Fe}(\text{L}^{\text{Naph-ODA-(S)-Al}})(\text{NCBH}_3)_2] \cdot 0.5 \text{ CH}_3\text{CN}$ (**C3**) (left), $[\text{Fe}(\text{L}^{\text{Naph-ODA-(Rac)-Al}})(\text{NCBH}_3)_2] \cdot 0.5 \text{ CH}_3\text{CN}$ (**C1**) (middle) and $[\text{Fe}(\text{L}^{\text{Naph-ODA-(R)-Al}})(\text{NCBH}_3)_2] \cdot 0.5 \text{ CH}_3\text{CN}$ (**C2**) (right). The methyl group is disordered in the case of the racemic mixture.

A possible facial coordination isomer would introduce chirality to the iron center, allowing for the formation of either the Λ - or Δ -isomers, by the positioning of the pyridine units, looking on the triangle area imparting NCBH_3 , 1,3,4-thiadiazole unit and on pyridine unit (**Figure S78**). Λ - and Δ -isomers refer to the two possible chiral arrangements of octahedral metal complexes, where the ligands wrap around the metal center in left-handed (Λ) or right-handed (Δ) helicity. These stereoisomers can exhibit subtle differences in intermolecular packing and lattice interactions, which may influence the spin crossover properties (**Figure S78**).

Since the molecular structures of the complex units in **C1-C3** are similar, the impact of chirality on the packing should be considered. Investigation of the crystal structures along the a -axis reveals a consistent overall packing arrangement among the three complexes, as illustrated in **Figure 2**. The only difference in packing arises from the orientation of the chiral methyl group. In all three complexes, the naphthyl groups from two complex units interact via π - π interactions, forming pairs. Similar interactions have been observed in related complexes.^[16,24,25] Within the crystal lattice, the iron(II) centers of each pair are interlocked, with one NCBH_3 co-ligand pointing toward the adjacent complex. This interlocking arrangement results in a stair-like chain of pairs (**Figure S67**), further stabilized by interactions with neighboring pairs. Key π - π -stacking parameters, such as offset, normal vector, and centroid-centroid distances, were evaluated (**Figure S32, S37, S44, S49, S57 and S62 and Table S13**), revealing consistent values across the series. This structural similarity reflects the conserved packing motif among **C1-C3**. No significant hydrogen bonding interactions were identified using Mercury, emphasizing the dominant role of π - π interactions in directing the supramolecular architecture. Notably, these π - π contacts between naphthyl units are the primary contributors to the observed cooperativity.^[16]

To the best of our knowledge, such an identical packing between racemate and enantiopure complexes has not previously been reported for chirality imparted spin crossover complexes, as the introduction of the chiral center alters the packing which in turn always in many cases change the *SCO* behavior. This

identical packing between the racemate and the enantiopure complexes can be attributed to the minimal change ligand backbone with a methyl group.

The temperature-dependent magnetic susceptibility behavior of all three complexes (**C1–C3**) was determined using pure microcrystalline samples from 10 - 300 K in both heating and cooling modes. A constant value of approximately $3.45 \text{ cm}^3 \cdot \text{K} \cdot \text{mol}^{-1}$ is observed for $\chi_M T$ at temperatures above 200 K for all complexes, confirming the high spin state concluded from single-crystal X-ray diffraction data. Upon decreasing the temperature, the $\chi_M T$ values decrease, showing a gradual spin-state transition with a $T_{1/2} = 150 \text{ K}$ for all three complexes, leading to a plateau below 75 K with an average $\chi_M T$ value of $1.06 \text{ cm}^3 \cdot \text{K} \cdot \text{mol}^{-1}$. The gradual nature of the spin-state transition can be attributed to the presence of only weak or moderate interactions. These findings support an incomplete transition with approximately 30% of the iron(II) centers remaining in the high-spin state as deduced from the $\chi_M T$ values. Further decreasing the temperature results in a drop in the magnetic moment below 10 K, which can be attributed to a combination of weak intermolecular dipolar interaction, zero-field splitting, and possible weak antiferromagnetic coupling effects between the iron centers.

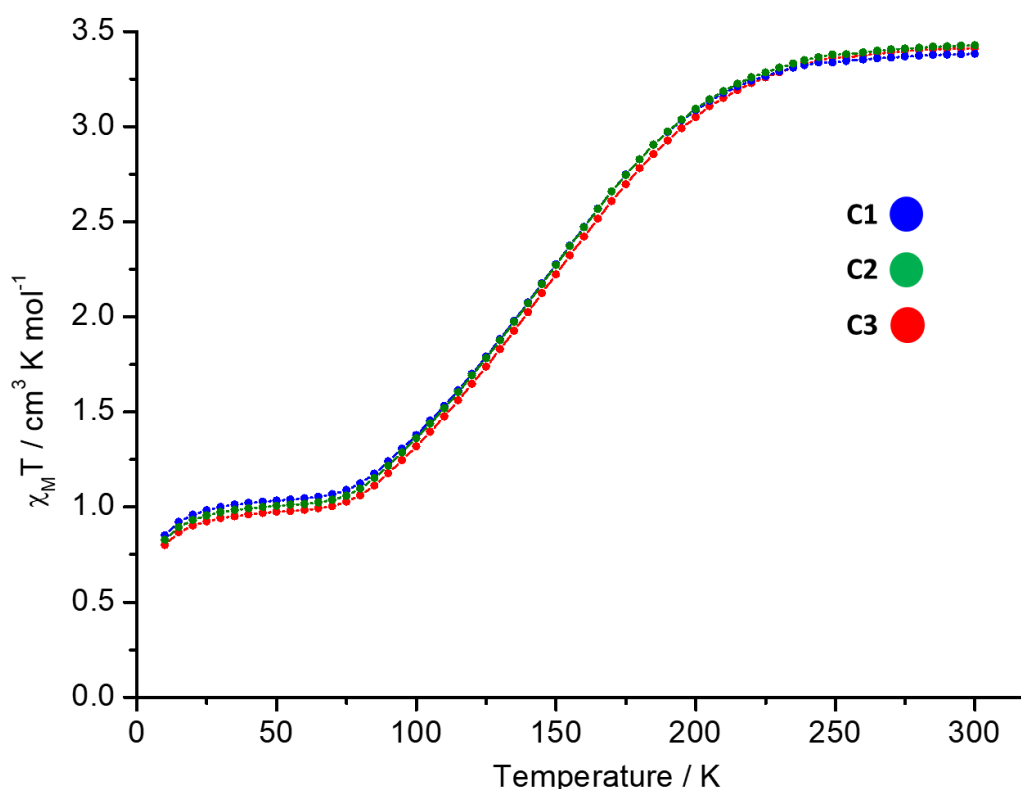


Figure 3: χ_M vs. T measured of powder product of $[\text{Fe}(\text{L}^{\text{Naph-ODA-(Rac)-Al}})(\text{NCBH}_3)_2]$ (**C1**) (blue), $[\text{Fe}(\text{L}^{\text{Naph-ODA-(R)-Al}})(\text{NCBH}_3)_2]$ (**C2**) (green) and $[\text{Fe}(\text{L}^{\text{Naph-ODA-(S)-Al}})(\text{NCBH}_3)_2]$ (**C3**) (red) in the form of the resulting $\chi_M T$ vs.T plot. Magnetic susceptibility was determined between 300 - 10 K.

This work presents an unprecedented example of introducing chirality into spin-crossover (SCO) complexes via the chirality of an amino acid point, with no significant difference in packing between the racemic and enantiopure polymorphs. Identical powder *X-ray* diffraction (PXRD) patterns and a detailed structural analysis using single-crystal *X-ray* data confirm that all three complexes have the same crystal packing. This highlights the rare phenomenon of enantiomers sharing an identical packing motif and nearly identical SCO behavior. All complexes undergo a gradual, incomplete spin-state transition with a transition temperature ($T_{1/2}$) of 150 K.

Further investigations are underway to study the circular dichroism (CD)-light induced spin state transition (LIESST) phenomenon using polarized light in both racemic and enantiopure complexes. The goal is to elucidate the spin-selective photoresponse in this system. If successful, this system could be the first of its kind: a reversible optical handle for reading and writing spin states with chiral sensitivity.

The authors thank Dr. Thomas and Prof. Besenius (JGU) for the CD spectra measurements and Mr. Hagenow (JGU) for the evaluation of the CD data. JGB and ER acknowledge funding by the Deutsche Forschungsgemeinschaft (DFG, German Research Foundation)-TRR 173-268565370 Spin+X (Project No. A04).

Data Availability Statement:

All the raw data from this manuscript have been uploaded to Zenodo and freely and fair available via the Doi: 10.5281/zenodo.15798534. All the processed data supporting the findings of this study are available within the article and ESI.

Conflicts of interest

There are no conflicts to declare.

Notes and references

- [1] P. Gutlich, V. Ksenofontov, A. Gaspar, *Coor. Chem. Rev.* **2005**, *249*, 1811–1829.
- [2] J.-F. Létard, *J. Mater. Chem.* **2006**, *16*, 2550–2559.
- [3] Y. Liu, Z. Wu, D. W. Armstrong, H. Wolosker, Y. Zheng, *Nat. Rev. Chem.* **2023**, *7*, 355–373.
- [4] S. Ohkoshi, S. Takano, K. Imoto, M. Yoshikiyo, A. Namai, H. Tokoro, *Nature Photon* **2014**, *8*, 65–71.
- [5] W.-K. Han, L.-F. Qin, C.-Y. Pang, C.-K. Cheng, W. Zhu, Z.-H. Li, Z. Li, X. Ren, Z.-G. Gu, *Dalton Trans.* **2017**, *46*, 8004–8008.

- [6] V. B. Jakobsen, L. O'Brien, G. Novitchi, H. Müller-Bunz, A. Barra, G. G. Morgan, *Eur. J. Inorg. Chem.* **2019**, 2019, 4405–4411.
- [7] A. Iazzolino, A. Ould Hamouda, A. Naïm, O. Stefánczyk, P. Rosa, E. Freysz, *Appl. Phys. Lett.* **2017**, *110*, 161908.
- [8] C. Bartual-Murgui, L. Piñeiro-López, F. J. Valverde-Muñoz, M. C. Muñoz, M. Seredyuk, J. A. Real, *Inorg. Chem.* **2017**, *56*, 13535–13546.
- [9] C. T. Kelly, R. Jordan, S. Felton, H. Müller-Bunz, G. G. Morgan, *Chem. Eur. J.* **2023**, *29*, e202300275.
- [10] V. Maliuzhenko, M. Weselski, J. Gregoliński, M. Książek, J. Kusz, R. Bronisz, *Inorg. Chem.* **2024**, *63*, 17762–17773.
- [11] N. Suryadevara, A. Pausch, E. Moreno-Pineda, A. Mizuno, J. Bürck, A. Baksi, T. Hochdörffer, I. Šalitroš, A. S. Ulrich, M. M. Kappes, V. Schünemann, W. Klopfer, M. Ruben, *Chem. Eur. J.* **2021**, *27*, 15172–15180.
- [12] X. Zhao, Y. Deng, J. Xi, J. Huang, Y. Zhang, *Angew. Chem.* **2025**, *137*, e202414826.
- [13] Y. Sekimoto, M. R. Karim, N. Saigo, R. Ohtani, M. Nakamura, S. Hayami. *Eur. J. Inorg. Chem.* **2017**, 2017, 1049–1053.
- [14] N. Shahid, K. E. Burrows, C. M. Pask, O. Cespedes, M. J. Howard, P. C. McGowan, M. A. Halcrow, *Dalton Trans.* **2022**, *51*, 4262–4274.
- [15] K. E. Burrows, S. E. McGrath, R. Kulmaczewski, O. Cespedes, S. A. Barrett, M. A. Halcrow, *Chem. Eur. J.* **2017**, *23*, 9067–9075.
- [16] S. Sundaresan, J.-G. Becker, J. Eppelsheimer, A. E. Sedykh, L. M. Carrella, K. Müller-Buschbaum, E. Rentschler, *Dalton Trans.* **2023**, *52*, 13181–13189.
- [17] S. Sundaresan, J. Eppelsheimer, E. Gera, L. Wiener, L. M. Carrella, K. R. Vignesh, E. Rentschler, *Dalton Trans.* **2024**, *53*, 10303–10317.
- [18] S. Sundaresan, J. Eppelsheimer, L. M. Carrella, E. Rentschler, *Eur. J. Inorg. Chem.* **2025**, *28*, e202400690.
- [19] P. N. Basa, C. A. Barr, K. M. Oakley, X. Liang, S. C. Burdette, *J. Am. Chem. Soc.* **2019**, *141*, 12100–12108.
- [20] H. A. Rajapakse, H. Zhu, M. B. Young, B. T. Mott, *Tetrahedron Letters* **2006**, *47*, 4827–4830.

- [21] S. Sundaresan, J. A. Kitchen, S. Brooker, *Inorg. Chem. Front.* **2020**, *7*, 2050–2059.
- [22] J. K. McCusker, A. L. Rheingold, D. N. Hendrickson, *Inorg. Chem.* **1996**, *35*, 2100–2112.
- [23] G. S. Matouzenko, A. Bousseksou, S. Lecocq, P. J. Van Koningsbruggen, M. Perrin, O. Kahn, A. Collet, *Inorg. Chem.* **1997**, *36*, 5869–5879.
- [24] J. Kiehl, T. Hochdörffer, L. M. Carrella, V. Schünemann, M. H. Nygaard, J. Overgaard, E. Rentschler, *Inorg. Chem.* **2022**, *61*, 3141–3151.
- [25] S. Sundaresan, J. Kiehl, L. M. Carrella, E. Rentschler, *Crystal Growth & Design* **2023**, *23*, 1648–1655.

ESI: Chirality Without Compromise: Identical Spin Crossover

Behavior between the Racemate and Enantiopure Fe(II) Complexes

Jens-Georg Becker,^a Sriram Sundaresan,^a Luca. M. Carrella,^a and Eva Rentschler^{a*}

^aDepartment Chemie, Johannes-Gutenberg-Universität Mainz, Duesbergweg 10–14, 55128 Mainz, Germany.

E-mail: rentschl@uni-mainz.de

Table of Contents

1. Experimental Details:.....	256
2. Synthesis:.....	257
3. <i>NMR</i> -Spectra:	260
4. <i>IR</i> -spectra:.....	270
5. Mass spectra:.....	272
6. Crystallographic Data:.....	277
7. Powder XRD:.....	309
8. Magnetic Data:	311
9. Chiral <i>HPLC</i> and <i>CD</i> -spectra	312

1. Experimental Details:

All chemicals were purchased from Carbolution, Deutero, Fisher Chemicals, TCI and Bld-Pharma and used without further purification. Solvents were dried according to the literature known procedures and used freshly distilled. NMR spectra were recorded at room temperature with a Bruker Avance DSX 400 and analyzed with the program MestReNova.^[1] Impurities of pyridin-2-ylmethanol were detected by ¹H-NMR for **I-R** and **I-S** and the product was used with this minimal impurity due to difficulties by separation of column chromatography without further purification. Additionally, solvents of the column purification for all products (**I-R**, **I-S**, **L^{Naph-ODA-(R)-Al}** and **L^{Naph-ODA-(R)-Al}**) were characterized by ¹H-NMR and the products were used without further drying, due to the not observed impact on the complex synthesis. Magnetic susceptibility measurements were performed on a Quantum Design SQUID magnetometer MPMSXL in a temperature range between 5 and 300 K with an applied field of 1 kOe. The samples for the LIESST-measurement were filled in a glass capsule. The magnetometer was equipped with a Vhos quantum design attachment and a glass fibre was used to connect the attachment with the light source. The sample was irradiated with the Hyperchromator II of Mountain Photonics GmbH and as a light source the XWS-30 LASER PLASMA LIGHT SOURCE was used. The wavelength ($\lambda = 520$ nm) was adjusted with the program monochromator of the company Mountain Photonics GmbH. HRes ESI mass spectra were recorded on *Agilent 6200 series TOF/6500 series G-TOF* (11.0.203.0) at Johannes Gutenberg-University Mainz in acetonitrile. Elemental analysis (vario Micro Cube Elementar: C, H and N) were measured at the microanalytical laboratories of the RPTU (Rheinland-Pfälzische Technische Universität Kaiserslautern-Landau). Analyses were performed on a 1260 Infinity II HPLC system equipped with a binary pump, high-performance degasser, automated liquid sampler, thermostatted column oven, and diode array detector from Agilent Technologies. A mixture of n-hexane (HPLC grade, various suppliers) and ethanol (both HPLC grade, various suppliers) (80 / 20) was used as the mobile phase on both systems. All chiral separations were performed at a column temperature of 40 °C and a flow rate of 1.0 ml/min. The data were analyzed using the MestReNova software from Mestrelab Research. CD spectroscopy was performed on a J-815 spectrometer (JASCO, Easton, MD). Samples were baseline corrected and measured using 1000 QS (HELLMA) quartz glass cuvettes with a path length of 1 mm or 10 mm at varying temperatures, controlled by a PTC-423S/15 Peltier element at 20°C. Each measurement was repeated twice to minimize errors. The ATR-IR spectra were recorded at room temperature on a Bruker ALPHAII ATR-IR, analysed with the software OPUS and plotted in Origin 7.5 V5. Powder XRD data were collected with Bruker D2 Phaser at room temperature and analysed by the program Mercury. X-ray diffraction data were collected with STOE STADIVARI at the Johannes Gutenberg University Mainz. The structures were

solved with ShelXT^[2] and refined with ShelXL^[3,4] implemented in the program Olex2.^[5] The X-ray cif file data are deposited on the Cambridge CCDC database with identification numbers 2467465-2467470.

2. Synthesis:

Ligand synthesis:

Naphthohydrazide was synthesized following literature reported procedure.^[6]

Bis(pyridin-2-ylmethyl)-R-alanine (I-R)

The synthesis was carried out with appropriate modification from the literature.^[7,8]

R-Alanine (3.00 g, 33.67 mmol, 1.0 eq.) was suspended in 80 mL dichloromethane under nitrogen atmosphere. 2-Pyridinecarbaldehyde (6.75 mL, 70.96 mmol, 2.1 eq.) was added to the white solid containing suspension, resulting in a colour change to dark brown suspension after 30 minutes. Sodium triacetoxyborohydride (17.84 g, 84.18 mmol, 2.5 eq.) was added carefully after cooling the reaction mixture under ice. The reaction mixture (yellow suspension) was stirred overnight. Saturated sodium bicarbonate solution (70 ml) was added and after 30 minutes the two phases were extracted, the aqueous phase was extracted twice with 150 mL dichloromethane. The organic phase was dried over sodium sulphate and the solvent was removed under reduced pressure. The crude product obtained was further purified *via* column chromatography (dichloromethane: methanol; 90:10). The product was isolated as brown oil in moderate yields (4.962 g, 18.29 mmol, 54 %). ¹H NMR (400 MHz, Chloroform-d δ(ppm)): 8.53 (ddd, *J* = 5.0, 1.8, 0.9 Hz, 2H), 7.63 (td, *J* = 7.7, 1.8 Hz, 2H), 7.29 (dd, *J* = 7.5, 1.2 Hz, 3H), 7.19 (ddd, *J* = 7.6, 5.0, 1.2 Hz, 2H), 4.00 (d, *J* = 2.6 Hz, 4H), 3.68 (q, *J* = 7.1 Hz, 1H), 1.44 (d, *J* = 7.1 Hz, 3H).

Bis(pyridin-2-ylmethyl)-S-alanine (I-S)

The synthesis was carried out with appropriate modification from the literature.^[7,8] S-Alanine (3.00 g, 33.67 mmol, 1.0 eq.) was suspended in 80 mL dichloromethane under nitrogen atmosphere. 2-Pyridinecarbaldehyde (6.75 mL, 70.96 mmol, 2.1 eq.) was added to the white solid containing suspension, resulting in a colour change to dark brown suspension after 30 minutes. Sodium triacetoxyborohydride (17.84 g, 84.18 mmol, 2.5 eq.) was added carefully after cooling the reaction mixture under ice. The reaction mixture (yellow suspension) was stirred overnight. Saturated sodium bicarbonate solution (70 ml) was added and after 30 minutes the two phases were extracted, the aqueous phase was extracted twice with 150 mL dichloromethane. The organic phase was dried over sodium sulphate and the solvent was removed under reduced pressure. The crude product obtained was further purified *via* column chromatography (dichloromethane: methanol; 90:10). The product was isolated as brown oil in moderate yields (2.743 g, 10.11 mmol, 30 %). ¹H NMR (400 MHz,

Chapter 4: Unique packing properties of chiral 1,3,4-Oxadiazole Spin Crossover complexes

Chloroform-*d* δ (ppm): 8.60 – 8.50 (m, 1H), 7.74 – 7.58 (m, 1H), 7.29 (dd, $J = 7.5, 1.2$ Hz, 1H), 7.19 (ddd, $J = 7.6, 5.0, 1.2$ Hz, 1H), 4.00 (d, $J = 2.6$ Hz, 2H), 3.68 (q, $J = 7.1$ Hz, 0H), 1.44 (d, $J = 7.1$ Hz, 1H).

(R)-1-(5-(naphthalen-2-yl)-1,3,4-oxadiazol-2-yl)-N,N-bis(pyridin-2-ylmethyl)ethan-1-amine (L^{Naph-ODA}-_{(R)-Al})

The synthesis was carried out with appropriate modification from the literature. ^[9]

Bis(pyridin-2-ylmethyl)-R-alanine (2.460 g, 9.067 mmol, 1 eq.) was dissolved in dry dichloromethane under nitrogen atmosphere. The solution was cooled in an ice bath, and carbonyldiimidazole (1.470 g, 9.067 mmol, 1 eq.) was added. The resulting clear brown solution was stirred for 1 hour. Subsequently, naphthohydrazide (1.688 g, 9.067 mmol, 1 eq.) was added, and the reaction mixture was stirred for an additional 2 hours. Carbontetrabromide (6.014 g, 18.13 mmol, 2 eq.) and triphenylphosphine (4.756g, 18.13 mmol, 2 eq.) were then added simultaneously. The solution immediately turned red. After stirring for 2 hours, the solvent was evaporated under reduced pressure. The crude residue was purified by column chromatography (ethyl acetate:methanol,99.5:0.5 \rightarrow 90:20 gradient). The target compound was obtained as a brown oil (2.547 g, 6.043 mmol, 67 % yield). $R_f = 0.23$ (ethyl acetate: methanol, 19:1). ¹H NMR (400 MHz, Chloroform-*d* δ (ppm)): 8.57 – 8.47 (m, 3H), 8.14 (dd, $J = 8.6, 1.7$ Hz, 1H), 8.03 – 7.95 (m, 2H), 7.95 – 7.88 (m, 1H), 7.73 – 7.53 (m, 7H), 7.19 – 7.11 (m, 3H), 4.46 (q, $J = 7.0$ Hz, 1H), 4.16 – 3.98 (m, 5H), 1.75 (d, $J = 7.0$ Hz, 3H). ¹³C NMR (101 MHz, Chloroform-*d* δ (ppm)): 167, 165, 159, 149, 136, 134, 132, 129, 128, 127, 127, 127, 123, 122, 122.17, 56, 52, 14. FT-IR: $\tilde{\nu}$ (cm⁻¹) = 3053, 1672, 1588, 1568, 1542, 1502, 1472, 1432, 1362, 1299, 1193, 1148, 1130, 1047, 994, 967, 899, 863, 845, 820, 752, 617, 593, 542, 474, 403. ESI-MS (m/z): calc. for [C₂₇H₂₃N₅O₁]⁺ expected: 422.20 (100.00 %); found: 422.20 (100.00 %)

(S)-1-(5-(naphthalen-2-yl)-1,3,4-oxadiazol-2-yl)-N,N-bis(pyridin-2-ylmethyl)ethan-1-amine (L^{Naph-ODA}-_{(S)-Al})

The synthesis was carried out with appropriate modification from the literature. ^[9]

Bis(pyridin-2-ylmethyl)-R-alanine (2.460 g, 9.067 mmol, 1 eq.) was dissolved in dry dichloromethane under a nitrogen atmosphere. The solution was cooled in an ice bath, and carbonyldiimidazole (1.470 g, 9.067 mmol, 1 eq.) was added. The resulting clear brown solution was stirred for 1 hour. Subsequently, naphthohydrazide (1.688 g, 9.067 mmol, 1 eq.) was added, and the reaction mixture was stirred for an additional 2 hours. Carbontetrabromide (6.014 g, 18.13 mmol, 2 eq.) and triphenylphosphine (4.756g, 18.13 mmol, 2 eq.) were then added simultaneously. The solution immediately turned red. After stirring for 2 hours, the solvent was evaporated under reduced pressure. The crude residue was purified by column chromatography (ethyl acetate:methanol,99.5:0.5 \rightarrow 90:20

gradient). The target compound was obtained as a brown oil (1.629 g, 3.87 mmol, 43 % yield). $R_f = 0.23$ (ethyl acetate: methanol, 19:1). $^1\text{H NMR}$ (400 MHz, Chloroform-*d* δ (ppm)): 8.59 – 8.49 (m, 3H), 8.15 (dd, $J = 8.6, 1.7$ Hz, 1H), 8.06 – 7.87 (m, 3H), 7.72 – 7.56 (m, 6H), 7.15 (ddd, $J = 6.8, 4.9, 1.7$ Hz, 2H), 4.46 (q, $J = 7.0$ Hz, 1H), 4.20 – 3.92 (m, 4H), 1.76 (d, $J = 7.0$ Hz, 3H). $^{13}\text{C NMR}$ (101 MHz, Chloroform-*d* δ (ppm)): 167, 165, 159, 149, 136, 134, 132, 128 (d, $J = 12$ Hz), 127, 127.11, 123, 123, 122, 57, 52, 15. FT-IR: $\tilde{\nu}$ (cm^{-1}) = 2984, 2857, 1682, 1589, 1564, 1542, 1500, 1470, 1431, 1358, 1270, 1191, 1156, 1135, 1057, 1012, 994, 967, 937, 897, 858, 845, 823, 749, 660, 630, 610, 593, 547, 470, 403. ESI-MS (m/z): calc. for $[\text{C}_{27}\text{H}_{23}\text{N}_5\text{O}_1]^+$ expected: 422.20 (100.00 %); found: 422.20 (100.00 %)

Complex synthesis:

The Precursor complex $[\text{Fe}(\text{py})_4(\text{NCBH}_3)_2]$ was synthesized accordingly to literature known procedure.^[6]

$[\text{Fe}(\text{L}^{\text{Naph-ODA-(Rac-Al)}})(\text{NCBH}_3)_2] \cdot 0.5 \text{ CH}_3\text{CN}$ (**C1**)

The following reaction was carried out in a glovebox under an inert atmosphere. $[\text{Fe}(\text{py})_4(\text{NCBH}_3)_2]$ (217.0 mg, 0.475 mmol, 1 eq.) was suspended in 9 mL dry methanol and stirred for 30 minutes. The clear solution was added to a solution of $\text{L}^{\text{Naph-ODA-(S-Al)}}$ (100 mg, 0.237 mmol, 0.5 eq.) and $\text{L}^{\text{Naph-ODA-(S-Al)}}$ (87.25 mg, 0.237 mmol, 0.5 eq.) in 1 mL of methanol and the resulting mixture was stirred for 1 h. A yellow precipitate was observed, and the suspension was filtered. The product was obtained in moderate yields as yellow powder. (135 mg, 0.2424 mmol, 51%). Single Crystals suitable for X-ray diffraction were obtained by recrystallisation out of acetonitrile after five days of slow evaporation.

FT-IR: $\tilde{\nu}$ (cm^{-1}) = 2326, 2276, 2218, 2188, 2141, 1604, 1573, 1547, 1485, 1440, 1355, 1293, 1272, 1195, 1145, 1115, 1052, 1023, 996, 967, 894, 865, 848, 821, 761, 718, 671, 643, 595, 560, 477, 417. ESI-MS (m/z): calc. for $[\text{C}_{27}\text{H}_{26}\text{BFeN}_6\text{O}]^+$ expected: 517.16 (100.00 %); found: 517.16 (100.00 %). Elemental Analysis calculated for $[\text{Fe}(\text{L}^{\text{Naph-ODA-(Rac-Al)}})(\text{NCBH}_3)_2]$: C, 60.37, H, 5.25, N, 17.60. found: C, 59.89, H, 5.16, N, 17.53.

$[\text{Fe}(\text{L}^{\text{Naph-ODA-(R-Al)}})(\text{NCBH}_3)_2] \cdot 0.5 \text{ CH}_3\text{CN}$ (**C2**)

The following reaction was carried out in a glovebox under an inert atmosphere. $[\text{Fe}(\text{py})_4(\text{NCBH}_3)_2]$ (217.0 mg, 0.475 mmol, 1 eq.) was suspended in 9 mL dry methanol and stirred for 30 minutes. The clear solution was added to a solution of $\text{L}^{\text{Naph-ODA-(R-Al)}}$ (217 mg, 0.475 mmol, 1 eq.) in 1 mL of methanol and the resulting mixture was stirred for 1 h. A yellow precipitate was observed, and the suspension was filtered. The product was obtained in moderate yields as yellow powder (189 mg, 0.3393 mmol, 72%). Single Crystals suitable for X-ray diffraction were achieved by recrystallisation out of acetonitrile after five days of slow evaporation. FT-IR: $\tilde{\nu}$ (cm^{-1}) = 2326, 2188, 2020, 1979, 1632, 1604, 1573, 1547, 1484, 1440, 1391, 1355, 1293, 1232, 1195, 1144, 1116, 1052, 1023, 995, 966, 950, 894, 865, 848, 821,

Chapter 4: Unique packing properties of chiral 1,3,4-Oxadiazole Spin Crossover complexes

761, 717, 670, 643, 595, 559, 476, 418. ESI-MS (m/z): calc. for $[C_{27}H_{26}BFeN_6O]^+$ expected: 517.16 (100.00 %); found: 517.16 (100.00 %). Elemental Analysis calculated for $[Fe(L^{Naph-ODA-(R)-Al})(NCBH_3)_2]$: C, 60.37, H, 5.25, N, 17.60. found: C, 59.89, H, 5.13, N, 17.51.

$[Fe(L^{Naph-ODA-(S)-Al})(NCBH_3)_2] \cdot 0.5 CH_3CN$ (**C3**)

The following reaction was carried out in a glovebox under an inert atmosphere. $[Fe(py)_4(NCBH_3)_2]$ (217.0 mg, 0.475 mmol, 1 eq.) was suspended in 9 mL dry methanol and stirred for 30 minutes. The clear solution was added to a solution of $L^{Naph-ODA-(S)-Al}$ (217 mg, 0.475 mmol, 1 eq.) in 1 mL of methanol and the resulting mixture was stirred for 1 h. A yellow precipitate was observed, and the suspension was filtered. The product was obtained in moderate yields as yellow powder (182 mg, 0.3267 mmol, 69%). Single Crystals suitable for X-ray diffraction were achieved by recrystallisation out of acetonitrile after five days of slow evaporation. FT-IR: $\tilde{\nu}$ (cm^{-1}) = 2333, 2177, 1602, 1574, 1547, 1481, 1460, 1443, 1429, 1393, 1340, 1284, 1250, 1155, 1113, 1067, 1055, 1039, 1016, 1001, 927, 900, 873, 813, 763, 731, 687, 670, 636, 581, 552, 507, 492, 476, 416, 405. ESI-MS (m/z): calc. for $[C_{27}H_{26}BFeN_6O]^+$ expected: 517.16 (100.00 %); found: 517.16 (100.00 %). Elemental Analysis calculated for $[Fe(L^{Naph-ODA-(S)-Al})(NCBH_3)_2]$: C, 60.37, H, 5.25, N, 17.60. found: C, 59.87, H, 5.13, N, 17.48.

3. NMR-Spectra:

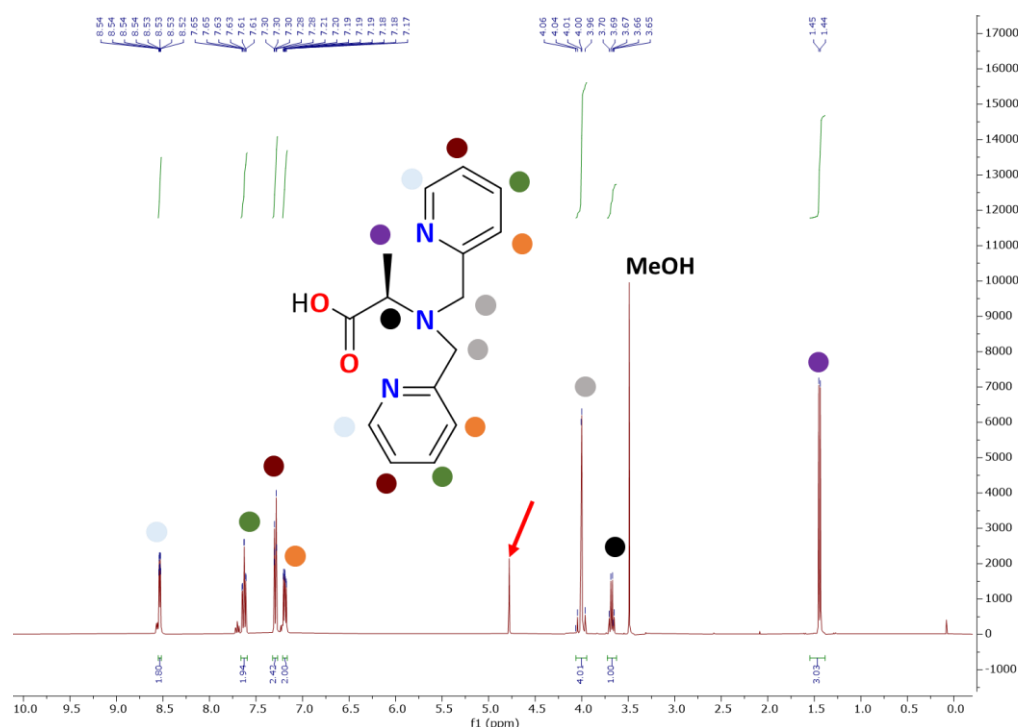


Figure S1: 1H -NMR spectrum of the Bis(pyridin-2-ylmethyl)-D-alanine (**I-R**) in $CDCl_3$ [400 MHz]. All signals can be assigned. The signal at 4.78 ppm (red arrow) can be assigned to pyridin-2-ylmethanol.^[10] And the signal at 3.49 ppm can be assigned to methanol.^[11]

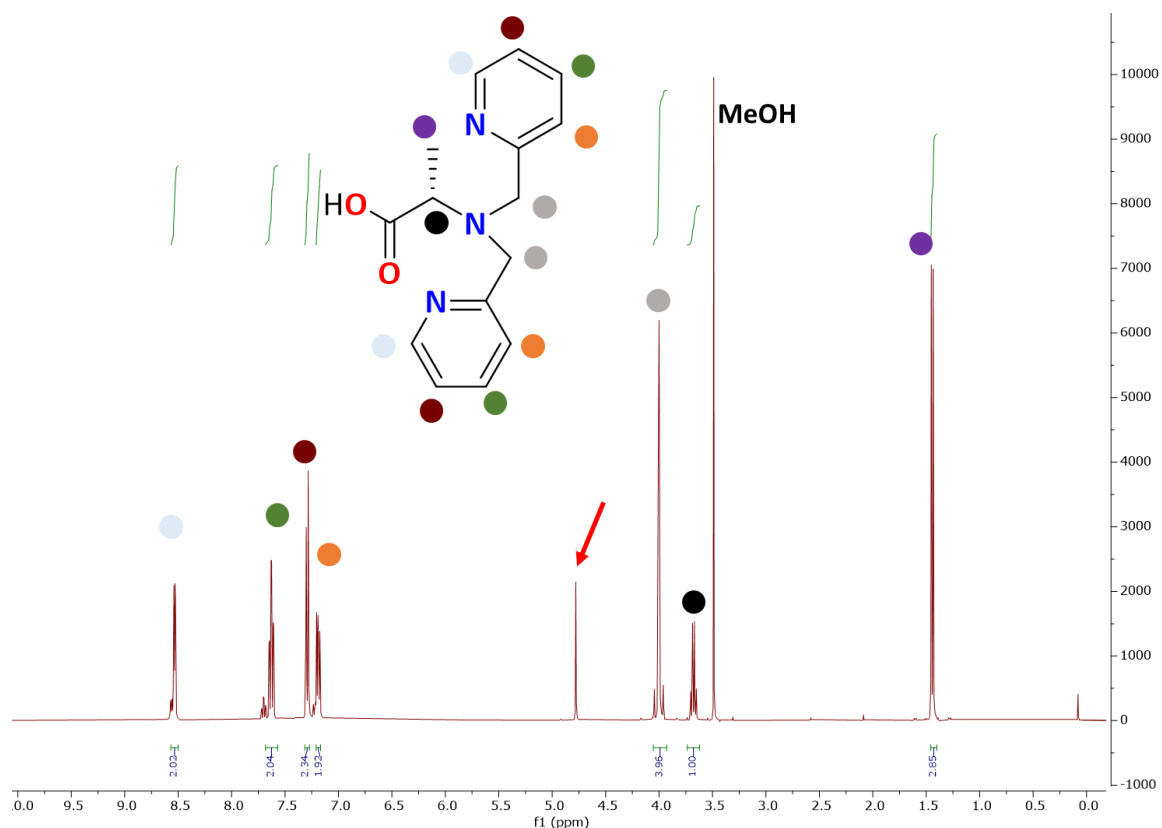


Figure S2: $^1\text{H-NMR}$ spectrum of the Bis(pyridin-2-ylmethyl)-S-alanine (**I-S**) in CDCl_3 [400 MHz]. All signals can be assigned. The signal at 4.78 ppm (red) can be assigned to pyridin-2-ylmethanol.^[10] And the signal at 3.49 ppm can be assigned to methanol.^[11]

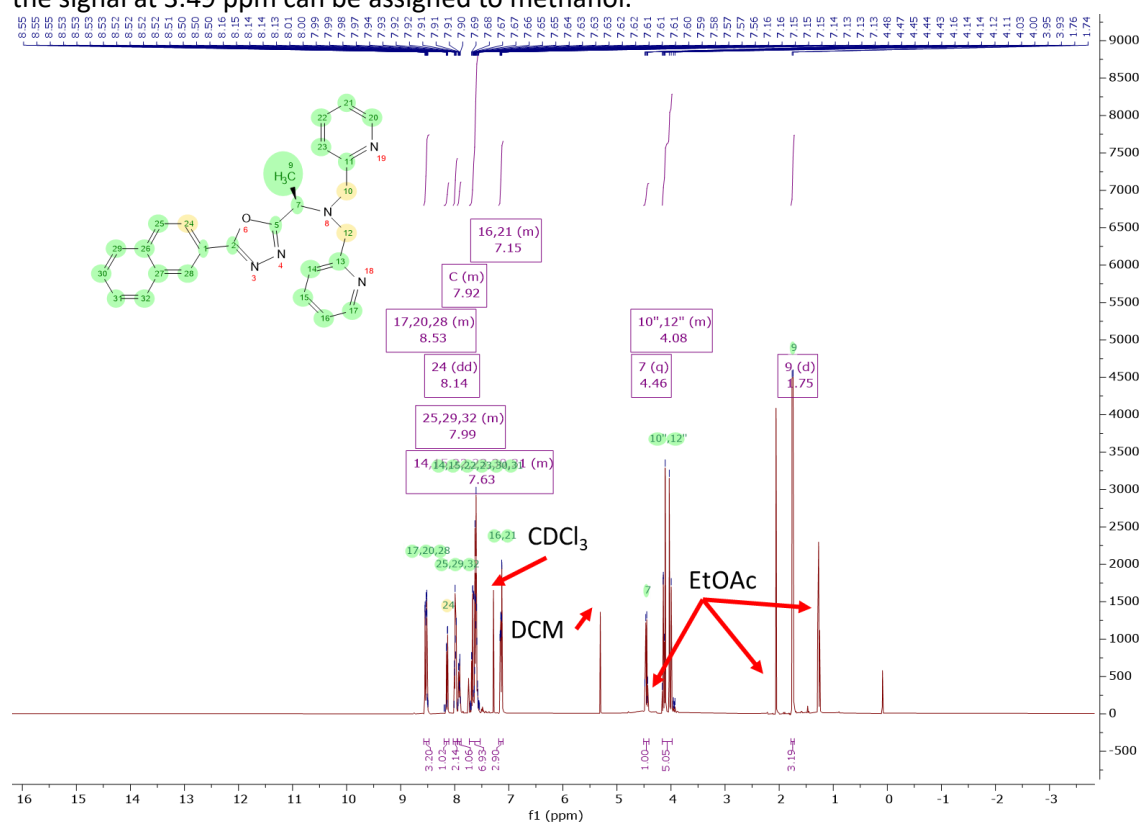


Figure S3: $^1\text{H-NMR}$ spectrum of (**R**)-1-(5-(naphthalen-2-yl)-1,3,4-oxadiazol-2-yl)-*N,N*-bis(pyridin-2-ylmethyl)ethan-1-amine (**L^{Naph}-ODA-(R)-Al**) in CDCl_3 [400 MHz]. All signals can be assigned. Signals at 1.27 ppm, 2.06 ppm and 4.14 ppm are assigned to ethyl acetate and the signal at 5.30 ppm is assigned to dichloromethane (red arrows).^[11]

Chapter 4: Unique packing properties of chiral 1,3,4-Oxadiazole Spin Crossover complexes

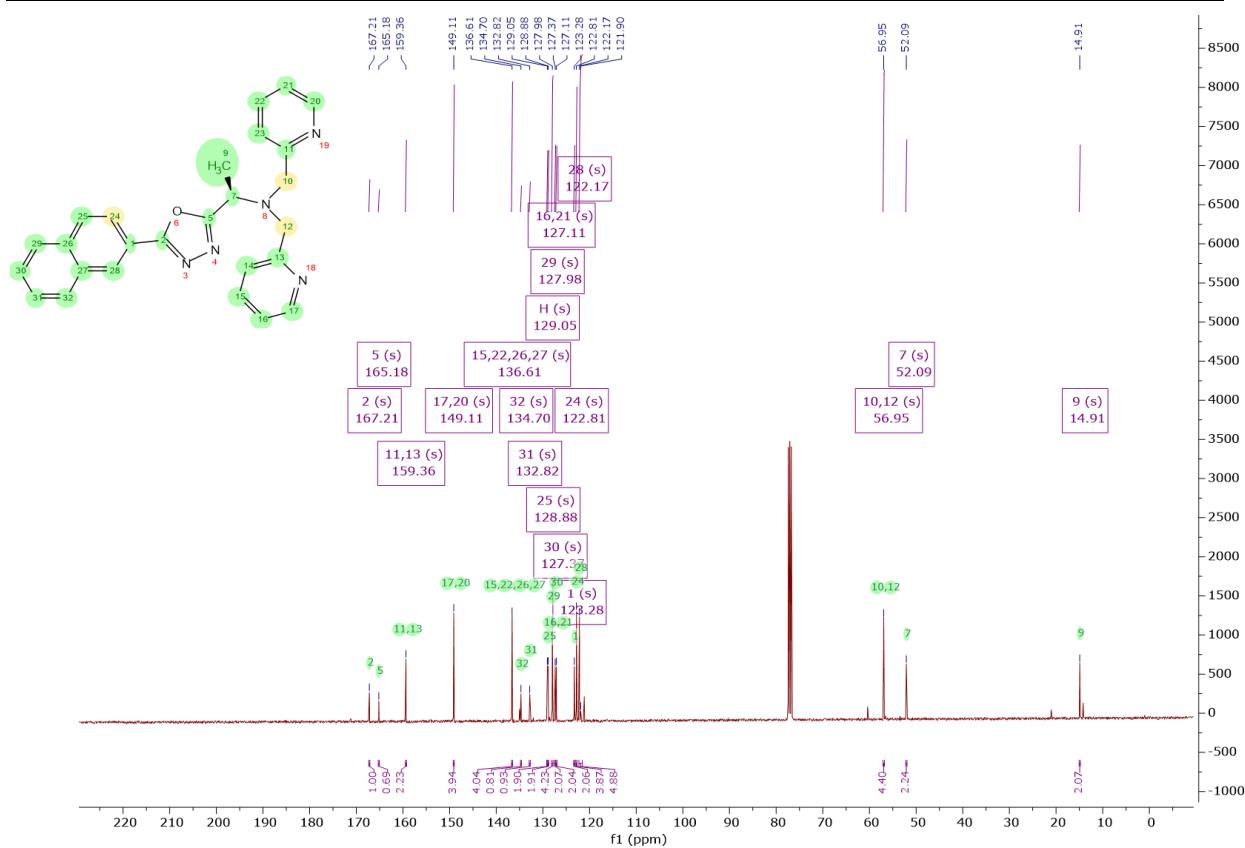


Figure S4: ^{13}C -NMR spectrum of $(R)\text{-}1\text{-}(5\text{-}(\text{naphthalen-2-yl})\text{-}1,3,4\text{-oxadiazol-2-yl})\text{-}N,N\text{-bis}(\text{pyridin-2-ylmethyl})\text{ethan-1-amine}$ ($\text{L}^{\text{Naph-ODA-(R)-Al}}$) in CDCl_3 [400 MHz].

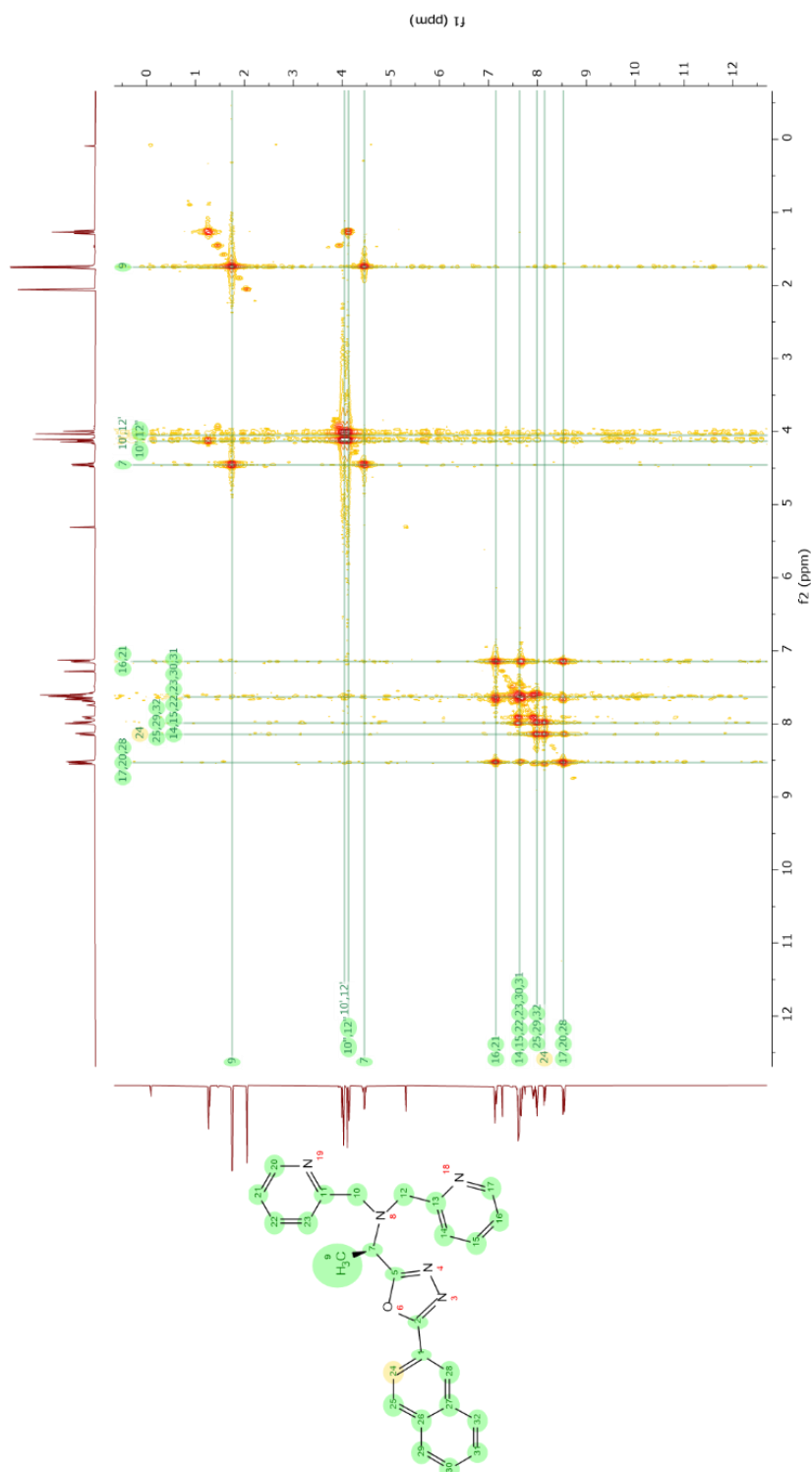


Figure S5: COSY-NMR spectrum of (R)-1-(5-(naphthalen-2-yl)-1,3,4-oxadiazol-2-yl)-N,N-bis(pyridin-2-ylmethyl)ethan-1-amine ($L^{\text{Naph-ODA-(R)-Al}}$) in CDCl_3 [400 MHz].

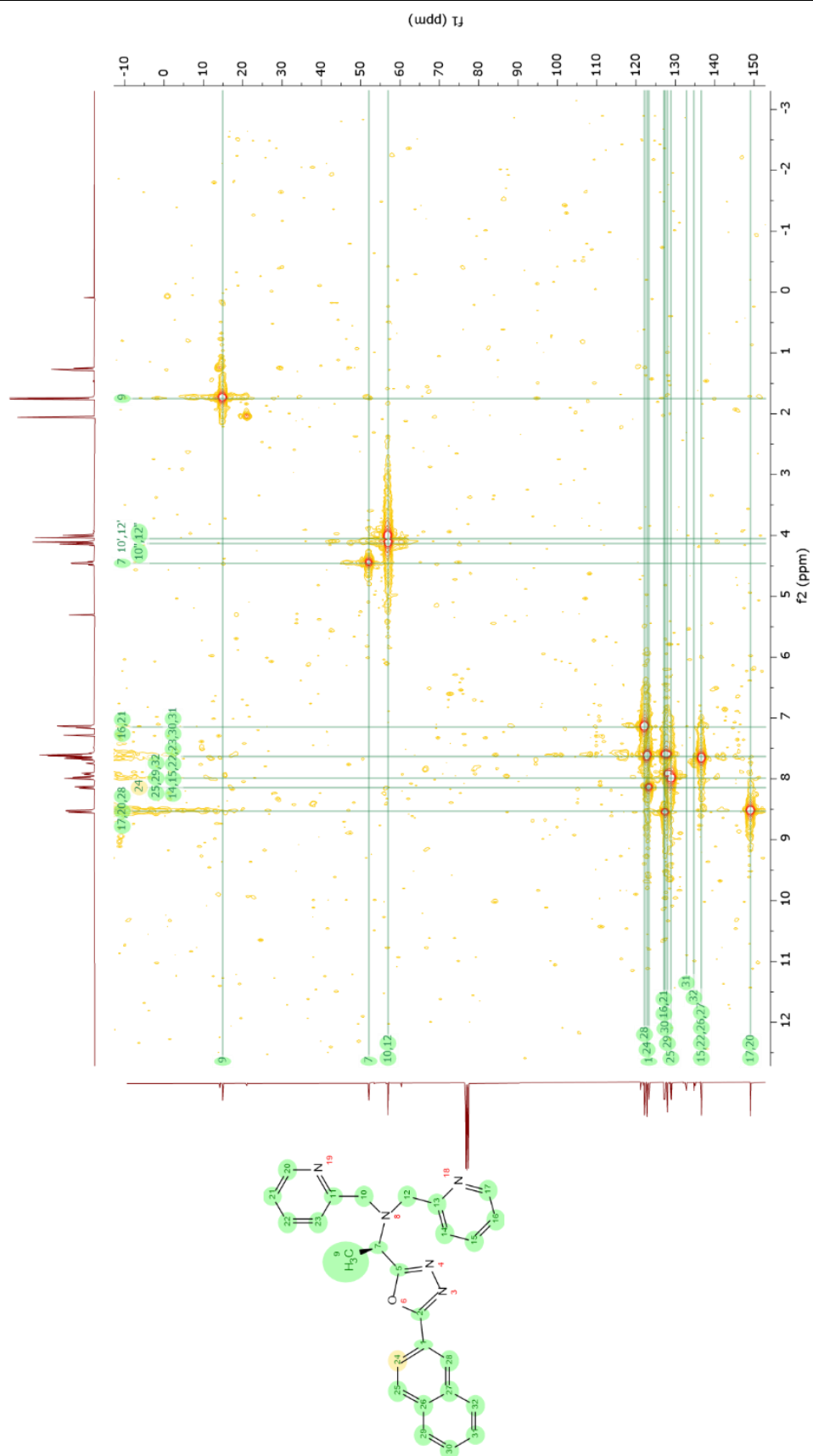


Figure S6: HSQC-NMR spectrum of (R)-1-(5-(naphthalen-2-yl)-1,3,4-oxadiazol-2-yl)-N,N-bis(pyridin-2-ylmethyl)ethan-1-amine ($L^{\text{Naph-ODA-(R)-Al}}$) in CDCl_3 [400 MHz].

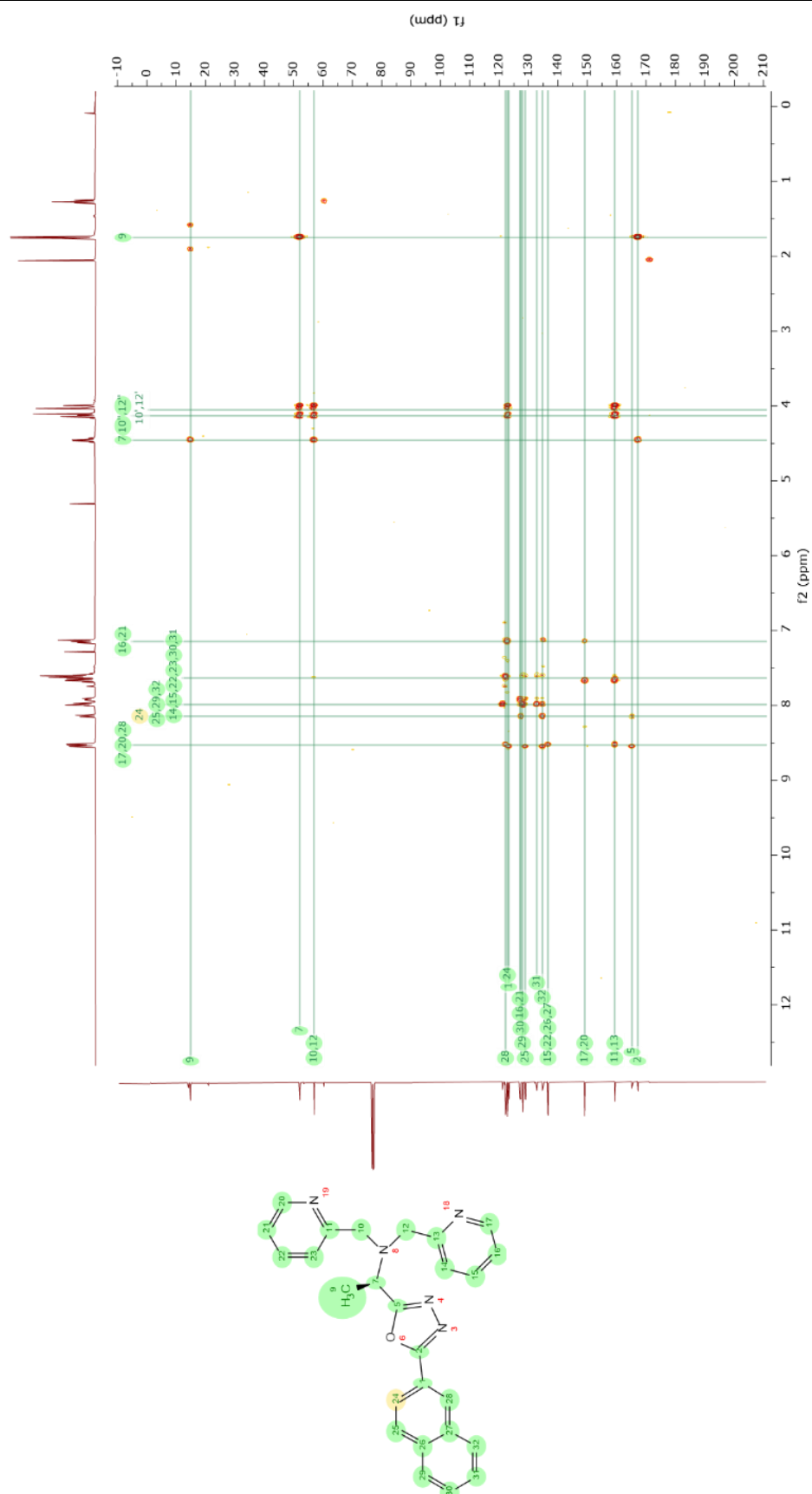


Figure S7: HMBC-NMR spectrum of (R)-1-(5-(naphthalen-2-yl)-1,3,4-oxadiazol-2-yl)-N,N-bis(pyridin-2-ylmethyl)ethan-1-amine ($\text{L}^{\text{Naph-ODA-(R)-Al}}$) in CDCl_3 [400 MHz].

Chapter 4: Unique packing properties of chiral 1,3,4-Oxadiazole Spin Crossover complexes

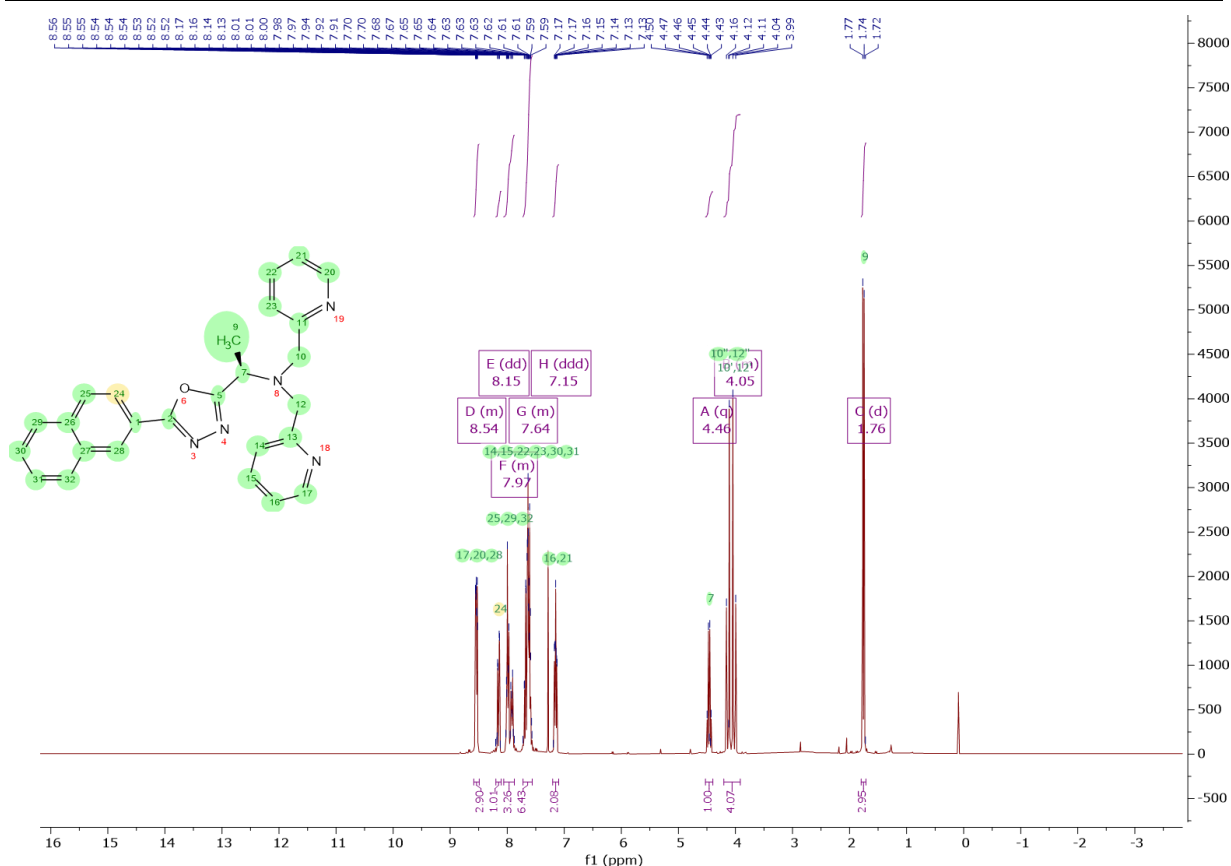


Figure S8: $^1\text{H-NMR}$ spectrum of (S)-1-(5-(naphthalen-2-yl)-1,3,4-oxadiazol-2-yl)-N,N-bis(pyridin-2-ylmethyl)ethan-1-amine ($\text{L}^{\text{Naph-ODA-(S)-Al}}$) in CDCl_3 [400 MHz]. All signals can be assigned.

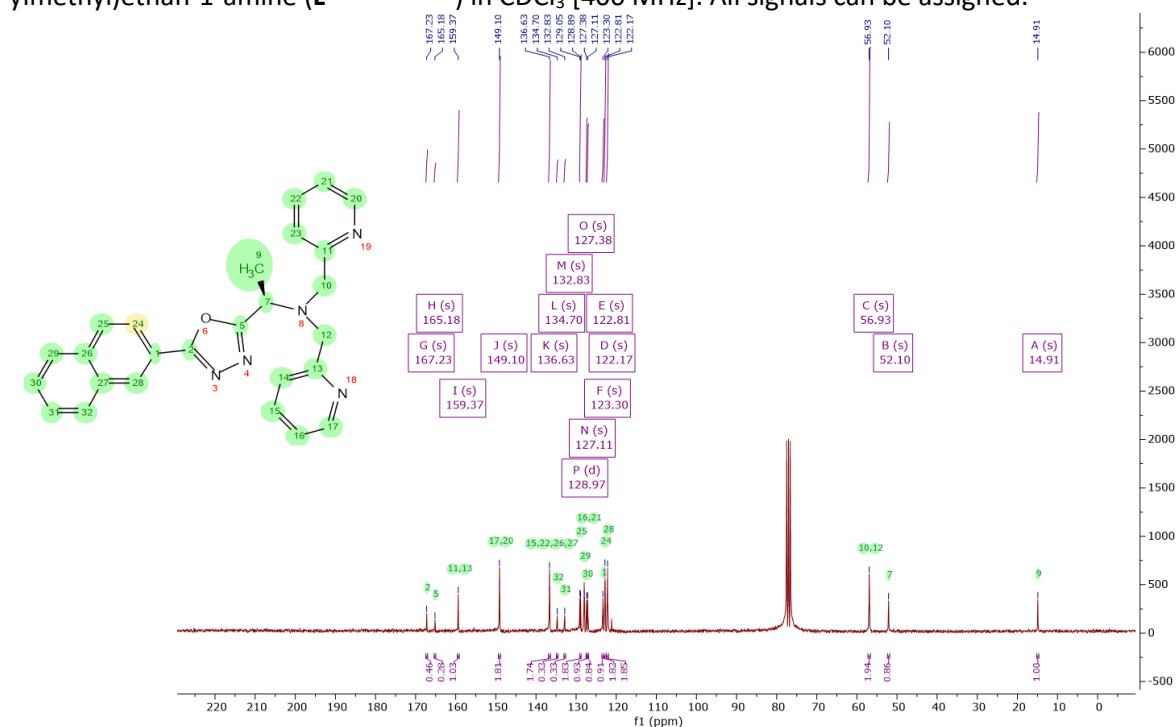


Figure S9: $^{13}\text{C-NMR}$ spectrum of (S)-1-(5-(naphthalen-2-yl)-1,3,4-oxadiazol-2-yl)-N,N-bis(pyridin-2-ylmethyl)ethan-1-amine ($\text{L}^{\text{Naph-ODA-(S)-Al}}$) in CDCl_3 [400 MHz].

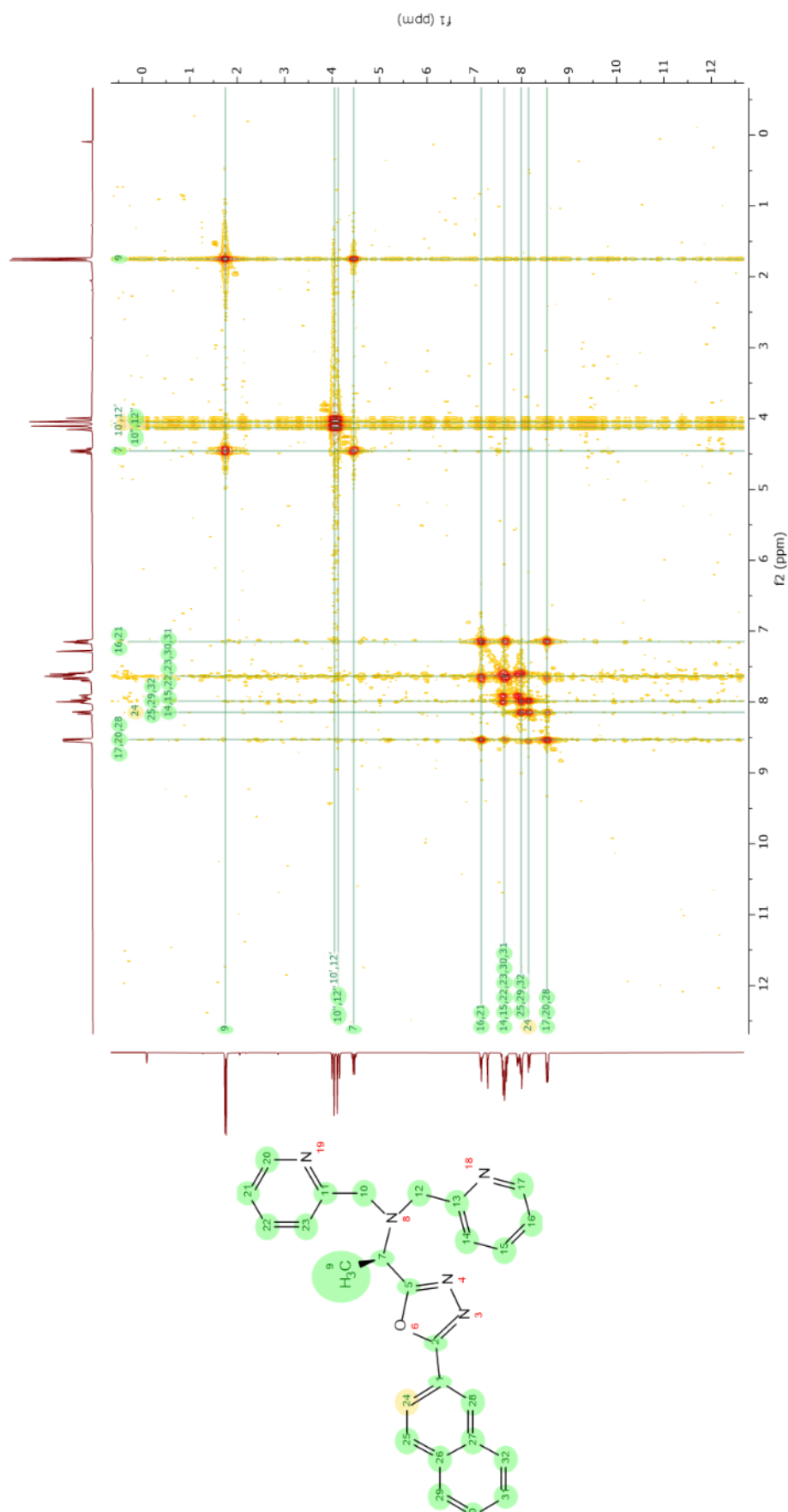


Figure S10: COSY-NMR spectrum of (S)-1-(5-(naphthalen-2-yl)-1,3,4-oxadiazol-2-yl)-N,N-bis(pyridin-2-ylmethyl)ethan-1-amine (**L^{Naph-ODA-(S)-Al}**) in CDCl₃ [400 MHz].

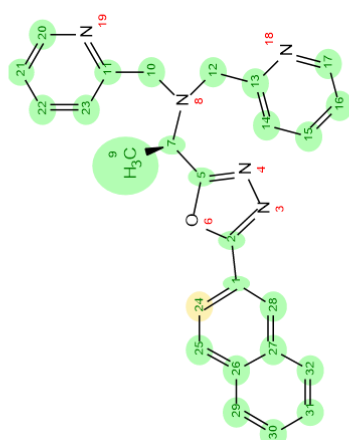
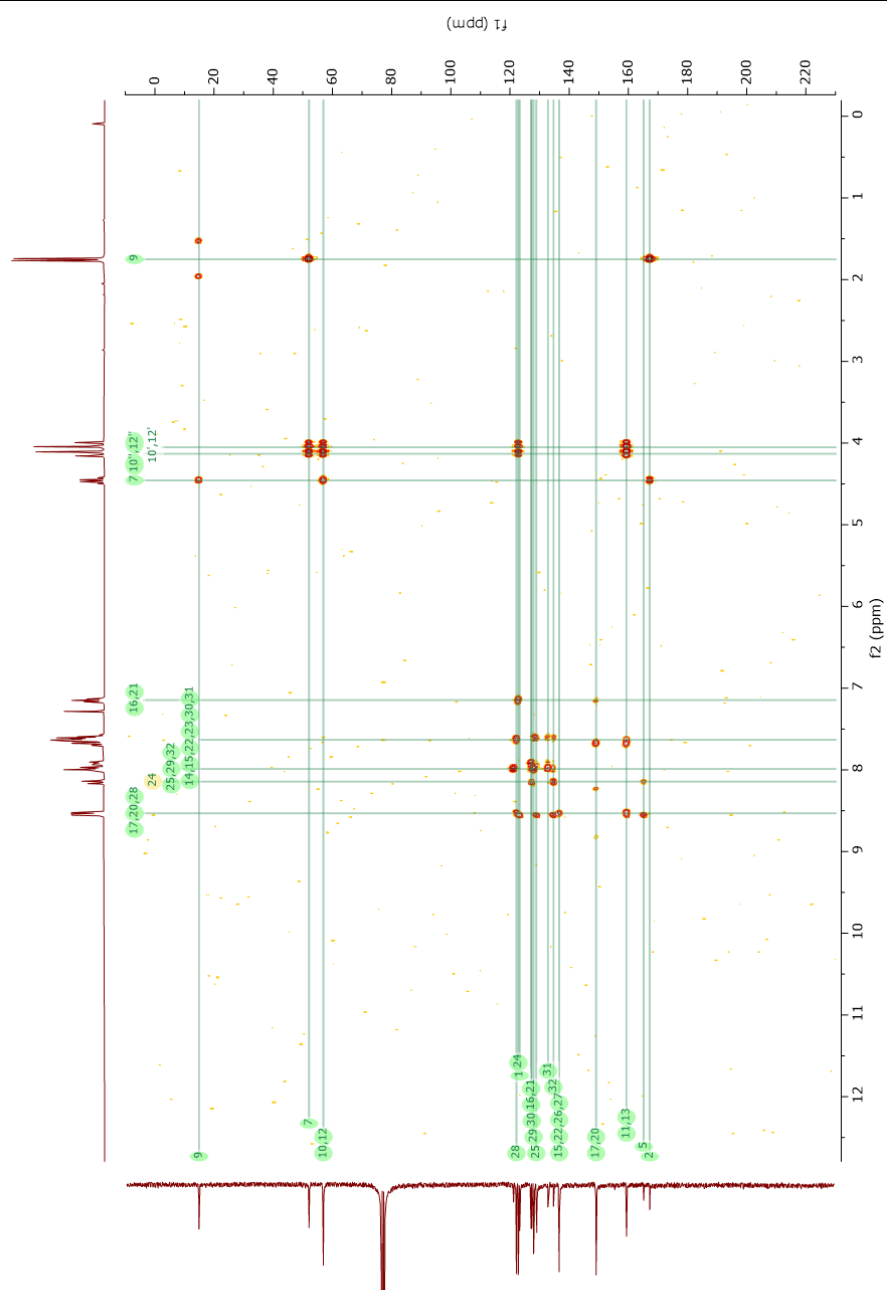


Figure S12: HMBC-NMR spectrum of (S)-1-(5-(naphthalen-2-yl)-1,3,4-oxadiazol-2-yl)-N,N-bis(pyridin-2-ylmethyl)ethan-1-amine ($L^{\text{Naph-ODA-(S)-Al}}$) in CDCl_3 [400 MHz].

4. IR-spectra:

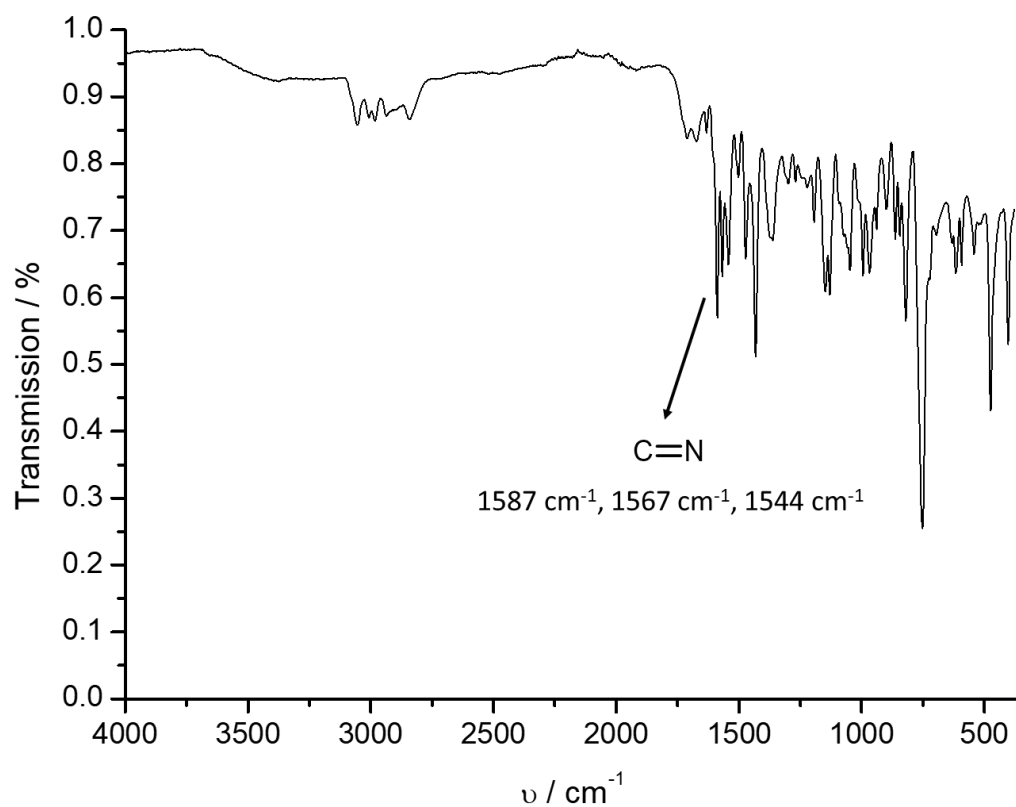


Figure S13: IR spectrum of Ligand $L^{\text{Naph-ODA-(R)-Al}}$.

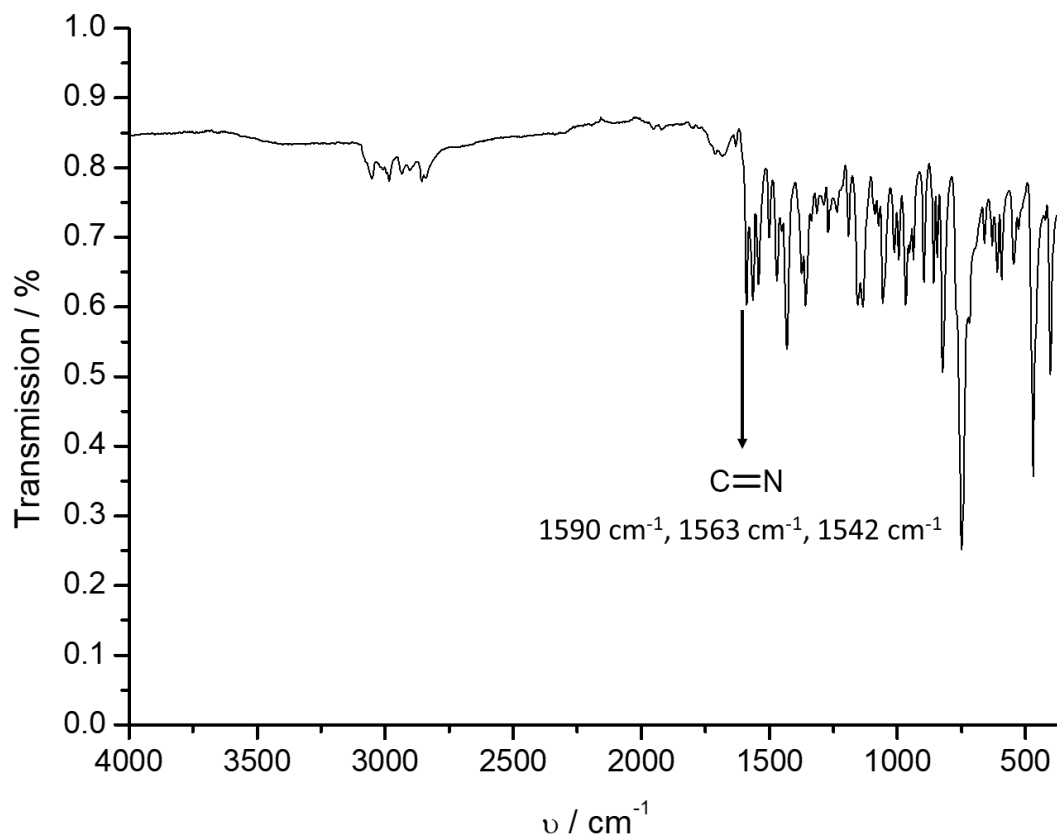


Figure S14: IR spectrum of Ligand $L^{\text{Naph-ODA-(S)-Al}}$.

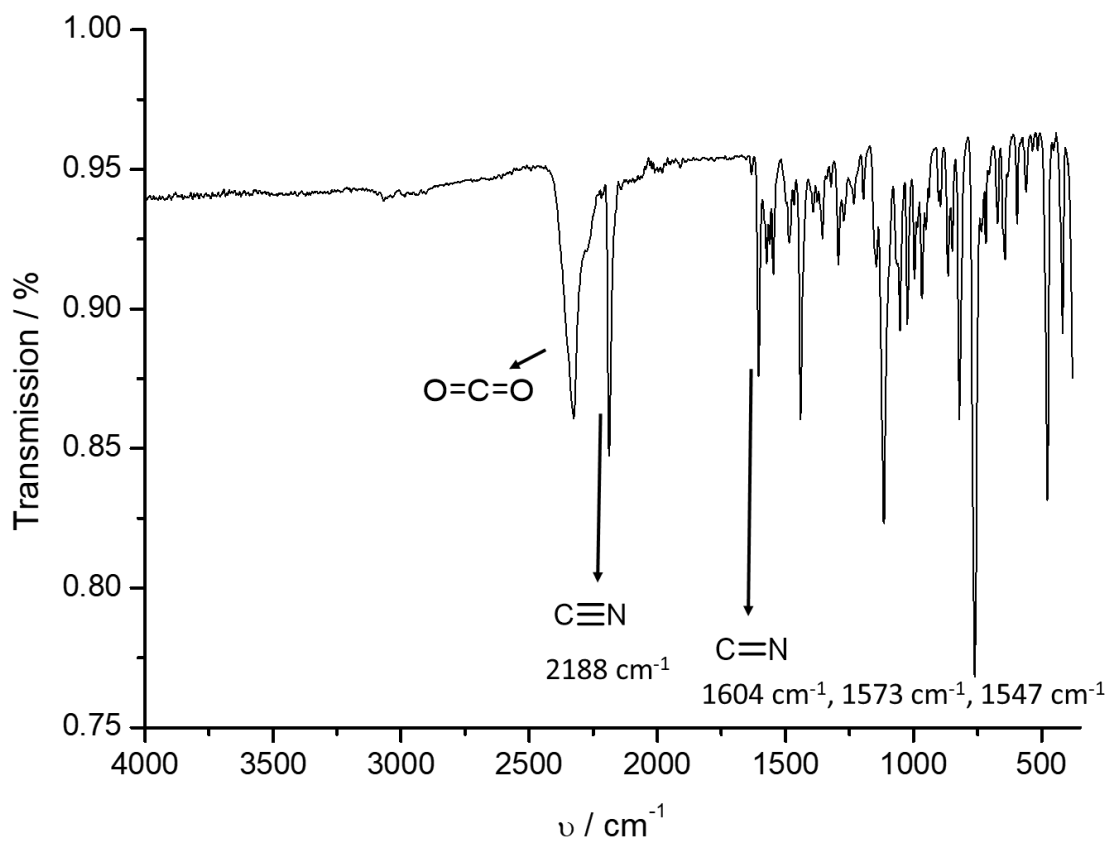


Figure S15: IR spectrum of $[\text{Fe}(\text{L}^{\text{Naph-ODA-(Rac)-Al})(\text{NCBH}_3)_2] \cdot 0.5 \text{CH}_3\text{CN}$ (C1).

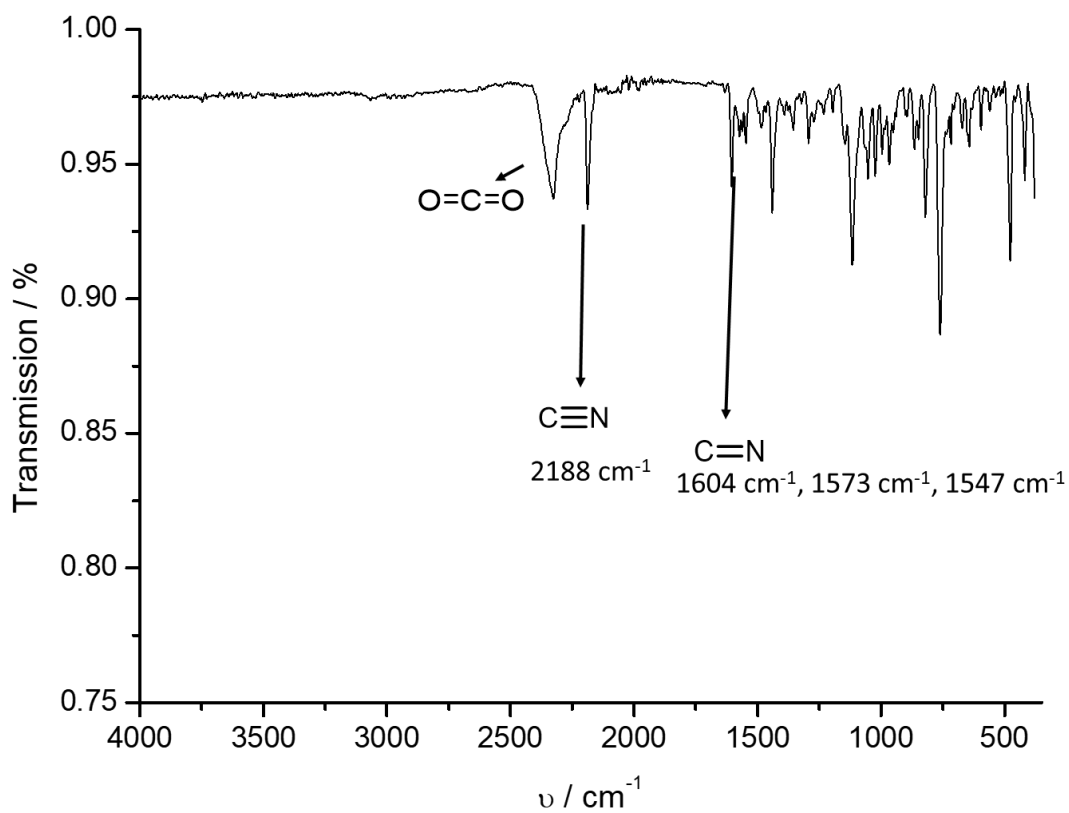


Figure S16: IR spectrum of $[\text{Fe}(\text{L}^{\text{Naph-ODA-(R)-Al})(\text{NCBH}_3)_2] \cdot 0.5 \text{CH}_3\text{CN}$ (C2).

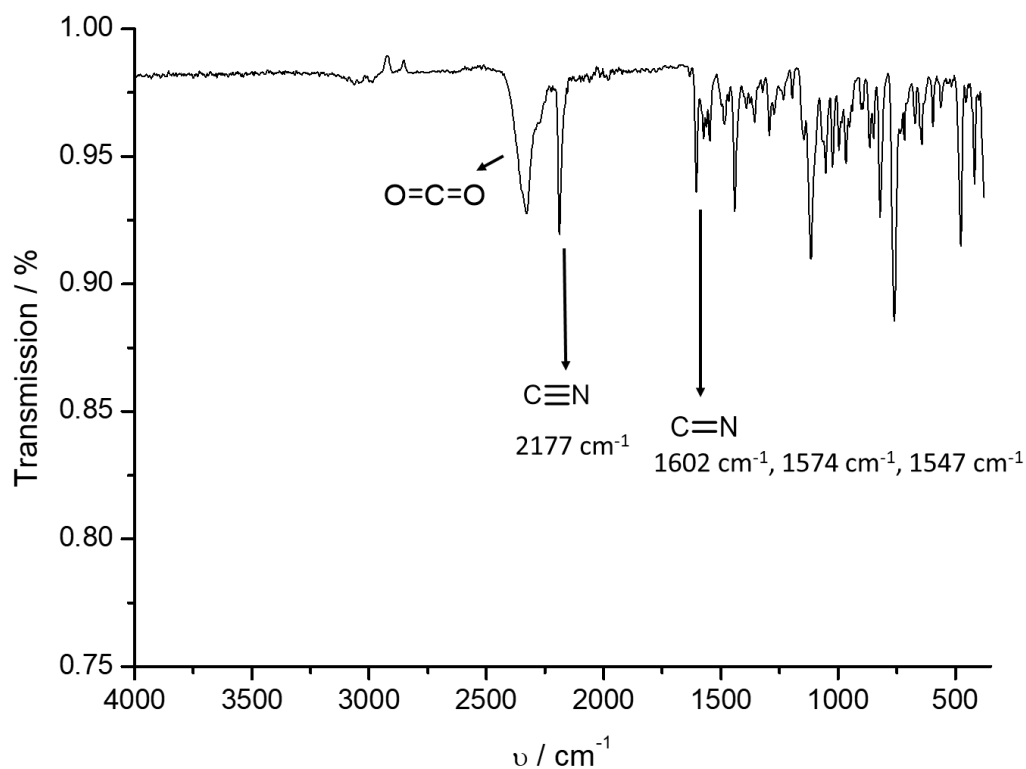


Figure S17: IR spectrum of $[\text{Fe}(\text{L}^{\text{Naph-ODA-(S)-Al}})(\text{NCBH}_3)_2] \cdot 0.5 \text{ CH}_3\text{CN}$ (**C3**).

5. Mass spectra:

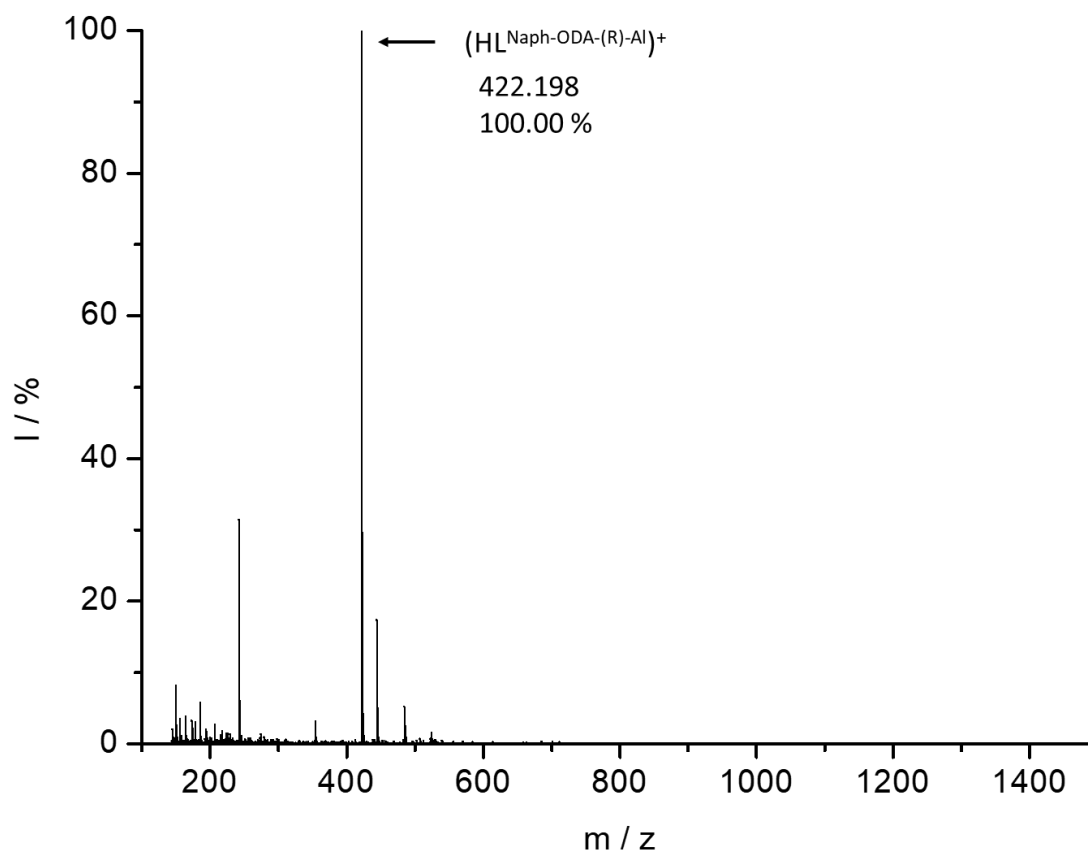


Figure S18: Mass spectrum (ESI positive) spectrum of $\text{L}^{\text{Naph-ODA-(R)-Al}}$.

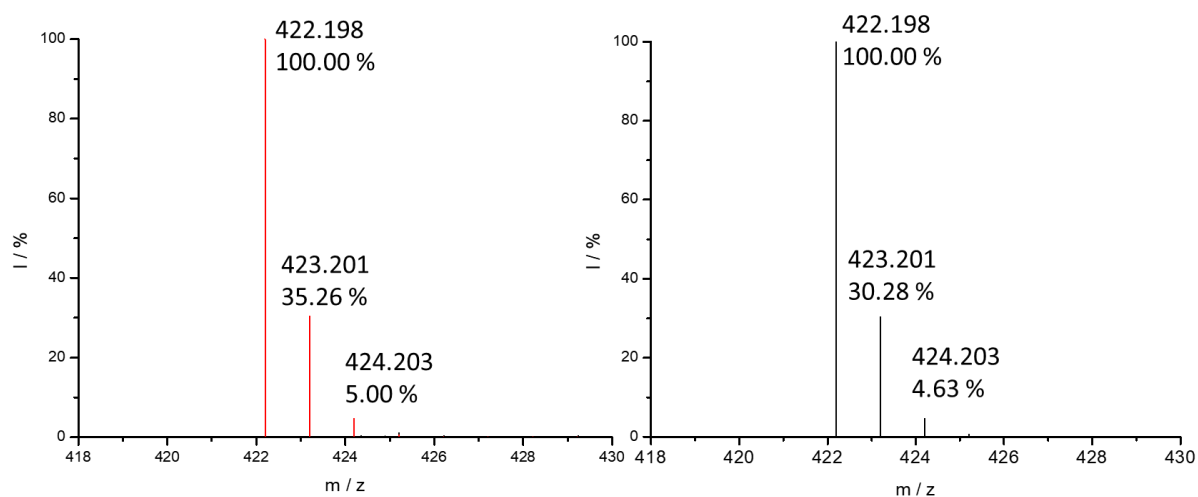


Figure S19: Isotopic pattern of ESI mass spectra of $L^{\text{Naph-ODA-(R)-Al}}$ measured (left with red overlap of the isotopic pattern) predicted (right).

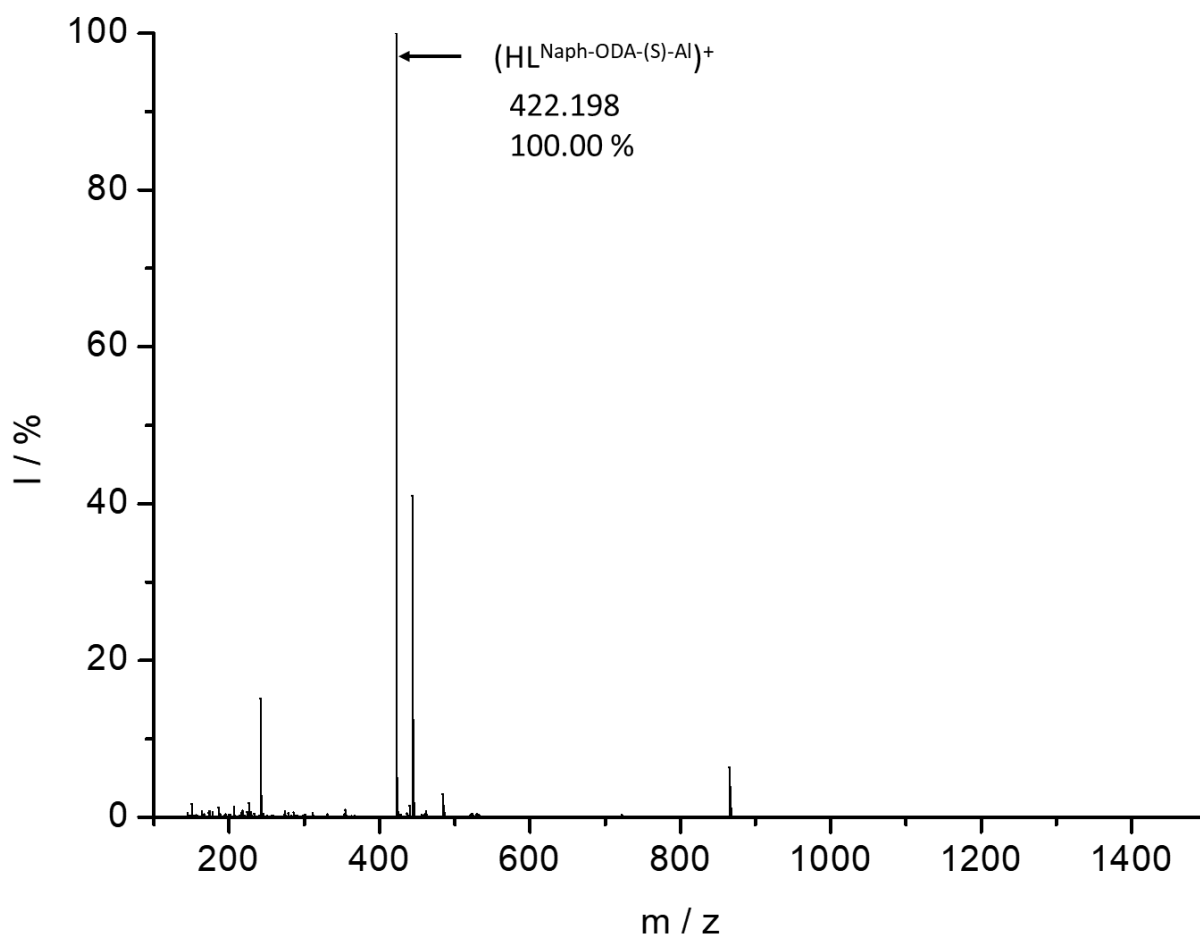


Figure S20: Mass spectrum (ESI positive) spectrum of $L^{\text{Naph-ODA-(S)-Al}}$.

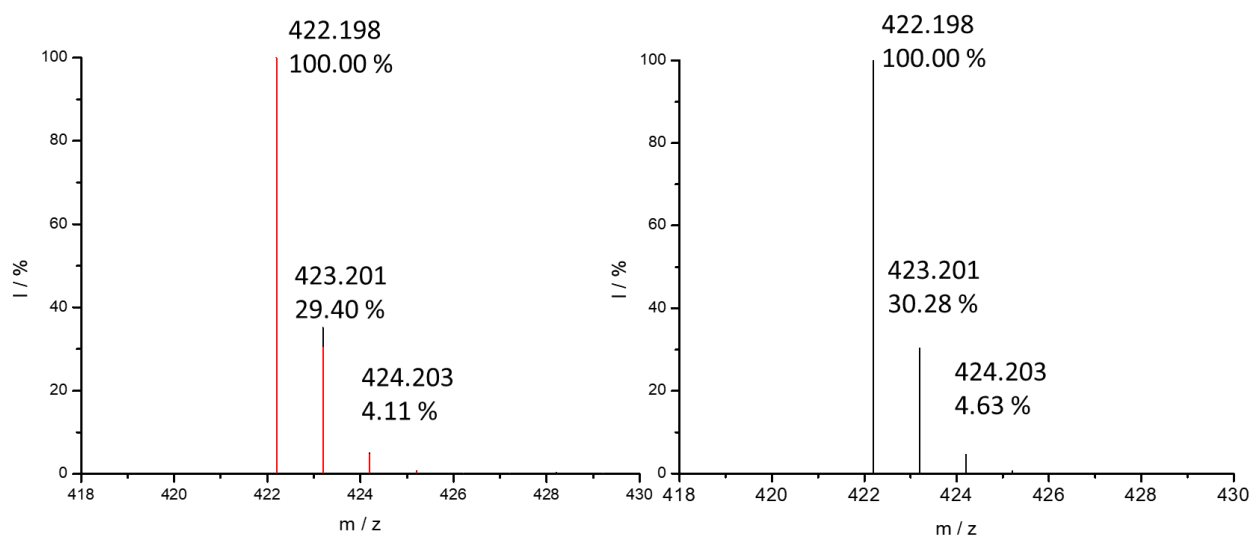


Figure S21: Isotopic pattern of *ESI* mass spectra of $L^{\text{Naph-ODA-(S)-Al}}$ measured (left with red overlap of the isotopic pattern) predicted (right).

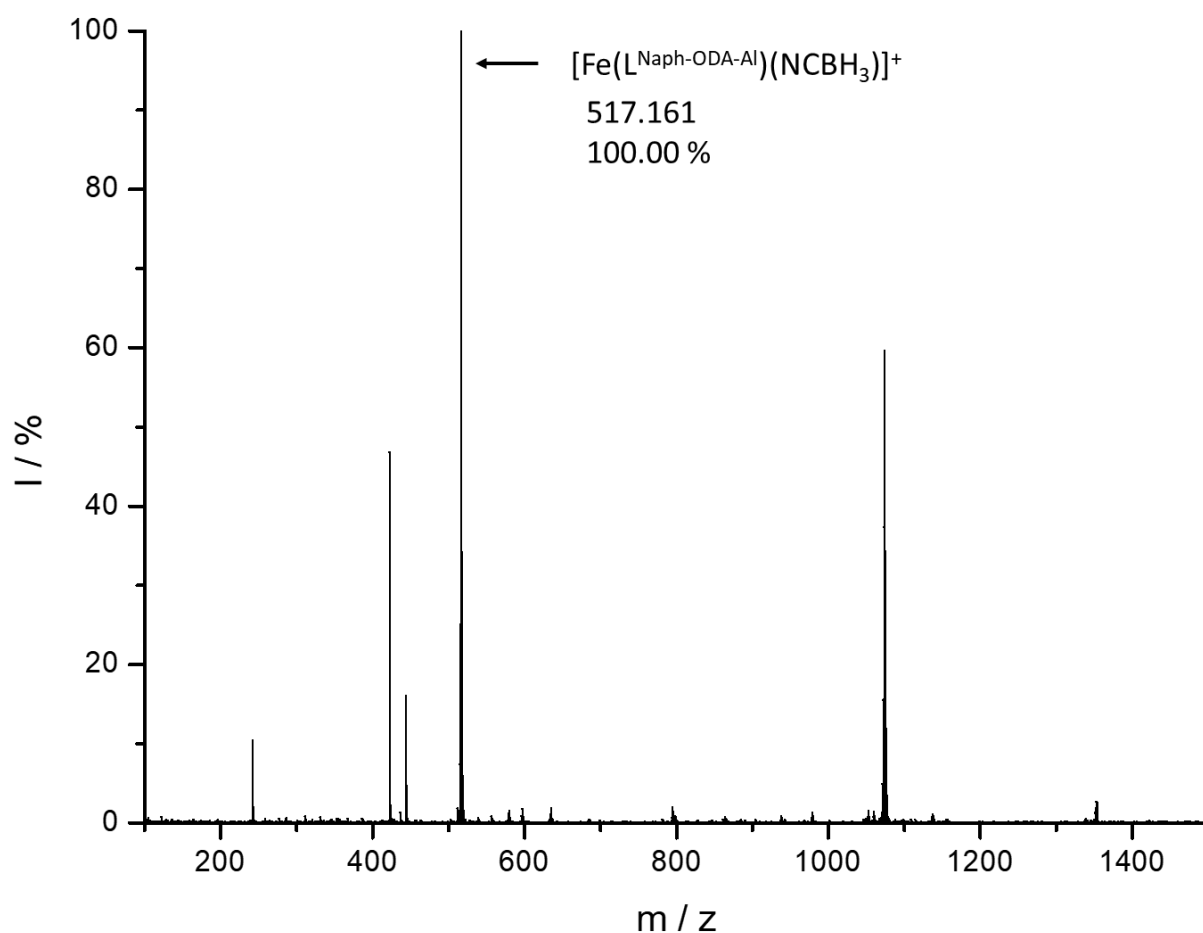


Figure S22: Mass spectrum (*ESI* positive) spectrum of $[\text{Fe}(L^{\text{Naph-ODA-(Rac)-Al}})(\text{NCBH}_3)_2] \cdot 0.5 \text{CH}_3\text{CN}$ (**C1**).

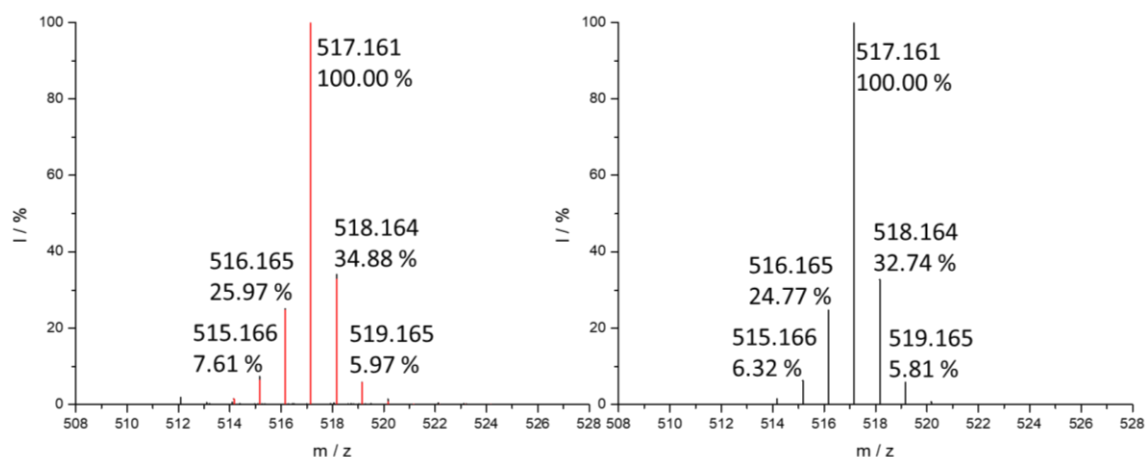


Figure S23: Isotopic pattern of *ESI* mass spectra of $[\text{Fe}(\text{L}^{\text{Naph-ODA-(Rac)-Al}})(\text{NCBH}_3)_2] \cdot 0.5 \text{CH}_3\text{CN}$ measured (left with red overlap of the isotopic pattern) predicted (right).

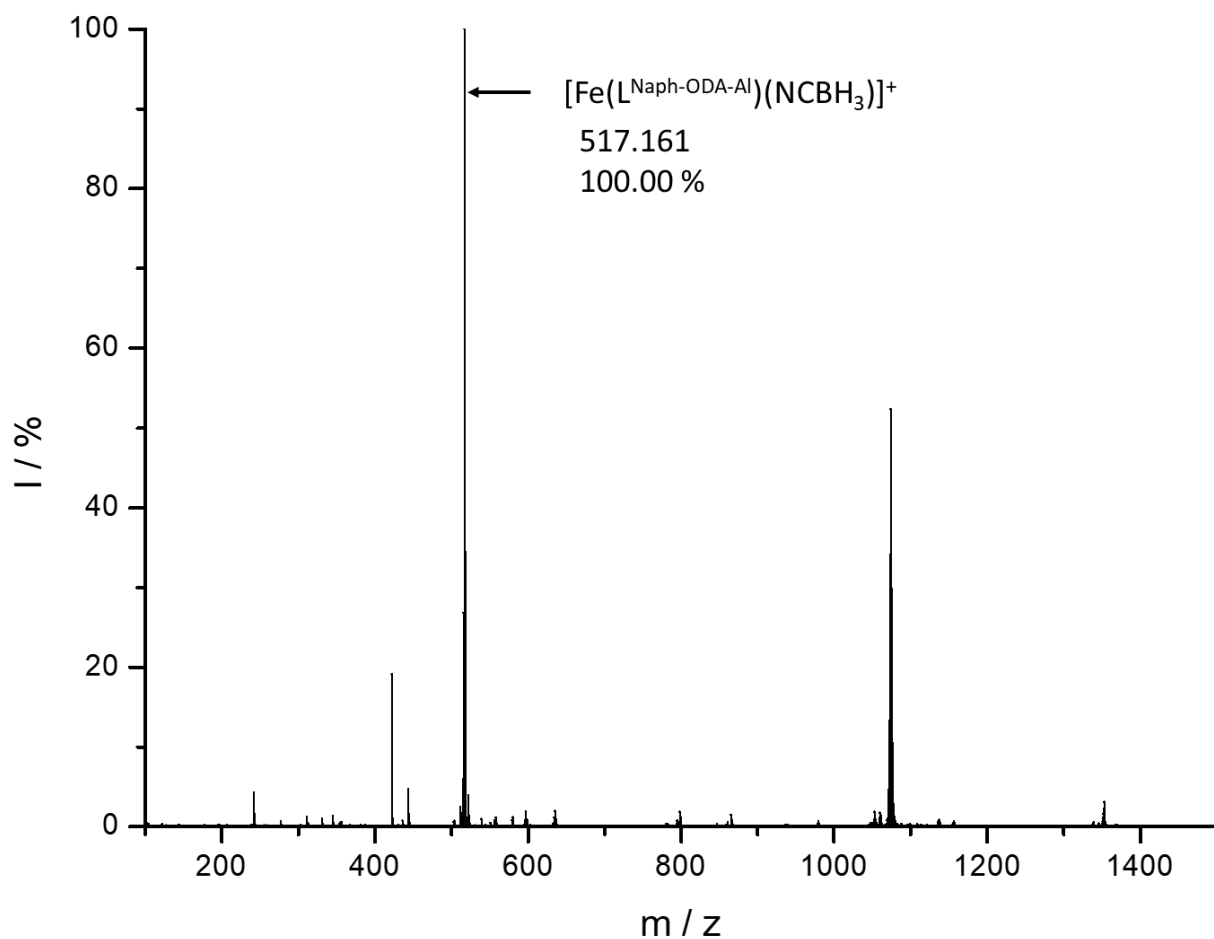


Figure S24: Mass spectrum (*ESI* positive) spectrum of $[\text{Fe}(\text{L}^{\text{Naph-ODA-(R)-Al}})(\text{NCBH}_3)_2] \cdot 0.5 \text{CH}_3\text{CN}$ (**C2**).

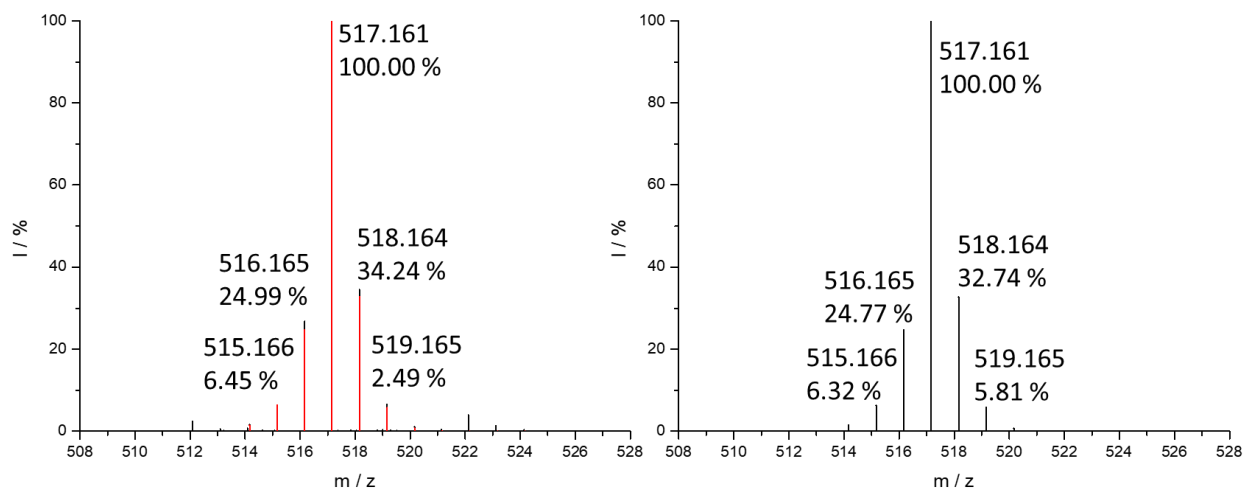


Figure S25: Isotopic pattern of *ESI* mass spectra of $[\text{Fe}(\text{L}^{\text{Naph-ODA-(R)-Al}})(\text{NCBH}_3)_2] \cdot 0.5 \text{CH}_3\text{CN}$ measured (left with red overlap of the isotopic pattern) predicted (right).

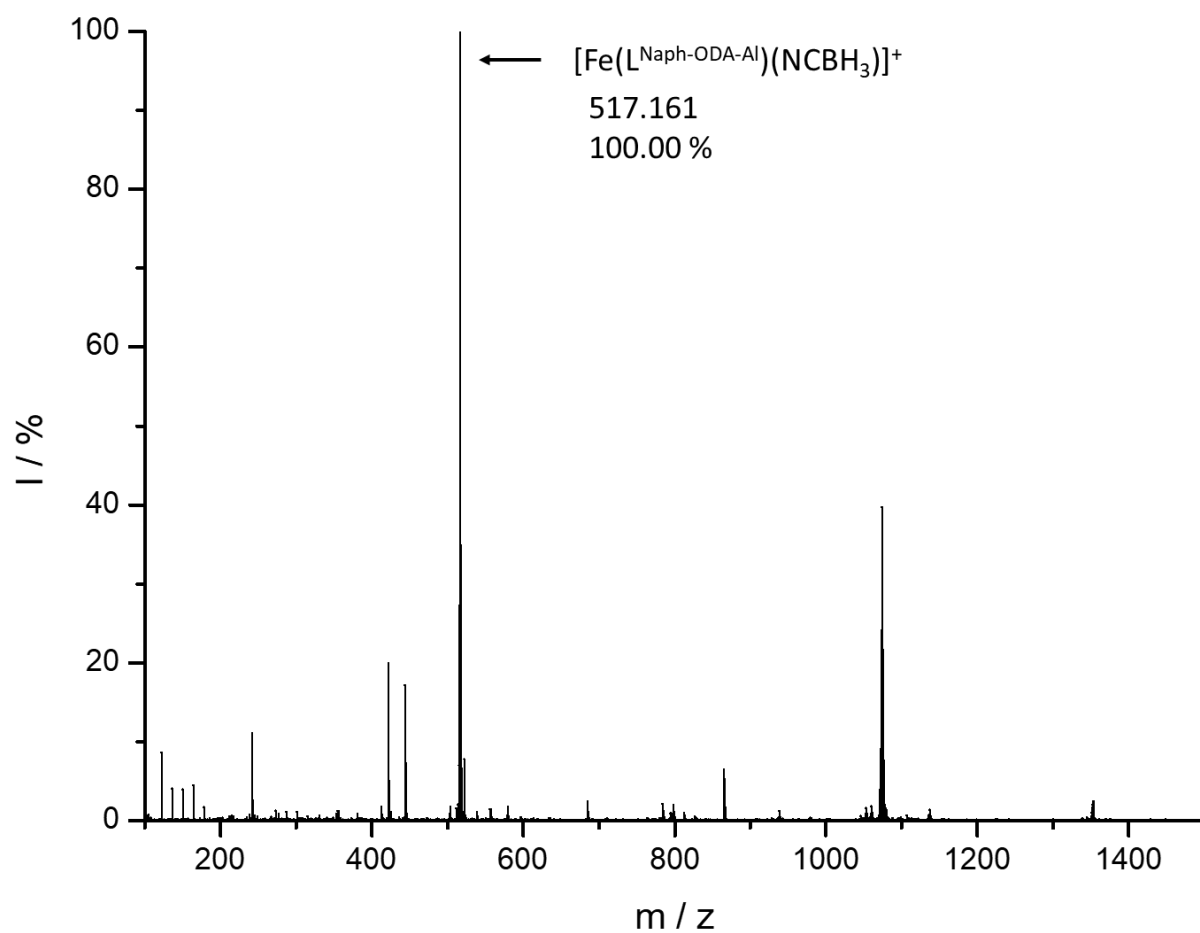


Figure S26: Mass spectrum (*ESI* positive) spectrum of $[\text{Fe}(\text{L}^{\text{Naph-ODA-(S)-Al}})(\text{NCBH}_3)_2] \cdot 0.5 \text{CH}_3\text{CN}$ (**C3**).

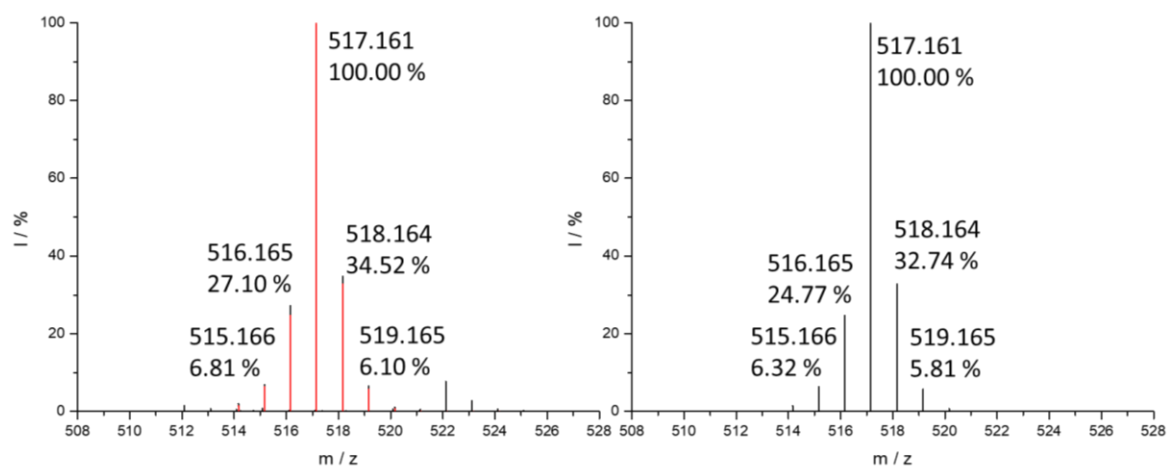


Figure S27: Isotopic pattern of *ESI* mass spectra of $[\text{Fe}(\text{L}^{\text{Naph-ODA-(S)-Al}})(\text{NCBH}_3)_2] \cdot 0.5 \text{CH}_3\text{CN}$ measured (left with red overlap of the isotopic pattern) predicted (right).

6. Crystallographic Data:

6.1. Packing of $[\text{Fe}(\text{L}^{\text{Naph-ODA-(Rac)-Al}})(\text{NCBH}_3)_2] \cdot 0.5 \text{CH}_3\text{CN}$

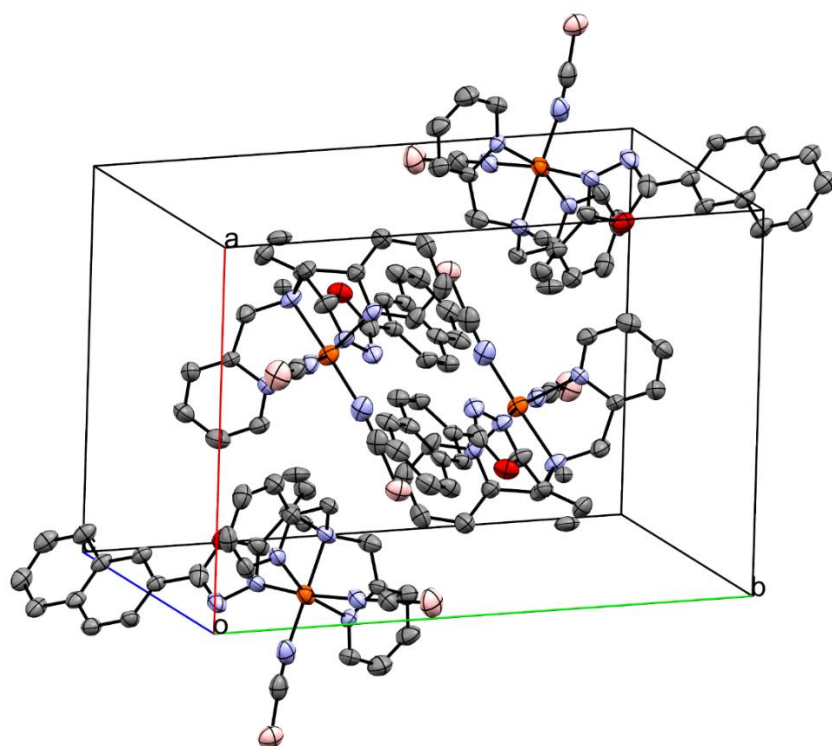


Figure S28: Unit cell of $[\text{Fe}(\text{L}^{\text{Naph-ODA-(Rac)-Al}})(\text{NCBH}_3)_2] \cdot 0.5 \text{CH}_3\text{CN}$ (**C1**) at 90 K. Solvent molecules and Hydrogen atoms were removed for better overview.

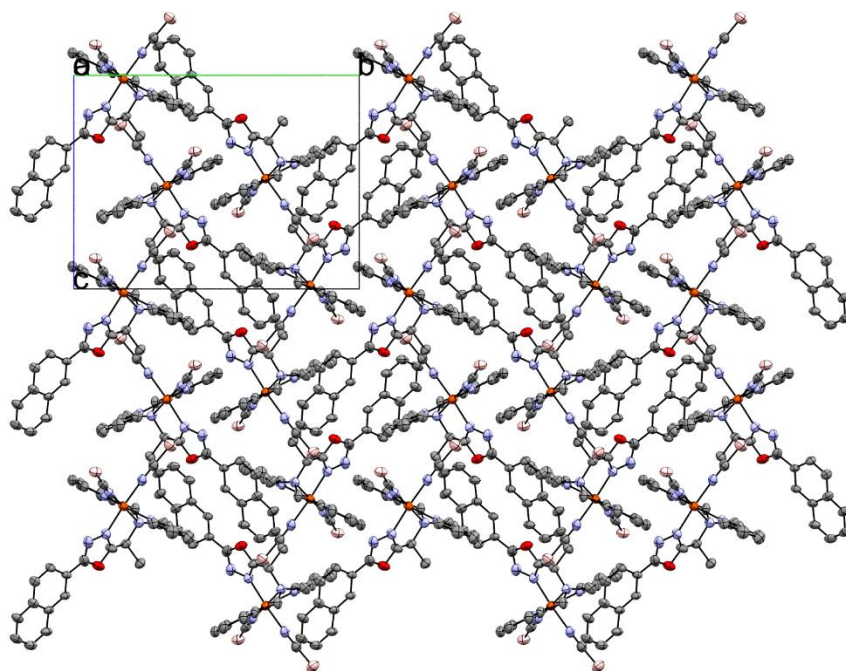


Figure S29: Visualisation of the packing for $[\text{Fe}(\text{L}^{\text{Naph-ODA-(Rac)-Al}})(\text{NCBH}_3)_2] \cdot 0.5 \text{CH}_3\text{CN}$ (**C1**) along a-axis at 90 K. Solvent molecules and Hydrogen atoms were removed for better overview.

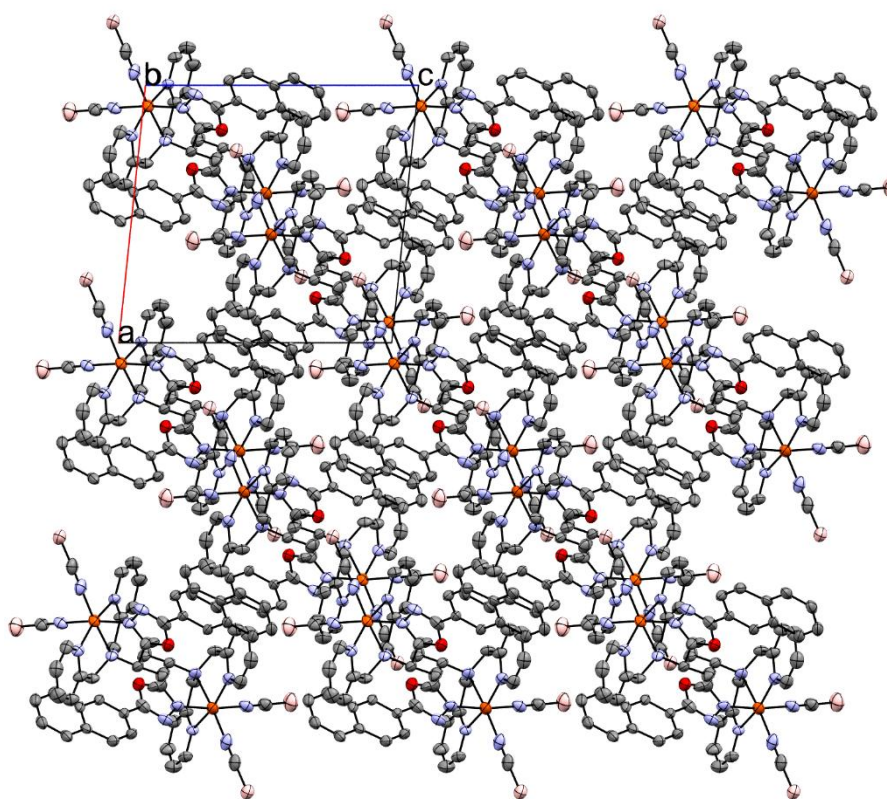


Figure S30: Visualisation of the packing for $[\text{Fe}(\text{L}^{\text{Naph-ODA-(Rac)-Al}})(\text{NCBH}_3)_2] \cdot 0.5 \text{CH}_3\text{CN}$ (**C1**) along b-axis at 90 K. Solvent molecules and Hydrogen atoms were removed for better overview.

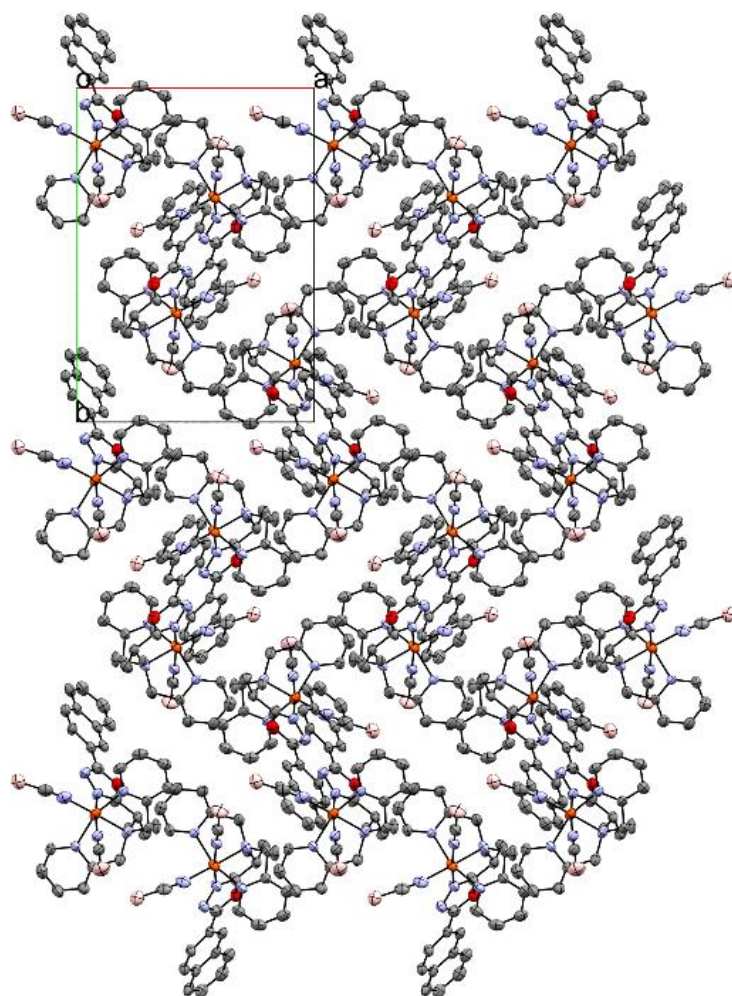


Figure S31: Visualisation of the packing for $[\text{Fe}(\text{L}^{\text{Naph-ODA-(Rac)-Al}})(\text{NCBH}_3)_2] \cdot 0.5 \text{CH}_3\text{CN}$ (**C1**) along c-axis at 90 K. Solvent molecules and Hydrogen atoms were removed for better overview.

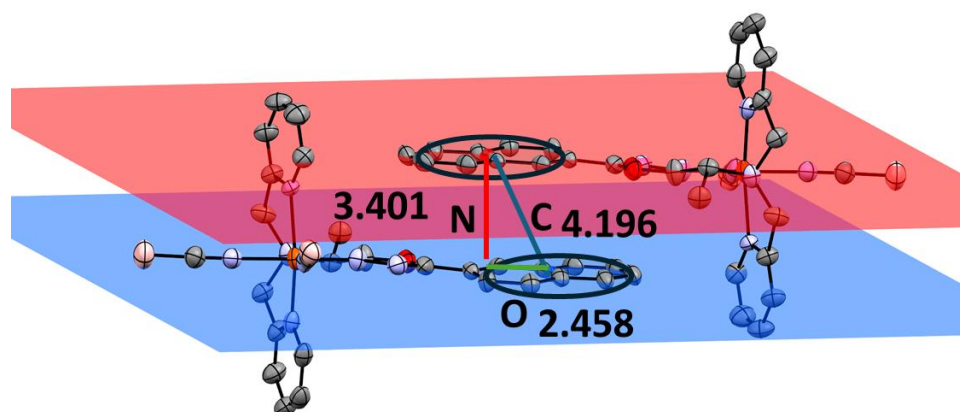


Figure S32: Visualisation of the π - π -interaction between Naphthyl units with off-set (green), normal vector (red) and centroid-centroid-distance (blue) and their values in Å for complex $[\text{Fe}(\text{L}^{\text{Naph-ODA-(Rac)-Al}})(\text{NCBH}_3)_2] \cdot 0.5 \text{CH}_3\text{CN}$ (**C1**) at 90 K.

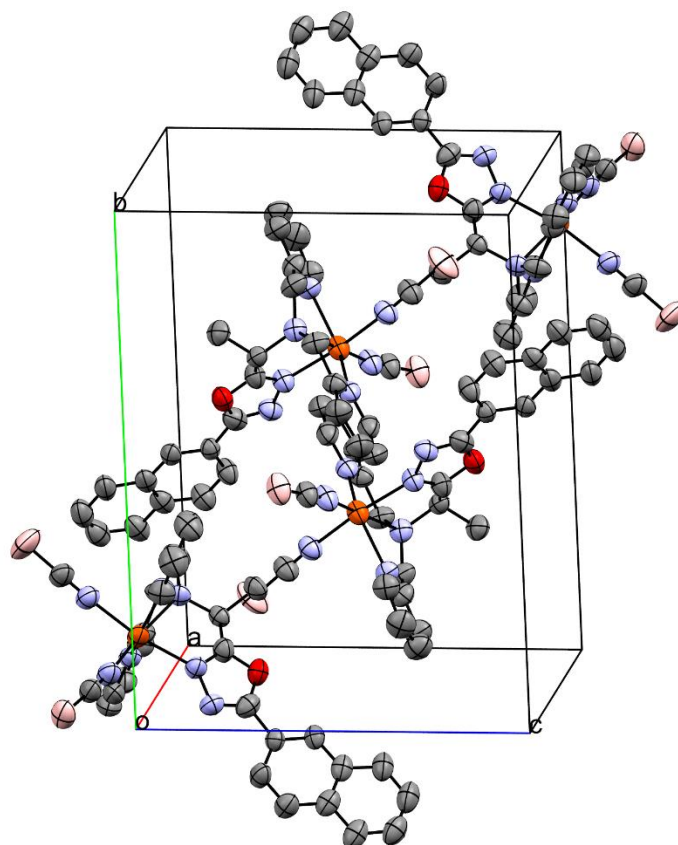


Figure S33: Unit cell of $[\text{Fe}(\text{L}^{\text{Naph-ODA-(Rac)-Al}})(\text{NCBH}_3)_2] \cdot 0.5 \text{CH}_3\text{CN}$ (**C1**) at 220 K. Solvent molecules and Hydrogen atoms were removed for better overview.

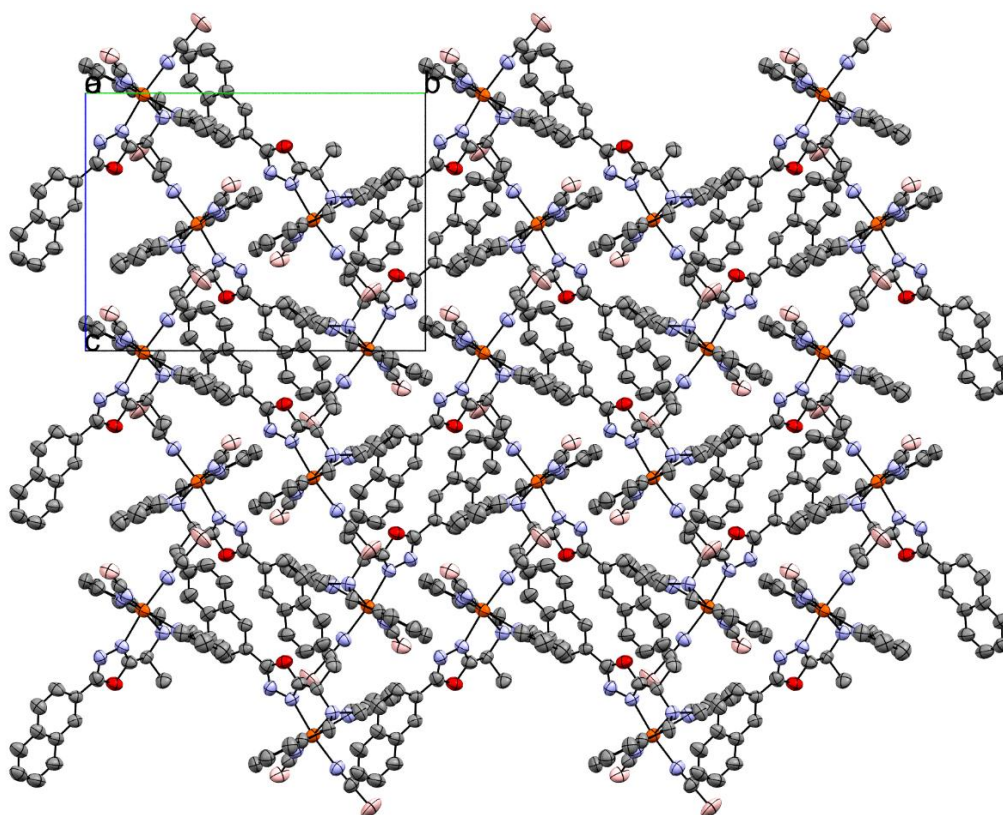


Figure S34: Visualisation of the packing for $[\text{Fe}(\text{L}^{\text{Naph-ODA-(Rac)-Al}})(\text{NCBH}_3)_2] \cdot 0.5 \text{CH}_3\text{CN}$ (**C1**) along a-axis at 220 K. Solvent molecules and Hydrogen atoms were removed for better overview.

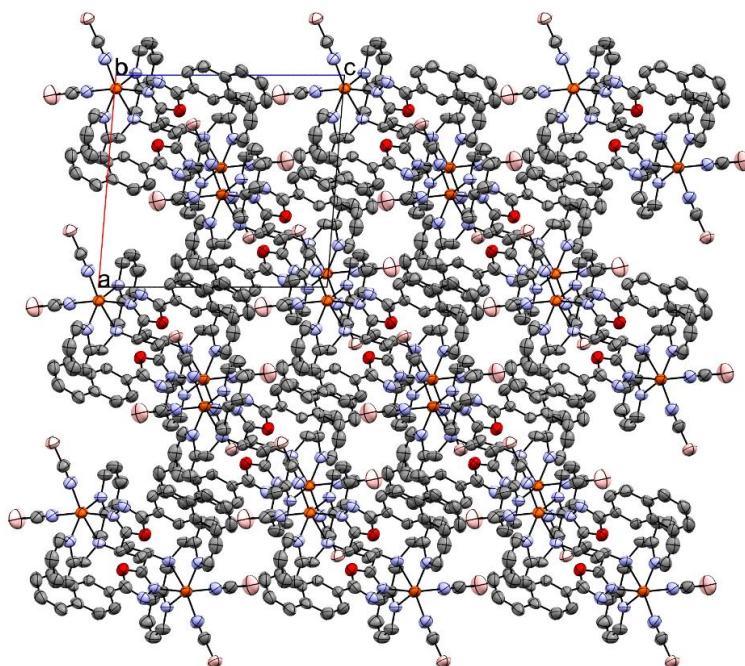


Figure S35: Visualisation of the packing for $[\text{Fe}(\text{L}^{\text{Naph-ODA-(Rac)-Al}})(\text{NCBH}_3)_2] \cdot 0.5 \text{CH}_3\text{CN}$ (**C1**) along a-axis at 220 K. Solvent molecules and Hydrogen atoms were removed for better overview.

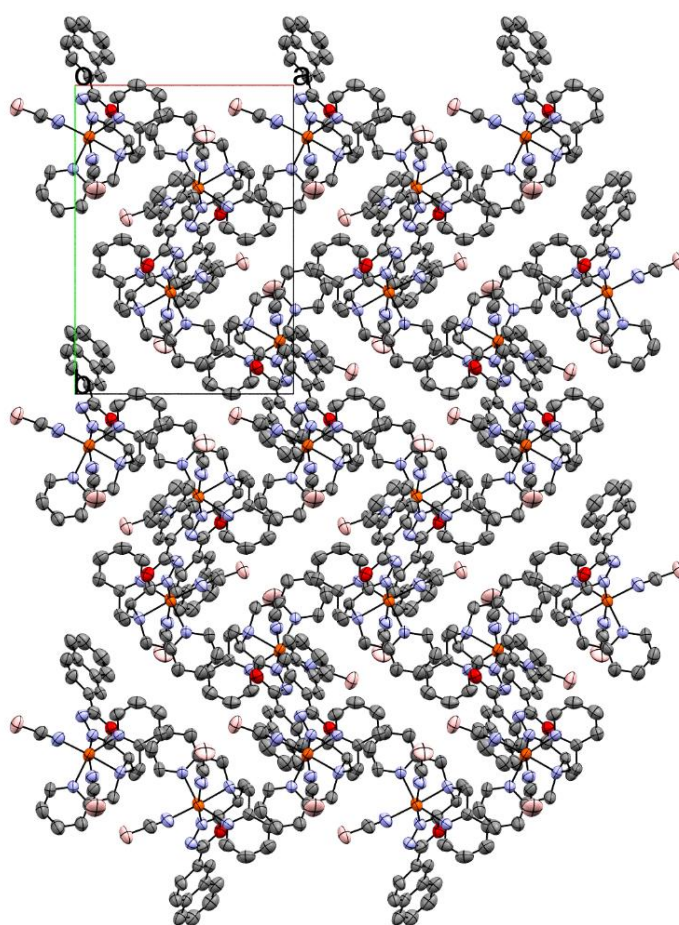


Figure S36: Visualisation of the packing for $[\text{Fe}(\text{L}^{\text{Naph-ODA-(Rac)-Al}})(\text{NCBH}_3)_2] \cdot 0.5 \text{CH}_3\text{CN}$ (**C1**) along c-axis at 220 K. Solvent molecules and Hydrogen atoms were removed for better overview.

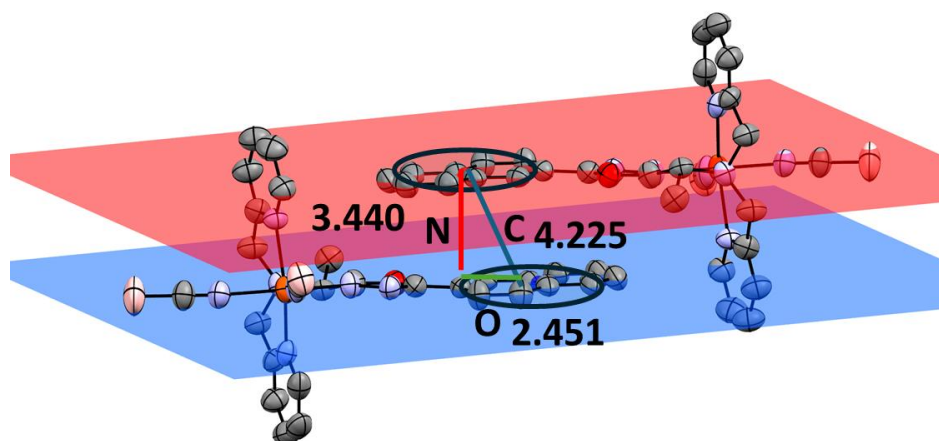


Figure S37: Visualisation of the π - π -interaction between Naphthyl units with off-set (green), normal vector (red) and centroid-centroid-distance (blue) and their values in Å for complex $[\text{Fe}(\text{L}^{\text{Naph-ODA-(Rac-Al)}})(\text{NCBH}_3)_2] \cdot 0.5 \text{CH}_3\text{CN}$ (**C1**) at 220 K.

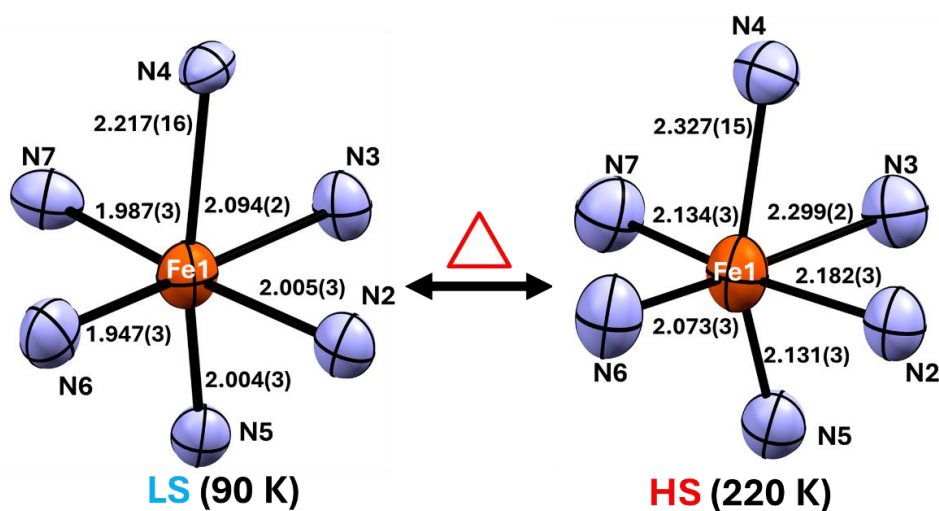


Figure S38: Fe-N bond length changing of the complex $[\text{Fe}(\text{L}^{\text{Naph-ODA-(Rac-Al)}})(\text{NCBH}_3)_2] \cdot 0.5 \text{CH}_3\text{CN}$ (**C1**). by visualization of the first coordination environment around the Fe(II) at 90 K and 220 K temperature.

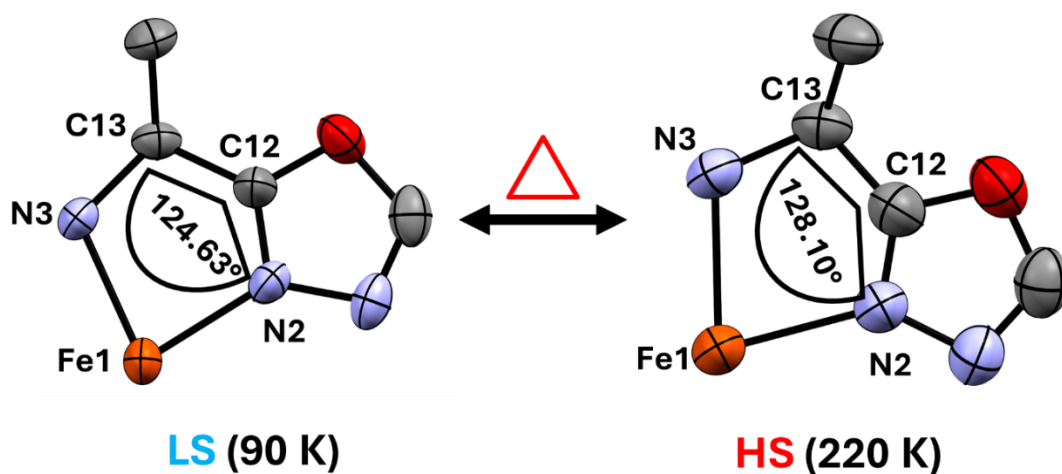


Figure S39: Bite Angles for the coordination pocket of the complex $[\text{Fe}(\text{L}^{\text{Naph-ODA-(Rac-Al)}})(\text{NCBH}_3)_2] \cdot 0.5 \text{CH}_3\text{CN}$ (**C1**). by visualization at 90 K and 220 K temperature.

6.2. Packing of $[\text{Fe}(\text{L}^{\text{Naph-ODA-(R)-Al}})(\text{NCBH}_3)_2] \cdot 0.5 \text{CH}_3\text{CN}$

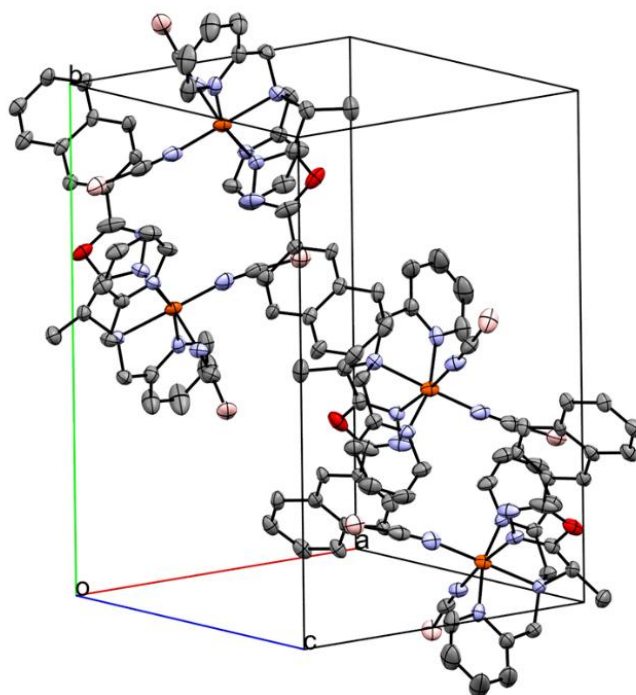


Figure S40: Unit cell of $[\text{Fe}(\text{L}^{\text{Naph-ODA-(R)-Al}})(\text{NCBH}_3)_2] \cdot 0.5 \text{CH}_3\text{CN}$ (**C2**) at 90 K. Solvent molecules and Hydrogen atoms were removed for better overview.

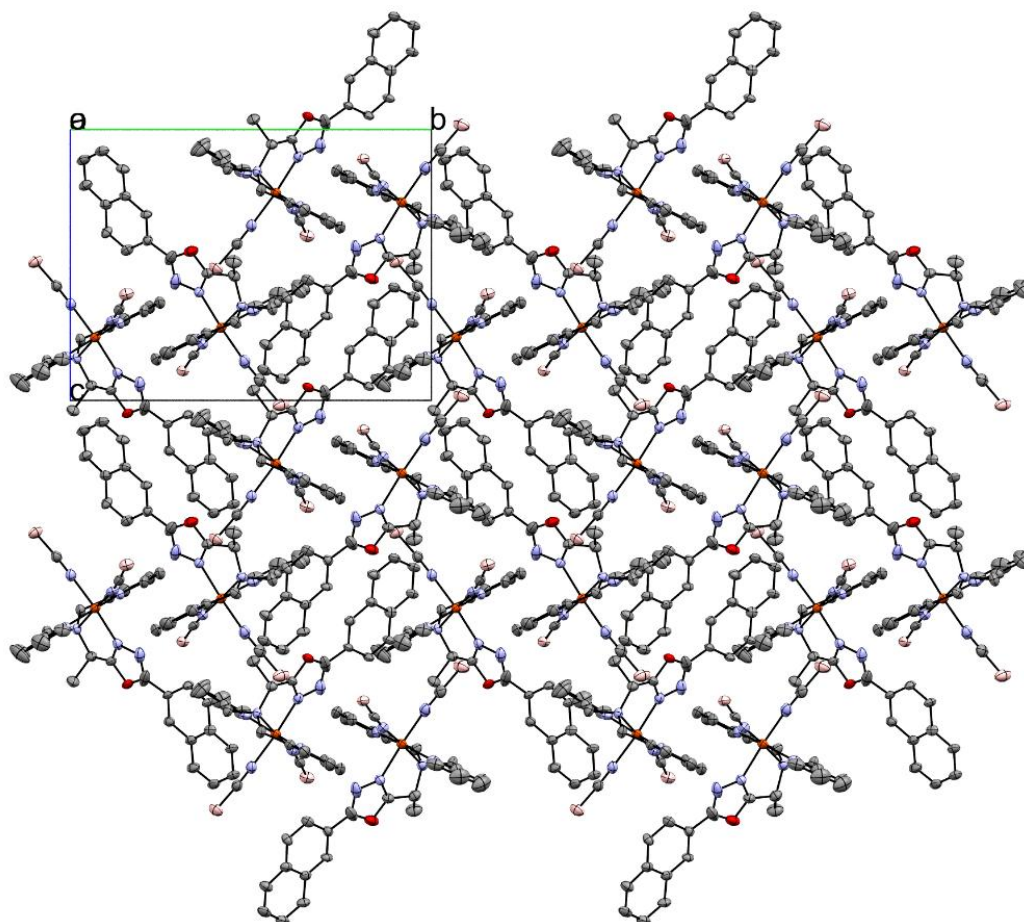


Figure S41: Visualisation of the packing for $[\text{Fe}(\text{L}^{\text{Naph-ODA-(R)-Al}})(\text{NCBH}_3)_2] \cdot 0.5 \text{CH}_3\text{CN}$ (**C2**) along a-axis at 90 K. Solvent molecules and Hydrogen atoms were removed for better overview.

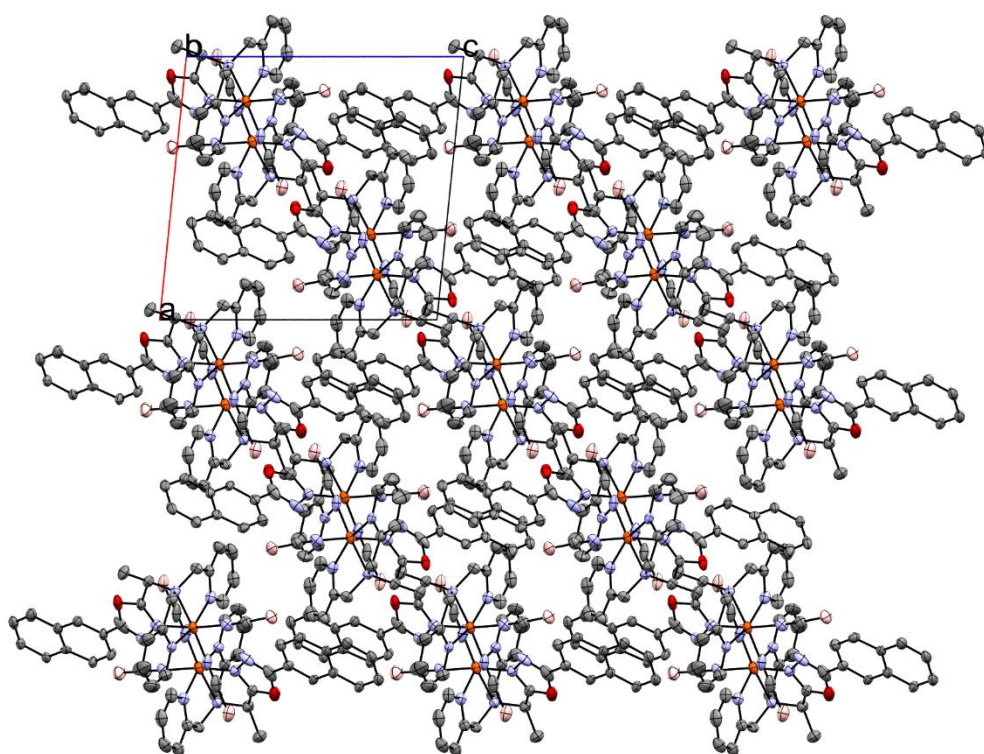


Figure S42: Visualisation of the packing for $[\text{Fe}(\text{L}^{\text{Naph-ODA-(R)-Al}})(\text{NCBH}_3)_2] \cdot 0.5 \text{CH}_3\text{CN}$ (**C2**) along a-axis at 90 K. Solvent molecules and Hydrogen atoms were removed for better overview.

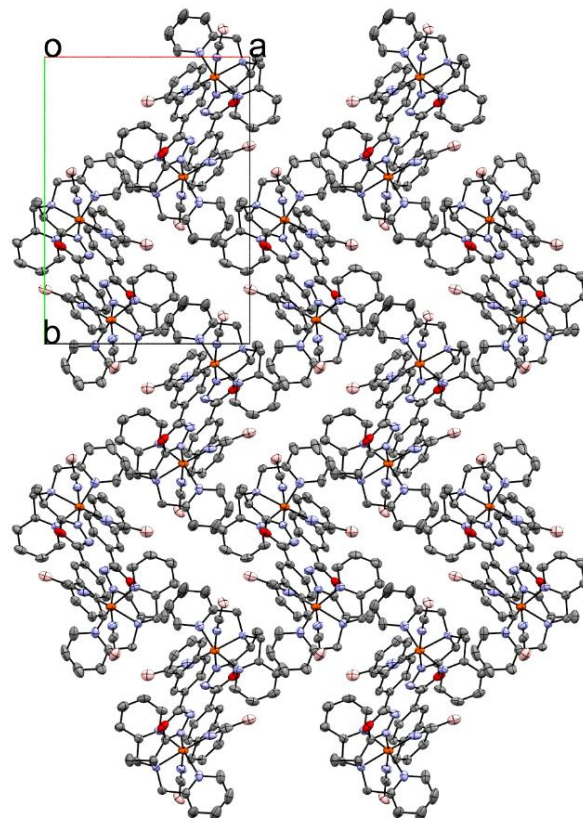


Figure S43: Visualisation of the packing for $[\text{Fe}(\text{L}^{\text{Naph-ODA-(R)-Al}})(\text{NCBH}_3)_2] \cdot 0.5 \text{CH}_3\text{CN}$ (**C2**) along c-axis at 90 K. Solvent molecules and Hydrogen atoms were removed for better overview.

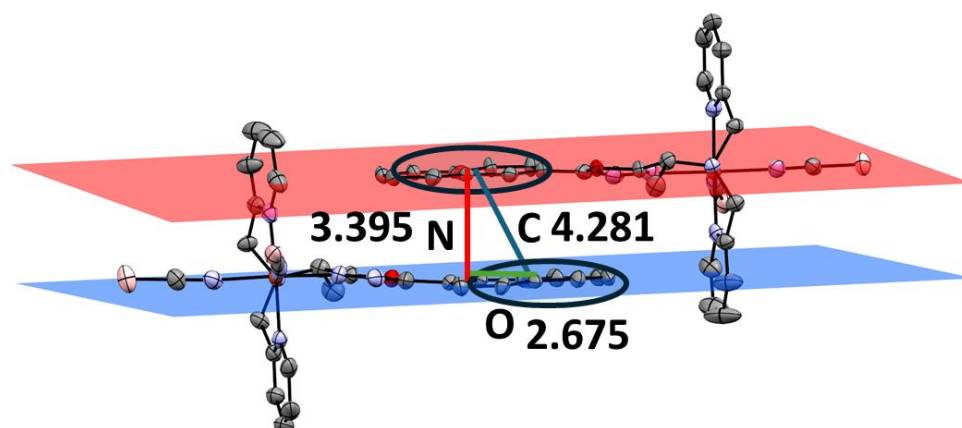


Figure S44: Visualisation of the π - π -interaction between Naphthyl units with off-set (green), normalvector (red) and centroid-centroid-distance (blue) and their values in Å for complex $[\text{Fe}(\text{L}^{\text{Naph-ODA-(R-Al)}})(\text{NCBH}_3)_2] \cdot 0.5 \text{ CH}_3\text{CN}$ (**C2**) at 90 K.

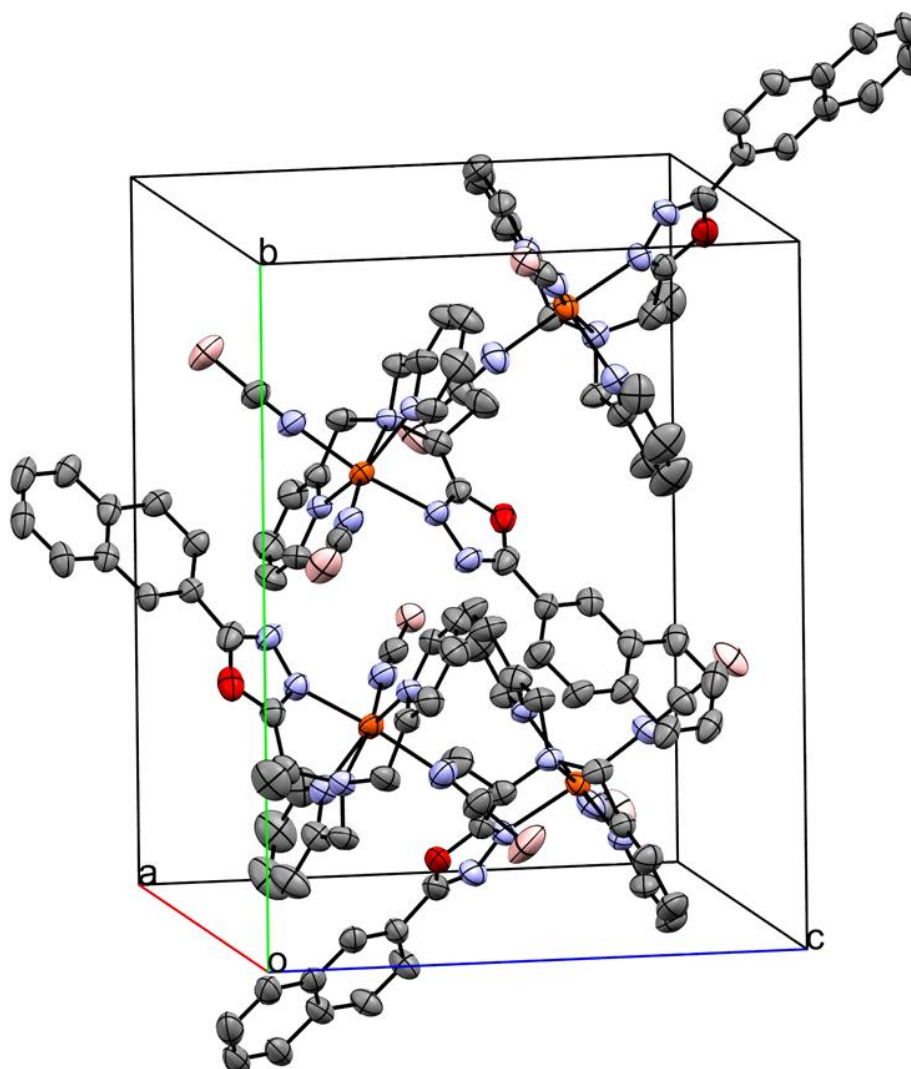


Figure S45: Unit cell of $[\text{Fe}(\text{L}^{\text{Naph-ODA-(R-Al)}})(\text{NCBH}_3)_2] \cdot 0.5 \text{ CH}_3\text{CN}$ (**C2**) at 220 K. Solvent molecules and Hydrogen atoms were removed for better overview.

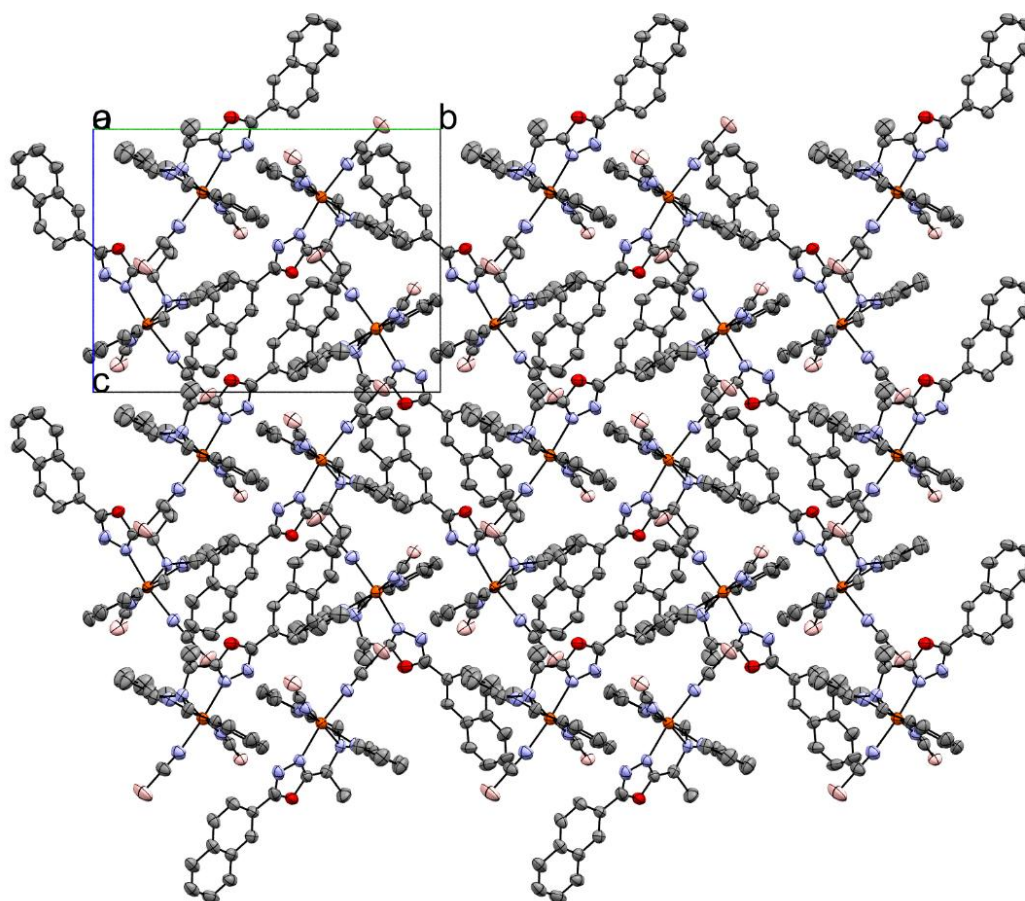


Figure S46: Visualisation of the packing for $[\text{Fe}(\text{L}^{\text{Naph-ODA-(R)-Al}})(\text{NCBH}_3)_2] \cdot 0.5 \text{CH}_3\text{CN}$ (**C2**) along a-axis at 220 K. Solvent molecules and Hydrogen atoms were removed for better overview.

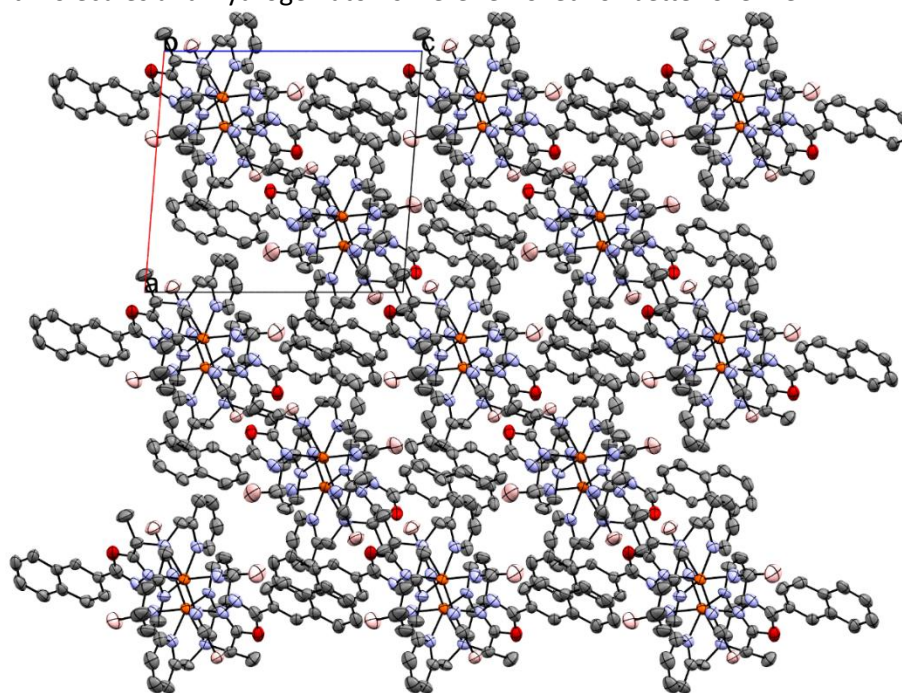


Figure S47: Visualisation of the packing for $[\text{Fe}(\text{L}^{\text{Naph-ODA-(R)-Al}})(\text{NCBH}_3)_2] \cdot 0.5 \text{CH}_3\text{CN}$ (**C2**) along a-axis at 220 K. Solvent molecules and Hydrogen atoms were removed for better overview.

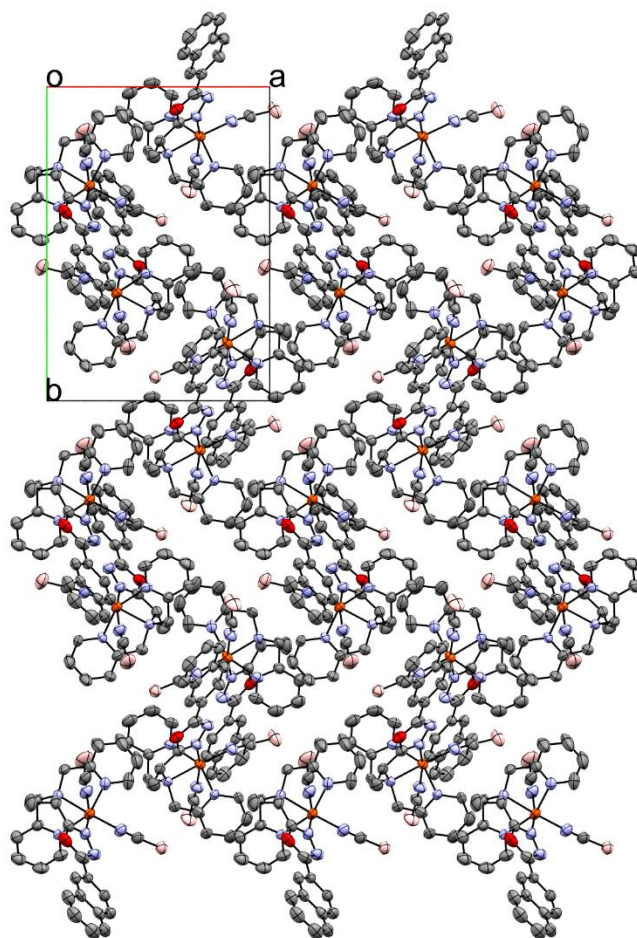


Figure S48: Visualisation of the packing for $[\text{Fe}(\text{L}^{\text{Naph-ODA-(R)-Al}})(\text{NCBH}_3)_2] \cdot 0.5 \text{CH}_3\text{CN}$ (**C2**) along c-axis at 220 K. Solvent molecules and Hydrogen atoms were removed for better overview.

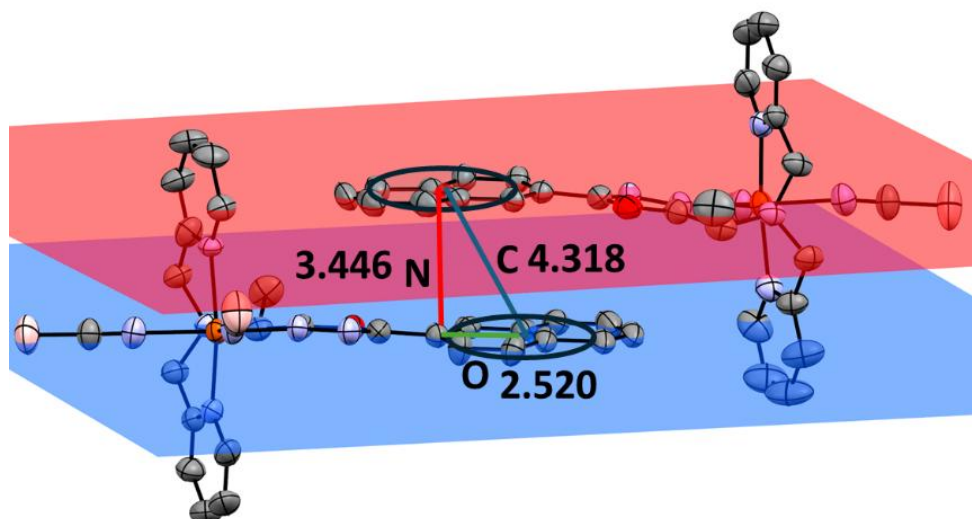


Figure S49: Visualisation of the π - π -interaction between Naphthyl units with off-set (green), normal vector (red) and centroid-centroid-distance (blue) and their values in Å for complex $[\text{Fe}(\text{L}^{\text{Naph-ODA-(R)-Al}})(\text{NCBH}_3)_2] \cdot 0.5 \text{CH}_3\text{CN}$ (**C2**) at 220 K.

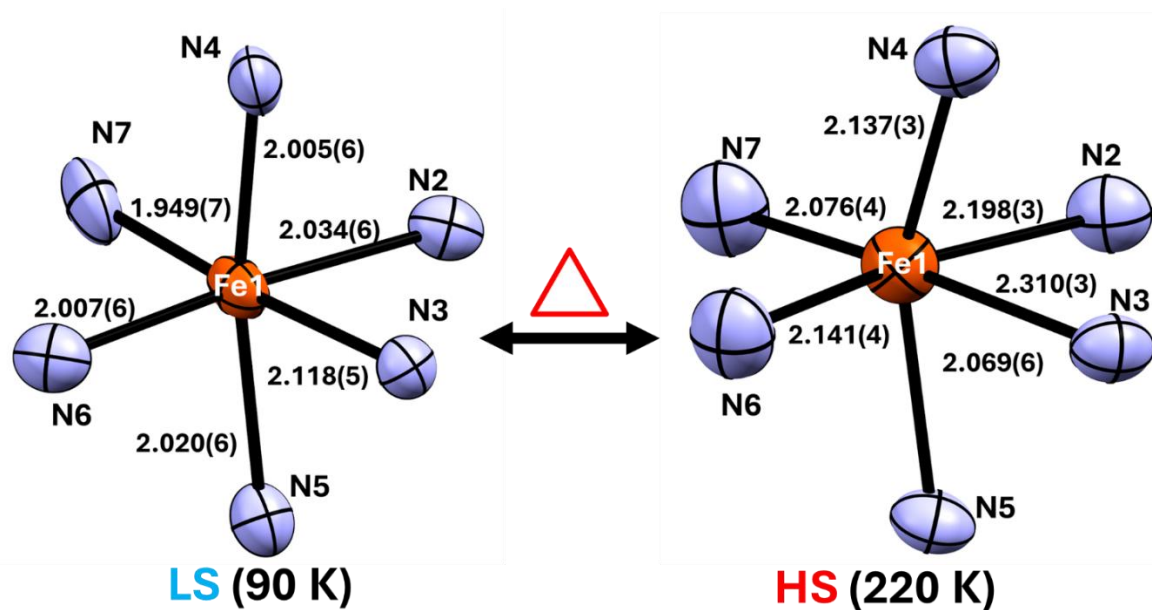


Figure S50: Fe-N bond length changing for Fe1 of the complex $[\text{Fe}(\text{L}^{\text{Naph-ODA-(R)-Al}})(\text{NCBH}_3)_2] \cdot 0.5 \text{CH}_3\text{CN}$ (C2). by visualization of the first coordination environment around the Fe(II) at 90 K and 220 K temperature.

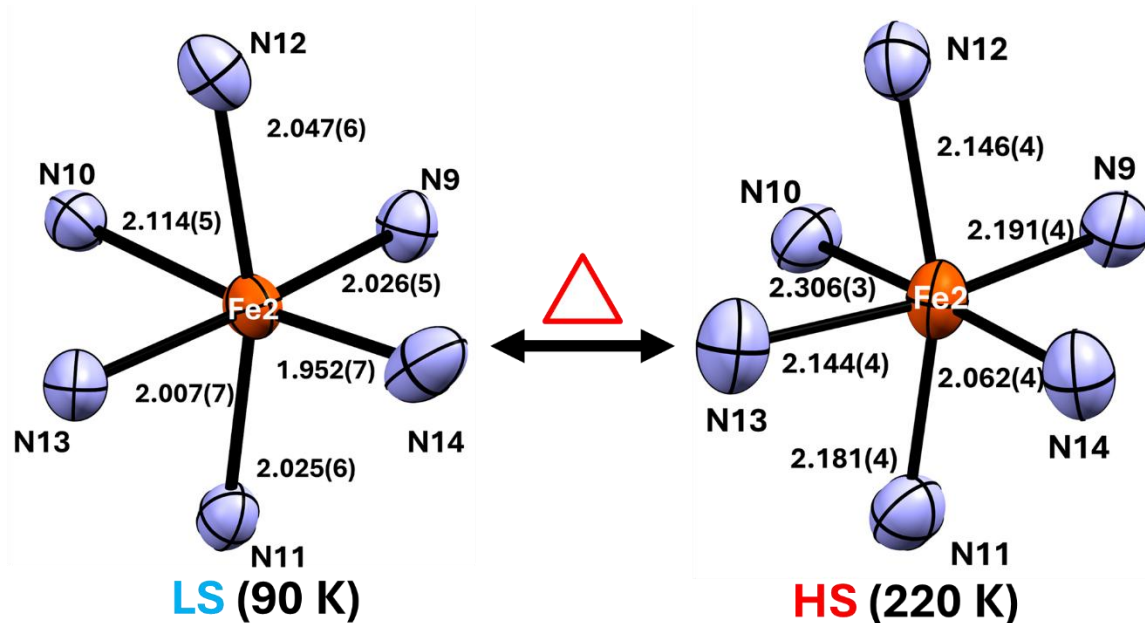


Figure S51: Fe-N bond length changing for Fe2 of the complex $[\text{Fe}(\text{L}^{\text{Naph-ODA-(R)-Al}})(\text{NCBH}_3)_2] \cdot 0.5 \text{CH}_3\text{CN}$ (C2). by visualization of the first coordination environment around the Fe(II) at 90 K and 220 K temperature.

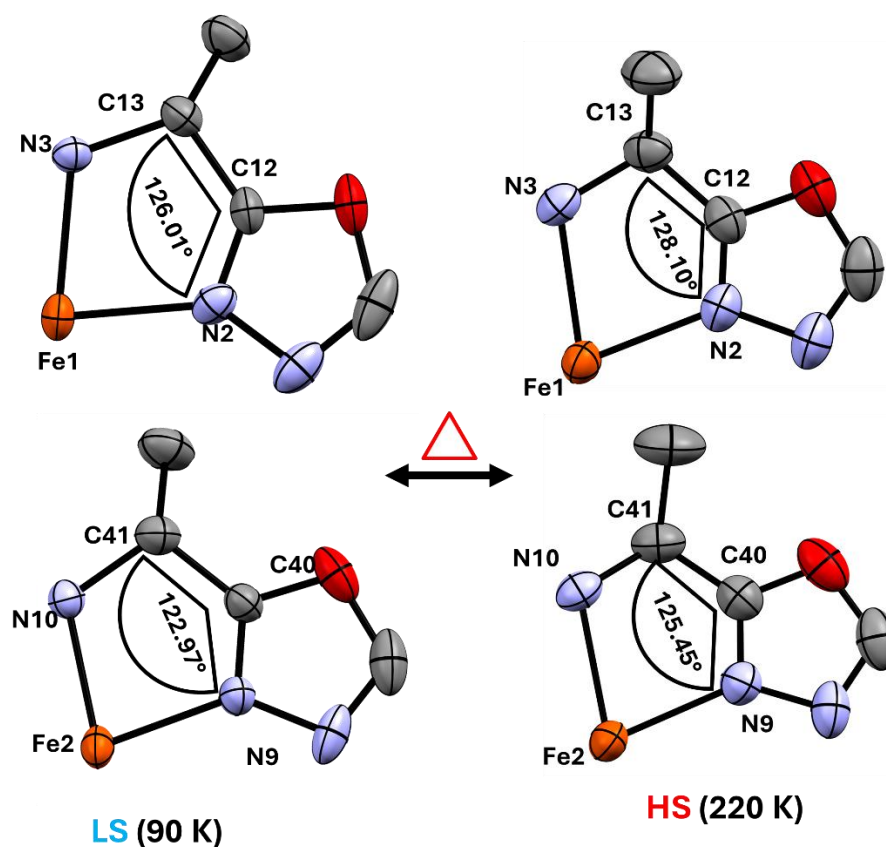


Figure S52: Bite Angles for the coordination pocket of Fe1 and Fe2 of the complex $[\text{Fe}(\text{L}^{\text{Naph-ODA-(R)-A}})(\text{NCBH}_3)_2] \cdot 0.5 \text{CH}_3\text{CN}$ (**C1**), by visualization at 90 K and 220 K temperature.

6.3. Packing of $[\text{Fe}(\text{L}^{\text{Naph-ODA-(S)-Al}})(\text{NCBH}_3)_2] \cdot 0.5 \text{ CH}_3\text{CN}$ (C3)

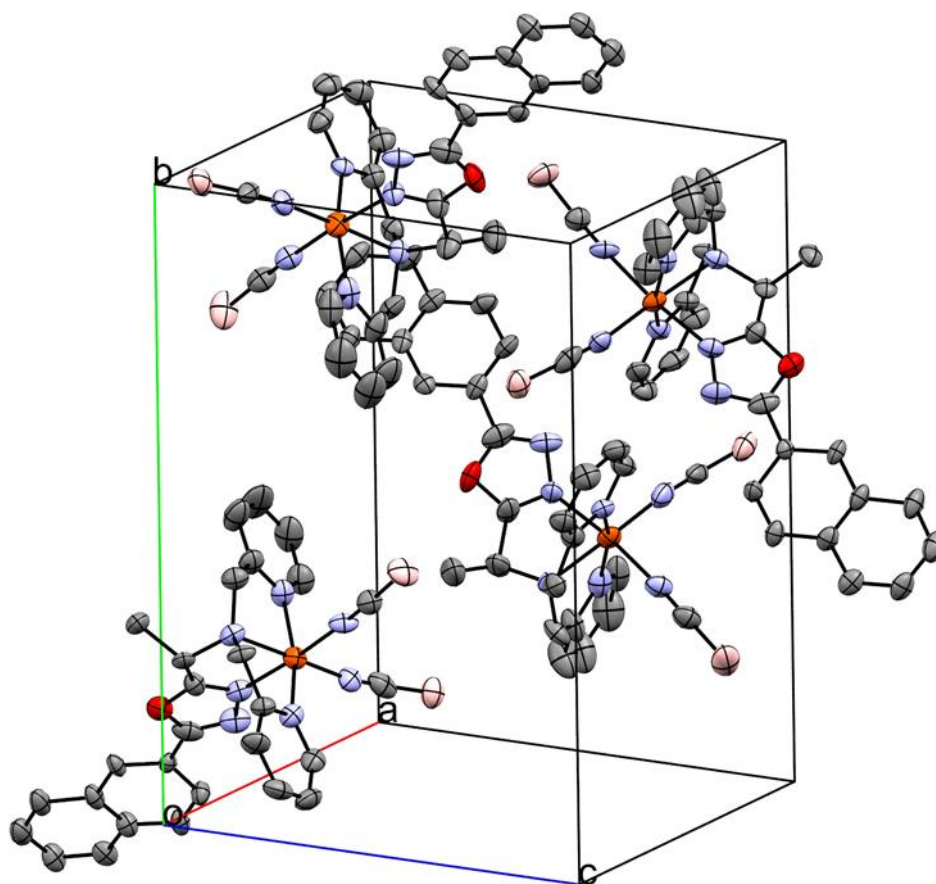


Figure S53: Unit cell of $[\text{Fe}(\text{L}^{\text{Naph-ODA-(S)-Al}})(\text{NCBH}_3)_2] \cdot 0.5 \text{ CH}_3\text{CN}$ (C3) at 90 K. Solvent molecules and Hydrogen atoms were removed for better overview.

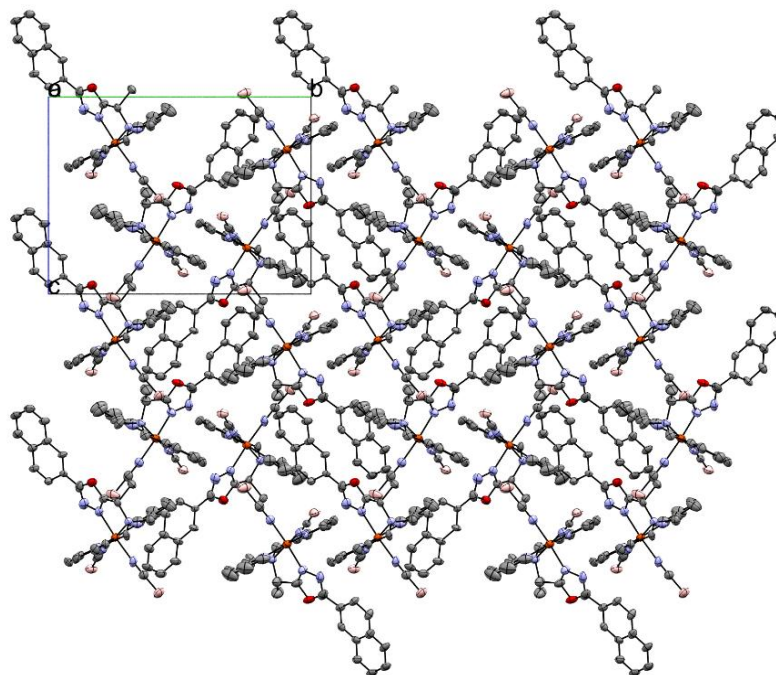


Figure S54: Visualisation of the packing for $[\text{Fe}(\text{L}^{\text{Naph-ODA-(S)-Al}})(\text{NCBH}_3)_2] \cdot 0.5 \text{ CH}_3\text{CN}$ (C3) along a-axis at 90 K. Solvent molecules and Hydrogen atoms were removed for better overview.

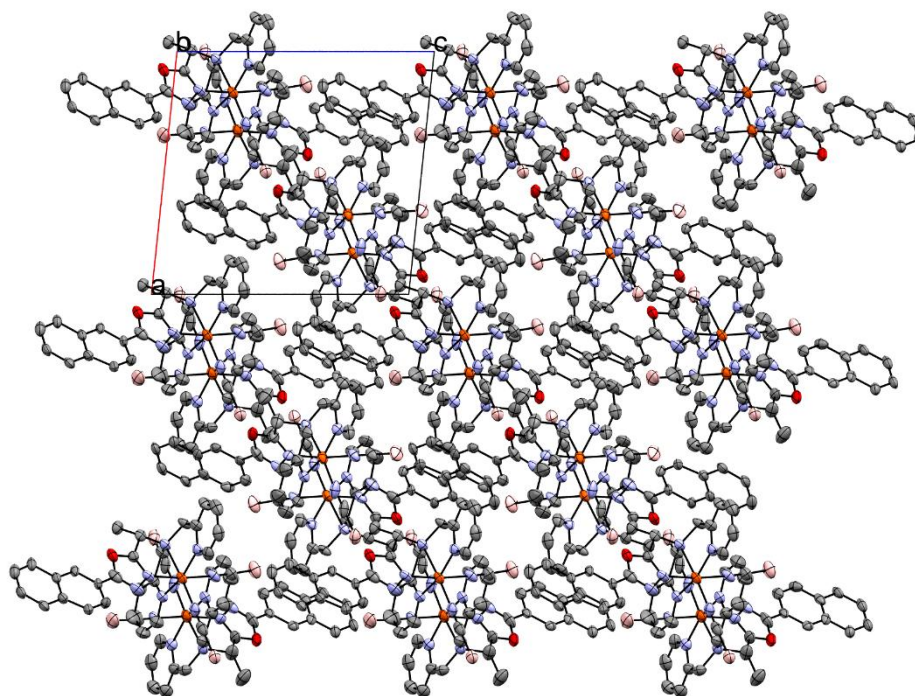


Figure S55: Visualisation of the packing for $[\text{Fe}(\text{L}^{\text{Naph-ODA-(S)-Al}})(\text{NCBH}_3)_2] \cdot 0.5 \text{CH}_3\text{CN}$ (**C3**) along a-axis at 90 K. Solvent molecules and Hydrogen atoms were removed for better overview.

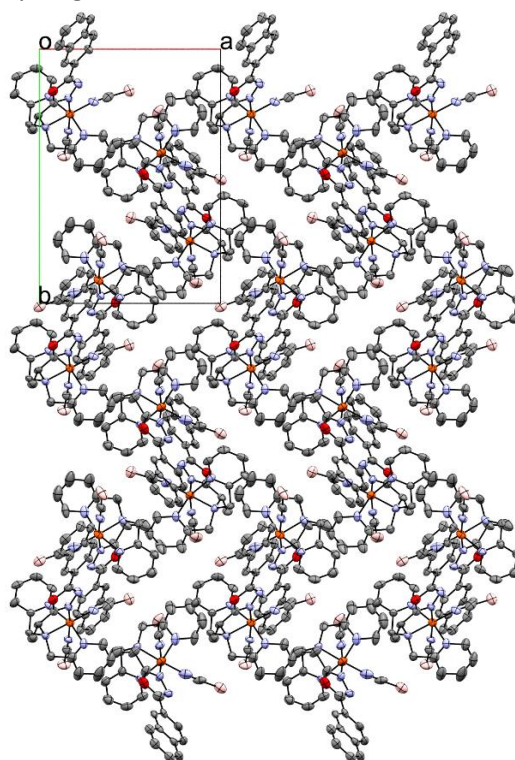


Figure S56: Visualisation of the packing for $[\text{Fe}(\text{L}^{\text{Naph-ODA-(S)-Al}})(\text{NCBH}_3)_2] \cdot 0.5 \text{CH}_3\text{CN}$ (**C3**) along c-axis at 90 K. Solvent molecules and Hydrogen atoms were removed for better overview.

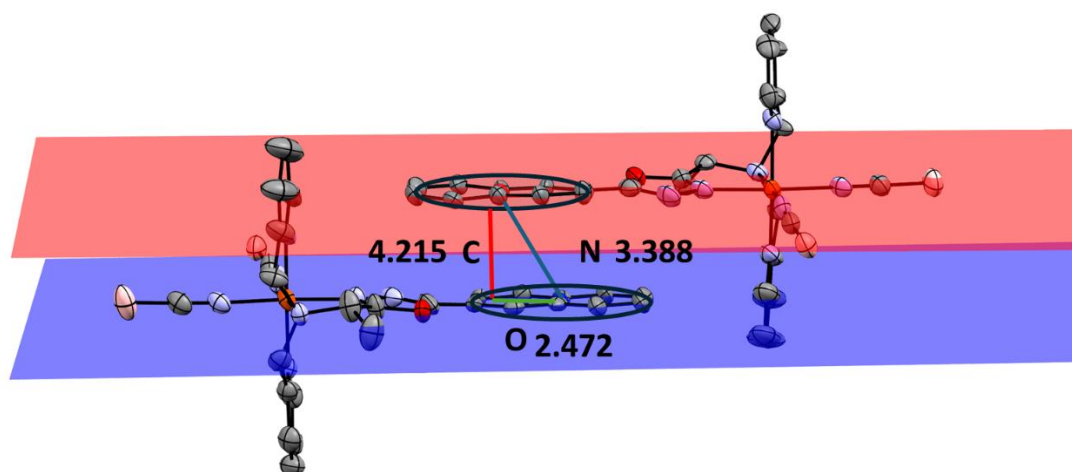


Figure S57: Visualisation of the π - π -interaction between Naphthyl units with off-set (green), normal vector (red) and centroid-centroid-distance (blue) and their values in Å for complex $[\text{Fe}(\text{L}^{\text{Naph-ODA-(S)-Al}})(\text{NCBH}_3)_2] \cdot 0.5 \text{CH}_3\text{CN}$ (**C3**) at 90 K.

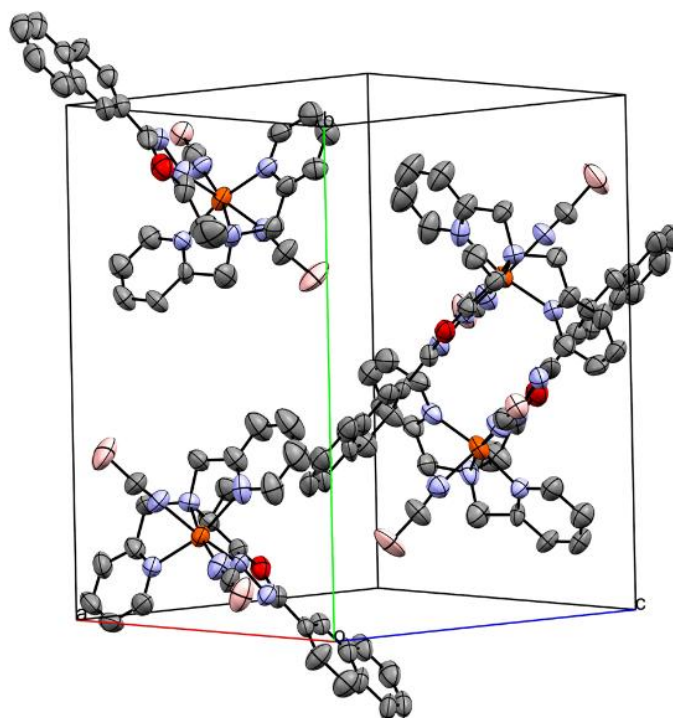


Figure S58: Unit cell of $[\text{Fe}(\text{L}^{\text{Naph-ODA-(S)-Al}})(\text{NCBH}_3)_2] \cdot 0.5 \text{CH}_3\text{CN}$ (**C3**) at 220 K. Solvent molecules and Hydrogen atoms were removed for better overview.

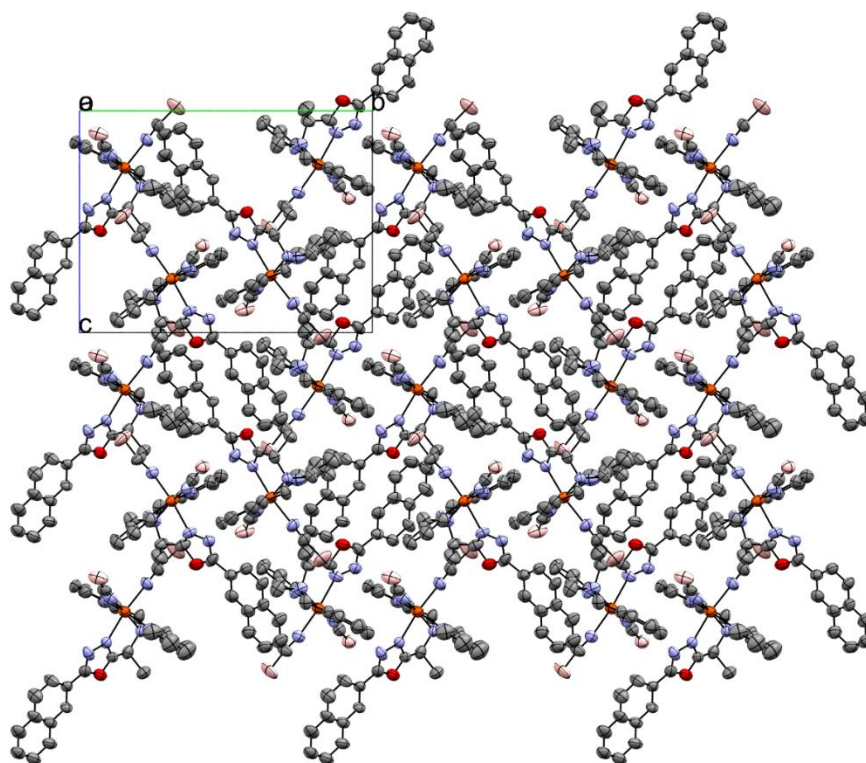


Figure S59: Visualisation of the packing for $[\text{Fe}(\text{L}^{\text{Naph-ODA-(S)-Al}})(\text{NCBH}_3)_2] \cdot 0.5 \text{CH}_3\text{CN}$ (**C3**) along a-axis at 220 K. Solvent molecules and Hydrogen atoms were removed for better overview.

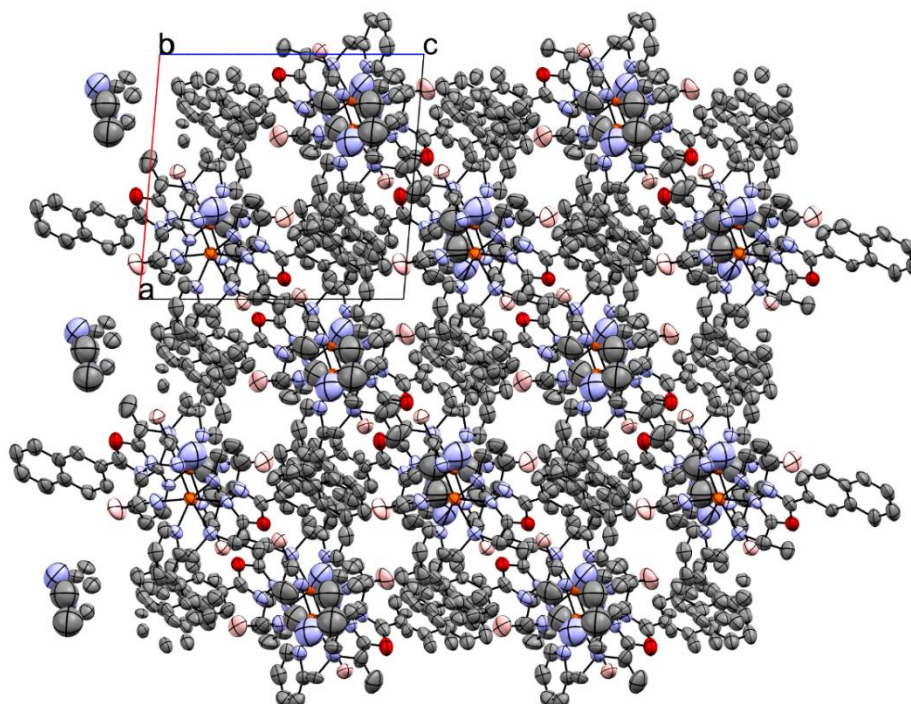


Figure S60: Visualisation of the packing for $[\text{Fe}(\text{L}^{\text{Naph-ODA-(S)-Al}})(\text{NCBH}_3)_2] \cdot 0.5 \text{CH}_3\text{CN}$ (**C3**) along a-axis at 220 K. Solvent molecules and Hydrogen atoms were removed for better overview.

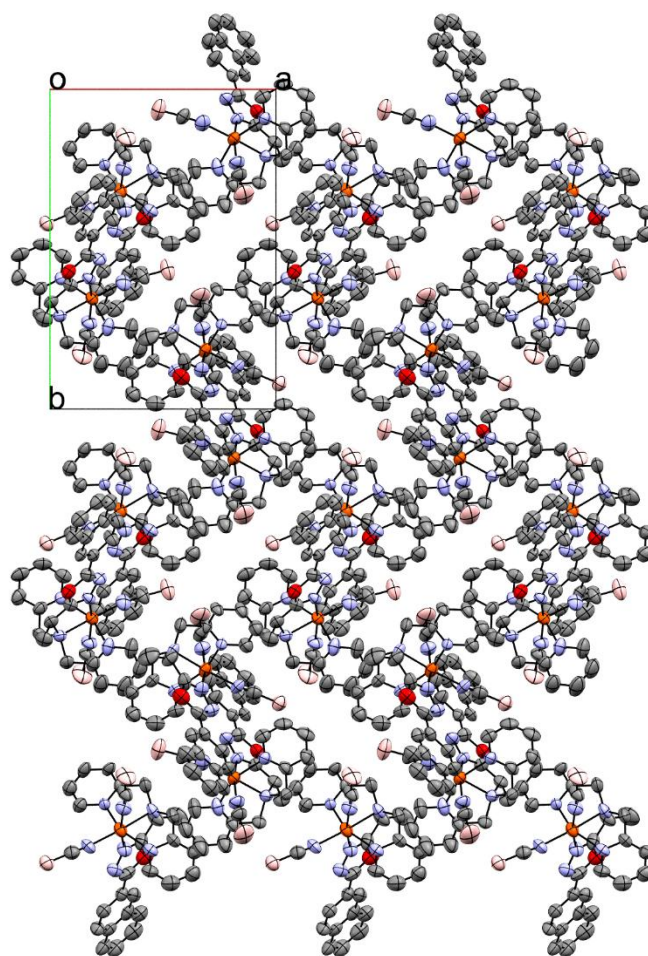


Figure S61: Visualisation of the packing for $[\text{Fe}(\text{L}^{\text{Naph-ODA-(S)-Al}})(\text{NCBH}_3)_2] \cdot 0.5 \text{CH}_3\text{CN}$ (**C3**) along c-axis at 220 K. Solvent molecules and Hydrogen atoms were removed for better overview.

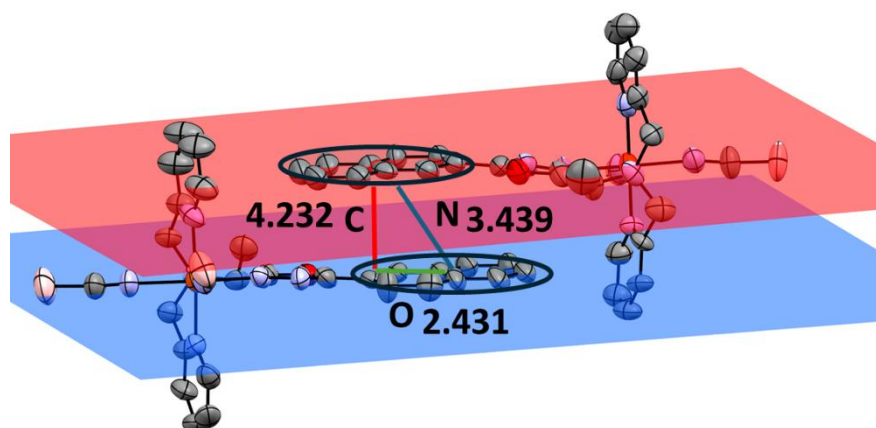


Figure S62: Visualisation of the π - π -interaction between Naphthyl units with off-set (green), normal vector (red) and centroid-centroid-distance (blue) and their values in Å for complex $[\text{Fe}(\text{L}^{\text{Naph-ODA-(S)-Al}})(\text{NCBH}_3)_2] \cdot 0.5 \text{CH}_3\text{CN}$ (**C3**) at 220 K.

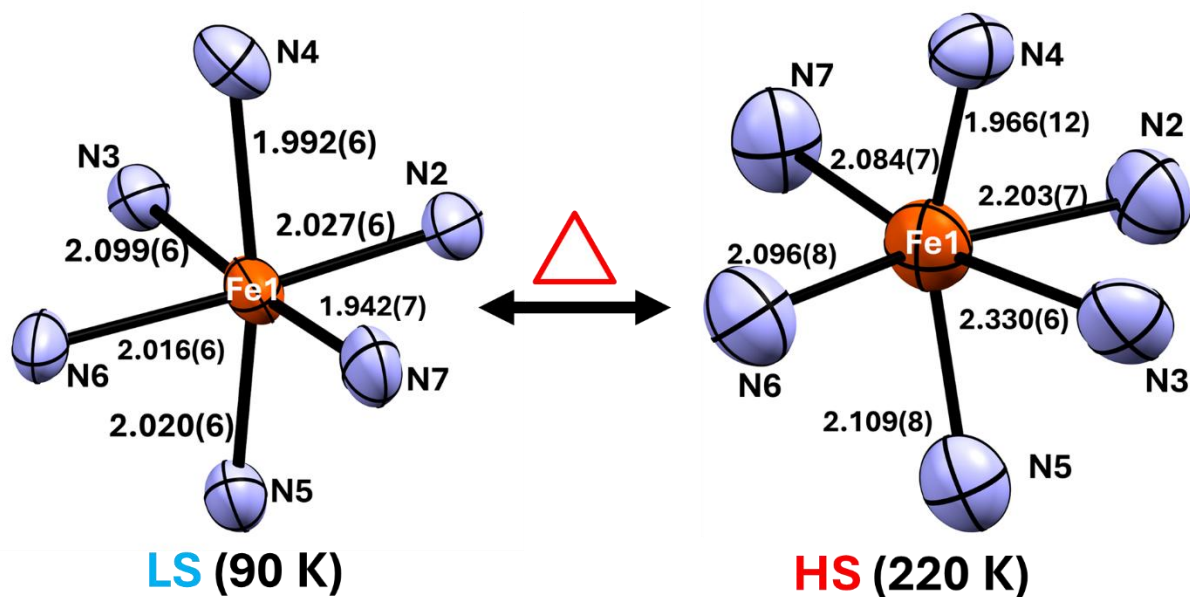


Figure S63: Fe-N bond length changing for Fe1 of the complex $[\text{Fe}(\text{L}^{\text{Naph-ODA-(S)-Al}})(\text{NCBH}_3)_2] \cdot 0.5 \text{CH}_3\text{CN}$ (**C3**). by visualization of the first coordination environment around the Fe(II) at 90 K and 220 K temperature.

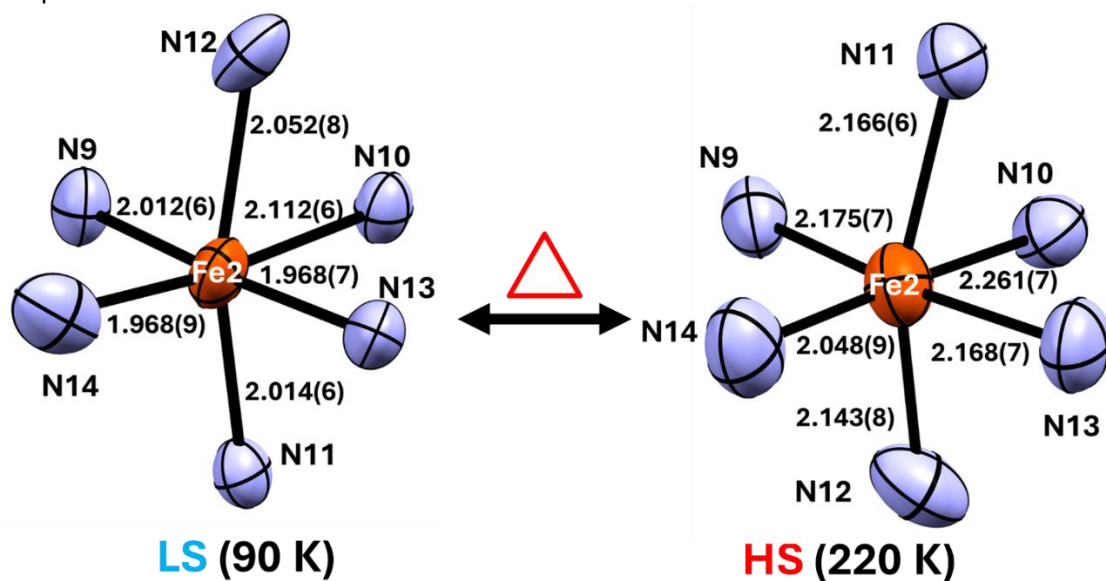


Figure S64: Fe-N bond length changing for Fe2 of the complex $[\text{Fe}(\text{L}^{\text{Naph-ODA-(R)-Al}})(\text{NCBH}_3)_2] \cdot 0.5 \text{CH}_3\text{CN}$ (**C3**). by visualization of the first coordination environment around the Fe(II) at 90 K and 220 K temperature.

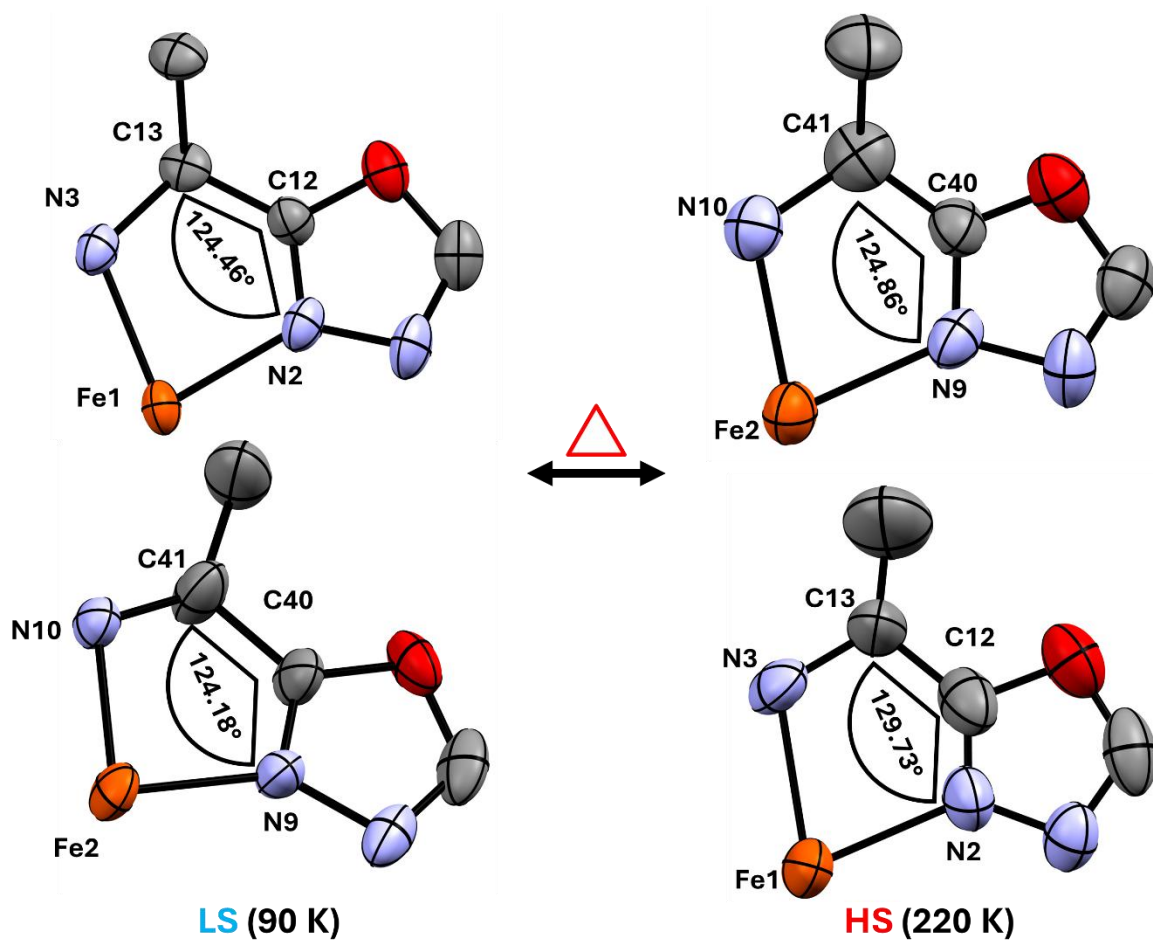


Figure S65: Bite Angles for the coordination pocket of the complex $[\text{Fe}(\text{L}^{\text{Naph-ODA-(S)-Al}})(\text{NCBH}_3)_2] \cdot 0.5 \text{CH}_3\text{CN}$ (**C3**), by visualization at 90 K and 220 K temperature.

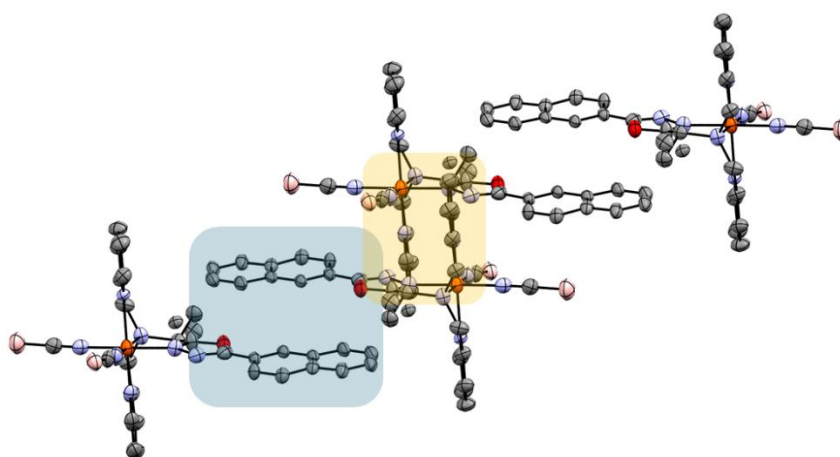


Figure S66: Stairs-like packing of the complex units $[\text{Fe}(\text{L}^{\text{Naph-ODA-Al}})(\text{NCBH}_3)_2]$ for complex $[\text{Fe}(\text{L}^{\text{Naph-ODA-(Rac)-Al}})(\text{NCBH}_3)_2] \cdot 0.5 \text{CH}_3\text{CN}$ (**C1**), with Naphthyl-Naphthyl-Interactions (blue) and opposite interlocked iron(II) centers (orange).

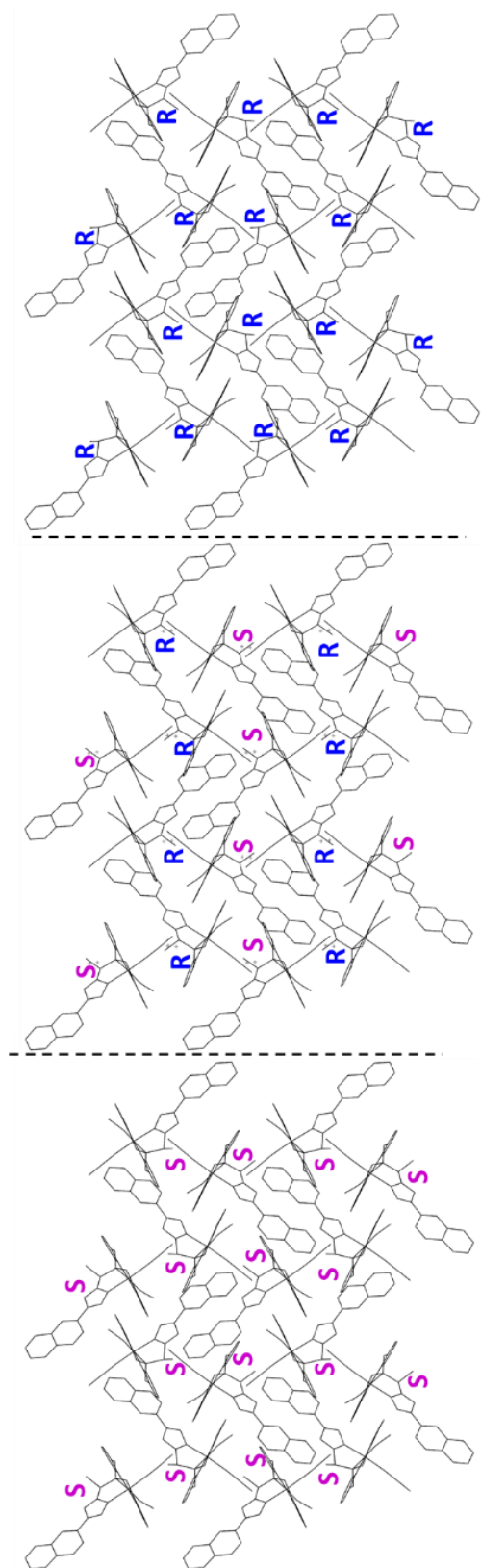


Figure S67: Packing diagram to visualize the similarity in packing between the complexes $[\text{Fe}(\text{L}^{\text{Naph-ODA-(S)-Al}})(\text{NCBH}_3)_2] \cdot 0.5 \text{CH}_3\text{CN}$ (**C3**) (left), $[\text{Fe}(\text{L}^{\text{Naph-ODA-(Rac)-Al}})(\text{NCBH}_3)_2] \cdot 0.5 \text{CH}_3\text{CN}$ (**C1**) and $[\text{Fe}(\text{L}^{\text{Naph-ODA-(R)-Al}})(\text{NCBH}_3)_2] \cdot 0.5 \text{CH}_3\text{CN}$ (**C2**) (right).

6.4. XRD Tables:

Table S1: Measurement parameters for $[\text{Fe}(\text{L}^{\text{Naph-ODA-(Rac-Al)}})(\text{NCBH}_3)_2] \cdot 0.5 \text{CH}_3\text{CN}$ (**C1**) at 90 K.

Parameter	Result
Empirical formula	C ₂₉ H _{30.50} B ₂ Fe N _{7.5} O [C ₂₈ H ₂₉ B ₂ Fe N ₇ O, 0.5(C ₂ H ₃ N)]
Formula weight	577.58
Temperature/K	90
Crystal system	monoclinic
Space group	P2 ₁ /n
a/Å	12.4656(4)
b/Å	17.4511(5)
c/Å	13.1482(4)
α/°	90
β/°	95.936(3)
γ/°	90
Volume/Å ³	2844.90(15)
Z	4
ρ _{calc} g/cm ³	1.349
μ/mm ⁻¹	0.567
F(000)	1204
Radiation	MoK α (λ = 0.71073)
2θ range for data collection/°	2.378 to 32.811
Index ranges	-18 ≤ h ≤ 16, -21 ≤ k ≤ 26, -18 ≤ l ≤ 19
Reflections collected	28641
Independent reflections	7594 [R _{int} = 0.0495, R _{sigma} = 0.0342]
Data/restraints/parameters	28641/150/559
Goodness-of-fit on F ²	1.181
Final R indexes [I ≥ 2σ (I)]	R ₁ = 0.0845, wR ₂ = 0.2025
Final R indexes [all data]	R ₁ = 0.0934, wR ₂ = 0.2079

Chapter 4: Unique packing properties of chiral 1,3,4-Oxadiazole Spin Crossover complexes

Table S2: Measurement parameters for $[\text{Fe}(\text{L}^{\text{Naph-ODA-(Rac-Al)}})(\text{NCBH}_3)_2] \cdot 0.5 \text{CH}_3\text{CN}$ (**C1**) at 220 K.

Parameter	Results
Empirical formula	C ₂₉ H _{30.50} B ₂ Fe N _{7.5} O [C ₂₈ H ₂₉ B ₂ Fe N ₇ O, 0.5(C ₂ H ₃ N)]
Formula weight	576.57
Temperature/K	220
Crystal system	monoclinic
Space group	P2 ₁ /n
a/Å	12.5019(5)
b/Å	17.6496(5)
c/Å	13.4172(5)
α/°	90
β/°	94.690(3)
γ/°	90
Volume/Å ³	2950.64(18)
Z	4
ρ _{calc} g/cm ³	1.298
μ/mm ⁻¹	0.547
F(000)	1200
Radiation	MoK α (λ = 0.71073)
2θ range for data collection/°	2.141 to 32.702
Index ranges	-18 ≤ h ≤ 17, -21 ≤ k ≤ 26, -18 ≤ l ≤ 20
Reflections collected	27570
Independent reflections	6471 [R _{int} = 0.0304, R _{sigma} = 0.0245]
Data/restraints/parameters	27570/246/558
Goodness-of-fit on F ²	1.134
Final R indexes [I ≥ 2σ (I)]	R ₁ = 0.0777, wR ₂ = 0.2016
Final R indexes [all data]	R ₁ = 0.1007, wR ₂ = 0.2156

Chapter 4: Unique packing properties of chiral 1,3,4-Oxadiazole Spin Crossover complexes

Table S3: Measurement parameters for $[\text{Fe}(\text{L}^{\text{Naph-ODA-(R)-Al}})(\text{NCBH}_3)_2] \cdot 0.5 \text{ CH}_3\text{CN}$ (**C2**) at 90 K.

Parameter	Results
Empirical formula	C58 H61 B4 Fe2 N15 O2 [2(C28 H29 B2 Fe N7 O), C2 H3 N]
Formula weight	1155.15
Temperature/K	90
Crystal system	monoclinic
Space group	P2 ₁
a/Å	12.5090(4)
b/Å	17.4132(5)
c/Å	13.1212(4)
α/°	90
β/°	95.783(2)
γ/°	90
Volume/Å³	2843.54(15)
Z	2
ρ_{calc} g/cm³	1.349
μ/mm⁻¹	0.568
F(000)	1204
Radiation	MoK α (λ = 0.71073)
2θ range for data collection/°	2.144 to 32.656
Index ranges	-18 ≤ h ≤ 17, -25 ≤ k ≤ 25, -18 ≤ l ≤ 19
Reflections collected	51990
Independent reflections	14655 [R _{int} = 0.0444, R _{sigma} = 0.0402]
Data/restraints/parameters	51990/505/930
Goodness-of-fit on F²	1.025
Final R indexes [I >= 2σ (I)]	R ₁ = 0.0858, wR ₂ = 0.2265
Final R indexes [all data]	R ₁ = 0.0987, wR ₂ = 0.2412

Chapter 4: Unique packing properties of chiral 1,3,4-Oxadiazole Spin Crossover complexes

Table S4: Measurement parameters for $[\text{Fe}(\text{L}^{\text{Naph-ODA-(R)-Al}})(\text{NCBH}_3)_2] \cdot 0.5 \text{ CH}_3\text{CN}$ (**C2**) at 220 K.

Parameter	Results
Empirical formula	C ₅₈ H ₆₁ B ₄ Fe ₂ N ₁₅ O ₂ [2(C ₂₈ H ₂₉ B ₂ Fe N ₇ O), C ₂ H ₃ N]
Formula weight	1155.15
Temperature/K	220
Crystal system	monoclinic
Space group	P2 ₁
a/Å	12.5324(2)
b/Å	17.6041(3)
c/Å	13.3803(3)
α/°	90
β/°	94.564(2)
γ/°	90
Volume/Å ³	2942.62(10)
Z	2
ρ _{calc} g/cm ³	1.304
μ/mm ⁻¹	0.549
F(000)	1204
Radiation	MoK α (λ = 0.71073)
2θ range for data collection/°	2.143 to 32.624
Index ranges	-16 ≤ h ≤ 18, -25 ≤ k ≤ 25, -20 ≤ l ≤ 18
Reflections collected	57456
Independent reflections	15064 [R _{int} = 0.0203, R _{sigma} = 0.0205]
Data/restraints/parameters	57456/1086/946
Goodness-of-fit on F ²	1.026
Final R indexes [I >= 2σ (I)]	R ₁ = 0.0515, wR ₂ = 0.1397
Final R indexes [all data]	R ₁ = 0.0631, wR ₂ = 0.1501

Chapter 4: Unique packing properties of chiral 1,3,4-Oxadiazole Spin Crossover complexes

Table S5: Measurement parameters for $[\text{Fe}(\text{L}^{\text{Naph-ODA-(S)-Al}})(\text{NCBH}_3)_2] \cdot 0.5 \text{ CH}_3\text{CN}$ (**C3**) at 90 K.

Parameter	Results
Empirical formula	C ₅₈ H ₆₁ B ₄ Fe ₂ N ₁₅ O ₂ [2(C ₂₈ H ₂₉ B ₂ Fe N ₇ O), C ₂ H ₃ N]
Formula weight	1155.15
Temperature/K	90
Crystal system	monoclinic
Space group	P2 ₁
a/Å	12.4828(3)
b/Å	17.4584(3)
c/Å	13.1586(3)
α/°	90
β/°	96.006(2)
γ/°	90
Volume/Å ³	2851.91(11)
Z	2
ρ _{calc} g/cm ³	1.345
μ/mm ⁻¹	0.566
F(000)	1204
Radiation	MoK α (λ = 0.71073)
2θ range for data collection/°	2.333 to 32.688
Index ranges	-18 ≤ h ≤ 17, -23 ≤ k ≤ 26, -18 ≤ l ≤ 19
Reflections collected	51119
Independent reflections	14454 [R _{int} = 0.0286, R _{sigma} = 0.0263]
Data/restraints/parameters	51119/667/899
Goodness-of-fit on F ²	1.113
Final R indexes [I ≥ 2σ (I)]	R ₁ = 0.0838, wR ₂ = 0.2155
Final R indexes [all data]	R ₁ = 0.0962, wR ₂ = 0.2269

Chapter 4: Unique packing properties of chiral 1,3,4-Oxadiazole Spin Crossover complexes

Table S6: Measurement parameters for $[\text{Fe}(\text{L}^{\text{Naph-ODA-(S)-Al}})(\text{NCBH}_3)_2] \cdot 0.5 \text{ CH}_3\text{CN}$ (**C3**) at 220 K.

Parameter	Results
Empirical formula	C58 H61 B4 Fe2 N15 O2 [2(C28 H29 B2 Fe N7 O), C2 H3 N]
Formula weight	1155.15
Temperature/K	220
Crystal system	monoclinic
Space group	P2 ₁
a/Å	12.4966(4)
b/Å	17.6717(4)
c/Å	13.4291(4)
α/°	90
β/°	94.771(2)
γ/°	90
Volume/Å ³	2955.35(15)
Z	2
ρ _{calc} g/cm ³	1.298
μ/mm ⁻¹	0.546
F(000)	1204
Radiation	MoK α (λ = 0.71073)
2θ range for data collection/°	2.325 to 32.691
Index ranges	-17 ≤ h ≤ 18, -23 ≤ k ≤ 26, -19 ≤ l ≤ 18
Reflections collected	54398
Independent reflections	11738 [R _{int} = 0.0305, R _{sigma} = 0.0288]
Data/restraints/parameters	54398/1159/882
Goodness-of-fit on F ²	1.086
Final R indexes [I >= 2σ (I)]	R ₁ = 0.0858, wR ₂ = 0.2394
Final R indexes [all data]	R ₁ = 0.1183, wR ₂ = 0.2701

6.5. Bond length tables:

Table S7: Iron(II) -Nitrogen bond length and average bond length for complex [Fe(L^{Naph-ODA-(Rac)-Al})(NCBH₃)₂] · 0.5 CH₃CN (**C1**) 90 K and 220K.

	Bond length / Å at 90 K	Bond length / Å at 220 K
Fe1-N2	2.005(3)	2.182(3)
Fe1-N3	2.094(2)	2.299(2)
Fe1-N5	2.004(3)	2.131(3)
Fe1-N6	1.947(3)	2.073(3)
Fe1-N7	1.987(3)	2.134(3)
Fe1-N4	2.217(16)	2.327(15)
Average bond length	2.042	2.191
Spin State	LS	HS

Table S8: Iron(II) -Nitrogen bond length and average bond length for complex [Fe(L^{Naph-ODA-(R)-Al})(NCBH₃)₂] · 0.5 CH₃CN (**C2**) 90 K and 220K.

Fe1	Bond length / Å at 90 K	Bond length / Å at 220 K
Fe1-N2	2.034(6)	2.198(3)
Fe1-N3	2.118(5)	2.310(3)
Fe1-N4	2.005(6)	2.137(3)
Fe1-N5	2.020(6)	2.069(6)
Fe1-N6	2.007(6)	2.141(4)
Fe1-N7	1.949(7)	2.076(4)
Average bond length	2.022	2.155
Spin State	LS	HS

Fe2	Bond lengths / Å at 90 K	Bond lengths / Å at 220 K
Fe2-N9	2.026(5)	2.191(4)
Fe2-N10	2.114(5)	2.306(3)
Fe2-N11	2.025(6)	2.181(4)
Fe2-N12	2.047(6)	2.146(4)

Chapter 4: Unique packing properties of chiral 1,3,4-Oxadiazole Spin Crossover complexes

Fe2-N13	2.007(7)	2.144(4)
Fe2-N14	1.952(7)	2.062(4)
Average bond length	2.029	2.172
Spin State	LS	HS

Table S9: Iron(II) -Nitrogen bond length and average bond length for complex $[\text{Fe}(\text{L}^{\text{Naph-ODA-(S)-A}})(\text{NCBH}_3)_2] \cdot 0.5 \text{CH}_3\text{CN}$ (**C3**) 90 K and 220K.

Fe1	Bond lengths / Å at 90 K	Bond lengths / Å at 220 K
Fe1-N2	2.027(6)	2.203(7)
Fe1-N3	2.099(6)	2.330(6)
Fe1-N4	1.992(6)	1.966(12)
Fe1-N5	2.020(6)	2.109(8)
Fe1-N6	2.016(6)	2.096(8)
Fe1-N7	1.942(7)	2.084(7)
Average bond length	2.016	2.131
Spin State	LS	HS
Fe2	Bond lengths / Å at 90 K	Bond lengths / Å at 220 K
Fe2-N9	2.012(6)	2.175(7)
Fe2-N10	2.112(6)	2.261(7)
Fe2-N11	2.014(6)	2.166(6)
Fe2-N12	2.052(8)	2.143(8)
Fe2-N13	1.968(7)	2.168(7)
Fe2-N14	1.968(9)	2.048(9)
Average bond length	2.021	2.160
Spin State	LS	HS

6.6. Bond angle tables:

Table S10: N-Fe-N bond angles for the complex $[\text{Fe}(\text{L}^{\text{Naph-ODA-(Rac-Al)}})(\text{NCBH}_3)_2] \cdot 0.5 \text{CH}_3\text{CN}$ (**C1**) 90 K and 220K.

Fe1	Bond angle / ° at 90 K	Bond angle / ° at 220 K
N2-Fe1-N3	81.64(10)	76.36(9)
N2-Fe1-N4	93.4(5)	90.4(5)
N3-Fe1-N4	81.4(5)	74.8(4)
N5-Fe1-N2	89.31(11)	87.44(10)
N5-Fe1-N3	81.49(11)	76.25(10)
N6-Fe1-N2	95.66(11)	97.48(10)
N6-Fe1-N5	101.69(12)	110.28(12)
N6-Fe1-N7	91.21(11)	94.24(11)
N6-Fe1-N4	95.6(5)	99.1(4)
N7-Fe1-N3	91.52(11)	91.96(10)
N7-Fe1-N5	88.86(11)	88.70(11)
N7-Fe1-N4	86.4(5)	87.5(5)
Distortion parameter	59.98	92.41
Spin State	LS	HS

Table S11: N-Fe-N bond angles for the complex $[\text{Fe}(\text{L}^{\text{Naph-ODA-(R)-Al}})(\text{NCBH}_3)_2] \cdot 0.5 \text{CH}_3\text{CN}$ (**C2**) 90 K and 220 K.

Fe1	Bond angle / ° at 90 K	Bond angle / ° at 220 K
N2-Fe1-N3	81.3(2)	76.37(13)
N4-Fe1-N2	89.2(2)	89.11(13)
N4-Fe1-N3	82.1(2)	75.80(12)
N4-Fe1-N6	90.2(2)	87.96(15)
N5-Fe1-N2	90.5(2)	85.4(4)
N5-Fe1-N3	80.7(2)	79.5(3)
N6-Fe1-N3	91.1(2)	91.52(14)
N6-Fe1-N5	87.9(2)	92.4(4)

Chapter 4: Unique packing properties of chiral 1,3,4-Oxadiazole Spin Crossover complexes

N7-Fe1-N2	96.1(2)	98.08(15)
N7-Fe1-N4	95.4(2)	110.54(16)
N7-Fe1-N5	101.9(3)	94.1(3)
N7-Fe1-N6	91.5(2)	93.95(16)
Distortion parameter	55.50	86.45
Spin State	LS	HS

Fe2	Bond angle / ° at 90 K	Bond angle / ° at 220 K
N9-Fe2-N10	81.3(2)	76.9(2)
N9-Fe2-N11	88.8(2)	88.6(2)
N9-Fe2-N12	91.0(3)	87.4(3)
N11-Fe2-N10	81.9(2)	76.0(2)
N12-Fe2-N10	80.2(3)	76.9(3)
N13-Fe2-N10	91.4(2)	91.7(3)
N13-Fe2-N11	89.0(2)	89.0(3)
N13-Fe2-N12	88.9(3)	89.6(3)
N13-Fe2-N14	91.8(3)	93.7(3)
N14-Fe2-N9	95.6(3)	97.6(3)
N14-Fe2-N11	102.9(3)	109.7(3)
N14-Fe2-N12	95.2(3)	97.6(3)
Distortion parameter	57.80	85.90
Spin State	LS	HS

Table S12: N-Fe-N bond angles for the complex $[\text{Fe}(\text{L}^{\text{Naph-ODA-(S)-Al}})(\text{NCBH}_3)_2] \cdot 0.5 \text{CH}_3\text{CN}$ (**C3**) 90 K and 220 K.

Fe1	Bond angle / ° at 90 K	Bond angle / ° at 220 K
N2-Fe1-N3	81.1(2)	75.5(3)
N4-Fe1-N2	89.6(2)	86.1(8)
N4-Fe1-N3	82.9(2)	77.1(6)
N4-Fe1-N6	90.2(2)	93.4(8)

Chapter 4: Unique packing properties of chiral 1,3,4-Oxadiazole Spin Crossover complexes

N5-Fe1-N2	89.9(2)	86.5(3)
N5-Fe1-N3	80.5(2)	77.2(3)
N6-Fe1-N3	92.1(2)	92.6(3)
N6-Fe1-N5	88.3(2)	88.8(3)
N7-Fe1-N2	95.8(2)	97.3(3)
N7-Fe1-N4	95.4(3)	94.9(6)
N7-Fe1-N5	101.4(3)	110.4(3)
N7-Fe1-N6	91.0(3)	94.7(3)
Distortion parameter	53.60	92.10
Spin State	LS	HS
Fe2	Bond angle / ° at 90 K	Bond angle / ° at 220 K
N9-Fe2-N10	80.9(2)	76.37(13)
N9-Fe2-N12	92.6(2)	84.73(14)
N11-Fe2-N9	87.0(2)	91.21(14)
N11-Fe2-N10	81.9(2)	74.51(13)
N12-Fe2-N10	79.7(2)	77.27(12)
N13-Fe2-N10	91.6(2)	92.45(15)
N13-Fe2-N11	89.8(2)	88.79(17)
N13-Fe2-N12	88.2(2)	89.76(16)
N14-Fe2-N9	95.5(2)	96.71(14)
N14-Fe2-N11	102.5(3)	98.62(16)
N14-Fe2-N12	96.0(3)	109.71(16)
N14-Fe2-N13	92.1(3)	94.78(16)
Distortion parameter	62.80	92.05
Spin State	LS	HS

6.7. Stacking Parameters:

Table S13: Stacking parameter for the Naphthyl-Naphthyl-Stacking: lengths of off-set, normal vector and centroid-centroid distance for the complexes $[\text{Fe}(\text{L}^{\text{Naph-ODA-(Rac-Al)}})(\text{NCBH}_3)_2] \cdot 0.5 \text{ CH}_3\text{CN}$ (**C1**), $[\text{Fe}(\text{L}^{\text{Naph-ODA-(R-Al)}})(\text{NCBH}_3)_2] \cdot 0.5 \text{ CH}_3\text{CN}$ (**C2**) and $[\text{Fe}(\text{L}^{\text{Naph-ODA-(S-Al)}})(\text{NCBH}_3)_2] \cdot 0.5 \text{ CH}_3\text{CN}$ (**C3**) 90 K and 220 K.

	off-set / Å	normal vector / Å	centroid-centroid / Å
C1 (90 K)	2.458	3.401	4.197
C1 (220 K)	2.451	3.440	4.224
C2 (90 K)	2.675	3.395	4.281
C2 (220 K)	2.520	3.446	4.318
C3 (90 K)	2.472	3.388	4.215
C3 (220 K)	2.431	3.439	4.238

7. Powder XRD:

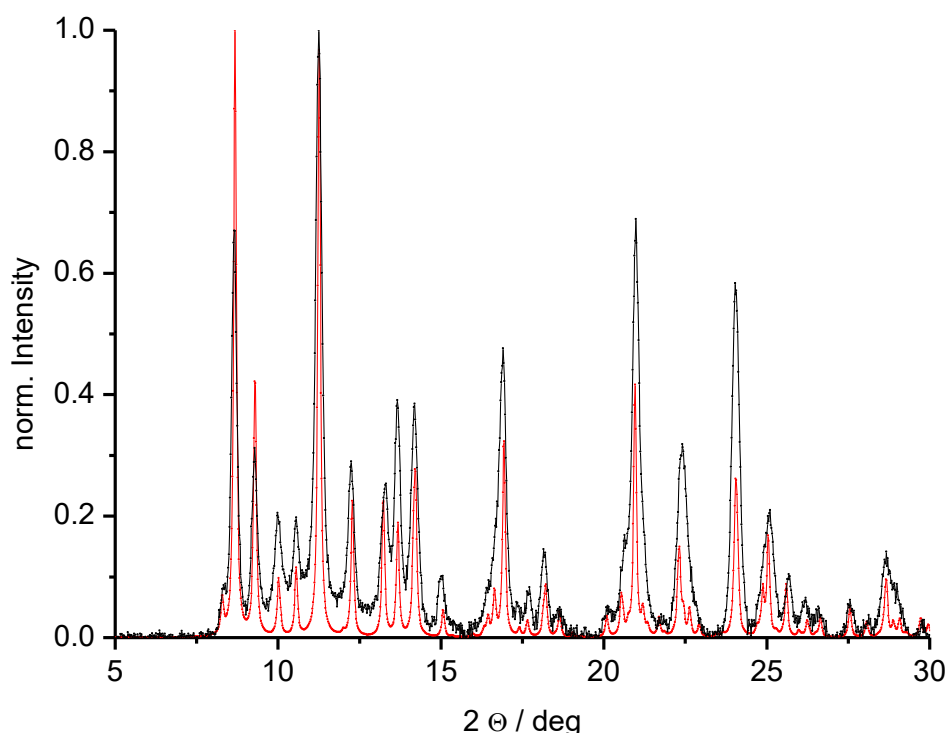


Figure S68: Powder XRD Pattern of the product of $[\text{Fe}(\text{L}^{\text{Naph-ODA-(Rac-Al)}})(\text{NCBH}_3)_2] \cdot 0.5 \text{ CH}_3\text{CN}$ (**C1**) (black) against the predicted Pattern based on the single crystal XRD measurement (red) at 220 K.

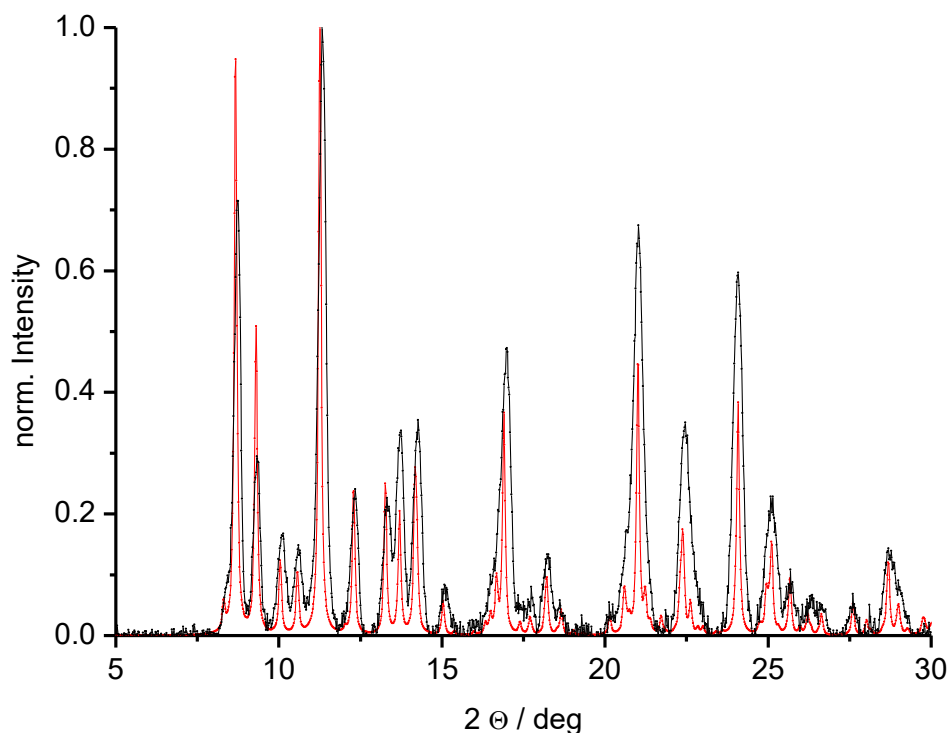


Figure S69: Powder XRD Pattern of the of product of $[\text{Fe}(\text{L}^{\text{Naph-ODA-(R)-Al}})(\text{NCBH}_3)_2] \cdot 0.5 \text{CH}_3\text{CN}$ (**C2**) (black) against the predicted Pattern based on the single crystal XRD measurement (red) at 220 K.

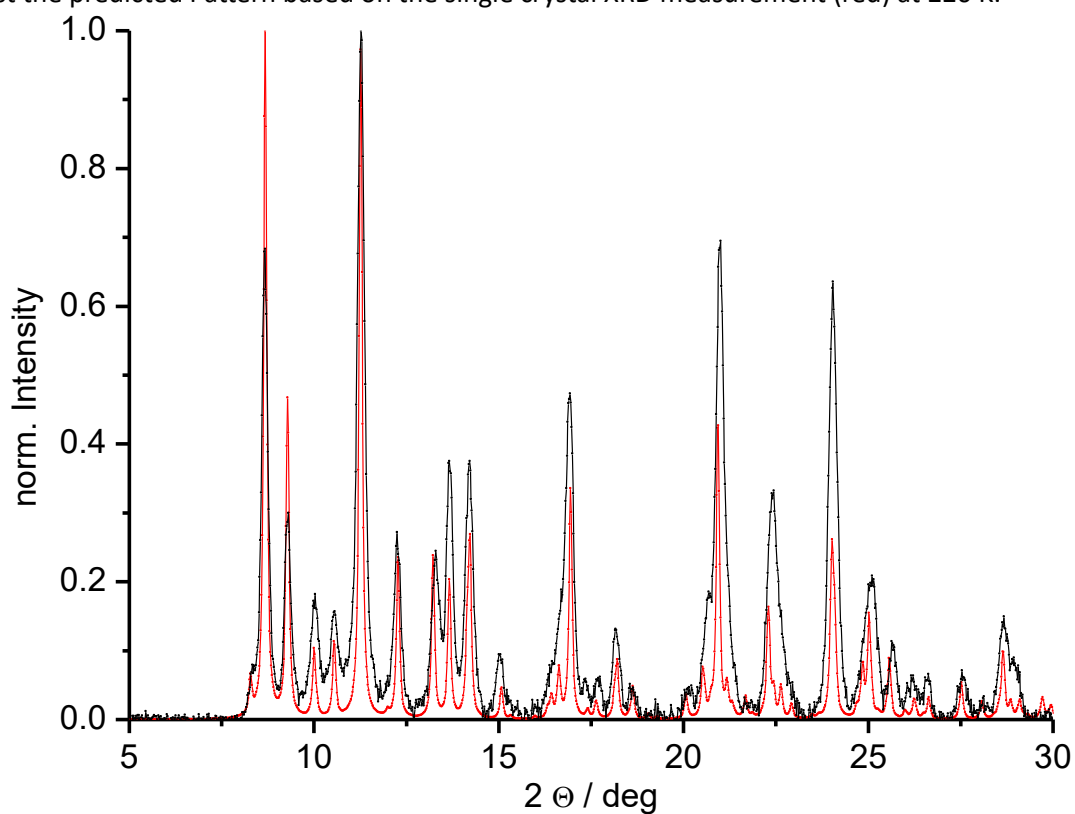


Figure S70: Powder XRD Pattern of the of product of $[\text{Fe}(\text{L}^{\text{Naph-ODA-(S)-Al}})(\text{NCBH}_3)_2] \cdot 0.5 \text{CH}_3\text{CN}$ (**C3**) (black) against the predicted Pattern based on the single crystal XRD measurement (red) at 220 K.

8. Magnetic Data:

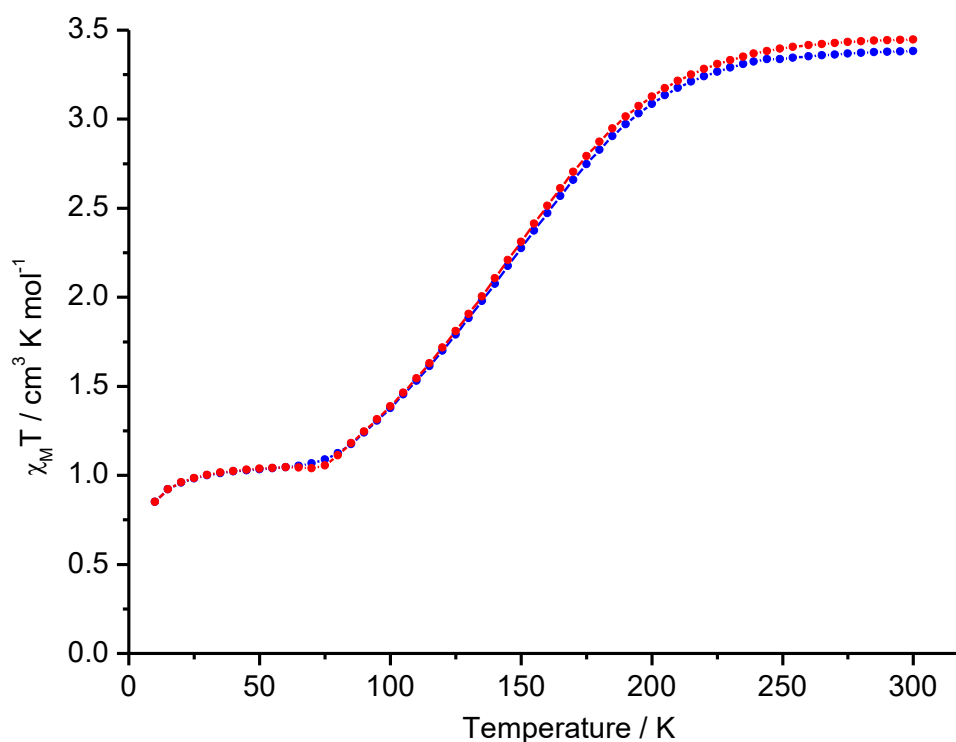


Figure S71: χ_M vs. T measured of powder product of $[\text{Fe}(\text{L}^{\text{Naph-ODA-(Rac-Al)}})(\text{NCBH}_3)_2] \cdot 0.5 \text{CH}_3\text{CN}$ (**C1**) in the form of the resulting $\chi_M T$ vs. T plot. Magnetic susceptibility was determined between 300 - 10 K (blue) and 10-300 K (red).

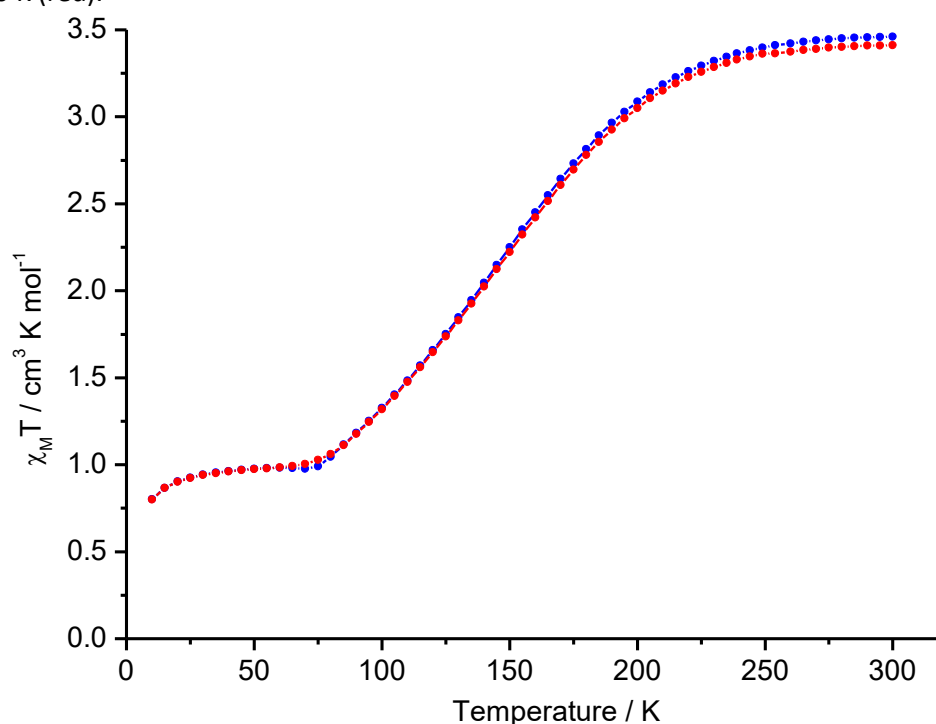


Figure S72: χ_M vs. T measured of powder product of $[\text{Fe}(\text{L}^{\text{Naph-ODA-(R-Al)}})(\text{NCBH}_3)_2] \cdot 0.5 \text{CH}_3\text{CN}$ (**C2**) in the form of the resulting $\chi_M T$ vs. T plot. Magnetic susceptibility was determined between 300 - 10 K (blue) and 10-300 K (red).

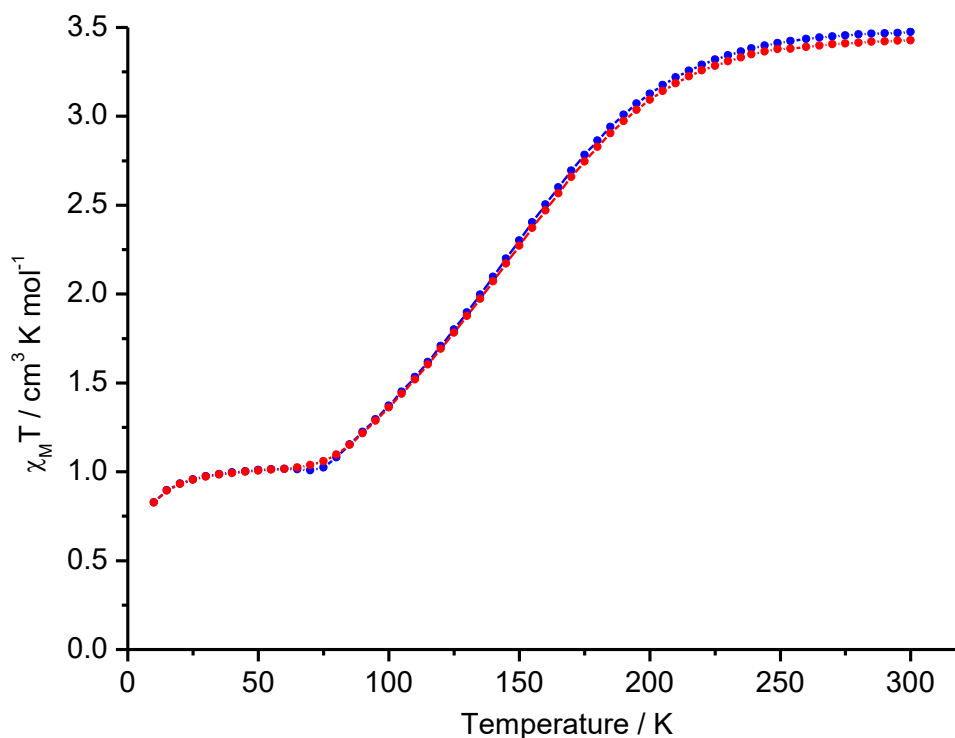


Figure S73: $\chi_M T$ vs. T measured of powder product of $[\text{Fe}(\text{L}^{\text{Naph-ODA-(S)-Al}})(\text{NCBH}_3)_2] \cdot 0.5 \text{CH}_3\text{CN}$ (**C3**) in the form of the resulting $\chi_M T$ vs. T plot. Magnetic susceptibility was determined between 300-10 K (blue) and 10 - 300 K (red).

9.1 Chiral HPLC

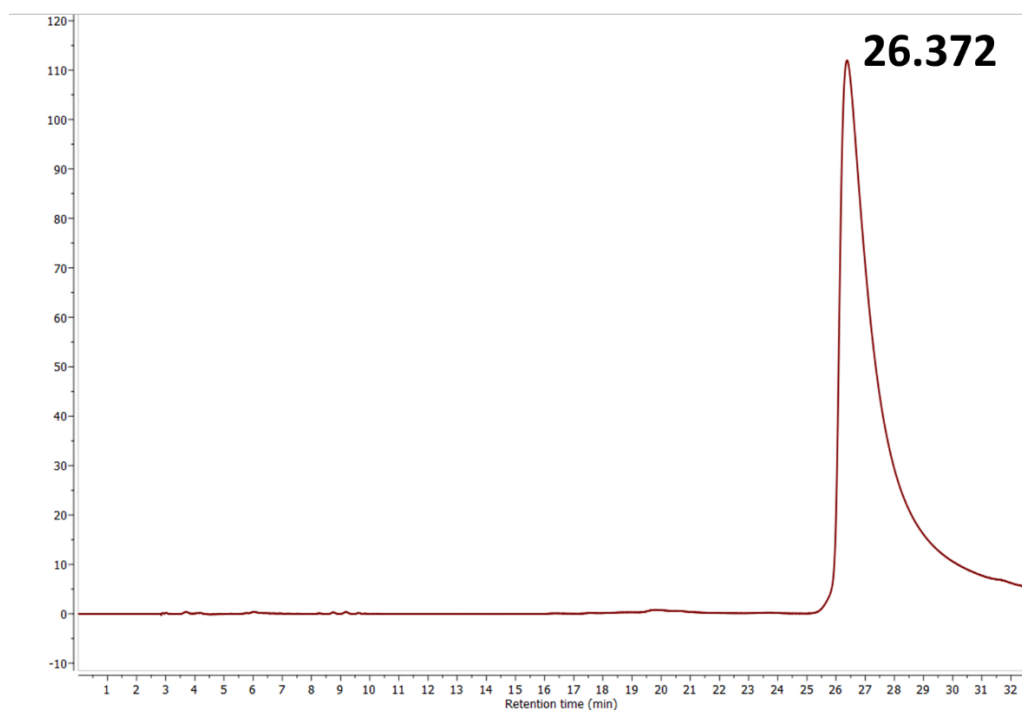


Figure S74: Chromatogram of chiral HPLC measurement of $\text{L}^{\text{Naph-ODA-(R)-Al}}$ with Absorption (mAu) against Retention time (min).

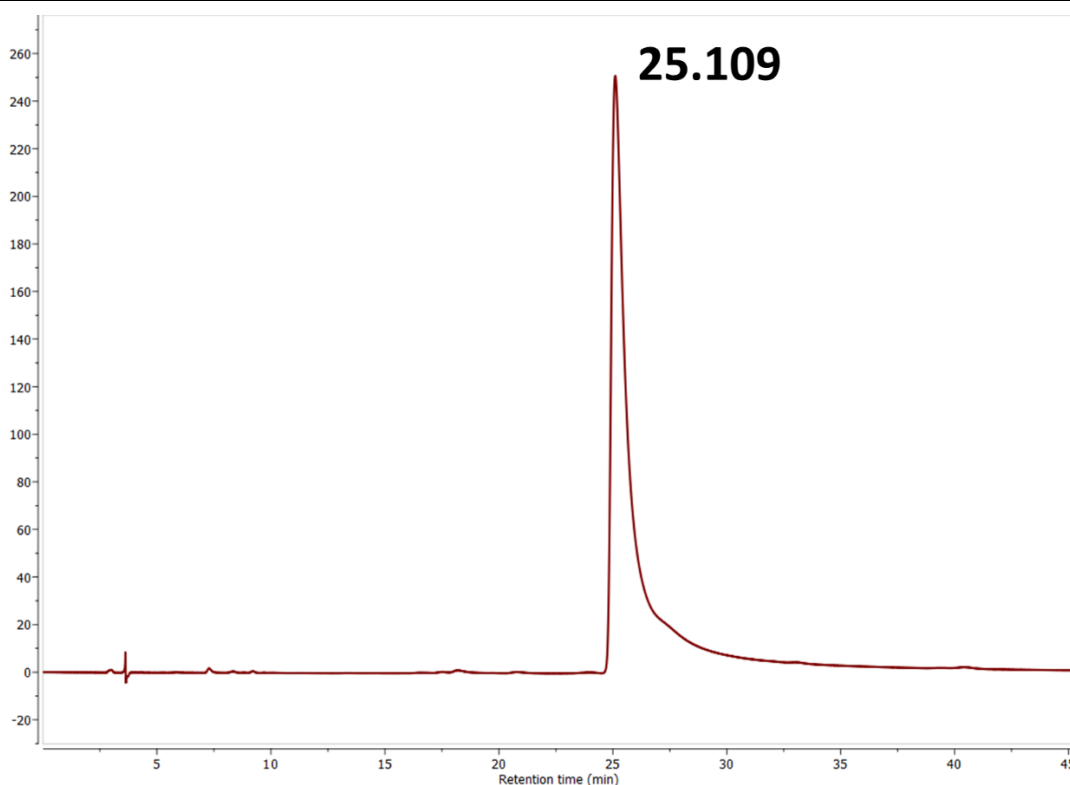


Figure S75: Chromatogram of chiral HPLC measurement of $L^{\text{Naph-ODA-(S)-Al}}$ with Absorption (mAu) against Retention time (min).

9.2 CD-spectra:

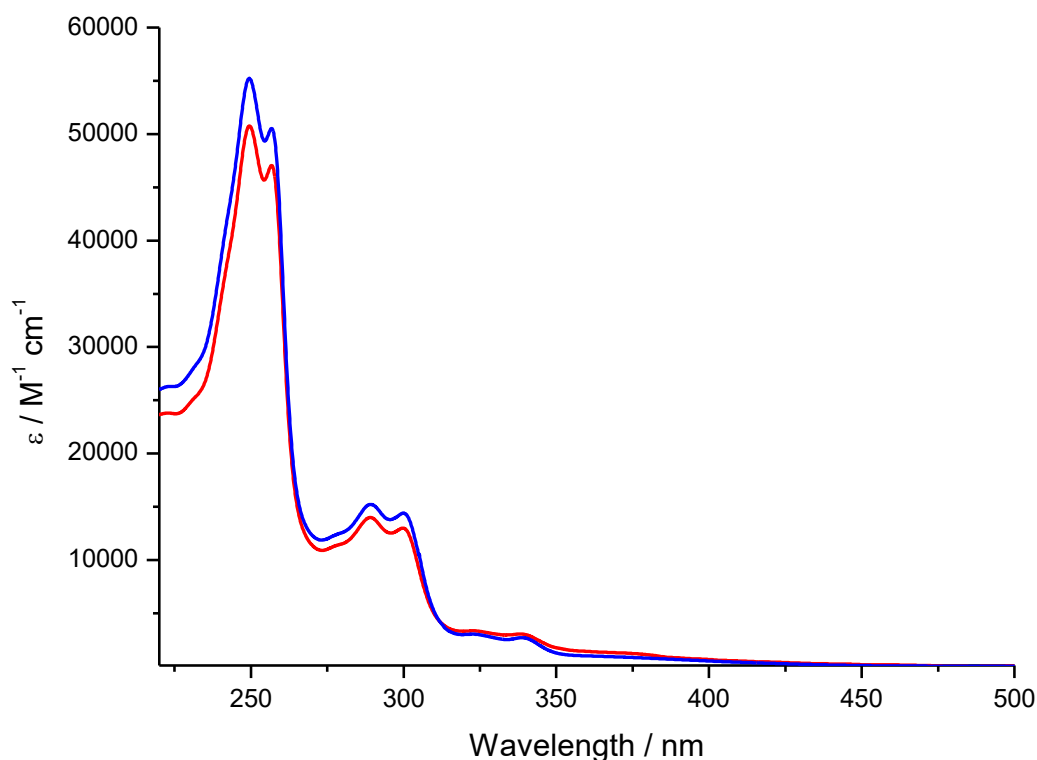


Figure S76: Absorption spectra of $[\text{Fe}(\text{L}^{\text{Naph-ODA-(R)-Al}})(\text{NCBH}_3)_2] \cdot 0.5 \text{CH}_3\text{CN}$ (C2) (blue), $[\text{Fe}(\text{L}^{\text{Naph-ODA-(S)-Al}})(\text{NCBH}_3)_2] \cdot 0.5 \text{CH}_3\text{CN}$ (C3) (red). The difference in molar absorption coefficient is due to concentration inaccuracy.

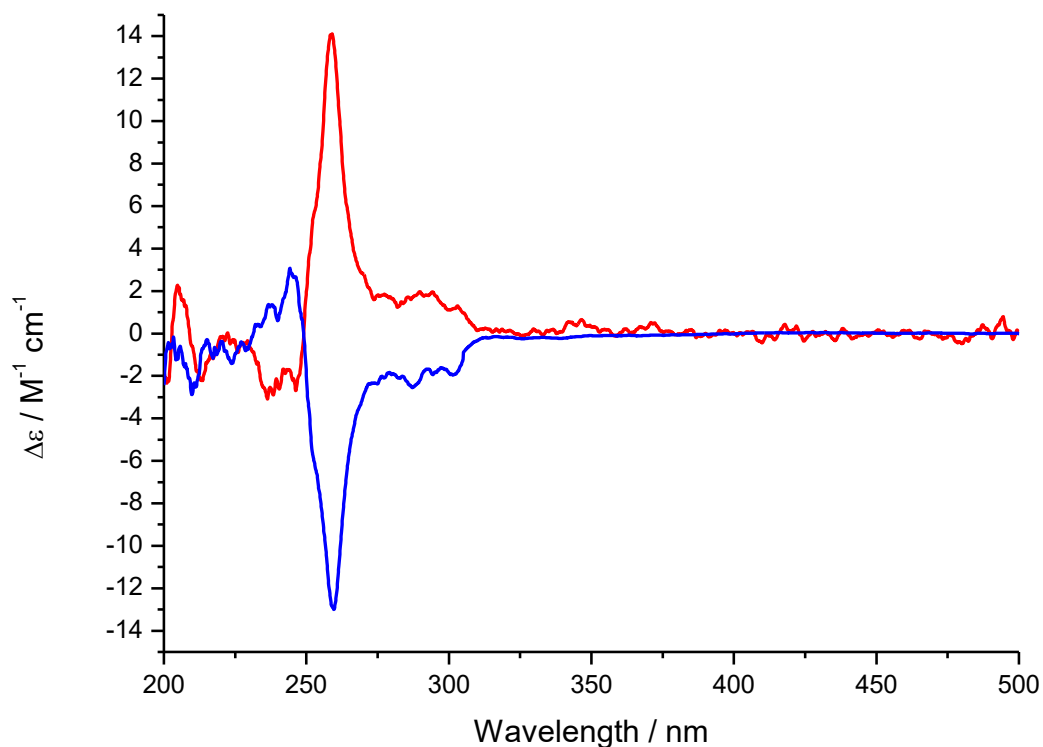


Figure S77: CD-spectra of $[\text{Fe}(\text{L}^{\text{Naph-ODA-(R)-Al}})(\text{NCBH}_3)_2] \cdot 0.5 \text{CH}_3\text{CN}$ (**C2**) (blue), $[\text{Fe}(\text{L}^{\text{Naph-ODA-(S)-Al}})(\text{NCBH}_3)_2] \cdot 0.5 \text{CH}_3\text{CN}$ (**C3**) (red). The difference in molar absorption coefficient difference is due to concentration inaccuracy.

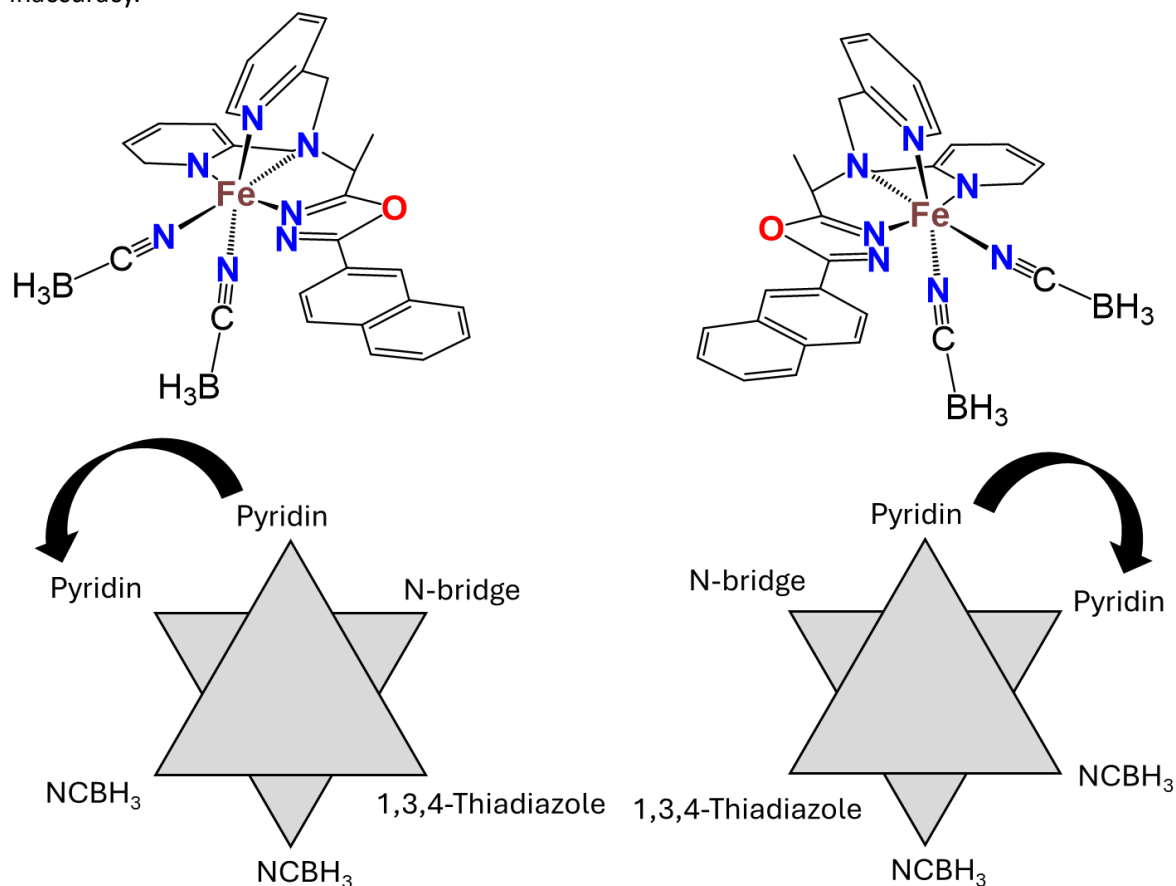


Figure S78: schematic representation of the intrinsic chirality for a possible facial isomer with Λ -isomer (left) and Δ -isomer (right).

10. References:

- [1] J. C. Cobas, F. J. Sardina, *Concepts Magnetic Resonance* **2003**, *19A*, 80–96.
- [2] G. M. Sheldrick, *Acta Crystallogr. A. Found. Adv.* **2015**, *71*, 3–8.
- [3] G. M. Sheldrick, *Acta Crystallogr. A. Found. Crystallogr.* **2008**, *64*, 112–122.
- [4] G. M. Sheldrick, T. R. Schneider, *Elsevier*, **1997**, pp. 319–343.
- [5] O. V. Dolomanov, L. J. Bourhis, R. J. Gildea, J. A. K. Howard, H. Puschmann, *J. Appl. Crystallogr.* **2009**, *42*, 339–341.
- [6] S. Sundaresan, J.-G. Becker, J. Eppelsheimer, A. E. Sedykh, L. M. Carrella, K. Müller-Buschbaum, E. Rentschler, *Dalton Trans.* **2023**, *52*, 13181–13189.
- [7] P. N. Basa, C. A. Barr, K. M. Oakley, X. Liang, S. C. Burdette, *J. Am. Chem. Soc.* **2019**, *141*, 12100–12108.
- [8] Sm. K. Levadala, S. R. Banerjee, K. P. Maresca, J. W. Babich, J. Zubieta, *Synthesis* **2004**, *11*, 1759–1766
- [9] H. A. Rajapakse, H. Zhu, M. B. Young, B. T. Mott, *Tetrahedron Letters* **2006**, *47*, 4827–4830.
- [10] C. Kuloor, Akash, V. Goyal, R. Zbořil, M. Beller, R. V. Jagadeesh, *Angew. Chem. Int. Ed.* **2025**, *64*, e202414689.
- [11] G. R. Fulmer, A. J. M. Miller, N. H. Sherden, H. E. Gottlieb, A. Nudelman, B. M. Stoltz, J. E. Bercaw, K. I. Goldberg, *Organometallics* **2010**, *29*, 2176–2179.

Chapter 5: Solvent induced coordination Isomers of 1,3,4-Thiadiazole complexes

The investigations on the impact of the coordination mode (facial vs. meridional) were conducted and discussed in this chapter, using two solvatomorphic iron(II) complexes $[\text{Fe}(\text{L}^{\text{Naph-TDA}})(\text{NCBH}_3)_2]$, obtained from mixtures of dichloromethane and methanol, as well as from acetonitrile. Both were characterised by various analytic methods such as *IR*-and *UV-Vis* spectroscopy, *ESI-MS*-spectrometry and elemental analysis and both are based on the ligand $\text{L}^{\text{Naph-TDA}}$, which was synthesised and characterised by various analytic methods. A rare example of solvent-dependent coordination isomerism was observed: the complex crystallizes in a meridional coordination geometry when dichloromethane is present as the lattice solvent, and in a facial geometry when acetonitrile is incorporated in the packing. These structural differences were investigated by single-crystal *X-ray* diffraction and correlated with magnetic properties studied via *SQUID* magnetometry. A structure-property relationship was established, particularly highlighting the asymmetric hysteresis behaviour of the acetonitrile solvatomorph, attributed to the rotational dynamics of the π - π -stacked naphthyl groups.

The results are presented as scientific article planned to be published.

Author contribution:

The general synthesis of the ligand system and the complexes was developed by [REDACTED], while the laboratory work on the ligand was performed by [REDACTED] and [REDACTED] and the complex synthesis was performed by [REDACTED]. The *IR*-spectroscopy was collected by [REDACTED] as well as the sample preparation for elemental analysis, *NMR*-spectroscopy and *ESI-MS*-spectrometry. [REDACTED] collected the single crystal *XRD* data and refined the structure. The evaluation of the magnetic and structural data was done by [REDACTED].

The Manuscript was written by [REDACTED], with input from [REDACTED] and [REDACTED]. [REDACTED] had the supervision during the manuscript process. All Authors have read and agreed to the submitted version of the manuscript.

Manuscript: Lattice Solvent as a Structural Switch: *Mer-Fac* Isomerism and Spin Crossover in Fe(II) complexes based on 1,3,4- Thiadiazole

Jens-Georg Becker,¹ Sriram Sundaresan,^{1,2} Luca M. Carrella,¹ and Eva Rentschler^{1*}

¹Department Chemie, Johannes-Gutenberg-Universität Mainz, Duesbergweg 10–14, 55128 Mainz, Germany.
Email: rentschl@uni-mainz.de

²Institute of Physics, Czech Academy of Sciences, Cukrovarnická 10, 162 00 Prague, Czech Republic.

Abstract

We report a direct correlation between solvent effects and coordination isomerism in iron(II) spin crossover complexes using the novel ligand 1-(5-(naphthalen-2-yl)-1,3,4-thiadiazol-2-yl)-N,N-bis(pyridin-2-ylmethyl)methanamine ($L^{\text{Naph-TDA}}$). The facial and meridional coordination isomers of the complex $[\text{Fe}(L^{\text{Naph-TDA}})(\text{NCBH}_3)_2] \cdot \text{solv.}$ were obtained by crystallization from a mixture of dichloromethane and methanol (solv. = DCM \rightarrow meridional = **C2**) and from acetonitrile (solv. = MeCN \rightarrow fac = **C1**). Both complexes were thoroughly characterized using variable-temperature single-crystal X-ray diffraction and SQUID magnetometry. Both solvatomorphs exhibit an abrupt spin transition; notably, the MeCN solvatomorph displays asymmetric hysteresis, which is attributed to the rotation of stacked naphthyl rings. Further investigation of the isomerism in solutions was conducted via absorption spectroscopy.

Introduction

Molecular bistability lies at the heart of functional molecular materials, enabling switchable responses to external stimuli such as temperature, light, or pressure.^[1–4] Systems capable of switching between two distinct physical states are highly sought after for applications in information storage, molecular logic gates, sensors, and actuators.^[5–7] Among the various molecular switching motifs, spin crossover (SCO) compounds represent one of the most appealing classes, where a transition between low-spin (LS) and high-spin (HS) electronic configurations of a transition metal ion can be reversibly triggered by subtle changes in the environment.^[8] This interplay between molecular structure, spin state, and collective solid-state effects continues to offer a fertile playground bridging coordination chemistry and condensed matter physics.

A defining feature of SCO materials is their sensitivity to the crystal lattice environment.^[9–11] Minute perturbations in molecular packing, hydrogen-bonding networks, or lattice solvation can dramatically alter the cooperative interactions responsible for the spin transition in solid state.^[12,13] Solvent molecules, in particular, often play a pivotal role in stabilising distinct coordination geometries and

governing the communication pathways between neighbouring metal centres.^[14,15] In some cases, the loss of this lattice solvent may lead to locking of the metal ions in one spin state.^[16] In this work we report a rare example of 1,3,4-Thiadiazole based Fe(II) complex where, changes in lattice solvent has aided to reorganise the primary coordination sphere of the metal ion, leading to coordination isomerism interchangeable reversibly between *meridional* (*mer*) to *facial* (*fac*).

Such solvent-driven geometric rearrangements are not more structural curiosities as they fundamentally reshape the ligand field symmetry and, consequently, the spin-state energetics. The resulting reorganisation within the crystal lattice has modified packing density, symmetry relations, and magnetic cooperativity which has its influence in the spin states and is thoroughly investigated. These class of spin crossover system has their potential applications as molecular sensors especially shape-memory materials.

Results and Discussion:

Synthesis:

The ligand 1-(5-(naphthalen-2-yl)-1,3,4-thiadiazol-2-yl)-N,N-bis(pyridin-2-ylmethyl)methanamine ($L^{\text{Naph-TDA}}$) was synthesized in two steps based on a previously reported procedure and is shown **Figure 1**.^[9] The synthesis procedure was modified by using Lawesson's reagent to obtain the 1,3,4-thiadiazole in contrast to tetrabrommethane and Triphenylphosphane used for the 1,3,4-oxadiazole.^[9] The intermediate coupling product was obtained by reacting compound (**I**) with carbonyl diimidazole and naphthylhydrazide in dry dichloromethane. After removing the solvent and dissolving the residue in tetrahydrofuran, cyclization and simultaneous substitution was achieved using Lawesson's reagent, yielding the desired product $L^{\text{Naph-TDA}}$ in moderate yield. Detailed description is provided in the experimental section. The newly obtained ligand was fully characterized using a range of techniques, including $^1\text{H-NMR}$, $^{13}\text{C-NMR}$, 2D-NMR (**Figure S3-S7**), IR spectroscopy (**Figure S8**), mass spectrometry (**Figure S11-S12**) and elemental analysis.

The obtained ligand $L^{\text{Naph-TDA}}$ was subsequently reacted with the well-known precursor $[\text{Fe}(\text{NCBH}_3)_2(\text{py})_4]$ in two different solvents acetonitrile (**C1**) and dichloromethane (**C2**) to study the influence of the solvent. The complex synthesis in both cases were carried out at inert atmosphere because of the air sensitivity of the complex precursor used. Both complexes **C1** and **C2** obtained are air stable. Single crystals suitable for X -ray diffraction was obtained from both complexes in different crystallization conditions. In the case of **C1**. Single crystals were obtained from slow evaporation of acetonitrile, whereas in the case of **C2** layering method was used to obtain single crystals with dichloromethane and methanol.

Both complexes were characterized by IR spectroscopy. A minor shift of the C=N stretching vibration within the aromatic ring was observed from 1586 cm^{-1} and 1567 cm^{-1} (free ligand) to 1603 cm^{-1} and 1571 cm^{-1} for **C1**, and to 1603 cm^{-1} and 1571 cm^{-1} for **C2** due to electron density changes upon coordination to iron(II). Additionally, the $\text{N}\equiv\text{C}$ stretching vibration of the NCBH_3 co-ligand was observed at 2184 cm^{-1} (**C1**) and 2179 cm^{-1} (**C2**) (Figure S9 and S10) ^[9,17,18] Further confirmation of complex formation was provided by mass spectrometry, which revealed fragments such as $[\text{Fe}(\text{L}^{\text{Naph-TDA}})\text{NCBH}_3]^+$ (m/z : 505.089; 100%) (see Figure S13 – S16). This is explained by the loss of one NCBH_3 co-ligand and cleavage of the B–C bond, likely due to the acidic conditions during sample preparation or the measurement process.^[19]

Elemental analysis confirmed solvent exchange in **C1**, from acetonitrile to water, while in **C2** dichloromethane was retained as the lattice solvent which is consistent with the solvent molecules observed in single-crystal XRD.

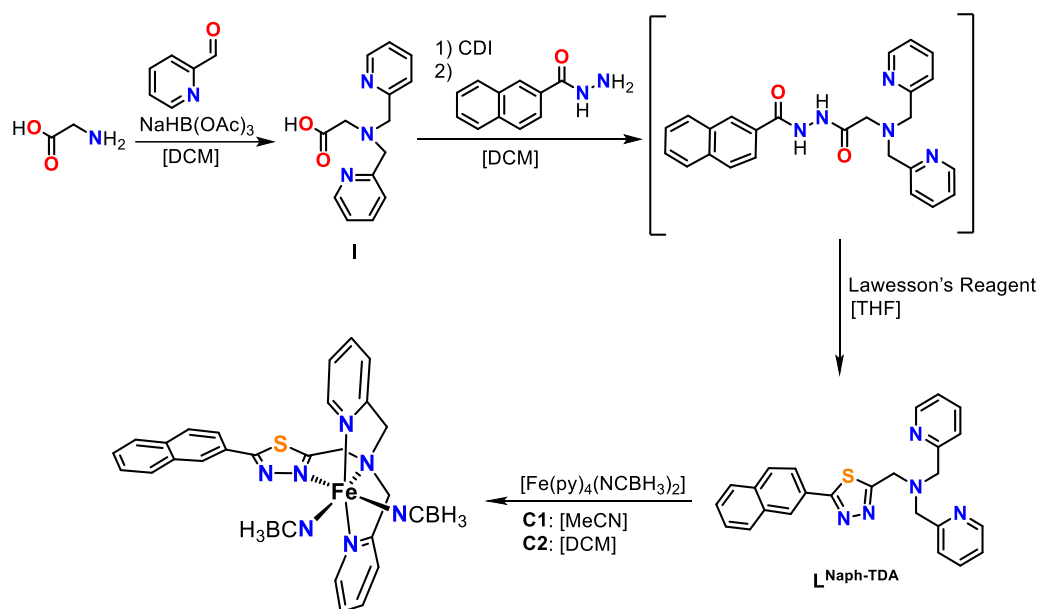


Figure 1: Multistep ligand synthesis of $\text{L}^{\text{Naph-TDA}}$ along with complex synthesis of **C1** and **C2**.

Structural determination:

Single crystal of both complexes **C1** and **C2** were crystallised in the same monoclinic crystal system. The change in the lattice solvent was responsible for the variation of the space groups these complexes crystallised. In the case of **C1**, the complex crystallised in $P2_1/c$ space group with two acetonitrile complex per complex in unit cell. Whereas **C2** crystallised in $C2/c$ space group with 1.5 DCM per complex unit. All the crystallography data are tabulated in **Table S1-S4**.

Given that the different solvents lead to different space groups, the influence on the molecular structure was further investigated. Complex **C1** exhibits a *fac*-isomer, characterized by the *cis*-coordination of the two pyridine rings among the four coordinating nitrogen atoms of the tetradentate ligand $L^{\text{Naph-TDA}}$, in addition to two NCBH_3 co-ligands (see **Figure 2**). On the other hand, complex **C2** shows the same N-donor coordination but with *trans*-coordinating pyridine units, leading to the *mer*-isomer, also illustrated in **Figure 2**.

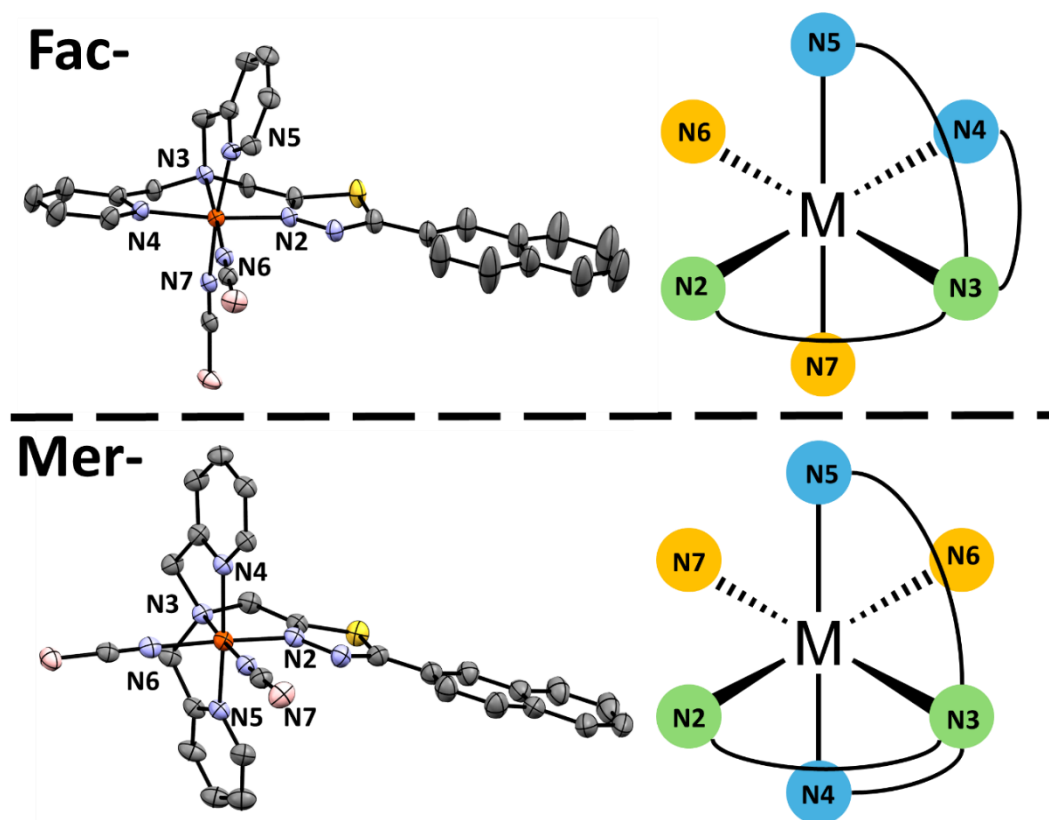


Figure 2: Visualization of the coordination mode difference between the *fac*-shaped $[\text{Fe}(\text{L}^{\text{Naph-TDA}})(\text{NCBH}_3)_2] \cdot 0.5 \text{H}_2\text{O}$ (above) (**C1**) and the *mer*-shaped $[\text{Fe}(\text{L}^{\text{Naph-TDA}})(\text{NCBH}_3)_2] \cdot 0.9 \text{DCM}$ (**C2**) (down) by the molecular structure (left) at 120 K with orange NCBH_3 , blue Pyridine-units, bridging nitrogen and green 1,3,4-thiadiazole unit.

The influence of the heteroatom on the bite angle and ligand flexibility was previously reported by some of us where we investigated the formation of helically chiral dinuclear complexes which also crystallized from acetonitrile.^[20] Since this complex also adopts the *mer*-isomer, it suggests that the presence of the 1,3,4-thiadiazole unit alone does not determine the coordination geometry. Instead, the introduction of the bulky naphthyl group in $L^{\text{Naph-TDA}}$ may contribute to a solvent-dependent isomerization through increased steric strain. These are also in line with the literature reports from Kisslinger *et al.* where they examined a series of complexes with comparable coordination motifs, varying the terminal N-donor functionalities.^[21] The introduction of steric strain through substitution of the terminal amine with two methyl groups, or with bulkier groups such as *propan-2-ylidene-imin* and *1,1,3,3-tetramethylguanidine*, showed that increasing strain favored *mer*-to-*fac* isomerization. These findings support the hypothesis that coordination strain governs isomerism.^[18] In another example by Matouzenko *et al.* The stereoisomerism of tetradentate ligands with a similar *motif* has been investigated in the complexes *fac*-[Fe(DPPA)(NCS)₂] (DPPA = (3-aminopropyl)bis(2-pyridylmethyl)amine) and *mer*-[Fe(DPEA)(NCS)₂] (DPEA = (3-aminoethyl)bis(2-pyridylmethyl)amine). In these studies, elongation of the ligand's coordination arm led to a change in the coordination geometry from *fac* to *mer*.^[22,23] But all in all the literature reported cases the complexes are either locked in LS state or HS state. The influence of the magnetic behaviour associated with this structural reorganization cannot be investigated.

In solution, a significant contribution to understanding the influence of coordination isomerism on the ligand field and, consequently, spin crossover properties was made by Lathion *et al.*. They studied the complex [Fe(Lk)₃]²⁺, where **Lk** represents ligands based on the 1-methyl-2-(pyridin-2-yl)-1H-benzo[d]imidazole motif, using various *NMR* techniques, including *Evans NMR*.^[9,18,24] Their work demonstrated that the thermodynamic trans-influence enthalpically favors the facial coordination, while the meridional geometry is favoured entropically due to its larger dipole moment. Since the entropic contribution is influenced by the dipole moment, solvent effects - particularly the dielectric constant - must also be considered. In solution, the facial isomer exhibits spin crossover with a higher transition temperature, indicating greater stabilization of the low-spin state for the facial isomer. However, temperature-dependent *Evans NMR* measurements must be interpreted carefully, considering the temperature-dependent equilibrium between *fac* and *mer* isomers as well as the spin crossover process.

The effect of strain on the coordination pocket is illustrated by the observed out-of-plane distortions, visualized in **Figure 3**. The distortion is more pronounced in the *fac*-isomer of **C1**, in contrast to the more planar arrangement found in **C2**. Moreover, the 1,3,4-thiadiazole-naphthyl unit in **C2** is significantly more bent, providing additional structural insight into the distortion induced by ligand strain.

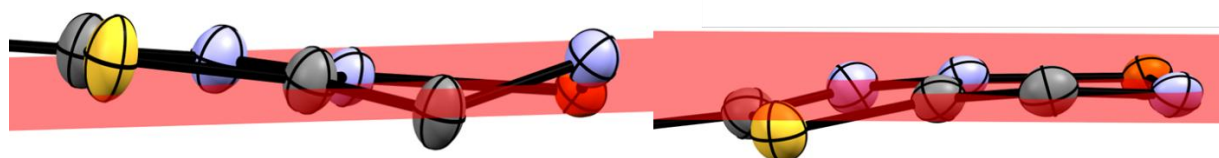


Figure 3: Visualization of the out-of-plane distortion for of the coordination pocket for the *fac*-shaped $[\text{Fe}(\text{L}^{\text{Naph-TDA}})(\text{NCBH}_3)_2] \cdot 0.5 \text{ H}_2\text{O}$ (left) (**C1**) and the *mer*-shaped $[\text{Fe}(\text{L}^{\text{Naph-TDA}})(\text{NCBH}_3)_2] \cdot 0.9 \text{ DCM}$ (**C2**) (right), with the calculated ideal plane (red).

The distortion in complexes **C1** and **C2** was further analyzed by comparing distortion parameters. These are summarized in **Table S6** and **S7**. At 120 K, the distortion parameter $\Sigma_0(\text{FeN}_6)$ for complex **C1** was found to be 52.17° . In contrast, complex **C2** exhibits a smaller distortion parameter of $\Sigma_0 = 48.35^\circ$, which is comparable to other reported *mer*-isomers such $[\text{Fe}(\text{L}^{\text{Ph-ODA}})(\text{NCBH}_3)_2] \cdot \text{MeCN}$ ($\Sigma_0 = 49.44^\circ$) and $[\text{Fe}(\text{L}^{\text{Naph-ODA}})(\text{NCBH}_3)_2] \cdot 1.5 \text{ MeOH}$ ($\Sigma_0 = 47.04^\circ$) in contrast to the recently reported chiral $[\text{Fe}(\text{L}^{\text{Naph-ODA-Al}})(\text{NCBH}_3)_2] \cdot 0.5 \text{ MeCN}$ ($\Sigma_0 = 57.94^\circ$), where the different can be explained by the steric impact of an introduced methyl group in the coordination environment.^[9,18,24] Since all these complexes are known to be in a low-spin state at this temperature, the observed difference in distortion between the two isomers - $\Delta\Sigma_0 = 3.82^\circ$ - can be considered significant.^[25,26] The average Fe-N bond lengths for **C1** and **C2**, also listed in table S5, are very similar (**C1**: $\bar{d}_{\text{Fe-N}} = 1.969 \text{ \AA}$; **C2**: $\bar{d}_{\text{Fe-N}} = 1.968 \text{ \AA}$), supporting their low-spin configuration.^[27] The values of the meridional coordinated complex are also in line with those reported for comparable complexes at 120 K, including and $[\text{Fe}(\text{L}^{\text{Ph-ODA}})(\text{NCBH}_3)_2] \cdot \text{MeCN}$ (1.971 \AA), $[\text{Fe}(\text{L}^{\text{Naph-ODA}})(\text{NCBH}_3)_2] \cdot 1.5 \text{ MeOH}$ (1.970 \AA).^[18,24] The value of the chiral complex $[\text{Fe}(\text{L}^{\text{Naph-ODA-Al}})(\text{NCBH}_3)_2] \cdot 0.5 \text{ MeCN}$ (2.026 \AA) distinguishes due to the observed incomplete spin crossover of these complex.^[9]

Given the similar bond lengths and distortion parameters among $[\text{Fe}(\text{L}^{\text{Naph-Q}})(\text{NCBH}_3)_2]$ complexes (Q = ODA-Al and ODA), the spin crossover (SCO) behavior of **C1** and **C2** was investigated using single-crystal X-ray diffraction at elevated temperatures (230 K and 240 K). A transition to the high-spin state is expected to result in increased average Fe-N bond lengths and larger distortion parameters due to the population of e_g^* orbitals. For **C1**, a marked increase in average bond length was observed at 230 K

($\bar{d}_{\text{Fe-N}} = 2.160 \text{ \AA}$), indicating that the SCO occurs between 120 K and 230 K. The distortion parameter also increased substantially to $\Sigma_0 = 102.76^\circ$, indicating the spin state transition.^[26] The bond lengths of both complexes **C1** and **C2** at both measured temperatures are shown in **Figure S43**.

In contrast, **C2** displays a relatively low distortion parameter of $\Sigma_0 = 65.35^\circ$ at 230 K, significantly below those of reported high-spin *mer*-isomers $[\text{Fe}(\text{L}^{\text{Ph-ODA}})(\text{NCBH}_3)_2] \cdot \text{MeCN}$ ($\Sigma_0 = 97.26^\circ$), $[\text{Fe}(\text{L}^{\text{Naph-ODA}})(\text{NCBH}_3)_2] \cdot 1.5 \text{ MeOH}$ ($\Sigma_0 = 92.92^\circ$) and $[\text{Fe}(\text{L}^{\text{Naph-ODA-Al}})(\text{NCBH}_3)_2] \cdot 0.5 \text{ MeCN}$ ($\Sigma_0 = 89.78^\circ$), which are high-spin at 230 K and 240 K, respectively.^[9,18,24] The Fe–N bond lengths for **C2** at these temperatures also remain relatively short ($\bar{d}_{\text{Fe-N}} = 2.034 \text{ \AA}$), further indicating that SCO is incomplete or only partially occurring at this temperature, as well as this value is close to the average Fe-N bond length of the chiral $[\text{Fe}(\text{L}^{\text{Naph-ODA-Al}})(\text{NCBH}_3)_2] \cdot 0.5 \text{ MeCN}$ at 90K ($\bar{d}_{\text{Fe-N}} = 2.160 \text{ \AA}$). This is in contrast to the significantly longer bond lengths observed for the high-spin analogues $[\text{Fe}(\text{L}^{\text{Ph-ODA}})(\text{NCBH}_3)_2] \cdot \text{MeCN}$ (2.174 Å), $[\text{Fe}(\text{L}^{\text{Naph-ODA}})(\text{NCBH}_3)_2] \cdot 1.5 \text{ MeOH}$ (2.165 Å) and $[\text{Fe}(\text{L}^{\text{Naph-ODA-Al}})(\text{NCBH}_3)_2] \cdot 0.5 \text{ MeCN}$ (2.162 Å).^[9,18,18]

The space groups of **C1** and **C2** differ, suggesting that their intermolecular interactions, particularly π - π stacking - which are known to affect the cooperativity and abruptness of spin crossover - must also differ. Other factors such as hydrogen bonding or solvent–solute interactions were not observed in the crystal structures. The apolar nature of the lattice solvents (DCM and MeCN) further supports this conclusion, limiting the discussion to π - π interactions.^[28]

In the crystal structure of both complexes the complex fragment $[\text{Fe}(\text{L}^{\text{Naph-TDA}})(\text{NCBH}_3)_2]$ occurs as pairs connected by the π - π -interaction of the Naphthyl-1,3,4-Thiadiazole-unit (shown in **Figure S23**, **S30**, **S35** and **S42**) According to the different positioning of the coordinating pyridine groups in relation to the Naphthyl-1,3,4-Thiadiazole based on the isomer, both complexes show packing with different linkages.

In case of **C2** the complexes forming linear chains along the unit cell diagonal, stabilized by sequential naphthyl-naphthyl and pyridine-pyridine interactions (see **Figure S37**). These motifs is in contrast to both reported 1,3,4-oxadiazole complexes $[\text{Fe}(\text{L}^{\text{Naph-ODA-Al}})(\text{NCBH}_3)_2] \cdot 0.5 \text{ MeCN}$ and $[\text{Fe}(\text{L}^{\text{Naph-ODA}})(\text{NCBH}_3)_2] \cdot 1.5 \text{ MeOH}$, where the connection between the pairs occurs by interlocked iron(II) coordination pockets.^[9,18] The stacking parameters for pyridine–pyridine interactions, calculated using the geometrical methods of B.K. Saha et al., are comparable across all systems and show minimal temperature dependence (**Table S8**, **Figure S36**).^[29] The resulted chains of the complex pairs in the packing of **C2** are oriented along *a-b*-face diagonal and the next neighbour chain is turned by 45° .

Solvent channels of dichloromethane are observed along the *c*-axis as the C-H-bonds of the dichloromethane are oriented in the direction of the naphthyl group.

In **C1**, *fac*-coordination also facilitates naphthyl-naphthyl interactions but introduces additional interactions: thiadiazole-naphthyl and thiadiazole-pyridine stacking, which are oriented along the *a*-axis (**Figure S21, S22, S24 and S25**). This interaction results in a rectangle network along the *a*-axis with solvent channels of acetonitrile along the *a*-direction in the middle located in the middle of the *c*-axis (**Figure S22**). The additional interactions between the aryl systems lead to a stronger network compared to **C2**, which should affect the profile of the spin state transition. The stacking parameters suggest that the naphthyl–naphthyl interactions in **C1** are stronger, as indicated by a 1.3 Å smaller offset compared to **C2** (**Table S8**).

Upon heating, a modest unit cell expansion is observed, consistent with SCO. For **C1**, the unit cell volume increases by 2%, and for **C2**, by 4%. These expansions are relatively small when compared to the 9% volume change reported for the oxygen analogue $[\text{Fe}(\text{L}^{\text{Naph-ODA}})((\text{NCBH}_3)_2)] \cdot 3 \text{ MeOH}$.^[18]

Notably, the naphthyl-naphthyl interactions in **C1** undergo a decrease in offset upon heating, coupled with a rotation around the 1,3,4-thiadiazole–naphthyl bond (shown in **Figure 4**). This is quantified by a change in the torsion angle C1–C10–C11–N1 (with C10–C11 being the bond between the naphthyl and thiadiazole units), which shifts by approximately 22°. This rotational flexibility may significantly influence the cooperative behavior of spin transition.

A similar concept was demonstrated by Zhao *et al.* for the enantiopure complex $[(\text{R-L})\text{Fe}\{\text{Au}(\text{CN})_2\}_2]$ (R-L = (R)-N¹-N²-dibenzyl-N¹-N²-bis(pyridine-2-ylmethyl)propan-1,2-diamine), where a symmetry-breaking transition due to the spring-like motion of benzyl rings enabled hysteresis in the magnetic response.^[30] In their study, motion of the benzylic groups between 280 K and 380 K led to a two-step spin transition, including a symmetry change from P2₁2₁2₁ to P2₁ and a spin transition from high-spin to low-spin states, demonstrating the profound impact of intramolecular flexibility on SCO hysteresis.

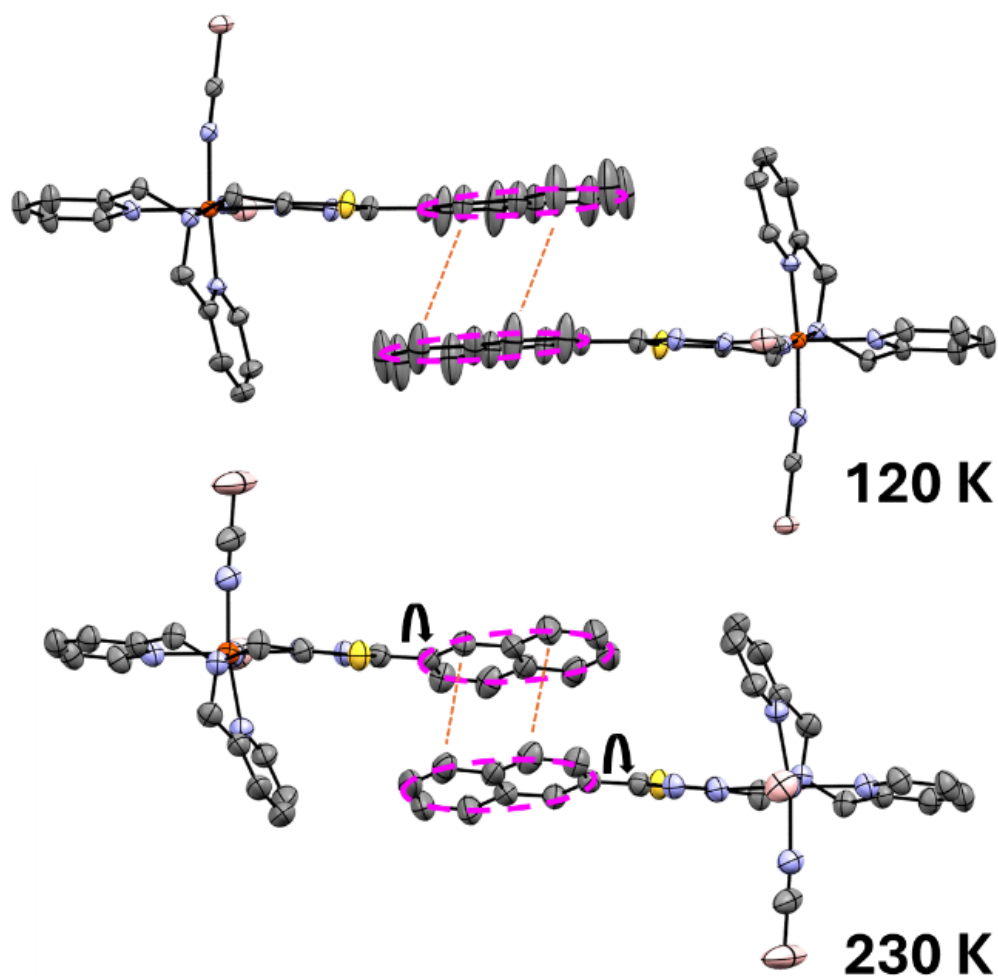


Figure 4: Visualization of the Naphthyl-Naphthyl-Rotation observed by VT single crystal XRD for the fac-shaped complex $[\text{Fe}(\text{L}^{\text{Naph-TDA}})(\text{NCBH}_3)_2] \cdot 0.5 \text{H}_2\text{O}$ (**C1**) at 120 K (above) and 230 K (bottom).

Solid Magnetic data:

To Investigate the influence of the coordination isomer in solid state SQUID measurements from 300 K and 10 K (cooling) and 10 K to 300 K (heating) were performed in 10 K steps as shown in **Figure 5** on microcrystalline powder

Both complexes exhibit a $\chi_M T$ plateau at high temperatures of approximately $3.5 \text{ cm}^3 \cdot \text{K} \cdot \text{mol}^{-1}$, characteristic of the T_{2g} high-spin state of Fe(II).^[31] Upon cooling, complex **C2** displays a gradual decrease in $\chi_M T$ between 250 K and 100 K, with a critical temperature of $T_c^\uparrow = T_c^\downarrow = 165 \text{ K}$. The $\chi_M T$ value reaches a low-temperature plateau of $0.09 \text{ cm}^3 \cdot \text{K} \cdot \text{mol}^{-1}$, consistent with complete conversion to the A_{1g} low-spin state via spin crossover.^[31] For complex **C1**, $\chi_M T$ drops abruptly from 230 K to 210 K, reaching an intermediate value of $0.84 \text{ cm}^3 \cdot \text{K} \cdot \text{mol}^{-1}$, followed by a gradual decrease to a low-spin plateau of $0.08 \text{ cm}^3 \cdot \text{K} \cdot \text{mol}^{-1}$, indicative of full conversion to the A_{1g} low-spin state. The critical temperature during cooling was determined by the first derivative of $\chi_M T$ with respect to temperature,

yielding $T_c^\downarrow = 220$ K. Upon heating, an asymmetric hysteresis is observed between 205 K and 230 K, with a hysteresis width ΔT_c of 5 K and a heating branch critical temperature of $T_c^\uparrow = 225$ K.

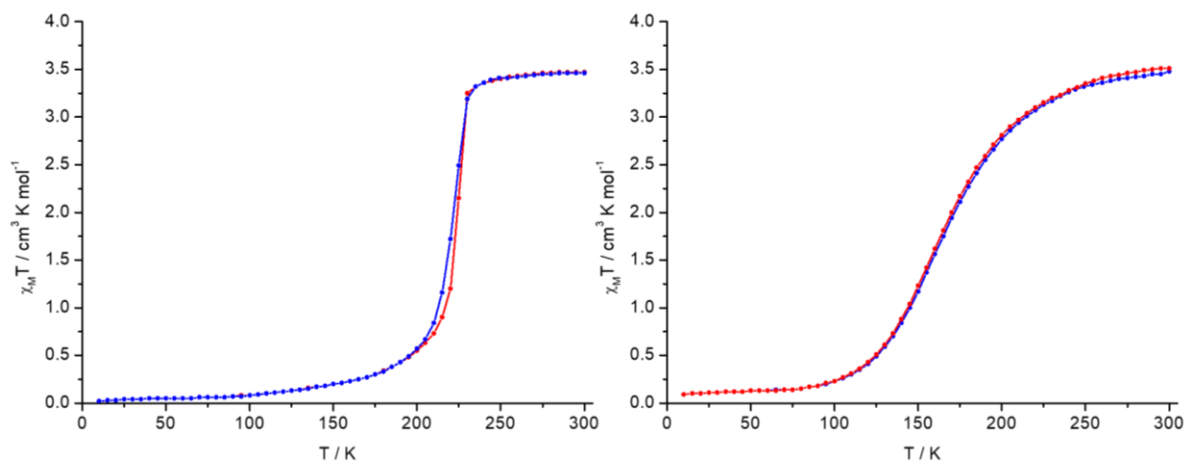


Figure 5: χ_M vs. T of $[\text{Fe}(\text{L}^{\text{Naph-TDA}})(\text{NCBH}_3)_2] \cdot 0.5 \text{ H}_2\text{O}$ (**C1**) (left) and $[\text{Fe}(\text{L}^{\text{Naph-TDA}})(\text{NCBH}_3)_2] \cdot 0.9 \text{ DCM}$ (**C2**) (right) between 300 K–10 K (blue) and 10 K–300 K (red).

This type of hysteresis has also been reported by Zhao *et al.* for the enantiopure complex $[(\text{R-L})\text{Fe}\{\text{Au}(\text{CN})_2\}_2]$, where R-L = (R)-N¹-N²-dibenzyl-N¹-N²-bis(pyridine-2-ylmethyl)propan-1,2-diamine. In that system, the hysteresis was attributed to a phase transition induced by cooperative interactions involving spring-like motion of flexible phenyl rings.^[30]

Analogously, in complex **C1**, the observed asymmetric hysteresis may be explained by restricted rotational motion along the 1,3,4-thiadiazole–naphthyl bond. This rotational change, required during the spin transition, could be kinetically hindered due to the substantial structural rearrangement involved, thereby delaying the reverse transition and introducing thermal hysteresis (shown in **Figure 4**).

As we could observed in the packing of **C1**, the additional interactions between the aryl groups are leading to a stronger network compared to **C2**. This is represented on the abrupt spin state transition in case of **C1**, which is in contrast to the gradual spin transition of **C2** with less linkage between the complex units. The lattice solvent is as well known for influencing the profil of the spin crossover, due to intermolecular interaction, which was shown by Phonsri *et al.*^[32,33]

The two solvatomorphs of the 1,3,4-thiadiazole-based Fe(II) complex display distinct coordination modes and spin-crossover behaviours, reflecting the coupled influence of lattice polarity and coordination geometry. The acetonitrile solvate ($\epsilon \approx 37$) stabilises a facial (fac) arrangement of the FeN_6 core, resulting in a more symmetric ligand field and shorter average Fe–N distances, consistent with a dominant low-spin character and higher T_m . In contrast, the dichloromethane solvate ($\epsilon \approx 9$) favours a

meridional (mer) configuration, introducing greater angular distortion and a weaker ligand field, correlating with the predominance of the high-spin state. These observations suggest that the dielectric nature of the lattice solvent exerts an indirect but significant effect: the more polar acetonitrile lattice enhances electrostatic screening and intermolecular coupling, thereby stabilising the low-spin configuration, while the less polar DCM lattice weakens these interactions and promotes high-spin behaviour. This solvent-driven reorganisation of coordination geometry and spin state exemplifies how lattice polarity and local structure cooperatively govern the electronic bistability in spin-crossover materials.

Solution Phase measurements: UV-Vis Absorption spectroscopy:

To visualize potential isomerization in solution, UV-absorption studies were performed for both complexes in corresponding solvents present in their crystal lattice. In the case of **C2** in acetonitrile and for **C1** in dichloromethane, **Figure 6**. Differences in the molar absorption coefficients are attributed to sample preparation and the low solubility of both complexes in these solvents.

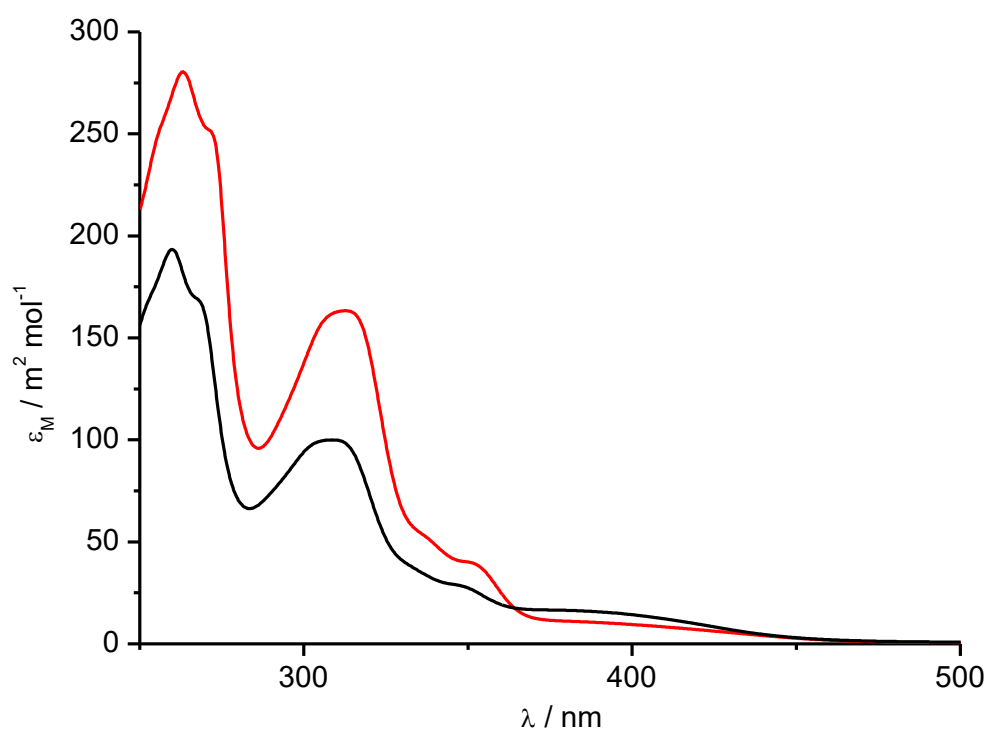


Figure 6: Plot of the molar absorption coefficient against the wavelength obtained by solution absorption spectroscopy with a concentration of 1 mM for **C2** in acetonitrile (black) and **C1** in dichloromethane (red). The differences in molar absorption coefficient are explained by concentration issues due to the low solubility of **C1** and **C2** in both solvents.

The symmetry change between the two isomers should result in a change of the transition bands, as the transition dipole moment is affected by the coordination symmetry. However, the absorption spectra

of all samples show similar transition profiles, suggesting that the geometry does not significantly affect the ligand field symmetry or that isomerization occurs in solution, preventing the observation of distinct isomers.

The mer-fac isomerisation between **C1** and **C2** and its influence on the magnetic behaviour in solid state is investigated. We also attempted to investigate the influence of solvent in solution. As we know from the literature reports from Halcrow *et al.* and Brooker *et al.* Solvents which readily participate in hydrogen bonding stabilises the complexes more in *LS* state in comparison to the apolar solvents. To investigate the influence of the solvent on the spin state transition Evans method NMR technique is as a literature known tool.^[34,35] We first investigated the stability of the complexes in solution as we know, speciation is a real hurdle in solution spin crossover. Since all the complexes are neutral, molar conductivity were measured in 1 M solution in both the cases (**C1** and **C2**). The values obtained ideally should be close to zero for neutral complexes but unfortunately in both the cases the values obtained are quite higher Δ_m of $74.014 \text{ S}\cdot\text{cm}^2\cdot\text{mol}^{-1}$ for **C2** and $68.341 \text{ S}\cdot\text{cm}^2\cdot\text{mol}^{-1}$ for **C1** which are more close to 1:1 electrolyte. This can be explained by coordination ability a^{TM} parameter reported on these co-ligands by Alveraz where in the case of NCBH_3 the value is 1 and this is quite weak and can be easily replaced with acetonitrile in solution which has a higher a^{TM} value of -0.2.^[36] Since the complexes are not stable in solution, the magnetic properties were not investigated in solution. Further a ligand dissociative complex isomerism between both isomers is possible, which makes the investigation of the impact of the isomer impossible.

Conclusion:

In summary, we demonstrated the synthesis and characterization of the novel ligand 1-(5-(naphthalen-2-yl)-1,3,4-thiadiazol-2-yl)-N,N-bis(pyridin-2-ylmethyl)methanamine $\text{L}^{\text{Naph-TDA}}$ and two solvatomorph complexes: **C1** $[\text{Fe}(\text{L}^{\text{Naph-TDA}})(\text{NCBH}_3)_2] \cdot 0.5 \text{ H}_2\text{O}$ and **C2** $[\text{Fe}(\text{L}^{\text{Naph-TDA}})(\text{NCBH}_3)_2] \cdot 0.9 \text{ DCM}$. The influence of the crystallization solvent is evident in the observed isomerization effect: acetonitrile yields the facial coordination isomer, while a layered mixture of dichloromethane and methanol produces the meridional isomer. Variable-temperature *SQUID* measurements reveal a shift in spin crossover behavior between the two solvatomorphs, attributable to both the coordination mode and the distinct packing arrangements determined by single-crystal XRD analysis. Notably, **C1** exhibits an asymmetric hysteresis, which is attributed to the rotation of stacked naphthyl units. Further investigation into the sensitive equilibrium between these isomers will be the focus of future research.

Experimental:

All chemicals were purchased from Alfa Aesar, Deutero, Fisher Chemicals, TCI, Sigma-Aldrich, and Acros Organics and used without further purification. Solvents were dried according to the literature known procedures and used freshly distilled.^[37] NMR spectra were recorded at room temperature with a Bruker Avance DSX 400 and analyzed with the program MestReNova.^[38] Magnetic susceptibility measurements were performed on a Quantum Design SQUID magnetometer MPMSXL in a temperature range between 5 and 300 K with an applied field of 1 kOe. All mass spectra (Advion expression-L CMS) as well as elemental analysis (Elementar vario EL Cube: C, H, and N) were measured at the microanalytical laboratories of the Johannes Gutenberg University Mainz. X-ray diffraction data were collected with STOE STADIVARI at the Johannes Gutenberg University Mainz. The structures were solved with ShelXT^[39] and refined with ShelXL^[40,41] implemented in the program Olex2.^[42] UV-Vis-Absorption-spectroscopy was performed using the JASCO V-770 in a single beam mode with a scanning speed of 400 nm/min was used. The data was plotted using Origin 7.5 V5. The ATR-IR spectra was recorded at room temperature on a Bruker ALPHAII ATR-IR, analysed with the software OPUS and plotted in Origin 7.5 V5. The conductivity measurements were performed for the samples in acetonitrile using a *SevenCompact™ S230* conductivity meter. The arithmetic mean of three measurements was used for the calculation of the molar conductivity.

Ligand synthesis:

The Synthesis of 1-(5-(naphthalen-2-yl)-1,3,4-thiadiazol-2-yl)-N,N-bis(pyridin-2-ylmethyl)methanamine of **L^{Naph-TDA}** was done similar to the reported.^[9]

2-Naphthohydrazide

2-Naphthohydrazide was prepared based on previously reported literature.^[18,43] **Naphthoicacid** (20.00 g, 116.20 mmol, 1.0 eq.) was dissolved in 300 mL ethanol and sulfuricacid (4 mL, conc.) was added. The solution was refluxed over 24 hours at 90°C. The solvent was removed under reduced pressure and the residue was dissolved in 300 mL dichloromethane. The organic phase was washed three times with 100 mL sodium bicarbonate (5%), the dried over magnesium sulfate and the solution was concentrated under reduced pressure. The residue was dissolved in 100 mL methanol, hydrazine hydrate (6.31 mL, 127,80 mmol, 1.1 eq.) was added to the solution and the solution was refluxed over 24 hours at 75°C. While cooling down the solution beige solid was obtained and separated by filtration. The resulted beige solid was washed three times with 30 mL cold methanol and with 30 mL n-pentane to yield 2-Naphthohydrazide (18.60 g, 99.89 mmol, 86%). ¹H-NMR (400 MHz, DMSO-*d*₆ δ(ppm)) 9.96 (s, 1H), 8.44 (d, *J* = 1.7 Hz, 1H), 8.04 – 7.89 (m, 5H), 7.65 – 7.54 (m, 2H), 4.61 (s, 2H).

Bis(pyridine-2-yl)glycine (I)

The synthesis procedure was of **Bis(pyridine-2-yl)glycine (I)** was reported by Levadala et al.^[44]

Glycine (3.00 g, 79.93 mmol, 1.0 eq.) was suspended in 80 mL DCM under nitrogen atmosphere. Under cooling with ice sodium trisacetoxyborohydride (21.18 g, 99.91 mmol, 2.5 eq.) was added and stirred. After 10 minutes a solution of 2-Pyridinecarbaldehyd (7.60 mL, 79.93 mmol, 2.0 eq.) in 20 mL dichloromethane was added. The cooling was replaced, and the yellowish suspension was allowed to warm up overnight. 70 ml saturated sodium bicarbonate solution was added and after 30 minutes the two phases were extracted, and the aqueous phase was extracted twice with 150 mL DCM. The organic phase was dried over sodium sulphate and the solvent was removed under reduced pressure. The crude product was purified via column chromatography (dichloromethane: methanol; 90:10). The product was isolated as brown powder (3.113 g, 12.10 mmol, 30 %). ¹H-NMR (400 MHz, Chloroform-*d* δ (ppm)): 8.59 – 8.53 (m, 2H), 7.67 (td, *J* = 7.7, 1.8 Hz, 1H), 7.33 – 7.29 (m, 1H), 7.23 (ddd, *J* = 7.6, 4.9, 1.2 Hz, 1H), 4.11 (s, 2H), 3.61 (s, 1H).

1-(5-(naphthalen-2-yl)-1,3,4-thiadiazol-2-yl)-N,N-bis(pyridin-2-ylmethyl)methanamine (L**^{Naph-TDA})**

Bis(pyridin-2-ylmethyl)glycine (**I**) (5.260 g, 20.44 mmol, 1 eq.) was dissolved under nitrogen atmosphere in dry dichloromethane and the solution was cooled with ice. Carbonyldiimidazole (3.708 g, 22.87 mmol, 1.1 eq.) was added and the clear solution was stirred under cooling for 30 minutes. Naphthohydrazide (3.807 g, 20.44 mmol, 1 eq.) was added and the suspension was allowed to warm up and stirred over the night. Then the solvent was evaporated under vacuum, and the residue was dissolved in dry tetrahydrofuran under nitrogen atmosphere. To the clear brown solution Lawesson's reagent was added (9.907 g, 24.53 mmol, 1.2 eq.) the resulting reddish-brown solution was heated under reflux at 80 °C over night. Then the solvent was removed under vacuum, and the residue was dissolved in 400 mL dichloromethane. The organic phase was washed three times with saturated sodiumbicarbonate solution and dried over sodium sulfate. The desired product 1-(5-(naphthalen-2-yl)-1,3,4-thiadiazol-2-yl)-N,N-bis(pyridin-2-ylmethyl)methanamine (**L**^{Naph-TDA}) (3.566 g, 8.43 mmol, 41%) was obtained after purification with flash chromatography as brown solid in moderate yields. ¹H NMR (400 MHz, Chloroform-*d* δ (ppm)): 8.59 (ddd, *J* = 4.9, 1.8, 0.9 Hz, 2H), 8.42 (d, *J* = 1.8 Hz, 1H), 8.12 (dd, *J* = 8.6, 1.8 Hz, 1H), 7.97 – 7.85 (m, 3H), 7.73 (td, *J* = 7.7, 1.8 Hz, 2H), 7.60 (dt, *J* = 7.9, 1.1 Hz, 2H), 7.58 – 7.53 (m, 2H), 7.21 (ddd, *J* = 7.5, 4.9, 1.2 Hz, 2H), 4.25 (s, 2H), 4.00 (s, 4H). ¹³C-NMR (101 MHz, CDCl₃, δ (ppm)): 158, 149, 137, 134, 133, 129, 128, 1278, 128 (d, *J* = 10.3 Hz), 127, 124, 123, 122, 59, 53. FT-IR: $\tilde{\nu}$ (cm⁻¹) = 3045, 3009, 2960, 2929, 2880, 2837, 1680, 1586, 1567, 1510, 1473, 1431, 1416, 1347, 1321, 1302, 1283, 1242, 1216, 1192, 1175, 1147, 1131, 1112, 1071, 1047, 992, 977, 937, 908, 871, 857, 842, 813, 770, 760, 743, 680, 653, 629, 606, 585, 565, 519, 481, 405. ESI-MS (*m/z*): calc.

for $[\text{C}_{25}\text{H}_{21}\text{N}_5\text{S}_1]^+$ expected: 424.159 (100.00 %); found: 424.160 (100.00 %). Elemental analysis calculated for $\text{L}^{\text{Naph-TDA}} \cdot 0.5 \text{H}_2\text{O}$ ($\text{C}_{25}\text{H}_{26}\text{N}_5\text{O}_{0.5}\text{S}$): C, 63.71; H, 4.08; N, 16.36. found: C, 69.70; H, 4.81; N, 15.90.

Complex synthesis:

$[\text{Fe}(\text{L}^{\text{Naph-TDA}})(\text{NCBH}_3)_2] \cdot 0.5 \text{H}_2\text{O}$ (C1)

The following reaction was carried out in a glovebox under an inert atmosphere. $[\text{Fe}(\text{py})_4(\text{NCBH}_3)_2]$ (109 mg, 0.24 mmol, 1 eq.) was dissolved in acetonitrile (8 ml) and stirred for 30 minutes. The solution was filtered with a syringe filter, to remove undissolved particles. The filtrate was added to a solution of 1-(5-(naphthalen-2-yl)-1,3,4-thiadiazol-2-yl)-N,N-bis(pyridin-2-ylmethyl)methanamine ($\text{L}^{\text{Naph-TDA}}$) (100 mg, 0.24 mmol, 1 eq.) in 1 mL acetonitrile. The solution was stirred for 30 minutes again and filtered in an empty vial using a syringe filter. The solution was kept undisturbed and set for slow evaporation of the solvent. After four days brown block shaped crystals had formed that were suitable for X-ray structure analysis. The crystals were collected by filtration dried at atmospheric pressure to afford $[\text{Fe}(\text{L}^{\text{Naph-TDA}})(\text{NCBH}_3)_2] \cdot 0.5 \text{H}_2\text{O}$ (101.00 mg, 0.181 mmol, 77%) at high yields. FT-IR: $\tilde{\nu}$ (cm^{-1}) = 3053, 2336, 2184, 1603, 1571, 1479, 1439, 1369, 1356, 1319, 1289, 1266, 1191, 1191, 1191, 1156, 1117, 1096, 1054, 1054, 1017, 995, 976, 958, 938, 897, 884, 863, 820, 796, 767, 752, 704, 652, 615, 560, 513, 475, 425, 410. ESI-MS (m/z): calc. for $[\text{C}_{26}\text{H}_{21}\text{FeN}_6\text{S}]^+$ expected: 505.089 (100.00 %); found: 505.089 (100.00 %). Elemental analysis calculated for $[\text{Fe}(\text{L}^{\text{Naph-TDA}})(\text{NCBH}_3)_2] \cdot 0.5 \text{H}_2\text{O}$ ($\text{C}_{27}\text{H}_{28}\text{N}_7\text{B}_2\text{FeO}_{0.5}\text{S}$): C, 57.09; H, 4.97; N, 17.26. found: C, 56.72; H, 5.09; N, 17.16.

$[\text{Fe}(\text{L}^{\text{Naph-TDA}})(\text{NCBH}_3)_2] \cdot 0.9 \text{DCM}$ (C2)

The following reaction was carried out in a glovebox under an inert atmosphere. $[\text{Fe}(\text{py})_4(\text{NCBH}_3)_2]$ (109 mg, 0.24 mmol, 1 eq.) was dissolved in 5 mL dry methanol and stirred for 30 Minutes results in a red solution. The solution was filtered using a syringe filter, to remove undissolved particles. The filtrate was layered above a spacer solution of 1:1 dichloromethane and methanol, which was layered on a solution of ($\text{L}^{\text{Naph-TDA}}$) (100 mg, 0.24 mmol, 1 eq.) in 5 mL dichloromethane. Crystals suitable for X-ray structure analysis were obtained after six days out of the reddish solution The crystals were collected by filtration dried at atmospheric pressure to afford $[\text{Fe}(\text{L}^{\text{Naph-TDA}})(\text{NCBH}_3)_2] \cdot 0.9 \text{DCM}$ (65.00 mg, 0.107 mmol, 45 %). FT-IR: $\tilde{\nu}$ (cm^{-1}) = 2916, 2337, 2179, 1603, 1571, 1478, 1440, 1349, 1305, 1283, 1217, 1192, 1155, 1110, 1049, 1019, 996, 956, 938, 897, 862, 821, 789, 758, 731, 705, 657, 642, 473, 421. ESI-MS (m/z): calc. for $[\text{C}_{26}\text{H}_{21}\text{FeN}_6\text{S}]^+$ expected: 505,089 (100.00 %); found: 505.089 (100.00 %). Elemental analysis calculated for $[\text{Fe}(\text{L}^{\text{Tetra-ODA}})(\text{NCBH}_3)_2] \cdot 0.9 \text{CH}_2\text{Cl}_2$ ($\text{C}_{28}\text{H}_{28.8}\text{N}_7\text{B}_2\text{FeSCl}_{1.8}$): C, 52.73; H, 4.57; N, 15.43. found: C, 52.53; H,4.73; N,15.62.

References:

- [1] G. Li, O. Stefanczyk, K. Kumar, L. Guérin, K. Okuzono, K. Tran, M. Seydi Kilic, K. Nakabayashi, K. Imoto, A. Namai, Y. Nakamura, S. Ranjan Maity, F. Renz, G. Chastanet, S. Ohkoshi, *Angew. Chem. Int. Ed.* **2025**, *64*, e202423095.
- [2] K. Lünser, E. Kavak, K. Gürpınar, B. Emre, O. Atakol, E. Stern-Taulats, M. Porta, A. Planes, P. Lloveras, J.-L. Tamarit, L. Mañosa, *Nat Commun.* **2024**, *15*, 6171.
- [3] A. Dürrmann, G. Hörner, D. Baabe, F. W. Heinemann, M. A. C. De Melo, B. Weber, *Nat Commun.* **2024**, *15*, 7321.
- [4] T. Charytanowicz, J. Wang, H. Tokoro, K. Tran, F. Renz, S. Ohkoshi, S. Chorazy, B. Sieklucka, *Angew. Chem.* **2025**, *137*, e202419242.
- [5] K. S. Woo, A. Zhang, A. Arabelo, T. D. Brown, M. Park, A. A. Talin, E. J. Fuller, R. S. Bisht, X. Qian, R. Arroyave, S. Ramanathan, L. Thomas, R. S. Williams, S. Kumar, *Nat Commun* **2024**, *15*, 4656.
- [6] F. Fiaz, A. Siddique, M. F. Rabbee, M. B. Hanif, S. M. Al-Baqami, S. M. S. Jillani, N. S. Almuqati, Md. R. Rahman, M. A. Chowdhury, M. N. Akhtar, M. M. R. Khan, M. M. Rahman, T. A. Sheikh, *Rev. Inorg. Chem.* **2025**,
- [7] Y. Zhang, R. Torres-Cavanillas, X. Yan, Y. Zeng, M. Jiang, M. Clemente-León, E. Coronado, S. Shi, *Chem. Soc. Rev.* **2024**, *53*, 8764–8789.
- [8] Y. Zhang, A. Rotaru, T. Ranquet, X. Yang, Y. Zan, B. Reig, I. Séguy, L. Salmon, G. Molnár, A. Bousseksou, *J. Mater. Chem. C* **2025**, *13*, 18905–18912.
- [9] J.-G. Becker, S. Sundaresan, Luca. M. Carrella, E. Rentschler, *Chem. Commun.* **2025**, *61*(71), 13389-13392.
- [10] T.-T. Ma, X.-P. Sun, Z.-S. Yao, J. Tao, *Inorg. Chem. Front.* **2020**, *7*, 1196–1204.
- [11] R. Mahbub, K. A. McElveen, M. Z. Zaz, T. K. Ekanayaka, E. Mishra, E. Bissell, P. Banerjee, D. Shapiro, R. Y. Lai, P. A. Dowben, J. E. Shield, *J. Phys.: Condens. Matter* **2025**, *37*, 085302.
- [12] J. Kiehl, T. Hochdörffer, L. M. Carrella, V. Schünemann, M. H. Nygaard, J. Overgaard, E. Rentschler, *Inorg. Chem.* **2022**, *61*, 3141–3151.
- [13] Y. P. Petrenko, J. Troya, V. García-López, D. M. Khomenko, R. O. Doroshchuk, R. D. Lampeka, M. Clemente-León, E. Coronado, *Inorg. Chem.* **2025**, *64*, 6442–6451.
- [14] S. L. Dabb, N. C. Fletcher, *Dalton Trans.* **2015**, *44*, 4406–4422.
- [15] T. Morozumi, R. Matsuoka, T. Nakamura, T. Nabeshima, *Chem. Sci.* **2021**, *12*, 7720–7726.
- [16] X.-H. Zhao, Y.-F. Deng, J.-Q. Huang, M. Liu, Y.-Z. Zhang, *Inorg. Chem. Front.* **2024**, *11*, 808–816.
- [17] E. Cuza, S. Benmansour, N. Cosquer, F. Conan, S. Pillet, C. J. Gómez-García, S. Triki, *Magnetochemistry* **2020**, *6*, 26.
- [18] S. Sundaresan, J.-G. Becker, J. Eppelsheimer, A. E. Sedykh, L. M. Carrella, K. Müller-Buschbaum, E. Rentschler, *Dalton Trans.* **2023**, *52*, 13181–13189.
-

- [19] J. Zhou, B.-W. Zhu, J. Luan, Z. Liu, J.-K. Fang, X. Bao, G. Peng, J. Tucek, S.-S. Bao, L.-M. Zheng, *Dalton Trans.* **2015**, *44*, 20551–20561.
- [20] J.-G. Becker, J. F. Nüsing, S. Sundaresan, R. Diego, M. Mondeshki, L. M. Carrella, E. Rentschler, *Cryst. Growth Des.* **2024**, *24*, 7662–7669.
- [21] S. Kisslinger, H. Kelm, S. Zheng, A. Beitat, C. Würtele, R. Wortmann, S. Bonnet, S. Herres-Pawlis, H. Krüger, S. Schindler, *Z. Anorg. Allg. Chem.* **2012**, *638*, 2069–2077.
- [22] G. S. Matouzenko, D. Luneau, G. Molnár, N. Ould-Moussa, S. Zein, S. A. Borshch, A. Bousseksou, F. Averseng, *Eur. J. Inorg. Chem.* **2006**, *2006*, 2671–2682.
- [23] G. S. Matouzenko, E. Jeanneau, A. Yu. Verat, A. Bousseksou, *Dalton Trans.* **2011**, *40*, 9608.
- [24] S. Sundaresan, J. Eppelsheimer, E. Gera, L. Wiener, L. M. Carrella, K. R. Vignesh, E. Rentschler, *Dalton Trans.* **2024**, *53*, 10303–10317.
- [25] M. A. Halcrow, *Chem. Soc. Rev.* **2011**, *40*, 4119.
- [26] S. Yuan, N. Natt, B. J. Powell, *Inorg. Chem.* **2025**, *64*, 7182–7193.
- [27] H. L. C. Feltham, C. Johnson, A. B. S. Elliott, K. C. Gordon, M. Albrecht, S. Brooker, *Inorg. Chem.* **2015**, *54*, 2902–2909.
- [28] S. Rodríguez-Jiménez, A. S. Barltrop, N. G. White, H. L. C. Feltham, S. Brooker, *Inorg. Chem.* **2018**, *57*, 6266–6282.
- [29] A. Banerjee, A. Saha, B. K. Saha, *Crystal Growth & Design* **2019**, *19*, 2245–2252.
- [30] X. Zhao, Y. Deng, J. Xi, J. Huang, Y. Zhang, *Angew. Chem.* **2025**, *137*, e202414826.
- [31] P. Gütllich, A. Hauser, H. Spiering, *Angew. Chem. Int. Ed. Engl.* **1994**, *33*, 2024–2054.
- [32] M. Fumanal, F. Jiménez-Grávalos, J. Ribas-Arino, S. Vela, *Inorg. Chem.* **2017**, *56*, 4474–4483.
- [33] W. Phonsri, P. Harding, L. Liu, S. G. Telfer, K. S. Murray, B. Moubaraki, T. M. Ross, G. N. L. Jameson, D. J. Harding, *Chem. Sci.* **2017**, *8*, 3949–3959.
- [34] S. De, S. Tewary, D. Garnier, Y. Li, G. Gontard, L. Lisnard, A. Flambard, F. Breher, M. Boillot, G. Rajaraman, R. Lescouëzec, *Eur. J. Inorg. Chem.* **2018**, *2018*, 414–428.
- [35] N. Ortega-Villar, A. L. Thompson, M. C. Muñoz, V. M. Ugalde-Saldívar, A. E. Goeta, R. Moreno-Esparza, J. A. Real, *Chem. Eur. J.* **2005**, *11*, 5721–5734.
- [36] S. Alvarez, *Chem. Eur. J.* **2020**, *26*, 4350–4377.
- [37] W. L. F. Armarego, Butterworth-Heinemann, Amsterdam, **2017**.
- [38] J. C. Cobas, F. J. Sardina, *Concepts Magnetic Resonance* **2003**, *19A*, 80–96.
- [39] G. M. Sheldrick, *Acta Crystallogr. A. Found. Adv.* **2015**, *71*, 3–8.
- [40] G. M. Sheldrick, *Acta Crystallogr. A. Found. Crystallogr.* **2008**, *64*, 112–122.
- [41] G. M. Sheldrick, T. R. Schneider, Elsevier, **1997**, pp. 319–343.
- [42] O. V. Dolomanov, L. J. Bourhis, R. J. Gildea, J. A. K. Howard, H. Puschmann, *J. Appl. Crystallogr.* **2009**, *42*, 339–341.

- [43] S. Sundaresan, J. Kiehl, L. M. Carrella, E. Rentschler, *Crystal Growth & Design* **2023**, *23*, 1648–1655.
- [44] Sm. K. Levadala, S. R. Banerjee, K. P. Maresca, J. W. Babich, J. Zubieta, *Synthesis* **2004**, *11*, 1759-1766

ESI: Lattice Solvent as a Structural Switch: *Mer-Fac* Isomerism and Spin Crossover in Fe(II) complexes based on 1,3,4-Thiadiazole

Jens-Georg Becker,¹ Sriram Sundaresan,² Luca M. Carrella,¹ and Eva Rentschler^{1*}

¹Department Chemie, Johannes-Gutenberg-Universität Mainz, Duesbergweg 10–14, 55128 Mainz, Germany.

Email: rentschl@uni-mainz.de

²Institute of Physics, Czech Academy of Sciences, Cukrovarnická 10, 162 00 Prague, Czech Republic.

Table of Contents

1. NMR-Spectra:	336
2. IR-spectra:.....	339
3. Mass spectra:.....	341
4. Crystolographic Data	344
5. Temperature dependent magnetization measurement	364
6. UV-Vis Absorption spectroscopy in solution	366

1. NMR-Spectra:

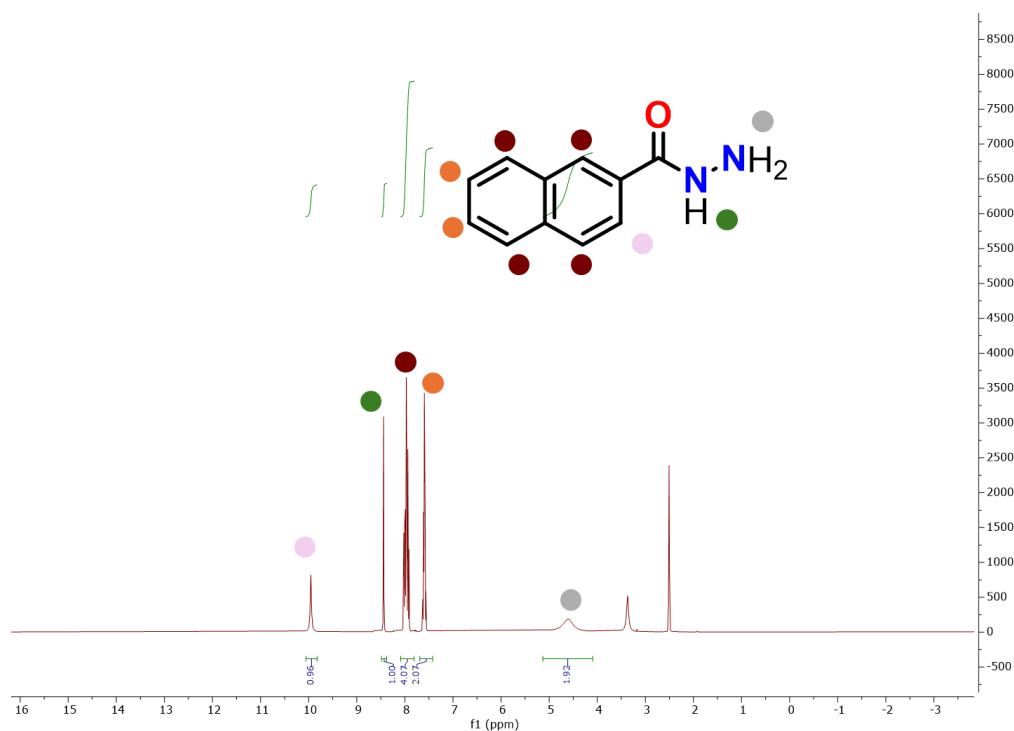


Figure S1: ¹H-NMR spectrum of the Naphthoichydrazide in DMSO [400 MHz]. The peak at 3.49 can be assigned to methanol and the peak at 1.44 could be assigned to water.^[1]

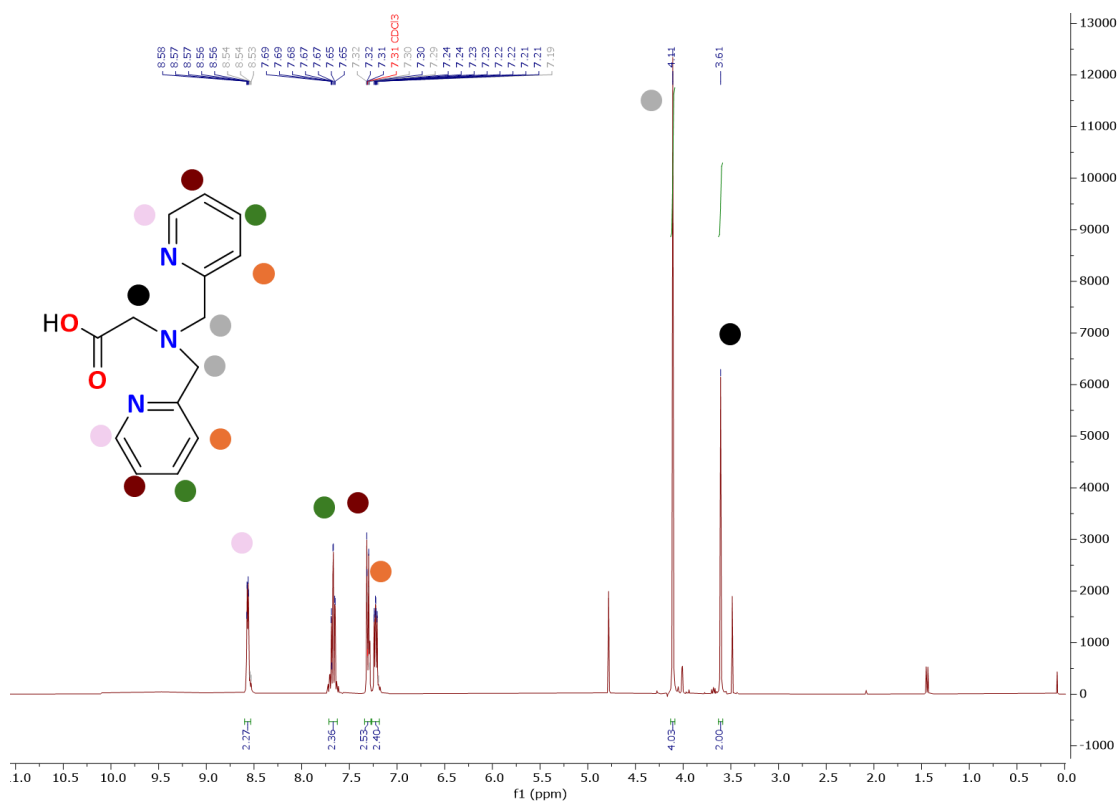


Figure S2: ¹H-NMR spectrum of the tert-butyl bis(pyridin-2-ylmethyl)glycine (**2.1**) in CDCl₃ [400 MHz]. The peak at 4.78 ppm could be assigned to impurity, which could be dichloromethane. The peak at 3.49 can be assigned to methanol and the peak at 1.44 could be assigned to water.^[1]

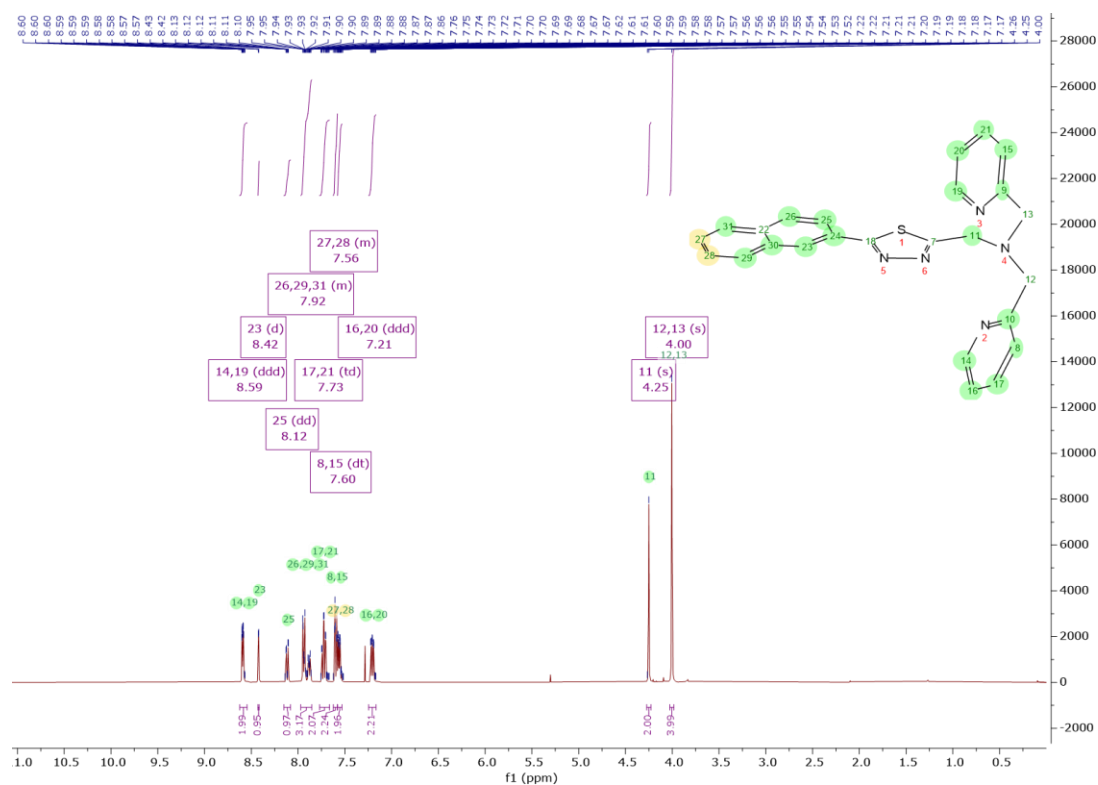
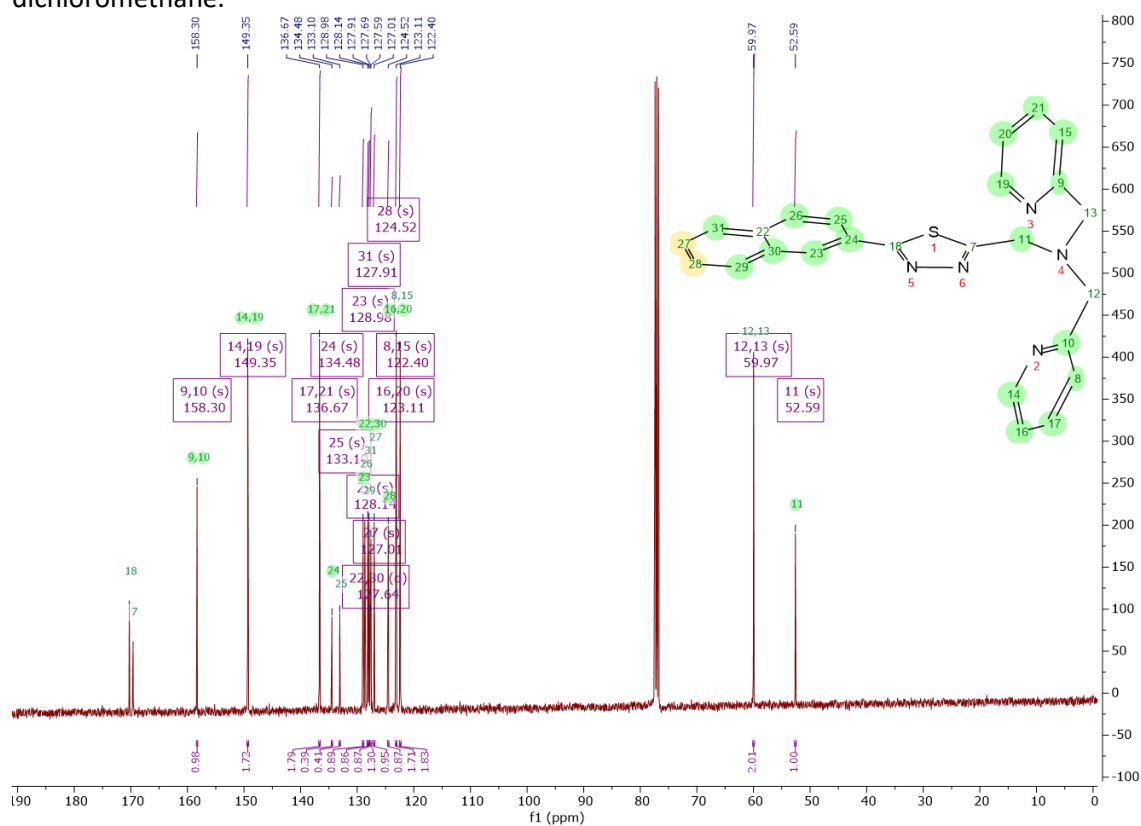


Figure S3: $^1\text{H-NMR}$ spectrum of the 1-(5-(naphthalen-2-yl)-1,3,4-thiadiazol-2-yl)-N,N-bis(pyridin-2-ylmethyl)methanamine ($\text{L}^{\text{Naph-TDA}}$) in CDCl_3 [400 MHz]. The peak at 5.31 ppm could be assigned to dichloromethane.^[1]



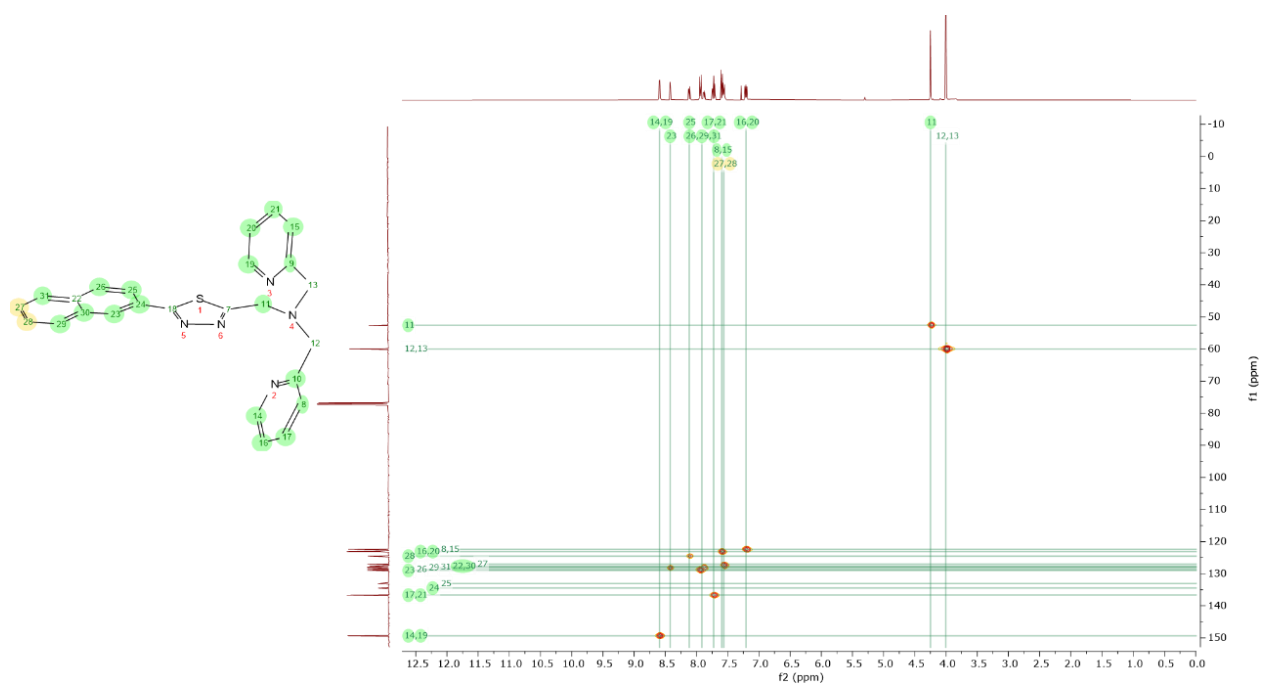


Figure S5: HSQC-NMR spectrum of ligand $L^{\text{Naph-TDA}}$ measured in CDCl_3 .

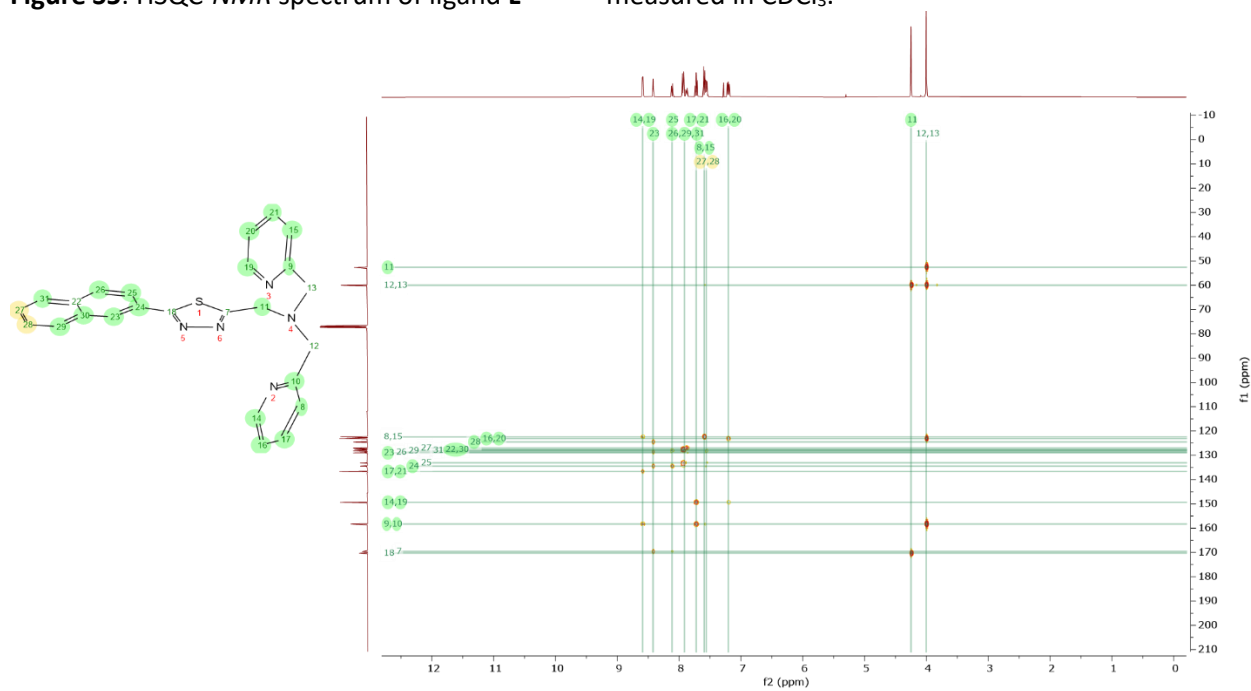


Figure S6: HMBC-NMR spectrum of ligand $L^{\text{Naph-TDA}}$ measured in CDCl_3 .

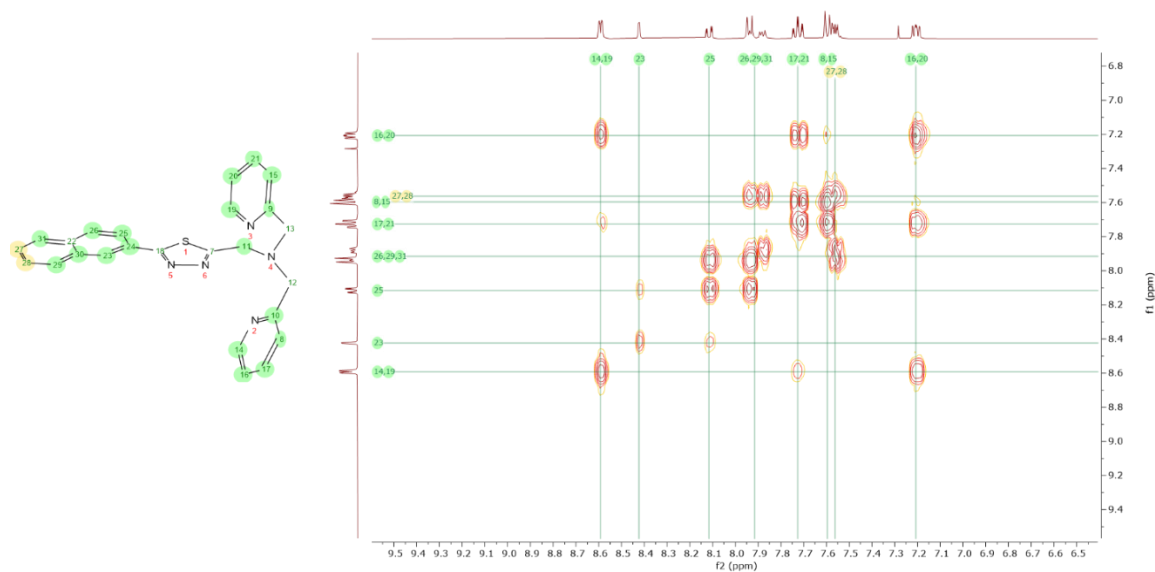


Figure S7: COSY-NMR spectrum of ligand $L^{\text{Naph-TDA}}$ measured in CDCl_3 [400 MHz].

2. IR-spectra:

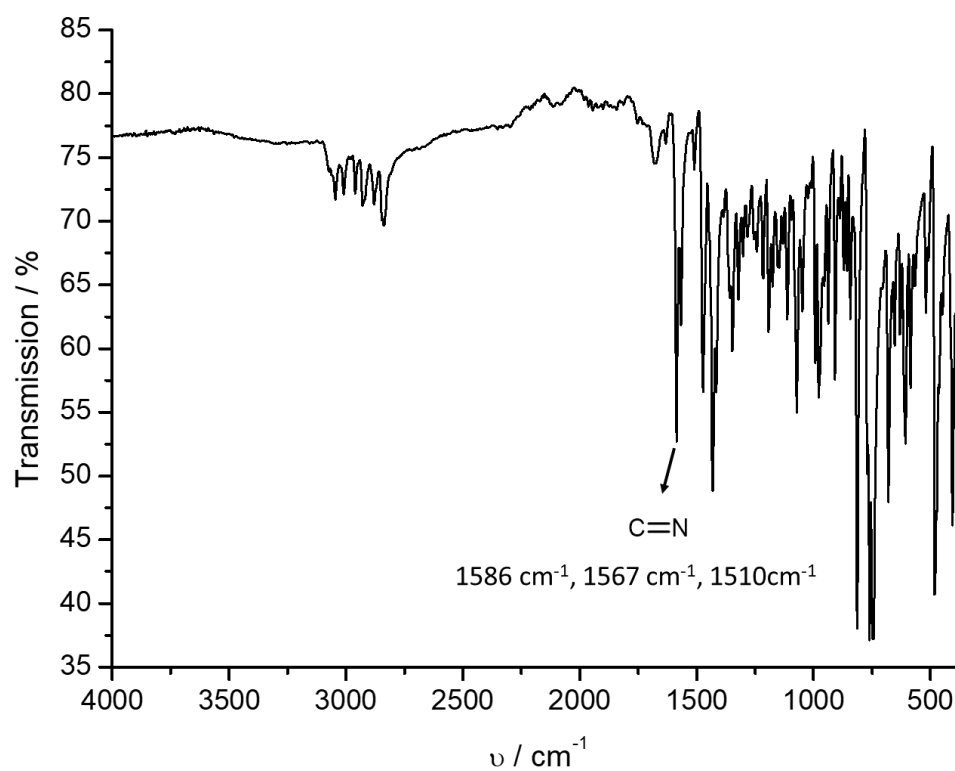


Figure S8: IR spectra of the final Ligand $L^{\text{Naph-TDA}}$.

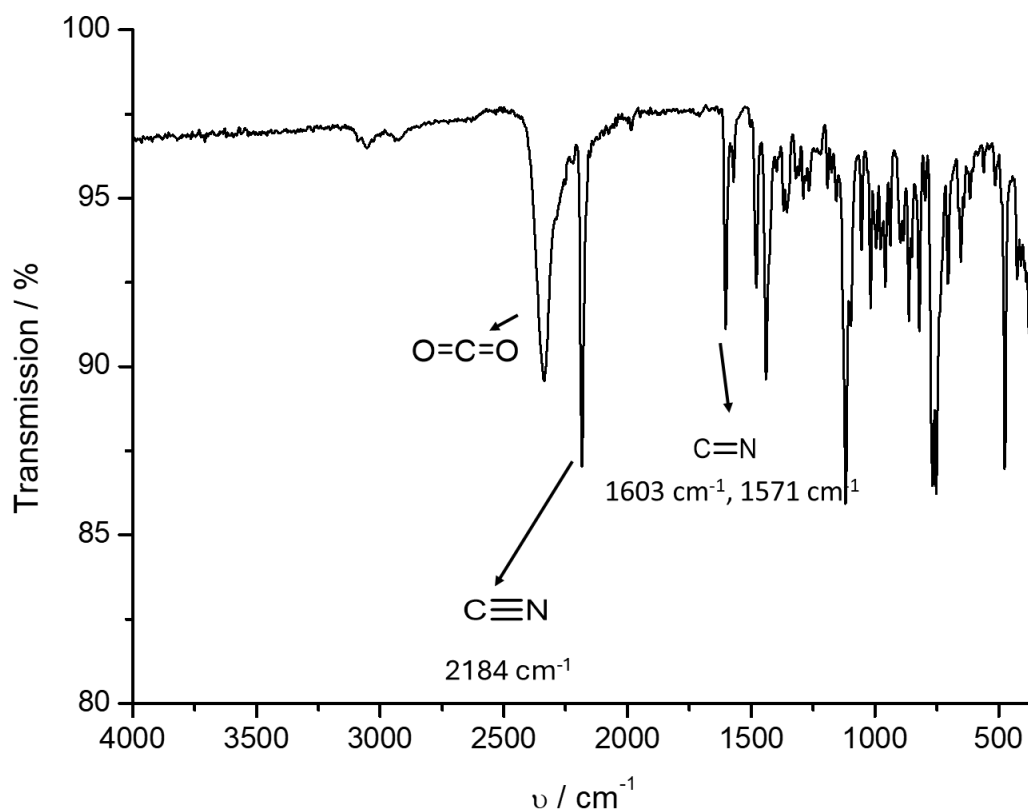


Figure S9: IR spectrum of $[\text{Fe}(\text{L}^{\text{Naph-TDA}})(\text{NCBH}_3)_2] \cdot 0.5 \text{H}_2\text{O}$ (**C1**).

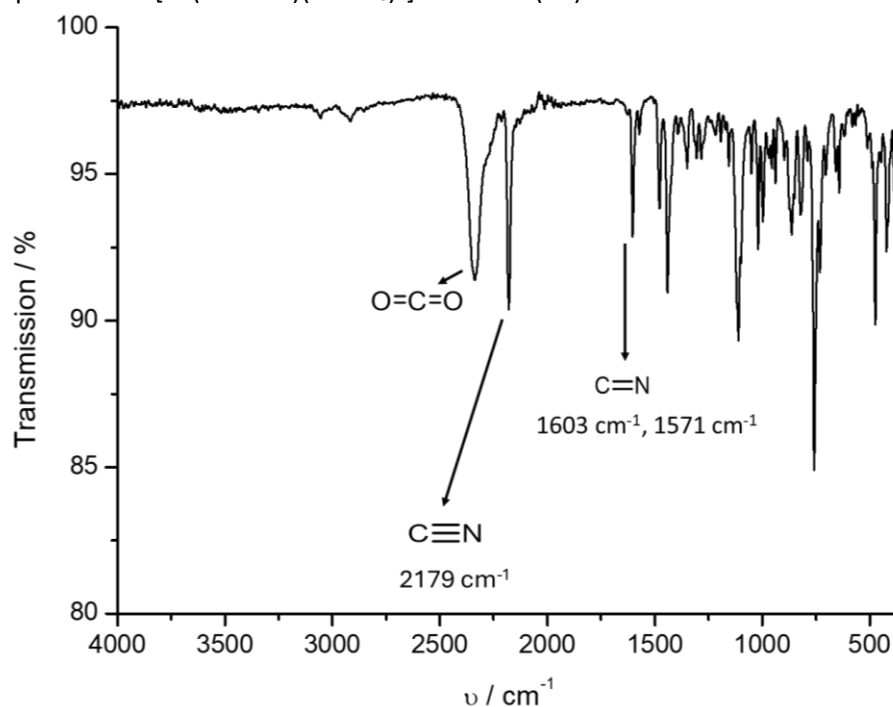


Figure S10: IR spectrum of $[\text{Fe}(\text{L}^{\text{Naph-TDA}})(\text{NCBH}_3)_2] \cdot 0.9 \text{DCM}$ (**C2**).

3. ESI-Mass spectrometry

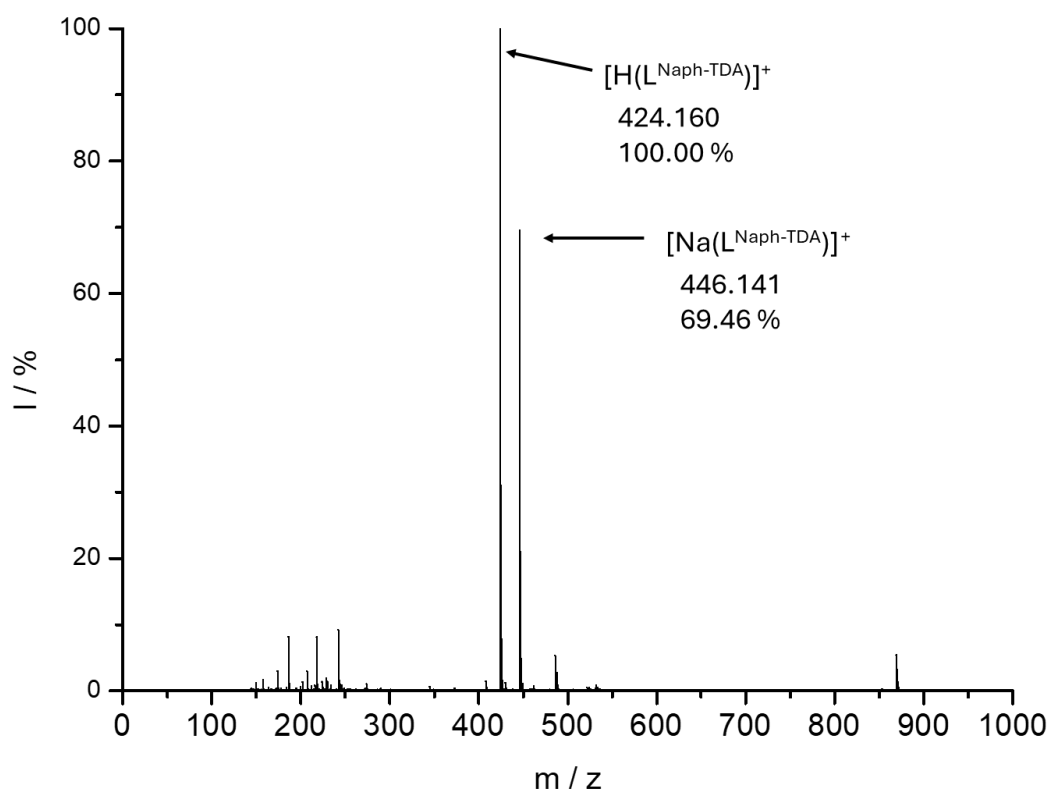


Figure S11: Mass spectrum (ESI positive) of the Ligand ($L^{\text{Naph-TDA}}$).

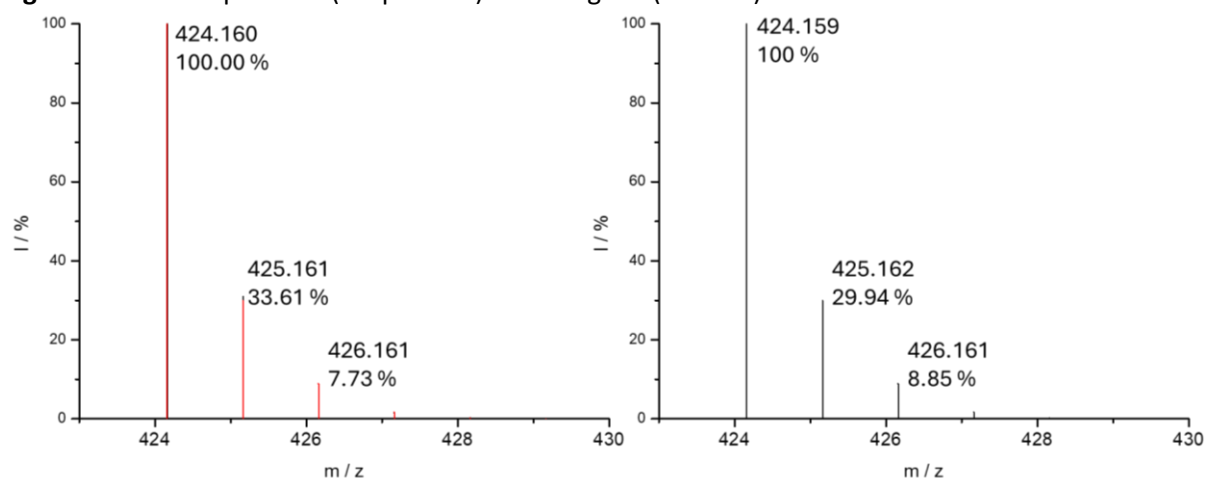


Figure S12: Isotopic pattern of ESI mass spectra of $L^{\text{Naph-TDA}}$ measured (left with red overlap of the isotopic pattern) predicted (right).

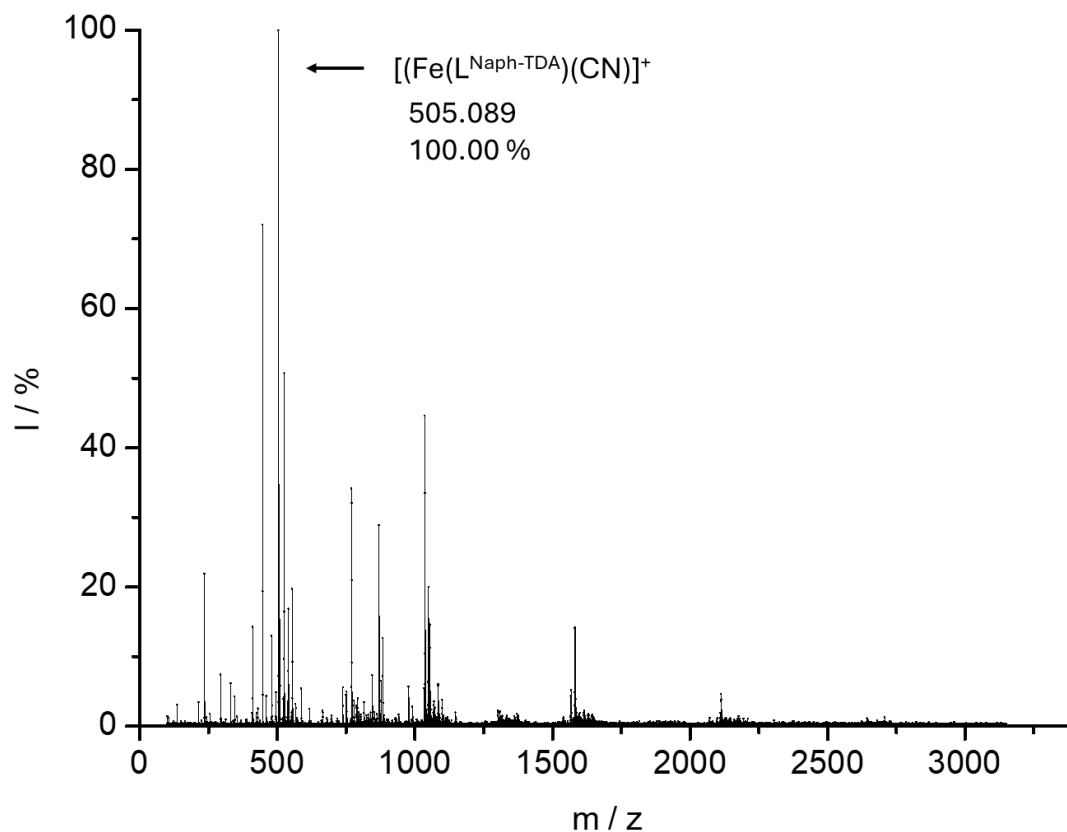


Figure S13: Mass spectrum (*ESI* positive) of the Complex $[\text{Fe}(\text{L}^{\text{Naph-TDA}})(\text{NCBH}_3)_2] \cdot 0.5 \text{H}_2\text{O}$ (**C1**).

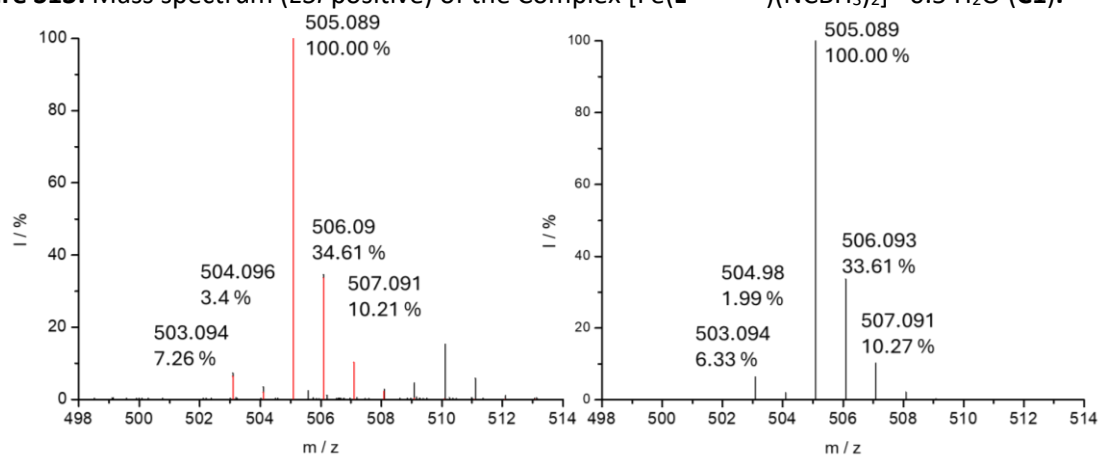


Figure S14: Isotopic pattern of *ESI* mass spectra of $[\text{Fe}(\text{L}^{\text{Naph-TDA}})(\text{NCBH}_3)_2] \cdot 0.5 \text{H}_2\text{O}$ (**C1**) measured (left with red overlap of the isotopic pattern) predicted (right).

4. Crystallographic Data

4.1. Packing description of $[\text{Fe}(\text{L}^{\text{Naph-TDA}})(\text{NCBH}_3)_2] \cdot 0.5 \text{H}_2\text{O}$ (**C1**)

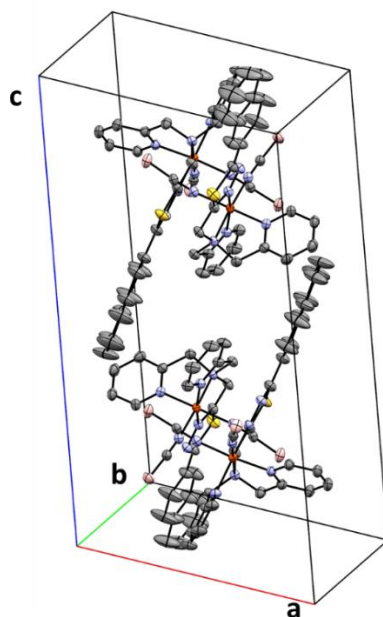


Figure S17: Unit cell of $[\text{Fe}(\text{L}^{\text{Naph-TDA}})(\text{NCBH}_3)_2] \cdot 0.5 \text{H}_2\text{O}$ (**C1**) at 120 K. Solvent molecules and Hydrogen atoms were removed for better overview.

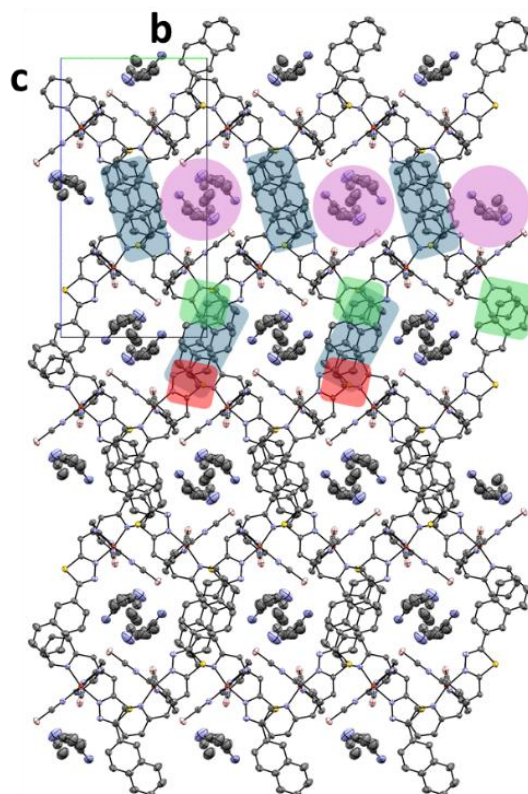


Figure S18: Visualisation of the packing for $[\text{Fe}(\text{L}^{\text{Naph-TDA}})(\text{NCBH}_3)_2] \cdot 0.5 \text{H}_2\text{O}$ (**C1**) along a-axis at 120 K. **Pink:** solvent channel; **Red** and **Green:** interaction due to Pyridine-Naphthyl- and 1,3,4-Thiadiazole-Naphthyl-Stacking; **Blue:** Naphthyl-Naphthyl-Stacking. Hydrogen atoms were removed for better overview.

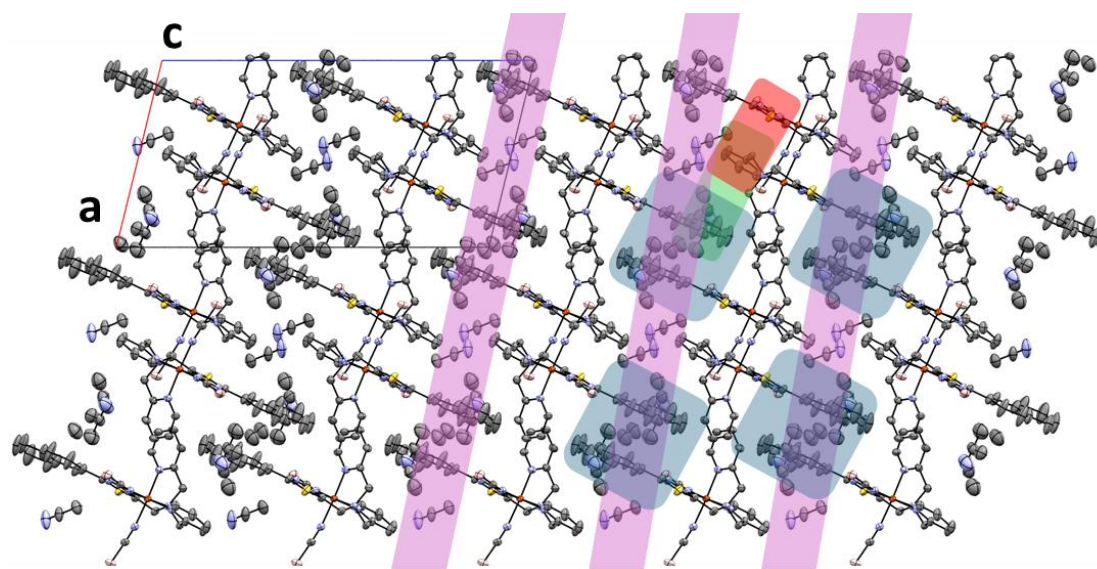


Figure S19: Visualisation of the packing for $[\text{Fe}(\text{L}^{\text{Naph-TDA}})(\text{NCBH}_3)_2] \cdot 0.5 \text{H}_2\text{O}$ (**C1**) along b-axis at 120 K. **Pinc:** solvent channel; **Red:** 1,3,4-Thiadiazole-Pyridine-interaction; **Green:** Naphthyl-Pyridine-interaction; **Blue:** Naphthyl-Naphthyl-interaction. Hydrogen atoms were removed for better overview.

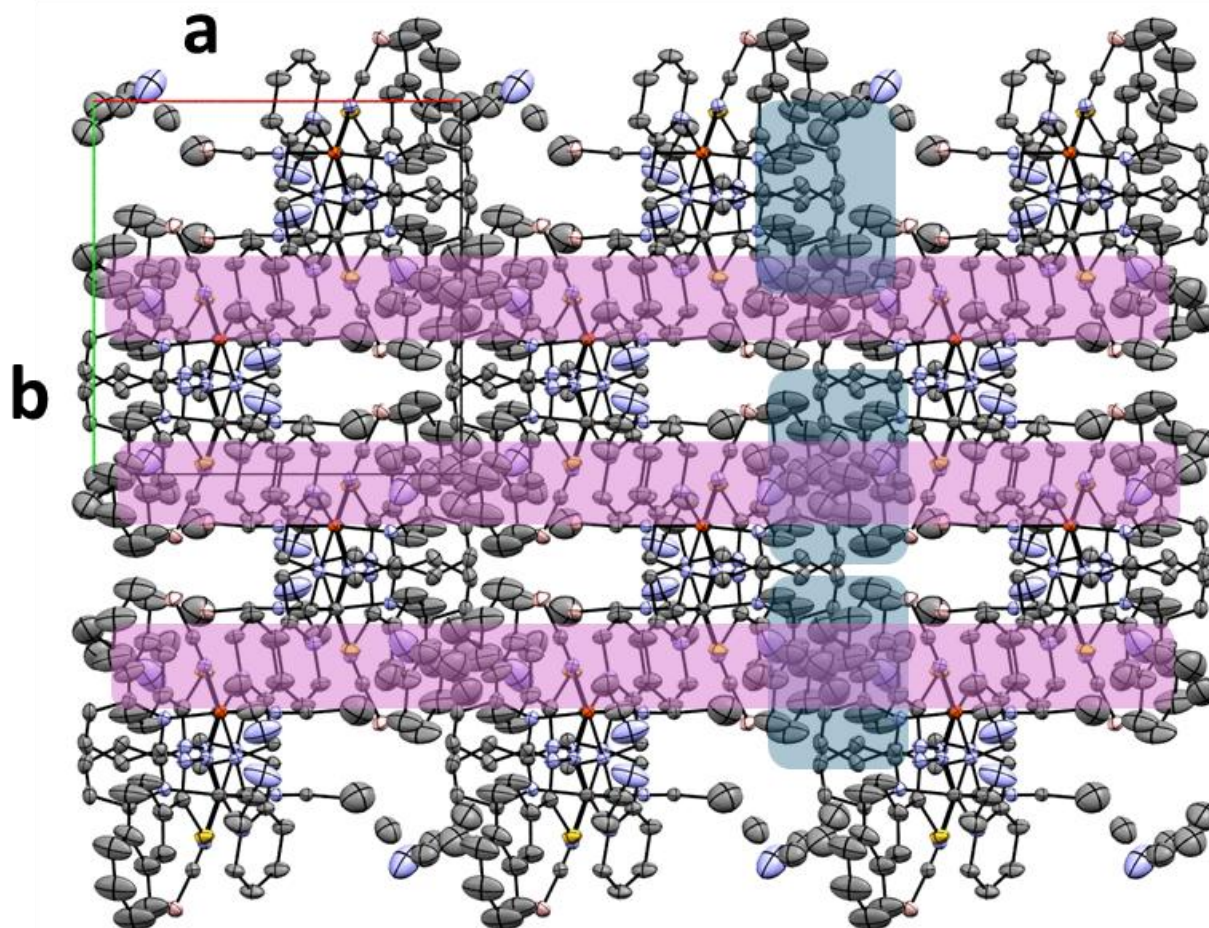


Figure S20: Visualisation of the packing for $[\text{Fe}(\text{L}^{\text{Naph-TDA}})(\text{NCBH}_3)_2] \cdot 0.5 \text{H}_2\text{O}$ (**C1**) along c-axis at 120 K. **Pinc:** solvent channel; **Blue:** Naphthyl-Naphthyl-interaction. Hydrogen atoms were removed for better overview.

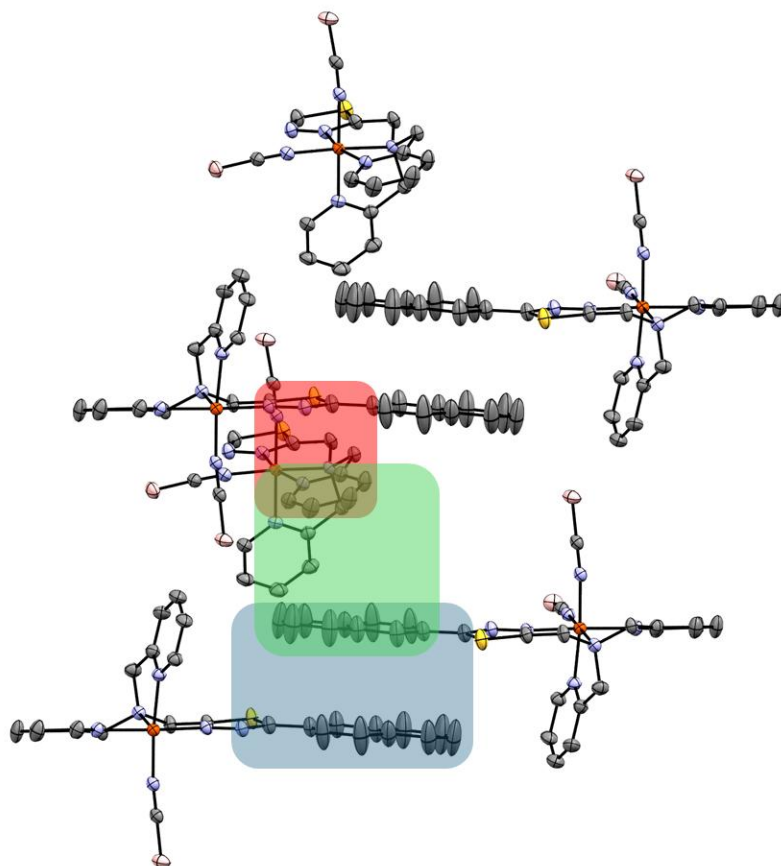


Figure S21: Visualisation of the π - π -interaction along a-axis between Naphthyl-units (Blue), the Pyridine- and Naphthyl-units (Green) and 1,3,4-Thiadiazole- and Pyridine-units (Red) for $[\text{Fe}(\text{L}^{\text{Naph-TDA}})(\text{NCBH}_3)_2] \cdot 0.5 \text{H}_2\text{O}$ (C1) at 120 K. Solvent were removed for better overview.

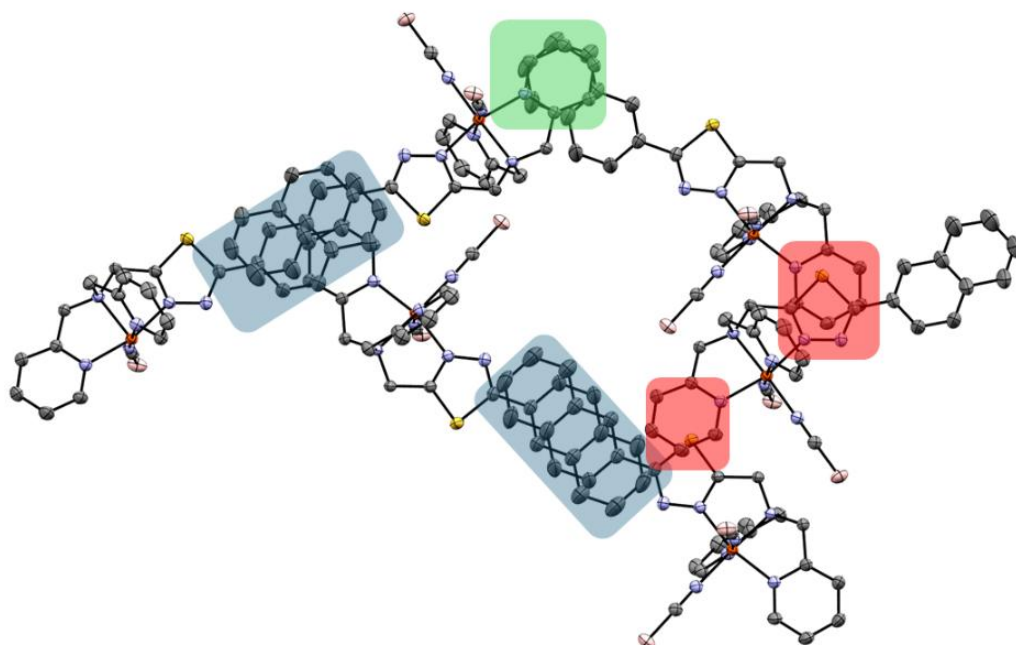


Figure S22: Visualisation of the π - π -interaction leading to the 3D network between Naphthyl-units (Blue), the Pyridine- and Naphthyl-units (Green) and 1,3,4-Thiadiazole- and Pyridine-units (Red) for $[\text{Fe}(\text{L}^{\text{Naph-TDA}})(\text{NCBH}_3)_2] \cdot 0.5 \text{H}_2\text{O}$ (C1) at 120 K. Solvent were removed for better overview.

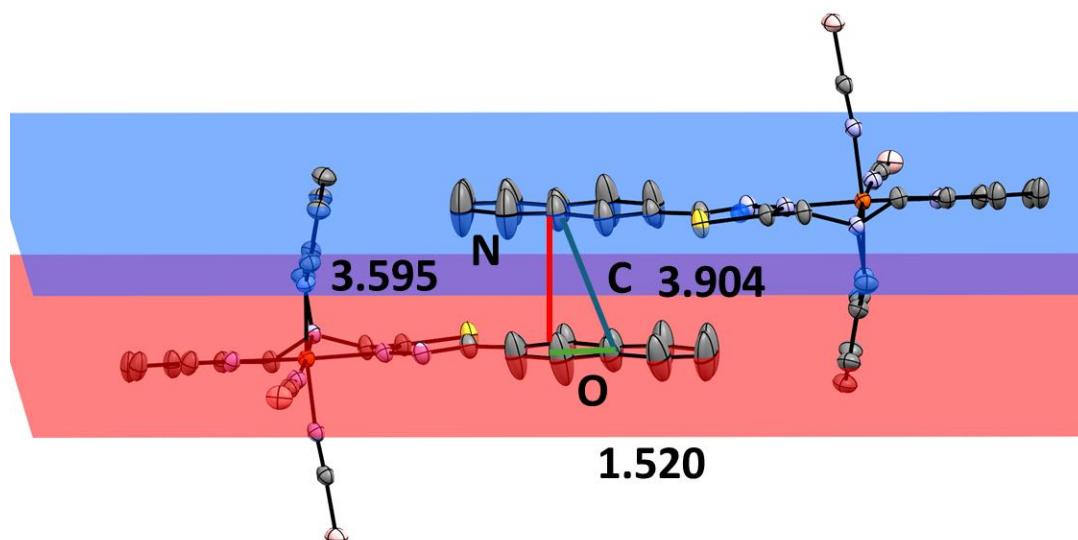


Figure S23: Visualisation of the π - π -interaction between Naphthyl units with Off-set (green), Normal vector (red) and centroid-centroid-distance (blue) and their values in Å for complex $[\text{Fe}(\text{L}^{\text{Naph-TDA}})(\text{NCBH}_3)_2] \cdot 0.5 \text{H}_2\text{O}$ (C1) at 120 K.

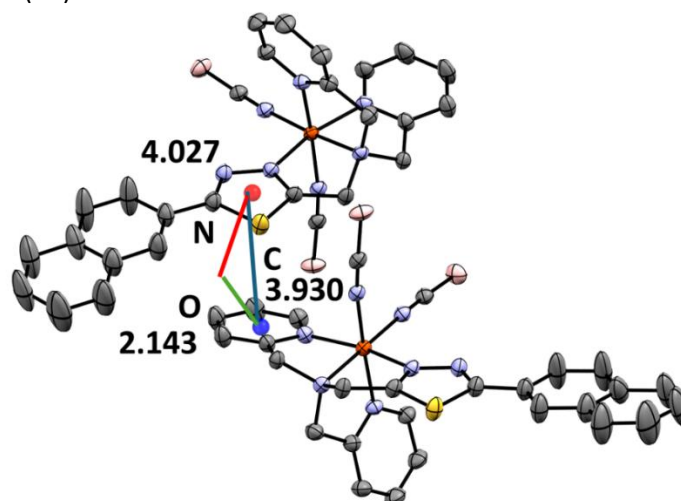


Figure S24: Visualisation of the π - π -interaction between 1,3,4-Thiadiazole and trans pyridine units with off-set (green), normalvector (red) and centroid-centroid-distance (blue) and their values in Å for complex $[\text{Fe}(\text{L}^{\text{Naph-TDA}})(\text{NCBH}_3)_2] \cdot 0.5 \text{H}_2\text{O}$ (C1) at 120 K.

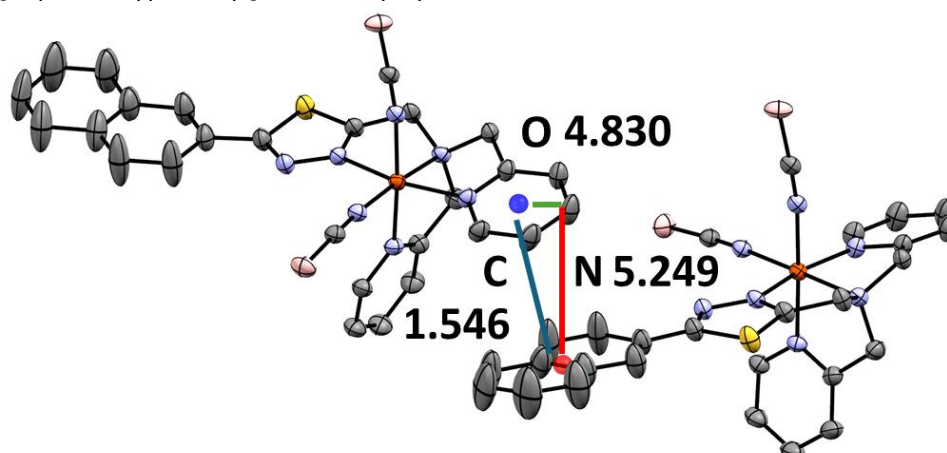


Figure S25: Visualisation of the π - π -interaction between Naphthyl- and trans pyridine units with off-set (green), normal vector (red) and centroid-centroid-distance (blue) and their values in Å for complex $[\text{Fe}(\text{L}^{\text{Naph-TDA}})(\text{NCBH}_3)_2] \cdot 0.5 \text{H}_2\text{O}$ (C1) at 120 K.

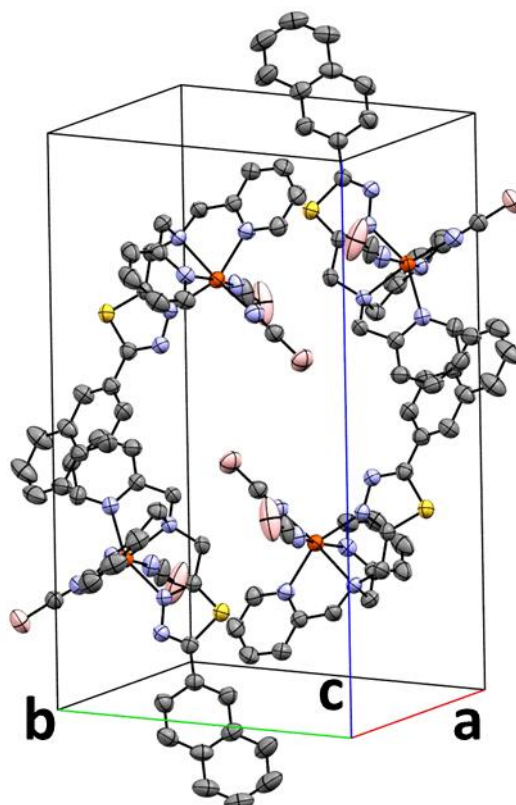


Figure S26: Unit cell of $[[\text{Fe}(\text{L}^{\text{Naph-TDA}})(\text{NCBH}_3)_2] \cdot 0.5 \text{H}_2\text{O}$ (**C1**) at 230 K. Solvent molecules and Hydrogen atoms were removed for better overview.

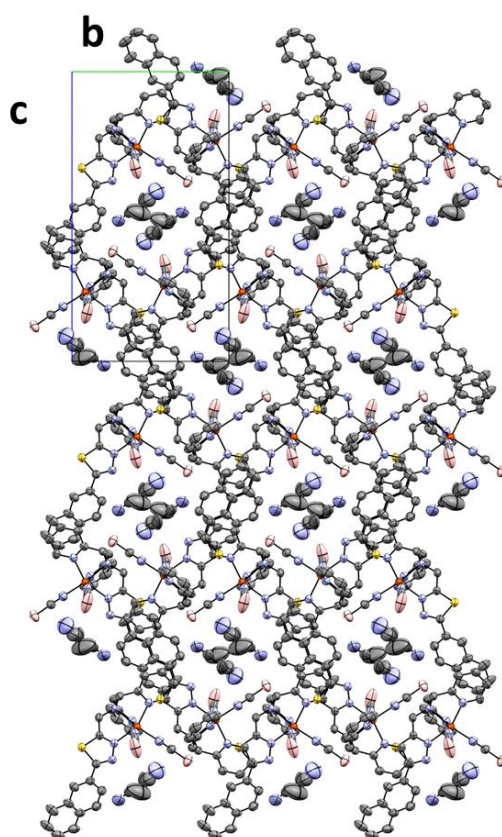


Figure S27: Visualisation of the packing for $[\text{Fe}(\text{L}^{\text{Naph-TDA}})(\text{NCBH}_3)_2] \cdot 0.5 \text{H}_2\text{O}$ (**C1**) along a-axis at 230 K. Hydrogen atoms were removed for better overview.

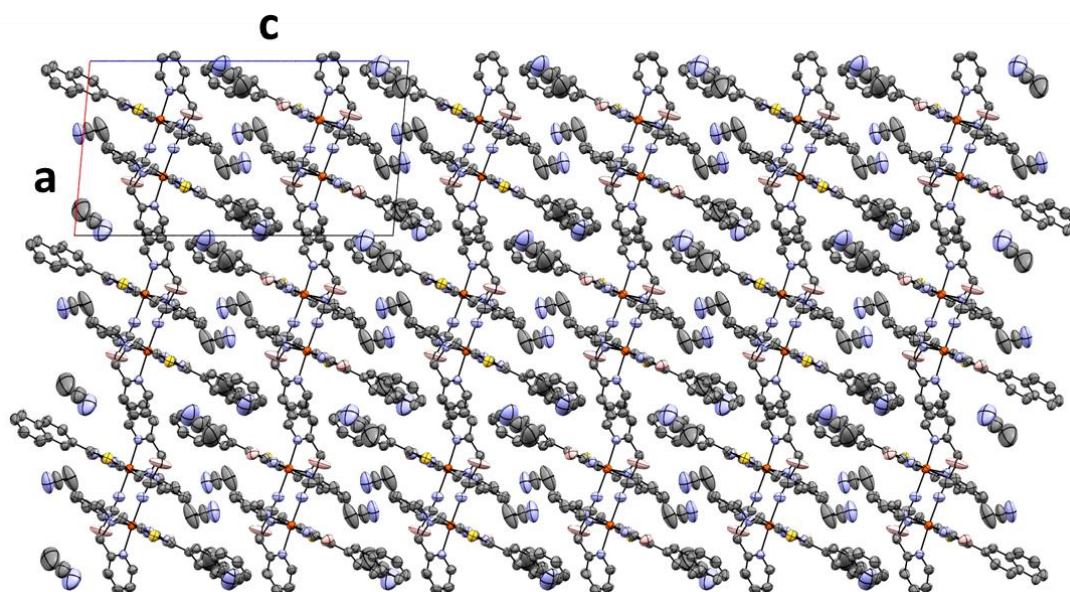


Figure S28: Visualisation of the packing for $[\text{Fe}(\text{L}^{\text{Naph-TDA}})(\text{NCBH}_3)_2] \cdot 0.5 \text{H}_2\text{O}$ (**C1**) along b-axis at 230 K. Hydrogen atoms were removed for better overview.

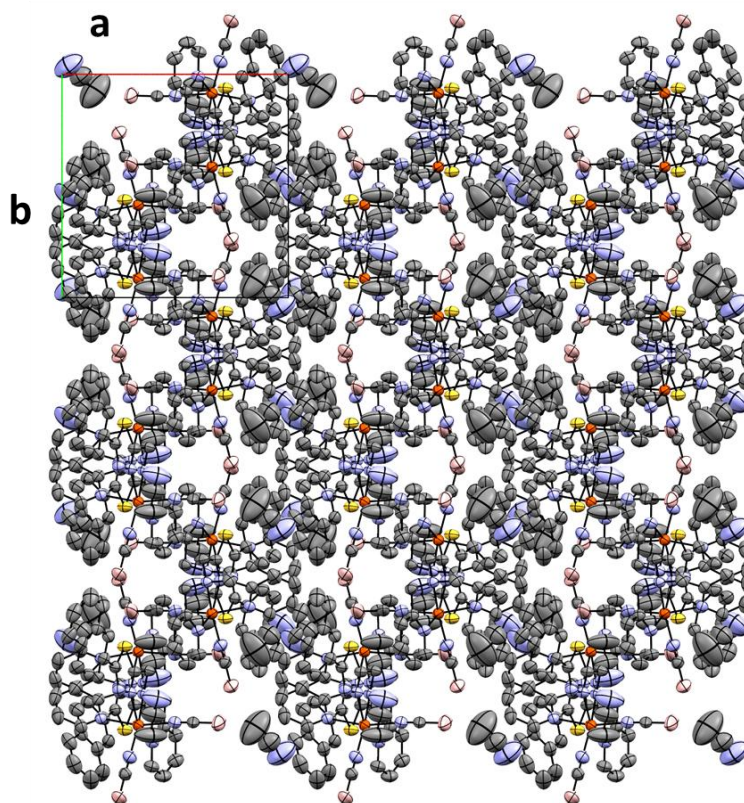


Figure S29: Visualisation of the packing for $[\text{Fe}(\text{L}^{\text{Naph-TDA}})(\text{NCBH}_3)_2] \cdot 0.5 \text{H}_2\text{O}$ (**C1**) along c-axis at 230 K. Hydrogen atoms were removed for better overview.

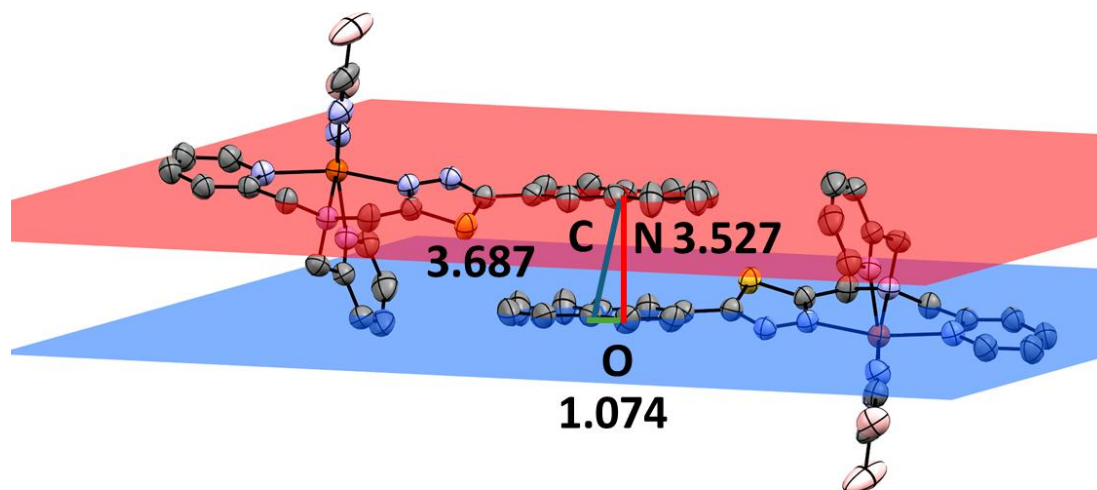


Figure S30: Visualisation of the π - π -interaction between Naphthyl units with off-set (green), normal vector (red) and centroid-centroid-distance (blue) and their values in Å for complex $[\text{Fe}(\text{L}^{\text{Naph-TDA}})(\text{NCBH}_3)_2] \cdot 0.5 \text{ H}_2\text{O}$ (C1) at 230 K.

4.2. Packing description of $[\text{Fe}(\text{L}^{\text{Naph-TDA}})(\text{NCBH}_3)_2] \cdot 0.9 \text{ DCM}$ (C2)

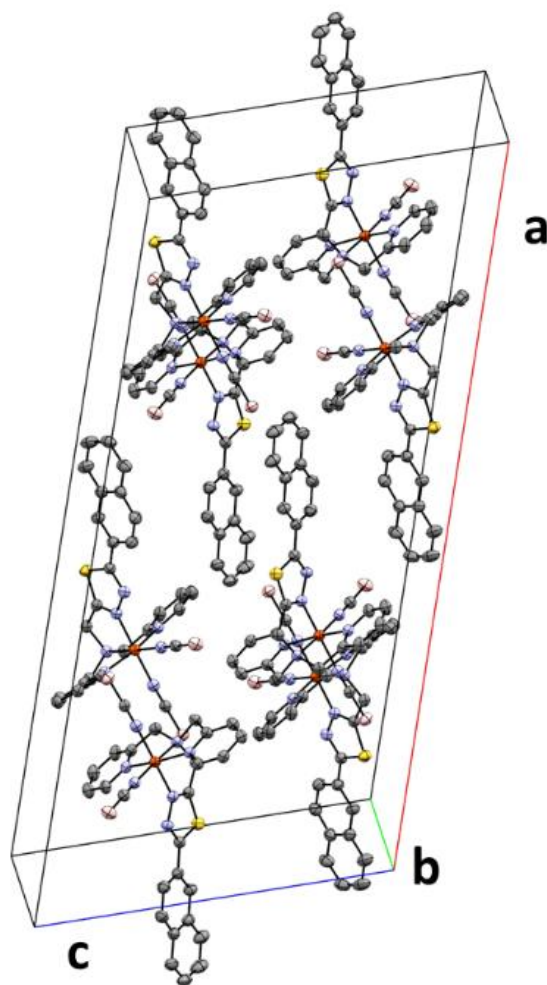


Figure S31: Unit cell of $[\text{Fe}(\text{L}^{\text{Naph-TDA}})(\text{NCBH}_3)_2] \cdot 0.9 \text{ DCM}$ (C2) at 120 K. Solvent molecules and Hydrogen atoms were removed for better overview.

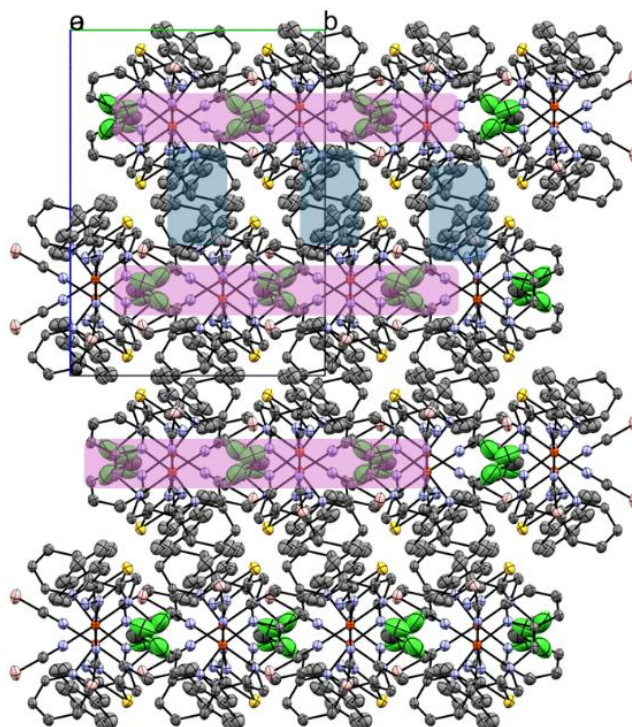


Figure S32: Visualisation of the packing for $[\text{Fe}(\text{L}^{\text{Naph-TDA}})(\text{NCBH}_3)_2] \cdot 0.9 \text{ DCM}$ (**C2**) along a-axis at 120 K. **Pink:** solvent channel; **Blue:** Naphthyl-Naphthyl-interaction. Hydrogen atoms were removed for better overview.

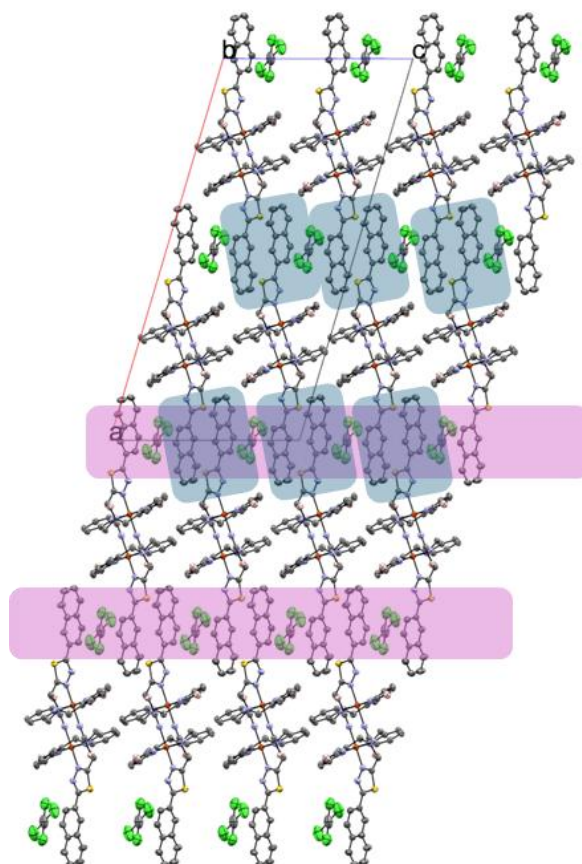


Figure S33: Visualisation of the packing for $[\text{Fe}(\text{L}^{\text{Naph-TDA}})(\text{NCBH}_3)_2] \cdot 0.9 \text{ DCM}$ (**C2**) along b-axis at 120 K. **Pink:** solvent channel; **Blue:** Naphthyl-Naphthyl-interaction. Hydrogen atoms were removed for better overview.

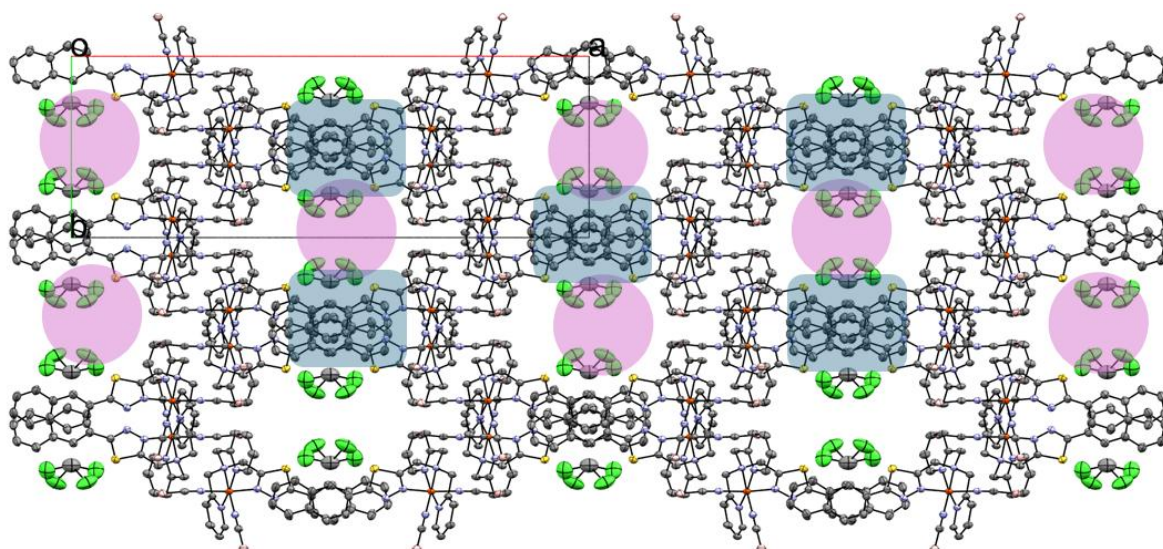


Figure S34: Visualisation of the packing for $[\text{Fe}(\text{L}^{\text{Naph-TDA}})(\text{NCBH}_3)_2] \cdot 0.9 \text{ DCM}$ (**C2**) along *c*-axis at 120 K. Pink: solvent channel; Blue: Naphthyl-Naphthyl-interaction. Hydrogen atoms were removed for better overview.

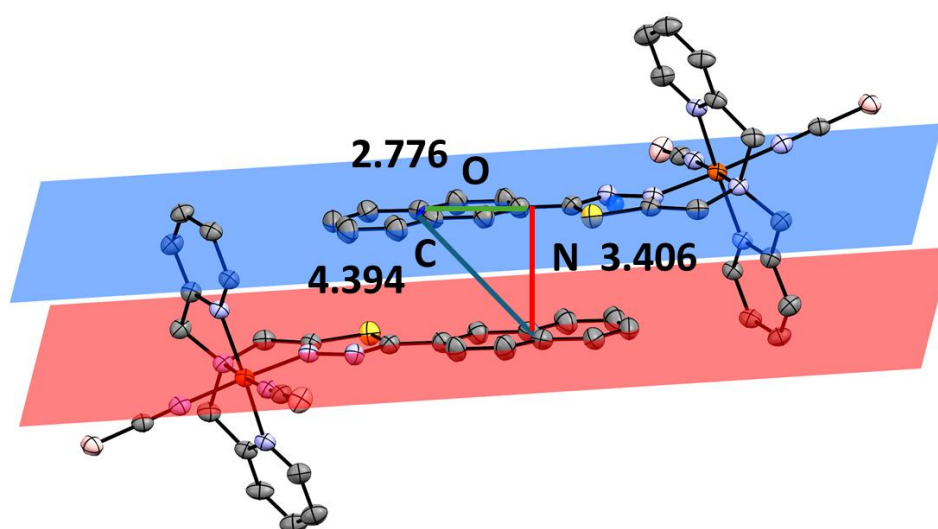


Figure S35: Visualisation of the π - π -interaction between Naphthyl units with off-set (green), normal vector (red) and centroid-centroid-distance (blue) and their values in Å for complex $[\text{Fe}(\text{L}^{\text{Naph-TDA}})(\text{NCBH}_3)_2] \cdot 0.9 \text{ DCM}$ (**C2**) at 120 K.

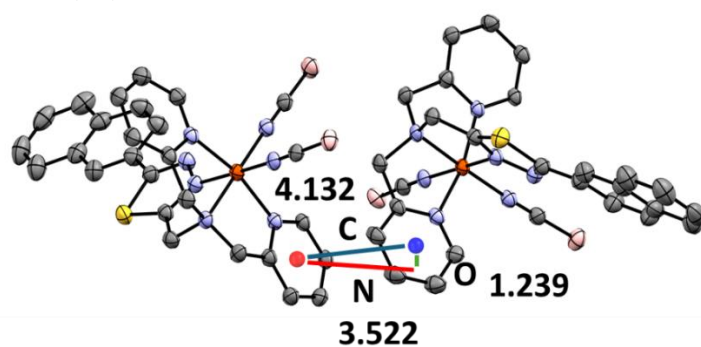


Figure S36: Visualisation of the π - π -interaction between Pyridine units with off-set (green), normal vector (red) and centroid-centroid-distance (blue) and their values in Å for complex $[\text{Fe}(\text{L}^{\text{Naph-TDA}})(\text{NCBH}_3)_2] \cdot 0.9 \text{ DCM}$ (**C2**) at 120 K.

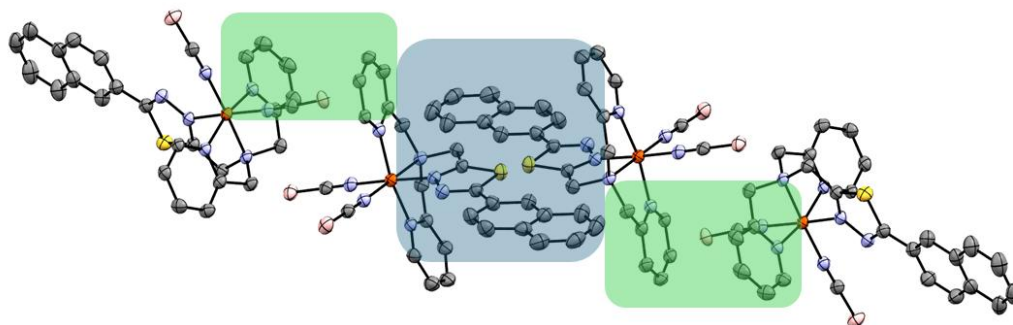


Figure S37: Visualisation of the π - π -interaction between along the unit cell diagonal between Naphthyl-units (Blue), the Pyridine- and Naphthyl-units (Green) and 1,3,4-Thiadiazole- and Pyridine-units (Red) for $[\text{Fe}(\text{L}^{\text{Naph-TDA}})(\text{NCBH}_3)_2] \cdot 0.9 \text{ DCM (C2)}$ at 120 K.

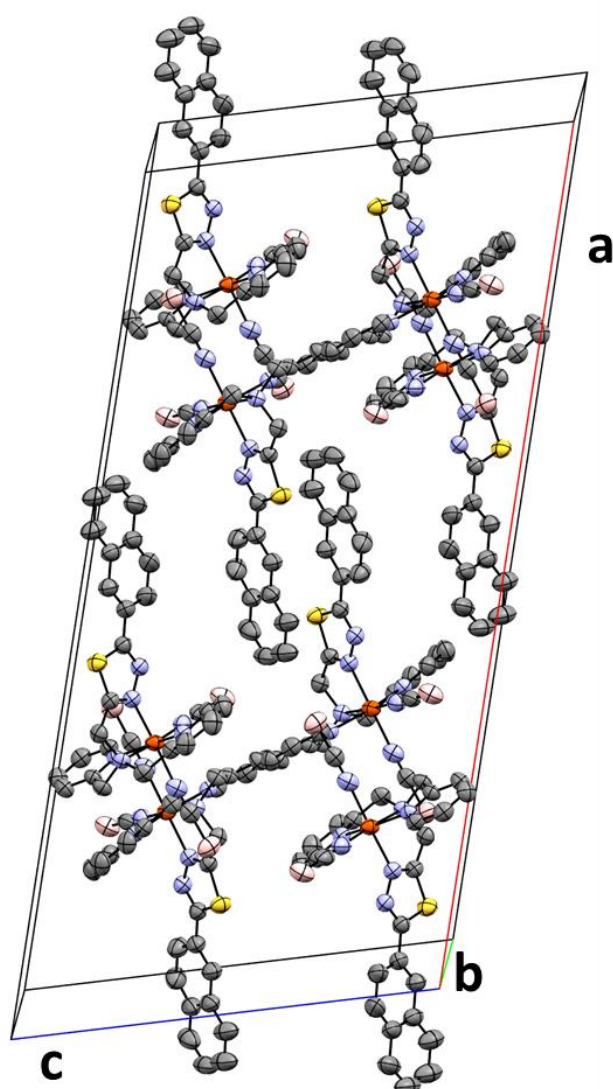


Figure S38: Unit cell of $[[\text{Fe}(\text{L}^{\text{Naph-TDA}})(\text{NCBH}_3)_2] \cdot 0.9 \text{ DCM (C2)}$ at 240 K. Solvent molecules and Hydrogen atoms were removed for better overview.

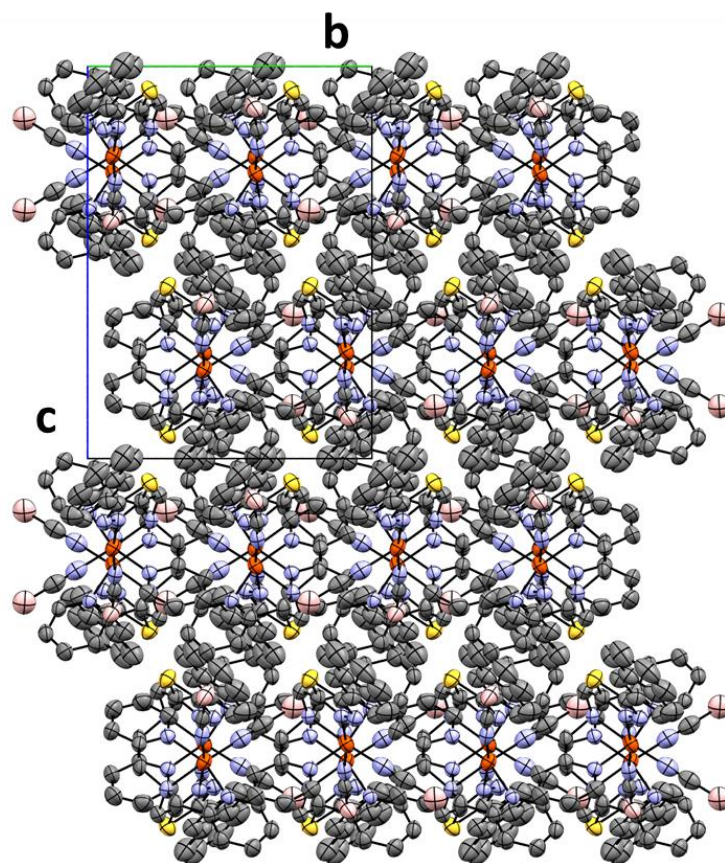


Figure S39: Visualisation of the packing for $[\text{Fe}(\text{L}^{\text{Naph-TDA}})(\text{NCBH}_3)_2] \cdot 0.9 \text{ DCM}$ (**C2**) along a-axis at 240 K. Solvent molecules and Hydrogen atoms were removed for better overview.

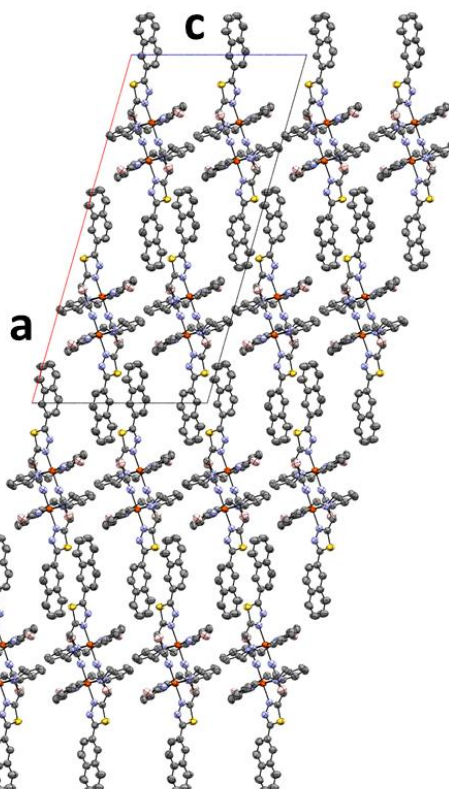


Figure S40: Visualisation of the packing for $[\text{Fe}(\text{L}^{\text{Naph-TDA}})(\text{NCBH}_3)_2] \cdot 0.9 \text{ DCM}$ (**C2**) along b-axis at 240 K. Solvent molecules and Hydrogen atoms were removed for better overview.

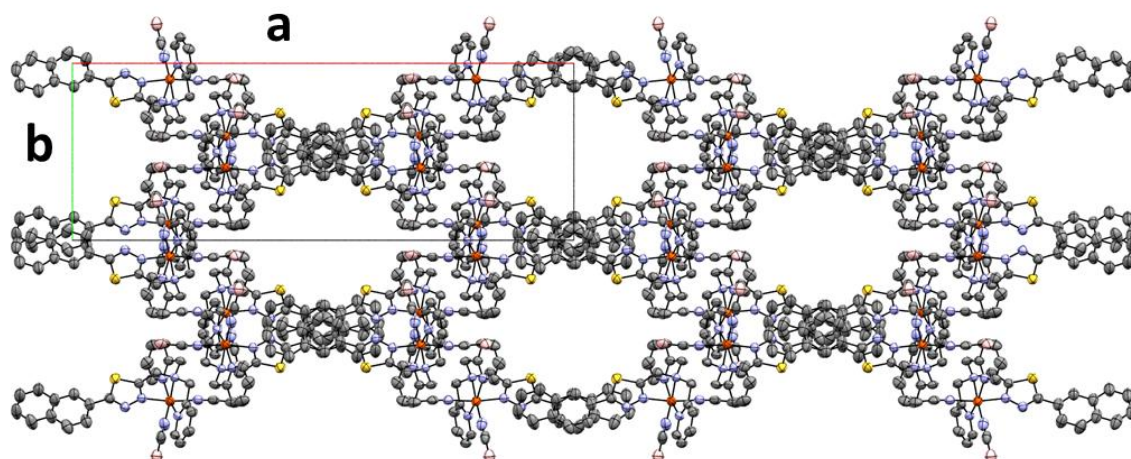


Figure S41: Visualisation of the packing for $[\text{Fe}(\text{L}^{\text{Naph-TDA}})(\text{NCBH}_3)_2] \cdot 0.9 \text{ DCM (C2)}$ along c-axis at 240 K. Solvent molecules and Hydrogen atoms were removed for better overview.

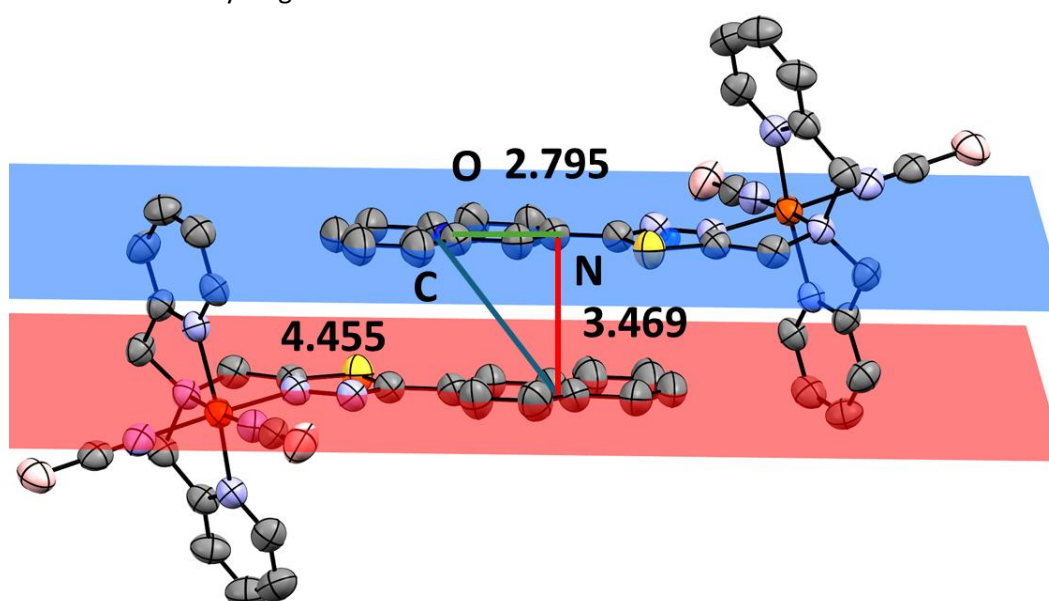


Figure S42: Visualisation of the π - π -interaction between Naphthyl units with off-set (green), normal vector (red) and centroid-centroid-distance (blue) and their values in Å for complex $[\text{Fe}(\text{L}^{\text{Naph-TDA}})(\text{NCBH}_3)_2] \cdot 0.9 \text{ DCM (C2)}$ at 240 K.

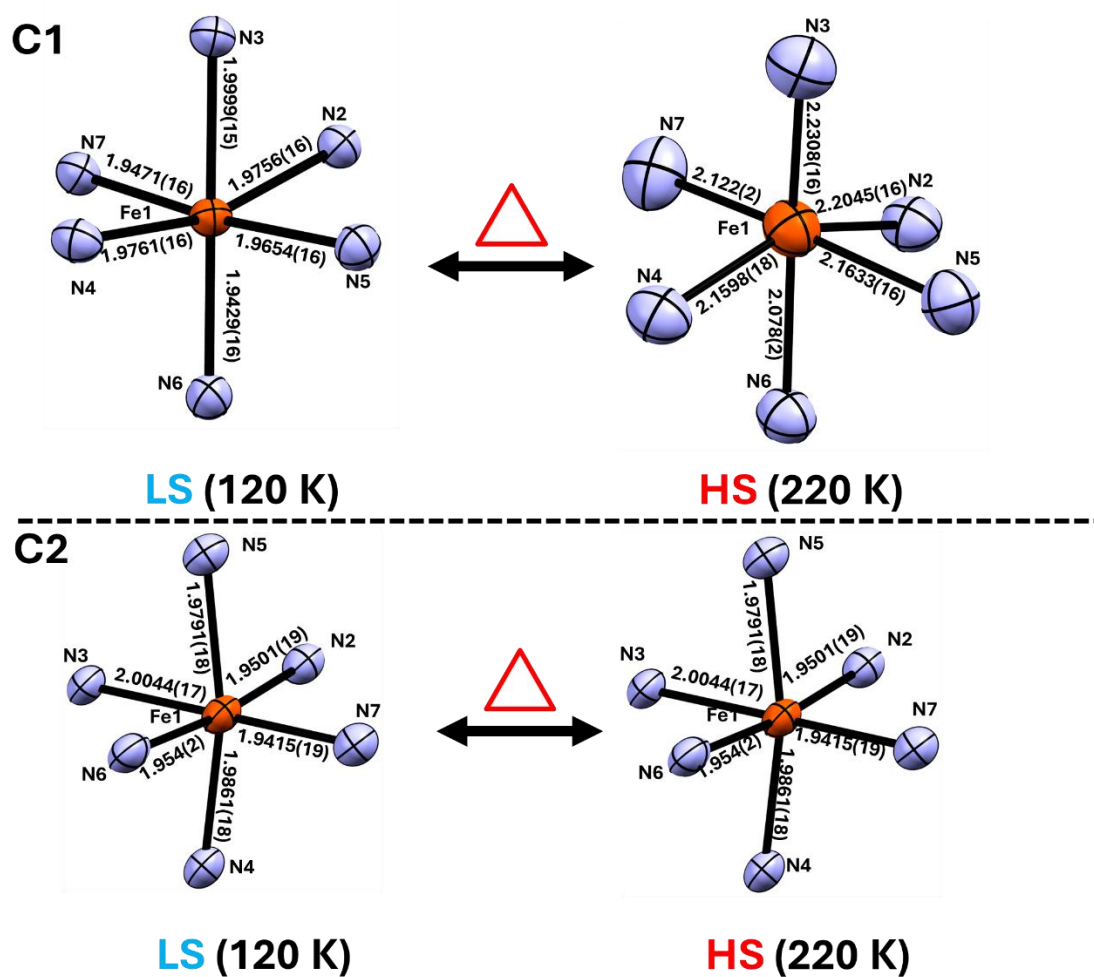


Figure S43: Fe-N Metal donor bond distances at 120 and 220 K for $[\text{Fe}(\text{L}^{\text{Naph-TDA}})(\text{NCBH}_3)_2] \cdot 0.5 \text{H}_2\text{O}$ (**C1**)(top) and $[\text{Fe}(\text{L}^{\text{Naph-TDA}})(\text{NCBH}_3)_2] \cdot 0.9 \text{DCM}$ (**C2**)(bottom)

Table S1: Measurement parameters for $[\text{Fe}(\text{L}^{\text{Naph-TDA}})(\text{NCBH}_3)_2] \cdot 0.5 \text{H}_2\text{O}$ (**C1**) at 120 K.

Parameter	Results
Empirical formula	$\text{C}_{27}\text{H}_{27}\text{B}_2\text{FeN}_7\text{S}_2 \cdot 0.5 \text{C}_2\text{H}_3\text{N}$
Formula weight	641.19
Temperature/K	120
Crystal system	monoclinic
Space group	$P2_1/c$
$a/\text{\AA}$	12.0952(4)
$b/\text{\AA}$	11.9012(3)
$c/\text{\AA}$	23.4101(8)
$\alpha/^\circ$	90
$\beta/^\circ$	103.764(3)
$\gamma/^\circ$	90
Volume/ \AA^3	3273.05(18)
Z	4
$\rho_{\text{calc}}/\text{g/cm}^3$	1.301
μ/mm^{-1}	0.561
F(000)	1336
Radiation	Mo K α ($\lambda = 0.71073$)
2 θ range for data collection/ $^\circ$	2.176 to 32.768
Index ranges	$-17 \leq h \leq 17, -15 \leq k \leq 18, -33 \leq l \leq 32$
Reflections collected	54520
Independent reflections	8913 [$R_{\text{int}} = 0.0277, R_{\text{sigma}} = 0.0216$]
Data/restraints/parameters	9619/0/346
Goodness-of-fit on F^2	1.026
Final R indexes [$ I \geq 2\sigma(I)$]	$R_1 = 0.0573, wR_2 = 0.1495$
Final R indexes [all data]	$R_1 = 0.0690, wR_2 = 0.1589$

Table S2: Measurement parameters for $[\text{Fe}(\text{L}^{\text{Naph-TDA}})(\text{NCBH}_3)_2] \cdot 0.5 \text{H}_2\text{O}$ (**C1**) at 230 K

Parameter	Results
Empirical formula	$\text{C}_{27}\text{H}_{27}\text{B}_2\text{FeN}_7\text{S} \cdot 2 \text{C}_2\text{H}_3\text{N}$
Formula weight	694.36
Temperature/K	230
Crystal system	monoclinic
Space group	$P2_1/c$
a/Å	12.3296(9)
b/Å	12.1188(7)
c/Å	22.4575(17)
$\alpha/^\circ$	90
$\beta/^\circ$	95.099(6)
$\gamma/^\circ$	90
Volume/Å³	3342.3(4)
Z	4
$\rho_{\text{calc}}/\text{cm}^3$	1.274
μ/mm^{-1}	0.549
F(000)	1336
Radiation	Mo K α ($\lambda = 0.71073$)
2θ range for data collection/$^\circ$	2.352 to 32.753
Index ranges	$-18 \leq h \leq 10, -16 \leq k \leq 17, -30 \leq l \leq 32$
Reflections collected	41144
Independent reflections	7599 [$R_{\text{int}} = 0.0296, R_{\text{sigma}} = 0.0245$]
Data/restraints/parameters	10719/51/346
Goodness-of-fit on F²	1.051
Final R indexes [$I \geq 2\sigma(I)$]	$R_1 = 0.0549, wR_2 = 0.1521$
Final R indexes [all data]	$R_1 = 0.0758, wR_2 = 0.1690$

Table S3: Measurement parameters for $[\text{Fe}(\text{L}^{\text{Naph-TDA}})(\text{NCBH}_3)_2] \cdot 0.9 \text{ DCM (C2)}$ at 120 K.

Parameter	Results
Empirical formula	$\text{C}_{27}\text{H}_{27}\text{B}_2\text{FeN}_7\text{S} \cdot 1.5 \text{ CH}_2\text{Cl}_2$
Formula weight	686.47
Temperature/K	120
Crystal system	monoclinic
Space group	C 2/c
a/Å	35.4986(10)
b/Å	11.9315(2)
c/Å	16.9166(5)
$\alpha/^\circ$	90
$\beta/^\circ$	106.555(2)
$\gamma/^\circ$	90
Volume/Å ³	6868.0(3)
Z	8
$\rho_{\text{calc}}/\text{cm}^3$	1.328
μ/mm^{-1}	0.763
F(000)	2824
Radiation	Mo K α ($\lambda = 0.71073$)
2 θ range for data collection/ $^\circ$	2.103 to 33.748
Index ranges	$-55 \leq h \leq 50, -18 \leq k \leq 15, -22 \leq l \leq 25$
Reflections collected	36245
Independent reflections	10505 [$R_{\text{int}} = 0.0333, R_{\text{sigma}} = 0.0304$]
Data/restraints/parameters	11671/0/346
Goodness-of-fit on F ²	1.069
Final R indexes [$ I \geq 2\sigma(I)$]	$R_1 = 0.0712, wR_2 = 0.2037$
Final R indexes [all data]	$R_1 = 0.0834, wR_2 = 0.2149$

Table S4: Measurement parameters for $[\text{Fe}(\text{L}^{\text{Naph-TDA}})(\text{NCBH}_3)_2] \cdot 0.9 \text{ DCM (C2)}$ at 240 K.

Parameter	Results
Empirical formula	$\text{C}_{27}\text{H}_{27}\text{B}_2\text{FeN}_7\text{S} \cdot 1.5 \text{ CH}_2\text{Cl}_2$
Formula weight	686.47
Temperature/K	240
Crystal system	monoclinic
Space group	C 2/c
a/Å	35.677(3)
b/Å	12.0580(6)
c/Å	17.2878(16)
$\alpha/^\circ$	90
$\beta/^\circ$	105.948(7)
$\gamma/^\circ$	90
Volume/Å ³	7150.9(10)
Z	8
$\rho_{\text{calc}}/\text{cm}^3$	1.275
μ/mm^{-1}	0.733
F(000)	2824
Radiation	Mo K α ($\lambda = 0.71073$)
2 θ range for data collection/ $^\circ$	2.075 to 33.693
Index ranges	$-55 \leq h \leq 50, -18 \leq k \leq 15, -23 \leq l \leq 26$
Reflections collected	38140
Independent reflections	7709 [$R_{\text{int}} = 0.0277, R_{\text{sigma}} = 0.0271$]
Data/restraints/parameters	12145/0/346
Goodness-of-fit on F ²	1.071
Final R indexes [$ I \geq 2\sigma(I)$]	$R_1 = 0.0516, wR_2 = 0.1481$
Final R indexes [all data]	$R_1 = 0.0779, wR_2 = 0.1651$

Table S5: Fe-N bond lengths in Å for Complex $[\text{Fe}(\text{L}^{\text{Naph-TDA}})(\text{NCBH}_3)_2] \cdot 0.5 \text{H}_2\text{O}$ (**C1**) and $[\text{Fe}(\text{L}^{\text{Naph-TDA}})(\text{NCBH}_3)_2] \cdot 0.9 \text{DCM}$ (**C2**) at 120 K and 240 K.

	C1 at 120 K	C1 at 230 K	C1 at 120 K	C1 at 240 K
Fe1 – N2	1.9756(16)	2.2045(16)	1.9501(19)	2.0347(15)
Fe1 – N3	1.9999(15)	2.2308(16)	2.0044(17)	2.0934(13)
Fe1 – N4	1.9761(16)	2.1598(18)	1.9861(18)	2.0521(14)
Fe1 – N5	1.9654(16)	2.1633(16)	1.9791(18)	2.0486(15)
Fe1 – N6	1.9429(16)	2.078(2)	1.954(2)	2.0169(19)
Fe1 – N7	1.9471(16)	2.122(2)	1.9415(19)	1.958(2)
Average bond length	1.968	2.160	1.969	2.034
Spin state	LS	HS	LS	HS

Table S6: N-Fe-N cis bond angles in degree /° for the complex for $[\text{Fe}(\text{L}^{\text{Naph-TDA}})(\text{NCBH}_3)_2] \cdot 0.5 \text{H}_2\text{O}$ (**C1**) at 120 K and 230 K.

	C1 120 K	C1 230 K
N2 Fe1 N3	83.69(7)	76.83(6)
N4 Fe1 N3	81.74(6)	75.43(6)
N5 Fe1 N2	86.44(7)	80.59(6)
N5 Fe1 N3	84.71(7)	78.49(6)
N5 Fe1 N4	94.58(7)	99.00(7)
N6 Fe1 N2	98.98(7)	109.71(7)
N6 Fe1 N4	95.69(7)	98.51(7)
N6 Fe1 N5	92.79(7)	95.01(8)
N6 Fe1 N7	90.26(7)	95.19(8)
N7 Fe1 N2	87.15(6)	86.28(7)
N7 Fe1 N3	92.52(6)	92.60(7)
N7 Fe1 N4	91.08(7)	89.64(7)
Distortion parameter	52.17	102.76
Spin state	LS	HS

Table S7: N-Fe-N cis bond angles in degree /° for the complex [Fe(L^{Naph-TDA})(NCBH₃)₂] · 0.9 DCM (**C2**) at 120 K and 240 K.

	C2 120 K	C2 240 K
N2 Fe1 N3	84.21(7)	81.48(6)
N2 Fe1 N4	92.42(7)	91.55(6)
N2 Fe1 N5	85.51(7)	84.73(6)
N4 Fe1 N3	82.63(7)	79.79(5)
N5 Fe1 N3	82.98(8)	80.38(6)
N6 Fe1 N3	91.63(7)	91.56(6)
N6 Fe1 N4	90.96(7)	91.55(6)
N6 Fe1 N5	90.07(7)	89.78(6)
N7 Fe1 N2	93.52(8)	95.14(7)
N7 Fe1 N4	96.31(7)	98.17(6)
N7 Fe1 N5	98.04(8)	101.57(7)
N7 Fe1 N6	90.73(8)	91.97(7)
Distortion parameter	48.35	65.35
Spin state	LS	HS

Table S8: Extracted parameter of off-set, the normal vector distance and the centroid-centroid distance and the Naphthyl-1,3,4-Thiadiazole-Torsion for **C1** and **C2** for the π - π -interaction between Naphthyl-units at 120 K and 230 K or 230 K.

Complex	off-set / Å	normal vector distance/ Å	centroid-centroid-distance/ Å	Torsion Naph-TDA/ °
C2 120 K	2.776	3.404	4.394	177.35
C2 230 K	2.796	3.469	4.455	178.18
C1 120 K	1.520	3.596	3.904	155.80
C1 230 K	1.074	3.527	3.687	176.94

Table S9: Extracted parameter of off-set, the normal vector distance and the centroid-centroid distance for **C2** for the π - π -interaction between Pyridine-units at 120 K and 230 K or 230 K.

	off-set / Å	normal vector distance/ Å	centroide-centroide-distance/ Å
C2 120 K	1.239	3.522	4.132
C2 230 K	1.259	3.579	4.179

5. Temperature dependent magnetization measurement

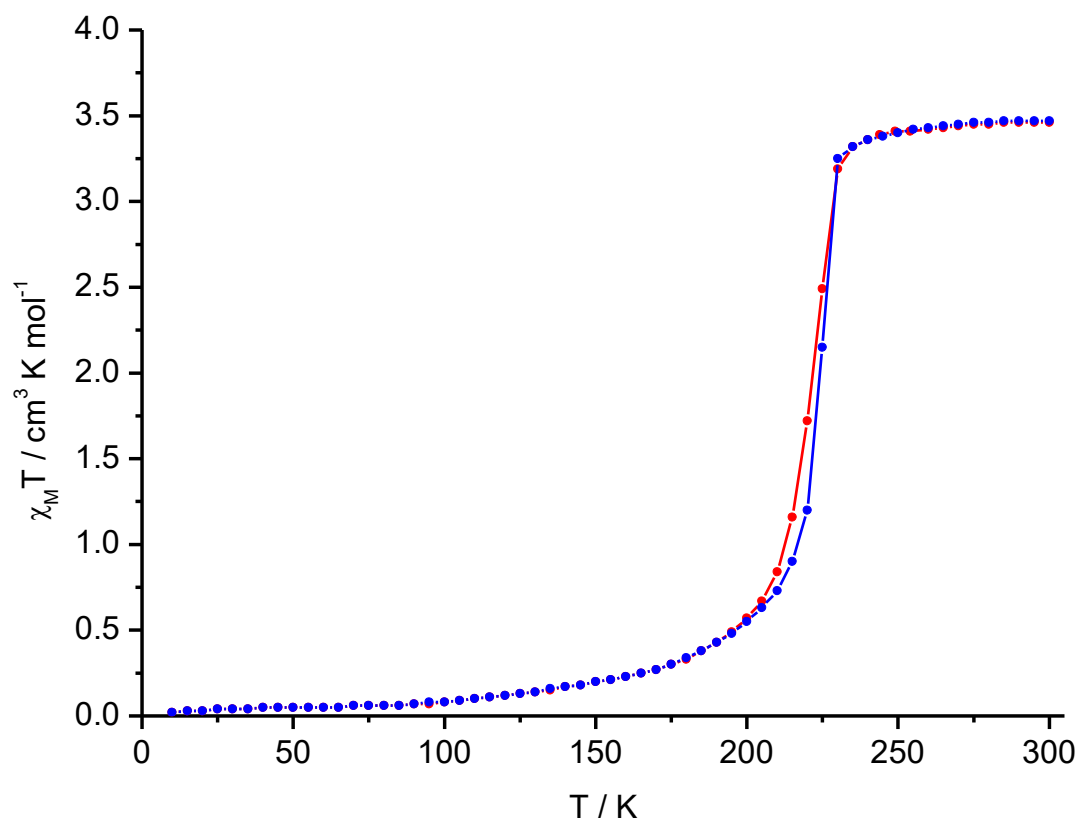


Figure S44: χ_M vs. T measured of powder product of $[\text{Fe}(\text{L}^{\text{Naph-TDA}})(\text{NCBH}_3)_2] \cdot 0.5 \text{ H}_2\text{O}$ (**C1**) in the form of the resulting $\chi_M T$ vs. T plot. Magnetic susceptibility was determined between 300 - 10 K (blue) and 10-300 K (red).

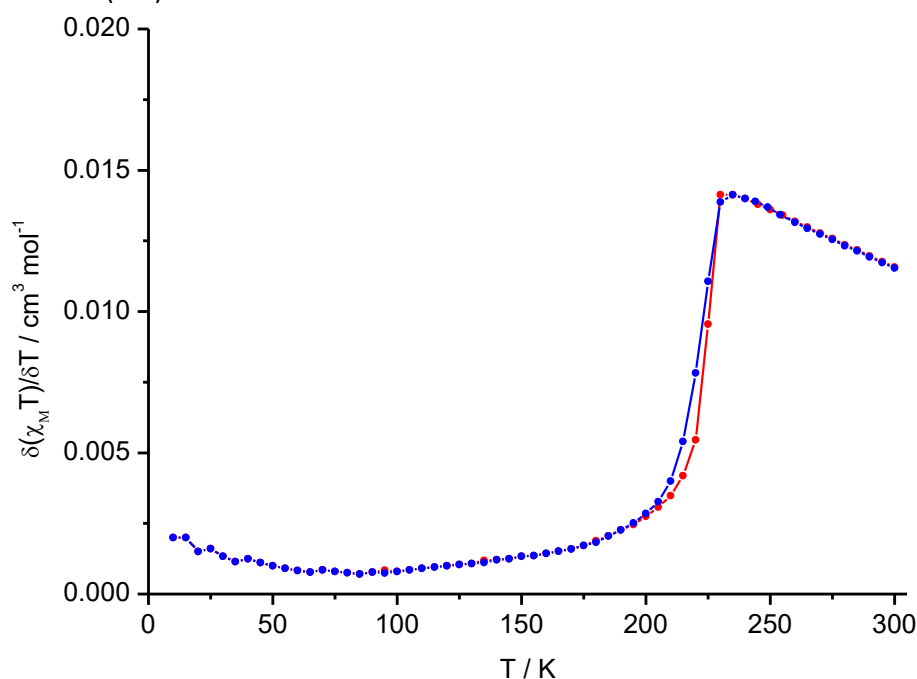


Figure S45: First derivative of $\frac{\delta \chi_M T}{\delta T}$ with respect to T for $[\text{Fe}(\text{L}^{\text{Naph-TDA}})(\text{NCBH}_3)_2] \cdot 0.5 \text{ H}_2\text{O}$ (**C1**) in the form of the resulting $\frac{\delta \chi_M T}{\delta T}$ vs. T plot. Magnetic susceptibility was determined between 300 - 10 K (blue) and 10-300 K (red).

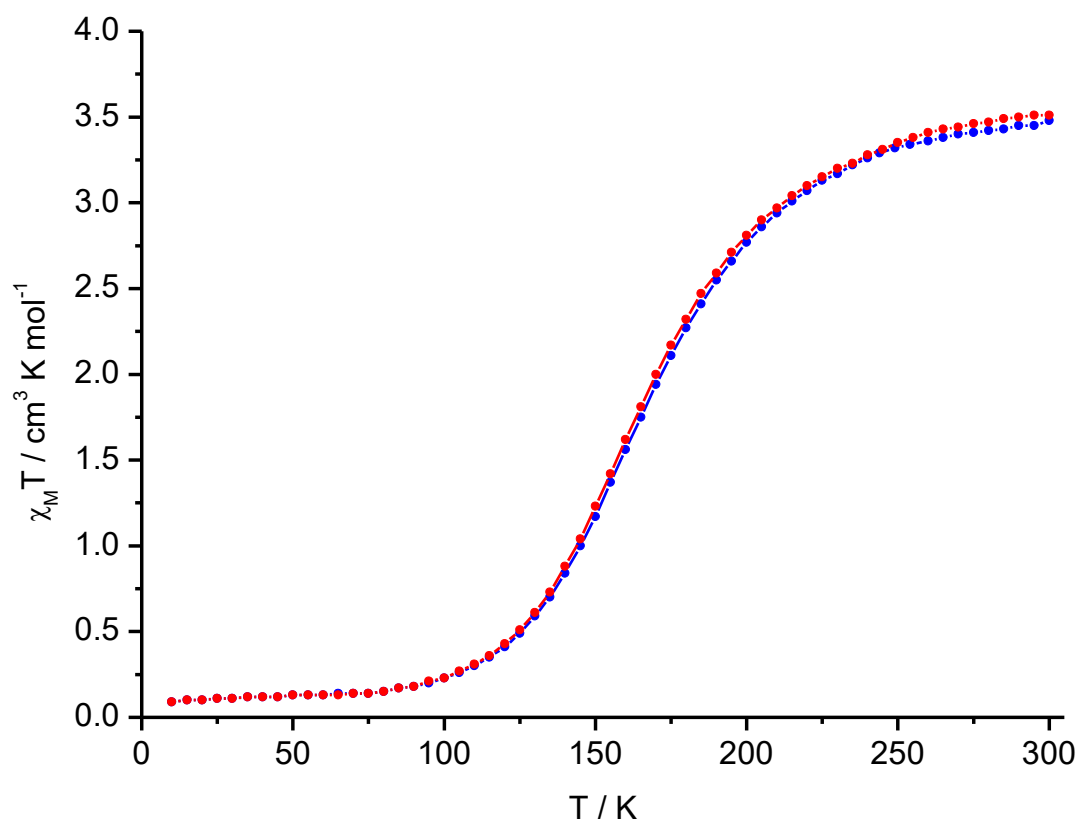


Figure S46: χ_M vs. T measured of powder product of $[\text{Fe}(\text{L}^{\text{Naph-TDA}})(\text{NCBH}_3)_2] \cdot 0.9 \text{ DCM}$ (**C2**) in the form of the resulting $\chi_M T$ vs. T plot. Magnetic susceptibility was determined between 300 - 10 K (blue) and 10-300 K (red).

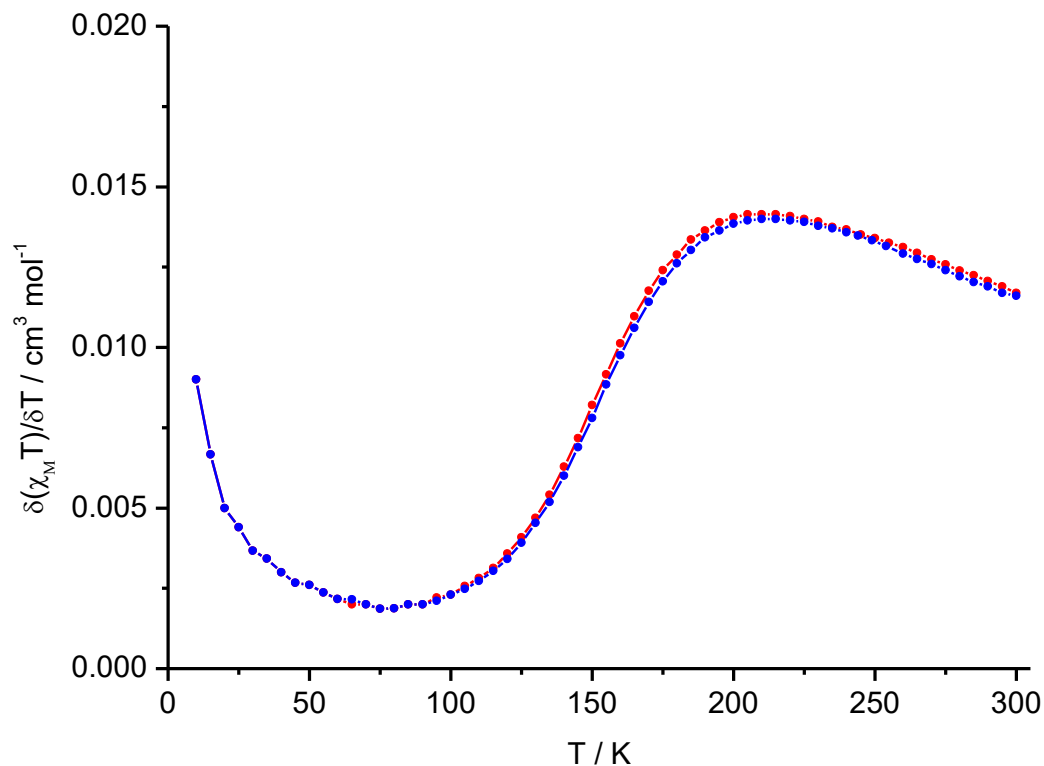


Figure S47: First derivative of $\frac{\delta \chi_M T}{\delta T}$ with respect to T for $[\text{Fe}(\text{L}^{\text{Naph-TDA}})(\text{NCBH}_3)_2] \cdot 0.9 \text{ DCM}$ (**C2**) in the form of the resulting $\frac{\delta \chi_M T}{\delta T}$ vs. T plot. Magnetic susceptibility was determined between 300-10 K (blue) and 10-300 K (red).

6. UV-Vis Absorption spectroscopy in solution

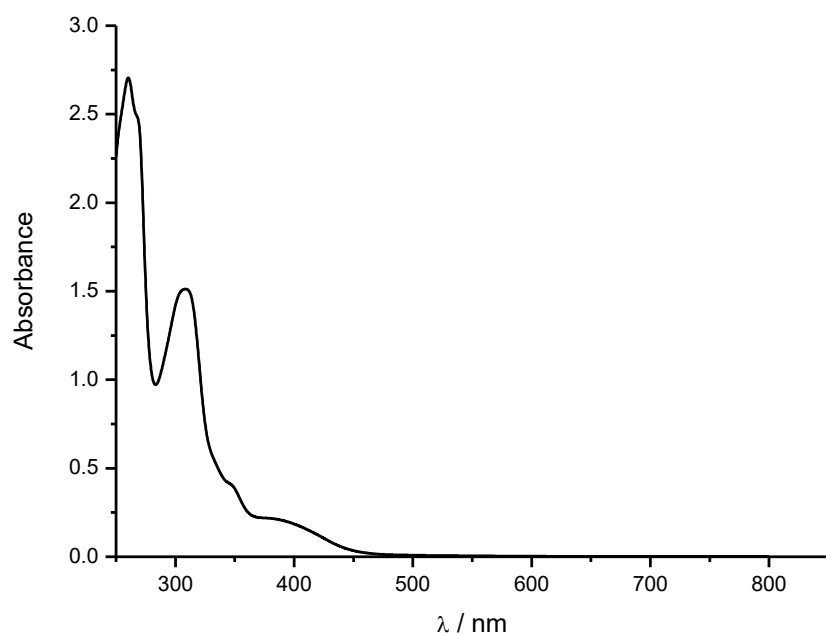


Figure S48: Absorption spectra of $[\text{Fe}(\text{L}^{\text{Naph-TDA}})(\text{NCBH}_3)_2] \cdot 0.5 \text{H}_2\text{O}$ (C1) in acetonitrile of the 1 mM solution.

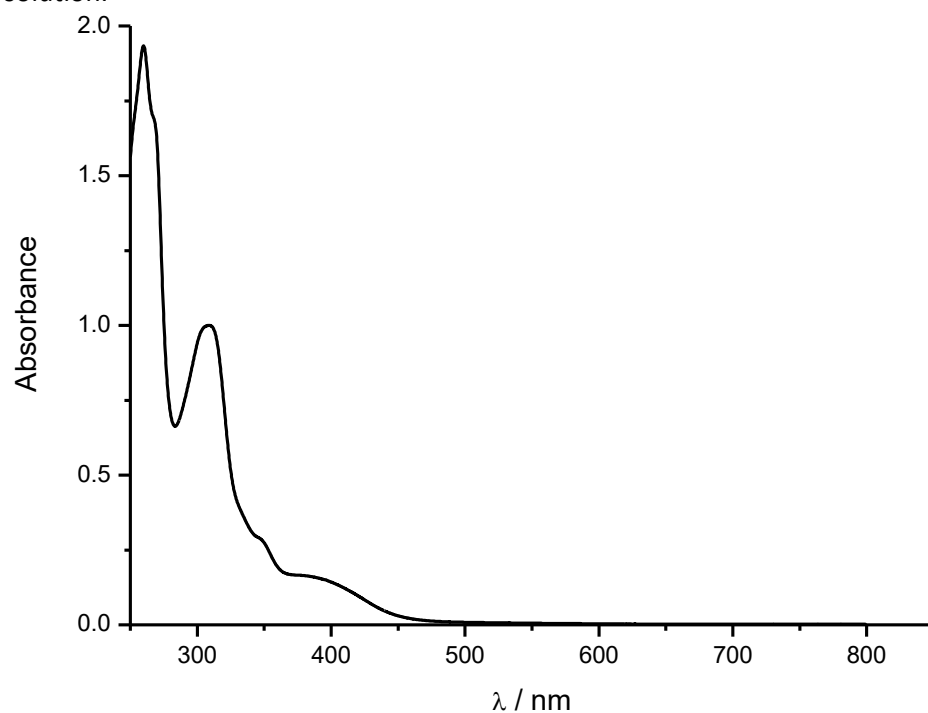


Figure S49: Absorption spectra of $[\text{Fe}(\text{L}^{\text{Naph-TDA}})(\text{NCBH}_3)_2] \cdot 0.9 \text{DCM}$ (C2) in dichloromethane of the 1 mM solution.

7. References:

- [1] G. R. Fulmer, A. J. M. Miller, N. H. Sherden, H. E. Gottlieb, A. Nudelman, B. M. Stoltz, J. E. Bercaw, K. I. Goldberg, *Organometallics* **2010**, 29, 2176–2179.

Chapter 6: Helical dinuclear iron(II) complexes with 1,3,4-Oxa- and 1,3,4-Thiadiazole coordination units

This chapter discusses the synthesis of two ligands - one based on a 1,3,4-oxadiazole and the other on a 1,3,4-thiadiazole - each featuring two coordination pockets designed for the formation of hypothetical helical dinuclear complexes of the type $[\text{Fe}_2(\text{L}^{(\text{T/O})\text{-DA-Hel}})_3](\text{ClO}_4)_4$. The helical dinuclear complex was successfully synthesized using the 1,3,4-thiadiazole-based ligand, whereas the 1,3,4-oxadiazole analogue led only to mononuclear complexes. Both complexes were structurally and magnetically characterized in the solid state using single-crystal *X-ray* diffraction and *SQUID* magnetometry. The influence of the heteroatom on complex formation was analysed in terms of bite angles. Furthermore, the incorporation of spin-crossover behaviour into the helical complex was explored for potential applications in supramolecular chemistry, with studies including *Evans NMR* and guest intercalation experiments using diffusion-ordered spectroscopy (*DOSY*), such as $^7\text{Li-DOSY}$, to investigate interactions with small guest molecules like lithium.

The results are presented as scientific article published in *ACS Publication* (DOI: <https://doi.org/10.1021/acs.cgd.4c00914>).

Reprinted with the permission from:

Copyright 2024 ACS Publications

Author contribution:

████████████████████ and ██████████ designed the ligand and complexes synthesis. The ligand and complex synthesis were performed by ██████████ and ██████████ as well as the characterisation via *IR*-spectroscopy and as well as the sample preparation of elemental analysis, *NMR*-spectroscopy and *ESI-MS*-spectrometry. The *NMR*-experiments (*Evans*- and *DOSY*-measurements) were performed under the supervision of ██████████. ██████████ collected the single crystal *XRD* data and refined the structure. The evaluation of the magnetic and structural data was done by ██████████.

The Manuscript was written by ██████████, with input from ██████████ and ██████████. ██████████ had the supervision during the manuscript process. All Authors have read and agreed to the published version of the manuscript.

Manuscript: The Crucial Role of the Heteroatom and Bite Angle Influencing Spin States and Dinuclear Fe(II) Helicate Formation in 1,3,4-Thia/Oxadiazole Ligand

Jens-Georg Becker,¹ Jan F. Nüsing,¹ Sriram Sundaresan,¹ Rosa Diego,¹ Mihail Mondeshki,¹ Luca M. Carrella,¹ and Eva Rentschler^{1*}

¹Department Chemie, Johannes-Gutenberg-Universität Mainz, Duesbergweg 10–14, 55128 Mainz, Germany. Email: rentschl@uni-mainz.de

Abstract:

Helical complexes can serve as sensors in various applications, detecting the presence of specific guest molecules by binding to them or responding to their presence. We report the synthesis of two novel iron (II) helicates, together with a mononuclear iron(II) compound. The new ligand $L^{\text{TDA-Hel}}$ formed the triple-stranded helicates $[\text{Fe}_2(L^{\text{TDA-Hel}})_3](\text{ClO}_4)_4 \cdot 3 \text{H}_2\text{O}$ (**C1**) and $[\text{Fe}_2(L^{\text{TDA-Hel}})_3](\text{BF}_4)_4 \cdot 5 \text{H}_2\text{O}$ (**C2**), as anticipated, whereas the new ligand $L^{\text{ODA-Hel}}$ formed a mononuclear Fe(II) complex $[\text{Fe}(\text{H}_2\text{O})_2(L^{\text{ODA-Hel}})_2](\text{ClO}_4)_2$ (**C3**) with coordinated aqua co-ligands. All three complexes have been studied by single crystal X-ray crystallography to investigate the effect of the size of the O/S hetero atom in the helix formation. Complexes **C1** and **C2** are diamagnetic in both solid and solution states, with solution *NMR* confirming their stability. Due to the small helical cavity, guest sensing with Li^+ ions was tested using *VT* ^7Li *NMR* spectra.

Introduction:

Self-assembly of metallo-supramolecular architecture driven by coordination chemistry of the metals is fascinating and heavily dependent on appropriate ligand design.^[1–5] It involves the spontaneous formation of complex molecular structures from simpler building blocks, driven by the self-assembly of metal centres and ligands together. By choosing the right ligand suitable for the metal centre several intricate supramolecular architectures can be obtained, including helicates, cages and grids.^[6–9]

Helical metal complexes are intricate molecular structures in which metal ions are coordinated by ligands to form triple-standard helical architectures.^[10,11] These complexes often exhibit chirality, meaning they exist in left- or right-handed forms that are non-superimposable mirror images of each other.^[12,13] Moreover, helicates, have emerged as versatile sensors for encapsulating various guest molecules.^[14,15] In some cases, the guest can even induce the appropriate self-assembly in triple-stranded helicate due to a template effect. Importantly, the helical cavities of helicates provide a unique

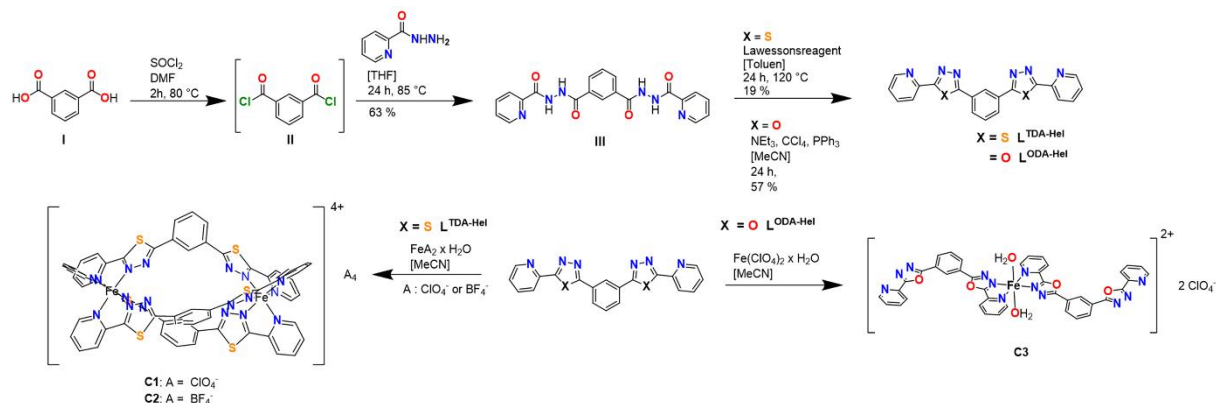
environment that can selectively bind to specific guest molecules through complementary interactions, leading to changes in their properties, such as fluorescence, conductivity, or spin states of the metal centres.^[15] This property has found applications in sensing various analytes, including ions, small molecules, and biomolecules, making helicates promising candidates for biosensing and environmental monitoring.^[14,16–18]

Ditopic helicates based on different 5-membered rings, such as diazole and triazole are recently reported in the literature and investigated for spin crossover properties.^[15,19] Fe(II) helicates, which show spin crossover, were also reported with other Schiff base ligands.^[20,21] Aromi *et al.* demonstrated the spin states of the Fe(II) centre can be tuned by choice of the encapsulated anion.^[22] In the past, we have reported a number of examples of *SCO* complexes based on 1,3,4-thiadiazole and 1,3,4-oxadiazole, including the first examples of 1,3,4-Oxadiazole mononuclear and dinuclear complexes.^[23–25, 26,27] In view of extending our approach to synthesise robust new ditopic helical complexes to study *SCO* phenomena, we have synthesised two ligands with a suitable bridging moiety, a disubstituted 1,3-phenyl group, to realise helix formation with an extended 1,3,4-oxa/thiadiazole binding pocket, **L**^{TDA-Hel} and **L**^{ODA-Hel}. The nitrogen of the pyridine unit and one of the thiadiazole form a bidentate coordination pocket. Three of these ligands then form a N₆ coordination environment for each iron(II) centre. One nitrogen atom from each ligand is available for electron pair interaction with the guest, which, when encapsulated, can tune the *SCO* behaviour. In fact, through self-assembly reactions of the ligands with iron salts, two helicates, **C1** and **C2**, were formed with the 1,3,4-thiadiazole-based ligand, whereas upon the reaction with the 1,3,4-oxadiazole ligand a mononuclear Fe(II) complex (**C3**) was isolated. The role of the heteroatom in helical complex formation, along with attempted guest interactions with the helicates in the case of **C2** are investigated in detail in the current study. Recently Crowley *et al.* attempted host guest chemistry with analogues Fe(II) helicates.^[28] Despite having a small cavity guest sensing attempts were also investigated by *NMR* spectroscopy.^[28] Attempts were made to make use of the lone pair nitrogen atoms from the ligand backbone to encapsulate cations such as lithium in the cavity and tune the spin states of the iron centres by guest encapsulation. To the best of our knowledge, this study would be the first of its kind to tune the spin states of iron centres by encapsulated cations.

Results and discussion:

Two new ligands **L**^{TDA-Hel} and **L**^{ODA-Hel} were prepared in two steps. The first step was a conversion of isophthalic acid (**I**), catalysed by DMF and thionylchloride to isophthaloyldichloride (**II**). The product was reacted, without any further purification, with picolyhydrazide in THF to the N'1,N'3-dipicolinoylisophthalohydrazide (**III**). The following ring closing was achieved with Lawesson's reagent, yielding to the ligand 1,3-bis(5-(pyridin-2-yl)-1,3,4-thiadiazole-2-yl)benzene (**L**^{TDA-Hel}) in low yields.^[23,24] The ring-closing reaction and dehydration to the 1,3-bis(5-(pyridin-2-yl)-1,3,4-oxadiazole-2-yl)benzene

($L^{\text{ODA-Hel}}$) were achieved in moderate yields with triethylamine, triphenylphosphane and tetrachlorocarbon in dry acetonitrile.^[27,29] The obtained $L^{\text{TDA-Hel}}$ and $L^{\text{ODA-Hel}}$ were fully characterized using a range of techniques, including $^1\text{H-NMR}$, $^{13}\text{C-NMR}$, 2D-NMR (**Figure S1-S11**), IR (**Figure S30-S32**), mass spectrometry (**Figure S36-37**), and elemental analysis.



Scheme 1: Top: Multistep ligand synthesis of $L^{\text{TDA-Hel}}$ and $L^{\text{ODA-Hel}}$. **Bottom:** Complex synthesis of **C1-C3**.

Three complexes **C1-C3** were prepared in aerobic ambient conditions. Complex **C1** and **C2** were obtained with $L^{\text{TDA-Hel}}$ as di-nuclear helicates with ClO_4^- and BF_4^- counterions. Complex **C3** was obtained $L^{\text{ODA-Hel}}$ as mononuclear iron(II) complex. All complexes are characterized by IR spectroscopy (**Figure S33-35**) and single crystal X-ray crystallography. Complex **C1** and **C2** are additionally characterised by a range of NMR techniques (**Figure S12-21**). The X-ray crystallography data were obtained from a crystal taken directly from the mother liquor, whereas all other analyses were carried out on a microcrystalline sample obtained by filtering the mother liquor and air drying it. The bulk sample analysed by EA shows that **C1** and **C2** contain water. This could be due to the air drying of the bulk product after filtration and the time delay between the measurement of EA and the measurement. The lattice solvent molecules such as acetonitrile and ether evaporate easily and are replaced by water.

Structural determination of complex **C1** and **C2** and ligand $L^{\text{ODA-Hel}}$:

Complex $[\text{Fe}_2(L^{\text{TDA-Hel}})_3](\text{ClO}_4)_4 \cdot 3 \text{H}_2\text{O}$ (**C1**) was crystallized as dark red rectangular crystals from acetonitrile by diethyl ether diffusion after two weeks. The X-ray structural data was collected at 120 K. The complex $[\text{Fe}_2(L^{\text{TDA-Hel}})_3](\text{ClO}_4)_4 \cdot 3 \text{H}_2\text{O}$ (**C1**) crystallizes in $P\bar{1}$ space group in a triclinic crystal system. The asymmetric unit consists of one molecule of the helical cation with the formula $[\text{C}_{60}\text{H}_{36}\text{Fe}_2\text{N}_{18}\text{S}_6]^{4+}$ (**Figure 1**). Four perchlorate anions compensate for the overall charge. The excess electron density is modelled as four acetonitrile molecules in the crystal lattice. The unit cell contains a total of two asymmetric units. The average Fe-N bond length for both iron centres, Fe1 and Fe2 are 1.959 \AA , indicating that both iron centres are in the LS state.^[30-33] All Fe-N bond lengths can be seen in **Table S5**. The key parameters from the X-ray crystallography data are tabulated in **Table S1**. The cationic helicate consists of two Fe(II) metal centres bridged by three $L^{\text{TDA-Hel}}$

ligands. As shown in **Figure 2**, the helical unit contains the same chiral environment around both iron centers. Due to the inversion symmetry of the $P\bar{1}$ space group one unit cell contains both enantiomeric helices (Λ and Δ), which indicates the racemization of the helices. Both enantiomeric helices are aligned in the bc plane, which is shown in **Figure S38**, and are interlinked which implies strong interaction between both.

The nitrogen from the Thiadiazole along with the pyridyl nitrogen forms a bis bidentate pocket and three of such ligands come together to wrap around the metal centre to satisfy the coordination sphere around each iron centre. The distortion parameters for the coordination pocket are in line with values for LS complexes known from literature.^[30–33] The distortion calculations give an Σ of 55.080 for Fe1 and 55.181 for Fe2 as well as θ of 128.956 for Fe1 and 133.812 for Fe2.

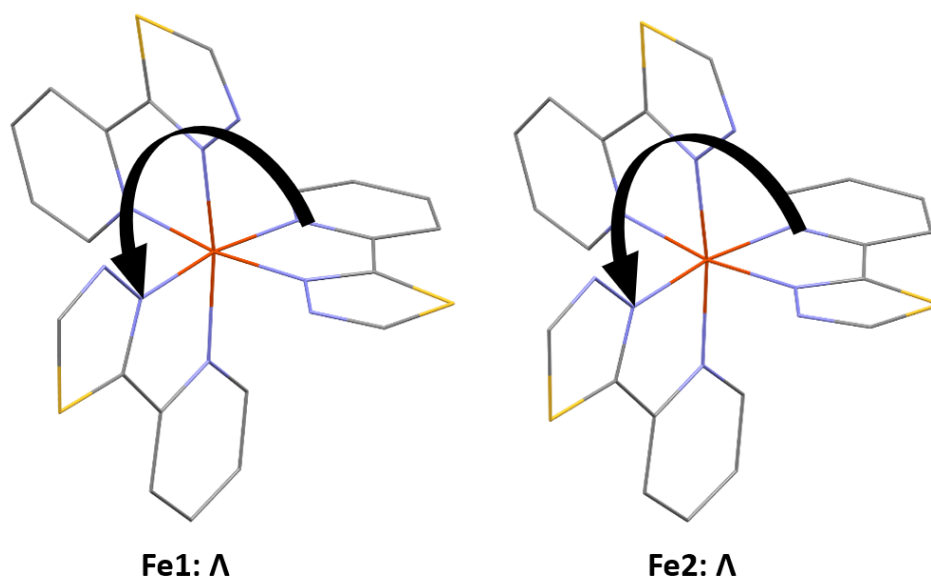


Figure 1: Representation of the Iron(II) environment in $[\text{Fe}_2(\text{L}^{\text{TDA-Hel}})_3](\text{ClO}_4)_4 \cdot 3 \text{H}_2\text{O}$ (**C1**), to show the chirality of one helical unit.

The complex $[\text{Fe}_2(\text{L}^{\text{TDA-Hel}})_3](\text{BF}_4)_4 \cdot 5\text{H}_2\text{O}$ (**C2**) was also crystallized as dark red rectangular crystals from acetonitrile by diethyl ether diffusion after fourteen days. The crystal structure $[\text{Fe}_2(\text{L}^{\text{TDA-Hel}})_3](\text{BF}_4)_4 \cdot 5 \text{H}_2\text{O}$ (**C2**) is isostructural to **C1**, but instead, the cation with the formula $[\text{C}_{60}\text{H}_{36}\text{Fe}_2\text{N}_{18}\text{S}_6]^{4+}$ is charge balanced by four disordered tetrafluoroborate anions. In addition, the lattice solvent has water along with acetonitrile. The crystal structure of **C2** is shown in **Figure S40**, the bond lengths can be seen in **Table S6**. The calculated distortion parameters are $\Sigma = 55.321$ and $\theta = 143.117$ for Fe1 and $\Sigma = 54.891$ and $\theta = 139.770$ for Fe2, which are in line with the values for the coordination sphere around low spin iron(II).^{30,31,34,35} The crystallographic data are tabulated in **Table S2**.

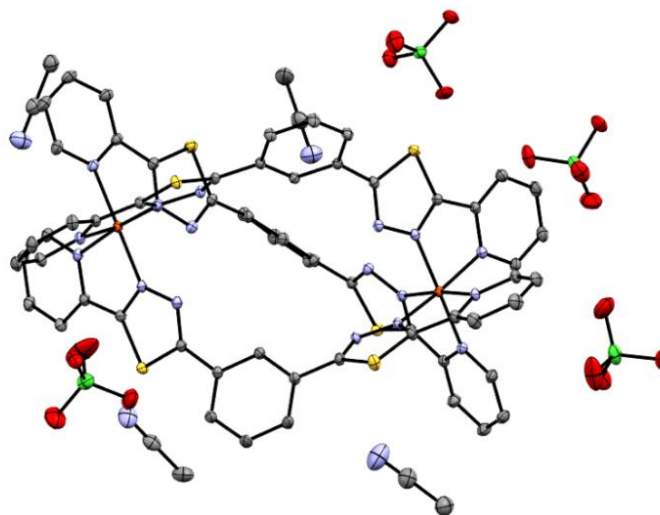


Figure 2: Molecular structure of $[\text{Fe}_2(\text{L}^{\text{TDA-Hel}})_3](\text{ClO}_4)_4 \cdot 4 \text{CH}_3\text{CN}$ (**C1**). Colours: carbon (grey), nitrogen (light blue) iron (orange), sulphur (yellow), chloride (green), oxygen (red).

Complexations with $\text{L}^{\text{ODA-Hel}}$ under the same conditions as for **C1** and **C2** lead to small crystals which were crystallized from acetonitrile as colourless needles by slow evaporation over two weeks. The X-ray data was collected 120 K show that $[\text{Fe}(\text{H}_2\text{O})_2(\text{L}^{\text{ODA-Hel}})_2](\text{ClO}_4)_2$ (**C3**) crystallizes in triclinic space group $P\bar{1}$, further information about the crystallographic data can be found in **Table S4**. The asymmetric unit consists of half of the complex with the molecular formula $[\text{C}_{20}\text{H}_{14}\text{FeN}_6\text{O}_3]^{2+}$ including an iron atom to which one aqua ligand and one equivalent of the ligand $\text{L}^{\text{ODA-Hel}}$ are coordinated. In addition, one equivalent of perchlorate is present as a counterion and one molecule of acetonitrile from the solvent. The complete structure $[\text{C}_{40}\text{H}_{28}\text{FeN}_{12}\text{O}_6]^{2+}$ of **C3** is obtained by inversion to the iron(II) centre as inversion centre. The ligand $\text{L}^{\text{ODA-Hel}}$ is present as a nearly planar unit and coordinates Fe^{2+} in one of the two coordination pockets as a bidentate ligand, as shown in **Figure S42**. The water molecules are coordinating in *trans*-configuration. The average bond length of the iron-nitrogen bonds is 2.181 Å while the average iron-oxygen bond length is 2.086 Å. The metal-ligand distances are listed in **Table S7**. The bond length indicates the complex stays at HS state at 120 K. ^[32–35] The crystal structure of **C3** shows hydrogen bonding interactions between the aqua ligand O3 and the nitrogen of the Oxadiazoles N4, N5 and the nitrogen of the pyridine arm N6, which through intramolecular interactions links the complex layers (**Table S4**). Furthermore, hydrogen bonds act between protons H1, H13, H17, H20, and the oxygen atoms O5, O6, O7 of the perchlorate, which is respectively located below or above the gap created by the *cis* position of the ligand arms, as shown in **Figure S43**. The formation of complex $[\text{Fe}(\text{H}_2\text{O})_2(\text{L}^{\text{ODA-Hel}})_2](\text{ClO}_4)_2$ suggests that despite the preferred 120° angle in the central benzylic unit for helical complexes, the angle of the coordination pocket significantly impacts both the spin state and the overall structure.

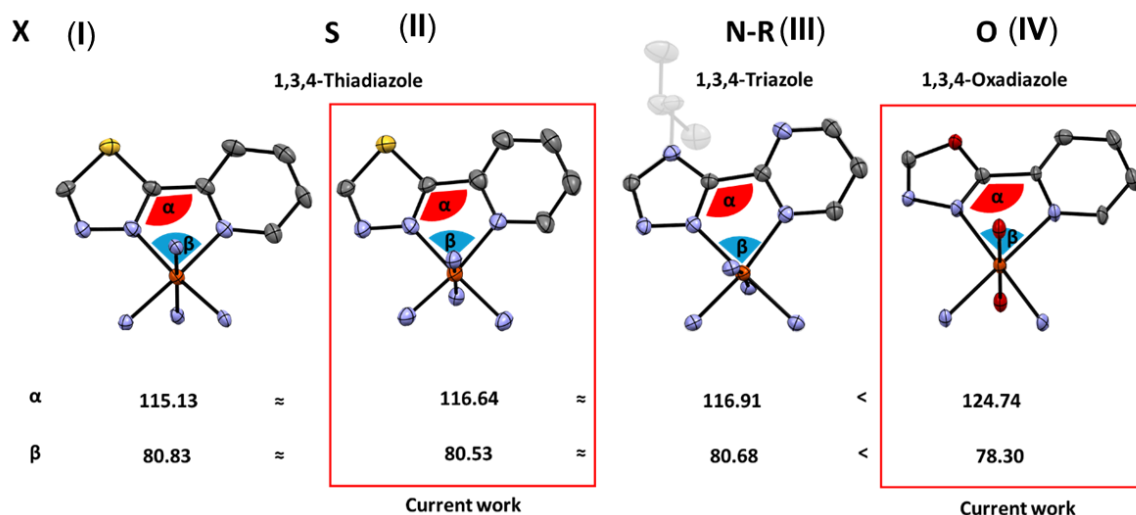


Figure 3: Comparison of the coordination pocket and the influence of the heteroatom on the bite angle. **(I)** $[\text{Fe}(\text{dptd})_3](\text{OTf})_2 \cdot 1.25 \text{ DCM} \cdot 0.5 \text{ H}_2\text{O}$ by Klingele *et al.* with Tris ligated mononuclear Fe(II) complex with thiadiazole. ^[36] **(II)** $[\text{Fe}_2(\text{L}^{\text{TDA-Hel}})_3](\text{ClO}_4)_4$ **C2** from the current study. **(III)** $[\text{Fe}_2(\text{L}^{2\text{pym-meta}})_3](\text{BF}_4)_4 \cdot 6 \text{ CH}_3\text{CN}$ by Brooker *et al.* ^[19] **(IV)** $[\text{Fe}(\text{H}_2\text{O})_2(\text{L}^{\text{ODA-Hel}})_2](\text{ClO}_4)_2$ from the current study.

As illustrated in **Figure 3** the bite angle β and backbone angle α of the ligand variations are dependent on the heteroatom in the five-membered ring. As the size of the heteroatom increases angle α decreases, which leads to a stronger ligand field stabilizing the complexes more in the *LS* state. This in turn, increases the bite angle and aligns the geometry closer to the optimal octahedron. It is important to note that from the current study, we also show that an increase in the α angle also affects the formation of the self-assembly of triple-stranded helicates. When the α angle is below 120° the formation of helicates is favored which is evident from the current work and also the work from Brooker *et al.* ^[19] The mononuclear complex $[\text{Fe}(\text{H}_2\text{O})_2(\text{L}^{\text{ODA-Hel}})_2](\text{ClO}_4)_2$ (**C3**) shows a parallel, staggered π -stacking between the oxadiazole ring and the benzyl ring with an average distance of 3.36 Å. Despite the entropically favoured formation of the helical unit (**Figure S44**), this π -stacking between the complexes in combination with a larger α -angle in the case of **C3** leads to the formation of the mononuclear complex. In contrast, a smaller α -angle and no π -stacking leads to the formation of dinuclear helicates in complexes **C1** and **C2**. α and β angles from the helicates reported by the Aromi *et al.* with anions such as Cl^- and Br^- encapsulated on them to tune the SCO behavior cannot be taken for direct comparison with the existing systems as the anions encapsulated also alters these angles as well as the spin states on these systems. ^[22]

The cavity inside the helicate was estimated by measuring the distance between the centre (red) to the nearest neighbour atom, hydrogens (grey) of the isophthalic unit (see **Figure 4**). With a small radius of 2.057 Å and with the presence of lone pair nitrogen atoms from thiadiazole only a small ion such as the lithium cation can be investigated as a guest.

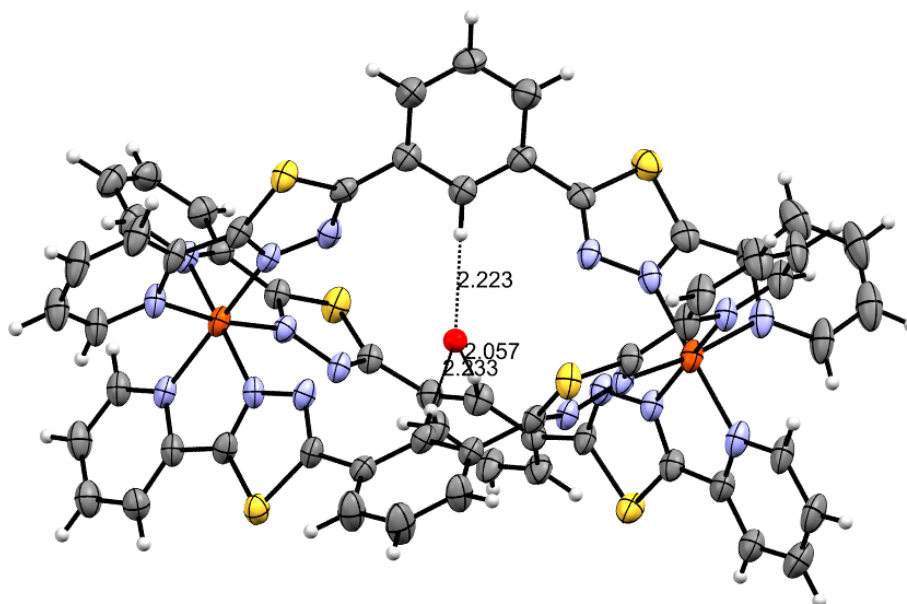


Figure 4: Calculation of the space of the defined spherical void inside the helical unit.

Solution Stability of the complex:

The stability of the complex **C1** in solution is initially tested by molar conductivity measurements in acetonitrile at a concentration of $1 \cdot 10^{-3}$ M. The values tabulated in **Table S9** clearly indicate that the complex stays as 2:1 conductor in solution.^[38] When the molar conductivity is measured after one hour the complex slightly dissociates but still within the range for a 2:1 conductor (**Section S8**). We have additionally recorded ^1H DOSY NMR spectra of the ligand and the complex and compared the extracted ^1H diffusion coefficients ($5.87 \times 10^{-10} \text{ m}^2 \cdot \text{s}^{-1}$ for the **C1** complex and $1.7 \times 10^{-9} \text{ m}^2 \cdot \text{s}^{-1}$ for the ligand). The higher diffusion coefficient suggests that the **C1** complex is stable on the millisecond time scale i.e., the time scale of the diffusion experiment. Finally, the UV-Vis studies on the complexes in MeCN, in comparison to the ligand, clearly show the presence of charge transfer bands centred around 370 - 530 nm (**Figure S45** and **Section S5**).^[39]

Cyclic Voltammetry:

The $[\text{Fe}_2(\text{L}^{\text{TDA-Hel}})_3](\text{ClO}_4)_4 \cdot 3 \text{ H}_2\text{O}$ (**C1**) and its redox properties were further characterized by CV measurements in acetonitrile ($1 \cdot 10^{-3}$ M, $n\text{-Bu}_4\text{PF}_6$) at a scan rate of $100 \text{ mV} \cdot \text{s}^{-1}$. The cyclic voltammogram of $[\text{Fe}_2(\text{L}^{\text{TDA-Hel}})_3](\text{ClO}_4)_4 \cdot 3 \text{ H}_2\text{O}$ (**C1**), the blank and the Fc/Fc^+ reference are shown in **Figure S46**. This oxidation process (I/I') was measured again at a scan rate of $50 \text{ mV} \cdot \text{s}^{-1}$ ($E_{1/2} = 1.37 \text{ V}$, $\Delta E_p = 182.8 \text{ mV}$) shown in **Figure 5**. The redox wave can be assigned to the redox process of the iron metal centre $\text{Fe}(\text{II})/\text{Fe}(\text{III})$, which is in the range of the literature.^[19,37] Correlation between the redox potential and the ligand field strength are well known from the literature for $3d$ metals. The redox

potential obtained in MeCN was compared to the analogue triazole based helicate reported by Brooker *et al.*^[19] The redox potential shifts to higher $E_{1/2}$ as expected due to the stronger ligand field imposed by the Thiadiazole moiety indicating greater stability of their oxidized forms. This is caused because ligands with stronger ligand field cause significant splitting of the d -orbitals, lowering the energy of iron oxidation state and thereby making the oxidation process more favourable and shifts the redox potential to more positive values. The spin states can be estimated from the redox potential of the metal centre in similar environments. In this case, since the helicates reported by Brooker *et al.* with 1,3,4-triazole ligands were stabilised in LS state, it is anticipated with the helicates **C1** and **C2** to be stabilised in LS state because of stronger ligand field imposed by 1,3,4-Thiadiazole. A scan rate study of this process in the area 1.0 V – 1.8 V has been recorded and is shown in **Figure S47** at scan rates of 50, 100, 150 and 200 $\text{mV}\cdot\text{s}^{-1}$. As expected for a quasi-reversible process, the oxidative and reductive peak potentials move apart as the current increases with increasing scan rate. The values for the current of the oxidation peaks of each scan rate were plotted against the square roots of the corresponding scan rates as can be seen in **Figure S48**. This further indicates a quasi-reversible process.

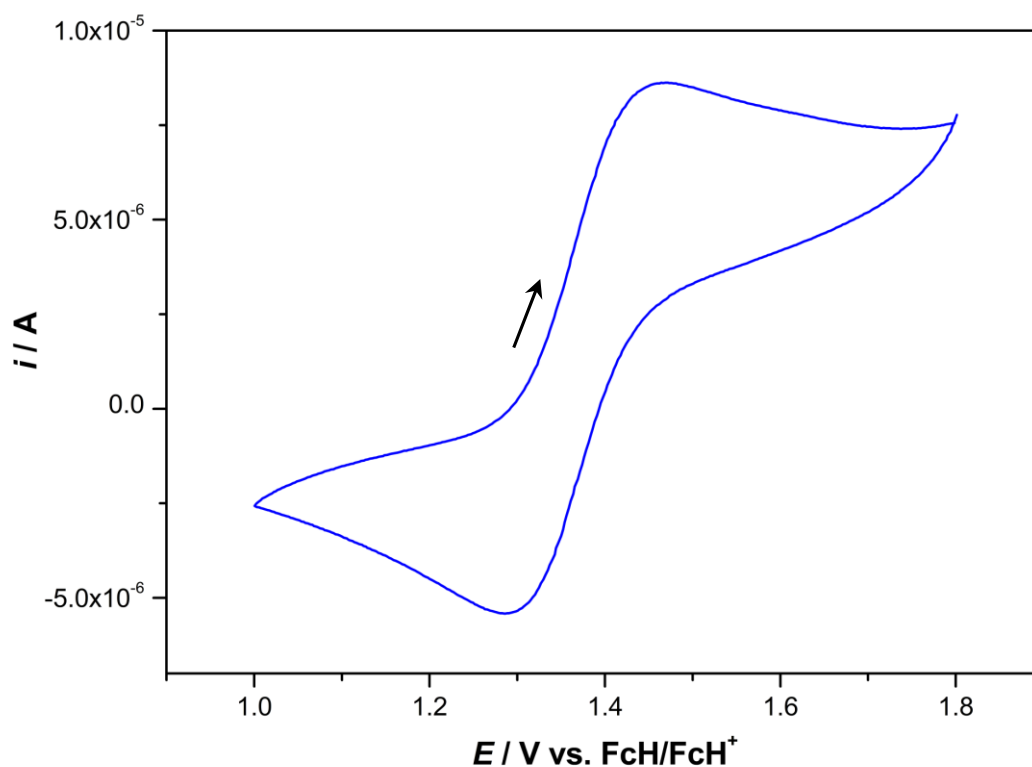


Figure 5: Cyclic voltammograms of 1 mM solutions of helicates $[\text{Fe}_2(\text{L}^{\text{TDA-Hel}})_3](\text{ClO}_4)_4 \cdot 3 \text{H}_2\text{O}$ (**C1**) in MeCN ($0.1 \text{ mol}\cdot\text{L}^{-1}$ TBAPF₆ vs Fc^+/Fc) at $50 \text{ mV}\cdot\text{s}^{-1}$.

Host-Guest chemistry:

The possible intercalation of monovalent Li^+ cation into the helical cavity of the **C1** host was investigated by ^7Li NMR techniques using lithium perchlorate as a source of lithium ions. The VT ^7Li NMR spectra of

the **C1** complex and LiClO₄ in a ratio 1:1 and the pure LiClO₄ as a reference (both samples dissolved in d³-MeCN) are presented in **Figure 6A** and **B**, respectively. The Li⁺ in the pure lithium perchlorate solution resonates at -2.28 ppm with a full width at half height (fwhh) of about 1.7 Hz. This signal shifts towards higher fields with decreasing temperature, however, with no effect on the fwhh. The difference between the signal maxima in two temperature steps is not constant, i.e., it is about 9 Hz for the signals recorded at 333 K and 318 K, while it is only about 1 Hz for the signal recorded between 273 K and 258 K. The VT ⁷Li NMR spectra of the perchlorate in the presence of the **C1** complex (**Figure 6A**) reveal deshielding of the lithium ions compared to pure salt with a ⁷Li shift of -1.3 ppm and *fwhh* of ca 2.5 Hz at 333 K. The change of the lithium shift between two temperature steps in the investigated temperature range is more pronounced ranging from ca. 15 Hz to 11 Hz. Also, *fwhh* increases by approximately 45% at the lowest temperature and by approx. 33% at 333 K.

This suggests an interaction between the lithium ions and the **C1** complex. Such an interaction could be further probed by diffusion and *NOE* based NMR techniques. For this reason, we recorded ⁷Li DOSY NMR spectra of both the C1-LiClO₄ mixture and the pure LiClO₄ solution and compared the diffusion coefficients obtained. The increase of the diffusion coefficient from 1.22 X 10⁻⁹ m²/s (LiClO₄) to 3.02 X 10⁻⁹ m²/s (**C1**-LiClO₄) is attributed to an (electrostatic) interaction between the lithium ion and the helical host. It should be noted that the lithium ions still diffuse faster than the **C1** complex i.e., no encapsulation takes place. The preferred location of the Li⁺ with respect to the complex **C1** was further investigated by ¹H-⁷Li HOESY NMR using different mixing times, but without success, possibly due to the fast lithium exchange. It should also be noted that the complex is strongly positively charged, so repulsion of the Li cation would be expected and any interaction would be mediated only by the perchlorate ions. This result explains the absence of spin state change due to the encapsulation of the lithium ion.

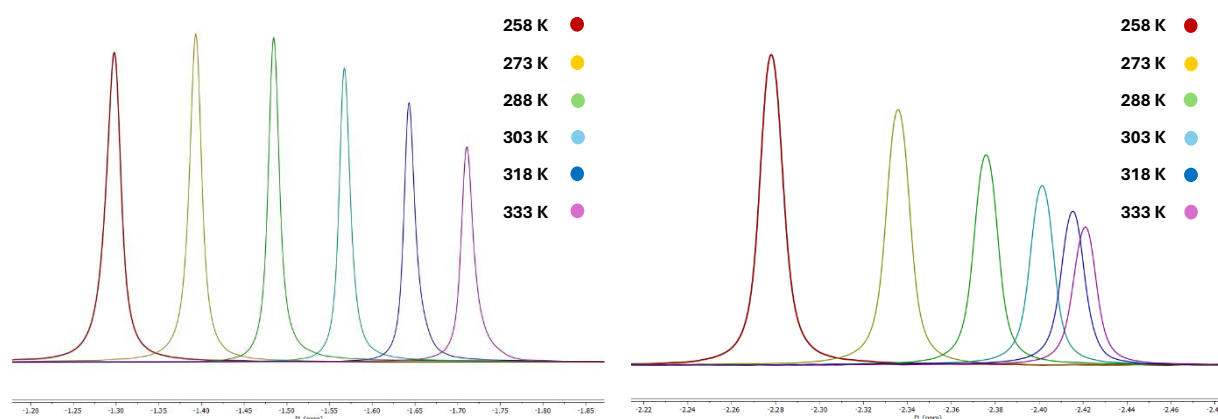


Figure 6: Left (A): VT- ⁷Li-NMR measurements between 258 to 333 K for complex **C1** (10 mg; 5.55 μmol) and LiClO₄ (0.580 mg; 5.55 μmol) in 0.7 mL in d³-MeCN. Right: VT- ⁷Li-NMR measurements between 258 to 333 K of pure LiClO₄ in d³-MeCN in the same concentration.

Conclusions:

In the current study we report the synthesis of two novel ligands with extended bis bidentate pockets with 1,3,4-thiadiazole and 1,3,4-oxadiazole, $L^{\text{TDA-Hel}}$ and $L^{\text{ODA-Hel}}$ respectively. The complexes with $L^{\text{TDA-Hel}}$ formed helicates as anticipated and two helical complexes $[\text{Fe}_2(L^{\text{TDA-Hel}})_3](\text{ClO}_4)_4 \cdot 3 \text{H}_2\text{O}$ (**C1**) and $[\text{Fe}_2(L^{\text{TDA-Hel}})_3](\text{BF}_4)_4 \cdot 5 \text{H}_2\text{O}$ (**C2**) are reported. Both complexes stay in *LS* state both in the solid state and in the solution phase. Both complexes were structurally characterized using *X-ray* crystallography. The solution stability of the helical complexes was also investigated through molar conductivity and *NMR*. The small helical cavity was used to probe the spin state switch by encapsulating Li^+ ion to tune the spin states of the iron centers. The *NMR* investigation reveals an interaction between the Li^+ ion and the **C1** complex, but without encapsulation, and the spin states of iron centers remain unchanged. The ligand field of the 1,3,4-thiadiazole will be further tuned by the choice of a different 5-membered ring to impart spin crossover in this system in the future. In the case of $L^{\text{ODA-Hel}}$ ligand, due to the larger bite angle by the change in the hetero atom from sulfur to oxygen, the desired helicate structures were not achieved. Instead, a mononuclear iron complex $[\text{Fe}(\text{H}_2\text{O})_2(L^{\text{ODA-Hel}})_2](\text{ClO}_4)_2$ (**C3**) was formed, despite the desired 120° angle imposed by the bridging benzyl unit. Further fine-tuning of the ligand design with $L^{\text{TDA-Hel}}$ is currently underway to impart *SCO* in this type of helical iron(II) complexes based on 1,3,4-thiadiazole ligands.

Experimental:

All chemicals were purchased from Alfa Aesar, Deutero, Fisher Chemicals, TCI, Sigma-Aldrich, and Acros Organics and used without further purification. Solvents were dried according to the literature known procedures and used freshly distilled. Dry DMF was purchased from Sigma Aldrich. Deuterated solvents were purchased from Deutero GmbH. Bruker Avance DRX 400 MHz *NMR* spectrometer (Bruker Biospin GmbH, Rheinstetten, Germany) at a ^1H frequency of 400.31 MHz and ^{13}C frequency of 100.66 MHz using a commercial Bruker 5 mm inverse 2 channel probe head equipped with z-gradients was used for the standard characterization of the synthesized ligands and complexes. For all ^1H spectra 32 scans were averaged using 2 s recycle delay. All ^1H COSY (correlation spectroscopy) *NMR* spectra were measured using pulsed field gradients for coherence selection. The experiments were performed recording 1024 data points in the direct dimension with 512 increments and 1 scan per increment with 2 sec recycle delay. The ^{13}C spectra were recorded with power gated decoupling averaging 1 k scans. All ^1H - ^{13}C HSQC (heteronuclear single quantum correlation) *NMR* experiments were recorded using the hsqcetgp sequence with 256 increments, 32 transients, a 2 s recycle delay, sweep widths of 20 and 180 ppm and offsets of 5.5 and 80 ppm for the ^1H and ^{13}C dimension resp. The sequence was optimized for 145 Hz couplings. The ^1H - ^{13}C HMBC (heteronuclear multiple bond correlation) *NMR* spectra were

recorded using the hmbcplpndqf pulse sequence with 256 increments, 32 transients, 2 s recycle delay, sweep widths of 20 and 240 ppm and offsets of 5.5 and 110 ppm for the ^1H and ^{13}C dimensions resp. The sequence was optimized for couplings of 10 Hz, which is a common compromise for long range ^1H – ^{13}C couplings. The data was processed using sine windows functions in both dimensions of total 1024 (F2) and 512 (F1) points. Stimulated echo sequence with bipolar gradient pulses and a longitudinal eddy current delay was used for the ^1H diffusion ordered spectroscopy (dosy) experiments. The gradient strength was incremented in 16 steps from 2 % to 95 % of the maximum gradient strength. The diffusion time and the gradient pulse length for all samples were 100 ms and 2.8 ms with 2 s recycle delay, respectively. After Fourier transformation and baseline correction, the diffusion dimension of the 2D dosy spectra was processed using the Topspin 1.3 software package (2007, patchlevel 8, Bruker Biospin GmbH, Rheinstetten, Germany). The diffusion analysis was performed using the Topspin T1/T2 relaxation package. All ^1H and ^{13}C NMR spectra were referenced using the solvent lock (^2H) signal in accordance with the IUPAC recommended secondary referencing methods.

Bruker Avance Neo NMR spectrometer (Bruker Biospin GmbH, Rheinstetten, Germany) equipped with a 5mm BBF/F/H TBO iProbe head and Sample Case Plus autosampler was used to record the variable temperature (VT) ^1H and all ^7Li NMR spectra at ^1H frequency of 400.3 MHz and ^7Li frequency of 155.6 MHz. The ^1H spectra were recorded applying a 30° pulse averaging 32 scans with a 2 s recycle delay. The ^7Li NMR spectra were measured exciting the sample with a 30° pulse averaging 32 scans with 3 s repetition time. Stimulated echo sequence with bipolar gradient pulses and one spoil gradient was used for the ^7Li diffusion ordered spectroscopy (dosy) experiments. The gradient strength was incremented in 16 steps from 2 % to 95 % of the maximum gradient strength. The diffusion time and the gradient pulse length for the studied ligand and C1 complex were 400 ms and 1.2 ms with 5 s recycle delay, respectively. The diffusion analysis was performed using the Topspin T1/T2 relaxation package of the Topspin 4.3 software package (2023, Bruker Biospin GmbH, Rheinstetten, Germany). The ^7Li spectra were referenced to 9.7 m LiCl in D_2O at 0 ppm. All NMR spectra were analysed using the program MestReNova (version 14.3.2-32681 / 23.03.2023, Mestrelab Research S. L.) if not stated otherwise. All mass spectra (Advion expression-L CMS) as well as elemental analysis (Elementar vario EL Cube: C, H, and N) were measured at the microanalytical laboratories of the Johannes Gutenberg University Mainz. Cyclic voltammetry measurements were performed on a PGSTAT 204 potentiostat was used and a TSC 1600 closed with an already built-in platinum counter electrode as a vessel wall from rhd instruments was used as the measuring cell. A glassy carbon electrode was used as the working electrode, this electrode was polished after every completed series of measurements using an aluminium oxide polishing paste with grain sizes of 0.1 μm and 0.05 μm from Buehler for at least half an hour on a microfiber cloth in figures of 8's. After the cleaning step the electrodes were washed with

water and acetonitrile and dried in an oven at 60°C for at least half an hour. A silver pseudo reference electrode was used as the reference electrode. For better comparability after every series a few milligrams of ferrocene was added, so all measurements can be referenced against ferrocene/ferrocenium. For the conducting salt tetrabutylammonium hexafluorophosphate was used with a concentration of 0.1 M. X-ray diffraction data were collected with STOE STADIVARI at the Johannes Gutenberg University Mainz. The structures were solved with ShelXT^[40] and refined with ShelXL^[41,42] implemented in the program Olex2.^[43] The X-ray cif file data are deposited on the Cambridge CCDC database with identification numbers 2366949-2366951.

Ligand Synthesis:

N'1,N'3-dipicolinoylisophthalohydrazide (III)

Isophthalic acid (4.01 g, 24.1 mmol, 1.00 eq.), 10 mL of SOCl₂ and 2 mL of DMF were combined under an inert N₂ atmosphere. The colourless solution was stirred and refluxed for 90 minutes until no further gas evolution could be observed. The solvent was then removed under reduced pressure, leaving a white colourless solid. The dry solid was suspended in 50 mL of dry THF and added to a solution of 2-picolinic hydrazide (6.62 g, 48.3 mmol, 2.00 eq.) in 150 mL dry THF resulting in a bright yellow solution with a yellow precipitate. The suspension was left to stir overnight and then filtered to obtain a colourless powder (6.15 g, 15.2 mmol, 63 %). ¹H-NMR (400 MHz, d⁶-DMSO, δ (ppm)): 11.75 – 11.47 (m, 2H), 10.74 (d, *J* = 17.4 Hz, 2H), 8.72 (ddt, *J* = 3.4, 2.4, 1.1 Hz, 2H), 8.63 – 8.50 (m, 1H), 8.21 – 8.01 (m, 6H), 7.77 – 7.60 (m, 3H).

1,3-bis(5-(pyridin-2-yl)-1,3,4-thiadiazol-2-yl)benzene (L^{TDA-Hel})

A suspension of N1,N4-di(pyridine-3-carbonyl)benzene-1,4-dicarbohydrazide (III) (4.36 g, 10.7 mmol, 1.00 eq.) and Lawesson's reagent (10.02 g, 23.5 mmol, 2.20 eq.) in 100 mL of dry toluene was stirred and refluxed for 72 h resulting in a red solid in an orange solution. Then 100 mL of a 1M NaOH solution were added, and the mixture was refluxed overnight giving a colourless solid at the phase boundary between an orange water and toluene phase. The solid was removed *via* filtration, obtaining a light brown powder (0.83 g, 2.1 mmol, 19.37%). ¹H-NMR (400 MHz, d-CDCl₃, δ (ppm)): 8.70 (ddd, *J* = 4.9, 1.7, 1.0 Hz 3H), 8.42 (dt, *J* = 7.9, 1.1 Hz, 2H), 8.21 (dd, *J* = 7.8, 1.8 Hz, 2H), 7.89 (td, *J* = 7.8, 1.7 Hz), 7.68 (t, 3*J* = 7.66 Hz, 1H), 7.43 (ddd, *J* = 7.6, 4.9, 1.2 Hz, 2H). ¹³C-NMR (400 MHz, CDCl₃, δ (ppm)): 170.80, 169.02, 150.10, 149.10, 137.40, 131.50, 130.40, 130.30, 127.40, 125.60, 121.20. FT-IR: $\tilde{\nu}$ (cm⁻¹) = 3048, 1583, 1565, 1487, 1427, 1399, 1301, 1271, 1247, 1221, 1144, 1081, 1045, 1010, 989, 915, 802, 777, 735, 716, 681, 633, 616, 597, 501, 470. ESI-MS (*m/z*): calc. for [C₂₀H₁₃N₆S₂]⁺ expected: 401.06; found: 401.0640. Elemental Analysis calculated for C₂₀H₁₂N₆S₂ · 2 H₂O · 0.15 C₇H₈: C, 56.14; H, 3.85; N, 18.66 Found (%): C, 56.16; H, 3.35; N, 18.19

1,3-bis(5-(pyridin-2-yl)-1,3,4-oxadiazol-2-yl)benzene ($L^{\text{ODA-Hel}}$)

The N'1,N'3-dipicolinoylisophthalohydrazide (**III**) (8.1 g; 20.0 mmol; 1.00 eq) was suspended in 300 mL of dry acetonitrile. Triethylamine (11.0 mL; 79.8 mmol; 4.00 eq), triphenylphosphane (20.9 g; 79.8 mmol; 4.00 eq) and tetrachloromethane (15.5 mL; 160 mmol; 8.00 eq) were added simultaneously under vigorous stirring and N_2 -atmosphere. A yellow suspension with colourless solid was formed. The reaction mixture heated up slightly which indicated that the reaction was still in progress, so it was stirred overnight. After 15 hours a red-orange suspension was formed. It was filtered and a slightly orange solid was obtained which was washed with acetonitrile. It was then suspended in water for one hour. After that 200 mL of DCM were added to form a solution. The aqueous phase was separated, then extracted five times with 15 mL DCM each. The organic phases were combined and extracted with water. The organic phase was then dried using sodium sulphate, filtered and DCM was removed by distillation. The 1,3-bis(5-(pyridin-2-yl)-1,3,4-oxadiazol-2-yl)benzene ($L^{\text{ODA-Hel}}$) was obtained as a colourless solid (4.13 g, 11.3 mmol, 56.6 %). $^1\text{H-NMR}$ (400 MHz, d^6 -DMSO, δ (ppm)): 9,00 (t, $^4J=1.7$, 1H), 8,82 (d, $^3J=4.7$, 2H), 8,42 (dd, $^3J=7.9$, 1.7, 2H), 8,33 (d, $^3J=8.3$, 2H), 7,92 (td, $^3J=7.8$, 7.8 1.7, 2H), 7,72 (t, $^3J=7.9$, 1H), 7,49 (ddd, $J=7.7$, 4.8, 1.2, 2H). FT-IR: $\tilde{\nu}$ (cm^{-1}): 3565, 3444, 3087, 1649, 1587, 1541, 1472, 1456, 1441, 1360, 1320, 1280, 1253, 1151, 1112, 1086, 1075, 1041, 1022, 996, 970, 918, 814, 797, 769, 742, 717. ESI-MS (m/z): calc. for $[\text{C}_{20}\text{H}_{13}\text{N}_6\text{O}_2]^+$ expected: 369.11, found: 369.1095. Elemental Analysis calculated for $\text{C}_{20}\text{H}_{12}\text{N}_6\text{O}_2 \cdot \text{H}_2\text{O}$: C 62.17, H 3.65, N 21.75 Found (%): C 62.47, H 3.77, N 21.81.

Complex Synthesis:



A suspension of $L^{\text{TDA-Hel}}$ (20 mg, 0.050 mmol, 3.0 eq.) in 10 mL acetonitrile was added dropwise to a solution of $\text{Fe}(\text{ClO}_4)_2 \cdot 6 \text{H}_2\text{O}$ (12 mg, 0.033 mmol, 2.0 eq.) in 10 mL acetonitrile, resulting in a dark red colour. The clear solution was then filtered and *via* ether diffusion with diethyl ether red, rectangular crystals were obtained (0.18 g, 0.010 mmol, 62 %). $^1\text{H-NMR}$ (400 MHz, d^3 -MeCN, δ (ppm)): 8.47 (d, $J=7.9$ Hz, 4H), 8.27 (tq, $J=5.9$, 3.5 Hz, 2H), 8.06 (s, 2H), 7.89 – 7.80 (m, 1H), 7.72 (t, $J=7.8$ Hz, 1H), 7.66 (q, $J=3.7$ Hz, 2H). FT-IR: $\tilde{\nu}$ (cm^{-1}): 3058, 2084, 1993, 1604, 1503, 1475, 1431, 1330, 1253, 1217, 1078, 1032, 996, 898, 862, 829, 801, 769, 746, 725, 683, 620, 555, 493, 453, 433, 409. Elemental Analysis calculated for $\text{C}_{60}\text{H}_{36}\text{Cl}_4\text{Fe}_2\text{N}_{18}\text{O}_{16}\text{S}_6 \cdot 3 \text{H}_2\text{O}$: C, 40.83; H, 2.40; N, 14.28 Found (%): C, 40.78; H, 2.48; N, 13.81.

$[\text{Fe}_2(\text{L}^{\text{TDA-Hel}})_3](\text{BF}_4)_4 \cdot 5 \text{H}_2\text{O}$ (**C2**)

A suspension of the ligand ($\text{L}^{\text{TDA-Hel}}$) (20 mg, 0.050 mmol, 3.0 eq.) in 10 mL acetonitrile was added dropwise to a solution of $\text{Fe}(\text{BF}_4)_2 \cdot 6 \text{H}_2\text{O}$ (11 mg, 0.032 mmol, 2.0 eq.) in 10 mL acetonitrile, resulting in a dark red colour. The clear solution was then filtered and *via* ether diffusion with diethyl ether red, rectangular crystals were obtained (0.17 g, 0.010 mmol, 60 %). $^1\text{H-NMR}$ (400 MHz, $\text{D}^3\text{-MeCN}$, δ (ppm)): 8.47 (d, $J = 7.9$ Hz, 4H), 8.27 (tq, $J = 5.9, 3.5$ Hz, 2H), 8.06 (s, 2H), 7.89 – 7.80 (m, 1H), 7.72 (t, $J = 7.8$ Hz, 1H), 7.66 (q, $J = 3.7$ Hz, 2H). FT-IR: $\tilde{\nu}$ (cm^{-1}): 3618, 3057, 1602, 1503, 1463, 1429, 1332, 1282, 1253, 1218, 1248, 1047, 1029, 895, 863, 830, 797, 774, 748, 726, 714, 684, 645, 611, 598, 520, 495, 453, 433, 408. Elemental Analysis calculated for $\text{C}_{60}\text{H}_{36}\text{B}_4\text{F}_{16}\text{Fe}_2\text{N}_{18}\text{S}_6 \cdot 5 \text{H}_2\text{O}$: C, 41.08; H, 2.80; N, 13.97 Found (%): C, 41.17; H, 2.65; N, 14.40

$[\text{Fe}(\text{H}_2\text{O})_2(\text{L}^{\text{ODA-Hel}})_2](\text{ClO}_4)_2$ (**C3**)

A suspension of $\text{L}^{\text{ODA-Hel}}$ (20 mg; 0.054 mmol; 3.0 eq) in 10 ml acetonitrile was dropped into a fresh solution of iron(II) perchlorate hexahydrate (13 mg; 0.036 mmol; 2.0 eq) in 10 mL acetonitrile with stirring. The solution turned immediately colourless. After 30 minutes of stirring, the reaction mixture was filtered and set for slow evaporation. Colourless needle shaped crystals were obtained in very low yields after one week of $[\text{Fe}(\text{H}_2\text{O})_2(\text{L}^{\text{ODA-Hel}})_2](\text{ClO}_4)_2$ (**C3**). FT-IR: $\tilde{\nu}$ (cm^{-1}): 3376, 1619, 1546, 1485, 1438, 1400, 1311, 1251, 1092, 1057, 950, 942, 815, 797, 778, 748, 717, 680, 622, 411.

Acknowledgement:

J.-G.B and E.R. sincerely thank the Deutsche Forschungsgemeinschaft (DFG, German Research Foundation) – TRR 173 – 268565370 (project A09) for the funding and support. All the authors thank the Johannes Gutenberg-University for the research facilities and infrastructure.

References:

- [1] Constable. *Coord. Chem. Rev.*, **2008**, 252 (8–9), 842–855.
- [2] Constable. *Chem. Soc. Rev.*, **2013**, 42, 1637.
- [3] Lehn, J. -M. *Angew. Chem. Int. Ed. Engl.* **1988**, 27 (1), 89–112.
- [4] Schnitzer, T.; Preuss, M. D.; Basten, J. van; Schoenmakers, S. M. C.; Spiering, A. J. H.; Vantomme, G.; Meijer, E. W. *Angew. Chem. Int. Ed. Engl.*, **2022**, 134 (41), e202206738.
- [5] Chan, M. H. Y.; Yam, V. W. W. *J. Am. Chem. Soc.*, **2022**, 144 (50), 22805–22825.
- [6] Piguet, C.; Bernardinelli, G.; Hopfgartner, G. *Chem. Rev.* **1997**, 97 (6), 2005–2062.
- [7] Pullen, S.; Tessarolo, J.; Clever, G. H. *Chem. Sci.*, **2021**, 12, 7269–7293.

- [8] Suryadevara, N.; Pausch, A.; Moreno-Pineda, E.; Mizuno, A.; Bürck, J.; Baksi, A.; Hochdörffer, T.; Šalitroš, I.; Ulrich, A. S.; Kappes, M. M.; Schünemann, V.; Klopper, W.; Ruben, M.; Pausch, A.; Kappes, M. M.; Klopper, W.; Moreno-Pineda, E.; Bürck, J.; Ulrich, A. S.; Šalitroš, I.; Ruben, M. *Chem. Eur. J.*, **2021**, *27*, 15172–15180.
- [9] Steinert, M.; Schneider, B.; Dechert, S.; Demeshko, S.; Meyer, F. *Inorg. Chem.*, **2016**, *55* (5), 2363–2373.
- [10] Zheng, X.-D.; Lu, T.-B. *Cryst. Eng. Comm.*, **2010**, *12*, 324–336.
- [11] Liu, Z.; Li, X.; Lu, Y.; Zhang, C.; Zhang, Y.; Huang, T.; Zhang, D.; Duan, L. *Nat. Commun.*, **2022**, *13.1*, 1215.
- [12] Jiao, J.; Dong, J.; Li, Y.; Cui, Y. *Angew. Chem. Int. Ed. Engl.*, **2021**, *60* (30), 16704–16711.
- [13] Cho, J.; Ho Jung, S.; Hwa Jung, J.; Ok, M.; Young Kim, K.; Choi, H.; Kim, S.; Shim Sung Lee. *Chem. Sci.*, **2022**, *13*, 3109–3117.
- [14] Zhu, X.; He, C.; Dong, D.; Liu, Y.; Duan, C. *Dalton Trans.*, **2010**, *39*, 10051–10055.
- [15] Diego, R.; Pavlov, A.; Darawsheh, M.; Aleshin, D.; Nehrkorn, J.; Nelyubina, Y.; Roubeau, O.; *Inorg. Chem.*, **2019**, *58*, 9562–9566.
- [16] Jia, C.; Zuo, W.; Yang, D.; Chen, Y.; Cao, L.; Custelcean, R.; Hostaš, J.; Hobza, P.; Glaser, R.; Wang, Y.-Y.; Yang, X.-J.; Wu, B. *Nat. Commun.*, **2017**, *8*, 938. DOI: 10.1038/s41467-017-00915-8.
- [17] Chen, W.; Tang, X.; Dou, W.; Wang, B.; Guo, L.; Ju, Z.; Liu, W. *Chem. Eur. J.*, **2017**, *23* (41), 9804–9811.
- [18] Sahoo, J.; Arunachalam, R.; Subramanian, P. S.; Suresh, E.; Valkonen, A.; Rissanen, K.; Albrecht, M.; Sahoo, J.; Arunachalam, R.; Subramanian, D. R. P. S.; Suresh, E.; Alkonen, A. V.; Rissanen, K.; Lbrecht, M. A. *Angew. Chem. Int. Ed.* **2016**, *55*, 625–9629.
- [19] Singh, S.; Hogue, R. W.; Feltham, H. L. C.; Brooker, S. *Dalton Transactions. Dalton Trans.*, **2019**, *48*, 15435–15444.
- [20] Struch, N.; Brandenburg, J. G.; Schnakenburg, G.; Wagner, N.; Beck, J.; Grimme, S.; Lützen, A. *Eur. J. Inorg. Chem.*, **2015**, *2015* (33), 5503–5510.
- [21] Tuna, F.; Lees, M. R.; Clarkson, G. J.; Hannon, M. J. *Chem. Eur. J.*, **2004**, *10* (22), 5737–5750.
- [22] Darawsheh, M. D.; Barrios, L. A.; Roubeau, O.; Teat, S. J.; Aromí, G.; Zaragoza, P.; San, F.; Zaragoza, S. *Chem. Commun.*, **2017**, *53*, 569–572.

- [23] Sundaresan, S.; Kiehl, J.; Carrella, L. M.; Rentschler, E. *Cryst. Growth Des.*, **2023**, 23, 3, 1648-1655.
- [24] Kiehl, J.; Hochdörffer, T.; Carrella, L. M.; Nygaard, M. H.; Overgaard, J.; Rentschler, E. *Inorg. Chem.*, **2022**, 61, 7, 3141-3151.
- [25] Fürmeyer, F.; Carrella, L. M.; Ksenofontov, V.; Möller, A.; Rentschler, E. *Inorg Chem* **2020**, 59 (5), 2843–2852.
- [26] Köhler, C.; Rentschler, E. *Eur. J. Inorg. Chem.*, **2016**, 1955–1960.
- [27] Sundaresan, S.; Becker, J.-G.; Eppelsheimer, J.; Sedykh, A. E.; Carrella, L.; Müller-Buschbaum, K.; Rentschler, E. *Dalton Trans.*, **2023**, 52, 13181-13189.
- [28] Lisboa, L. S.; Riisom, M.; Vasdev, R. A. S.; Jamieson, S. M. F.; Wright, L. J.; Hartinger, C. G.; Crowley, J. D. Cavity-Containing. *Front. Chem.* **2021**, 9.
- [29] Sundaresan, S.; Eppelsheimer, J.; Carrella, L. M.; Rentschler, E. *Crystals 2022, Vol. 12, Page 404*, **2022**, 12 (3), 404.
- [30] Herold, C. F.; Shylin, S. I.; Rentschler, E. *Inorg. Chem.*, **2016**, 55 (13), 6414–6419.
- [31] Herold, C. F.; Carrella, L. M.; Rentschler, E. A. *Eur. J. Inorg. Chem.*, **2015**, 3632–3636.
- [32] Halcrow, M. A. *John Wiley and Sons*, **2013**.
- [33] Gütlich, P.; Garcia, Y.; Goodwin, H. A. *Chem. Soc. Rev.*, **2000**, 29 (6), 419–427.
- [34] Gaspar, A. B.; Ksenofontov, V.; Seredyuk, M.; Gütlich, P. *Coord. Chem. Rev.* **2005**, 249 (23), 2661–2676.
- [35] Feltham, H. L. C.; Barltrop, A. S.; Brooker, S. *Coord. Chem. Rev.*, **2017**, 344, 26–53.
- [36] Klingele, J.; Kaase, D.; Schmucker, M.; Lan, Y.; Chastanet, G.; Letard J-F.,. *Inorg. Chem.*, **2013**, 52, 6000-6010.
- [37] Singh, S.; Brooker, S. *Chem. Sci.*, **2021**, 12, 10919-10929.
- (38) Sundaresan, S.; Brooker, S. *Inorg. Chem.*, **2023**, 62, 31, 12192-12202.
- [39] Sundaresan, S.; Kühne, I. A.; Kelly, C. T.; Barker, A.; Salley, D.; Müller-Bunz, H.; Powell, A. K.; Morgan, G. G. *Crystals (Basel)* **2019**, 9 (19).
- (40) Sheldrick, G. M. Foundations and Advances SHELXT-Integrated Space-Group and Crystal-Structure Determination. *Acta Cryst.*, **2015**, 71, 3–8.

- [41] Sheldrick, G. M. A. *Acta Crystallogr. A*, **2008**, *64*, 112-122.
- [42] Sheldrick, G. M.; Schneider, T. R. *Methods Enzymol* **1997**, *277*, 319–343.
- [43] Dolomanov, O. V; Bourhis, L. J.; Gildea, R. J.; Howard, J. A. K.; Puschmann, H. *J. Appl. Cryst.*, **2009**, *42*, 339–341.

ESI: The Crucial Role of the Heteroatom and Bite Angle Influencing Spin States and Dinuclear Fe(II) Helicate Formation in 1,3,4-Thia/Oxadiazole Ligand

Jens-Georg Becker,¹ Jan F. Nüsing,¹ Sriram Sundaresan,¹ Rosa Diego,¹ Mihail Mondeshki,¹ Luca M. Carrella,¹ and Eva Rentschler^{1*}

¹Department Chemie, Johannes-Gutenberg-Universität Mainz, Duesbergweg 10–14, 55128 Mainz, Germany. Email: rentschl@uni-mainz.de

Table of Contents

1. NMR-Spectra:	387
2. IR-spectra:.....	402
3. Mass spectra:.....	405
4. Crystolographic Data	406
5. UV-Vis-Spectra:	413
6. Cyclovoltammetry Data	414
7. Magnetic Data:.....	415

1. NMR-Spectra:

1.1 Ligand

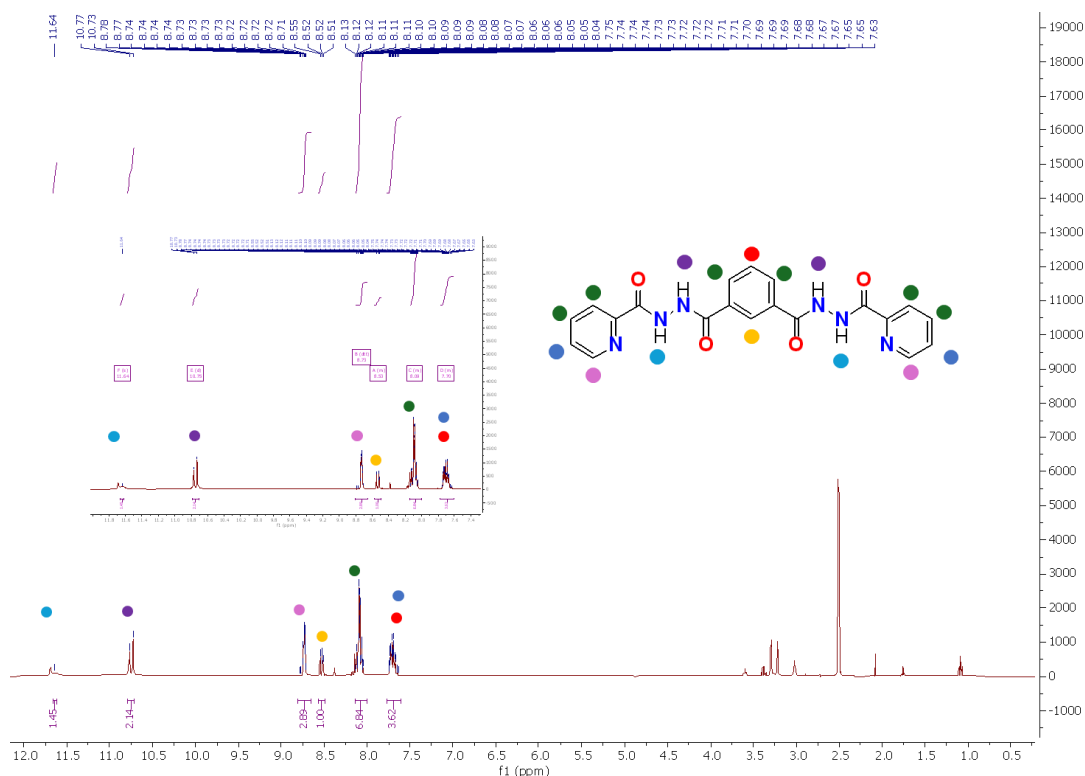


Figure S1: ¹H-NMR spectrum of N'1, N'3-dipicolinoylisophthalohydrazide (III) in DMSO [400 MHz]. All signals can be assigned. The signals in the aliphatic range are due to slight impurities and solvent residue.

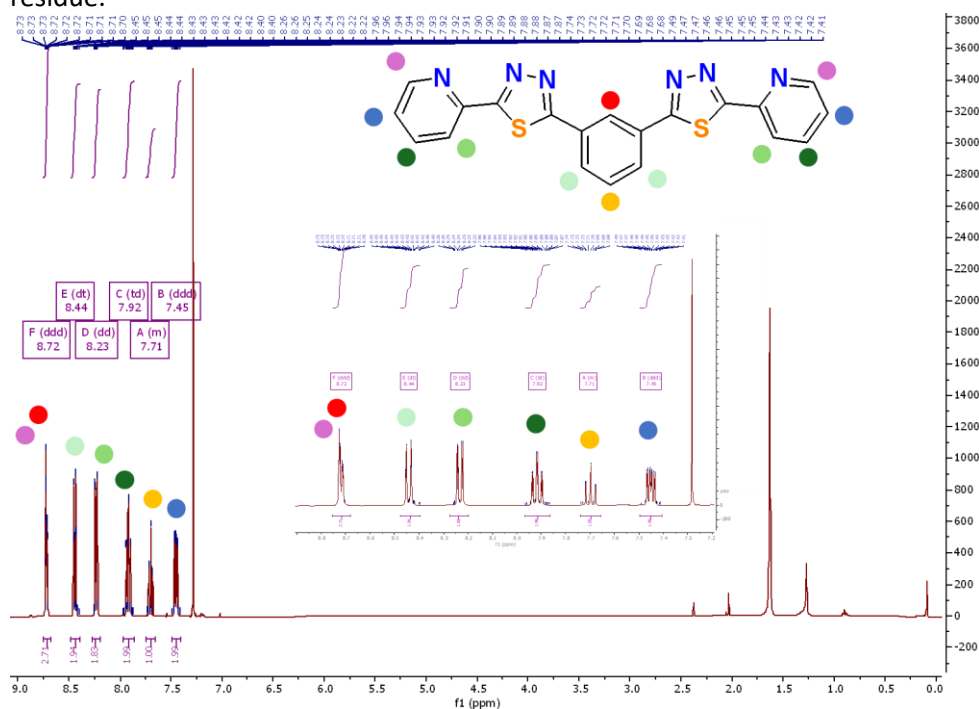


Figure S2: ¹H-NMR spectrum of the 1,3-bis(5-(pyridin-2-yl)-1,3,4-thiadiazol-2-yl)benzene (L^{TDA-Hel}) in CDCl₃ [400 MHz]. All signals can be assigned. The aliphatic peaks are due to grease and solvent residues of toluene.

Chapter 6: Helical dinuclear iron(II) complexes with 1,3,4-Oxa- and 1,3,4-Thiadiazole coordination units

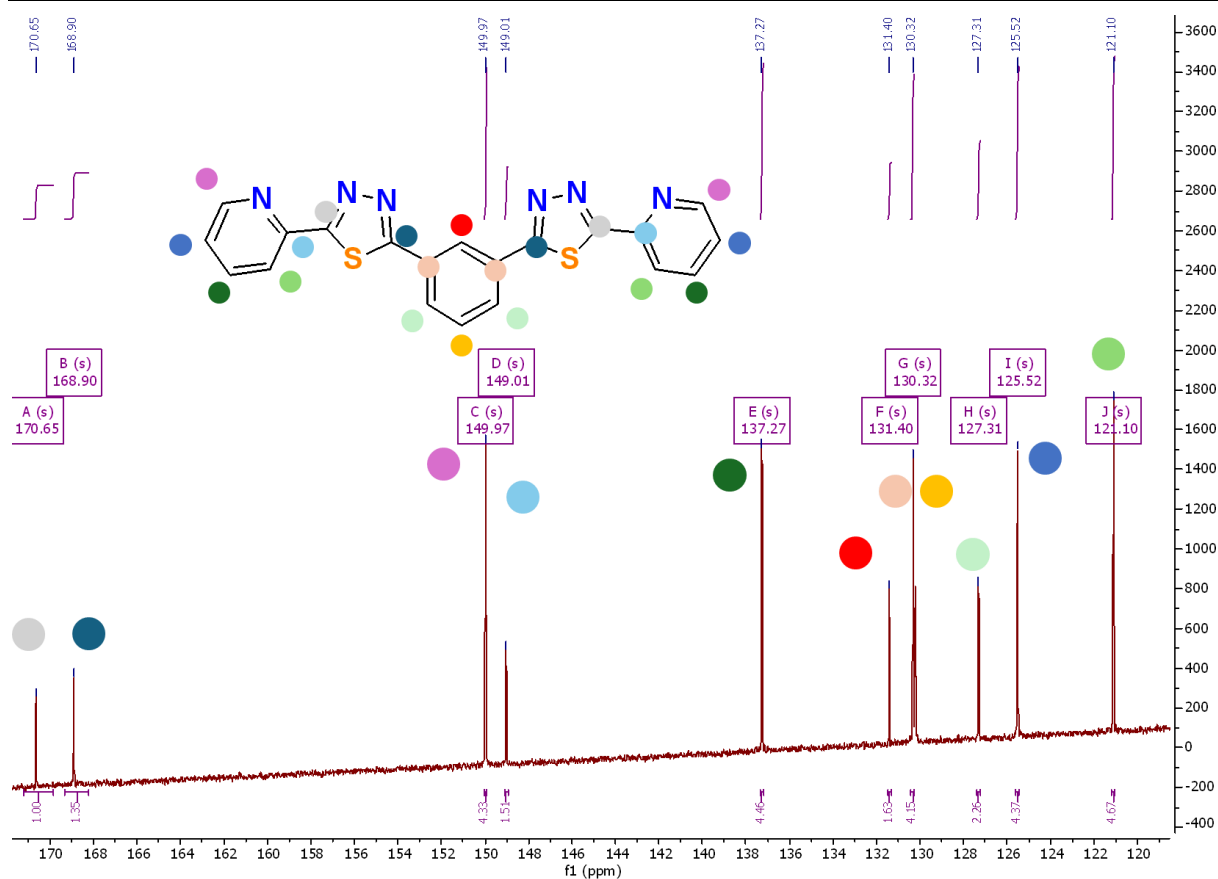


Figure S3: ^{13}C -NMR spectrum of the ligand ($\text{L}^{\text{TDA-Hel}}$) measured in CDCl_3 [101MHz].

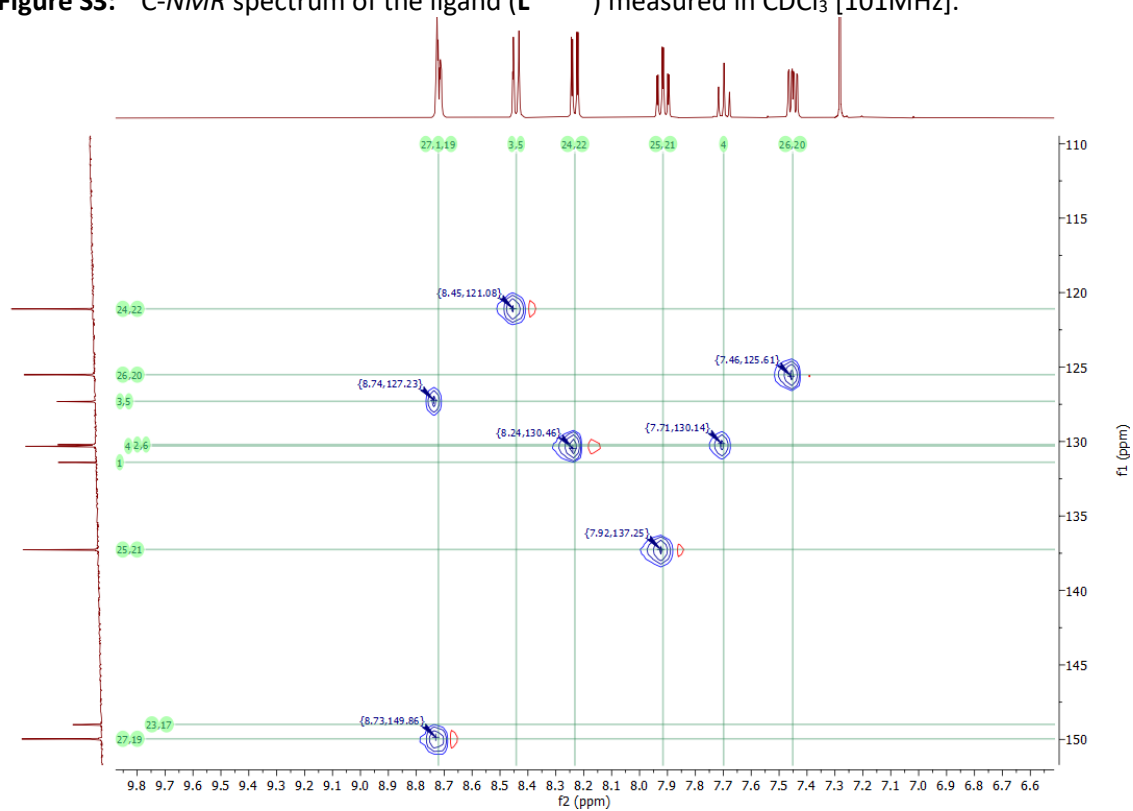


Figure S4: HSQC-NMR spectrum of ligand ($\text{L}^{\text{TDA-Hel}}$) measured in CDCl_3 .

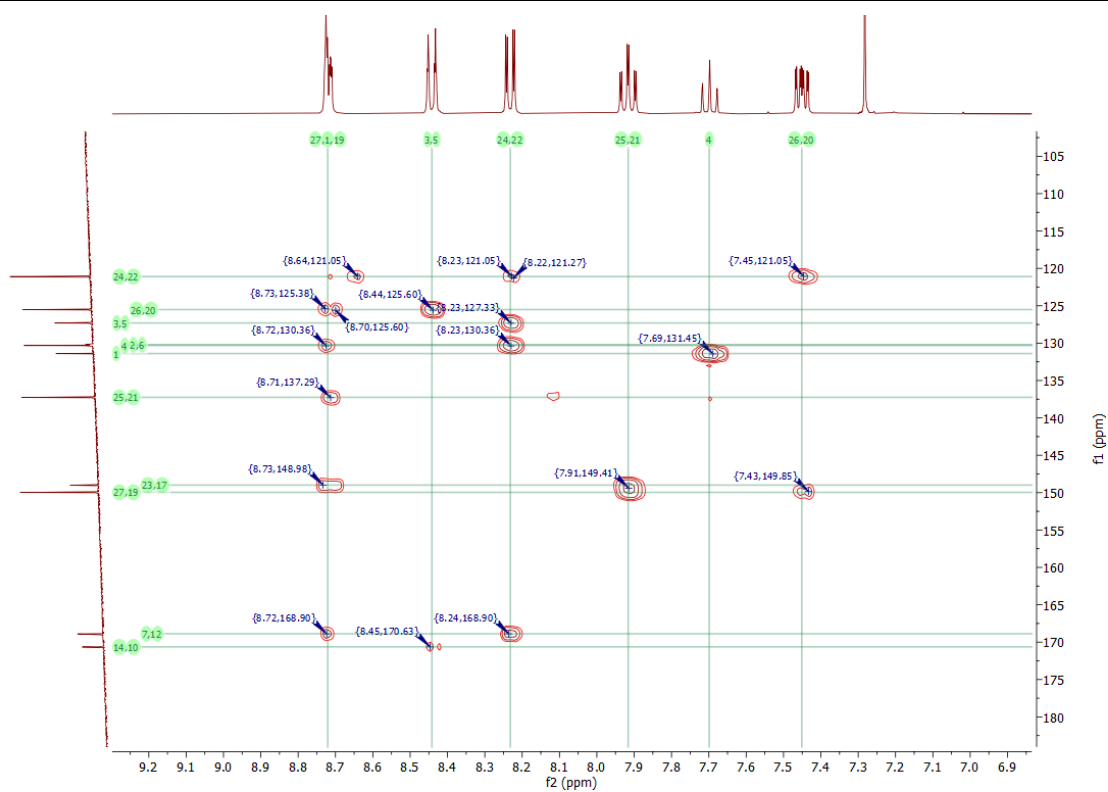


Figure S5: HMBC-NMR spectrum of ligand ($L^{\text{TDA-Hel}}$) measured in CDCl_3 .

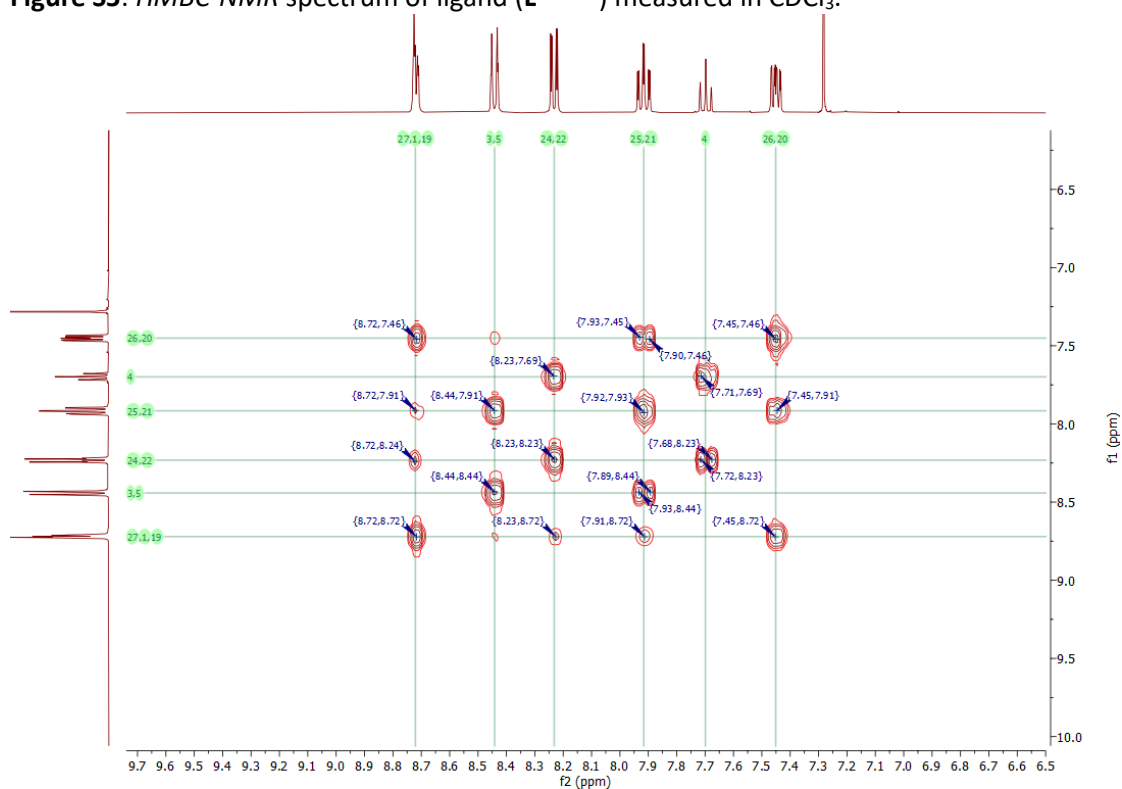


Figure S6: COSY-NMR spectrum of ligand ($L^{\text{TDA-Hel}}$) measured in CDCl_3 [400 MHz].

Chapter 6: Helical dinuclear iron(II) complexes with 1,3,4-Oxa- and 1,3,4-Thiadiazole coordination units

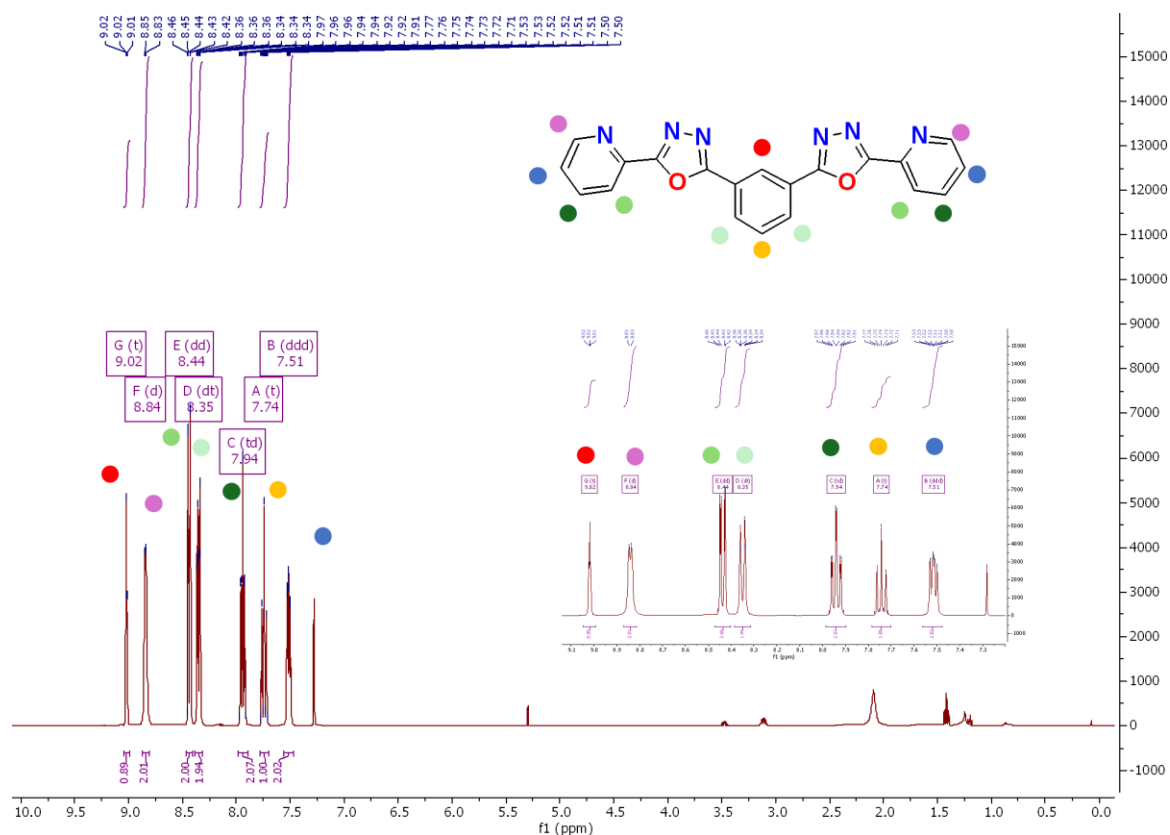


Figure S7: $^1\text{H-NMR}$ -spectrum of the ligand ($\text{L}^{\text{ODA-Hel}}$) in CDCl_3 [400 MHz]. All signals can be assigned. Some solvent residues of DCM and diethyl ether can be detected in the aliphatic region.

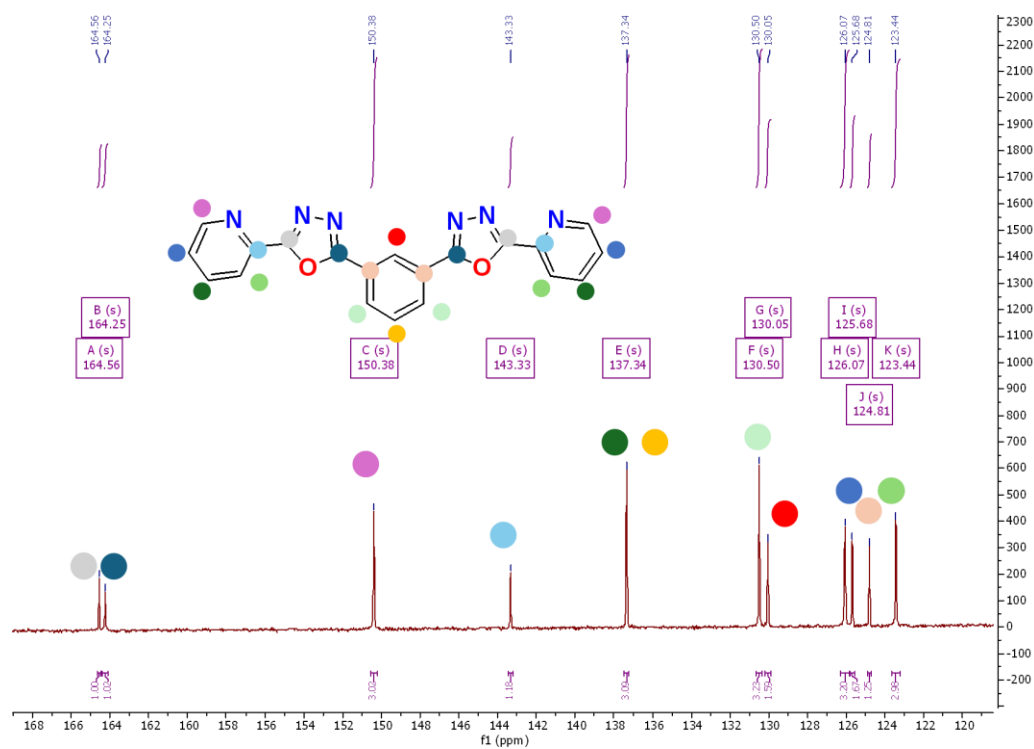


Figure S8: $^{13}\text{C-NMR}$ spectrum of ($\text{L}^{\text{ODA-Hel}}$) measured in CDCl_3 [101 MHz].

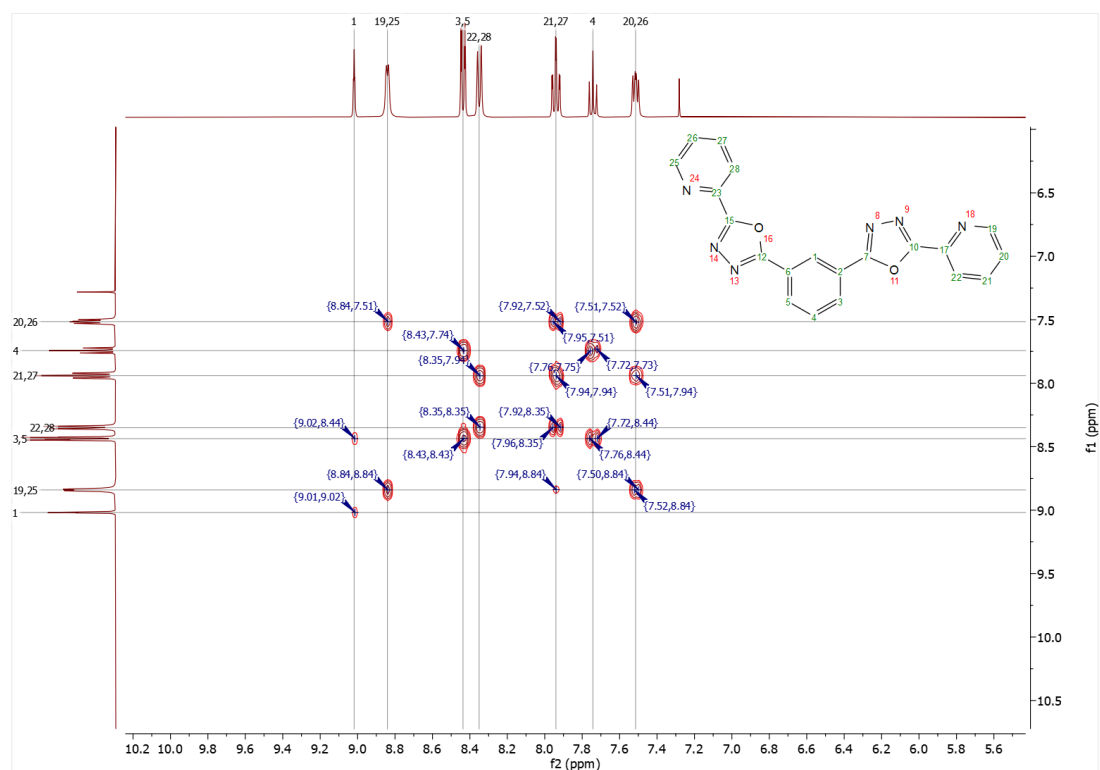


Figure S9: COSY-NMR spectrum of ligand ($L^{\text{ODA-Hel}}$) measured in CDCl_3 [400 MHz].

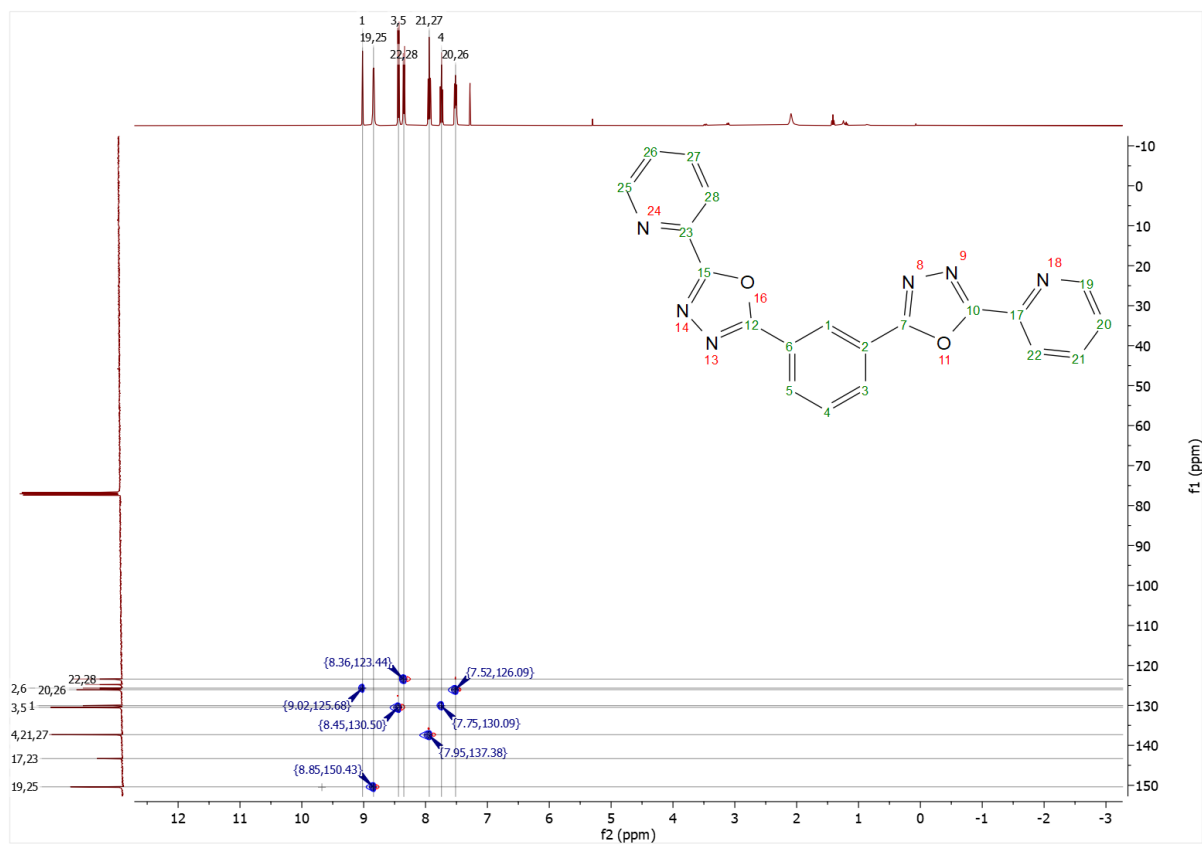


Figure S10: HSQC-NMR spectrum of $L^{\text{ODA-Hel}}$ measured in CDCl_3 [400 MHz].

1.2. Complex

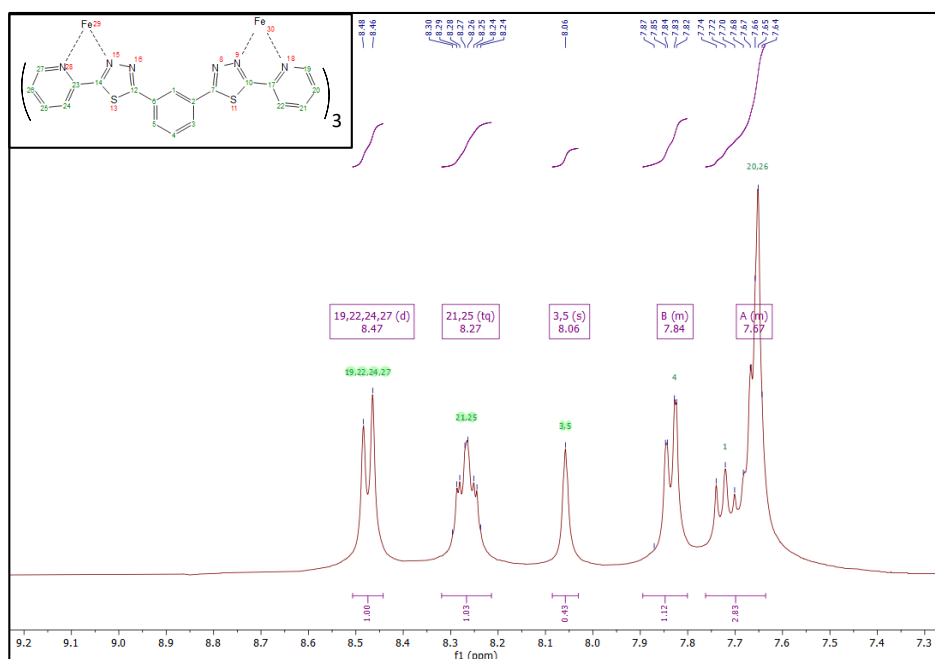


Figure S12: ¹H-NMR of Complex $[\text{Fe}_2(\text{L}^{\text{TDA-Hel}})_3](\text{ClO}_4) \cdot 3 \text{H}_2\text{O}$ (C1) in $\text{D}^3\text{-MeCN}$ zoomed in just the aromatic region clearly.

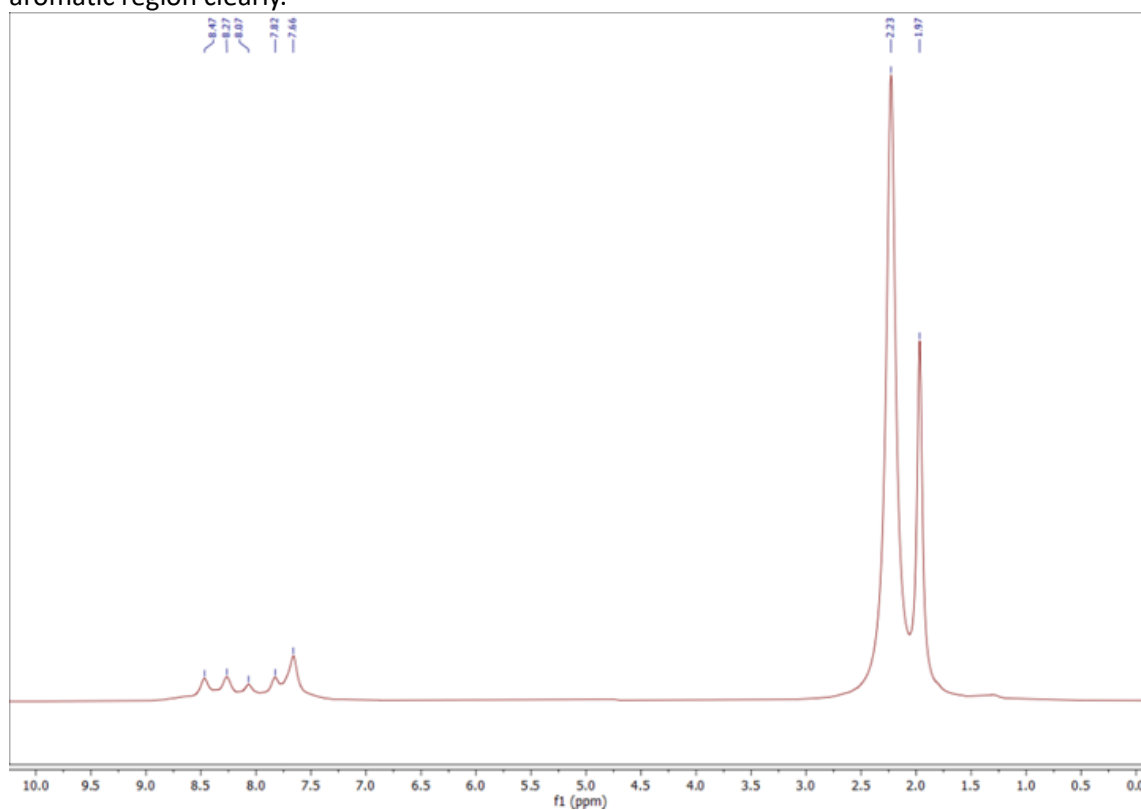


Figure S13: ¹H-NMR of Complex $[\text{Fe}_2(\text{L}^{\text{TDA-Hel}})_3](\text{ClO}_4) \cdot 3 \text{H}_2\text{O}$ (C1) in $\text{D}^3\text{-MeCN}$ full spectra.

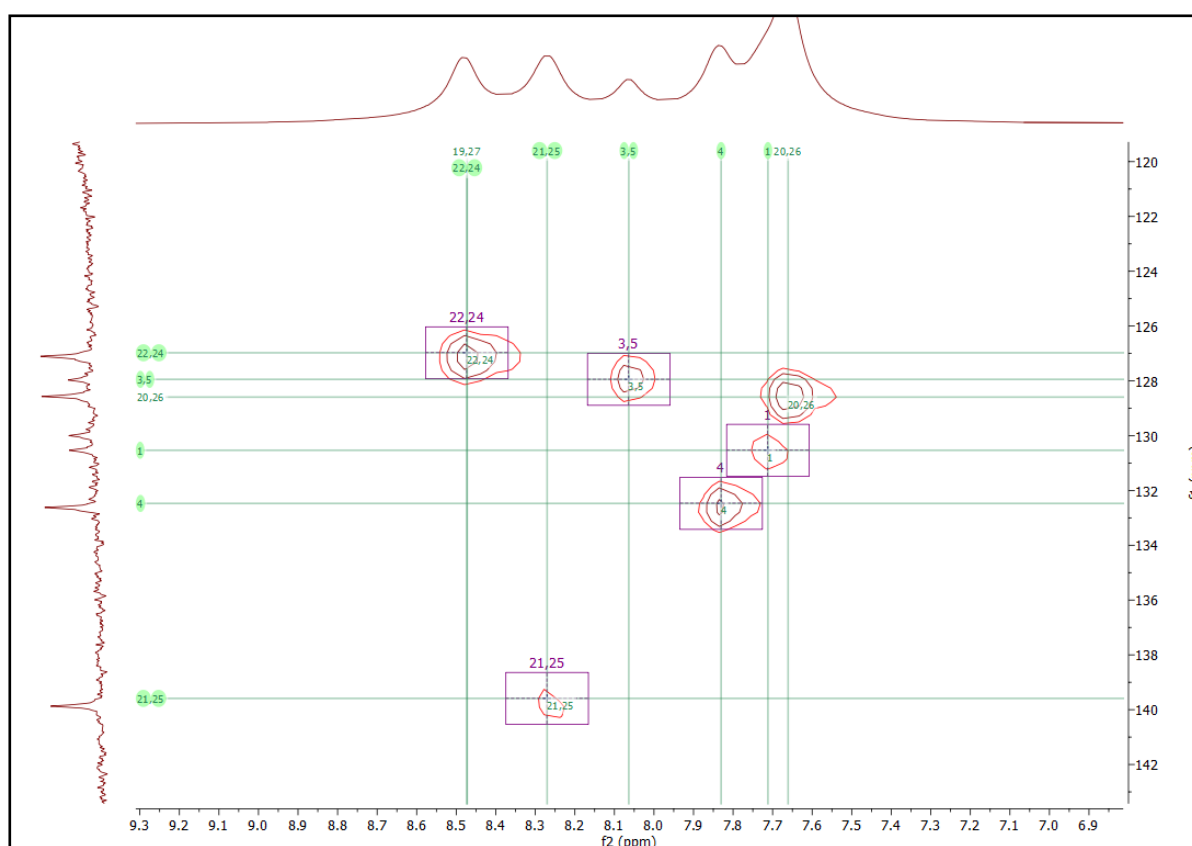


Figure S14: HSQC spectrum of complex $[\text{Fe}_2(\text{L}^{\text{TDA-Hel}})_3](\text{ClO}_4)_4 \cdot 3 \text{H}_2\text{O}$ (**C1**) in $\text{D}^3\text{-MeCN}$. These are the proposed assignments of the peaks in reference to the proton and 2D spectra of the ligand and the 2D spectra of the complex **C1**.

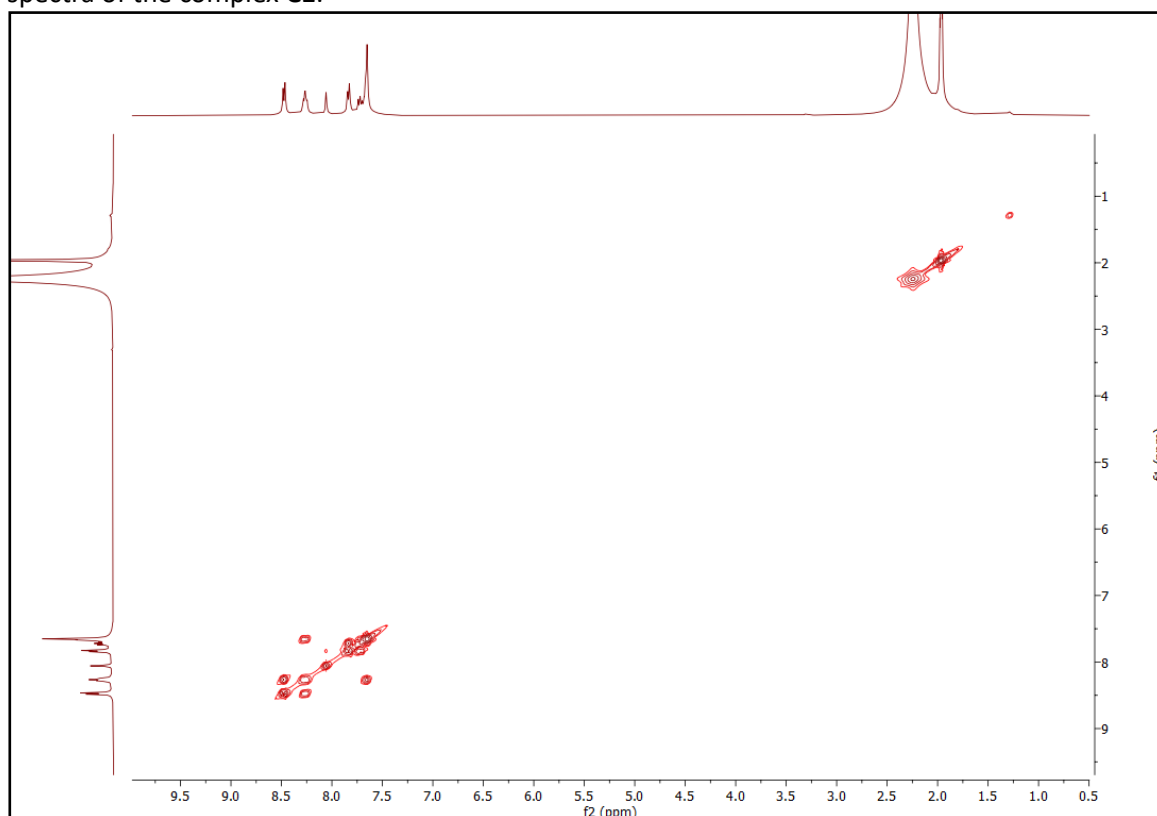


Figure S15: COSY spectrum of the complex $[\text{Fe}_2(\text{L}^{\text{TDA-Hel}})_3](\text{ClO}_4)_4 \cdot 3 \text{H}_2\text{O}$ (**C1**) in $\text{D}^3\text{-MeCN}$.

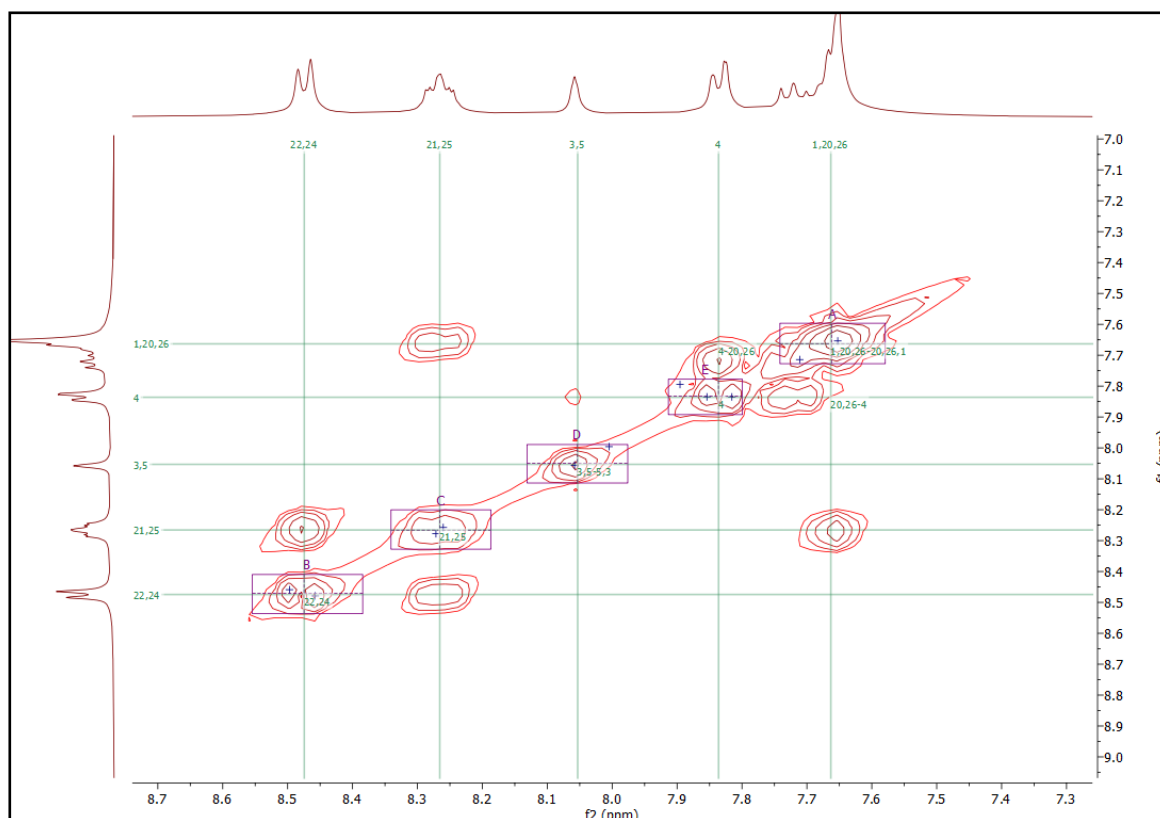


Figure S16: COSY spectrum of the complex $[\text{Fe}_2(\text{L}^{\text{TDA-Hel}})_3](\text{ClO}_4)_4 \cdot 3 \text{H}_2\text{O}$ (**C1**) in $\text{D}^3\text{-MeCN}$. These are the proposed assignments of the peaks in reference to the proton and 2D spectra of the ligand and the 2D spectra of the complex **C1**.

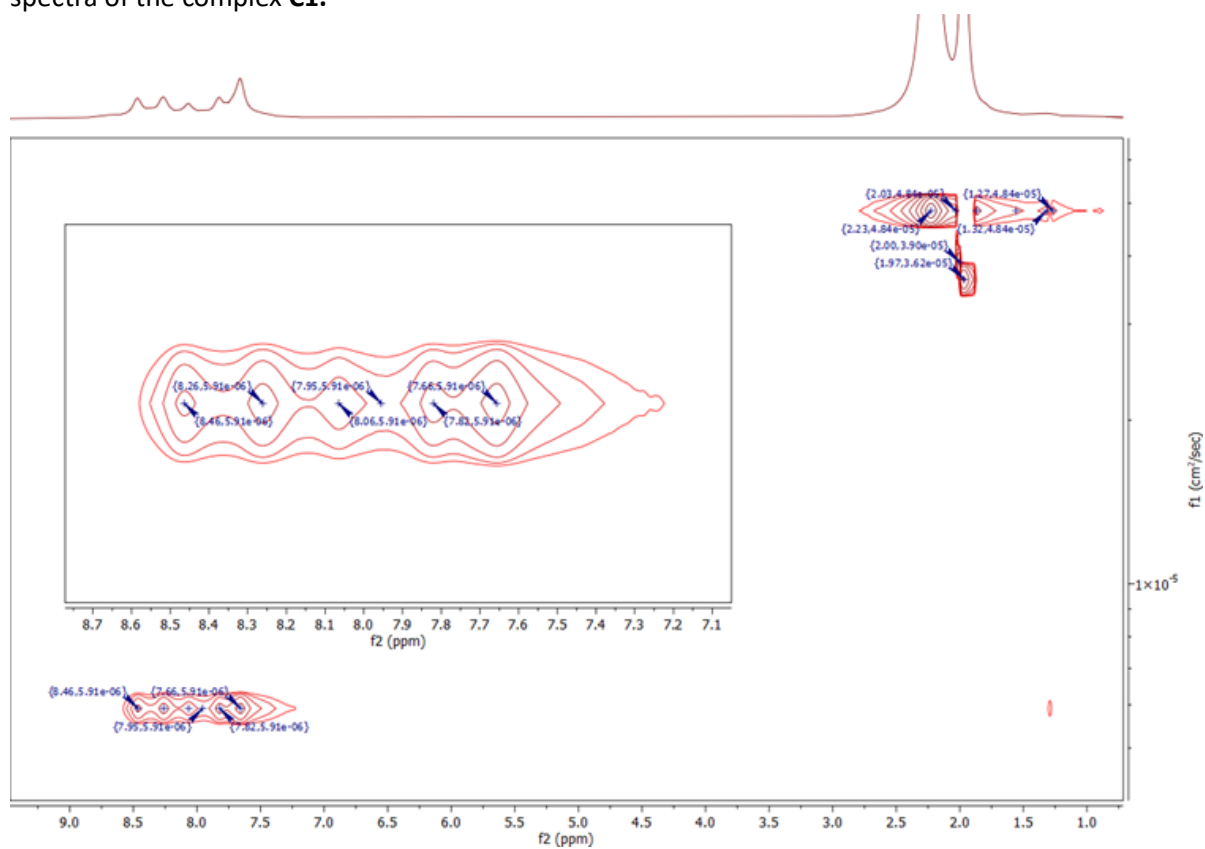


Figure S17: DOSY spectrum of complex $[\text{Fe}_2(\text{L}^{\text{TDA-Hel}})_3](\text{ClO}_4)_4 \cdot 3 \text{H}_2\text{O}$ (**C1**) in $\text{D}^3\text{-MeCN}$.

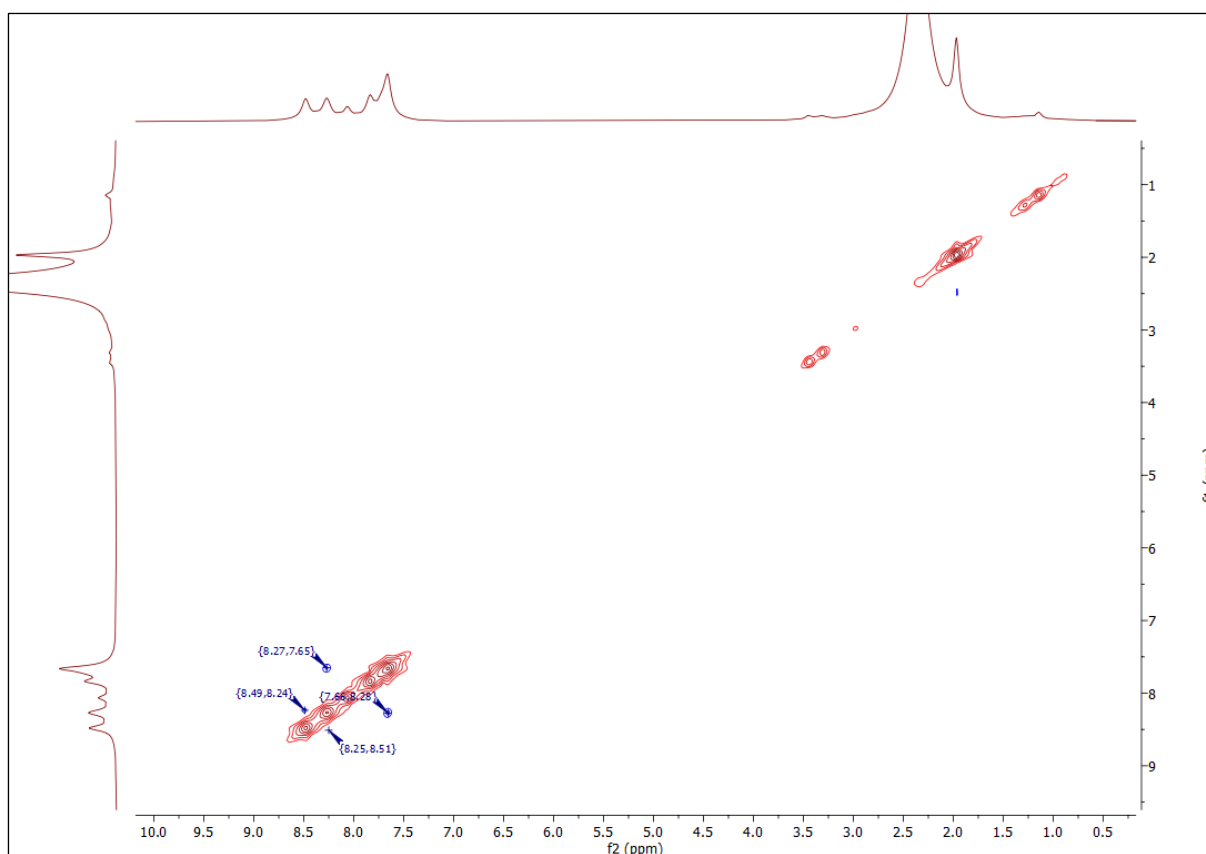


Figure S18: NOESY spectrum of complex $[\text{Fe}_2(\text{L}^{\text{TDA-Hel}})_3](\text{ClO}_4)_4 \cdot 3 \text{H}_2\text{O}$ (**C1**) in $\text{D}^3\text{-MeCN}$ with 1 s mixing time.

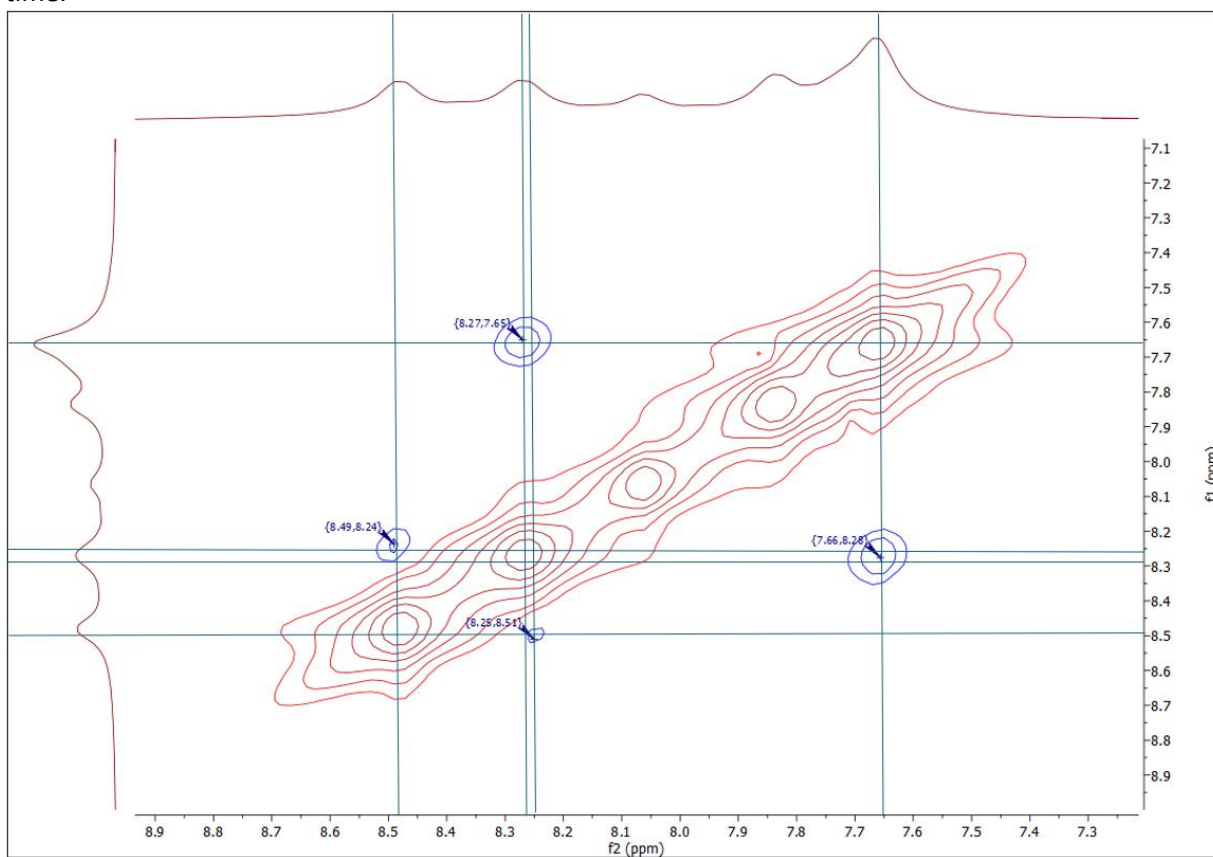


Figure 19: NOESY spectrum of complex $[\text{Fe}_2(\text{L}^{\text{TDA-Hel}})_3](\text{ClO}_4)_4 \cdot 3 \text{H}_2\text{O}$ (**C1**) in $\text{D}^3\text{-MeCN}$ recorded with 1 s mixing time.

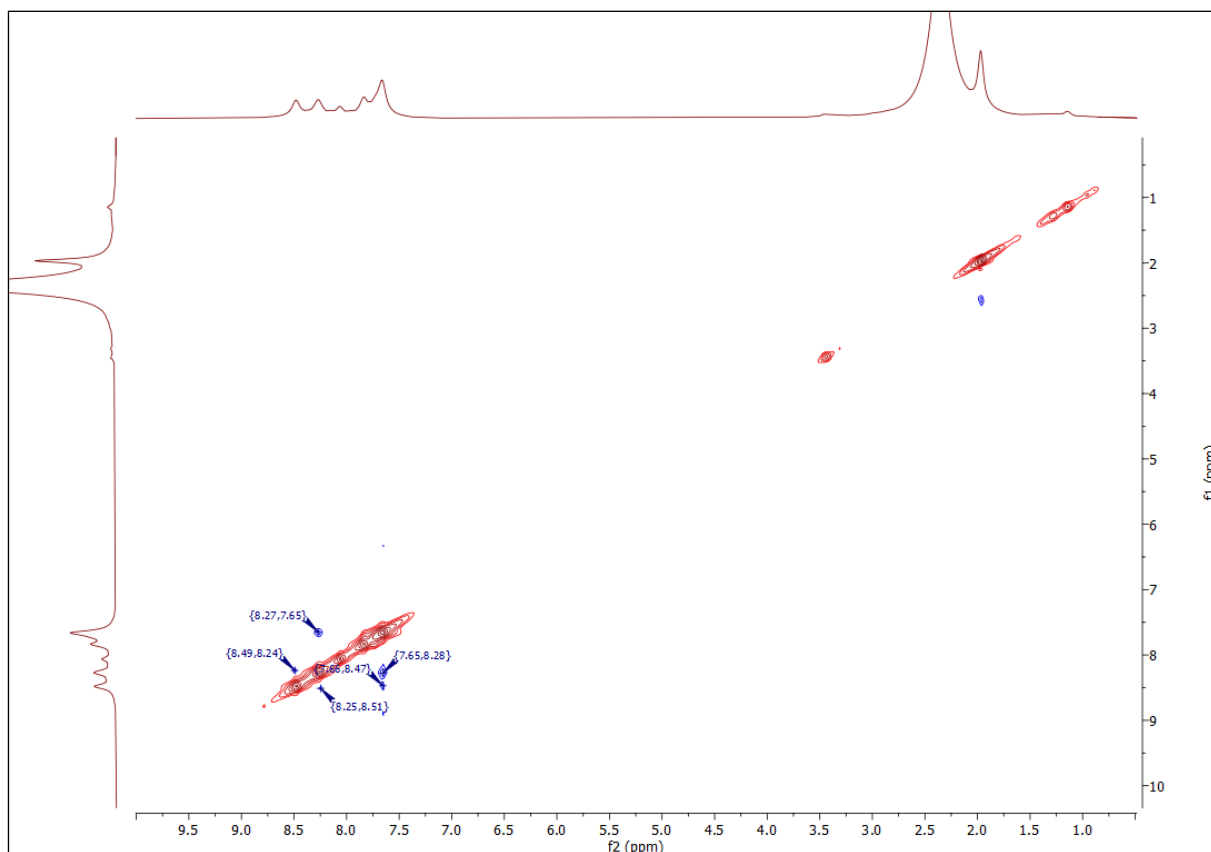


Figure S20: ROESY spectrum of complex $[\text{Fe}_2(\text{L}^{\text{TDA-Hel}})_3](\text{ClO}_4)_4 \cdot 3 \text{H}_2\text{O}$ (**C1**) in $\text{D}^3\text{-MeCN}$.

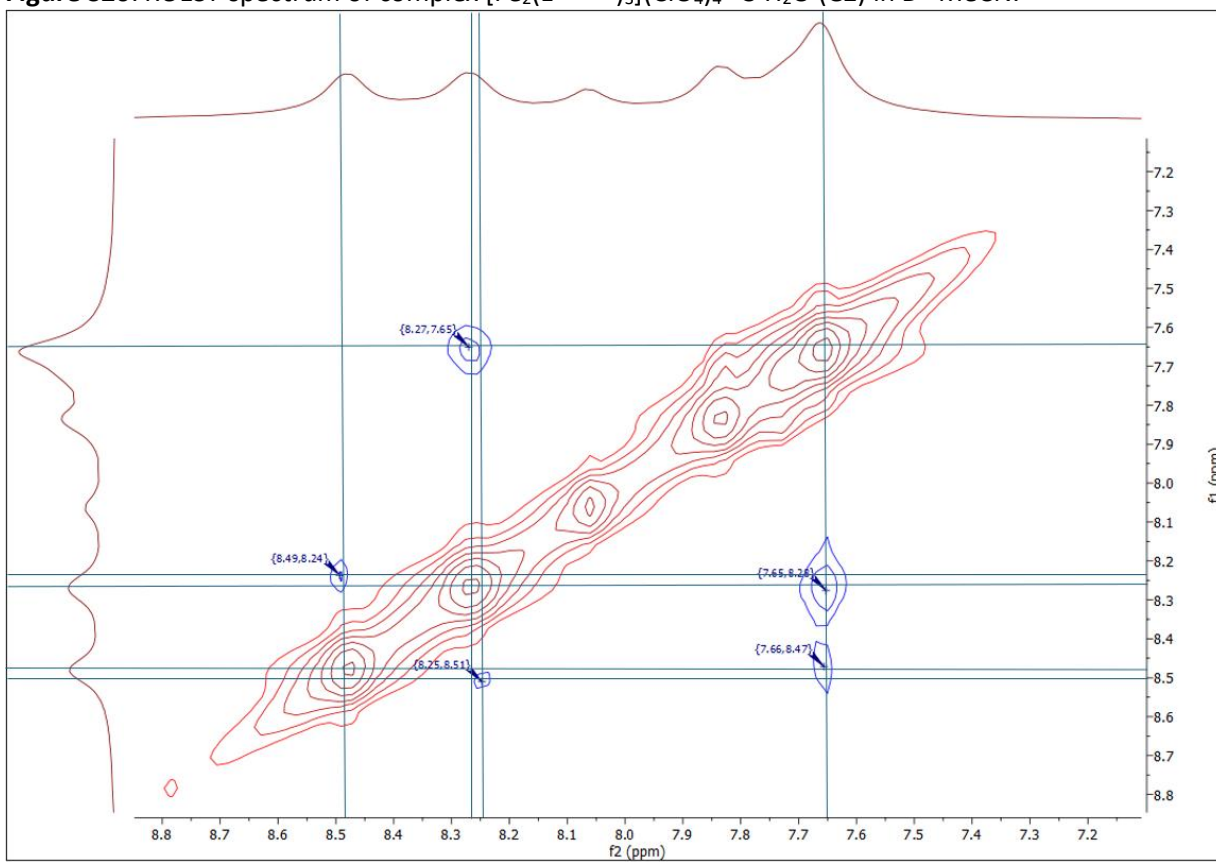


Figure 21: ROESY spectrum of complex $[\text{Fe}_2(\text{L}^{\text{TDA-Hel}})_3](\text{ClO}_4)_4 \cdot 3 \text{H}_2\text{O}$ (**C1**) in $\text{D}^3\text{-MeCN}$ zoomed for better clarity.

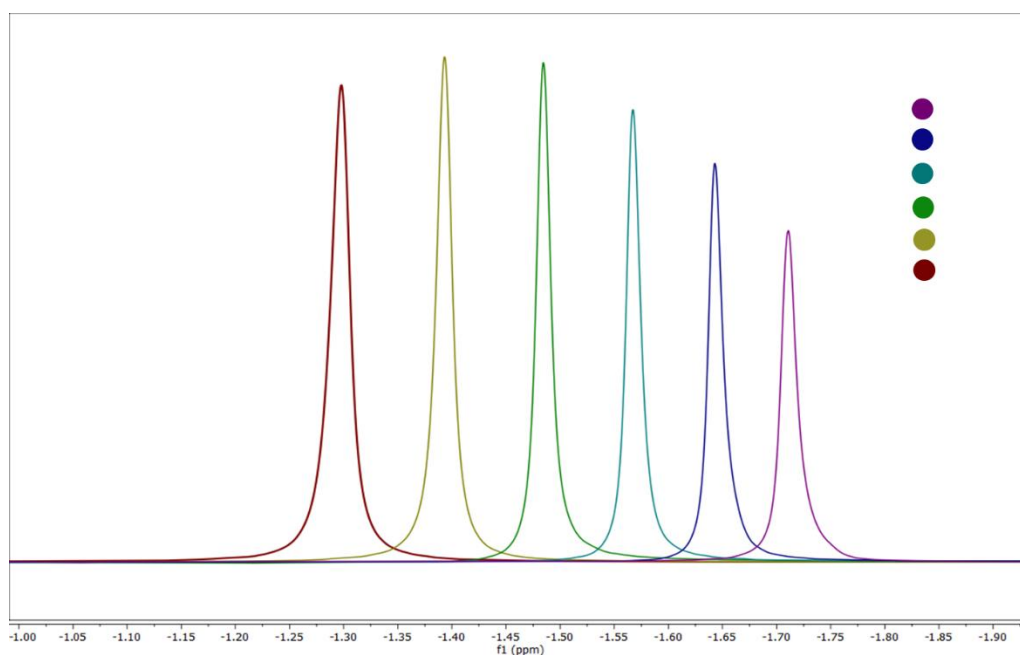


Figure S22: Variable temperature ⁷Li-NMR-measurements between 258 K and 333 K of complex **C1** and LiClO₄ in D³-MeCN.

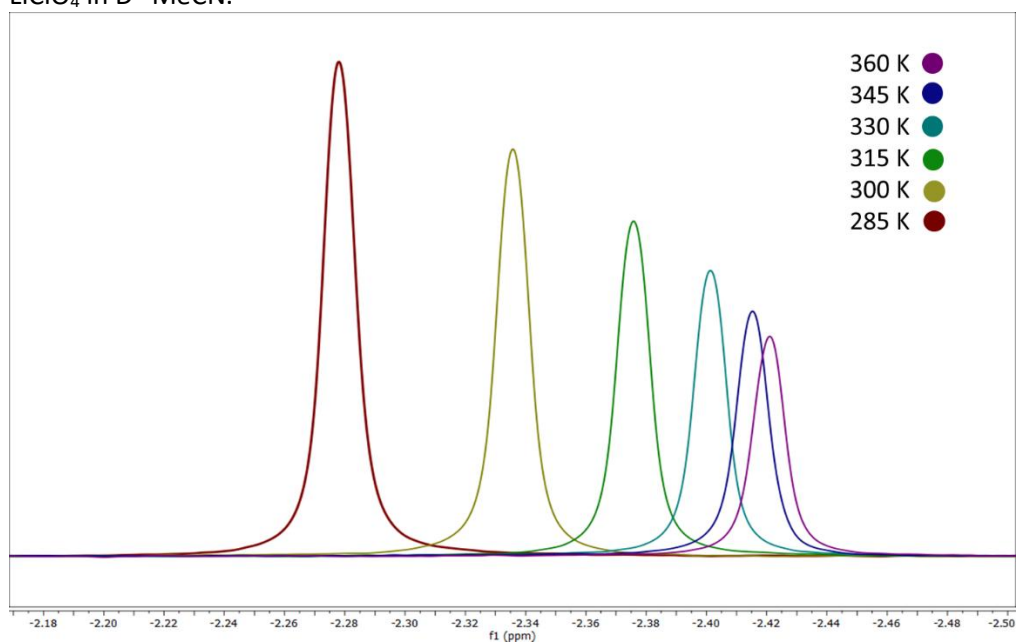


Figure S23: Variable temperature ⁷Li-NMR-measurements between 258 K and 333 K of LiClO₄ in D³-MeCN.

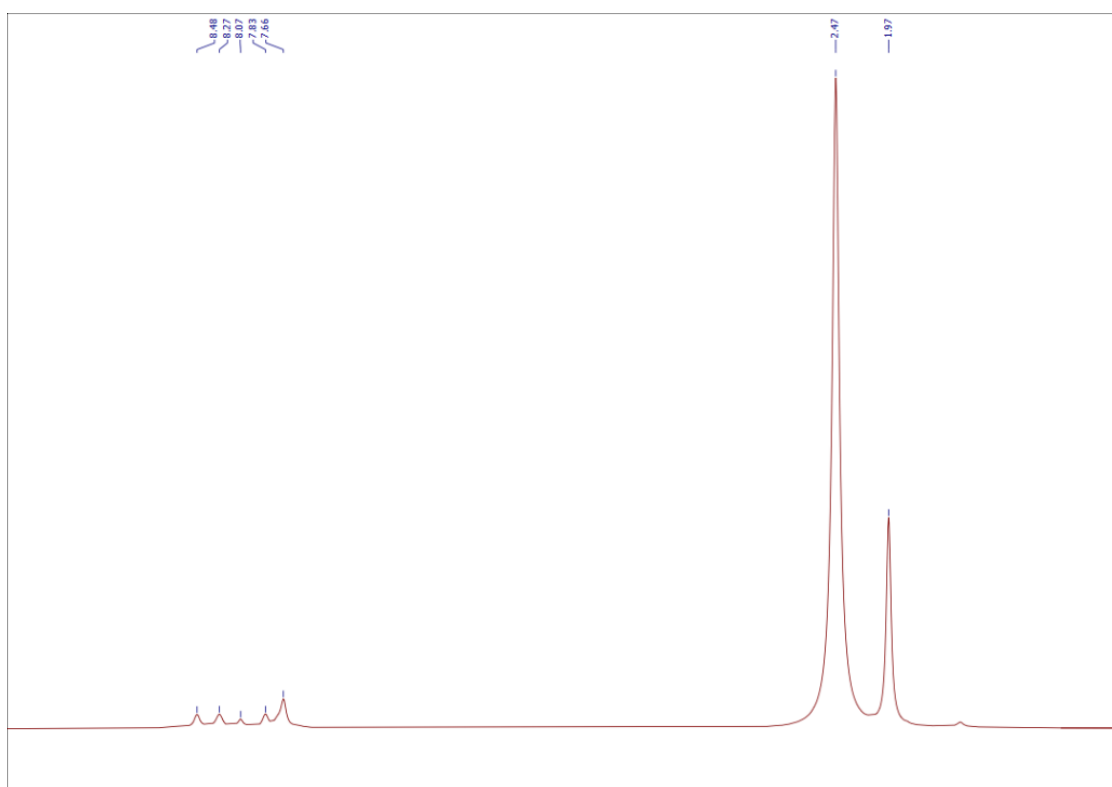


Figure S24: $^1\text{H-NMR}$ spectra of complex **C1** (10 mg; 5.55 μmol) with LiClO_4 (0.580 mg; 5.55 μmol) in 0.7 mL $\text{D}^3\text{-MeCN}$.

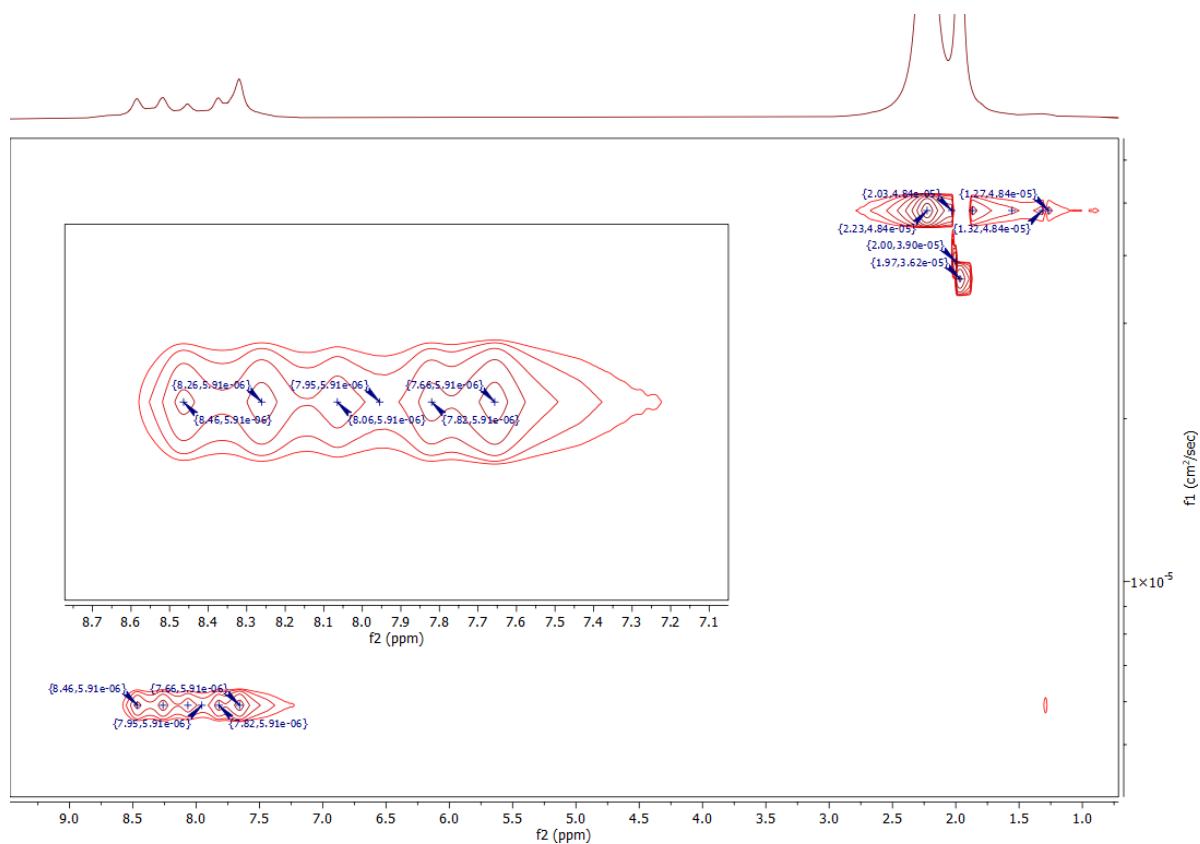


Figure S25: *DOSY* spectra of complex **C1** (10 mg; 5.55 μmol) in 0.7 mL $\text{D}^3\text{-MeCN}$.

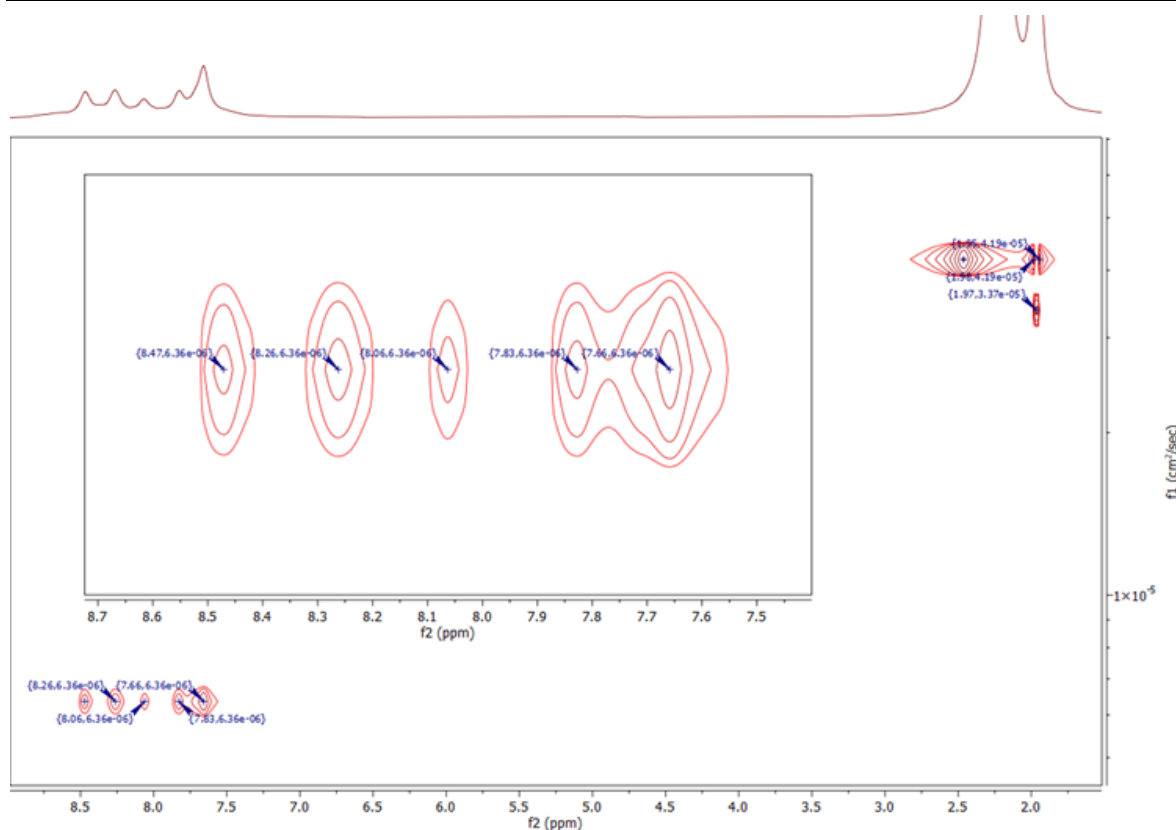


Figure S26: DOSY spectra of complex **C1** (10 mg; 5.55 μmol) with LiClO₄ (0.580 mg; 5.55 μmol) in 0.7 mL D³-MeCN.

c(LiClO₄)
 7.86 10⁻⁴ mol/L ●
 3.93 10⁻⁴ mol/L ●
 1.96 +10⁻⁴ mol/L ●

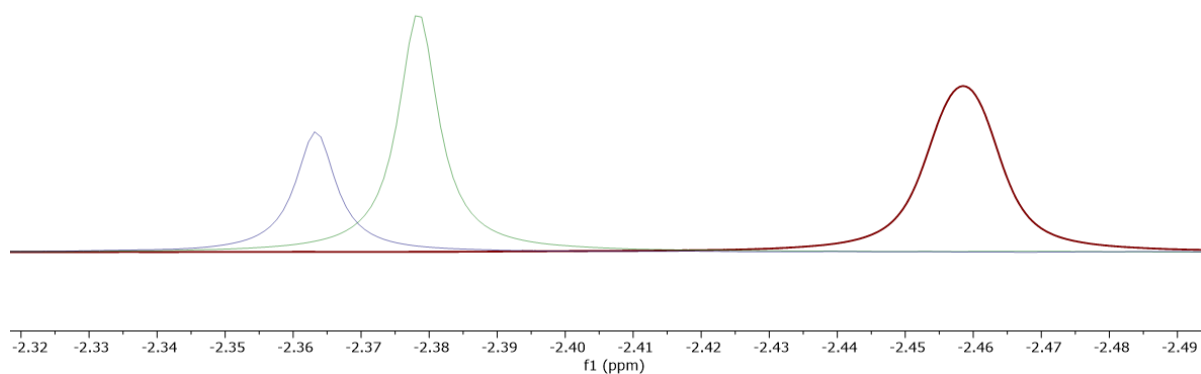


Figure S27: ⁷Li-NMR spectra of LiClO₄ with variable concentration of LiClO₄ (red 7.86 10⁻⁴ mol·L⁻¹; green 3.93 10⁻⁴ mol·L⁻¹; blue 1.96 +10⁻⁴ mol·L⁻¹).

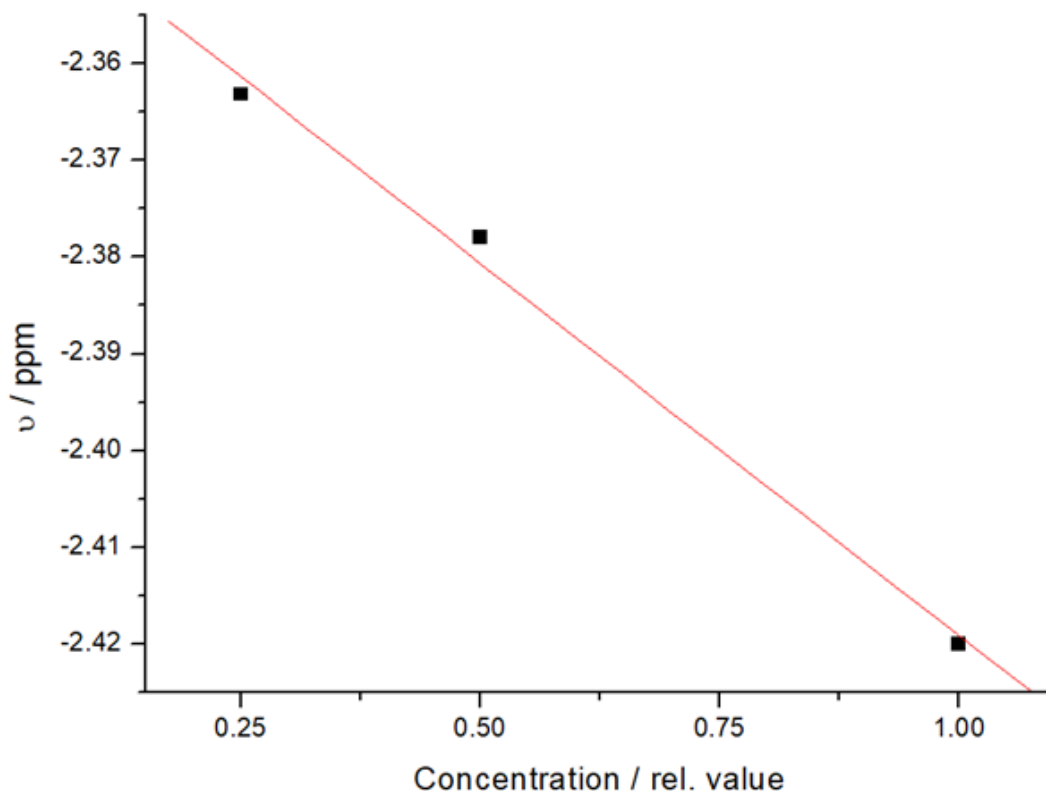


Figure S28: Visualization of changed shift of Li in $^7\text{Li-NMR}$ spectra by variable concentration of LiClO_4 .

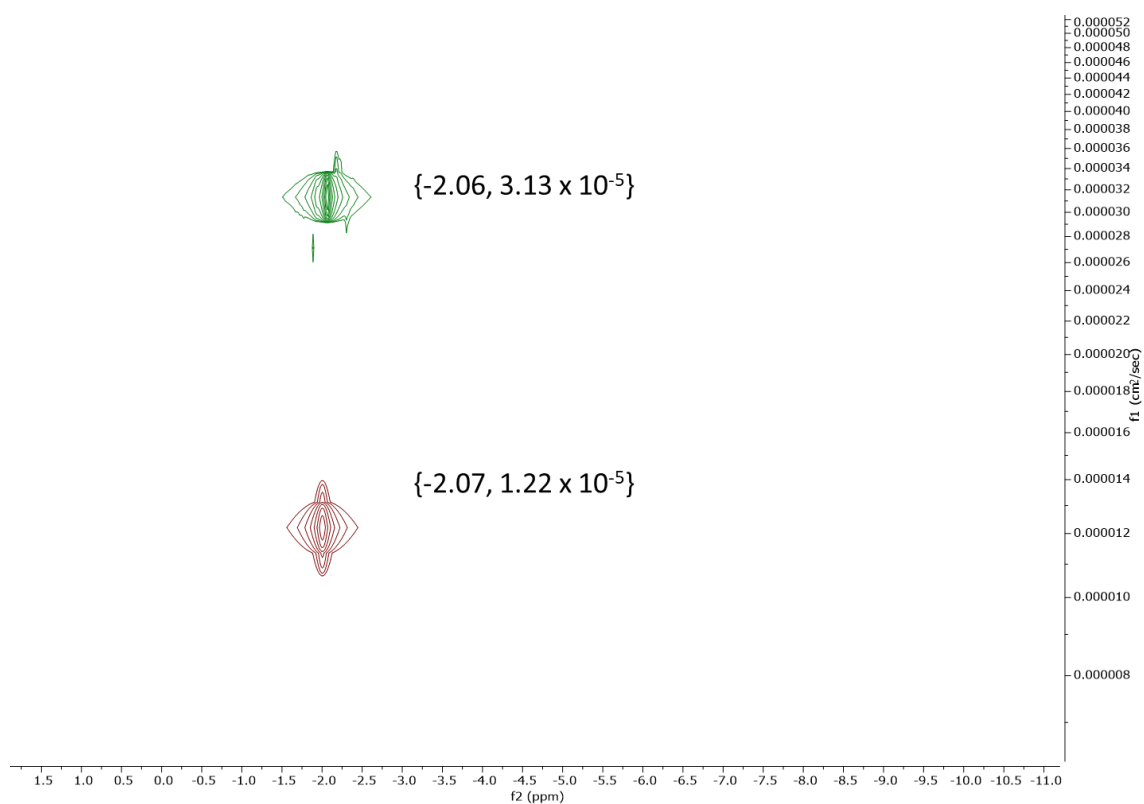


Figure S29: Stacked $^7\text{Li-NMR}$ DOSY of complex **C1** (10 mg; $5.55 \mu\text{mol}$) with LiClO_4 (0.580 mg; $5.55 \mu\text{mol}$) (red) and LiClO_4 (0.580 mg; $5.55 \mu\text{mol}$) (green) in 0.7 mL $\text{D}^3\text{-MeCN}$

2. IR-spectra:

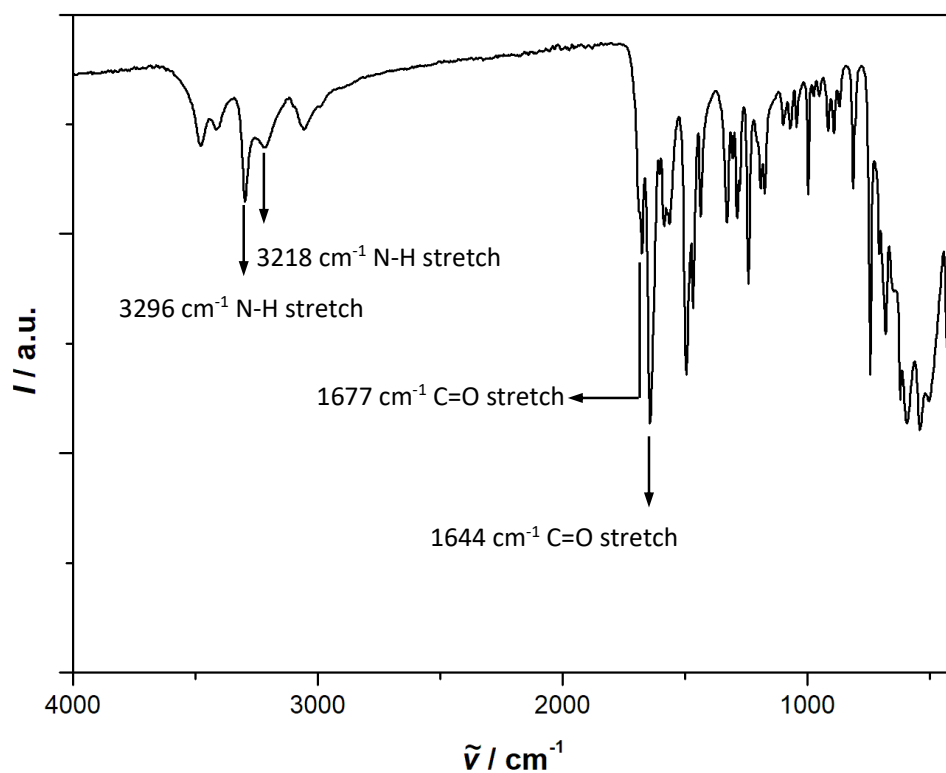


Figure S30: IR-Spectra of N'1,N'3-dipicolinoylisophthalohydrazide.

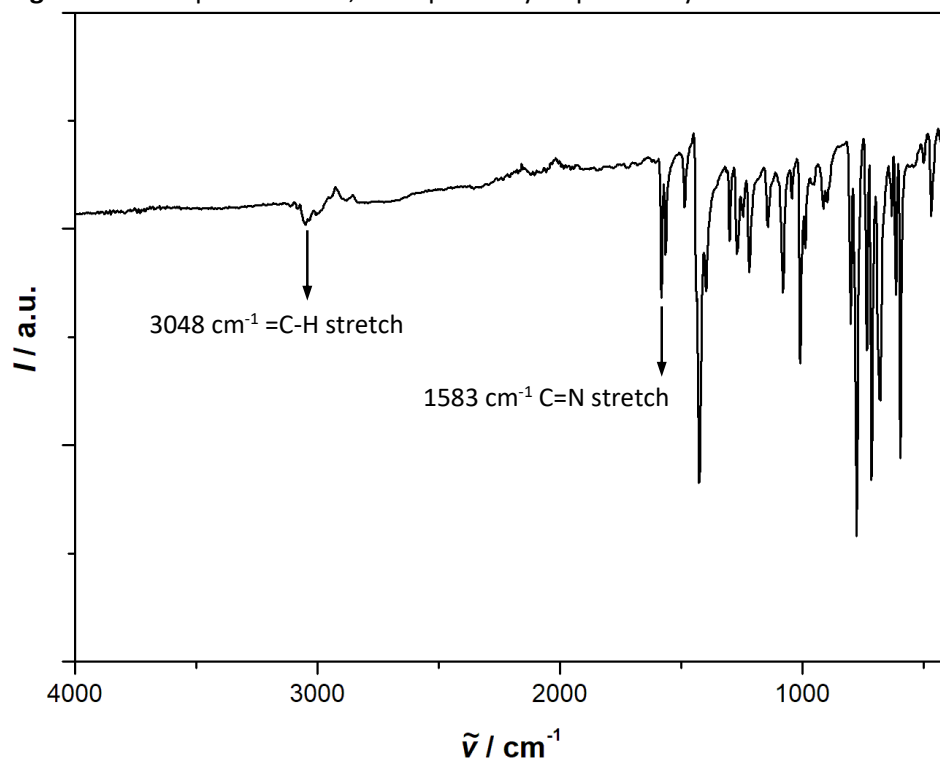


Figure S31: IR-Spectra of 1,3-bis(5-(pyridin-2-yl)-1,3,4-thiadiazol-2-yl)benzene ($\text{L}^{\text{TDA-Hel}}$).

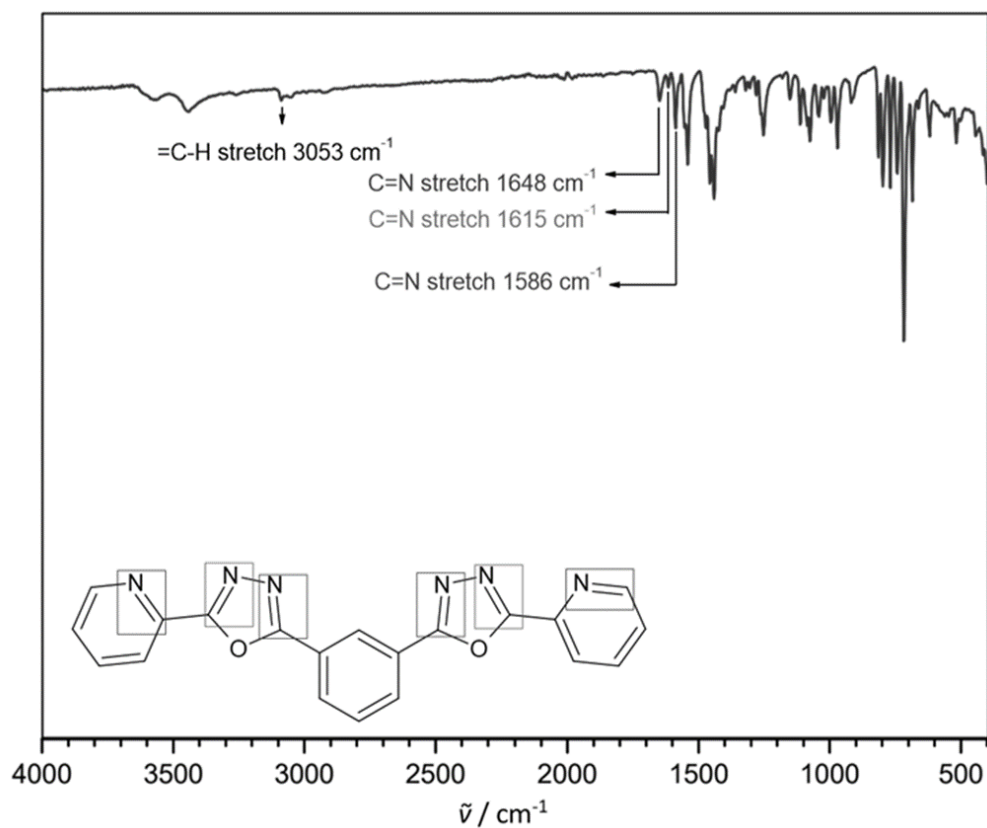


Figure S32: IR-Spectra of 1,3-bis(5-(pyridin-2-yl)-1,3,4-oxadiazol-2-yl)benzene ($L^{\text{ODA-Hel}}$).

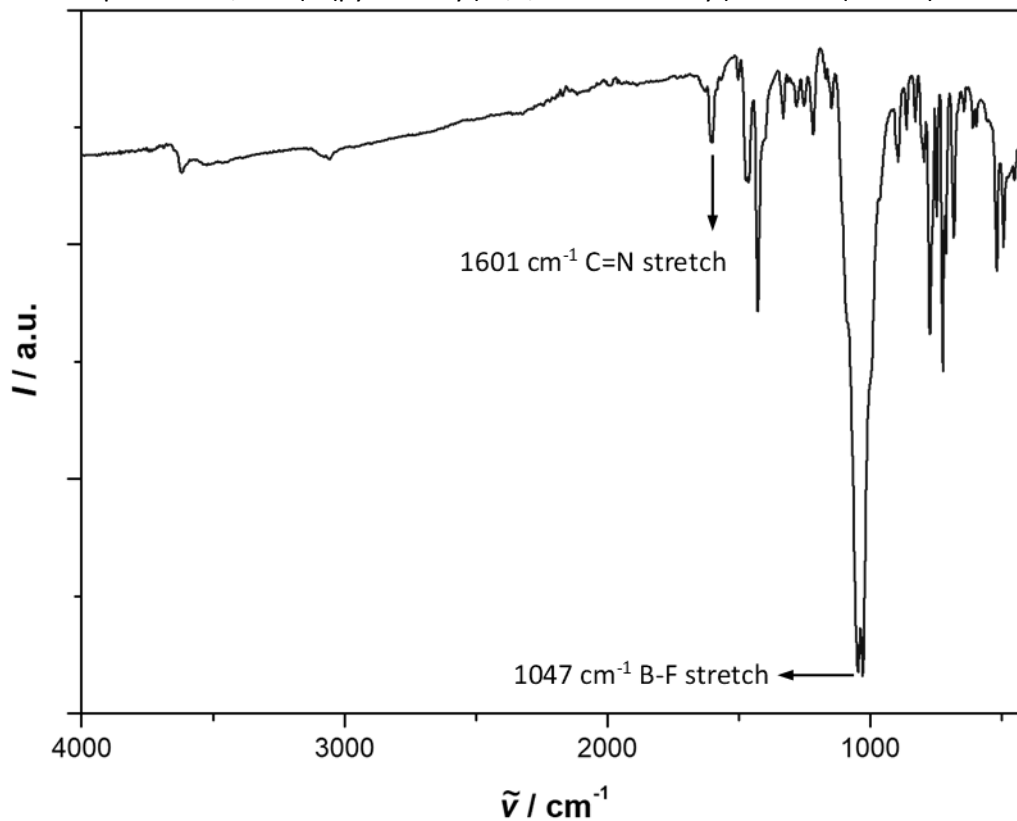


Figure S33: IR-spectra of the complex $[\text{Fe}_2(L^{\text{TDA-Hel}})_3](\text{BF}_4)_4 \cdot 5 \text{H}_2\text{O}$ (C2).

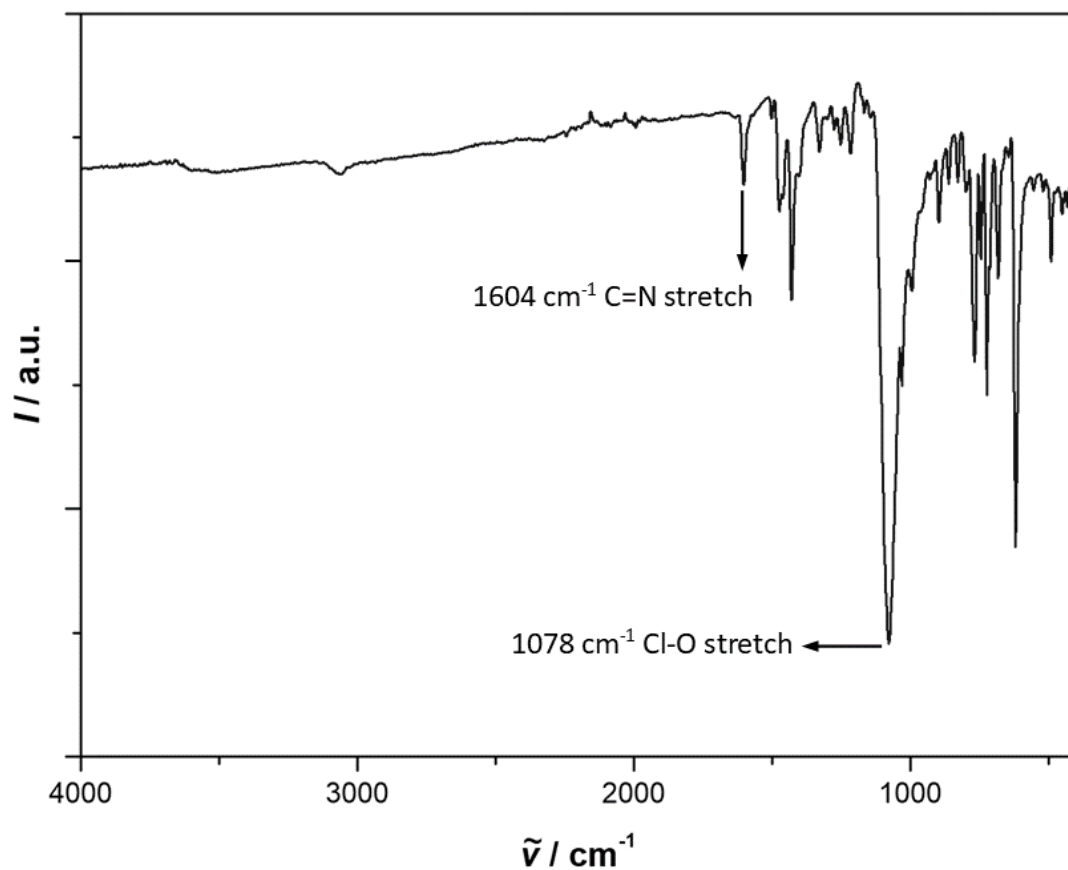


Figure S34: IR-spectra of the complex $[\text{Fe}_2(\text{L}^{\text{TDA-Hel}})_3](\text{ClO}_4)_4 \cdot 5 \text{H}_2\text{O}$ (**C1**).

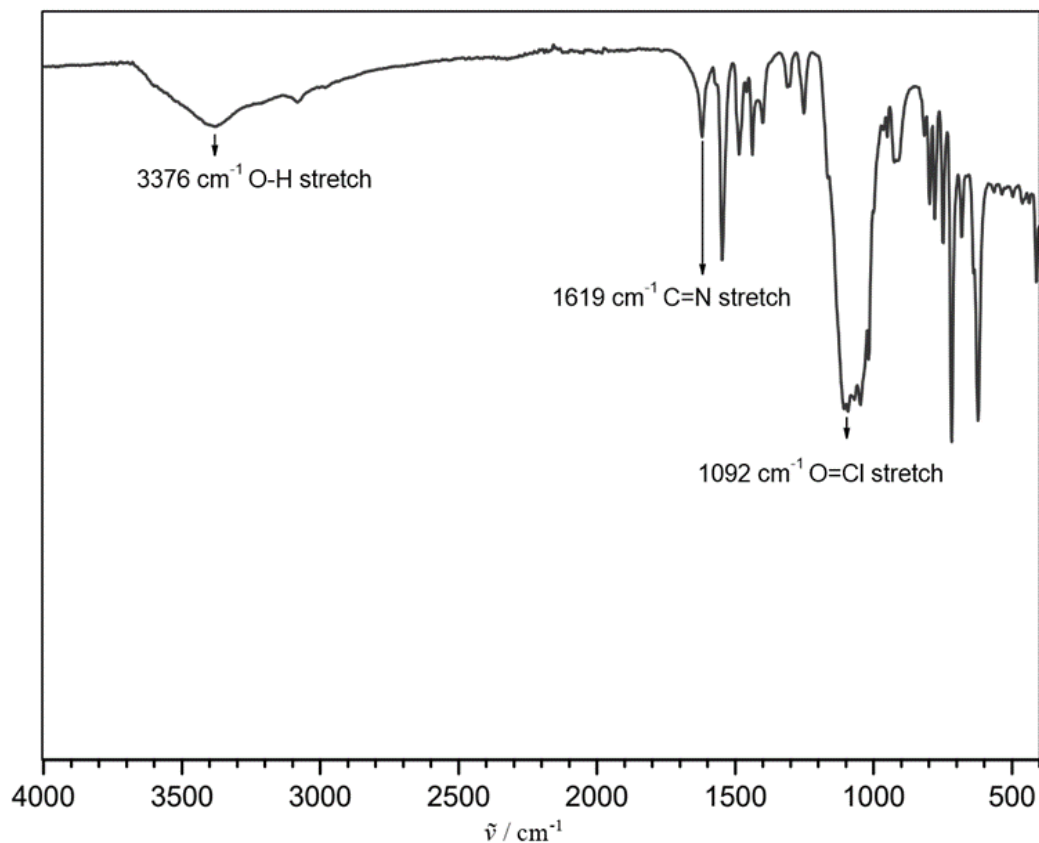


Figure S35: IR-spectra of $\text{Fe}(\text{H}_2\text{O})_2(\text{L}^{\text{ODA-Hel}})_2(\text{ClO}_4)$ (**C3**).

3. Mass spectra:

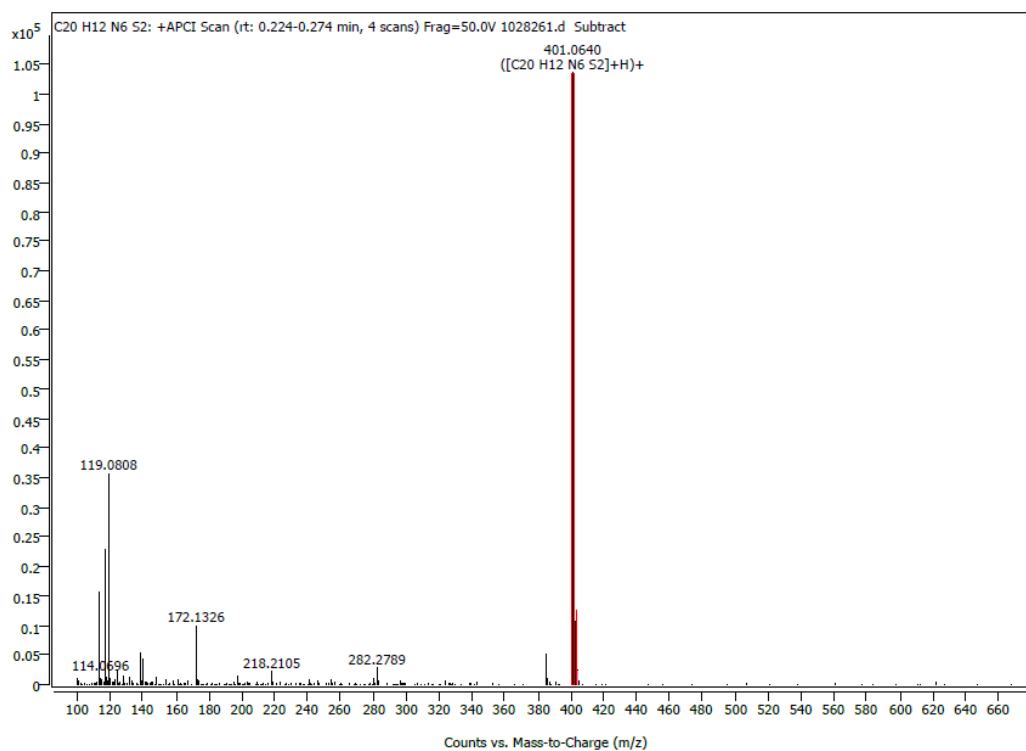


Figure S36: Mass spectrum (ESI positive) of the Ligand ($L^{\text{TDA-Hel}}$).

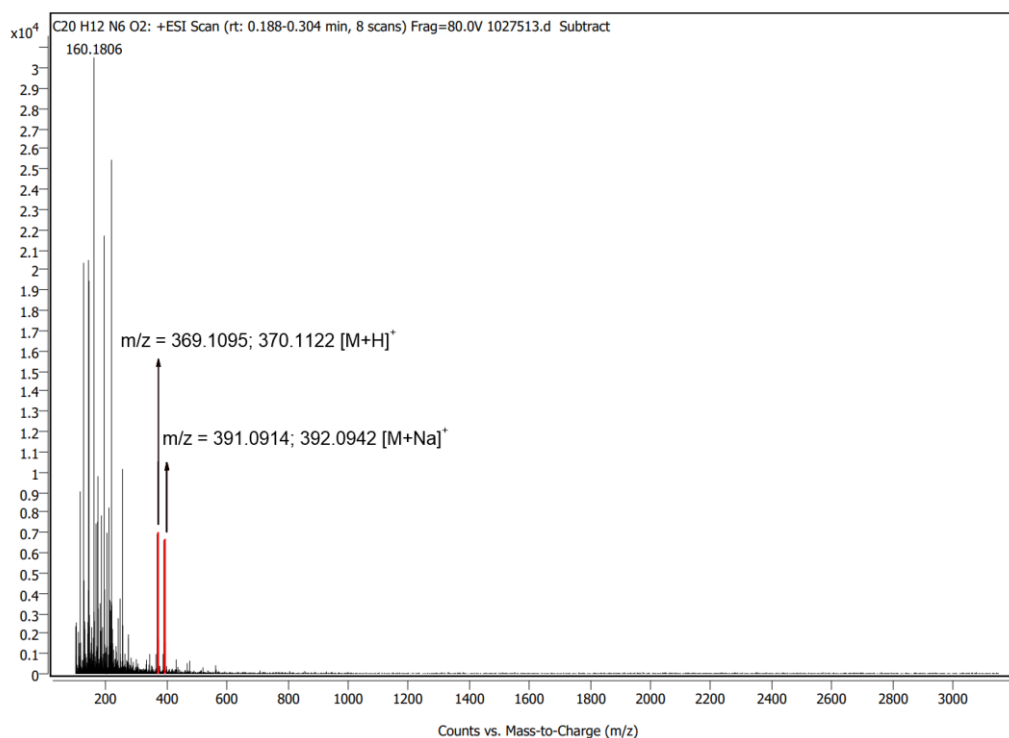


Figure S37: Mass spectrum (ESI positive) of the Ligand ($L^{\text{ODA-Hel}}$).

4. Crystallographic Data

Table S1: Measurement parameters for $[\text{Fe}_2(\text{L}^{\text{TDA-Hel}})_3](\text{ClO}_4)_4 \cdot 3 \text{H}_2\text{O}$ (**C1**).

Parameter	Result
Overall formula	$\text{C}_{68}\text{H}_{48}\text{Cl}_4\text{Fe}_2\text{N}_{22}\text{O}_{16}\text{S}_6$
Overall formula g/mol	1875.14
Crystal size / mm	0.56 x 0.23 x 0.06
Crystal system	triclinic
Space group	$P\bar{1}$
Unit cell dimensions	
a / Å	12.9312(4)
b / Å	17.3034(5)
c / Å	19.7718(6)
α / °	72.843(2)
β / °	72.223(2)
γ / °	68.146(2)
Volume / Å ³	3826.8(2)
Cell formula units	2
Density ρ_{calc} / g cm ⁻³	1.627
μ / mm ⁻¹	0.765
F(000)	1908
Temperature / K	120
Device type	STOE STADIVARI
Radiation	Mo-K α
Independent reflexes	$2.210 < \theta < 37.580$
Index ranges h	$-10 < h < 20$
Index ranges k	$-28 < k < 28$
Index ranges l	$-28 < l < 32$
Reflections collected	66489
Independent reflections	30572
Completeness	0.755
Max. and min transmission	0.8381 and 0.6522
R _{int}	0.0307
R _{sigma}	0.0335
Data/restraints/parameters	30572 / 0 / 1067
Goodness-of-fit on F ²	1.056
^a R ₁ [$I > 2\sigma(I)$]	0.0395
^b wR ₂ [$I > 2\sigma(I)$]	0.1069
R ₁ [all data]	0.0497
wR ₂ [all data]	0.1119

Table S2: Measurement parameters for $[\text{Fe}_2(\text{L}^{\text{TDA-Hel}})_3](\text{BF}_4)_4 \cdot 5 \text{H}_2\text{O}$ (**C2**).

Parameter	Results
Overall formula	$\text{C}_{71}\text{H}_{55}\text{B}_4\text{F}_{16}\text{Fe}_2\text{N}_{22.5}\text{O}_{0.75}\text{S}_6$
Overall formula g/mol	1886.67
Crystal size / mm	0.23 x 0.137 x 0.08
Crystal system	triclinic
Space group	$P\bar{1}$
Unit cell dimensions	
a / Å	12.8766(3)
b / Å	17.5125(4)
c / Å	21.0138(5)
$\alpha / ^\circ$	113.623(2)
$\beta / ^\circ$	91.539(2)
$\gamma / ^\circ$	109.492(2)
Volume / Å ³	4021.38(18)
Cell formula units	2
Density $\rho_{\text{calc}} / \text{g cm}^{-3}$	1.558
μ / mm^{-1}	0.614
F(000)	1913
Temperature / K	120
Device type	STOE STADIVARI
Radiation	Mo-K α
Independent reflexes	$1.741 < \theta < 37.774$
Index ranges h	$21 < h < 21$
Index ranges k	$-25 < k < 29$
Index ranges l	$-30 < l < 31$
Reflections collected	71938
Independent reflections	32227
Completeness	0.747
Max. and min transmission	0.8556 and 0.7451
R_{int}	0.0178
R_{sigma}	0.0230
Data/restraints/parameters	32227 / 120 / 1331
Goodness-of-fit on F ²	1.020
$^a R_1 [I > 2\sigma(I)]$	0.0458
$^b wR_2 [I > 2\sigma(I)]$	0.1186
R_1 [all data]	0.0620
wR_2 [all data]	0.1285

Chapter 6: Helical dinuclear iron(II) complexes with 1,3,4-Oxa- and 1,3,4-Thiadiazole coordination units

Table S3: Hydrogen bonding interactions of the complex $[\text{Fe}_2(\text{L}^{\text{TDA-Hel}})_3](\text{ClO}_4)_4 \cdot 3 \text{H}_2\text{O}$ (**C1**).

Hydrogen Bond	Bond Length (Å)
O9 --- S5	3.099
O10 --- 17	3.060
N10 --- S3	3.274
N21 --- S2	3.133

Table S4: Measurement parameters for $[\text{Fe}(\text{H}_2\text{O})_2(\text{L}^{\text{ODA-Hel}})_2](\text{ClO}_4)$ (**C3**).

Parameter	Results
Empirical formula	C ₄₄ H ₃₄ Cl ₂ FeN ₁₄ O ₁₄
Formula weight g/mol	1109.60
Crystal size / mm	0.06 x 0.037x0.02
Crystal system	triclinic
Space group	P-1
Unit cell dimensions	
a / Å	8.3987 (7)
b / Å	11.6916(9)
c / Å	13.3494(11)
α / °	112.090(6)
β / °	105.929(7)
γ / °	91.311(7)
Volume / Å ³	1156.22(17)
Cell formula units	1
Density ρ _{calc} / g cm ⁻³	1.594
μ / mm ⁻¹	0.528
F(000)	568
Temperature / K	120
Device type	STOE IPDS 2T
Radiation	MoKα
Independent reflexes	2.548 < θ < 25.993
Index ranges h	-9 < h < 10
Index ranges k	-14 < k < 14
Index ranges l	-16 < l < 16
Reflections collected	8753
Independent reflections	4519
Completeness	0.993
Max. and min transmission	0.9718 and 0.7187
R _{int}	0.0895
R _{sigma}	0.1063
Data/restraints/parameters	4519 / 0 / 342
Goodness-of-fit on F ²	1.177
R ₁ [I > 2σ (I)]	0.1058
wR ₂ [I > 2σ (I)]	0.2051
R ₁ [all data]	0.1715
wR ₂ [all data]	0.2397

Table S5: Metal to ligand bond length for the complex $[\text{Fe}_2(\text{L}^{\text{TDA-Hel}})_3](\text{ClO}_4)_4 \cdot 3 \text{H}_2\text{O}$ (**C1**).

	Fe1-N (Å)		Fe2-N (Å)
Fe1-N3	1.992	Fe2-N18	1.986
Fe1-N2	1.926	Fe2-N17	1.931
Fe1-N14	1.928	Fe2-N5	1.932
Fe1-N8	1.925	Fe2-N12	1.999
Fe1-N9	1.988	Fe2-N11	1.926
Fe1-N15	1.985	Fe2-N6	1.990

Table S6: Metal to ligand bond length for the complex $[\text{Fe}_2(\text{L}^{\text{TDA-Hel}})_3](\text{BF}_4)_4 \cdot 5 \text{H}_2\text{O}$ (**C2**).

	Fe1-N (Å)		Fe2-N (Å)
Fe1-N14	1.921	Fe2-N18	1.981
Fe1-N1	2.003	Fe2-N12	1.983
Fe1-N13	1.975	Fe2-N17	1.930
Fe1-N2	1.931	Fe2-N6	1.986
Fe1-N8	1.936	Fe2-N5	1.927
Fe1-N7	1.978	Fe2-N11	1.925

Table S7: Metal to ligand bond length for the complex $[\text{Fe}(\text{H}_2\text{O})_2(\text{L}^{\text{ODA-Hel}})_2](\text{ClO}_4)$ (**C3**).

Fe-N	Fe-N (Å)
Fe-N1	2.212
Fe-N2	2.149
Fe-O3	2.086

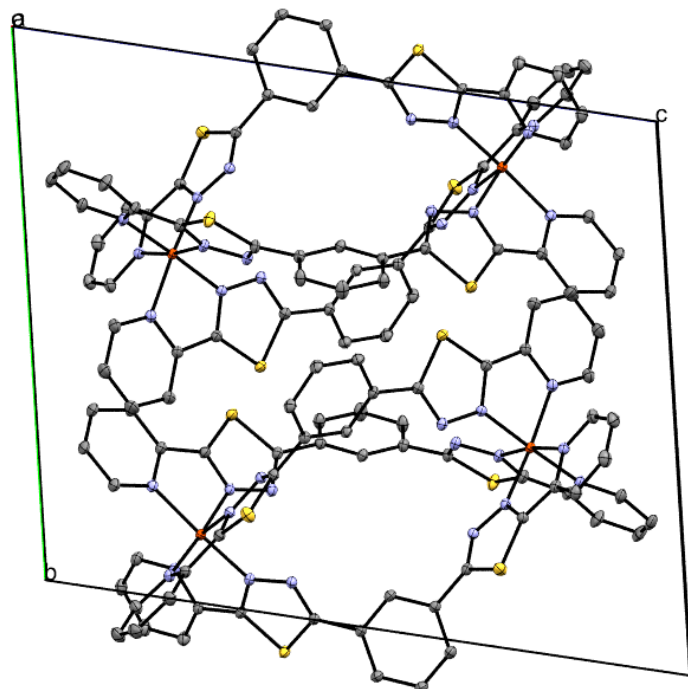


Figure S38: Aligned helical unites $[\text{Fe}_2(\text{L}^{\text{TDA-Hel}})_3]^{4+}$ with perspective on *bc* plane.

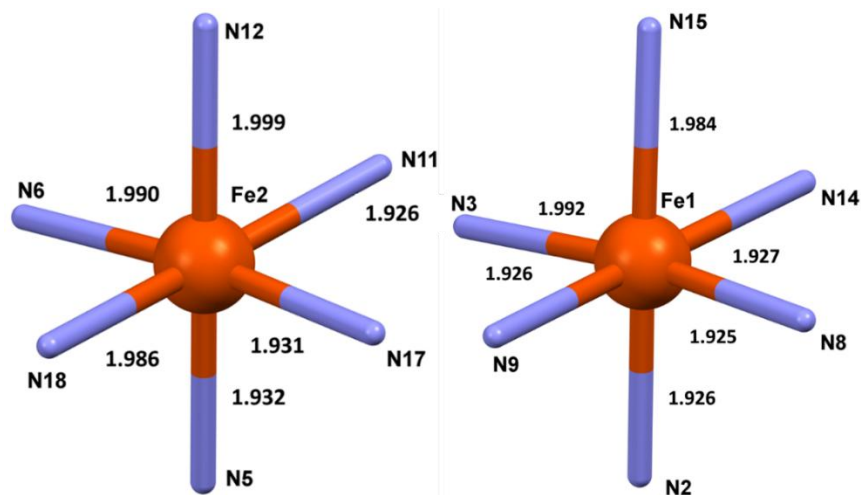


Figure S39: Representative bond length of the iron(II) contained in the helical unit for $[\text{Fe}_2(\text{L}^{\text{TDA-Hel}})_3](\text{ClO}_4)_4 \cdot 3 \text{H}_2\text{O}$ (**C1**).

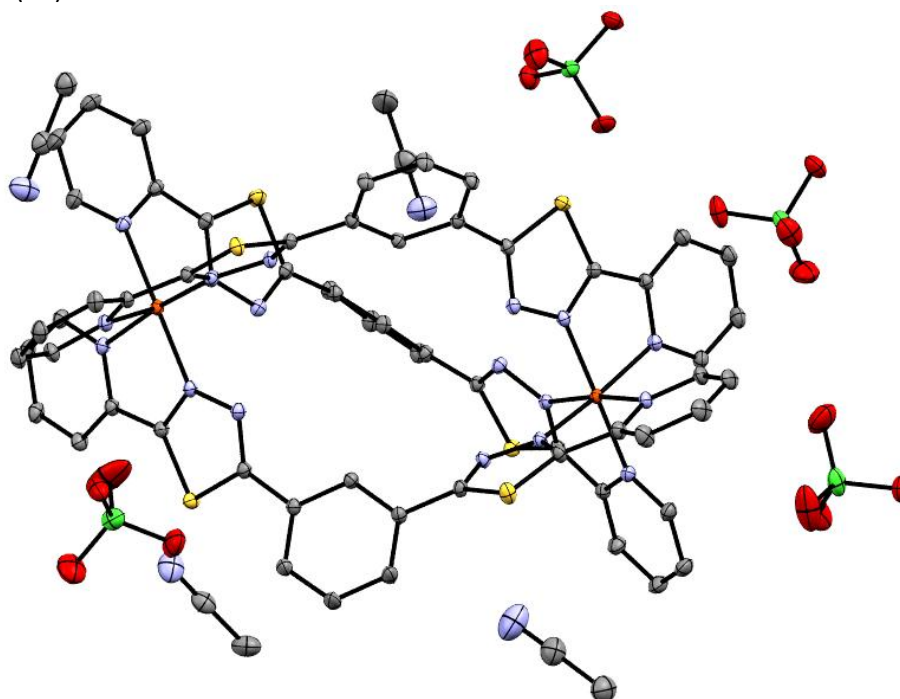


Figure S40: Molecular structure of $[\text{Fe}_2(\text{L}^{\text{TDA-Hel}})_3](\text{ClO}_4)_4 \cdot 4 \text{CH}_3\text{CN}$ (**C1**). Colours: carbon (grey), nitrogen (light blue) iron (orange), sulfur (yellow), chloride (green), oxygen (red) showing the hydrogen bonding interactions between the helical cations, the anions and the solvent molecules.

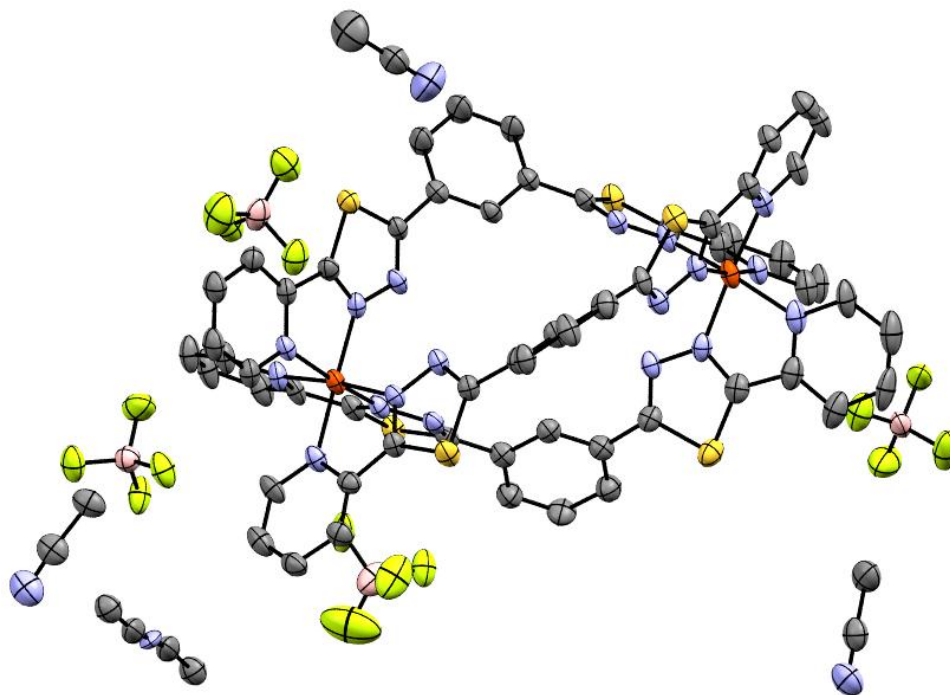


Figure S41: Molecular structure of $[\text{Fe}_2(\text{L}^{\text{TDA-Hel}})_3](\text{BF}_4)_4 \cdot 5 \text{H}_2\text{O}$ (**C2**). Colours: carbon (grey), nitrogen (light blue) iron (orange), sulphur (yellow), fluorine (light green), boron (light pink). The disordered solvent molecules and anions have been removed for clarity.

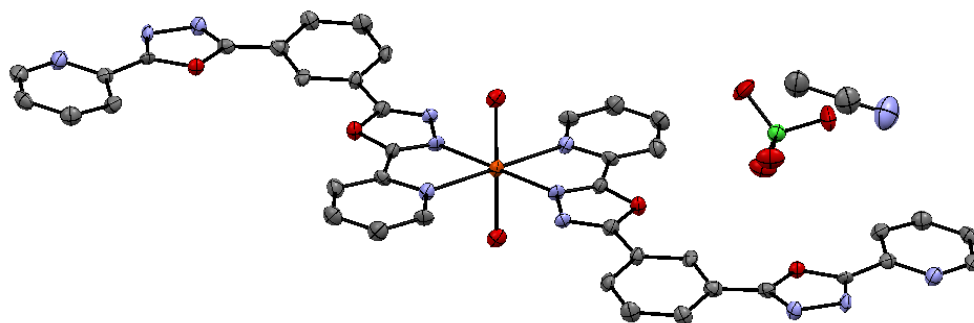


Figure S42: Molecular structure of $[\text{Fe}(\text{H}_2\text{O})_2(\text{L}^{\text{ODA-Hel}})_2](\text{ClO}_4)$ (**C3**). Colours: carbon (grey), nitrogen (light blue) iron (orange), sulphur (yellow), chlorine (green). The disordered solvent molecules and anions have been removed for clarity

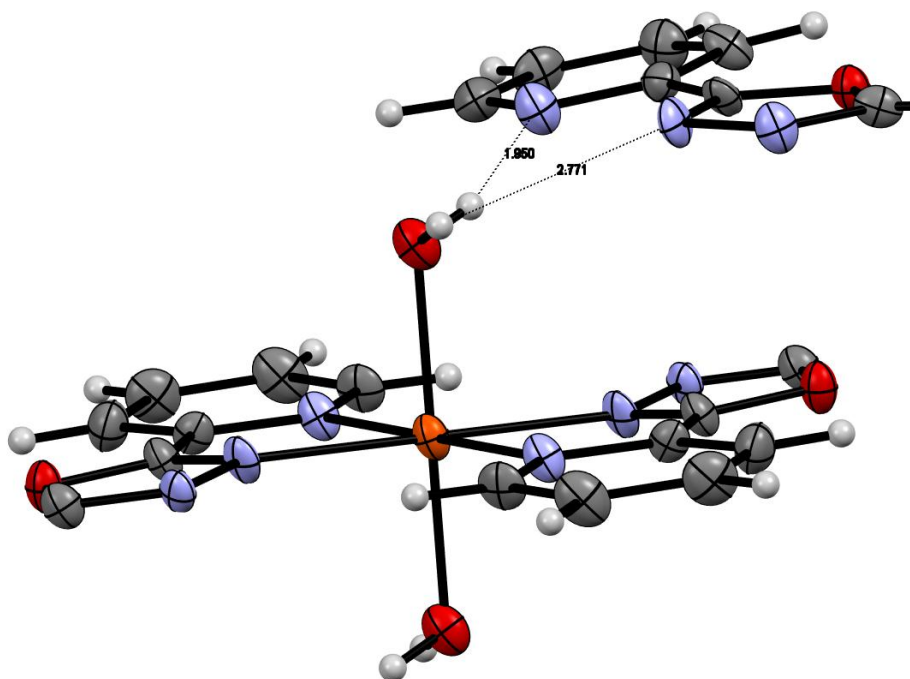


Figure S43: Hydrogen-interaction in the lattice of **C3** between axial coordinated aqua ligands and nitrogen of the thiadiazole.

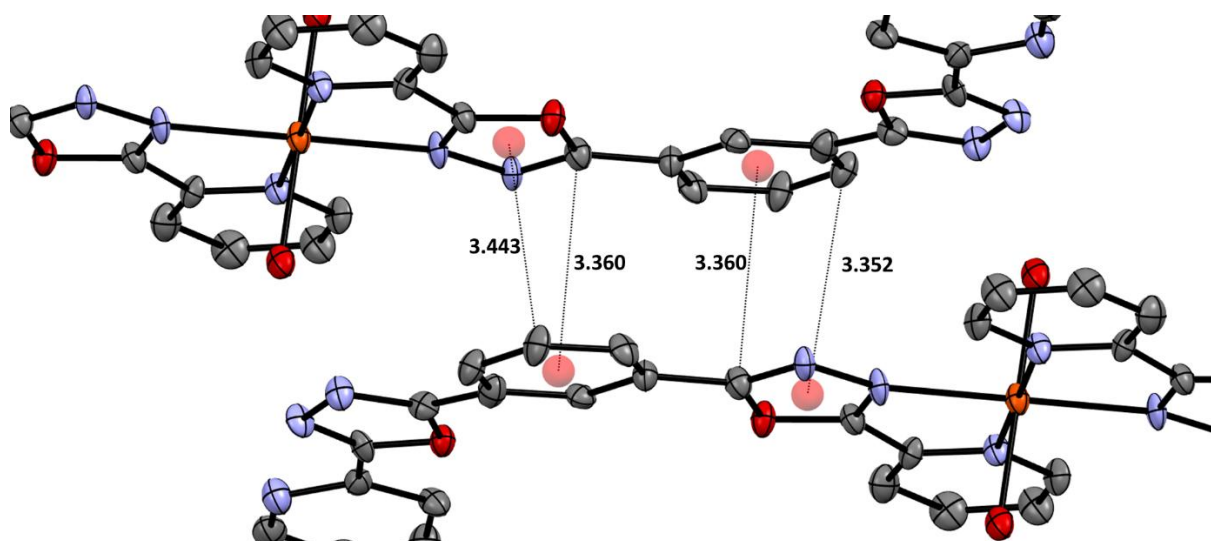


Figure S44: π - π -Interaction in the crystal lattice of complex **C3** between the isophthalic and oxadiazole units.

5. UV-Vis-Spectra:

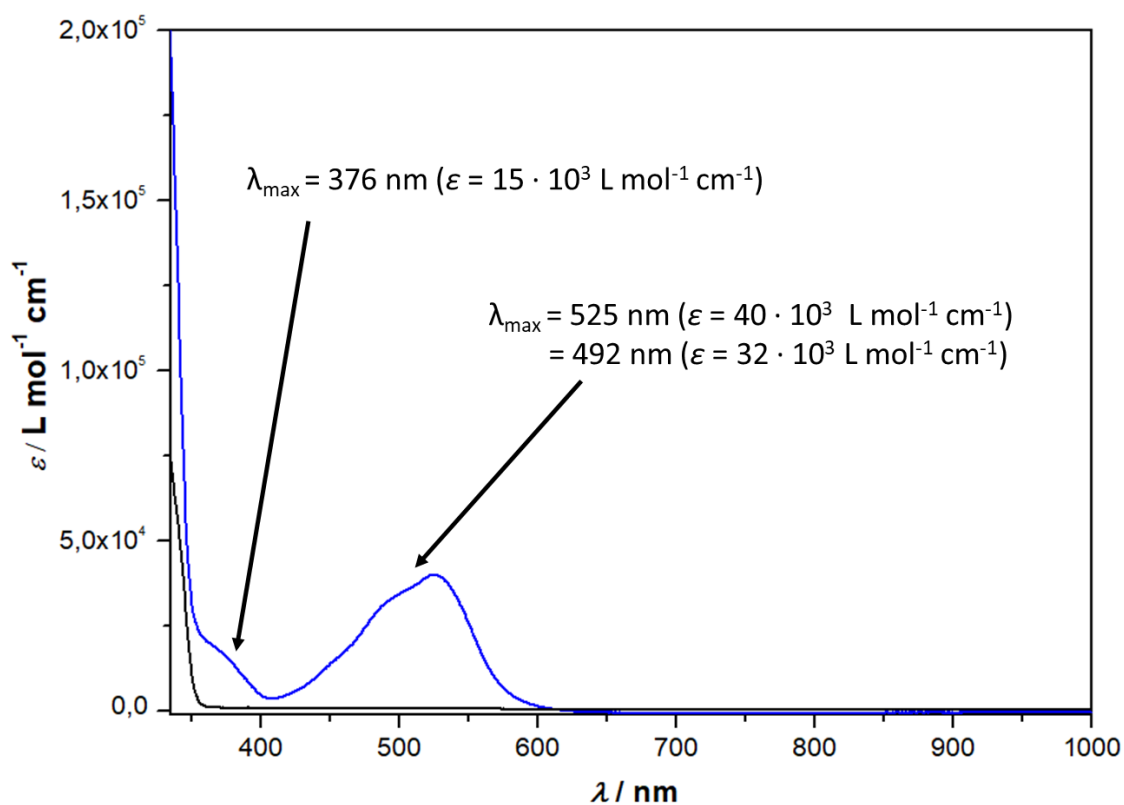


Figure S45: UV-Vis spectrum of $[\text{Fe}_2(\text{L}^{\text{TDA-Hel}})_3](\text{ClO}_4)_4 \cdot 3 \text{H}_2\text{O}$ (**C1**) (blue) with a concentration of $0.006 \text{ mol} \cdot \text{L}^{-1}$ in acetonitrile and of the Ligand $\text{L}^{\text{TDA-Hel}}$ (black) with a concentration of $0.025 \text{ mol} \cdot \text{L}^{-1}$. The Peak at 525.8 nm ($\epsilon = 40 \cdot 10^3 \text{ L} \cdot \text{mol}^{-1} \cdot \text{cm}^{-1}$) with a shoulder at 492.6 nm ($\epsilon = 32 \cdot 10^3 \text{ L} \cdot \text{mol}^{-1} \cdot \text{cm}^{-1}$) can be assigned to an LMCT.^[1] The Peak at 376.8 nm ($\epsilon = 15 \cdot 10^3 \text{ L} \cdot \text{mol}^{-1} \cdot \text{cm}^{-1}$) could be assigned to a MLCT-transition as it is known for Spin-Crossover complexes with pyridyl groups in the coordination pocket.^[2]

6. Cyclovoltammetry Data

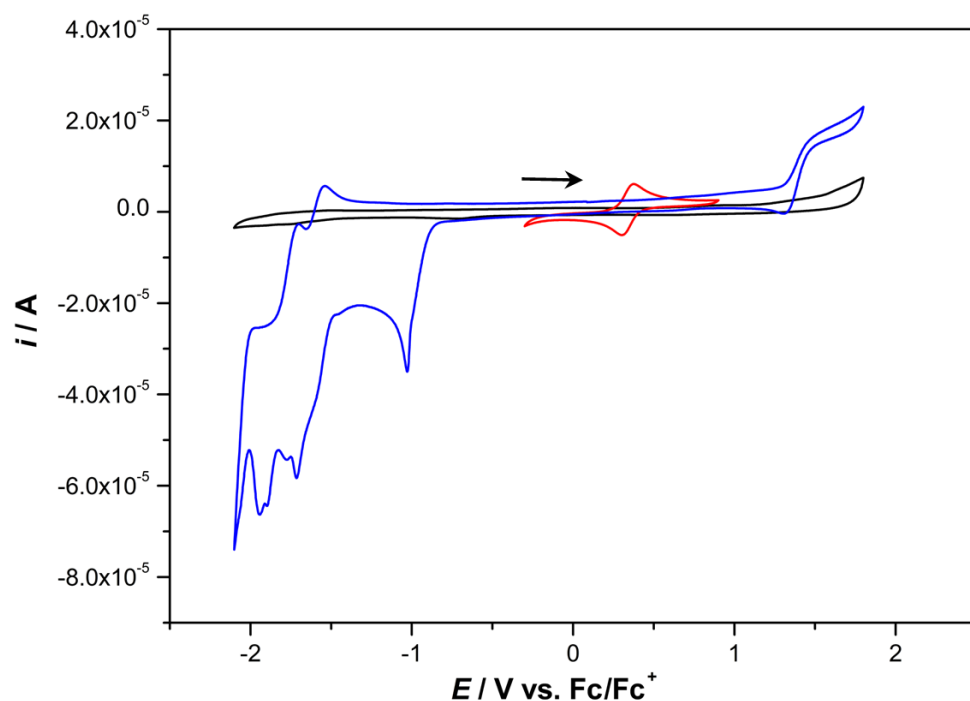


Figure S46: Cyclic voltammogram of $[\text{Fe}_2(\text{L}^{\text{TDA-Hel}})_3](\text{ClO}_4)_4 \cdot 3 \text{H}_2\text{O}$ (**C1**) in acetonitrile (10^{-3} M , $n\text{-Bu}_4\text{PF}_6$) at a scan rate of $100 \text{ mV}\cdot\text{s}^{-1}$ (blue), the blank (black) and the FcH/FcH^+ reference (red).

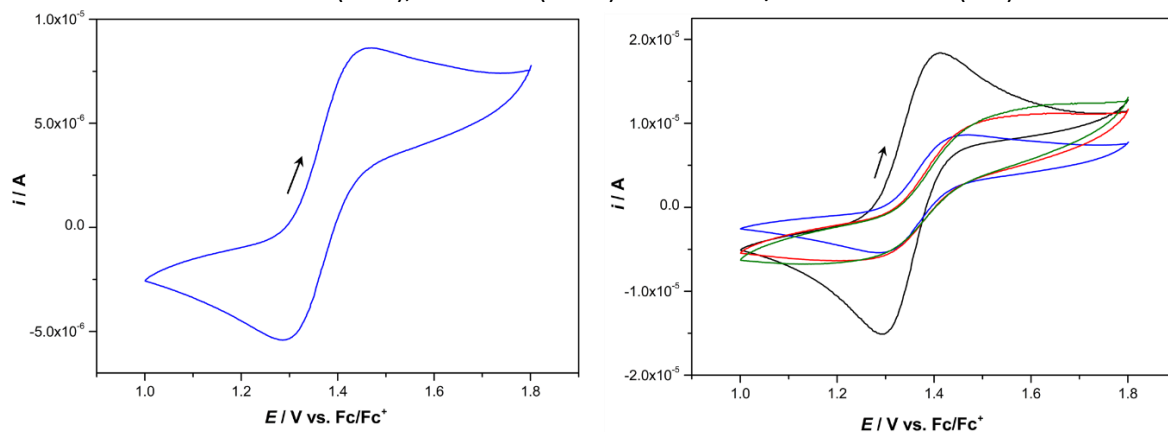


Figure S47: Cyclic voltammogram of $[\text{Fe}_2(\text{L}^{\text{TDA-Hel}})_3](\text{ClO}_4)_4 \cdot 3 \text{H}_2\text{O}$ (**C1**) in acetonitrile (10^{-3} M , $n\text{-Bu}_4\text{PF}_6$) at different scan rates ($50 \text{ mV}\cdot\text{s}^{-1}$ (blue), $100 \text{ mV}\cdot\text{s}^{-1}$ (black), $150 \text{ mV}\cdot\text{s}^{-1}$ (red) and $200 \text{ mV}\cdot\text{s}^{-1}$ (green)) of redox process (I/I') on the right and again at a scan rate of $50 \text{ mV}\cdot\text{s}^{-1}$ (blue) on the left.

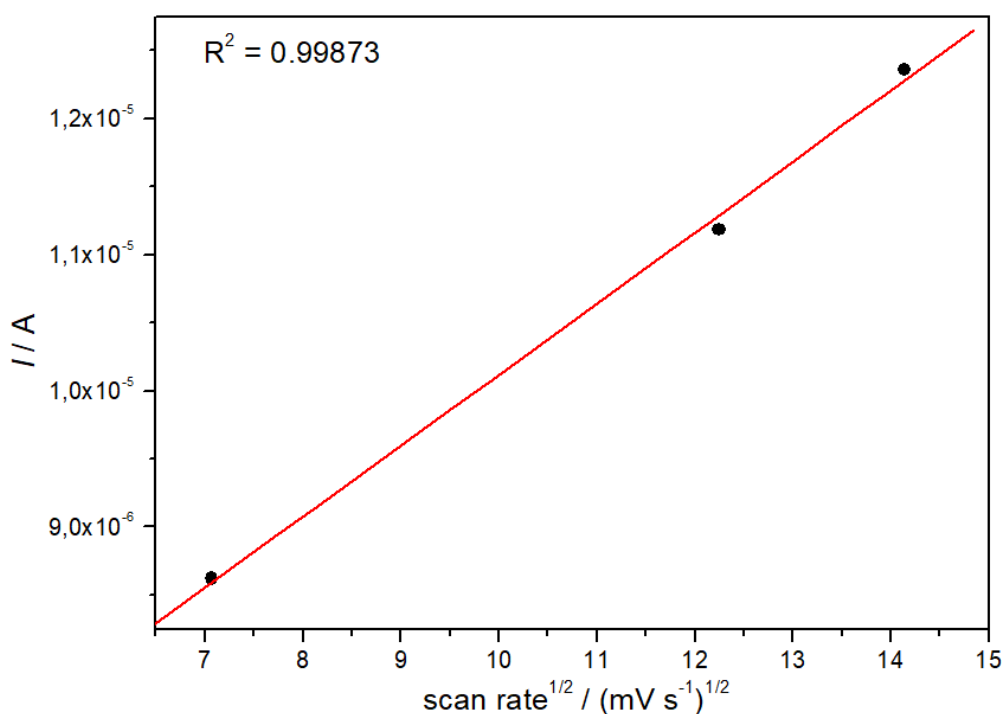


Figure S48: Linear plot of the current of the oxidation peaks versus the square root of the corresponding scan rate.

7. Magnetic Data:

Table S8: Calculated magnetic susceptibility at room temperature (293 K).

Complex	C1	C2
$M / \text{g} \cdot \text{mol}^{-1}$	1660.34	1710.91
χ_M^{20}	0	0

8. Molar Conductivity:

Table S9: Average molar conductivity Λ_m of the complexes **C1**, **C2** measured in acetonitrile.

Complex	C2	C1	C3
$M / \text{g} \cdot \text{mol}^{-1}$	1660.34	1710.91	1109.60
$\Lambda_m / \text{S} \cdot \text{cm}^2 \cdot \text{s}^{-1}$	360	419	321
$\Lambda_m / \text{S} \cdot \text{cm}^2 \cdot \text{s}^{-1}$ (after one hour)	376	443	321

The stability of the helical unit was investigated with molar conductivity, which was measured for both complexes $[\text{Fe}_2(\text{L}^{\text{TDA-Hel}})_3](\text{ClO}_4)_4 \cdot 3 \text{H}_2\text{O}$ (**C1**) and $[\text{Fe}_2(\text{L}^{\text{TDA-Hel}})_3](\text{BF}_4)_4 \cdot 5 \text{H}_2\text{O}$ (**C2**) in acetonitrile at room temperature and the measurements were repeated after one hour to ensure the stability of the complexes in solution. The molar conductivity for **C1** is slightly higher than expected for a 2:1 conductor with a value of 360 but still within an acceptable range. The standard range of molar conductivity for a 2:1 conductor is 220 – 300.^[3,4]

9. References:

- [1] Archer, R. J.; Scott, H. S.; Polson, M. I. J.; Williamson, B. E.; Mathonière, C.; Rouzières, M.; Clérac, R.; Kruger, P. E. *Dalton Trans.*, **2018**, 47 (24), 7965–7974.
- [2] Auböck, G.; Chergui, M. *Nat. Chem.* **2015**, 7 (8), 629–633.
- [3] Geary, W. J. *Coord. Chem. Rev.*, **1971**, 7 (1), 81–122.
- [4] Sundaresan, S.; Brooker, S. *Inorg. Chem.* **2023**, 62 (31), 12192–12202.

Summary and Perspectives

This work investigates the stepwise introduction of chirality into spin-crossover (SCO) complexes and the development of an ideal model system for studying SCO-chirality coupling. It was systematically probed how substitutions on the 1,3,4-chalcogendiazole heterocycle, the aryl backbone, NCE co-ligands (E = S, Se, BH₃), the solvent, the coordination mode, and chiral modifications in the ligand backbone affect SCO behavior.

We modulated the ligand field in the asymmetric mononuclear complex [Fe(L^{Ph-TDA})(NCE)₂] (E = S, Se, BH₃). The complex with co-ligand with E = Se remained high spin over the entire temperature range, whereas the E = BH₃ results in an abrupt spin crossover. Uniquely, for E = S, the complex crystallizes with two distinct iron(II) centers-forming two sublattices-unlike its isomorphous 1,3,4-oxadiazole analogues [Fe(L^{Ph-Py-ODA})(NCE)₂] (E = S, Se, BH₃). Upon cooling, one iron(II) center undergoes spin crossover, yielding a spin-state-ordered phase without a structural phase transition. Photoexcitation via the *LIESST* effect converts the mixed-spin [HS][LS] state partially into [HS][HS], but the reverse *LIESST* to [LS][LS] could not be achieved, likely due to the distorted geometry of the residual high-spin iron site. These findings were supported by single-crystal *XRD*, solid-state absorption spectroscopy, and temperature-dependent *Mössbauer* spectroscopy. In comparison to the oxadiazole analogue, the S-for-O substitution in the heterocycle produces a slight bite-angle change that shifts *T*_{1/2} from 166 K to 170 K. This influence of different heteroatoms in the core building block - the 1,3,4-chalcogendiazole - on the coordination geometry was further demonstrated through a helical approach. The smaller bite-angle results in comparison to literature known 1,2,4-triazole ligand based helical complex in locking the low spin state for both iron(II).

The 1,3,4-oxadiazole analogues, featuring two bidentate moieties, lead to a symmetric high-spin iron(II) complex. In contrast, the 1,3,4-thiadiazole ligand forms a solution-stable, helical dinuclear complex. This system was further analyzed for the intercalation of small guests, such as lithium cations, using ⁷Li-*NMR-DOSY* experiments. Remarkably, both in the solid state and in solution, this complex remains in the low-spin state across the entire measured temperature range.

The four-step ligand synthesis of L^{Ph-ODA} was streamlined to a two-step route for L^{Ph-TDA}, using glycine as the starting material. This allowed for the rapid introduction of chirality by substituting glycine with alanine. The resulting chiral complexes, [Fe(L^{Ph-TDA-(R/S)-Al})(NCBH₃)₂], and the racemic mixture [Fe(L^{Ph-TDA-(Rac)-Al})(NCBH₃)₂], adopt a facial coordination geometry-unlike the meridional, achiral complexes [Fe(L^{Ph-}

$\text{L}^{\text{TDA}}(\text{NCE})_2]$ ($\text{E} = \text{S}, \text{Se}, \text{BH}_3$). These complexes exhibit a known correlation between stereochemistry and packing behavior in the single crystal structure.

In the racemic complex, alternating R- Δ and S- Λ enantiomers create a robust network, resulting in a persistent high-spin state over the entire measured temperature range. Conversely, the enantiopure complex forms chains between solvent channels, allowing greater structural flexibility and defined cooperativity. This leads to an abrupt spin crossover at $T_{1/2} = 195 \text{ K}$, highlighting the significant impact of both methyl substitution (glycine to alanine) and the shift from meridional to facial geometry.

The chiral nature of the enantiopure complexes was confirmed via circular dichroism (CD) spectroscopy, while chiral HPLC was used for enantioselective ligand separation. Mössbauer spectroscopy was used to probe the electronic and structural environment of the iron(II) centers. Additionally, nuclear inelastic scattering (NIS) experiments, were performed on the complex to determine the $p\text{DOS}$ for the spin transition case.

The use of extended π -systems, such as naphthyl groups, serves as a powerful tool to enhance cooperativity. So we demonstrated this by substituting the phenyl group with a naphthyl group which on the 1,3,4-oxadiazole motive. These groups further improve system performance by coupling the temperature-dependent emission with the spin transition through energy transfer, as previously reported. We demonstrate this synergism by analyzing $[\text{Fe}(\text{L}^{\text{Naph-ODA}})(\text{NCBH}_3)_2]$ in both solid state and solution using Evans NMR, a robust method for studying spin crossover without interference from intermolecular interactions.

Synthesis via alanine-based routes introduced methyl groups stereoconservatively, with no racemization observed during ligand synthesis, as confirmed by chiral HPLC. In contrast to the 1,3,4-thiadiazole analog, the coordination geometry of $[\text{Fe}(\text{L}^{\text{Naph-ODA-Al}})(\text{NCBH}_3)_2]$ is meridional, resembling the achiral complex discussed above. A unique structure-property relationship emerged: the methyl group's point chirality induces similar packing across all complexes (R- and S-enantiomers and racemic mixtures), reflected in nearly identical temperature-dependent magnetization profiles from SQUID magnetometry. This positions the system as a model for studying chiral effects on circular dichroism (CD) in light-induced excited spin state trapping (LIESST) transitions without altering the transition temperature of the SCO.

The different coordination mode, observed for the substituted complexes $[\text{Fe}(\text{L}^{\text{Naph-ODA-Al}})(\text{NCBH}_3)_2]$ (meridional) and $[\text{Fe}(\text{L}^{\text{Ph-TDA-Al}})(\text{NCBH}_3)_2]$ (facial), was explored using $[\text{Fe}(\text{L}^{\text{Naph-TDA}})(\text{NCBH}_3)_2]$, which exhibits solvent-dependent polymorphism. Crystallization from DCM/MeOH yields the meridional isomer, while acetonitrile produces a facial complex with asymmetric hysteresis attributed to naphthyl group rotation. Strain within the coordination pocket drives isomerism, influenced not only by methyl

substitution (as in $[\text{Fe}(\text{L}^{\text{Ph-TDA-Al}})(\text{NCBH}_3)_2]$) but also by heteroatoms in 1,3,4-chalcogenadiazoles. For instance, $[\text{Fe}(\text{L}^{\text{Naph-ODA}})(\text{NCBH}_3)_2]$ adopts meridional geometry, whereas $[\text{Fe}(\text{L}^{\text{Naph-TDA}})(\text{NCBH}_3)_2]$ exhibits facial coordination. Expanding aryl groups from phenyl to naphthyl shifts isomerism from meridional to facial.

The geometry impact of the alkylic substituent on the mer-fac.isomerism and the spin crossover properties will be part of future studies for complex $[\text{Fe}(\text{L}^{\text{Naph-TDA-AS}})(\text{NCBH}_3)_2]$ (where AS denotes amino acid variants). If meridional geometry is retained, structure-property relationships of $[\text{Fe}(\text{L}^{\text{Naph-ODA-Al}})(\text{NCBH}_3)_2]$ are expected, enabling systematic investigations. Naphthyl group emission correlates with spin crossover (*SCO*); a similar effect should occur under *LIESST* conditions, with emission decreasing upon *LIESST* wavelength excitation. In ideal chiral systems with racemic mixtures, circularly polarized light may reduce *LIESST*-affected emission, detectable via cryo-*CD*-emission spectroscopy. To isolate polarization effects, enantiomers must share structural and *SCO* similarities to minimize packing (matrix) effects. These experiments will underpin research into *CD-LIESST* phenomena for multifunctional materials.

Improved synthesis protocols facilitate studies on chirality's role in *CD* effects and magnetism, leveraging affordable chiral building blocks like amino acids. Modifications with polyfunctional residues (e.g., lysine, aspartate, methionine) offer promising routes for linker-group incorporation and surface functionalization. This approach enables diverse experiments, including *NV*-magnetometry for domain dynamics under thermal/light stimuli and *CISS* effect measurements to probe spin-polarization switching via *SCO*-induced magnetic moment changes.



jensgeorgb@hotmail.com



0176 85986296



Kaiser-Wilhelm Ring 42
55118 Mainz



15.08.1994 in Lahnstein



Verheiratet

Schlüsselkompetenzen

Lösungsorientierung
Kreativität
Führungskompetenz
Kommunikation

Programmkenntnisse

Python
OriginLab
Blender

Sprachkenntnisse

Deutsch - Muttersprache
Englisch - B2 - C1

Curriculum Vitae

Jens-Georg Becker

Arbeitserfahrung

April 2022 - heute: Doktorand im Fach Chemie, Johannes Gutenberg-Universität Mainz, Arbeitsgruppe Prof. Dr. Rentschler:

- **Thema der Dissertation:** *Synthese und Untersuchung von chiralen Spin-Crossover-Komplexen auf Basis von 1,3,4-Chalkogendiazol-Liganden*

April 2021 - März 2022: Wissenschaftlicher Mitarbeiter, Max-Planck-Institut für Polymerforschung, Arbeitsgruppe Prof. Dr. Weber:

- Synthese und Untersuchung von Blei-Iodid-basierten Solarzellen durch Spin-Coating

Juli 2019 - November 2019: Wissenschaftliche Hilfskraft, Johannes Gutenberg-Universität Mainz

- Betreuung des Lehrpraktikums „*Chemische Grundlagen für Mediziner*“

Oktober 2016 - April 2021: Tutor: *Einführung in die Übergangsmetallchemie* im Fachbereich Chemie, Johannes Gutenberg-Universität Mainz

- Erstellung von Übungsblättern und Unterrichten von Lehrinhalten

Ausbildung

Oktober 2018 - September 2021: Master of Science Chemie, Johannes Gutenberg-Universität Mainz, (Gesamtnote: 1,0)

- **Masterarbeit:** *Synthese von radikaldekorierten Metallakronen* (Note: 1.1)
- **Stipendiat des Deutschlandstipendiums (2019)**

Oktober 2014 - Juli 2018: Bachelor of Science Chemie, Johannes Gutenberg-Universität Mainz, (Gesamtnote: 1,6)

- **Bachelorarbeit:** *Synthese von Metallakronen auf Basis von 2-Mercaptosalicylhydrazid* (Note: 1,0)

Allgemeine Hochschulreife (Abitur), Georg-Büchner-Gymnasium, Köln, (Gesamtnote: 2,7)

- **Berufsbildendes Praktikum** in der analytischen Abteilung der Quarzwerke GmbH

Workshops

- 2025:** "Projektmanagement and Teamleitung"
2024: "Entrepreneurship and Startups"
2024: "Blender für Beginner"
2023: "Good Scientific Practice"
2022: "Einführung in die Kristallographie zur Strukturbestimmung"
2022: "Programming in Python"
2022: "Grundlagen erfolgreicher Posterpräsentation"
2022: Erste-Hilfe-Kurs
2022: "Theoretical description of magnetic molecules on magnetic surfaces"
-

Publikationen

- 1. J.-G. Becker**, S. Sundaresan, Luca. M. Carrella, E. Rentschler *Chem. Commun.* **2025**, *61*, 13389-13392. DOI: <https://doi.org/10.1039/D5CC03779D>
 - Inside Front Cover: *Chem. Commun.* **2025**, *61*, 13210-13210.
 - 3. J.-G. Becker**, J. F. Nüsing, S. Sundaresan, R. Diego, M. Mondeshki, L. M. Carrella, E. Rentschler *Cryst. Growth Des.* **2024**, *24*, 7662-7669. DOI: <https://doi.org/10.1039/D3DT02420B>
 - S. Sundaresan, **J.-G. Becker**, J. Eppelsheimer, A. E. Sedykh, L. M. Carrella, K. Müller-Buschbaum, E. Rentschler *Dalton Trans.* **2023**, *52*, 13181-13189. DOI: <https://doi.org/10.1039/D3DT02420B>
-

Konferenzen und Beiträge

- 2024:** Mainzer Magnetic Moments, Mainz (Design des Programmhefts)
2024: Ligandendesign Workshop, Köln (Vortrag)
2024: 18. Koordinationschemiker-Treffen, Innsbruck (Vortrag)
2023: Gordon Research Conference on *Electron Spin Interactions with Chiral Molecules and Materials Conference*, Manchester, New Hampshire (Vortrag)
2022: 17. Koordinationschemiker-Treffen, Jena (Poster)
2017: 19. JungChemikerForum der Gesellschaft Deutscher Chemiker (GDCh), Mainz (Unterstützer)
-

Interessen und Hobbies

- Seit 2019:** Bouldering, Toprope- und Vorstiegsklettern (Mitglied im DAV)
2019 - 2023: Passives Mitglied, GDCh (Gesellschaft Deutscher Chemiker)
2017 - 2021: Mitglied Fachschaftsrat Fachbereich 09
2013 - 2014: Interkultureller Auseinandersetzung in Ostafrika
2010 - 2012: Standard-Paartanz
2005 - 2013: Basketball
2003 - 2013: Sankt Georg Pfadfinder
2002 - 2012: Ballett

Weitere:

- Wandern in Europa, Afrika und Asien
- Brettspiele

Nutzung von *KI*-Tools

<i>KI</i>-Tool	Genutzt für:	Warum?	Wann?
Chat GPT	Sprachliche Korrektur	Bessere Lesbarkeit	Während der Formulierung der Arbeit
Perplexity	Sprachliche Korrektur	Bessere Lesbarkeit	Während der Formulierung der Arbeit
